frontiers | Research Topics

Risk assessment and management of water conservancy projects

Edited by
Wei Ge, Pieter Van Gelder, Zongkun Li and Xihui Gu

Published in
Frontiers in Earth Science

ISSN 1664-8714
ISBN 978-2-8325-4160-9
DOI 10.3389/978-2-8325-4160-9

About Frontiers

Frontiers is more than just an open access publisher of scholarly articles: it is a pioneering approach to the world of academia, radically improving the way scholarly research is managed. The grand vision of Frontiers is a world where all people have an equal opportunity to seek, share and generate knowledge. Frontiers provides immediate and permanent online open access to all its publications, but this alone is not enough to realize our grand goals.

Frontiers journal series

The Frontiers journal series is a multi-tier and interdisciplinary set of open-access, online journals, promising a paradigm shift from the current review, selection and dissemination processes in academic publishing. All Frontiers journals are driven by researchers for researchers; therefore, they constitute a service to the scholarly community. At the same time, the *Frontiers journal series* operates on a revolutionary invention, the tiered publishing system, initially addressing specific communities of scholars, and gradually climbing up to broader public understanding, thus serving the interests of the lay society, too.

Dedication to quality

Each Frontiers article is a landmark of the highest quality, thanks to genuinely collaborative interactions between authors and review editors, who include some of the world's best academicians. Research must be certified by peers before entering a stream of knowledge that may eventually reach the public - and shape society; therefore, Frontiers only applies the most rigorous and unbiased reviews. Frontiers revolutionizes research publishing by freely delivering the most outstanding research, evaluated with no bias from both the academic and social point of view. By applying the most advanced information technologies, Frontiers is catapulting scholarly publishing into a new generation.

What are Frontiers Research Topics?

Frontiers Research Topics are very popular trademarks of the *Frontiers journals series*: they are collections of at least ten articles, all centered on a particular subject. With their unique mix of varied contributions from Original Research to Review Articles, Frontiers Research Topics unify the most influential researchers, the latest key findings and historical advances in a hot research area.

Find out more on how to host your own Frontiers Research Topic or contribute to one as an author by contacting the Frontiers editorial office: frontiersin.org/about/contact

Risk assessment and management of water conservancy projects

Topic editors

Wei Ge — Zhengzhou University, China

Pieter Van Gelder — Delft University of Technology, Netherlands

Zongkun Li — Zhengzhou University, China

Xihui Gu — China University of Geosciences Wuhan, China

Citation

Ge, W., Van Gelder, P., Li, Z., Gu, X., eds. (2023). *Risk assessment and management of water conservancy projects*. Lausanne: Frontiers Media SA.

doi: 10.3389/978-2-8325-4160-9

Table of contents

frontiers | Frontiers in Earth Science

TYPE Editorial
PUBLISHED 05 December 2023
DOI 10.3389/feart.2023.1330621

OPEN ACCESS

EDITED AND REVIEWED BY
Wouter Buytaert,
Imperial College London,
United Kingdom

*CORRESPONDENCE
Wei Ge,
gewei@zzu.edu.cn

RECEIVED 31 October 2023
ACCEPTED 21 November 2023
PUBLISHED 05 December 2023

CITATION
Ge W (2023), Editorial: Risk assessment and management of water conservancy projects.
Front. Earth Sci. 11:1330621.
doi: 10.3389/feart.2023.1330621

Editorial: Risk assessment and management of water conservancy projects

Wei Ge*

School of Water Conservancy and Transportation, Zhengzhou University, Zhengzhou, China

KEYWORDS

water resources allocation, flood risk control, hydraulic structural safety, risk criteria for reservoir dams, comprehensive risk management

Editorial on the Research Topic
Risk assessment and management of water conservancy projects

Water conservancy projects refer to various types of artificially constructed projects that promote water benefits and eliminate water hazards, mainly including dams, dikes, hydropower stations, channels, water gates, and so on. Water conservancy projects play extremely important roles in flood control (Ge et al., 2022), power generation, irrigation, water supply and shipping, and in promoting social and economic development and reducing carbon emissions. The construction, operation and decommissioning of water conservancy projects all have huge impacts on society and the environment (Zhang et al., 2022). In addition, due to the natural and human factors, such as super standard flood (Wu et al., 2021; Liu et al., 2022), natural aging (Zhang et al., 2023a), earthquake and improper management caused by extreme meteorological conditions, water conservancy projects are always faced with the risk of failure. The effective quantification of the water conservancy project risks and proposing corresponding management and control measures have always been a concern of researchers (Wang et al., 2023).

Experiments, theories and numerical methodologies are essential for quantitative characterization of water conservancy project risks. Hence, this Research Topic concentrates on the contributions regarding novel methodologies and applications to characterize the water conservancy project risk levels aiming at targeted management and control measures. After peer review, fifteen research articles were accepted and published, which can be helpful for improving the development of risk assessment methods, promoting the cross and integration of different subjects.

The main contributions of this Research Topic are mainly reflected in five aspects:

- Coordinated allocation and management of water resources

Taking the minimum relative water shortage rate as the objective function, an optimal allocation model (Chai et al.) of water resources was established, which solved the coordinated allocation of water resources between conventional and unconventional water resources. In addition, from the perspective of social welfare and water quality utility, a comprehensive optimization and coordination decision model (Jiao et al.) for water transfer was proposed, in which the cost-sharing contract was designed, and the Stackelberg game method was used to optimize the decision-making and coordination of the water supply chain, providing valuable references for water transfer decision-making.

- Flood risk control of reservoir dams

In view of the possible flood risk and catastrophic consequences caused by high dam failures induced by early impoundment, a multi-objective decision model which considers the failure probability, life loss, and early impoundment revenues brought by earlier power generation was proposed to acquire the satisfied initial impoundment scheme (Liu et al.). Based on the analysis of the uncertainty of flood volume and peak, a general risk analysis framework that integrates the Monte Carlo sampling method and the most likely event selection method was proposed to calculate the risk of operating a single reservoir (Du et al.).

- Analysis of hydraulic structural safety

Combined with indoor geotechnical tests, cloud theory was used to describe the distribution types of soil shear strength indicators, and a cloud model-Monte Carlo coupling method was proposed to analyze the stability of dam slopes (Han et al.). Furthermore, considering the effect of wetting deformation of coarse-grained materials on the safety of earth- dams during initial water storage, the P-Z (Pastor-Zienkiewicz) wetting model was established based on the P-Z model in the elastic-plastic theory and the wetting model formula. And then the BP (Back propagation) artificial neural network was introduced to establish the artificial neural network wetting deformation prediction model (Zhang et al.) based on the P-Z model. Finally, a novel prediction model, Levy flight-based grey wolf optimizer optimized support vector regression (LGWO-SVR) (He and Wu), was proposed to forecast the displacements of hydropower dams.

- Risk criteria for reservoir dams

Drawing on research ideas of ecological economics on ecosystem service values and equivalent factor methods, environmental values and effectively connected environmental criteria with existing standards were quantified using the ALARP (As low as reasonably practicable) principle and the F-N (Accumulated frequency—Number of fatalities) curve. Considering the differences in environmental and economic conditions in different regions, a risk preference matrix was established to determine the risk preference of each region and formulate the dam failure environmental risk criteria (Li et al.) for China, which presents a preliminary exploration of the formulation of dam failure environmental risk standards.

- Comprehensive risk management of water conservancy projects

A new model, which is based on the Shapley Value and the Utility Theory, was proposed to solve the risk sharing (Liu et al.) in quasi-public-welfare water conservancy public-private-participation (PPP) projects, encompassing a comprehensive analysis of multiple factors, such as the proportion of capital contribution, bargaining position, risk management capabilities, and risk-taking willingness of heterogeneous subjects. In addition, complex network theory and network immune strategies were used to identify relevant risks in urban river ecological governance projects (Xu et al.) and develop the corresponding risk response strategies, in which network global efficiency was set as a metric to assess the network's robustness under random and targeted attacks. The results revealed that the degree value attack immune strategy performed optimally under targeted attack scenarios.

Author contributions

WG: Writing–original draft, Writing–review and editing.

Funding

The author(s) declare financial support was received for the research, authorship, and/or publication of this article. This research was funded by the National Natural Science Foundation of China (Grant Nos 52079127, 52179144, U2243244, and U2040224), the Natural Science Foundation of Henan Province (Grant No. 232300421067), and the Program for Science and Technology Innovation Talents in Universities of Henan Province (HASTIT) (Grant No. 22HASTIT011).

Conflict of interest

The author declares that the research was conducted in the absence of any commercial or financial relationships that could be construed as a potential conflict of interest.

Publisher's note

References

Ge, W., Jiao, Y., Wu, M., Li, Z., Wang, T., Li, W., et al. (2022). Estimating loss of life caused by dam breaches based on the simulation of floods routing and evacuation potential of population at risk. *J. Hydrol.* 612, 128059. doi:10.1016/j.jhydrol.2022.128059

Liu, J., Feng, S., Gu, X., Zhang, Y., Beck, H. E., Zhang, J., et al. (2022). Global changes in floods and their drivers. *J. Hydrol.* 614, 128553. doi:10.1016/j.jhydrol.2022.128553

Wang, T., Li, Z., Ge, W., Zhang, H., Zhang, Y., Sun, H., et al. (2023). Risk consequence assessment of dam breach in cascade reservoirs considering risk transmission and superposition. *Energy* 265, 126315. doi:10.1016/j.energy.2022.126315

Wu, M., Wu, Z., Ge, W., Wang, H., Shen, Y., and Jiang, M. (2021). Identification of sensitivity indicators of urban rainstorm flood disasters: a case study in China. *J. Hydrol.* 599, 126393. doi:10.1016/j.jhydrol.2021.126393

Zhang, H., Ge, W., Zhang, Y., Li, Z., Li, W., Zhu, J., et al. (2023a). Risk management decision of reservoir dams based on the improved life quality index. *Water Resour. Manag.* 37, 1223–1239. doi:10.1007/s11269-023-03426-y

Zhang, Y., Li, Z., Wang, J., Ge, W., and Chen, X. (2022). Environmental impact assessment of dam-break floods considering multiple influencing factors. *Sci. Total Environ.* 837, 155853. doi:10.1016/j.scitotenv.2022.155853

frontiers | Frontiers in Earth Science

TYPE Original Research
PUBLISHED 19 January 2023
DOI 10.3389/feart.2023.1122937

OPEN ACCESS

EDITED BY
Wei Ge,
Zhengzhou University, China

REVIEWED BY
Zhen Wang,
Nanjing University of Science and Technology, China
Jie Li,
Army Engineering University of PLA, China

*CORRESPONDENCE
Peng He,
hepeng@ncwu.edu.cn

SPECIALTY SECTION
This article was submitted to Hydrosphere, a section of the journal Frontiers in Earth Science

RECEIVED 13 December 2022
ACCEPTED 03 January 2023
PUBLISHED 19 January 2023

CITATION
He P and Wu W (2023), Levy flight-improved grey wolf optimizer algorithm-based support vector regression model for dam deformation prediction.
Front. Earth Sci. 11:1122937.
doi: 10.3389/feart.2023.1122937

Levy flight-improved grey wolf optimizer algorithm-based support vector regression model for dam deformation prediction

Peng He[1]* and Wenjing Wu[2]

[1]College of Geosciences and Engineering, North China University of Water Resources and Electric Power, Zhengzhou, China, [2]School of Mechatronics Engineering, Zhongyuan University of Technology, Zhengzhou, China

Considering the strong non-linear time-varying behavior of dam deformation, a novel prediction model, called Levy flight-based grey wolf optimizer optimized support vector regression (LGWO-SVR), is proposed to forecast the displacements of hydropower dams. In the proposed model, the support vector regression is used to create the prediction model, whereas the Levy flight-based grey wolf optimizer algorithm is employed to search the penalty and kernel parameters for SVR. In this work, a multiple-arch dam was selected as a case study. To validate the proposed model, the predicted results of the model are compared with those derived from Grid Search algorithm, Particle Swarm Optimization, Grey Wolf Optimizer algorithm, and Genetic algorithm. The results indicate that the LGWO-SVR model performs well in the accuracy, stability, and rate of prediction. Therefore, LGWO-SVR model is suitable for dam engineering application.

KEYWORDS

dam deformation, support vector regression, grey wolf optimizer algorithm, levy flight, machine learning

Introduction

The safety of hyperpower dams has always been a widely-concerned issue of every country. To ensure the security of dam, dam safety monitoring model is built for monitoring the actual operation state of the dams (Li et al., 2021; Ge et al., 2020) . The deformation of a dam is commonly used to reflect the working condition during the operation period (Bui et al., 2016). Considering the non-linear and complex process of the deformation, it is difficult to forecast the dam behavior with high accuracy (Chen et al., 2018).

In recent years, various machine learning methods, such as artificial neural network, support vector machine, and random forest method, have been applied to establish the prediction models of dam deformation (Salazar F et al., 2017). The most widely used method is artificial neural networks (ANNs). However, an artificial neural network is more likely to fall into the situation that the trained ANN over-fits training samples, which reduces the accuracy of predicted dam deformation.

Support vector regression (SVR) has always been a hotspot in civil engineering to solve regression prediction (Su et al., 2015). SVR has distinctive superiority in solving non-linear problems with few samples and high dimensions. The prediction accuracy of SVR is influenced by the values of the penalty and kernel parameters in SVR. Therefore, a number of swarm intelligence algorithms were presented to optimize the parameters, including the Grid Search algorithm (GS), Particle Swarm Optimization algorithm (PSO), Cuckoo Search algorithm (CS), Genetic Algorithm (GA), *etc.* Su et al. (2018) employed the Particle Optimization algorithm (PSO) to seek the best parameter set

for SVR in predicting dam deformation. Ranković et al. (2014) proposed an SVR-based model for forecasting the dam deformation. In Rankovic's model, the parameters of SVR are specified with the trial-and-error method. Shu et al (2021) proposed a variational autoencoder-based model for dam displacement prediction. Li et al (2019) proposed a novel distributed time series evolution model for predicting the dam deformation. Meng et al. (2018) combined the Ant Colony Optimization algorithm (ACO) with SVR to forecast the price of stock. Kaltich et al. (2015) presented a wavelet genetic algorithm-support vector regression (GA-SVR) to forecast monthly river flows. Xue et al. (2018) proposed the Artificial Bee Colony algorithm (ABC) for global optimization to obtain the optimal solutions of several benchmark functions. In conclusion, the possible optimal solution can be obtained through these algorithms, but these algorithms are more likely to fall into the local optimal solutions and their convergence rates are very slow. Considering the lower speed and precision of these algorithms, a novel type of swarm intelligence algorithm called the Grey Wolf Optimizer (GWO) algorithm is introduced in this paper.

The Grey Wolf Optimizer algorithm has received much attention and been widely used in many fields such as optimal reactive power scheduling, multiple input and output problems, and truss structures with motive power restrict (Faris H et al., 2017). The GWO algorithm is easy to implement and has fewer control parameters. Numerical comparisons showed that the GWO algorithm could present a higher performance than other swarm intelligence algorithms (Zhang and Zhou, 2015). The search scope become more and more smaller with the increase of iterations in the GWO algorithm, which increase the possibility of falling into a local optimum. To expand the scope of the search, the Levy flight is combined with the GWO algorithm to optimize the parameters. The Levy flight is a random process that is inspired by the Levy distribution (Viswanathan et al., 1996). Application of the Levy flight can result in a more effective search because of the use of the long jumps. The Levy flight can reduce the possibility of falling into a local optimum, taking into account the short-range exploratory hopping and occasional long-distance walking simultaneously.

In this paper, the Levy flight-based Grey Wolf Optimizer (LGWO) algorithm is presented to optimize support vector regression model for forecasting dam deformation. Historical data of the water pressure, temperature, and time-varying effect values of a dam are taken as input variables and the model is constructed to forecast the deformation. To validate the performance of the LGWO algorithm, a comprehensive comparison is carried out among the prediction capability of some other swarm intelligence algorithms.

The rest of the paper is organized as follows: Section 2 presents a brief introduction to the Levy flight-based Grey Wolf Optimizer algorithm and the Support Vector Regression model, describes the framework of the LGWO-SVR model, and presents the criteria of prediction performance. Section 3 presents a description of a case study, the calculation of the input effects, and the initial parameters of each algorithm. The comprehensive comparison among those swarm intelligence algorithms and the prediction results of the LGWO-SVR model are also showed in Section 3. Finally, the conclusion for the current work is given in Section 4.

LGWO-SVR model

There are many factors affecting dam deformation, such as water pressure, seepage coupling, joint fissure, concrete temperature, etc (Wei et al., 2019). Limited by current monitoring technology and analysis theory, the prediction for dam deformation is complex. It is generally accepted that the displacements are composed of water pressure component, temperature component, and time-varying component. The relationships between these components and their relevant factors are non-linear. For example, water pressure component is the polynomials of the water depth. The prediction of dam deformation is a non-linear problem with high dimensions. As mentioned above, the SVR has distinctive superiority in solving non-linear problems with few samples and high dimensions. Therefore, it is suitable for the SVR to construct a prediction model.

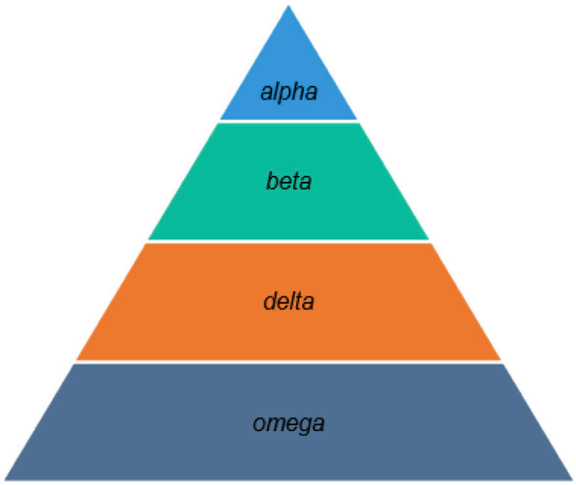

FIGURE 1
Social hierarchy of grey wolves (dominance decreases from top to bottom).

Support vector regression

The support vector regression (SVR) is data-based prediction model improved by the support vector classification. The basic idea of SVR is to find an optimal classification surface to minimize the error of all training samples from the optimal classification surface (Li et al., 2018). Suppose that there is a training sample set $\{(x_i; y_i)\}(i = 1,2, \ldots; n)$. x_i denotes the input variable vector of the i th training sample, y_i ($y_i \in R$) represents the corresponding output value, and n is the number of sample points.

The goal of SVR is to find a function relationship $f(x)$ between the input vector x_i and the output vector y_i under the premise that the relationship between input and output variables is unknown. The function can be expressed as a linear relationship as follows:

$$f(x) = w\phi(x) + b \tag{1}$$

where w represents the weight coefficient matrix, b represents the value of offsets, and $\phi(x)$ is a non-linear mapping function which is used to transform the complex non-linear problem in to a simple linear problem.

Based on the principle of structural risk minimization, the function $f(x)$ should loosely fit training data and avoid over-fitting problem by minimizing the norm of w (i.e., $\|w\|$). To cope with infeasible constrains, two slack variables ξ_i and ξ_i^* are introduced.

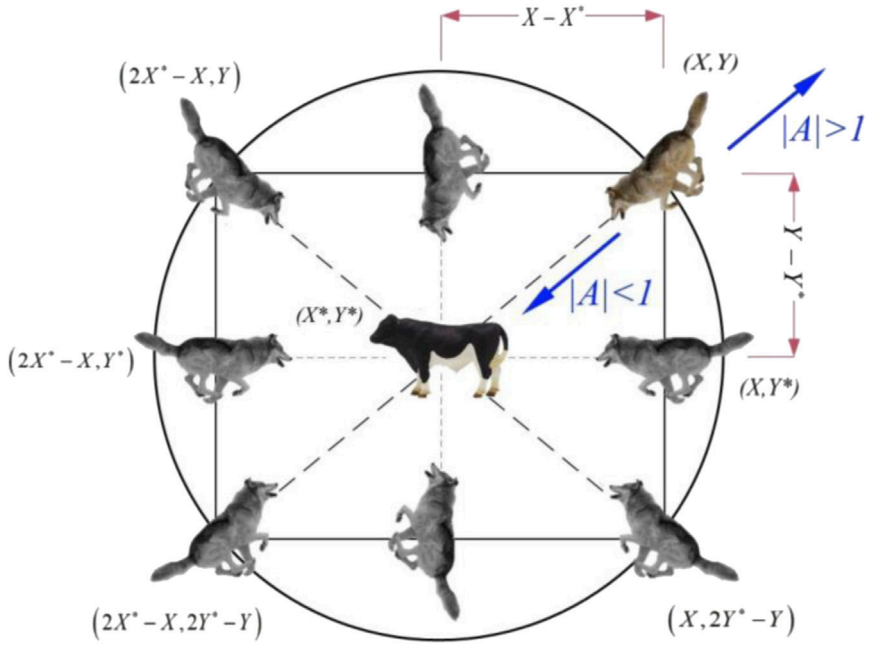

FIGURE 2
Position vectors and the possible next locations of a grey wolf.

Then the seeking process of minimizing w can be converted to solving the convex optimization problem:

$$\begin{cases} \min \frac{1}{2}\|w\|^2 + C\sum_{i=1}^{m}(\xi_i + \xi_i^*) \\ s.t. \begin{cases} y_i - w\phi(x) - b \le \varepsilon + \xi_i \\ -y_i + w\phi(x) + b \le \varepsilon + \xi_i^*, i = 1, 2, \cdots m \\ \xi_i \ge 0, \xi_i^* \ge 0 \end{cases} \end{cases} \tag{2}$$

where ε is the insensitive loss function which represents the error requirements for the regression function, and $C\,(C > 0)$ is the penalty factor. A larger C indicates that a larger penalty will be exerted on the samples when the training error is bigger than ε.

The convex optimization problem can be converted to solving the extremum of Lagrangian function L through the Lagrange multiplier method.

$$\begin{aligned} L(w, b, \xi_i, \xi_i^*, \alpha_i, \alpha_i^*, \eta_i, \eta_i^*) = {} & \frac{1}{2}\|w\|^2 + C\sum_{i=1}^{n}(\xi_i + \xi_i^*) \\ & -\sum_{i=1}^{n}\alpha_i(\xi_i + \varepsilon - y_i + w\phi(x_i) + b) \\ & -\sum_{i=1}^{n}\alpha_i^*(\xi_i^* + \varepsilon + yi - w\phi(x_i) - b) \\ & -\sum_{i=1}^{n}(\eta_i\xi_i + \eta_i^*\xi_i^*) \end{aligned} \tag{3}$$

where α_i, α_i^*, η_i, and η_i^* are the Lagrangian multipliers, which satisfy the positivity constraints.

According to the Karush-Kuhn-Tucher (KKT) condition which describes the necessary and sufficient conditions to meet the optimal solution, the derivatives of L about the original variable must be 0 to obtain optimal results (Smola and Scholkopf, 2004).

$$\frac{\partial L}{\partial b} = \sum_{i=1}^{n}(\alpha_i - \alpha_i^*) = 0, 0 \le \alpha_i, \alpha_i^* \le C \tag{4}$$

$$\frac{\partial L}{\partial w} = w - \sum_{i=1}^{n}(\alpha_i - \alpha_i^*)\varphi(x_i) = 0 \Rightarrow w = \sum_{i=1}^{n}(\alpha_i - \alpha_i^*)\varphi(x_i) \tag{5}$$

$$\frac{\partial L}{\partial \xi_I^*} = C - \alpha_i^* - \eta_i^* = 0 \Rightarrow C = \alpha_i^* + \eta_i^* \tag{6}$$

According to Eq. 5, the regression function of the SVR model can be transformed as follows.

$$f(x) = \sum_{i=1}^{n}(\alpha_i - \alpha_i^*)(\phi(x_i)\cdot\phi(x)) + b = \sum_{i=1}^{n}(\alpha_i - \alpha_i^*)K(x, x_i) + b \tag{7}$$

where $K(x, x_i)$ represents the kernel function.

When the SVR is used to solve the non-linear regression problem in practice, the non-linear problem is mapped to a high-dimensional space and the linear function is constructed in this space by selecting an appropriate kernel function. The selection of kernel function has a significant influence on the performance of the SVR because different kernel function is suitable for different data types (Huang et al., 2012). A radial basis kernel function is more favored than other kernel functions due to its facilitating implementation and strong mapping performance (Rasmussen, 2003). The expression of a radial basis kernel function is shown in Eq. 8.

$$K(x, x_i) = \exp\left(-\frac{\|x - x_i\|^2}{2\sigma^2}\right) \tag{8}$$

where σ denotes the parameter related to the width of kernel in statistics.

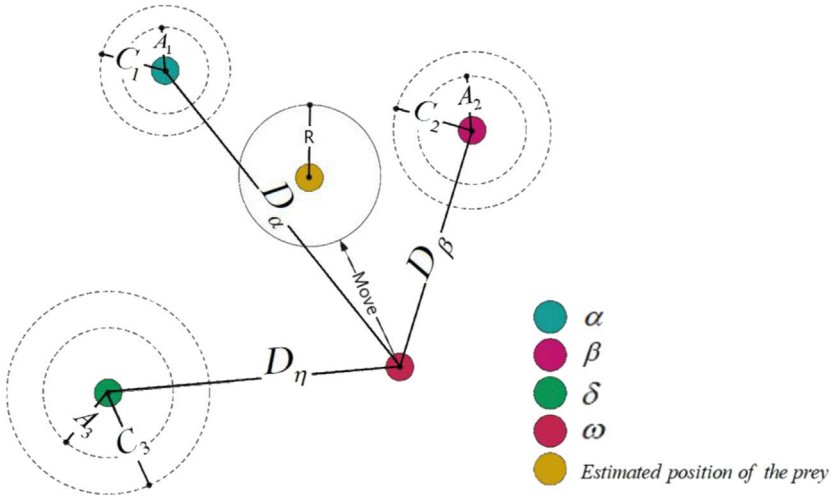

FIGURE 3
Location updating process of grey wolves in 2D space.

Using the Lagrangian multiplier method, duality principle, and the kernel function, the problem is transformed into a quadratic programming optimization one.

$$\max\left\{-\sum_{i,j=1}^{n}(\alpha_i-\alpha_i^*)(\alpha_j-\alpha_j^*)exp\left(-\frac{\|x_i-x_j\|^2}{2\sigma^2}\right)-\varepsilon\sum_{i=1}^{n}(\alpha_i+\alpha_i^*)+\sum_{i=1}^{n}y_i(\alpha_i-\alpha_i^*)\right\}$$
$$\text{subject to}\ \sum_{i=1}^{n}(\alpha_i-\alpha_i^*)=0\quad\text{and}\ \alpha_i,\alpha_i^*\in[0,C] \tag{9}$$

Obtaining the Lagrange multiplier α_i and α_i^* from the above quadratic optimization problem, the regression function of support vector machine can be expressed as Eq. 10.

$$f(x)=\sum_{i=1}^{n}(\alpha_i-\alpha_i^*)\exp\left(-\frac{\|x-x_i\|^2}{2\sigma^2}\right)+b \tag{10}$$

where α_i and α_i^* are the Lagrange multipliers, and σ denotes the parameter related to the width of kernel in statistics.

There are two essential parameters (the penalty parameter C and kernel parameter σ) in a SVR. The penalty parameter C controls the trade-off between the complexity of the function and the frequency in which errors are allowed. The parameter σ affects the mapping transformation of the input data to the feature space and controls the complexity of the model. Thus, it is important to select suitable parameters in the SVR.

A levy flight-based grey wolf optimizer (LGWO)

As mentioned above, the penalty parameter C and the kernel parameter σ are essential in a SVR. Many swarm intelligence algorithms mentioned above were presented to optimize those two parameters. However, these algorithms are more likely to fall into local optimum solutions. To cope with the problem, a novel algorithm called Levy flight-based Grey Wolf Optimizer (LGWO) is introduced to select the suitable parameters for the SVR.

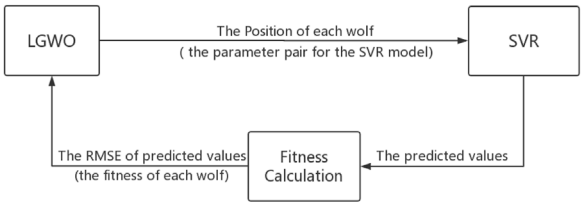

FIGURE 4
The process of training SVR using LGWO.

GWO is a swarm intelligence meta-heuristic algorithm given by Mirjalili et al. (2014). The inspiration of the GWO algorithm is based on the social hierarchy and hunting strategy of grey wolves in nature (Searemi et al., 2014). In each group of grey wolves, there is a very strict social dominant hierarchy shown in Figure 1.

To simulate the social hierarchy of grey wolves, four categories of wolves are defined--alpha (α), beta (β), delta (δ), and omega (ω). In the iterative calculation process, the first three best solutions are considered as alpha, beta, and delta, respectively. The rest of the candidate solutions are called omega. The wolves need to encircle the first three optimal solutions (alpha, beta, and delta) to find better solution for the problem (Mirjalili et al., 2014), which is modelled as:

$$\vec{D}=\left|\vec{C}\cdot\vec{X}_P(t)-\vec{X}(t)\right| \tag{11}$$
$$\vec{X}(t+1)=\vec{X}_P(t)-\vec{A}\cdot\vec{D} \tag{12}$$

where t denotes the current iteration, $\vec{X}_p$ denotes the position vector of the prey, $\vec{X}$ represents the position vector of a grey wolf, and $\vec{A}$, $\vec{C}$ are the random vectors.

The random vectors $\vec{A}$ and $\vec{C}$ are formulated as:

$$\vec{C}=2\vec{r}_2,\vec{A}=2\vec{a}\vec{g}\vec{r}_1-\vec{a} \tag{13}$$

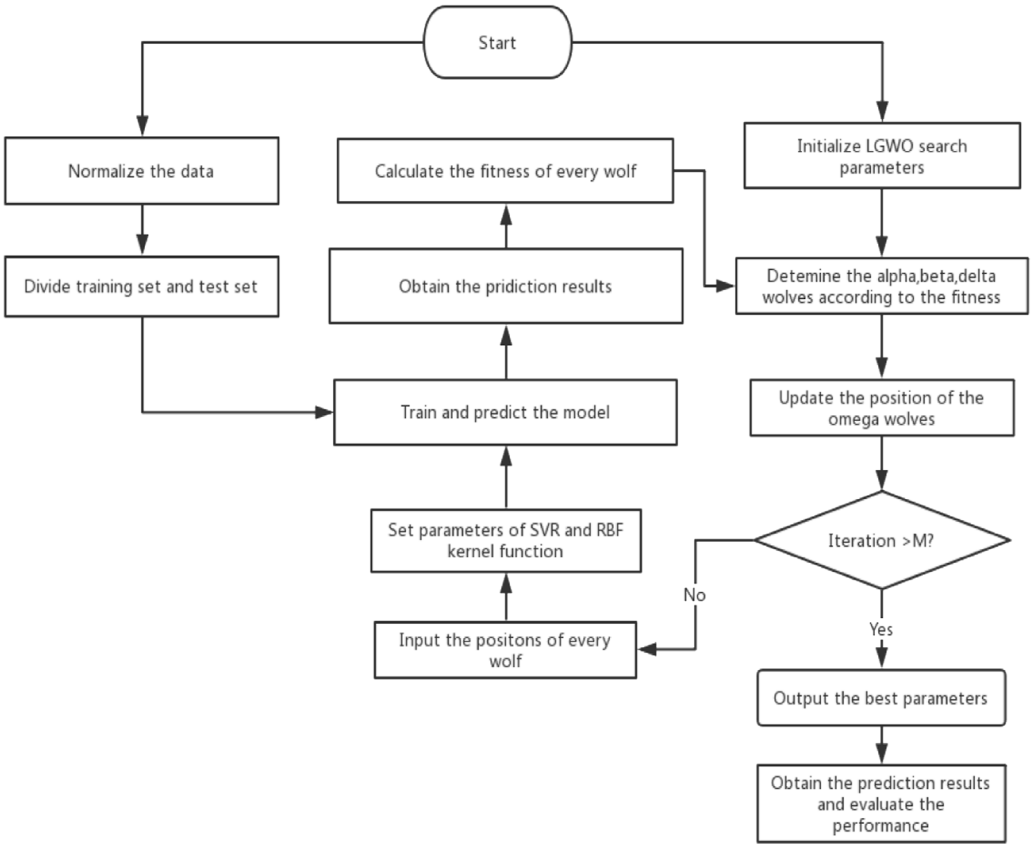

FIGURE 5
Structure of the proposed LGWO-SVR model.

where a is gradually linearly decreased from 2 to 0, and $\vec{r}_1$, Combination forecast model for concrete dam displacement considering residual correction $\vec{r}_2$ are random vectors in $[0, 1]$.

Different mathematical operators are defined in Eqs 11–13, which can be summarized as follows:

$$\vec{D}\mathrm{g}\vec{B} = (d_1 b_1, d_2 b_2, \mathrm{L}, d_n b_n)$$
$$\left|\vec{E}\right| = (|e_1|, |e_2|, \mathrm{L}, |e_n|)$$

where $\vec{D}$, $\vec{B}$, and $\vec{E}$ are N-dimensional vectors. $\vec{D} = (d_1, d_2, \cdots, d_n)$, $\vec{B} = (b_1, b_2, \cdots, b_n)$, and $\vec{E} = (e_1, e_2, \cdots, e_n)$.

Figure 2 shows how a grey wolf updates its position (X, Y) according to the position of the prey (X^*, Y^*). In the process of encircling prey, the grey wolf can reach different places around the best agent by adjusting the parameter values of A and C in Eqs 11, 12.

To simulate the hunting behavior of the grey wolves, the alpha, beta, and delta wolves in the GWO algorithm are three best solutions obtained so far. The omega wolves are obliged to update their positions according to the positions of the above best wolves. The hunting process can be mathematically described (Song et al., 2015):

$$\vec{D}_\alpha = \left|\vec{C}_1 \mathrm{g}\vec{X}_\alpha - \vec{X}\right|, \vec{D}_\beta = \left|\vec{C}_2 \mathrm{g}\vec{X}_\beta - \vec{X}\right|, \vec{D}_\delta = \left|\vec{C}_3 \mathrm{g}\vec{X}_\delta - \vec{X}\right| \quad (14)$$

$$\vec{X}_1 = \vec{X}_\alpha - \vec{A}_1 \mathrm{g}\vec{D}_\alpha, \vec{X}_2 = \vec{X}_\beta - \vec{A}_2 \mathrm{g}\vec{D}_\beta, \vec{X}_3 = \vec{X}_\delta - \vec{A}_3 \mathrm{g}\vec{D}_\delta \quad (15)$$

$$\vec{X}(t+1) = \frac{\vec{X}_1 + \vec{X}_2 + \vec{X}_3}{3} \quad (16)$$

where C_1, C_2, C_3, A_1, A_2, and A_3 represent the random vectors, X_α, X_β, and X_δ represent the positions of the alpha, beta, and delta wolves respectively, t represents the number of iteration, and $\vec{X}$ is the position of current solution.

As showed in Figure 3, a grey wolf can update its position according to the positions of alpha, beta, and delta wolves in a 2D search space. The final possible position of the prey is distributed in a circle determined by the positions of alpha, beta, and delta in the search space. The hunting process can be summarized that the position of the prey is estimated by the best three wolves, whereas the other wolves update their positions randomly around the prey.

When the grey wolves start to attack the prey, the encirclement of wolves became smaller and smaller. The GWO algorithm are more likely to fall into local optimum solutions under the small search encirclement (Mirjalili et al., 2015). Considering the small encirclement, the Levy flight is introduced to increase the ability of global and local search simultaneously.

The Levy flight is a category of random search process (Amirsadri et al., 2017). In this method, the short-range exploratory hopping and occasional long-distance walking are combined to result in a more effective search. The hopping behavior ensures that the search agents can search the small areas carefully, whereas the long-distance walking behavior ensures that the search agents can enter into another areas

FIGURE 6
Layout of the multiple-arch dam.

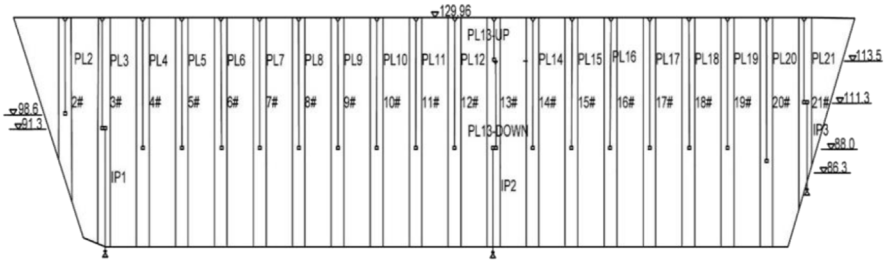

FIGURE 7
Pendulum systems for monitoring horizontal displacement.

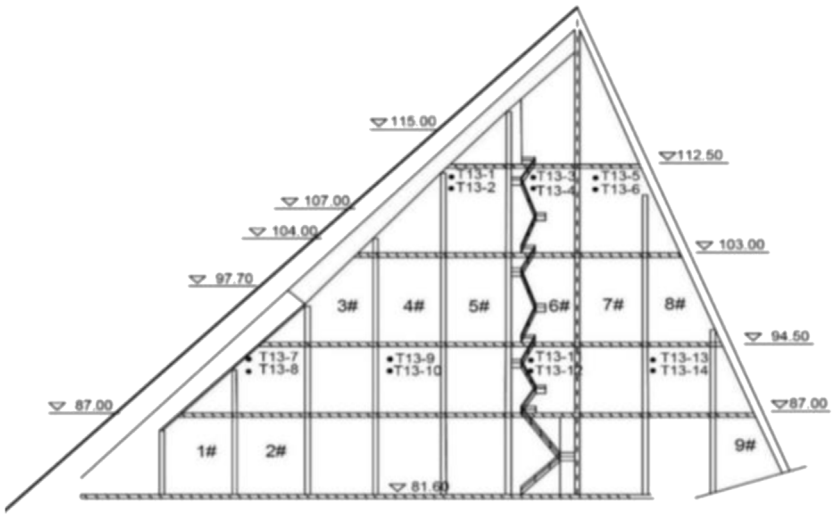

FIGURE 8
Thermometers installed in the dam section 13.

and search a wider range. The jump size in the Levy flight follows the Levy probability distribution function (Yang and Deb, 2009). Considering the difficulty of calculating the search path, a simple mathematical definition of the Levy distribution is described:

$$s = u/|v|^{\frac{1}{\beta}} \tag{17}$$

where s is the random step size obeying the Levy distribution, and u, v are the random numbers produced by normal distribution.

$$u : N\left(0, \sigma^2\right), v : N\left(0, 1\right) \tag{18}$$

with

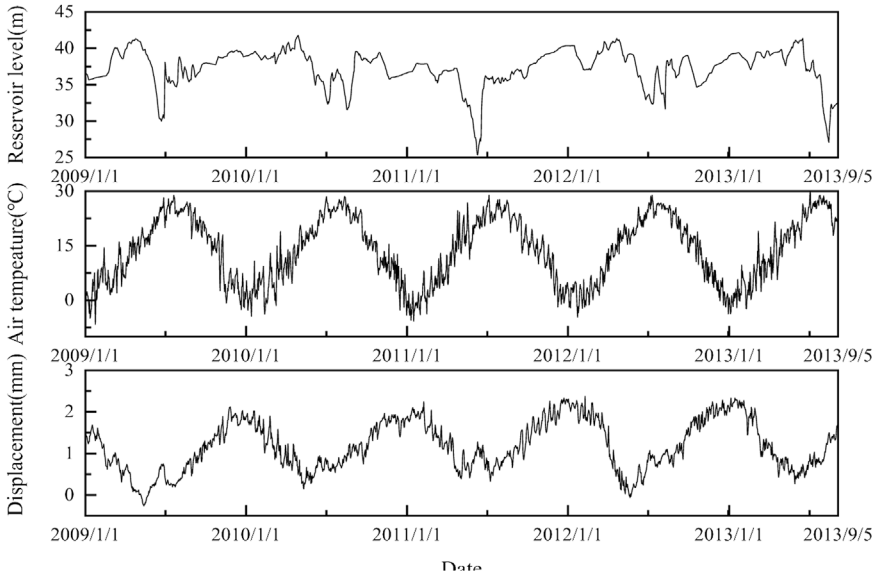

FIGURE 9
Reservoir level, air temperature, and displacements recorded in the dam section 13.

$$\sigma = \left\{ \frac{f(1+\beta)\mathrm{g}\sin\left(\frac{\pi\beta}{2}\right)}{\beta \mathrm{g} f\left(0.5+\frac{\beta}{2}\right)\mathrm{g}2^{(\beta/2-0.5)}} \right\}^{1/\beta} \tag{19}$$

where $f(x)$ is the standard gamma function, and the range of β is from 0 to 3.

In this study, a hybrid optimization algorithm which combines the GWO algorithm with the Levy flight is presented. In the proposed algorithm, all the wolves except the three leading wolves update their positions through the Levy flight. Therefore, the following equations can be used to update the position.

$$\vec{X}(t+1)_{LGWO} = \vec{X}(t+1) + S \tag{20}$$

where S is the step size determined by Eqs 17–19, $\vec{X}_{LGWO}(t+1)$ is the updated position of the wolf after the Levy flight, and $\vec{X}(t+1)$ is the updated position of the wolf without the Levy flight calculated by Eqs 14–16.

LGWO for parameter determination for SVR

As mentioned above, the penalty parameter C and the kernel function parameter σ in a SVR have a significant influence on the prediction performance. The LGWO algorithm is introduced to obtain the best series of parameters for the SVR. Therefore, the position of each wolf in the LGWO algorithm represents a parameter pair (C, σ) and the root mean squared error between the measured and predicted values is served as the fitness of each wolf.

Figure 4 shows the overall process of training the SVR using the LGWO algorithm at each iteration. At the beginning, the positions of wolves are obtained from the last iteration and served as the parameters of SVR. After giving the position of each wolf in SVR successively and training SVR, the predicted values of the testing sample are generated in SVR. Then the root mean squared error (RMSE) as the fitness of each wolf is given to the LGWO algorithm from SVR. The positions of the wolves are updated in the LGWO algorithm according to the fitness given by SVR. Finally, the best parameter pair (C, σ) is obtained from the

TABLE 1 Initial parameters.

Algorithm	Parameter	Value
LGWO	Population size	10
	$\vec{a}$	Linearly decreased from 2 to 0
	Max iteration	100
	Stopping criteria	Max iteration
	β	1.5
GWO	Population size	10
	$\vec{a}$	Linearly decreased from 2 to 0
	Max iteration	100
	Stopping criteria	Max iteration
PSO	Population size	10
	C_1, C_2	0.5,0.5
	W	0.8
	Max iteration	40
	Stopping criteria	Max iteration
GA	Population size	10
	C_1, C_2	0.6,0.001
	Max iteration	40
	Stopping criteria	Max iteration

TABLE 2 Experimental results of every algorithm.

Algorithm	RMSE		RAE		R^2	
	Averaged	Std dev	Averaged	Std dev	Averaged	Std dev
LGWO	0.1021	1.8E-05	0.0830	2.0E-05	0.9594	4.6E-05
GWO	0.1051	3.9E-03	0.0856	3.3E-03	0.9564	4.5E-03
PSO	0.2035	0.0782	0.1713	0.0685	0.7661	0.1411
GS	0.2755	0.0432	0.2378	0.0441	0.6036	0.1276
GA	0.3036	0.0681	0.2708	0.0703	0.4935	0.2234

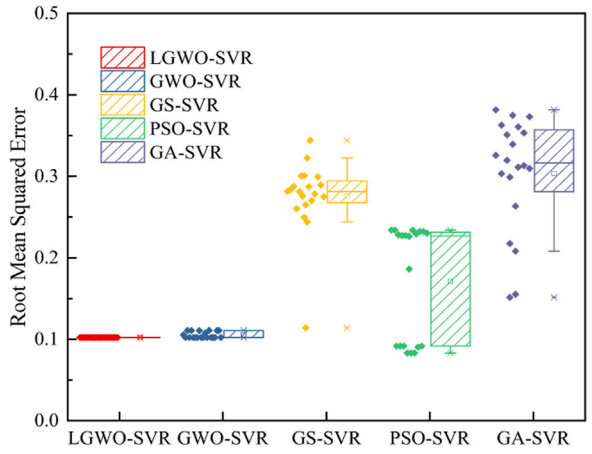

FIGURE 10
The distribution of RMSE at each run of each algorithm.

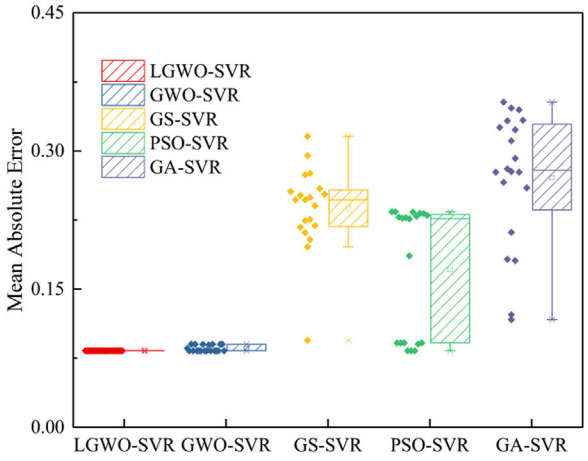

FIGURE 12
The distribution of MAE at each run of each algorithm.

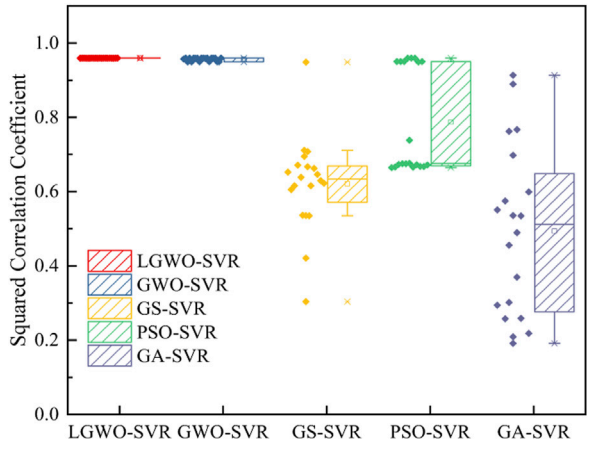

FIGURE 11
The distribution of R2 at each run of each algorithm.

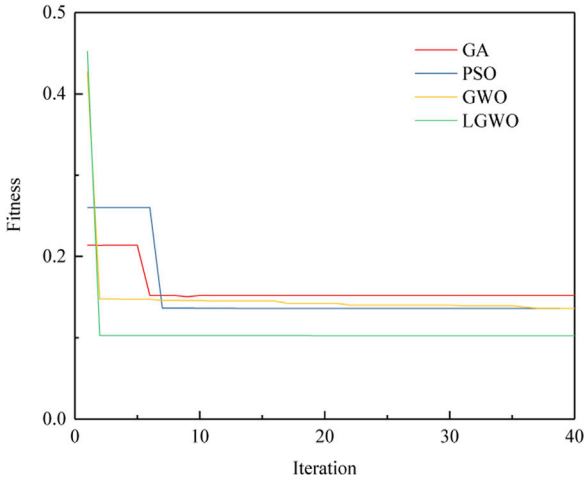

FIGURE 13
Convergence curves of the five algorithms over 20 independent runs.

LGWO algorithm and the predicted value with highest prediction accuracy is generated in SVR after reaching the maximum iteration.

In this paper, a novel hybrid model composed of the Levy flight-based grey wolf optimizer (LGWO) and support vector regression (SVR) was proposed and applied to make prediction for dam

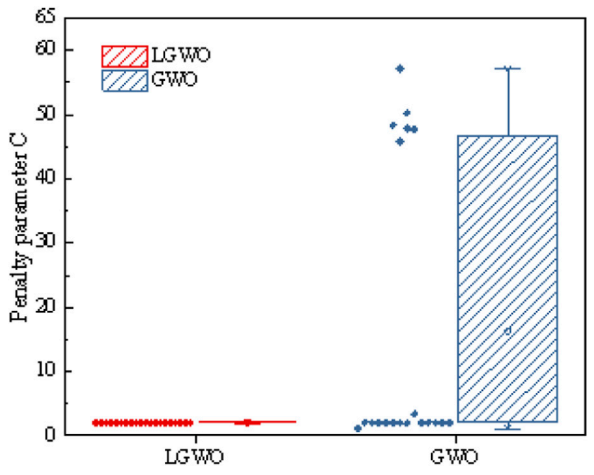

FIGURE 14
The distribution of parameter C for 20 independent runs of the LGWO and GWO algorithms.

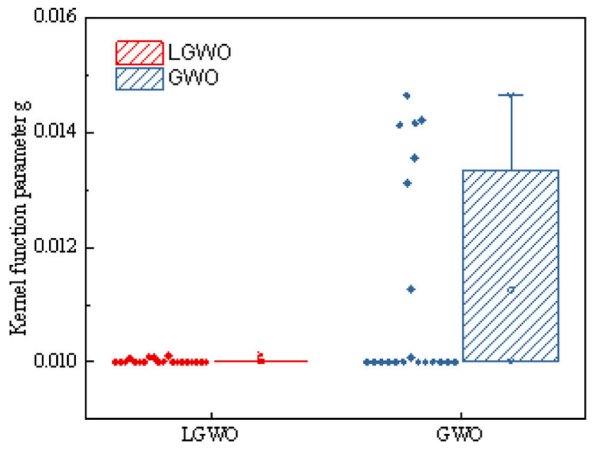

FIGURE 15
The distribution of parameter σ at 20 independent runs of the LGWO and GWO algorithms.

deformation. The structure of the proposed hybrid method for dam deformation prediction is shown in Figure 5. To avoid calculation error caused by numerical differences, the data is normalized and all the samples are divided into the training and testing samples. Main steps are as followed.

Step 1: Normalize the parameters of the LGWO-SVR model.

Step 2: Initialize the population of the wolf pack.

Step 3: Enter the position of each wolf to the SVR model and obtain the fitness of each wolf.

Step 4: Select the alpha, beta, and delta wolves in the wolf pack.

Step 5: Update the positions of the omega wolves.

Step 6: If the maximum iteration number reaches, the iteration is terminated and the position of the alpha wolf is outputted. Otherwise, repeat steps 3–6;

Step 7: Train the SVR model according to the outputted parameters and obtain the prediction values.

Criteria of prediction performance evaluation

To evaluate the performance of the proposed model, three widely used quantitative evaluation indicators are introduced. The specific expression of these indicators is shown as follows:

Squared correlation coefficient (R^2)

$$R^2 = \frac{\left[n\sum_{i=1}^{n}\hat{y}_i y_i - \sum_{i=1}^{n}\hat{y}_i\sum_{i=1}^{n}y_i\right]^2}{\left[n\sum_{i=1}^{n}\hat{y}_i^2 - \left(\sum_{i=1}^{n}y_i^2\right)^2\right]\left[n\left(\sum_{i=1}^{n}\hat{y}_i^2\right) - \left(\sum_{i=1}^{n}\hat{y}_i\right)^2\right]} \quad (21)$$

Mean absolute error (MAE)

$$MAE = \frac{1}{n}\sum_{i=1}^{n}|y_i - \hat{y}_i| \quad (22)$$

Root mean squared error (RMSE)

$$RMSE = \sqrt{\frac{1}{n}\sum_{i=1}^{n}(y_i - \hat{y}_i)^2} \quad (23)$$

where n is the number of testing samples, $\hat{y}_i$ is the predicted value of the i th testing sample, and y_i is the measured value of the i th testing sample.

Case study

General description of the project

The project used in this paper is situated on the Luo River (a tributary of the Huaihe River) in Anhui province, China. It is a multiple-arch dam consisting of 20 sections and 21 arches showed in Figure 6. The total height of the dam is 75.9 m, and the total length of the dam is 510 m. To understand the real-time working status of the dam during operation, the dam is installed with pendulum monitoring system. The aim is to monitor and assess the horizontal displacements of the dam. A total of 21 pendulum systems are installed in the arches. The pendulum monitoring system consists of 20 pendulum lines (PL) and three inverted pendulum lines (IP). The distribution of the pendulums is showed in Figure 7. The raw data was recorded by manual and automated equipment every day.

At the same time, some environmental data are also monitored, such as reservoir level, air temperature, water temperature. There are 57 thermometers embedded in the dam body, which are used to measure air, water, and concrete temperatures. In this study, the dam section 13 is selected for testing the model. The thermometer distribution of the dam section 13 is showed in Figure 8.

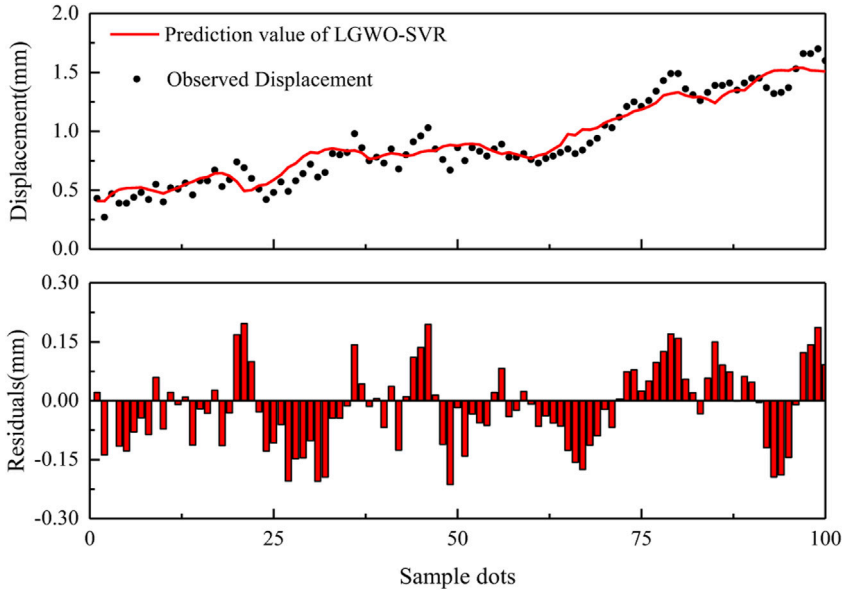

FIGURE 16
Measured and predicted displacements from the LGWO-SVR model.

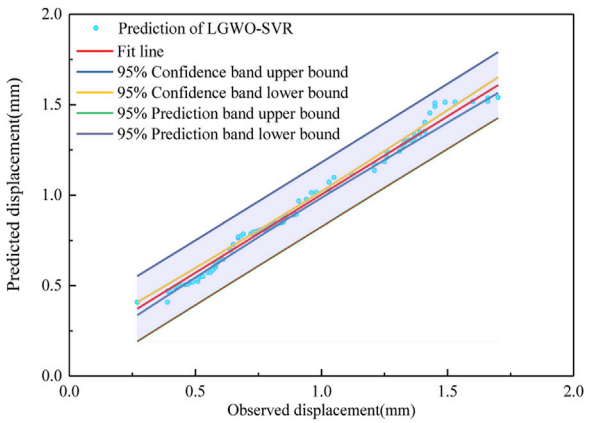

FIGURE 17
Linear regression analysis between the measured and the predicted values.

Input variables selection and data processing

In this study, the environmental monitoring data and displacements of the dam section 13 are used. Time series with 1700 data points from January 2009 to September 2013 are selected. The time series are divided into training and testing samples. The training time series are from January 2009 to June 2013. The testing time series are from June 2013 to September 2013. The amounts of training and testing samples are 1,000 and 260. The time series of air temperature, reservoir level, and displacements are presented in Figure 9.

Dam deformation is mainly influenced by hydraulic effect, thermal effect, and time-varying effect (Wei et al., 2019). For the hydraulic effect, it is usually considered as a reversible effect and can be represented by the polynomials(H^4; H^3; H^2; H) of the reservoir level. To consider the thermal effect, the measured temperatures including air, water, dam foundation, and concrete temperatures(T_{air}; T_{water}; $T_{foundation}$,; $T_{conctrete}$) are used. The time-varying effect represents the irreversible deformation of dam over the time effect. The effect could be represented by the combination of θ, $\ln(1+\theta)$, and $\theta/(\theta+1)$ where $\theta = t/100$ and t is the cumulative days from current data to initial monitoring date. Therefore, a total of 11variables are used as the input variables to construct the model and the displacements are the outputs.

Training the SVR model using LGWO

As mentioned above, there are two parameters (the penalty parameter C and kernel function parameter σ) in the SVR. The range of values of C and σ is [0.01,100] in SVR. In the LGWO algorithm, the number of the grey wolves is 20 and the maximum iteration is 100.

To describe the prediction performance of the LGWO-SVR model, four other algorithms are combined with SVR to predict the displacements: GS, PSO, GWO, and GA. Table 1 shows the initial parameters of these algorithms. To test the stability for each algorithm, 20 independent runs are carried out.

Results and discussion

The results from all the algorithms are presented in Table 2. The results are averaged over 20 independent runs. The Averaged and Std dev represent the mean evaluation indicators and standard deviation, respectively. As showed in Table 2, the squared correlation coefficients of the LGWO algorithm are 0.9594, which are higher than other four algorithms. In addition, the MAE and RMSE of the LGWO algorithm

are lower than the other four algorithms. It indicates that the LGWO algorithm performs better in the prediction accuracy.

To assess the solution stability of the LGWO algorithm, the distributions of evaluation indicators for the LGWO algorithm ais drew in Figures 10–12 with those for four other algorithms. It can be seen that the RMSE, MAE, R^2 of the LGWO algorithm are concentrated near 0.1, 0.8, and 0.96, respectively. However, the evaluation indicators of the other four algorithms are decentralized. The LGWO algorithm can obtain the parameter pair with the higher accuracy at each run. However, only one series of parameters is obtained in the GA and GS algorithm and eight series of parameters are obtained in the PSO algorithm at each independent 20 runs. It indicates that the LGWO algorithms perform well in the prediction stability.

Figure 13 shows the convergence curves of the five algorithms. The LGWO algorithm can reach the best solution at the third iteration although the initial fitness of the LGWO algorithm is much higher than the other algorithms, which indicates that the LGWO algorithm performs well in solution rate.

The above evaluations show that the LGWO algorithm performs better than the other algorithm in prediction accuracy, solution stability, and solution rate.

Considering the similar performance of the LGWO and GWO algorithms, the results of the 20 independent runs are presented in Figures 14, 15. The best series of the parameters is concentrated near (2.00,0.01) in the LGWO algorithm and the fitness of the result is all near 0.9595. However, the series of the parameter obtained from the GWO algorithm is decentralized and the fitness of six runs in 20 independent ones is about 0.9495. From this aspect, the GWO algorithm is more likely to fall into a local optimum and the LGWO algorithm can reduce the possibility of falling into a local optimum.

To further validate the performances of the LGWO-SVR model, the predicted displacements of the LGWO-SVR model and the measured displacements are shown in Figure 16. The best series of the parameters ($C = 2.029, \sigma = 0.010$) were found using the LGWO-SVR model. It can be seen from the figure that the LGWO-SVR model has better performance in prediction accuracy and reflect the variation of the dam displacements in a short time period. Figure 17 shows the linear fitting results of the measured and predicted displacements of the LGWO-SVR model. From the figure, the predicted values are within the 95% prediction band, which indicates the predicted results are very close to the actual values.

Conclusion

In this paper, a Levy flight-based grey wolf optimizer algorithm is applied into support vector regression for predicting dam deformation. In the proposed approach, the recently popular GWO algorithm was employed as the swarm intelligence algorithm to obtain the best parameters of the SVR model. Considering the possibility of falling into the local optimum, the Levy flight-based grey wolf optimizer was proposed to increase the chance of searching the potential global optimal solution. For verification, the results of the LGWO-SVR model were compared with four other swarm intelligence algorithms (PSO, GA, GS, and GWO). The prediction accuracy of the model is accessed by using MAE, RMSE, and R^2. The stability of the model can be seen from the distribution of the MAE, RMSE, and R^2 for 20 independent runs. The results showed that the LGWO-SVR model have higher prediction accuracy, stability, and solution rate than the other swarm intelligence algorithms, and the LGWO algorithm can obtain the global optimum of the SVR model for each run. This indicates that the LGWO algorithm is a good swarm intelligence algorithm to obtain the optimal parameter of SVR. Generally, the major contribution of this study of the dam deformation prediction are highlighted as follows:

(1) The LGWO algorithm was used to obtain the best series of the parameter in the SVR model and the results showed that the LGWO algorithm have the capability to obtain the global optimum accurately and swiftly.
(2) The dam deformation predicted by the LGWO-SVR model were compared with other swarm intelligence algorithms and the result showed that the LGWO-SVR model could reach better fitting accuracy and have lower residuals.
(3) The good performance of the LGWO-SVR model indicates that the Levy flight can reduce the possibility of falling into the local optimum.

Data availability statement

The original contributions presented in the study are included in the article/Supplementary Material, further inquiries can be directed to the corresponding author.

Author contributions

Conceptualization: PH; methodology: PH; validation: PH and WW; formal analysis: PH and WW; data curation: PH; writing—original draft preparation, PH; writing—review and editing, PH and WW; funding acquisition, PH.

Funding

This work was supported by the High-level Talent Start-up Research Foundation of North China University of Water Resources and Electric Power (201810001).

Conflict of interest

The authors declare that the research was conducted in the absence of any commercial or financial relationships that could be construed as a potential conflict of interest.

Publisher's note

References

Amirsadri, S., Mousavirad, S. J., and Ebrahimpour-Komleh, H. (2017). A Levy flight-based grey wolf optimizer combined with back-propagation algorithm for neural network training. *Neural Comput. Appl.* 30 (12), 3707–3720. doi:10.1007/s00521-017-2952-5

Bui, K-T. T., Tien Bui, D., Zou, J., Van Doan, C., and Revhaug, I. (2016). A novel hybrid artificial intelligent approach based on neural fuzzy inference model and particle swarm optimization for horizontal displacement modeling of hydropower dam. *Neural Comput. Appl.* 29 (12), 1495–1506. doi:10.1007/s00521-016-2666-0

Chen, B., Hu, T., Huang, Z., and Fang, C. (2018). A spatio-temporal clustering and diagnosis method for concrete arch dams using deformation monitoring data. *Struct. Health Monit.* 18, 1355–1371. doi:10.1177/1475921718797949

Faris, H., Aljarah, I., Al-Betar, M. A., and Mirjalili, S. (2017). Grey wolf optimizer: A review of recent variants and applications. *Neural Comput. Appl.* 30 (2), 413–435. doi:10.1007/s00521-017-3272-5

Ge, W., Li, Z., Li, W., Wu, M., Li, J., and Pan, Y. (2020). Risk evaluation of dam-break environmental impacts based on the set pair analysis and cloud model [J]. *Nat. Hazards* 104, 1641–1653. doi:10.1007/s11069-020-04237-9

Huang, G., Zhou, H., Ding, X., and Zhang, R. (2012). Extreme learning machine for regression and multiclass classification. *IEEE Trans. Syst. Man, Cybern. Part B Cybern.* 42 (2), 513–529. doi:10.1109/tsmcb.2011.2168604

Kaltich, A. M. (2015). Wavelet genetic algorithm-support vector regression (wavelet GA-SVR) for monthly flow forecasting. *Water Resour. Manag.* 29 (4), 1283–1293. doi:10.1007/s11269-014-0873-y

Li, M., Shen, Y., Ren, Q., and Li, H. (2019). A new distributed time series evolution prediction model for dam deformation based on constituent elements. *Adv. Eng. Inf.* 39, 41–52. doi:10.1016/j.aei.2018.11.006

Li, S., Fang, H., and Liu, X. (2018). Parameter optimization of support vector regression based on sine cosine algorithm. *Expert Syst. Appl.* 91, 63–77. doi:10.1016/j.eswa.2017.08.038

Li, Z., Zhang, Y., Wang, J., Ge, W., Li, W., Song, H., et al. (2021). Impact evaluation of geomorphic changes caused by extreme floods on inundation area considering geomorphic variations and land use types [J]. *Sci. Total Environ.* 754, 142424. doi:10.1016/j.scitotenv.2020.142424

Meng, Q. N., and Xu, X. (2018). Price forecasting using an ACO-based support vector regression ensemble in cloud manufacturing. *Comput. Industrial Eng.* 125, 171–177. doi:10.1016/j.cie.2018.08.026

Mirjalili, S. (2015). How effective is the Grey Wolf optimizer in training multi-layer perceptrons. *Appl. Intell.* 43 (1), 150–161. doi:10.1007/s10489-014-0645-7

Mirjalili, S., Mirjalili, S. M., and Lewis, A. (2014). Grey wolf optimizer. *Adv. Eng. Softw.* 69, 46–61. doi:10.1016/j.advengsoft.2013.12.007

Ranković, V., Grujović, N., Divac, D., and Milivojević, N. (2014). Development of support vector regression identification model for prediction of dam structural behaviour. *Struct. Saf.* 48, 33–39. doi:10.1016/j.strusafe.2014.02.004

Rasmussen, C. E. (2003). "Gaussian processes in machine learning," in *Lecture notes in computer science*, 63–71.

Salazar, F., Moran, R., Toledo, M. A., and Onate, E. (2017). Data-based models for the prediction of dam behaviour: A review and some methodological considerations. *Archives Comput. Methods Eng.* 24 (1), 1–21. doi:10.1007/s11831-015-9157-9

Searemi, S., Mirjalili, S. Z., and Mirjalili, S. M. (2014). Evolutionary population dynamics and grey wolf optimizer. *Neural Comput. Appl.* 26 (5), 1257–1263. doi:10.1007/s00521-014-1806-7

Shu, X., Bao, T., Li, Y., Gong, J., and Zhang, K. (2021). VAE-TALSTM: A temporal attention and variational autoencoder-based long short-term memory framework for dam displacement prediction. *Eng. Comput.* 38, 3497–3512. doi:10.1007/s00366-021-01362-2

Smola, A. J., and Scholkopf, B. (2004). A tutorial on support vector regression. *Statistics Comput.* 14 (3), 199–222. doi:10.1023/b:stco.0000035301.49549.88

Song, X., Tang, L., Zhao, S., Zhang, X., Li, L., Huang, J., et al. (2015). Grey Wolf Optimizer for parameter estimation in surface waves. *Soil Dyn. Earthq. Eng.* 75, 147–157. doi:10.1016/j.soildyn.2015.04.004

Su, H., Li, X., Yang, B., and Wen, Z. (2018). Wavelet support vector machine-based prediction model of dam deformation. *Mech. Syst. Signal Process.* 110, 412–427. doi:10.1016/j.ymssp.2018.03.022

Su, H., Wen, Z., Sun, X., and Yang, M. (2015). Time-varying identification model for dam behavior considering structural reinforcement. *Struct. Saf.* 57, 1–7. doi:10.1016/j.strusafe.2015.07.002

Viswanathan, G. M., Afanasyev, V., Buldyrev, S. V., Murphy, E. J., Prince, P. A., and Stanley, H. E. (1996). Lévy flight search patterns of wandering albatrosses. *Nature* 381 (6581), 413–415. doi:10.1038/381413a0

Wei, B., Yuan, D., Li, H., and Xu, Z. (2019). Combination forecast model for concrete dam displacement considering residual correction. *Struct. Health Monitoring-an Int. J.* 18 (1), 232–244. doi:10.1177/1475921717748608

Xue, Y., Jiang, J., Zhao, B., and Ma, T. (2018). A self-adaptive artificial bee colony algorithm based on global best for global optimization. *Soft Comput.* 22 (9), 2935–2952. doi:10.1007/s00500-017-2547-1

Yang, X., and Deb, S. (2009). "Cuckoo search via lévy flights," in 2009 World Congress on Nature & Biologically Inspired Computing (NaBIC), Coimbatore, India, 09-11 December 2009 (IEEE), 210–214.

Zhang, S., and Zhou, Y. (2015). Grey wolf optimizer based on powell local optimization method for clustering analysis. *Discrete Dyn. Nat. Soc.* 2015, 1–17. doi:10.1155/2015/481360

frontiers | Frontiers in Earth Science

TYPE Original Research
PUBLISHED 11 April 2023
DOI 10.3389/feart.2023.1187032

OPEN ACCESS

EDITED BY
Xihui Gu,
China University of Geosciences Wuhan, China

REVIEWED BY
Bo Li,
Changjiang River Scientific Research Institute (CRSRI), China
Li Hognen,
Nanjing Hydraulic Research Institute, China

*CORRESPONDENCE
Zelin Ding,
zzstar_ncwu_hs@163.com

SPECIALTY SECTION
This article was submitted to Hydrosphere, a section of the journal Frontiers in Earth Science

RECEIVED 15 March 2023
ACCEPTED 27 March 2023
PUBLISHED 11 April 2023

CITATION
Zhang H, Li X, Liu J, Han P, Yang Y, Ding Z, Han L, Zhang X and Wang S (2023), Study on wetting deformation model of coarse-grained materials based on P-Z model and BP neural network.
Front. Earth Sci. 11:1187032.
doi: 10.3389/feart.2023.1187032

Study on wetting deformation model of coarse-grained materials based on P-Z model and BP neural network

Hongyang Zhang[1,2], Xuan Li[1], Jianlong Liu[3], Pengju Han[1], Yige Yang[1], Zelin Ding[1,2]*, Liwei Han[1,2], Xianqi Zhang[1,2] and Shunsheng Wang[1,2]

[1]College of Water Conservancy, North China University of Water Resources and Electric Power, Zhengzhou, China, [2]Collaborative Innovation Center for Efficient Utilization of Water Resources in Yellow River Basin, Zhengzhou, China, [3]Management Division of Jiangsu Qinhuai River Hydraulic Engineering, Nanjing, China

The wetting deformation of coarse-grained materials can seriously affect the safety of earth and rock dams during initial water storage. The wetting model formulas are expressed in various forms and have complex parameters. Only a small amount of test data is fitted by mathematical statistics, and the universality of the obtained wetting model is unknown. Duncan-Chang E-B constitutive model cannot accurately reflect the wetting deformation characteristics of coarse-grained materials. Through the double-line wetting test of coarse-grained materials, the wetting model proposed by predecessors was verified and analyzed. Based on the indoor wetting test data, the parameters of each wetting model were fitted to analyze the accuracy of each wetting model in describing the wetting deformation characteristics. According to the P-Z model in the elastic-plastic theory and the wetting model formula, the P-Z wetting model is established, and the BP artificial neural network is introduced to establish the artificial neural network wetting deformation prediction model based on the P-Z model. The results show that the relationship between wetting axial strain and wetting stress level is best expressed by the exponential function. The relationship between wetting volumetric strain and wetting stress level is best described by Cheng's linear function. The relative errors between the predicted and experimental values of the proposed neural network prediction model are all within 6%. The relationship between wetting axial strain and wetting stress level is exponential function, and the relationship between wetting volumetric strain and wetting stress level is linear function. The P-Z wetting model proposed in this research can better reflect the wetting deformation characteristics of coarse-grained materials under complex stress paths. The artificial neural network prediction model based on P-Z wetting model is more reliable and accurate, which can meet the prediction requirements of actual engineering for wetting deformation of coarse-grained materials.

KEYWORDS

coarse-grained materials, triaxial wetting test, wetting deformation model, P-Z model, BP neural network

1 Introduction

The wetting and deformation of coarse-grained materials can lead to uneven settlement, cracks, and collapse of the dam during impoundment periods (Jia et al., 2020; Zhang et al., 2022), rainfall infiltration, and other processes. Severe wetting and deformation can increase the risk of dam failure (Ge et al, 2020; Wang et al, 2022), with serious implications for the safe operation of the dam as well as downstream areas (Wu et al, 2021; Ge et al, 2022; Wang et al, 2023). For example, when the Pubugou Rockfill Dam (Lin et al., 2017) was impounded to a high water level, When Laos sangpian reservoir (Xu, 2018) was impounded to a high water level, and when the Guanyinyan Composite Dam (Jia et al., 2018) was impounded for the first time, the coarse-grained materials both underwent significant wetting, resulting in uneven settlement and cracks in the dam (Jie et al., 2019), so it is especially important to research the wetting deformation of earth-rock dams. Cheng et al. (2010), Chi and Zhou (2017), Chen, (2019), and Zhou et al. (2019) fitted the empirical formula of the wetting model based on the test data on the basis of the triaxial wetting test. The functional relationship between wetting axial strain and wetting stress level is mainly summarized as an exponential, hyperbolic and linear function, while the functional relationship between wetting volumetric strain and wetting axial strain is basically a linear function. Wei and Zhu (2007) investigated the wetting stress-strain relationship of coarse-grained soils through a modified triaxial apparatus and suggested a double-line method test. In terms of the constitutive model, Ding and Qian (2022) proposed an improved wetting deformation model by the Duncan-Chang E-B model. Since the Duncan-Chang *E-B* model cannot reflect the complex stress path and the influence of stress on deformation, the fitting effect with the test results is not good. The P-Z model based on the generalized plastic model can well reflect the complex stress path correlation of the wetting deformation of coarse-grained materials (Zou et al., 2013), and more accurately simulate the wetting deformation law of coarse-grained materials.

However, the wetting models proposed by predecessors are different, and they are basically fitted by a small amount of data through mathematical statistics on the basis of some coarse-grained material experiments, which have problems such as low model accuracy, too many fitted parameters and complex expressions, and significant differences in results.

In this research, based on the wetting test data, the parameters of each wetting model are fitted and the wetting deformation is compared and analyzed to determine a more universal wetting strain model. The P-Z principal constitutive model is also combined with BP neural network to establish an artificial neural network wetting deformation prediction model based on the P-Z model, overcoming the problems of complex and heavy workload in the triaxial wetting test process and the inaccuracy of wetting deformation data due to the uncertainty in the test and numerical simulation stages.

2 triaxial wetting test

2.1 Test gradation

According to the standard of the geotechnical test method, the actual dry density of the materials used in the test was calculated to be 1.58×10^3 kg/m^3, and the relative density is 0.56. The content of each particle size group is shown in Table 1, and the gradation curve is shown in Figure 1.

TABLE 1 Content of each particle size group.

Particle size(mm)	50~40	40~30	30~20	20~10	10~5	<5
Content (%)	16.6	11.8	18.9	23.8	18.9	10.0

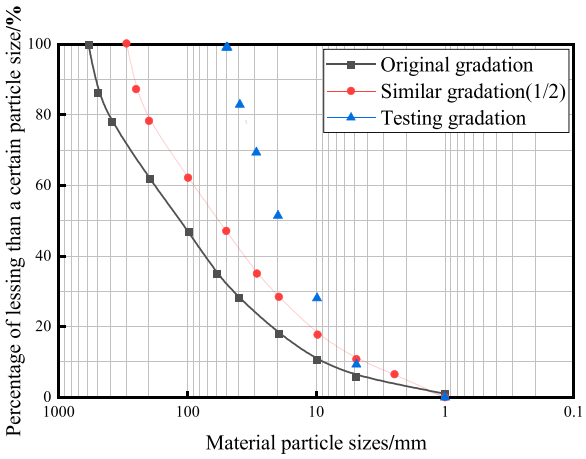

FIGURE 1
Original grading and test grading curves.

2.2 Triaxial test plan

The test was set under three confining pressure conditions of 800kPa, 1,600kPa, and 2,400 kPa, and five wetting stress levels of 0, 0.2, 0.40, 0.60, and 0.80 were set at each group of confining pressure. The wetting stress level is the ratio of the peak deviatoric stress in the wetting stage to the peak deviatoric stress in the conventional triaxial test, i.e., $s = (\sigma_1 - \sigma_3)/(\sigma_1 - \sigma_3)_f$. In this research, the conventional triaxial shear test of coarse-grained materials is first carried out. Then the peak deviatoric stress of specimen failure under confining pressure of 800kPa, 1,600kPa and 2,400 kPa is measured. Based on this, the stress levels of 0,0.2,0.40,0.60 and 0.80 are set, so that the corresponding deviatoric stress at each stress level can be calculated. In the test, the

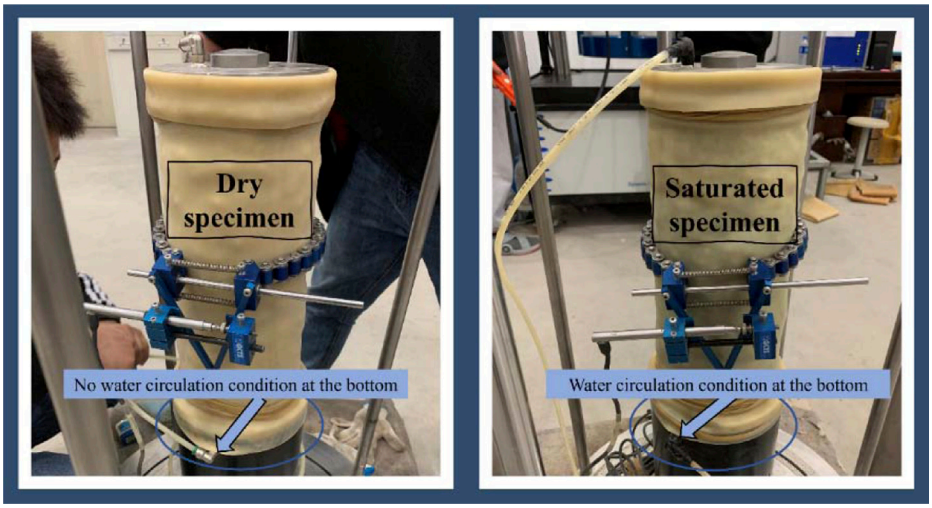

FIGURE 2
Comparison of dry and saturated specimens.

FIGURE 3
Comparison of coarse-grained materials in the dry state and saturated state.

effect of maintaining the level of wetting stress is achieved by keeping the numerical level of the deviatoric stress of the triaxial instrument constant. To reduce the influence of creep of coarse-grained materials, the material with initial water content of 5% is selected and the "double line method" is selected as the wetting test method (Miao, 2018; Jia et al., 2019). The strain difference between the wetting shear curve and the dry shear test curve under the same stress state is taken as the wetting deformation value under this stress state. Although the wetting volumetric strain obtained by this method is slightly larger, the prediction of deformation is safe and reasonable.

2.3 Test results

The results of the conventional triaxial test and wetting triaxial test of coarse-grained materials are shown in Figures 2, 3. The test values of wetting axial strain and wetting volumetric strain corresponding to the wetting deformation test are listed in Table 2.

3 Wettung model analysis and validation

3.1 Wetting axial strain model

At present, the functional relationship between wetting axial strain and wetting stress level is mainly hyperbolic function, exponential function, and linear function (Sun et al., 2023). To investigate the extent to which the level of wetting stress and the confining pressure affect the wetting axial strain and to compare the suitability of each wetting model to the test data. In this research,

TABLE 2 Wetting deformation of coarse-grained materials.

σ_3/kPa	S_L	ε_a/%	ε_v/%
800	0	0.03	0.05
	0.2	0.06	0.09
	0.4	0.12	0.22
	0.6	0.32	0.35
	0.8	0.70	0.40
1,600	0	0.05	0.13
	0.2	0.11	0.20
	0.4	0.21	0.34
	0.6	0.43	0.43
	0.8	0.80	0.51
2,400	0	0.08	0.18
	0.2	0.14	0.29
	0.4	0.26	0.48
	0.6	0.50	0.56
	0.8	0.82	0.64

TABLE 3 Fitting parameters of exponential function type I.

Parameters	k_1	b_1	k_2	b_2	Average fit $\overline{R^2}$
Numerical values	0.00391	−0.0047	−0.0831	4.7259	0.963

based on the results of the triaxial wetting test, the parameter fitting and wetting axial strain calculation of exponential function type, hyperbolic function type, and linear function type proposed by predecessors are carried out, respectively, and the best adaptation function is determined according to the results of comparative analysis.

(1) Expression for the exponential function relationship I (Cheng, et al., 2010):

$$\Delta\varepsilon_a = \left(k_1\frac{\sigma_3}{P_a} + b_1\right)e^{\left(k_2\frac{\sigma_3}{P_a}+b_2\right)S_L} \quad (1)$$

Where:
ε_a =wetting axial strain,
S_L =wetting stress level,
σ_3 =confining pressure, P_a is standard atmospheric pressure,
k_1, b_1, k_2, b_2 = material test parameters.

(2) Expression for the exponential function relationship II (Niu, 2020):

$$\Delta\varepsilon_a = f_1 e^{g_1\sigma_3+\left(f_2\sigma_3+g_2\right)S_L} \quad (2)$$

Where:
f_1, g_1, f_2, g_2 = model parameters.

TABLE 4 Fitting parameters of exponential function type II.

Parameters	f_1	g_1	f_2	$\overline{R^2}$	Average fit $\overline{R^2}$
Numerical values	0.0152	0.0008	−0.000812	4.7053	0.965

TABLE 5 Fitting parameters of hyperbolic functions.

Parameters	K_1	A	K_0	m	Average fit $\overline{R^2}$
Numerical values	0.00274	0.385	0.0595	0.722	0.932

TABLE 6 Fitting parameters of linear functions.

Parameters	c	d	e	f	Average fit $\overline{R^2}$
Numerical values	0.00008	0.7567	0.00004	−0.108	0.911

(3) Expression for the hyperbolic function relationship (Chi and Zhou, 2017):

$$\Delta\varepsilon_a = \frac{\left[K_1\left(\frac{\sigma_3}{P_a}\right)+A\right]S_L}{1-S_L} + \frac{1}{K_0}\left(\frac{\sigma_3}{P_a}\right)^m \quad (3)$$

Where:
K_1, A, K_0, m = model parameters.

(4) Expression for the linear functional relationship (Chen, 2019).

$$\Delta\varepsilon_a = (c\sigma_3 + d)S_L + (e\sigma_3 + f) \quad (4)$$

Where:
c, d, e, f = model parameters.

According to the triaxial wetting test data, the parameters of the above four function types are fitted. The fitting of each function model parameters and the determination coefficient of fitting $\overline{R^2}$ are shown in Tables 3–6. A comparison of the calculated and experimental values for each wetting axial variation model is shown in Figure 4. The results show that the model prediction curve of exponential function type I has the best fitting effect with the triaxial wetting test data, the fitting effect of hyperbolic function and exponential function type II is the second. The fitting effect of the linear function is the worst. Therefore, for the expression of the functional relationship between the wetting stress level and the wetting axial strain, the exponential function type I relational fitting of the wetting model has the highest accuracy. It is more in line with the test phenomenon. Its parameters are simple to derive and easy to calculate.

3.2 Wetting volumetric strain model

Zuo and Shen (1989) thought that the wetting volumetric strain was not related to the wetting stress level in the early stage, but was close to the hyperbolic relationship with the test confining pressure. With the progress of test instruments and

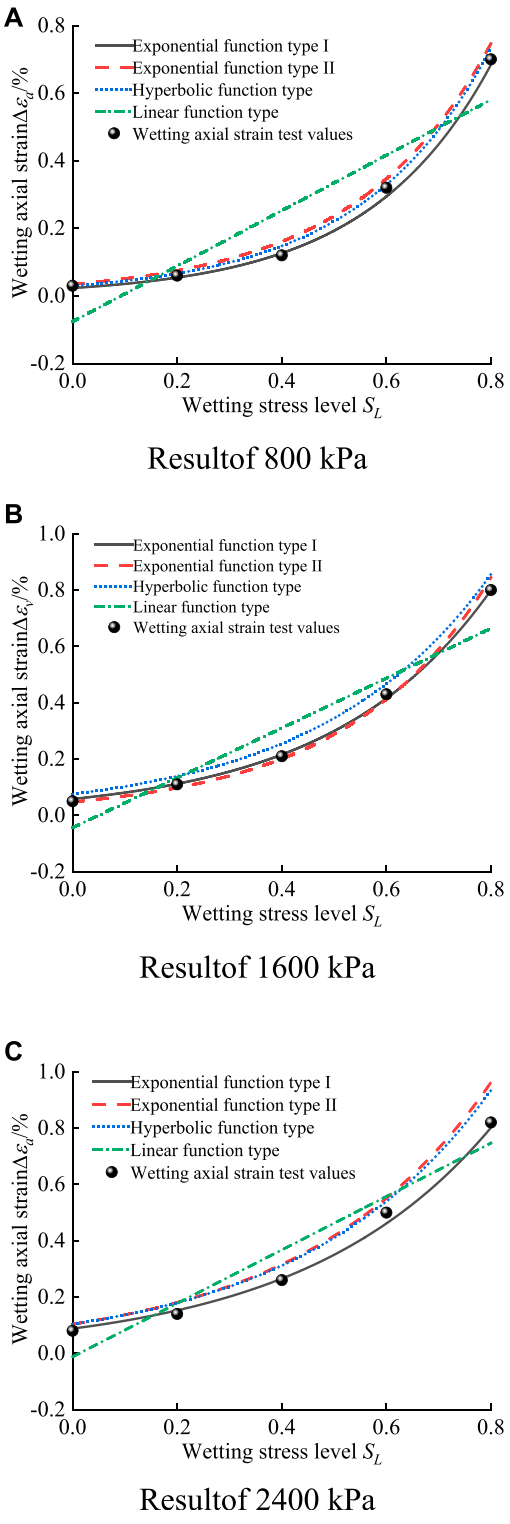

FIGURE 4
Comparison of simulation and test results of four wetting axial strain models. **(A)** Result of 800 kPa **(B)** Result of 1,600 kPa **(C)** Result of 2,400 kPa.

TABLE 7 Parameter fitting values of Cheng's linear model.

Parameters	k_3	b_3	k_4	b_4	Average fit $\overline{R^2}$
Numerical values	0.0022	0.4991	0.0111	−0.0545	0.992

research results, it is found that the wetting deformation of coarse aggregate under different stress paths is not the same, so there is a correlation between wetting volumetric strain and confining pressure and stress level. Cheng et al. (2010) considered that the wetting volumetric strain tends to vary linearly with the wetting stress level, and the relationship between wetting volumetric strain and wetting stress level was fitted by linear function expression (4 parameters):

$$\Delta\varepsilon_v = \left(k_3\frac{\sigma_3}{P_a} + b_3\right)S_L + k_4\frac{\sigma_3}{P_a} + b_4 \tag{5}$$

Where:
$\Delta\varepsilon_v$ = wetting volumetric strain,
S_L = wetting stress level,
σ_3 = confining pressure,
P_a = standard atmospheric pressure,
k_3, b_3, k_4, b_4 = material test parameters.

Zhou et al. (2019) introduced the average principal stress p and generalized shear stress q of the sample during the wetting process, deduced the method for calculating the ratio k of wetting volumetric strain to wetting axial strain, and summarized the wetting volumetric strain formula 6 parameters):

$$\Delta\varepsilon_v = \log_b\left(q/ap + b^3\right)\left\{\frac{\left[K_1\left(\frac{\sigma_3}{P_a}\right) + A\right]S_L}{1 - S_L} + \frac{1}{K_0}\left(\frac{\sigma_3}{P_a}\right)^m\right\} \tag{6}$$

Where:
a, b, K_1, A, K_0, m = material test parameters.

Peng et al. (2010) believed that the wetting volumetric strain is caused by spherical stress and partial stress, respectively. The relationship between the wetting volumetric strain caused by spherical stress and the confining pressure can be expressed by a hyperbola. The relationship between the wetting volumetric deformation caused by partial stress and the wetting stress level is fitted by linear and exponential functions. The wetting volumetric strain formula 6 parameters) is summarized as follows:

$$\Delta\varepsilon_v = a + b\left(\sigma_3/P_a\right) + \left[c\left(\sigma_3/P_a\right) + d\right]S_L + f\ln\left(\sigma_3/P_a\right) + g \tag{7}$$

Where:
a, b, c, d, f, g = material test parameters.

According to the triaxial wetting test data, the parameters of the wetting volumetric strain model of the above three function types are fitted. The fitting of each function model parameters and

TABLE 8 Parameter fitting values of Zhou's linear model.

Parameters	a	b	K_1	A	K_0	m	Average fit $\overline{R^2}$
Numerical values	2.9591	0.4365	0.00274	0.385	0.0595	0.722	0.983

TABLE 9 Parameter fitting values of Peng's linear model.

Parameters	a	b	c	d	f	g	Average fit $\overline{R^2}$
Numerical values	−0.01	0.0081	0.0072	0.4083	0.1462	−0.276	0.959

the determination coefficient of fitting $\overline{R^2}$ are shown in Tables 7–9. The comparison between the calculated values of each wetting volumetric strain model and the experimental values is shown in Figure 5. The results show that the prediction curve of Cheng's linear model fits the triaxial wetting test data the best; the Peng's function fits the second, and the Zhou's function fits the worst. Therefore, the Cheng's linear model has the highest accuracy in fitting the wetting volumetric strain model, and the Cheng's linear model is a 4-parameter; each parameter is easily derived from the test results, which is more concise and convenient than the 6-parameter models of Zhou and Peng.

4 BP neural network prediction model based on the P-Z model

4.1 P-Z wetting model

Zienkiewicz and Pastor proposed the generalized plasticity theory in 1985, then Pastor and Zienkiewicz extended their basic framework and on which they developed the constitutive model of soil, the Pastor-Zienkiewicz model (Pastor et al., 1985; Pastor et al., 1987) (hereafter referred to as the P-Z model).

The expression of the generalized plastic matrix of the P-Z model is:

$$D_{Lep} = D_e - \frac{D_e n_{gL} n^T D_e}{H_L + n_{gL}^T D_e n} \quad D_{Uep} = D_e - \frac{D_e n_{gU} n^T D_e}{H_U + n_{gU}^T D_e n} \tag{8}$$

Where:

L = loading,

U = unloading,

n_{gL} = direction vector of plastic potential,

n_{gU} = direction vector of plastic potential, meaning the direction of plastic strain increment,

n = loading direction vector, equivalent to the normal direction of yield surface,

H_L = the direction of plastic flow during loading, and represent the direction of plastic strain increment.

H_U = the direction of plastic flow during unloading, and represent the direction of plastic strain increment.

In the P-Z model, for each homogeneous material, the elastic matrix is determined by the bulk and shear modulus, which varies linearly with the mean stress.

$$K = K_{evo} p, G = G_{eso} p \tag{9}$$

Where:

K_{evo}, G_{eso} = the modulus of elasticity parameters.

The relationship curves of wetting stress level with wetting axial strain and wetting volumetric strain under different confining pressures are drawn by the wetting axial strain calculation model and the wetting volumetric strain calculation model determined in Section 2. In finite element numerical simulation, the corresponding confining pressure and stress level are calculated from the stress state of Gauss points of each element; through the interpolation calculation of the current confining pressure and stress level in the wetting calculation model, the wetting axial strain and wetting volumetric strain of each unit are obtained. The wetting deformation calculated by each unit is distributed to each strain component of the total strain of the current load step. The wetting deformation corresponding to each submerged unit is transformed into an equivalent nodal force applied to the sample, and the additional deformation is calculated as the wetting deformation.

4.2 Computational analysis of the P-Z wetting model

The finite element numerical simulation of the P-Z intrinsic model used in this research are carried out in the GEHOMadrid finite element program. The P-Z model framework is clear and easy to implement in finite element programs. The static and dynamic analysis process of soil structures can be completed with a set of parameters. According to Formula (8), Formula (9) and literature (Pastor et al., 1985; Pastor et al., 1987), there are 12 parameters in the P-Z constitutive model of coarse-grained materials, including eight dimensionless parameters: M_g, M_f, α_g, α_f, β_0, β_1, H_0, γ_{DM}, and four stress unit parameters: H_{u0}, γ_u, K_{evo}, G_{eso}. Where K_{evo}, G_{eso}, M_g, α_g, and H_0 can be determined by triaxial static tests, and the remaining 7 parameters can be determined from the above 5 parameters by derivation of empirical formulae. The calculation and optimization of the parameters of the P-Z model are described in detail by the author of the research (Zhang et al., 2019). Due to the limited space, this paper no longer lists the specific process of determining parameters. The calculation parameters of the P-Z model are shown in Table 10.

The GEHOMadrid finite element program was used to carry out numerical simulations of the wetting deformation of coarse-

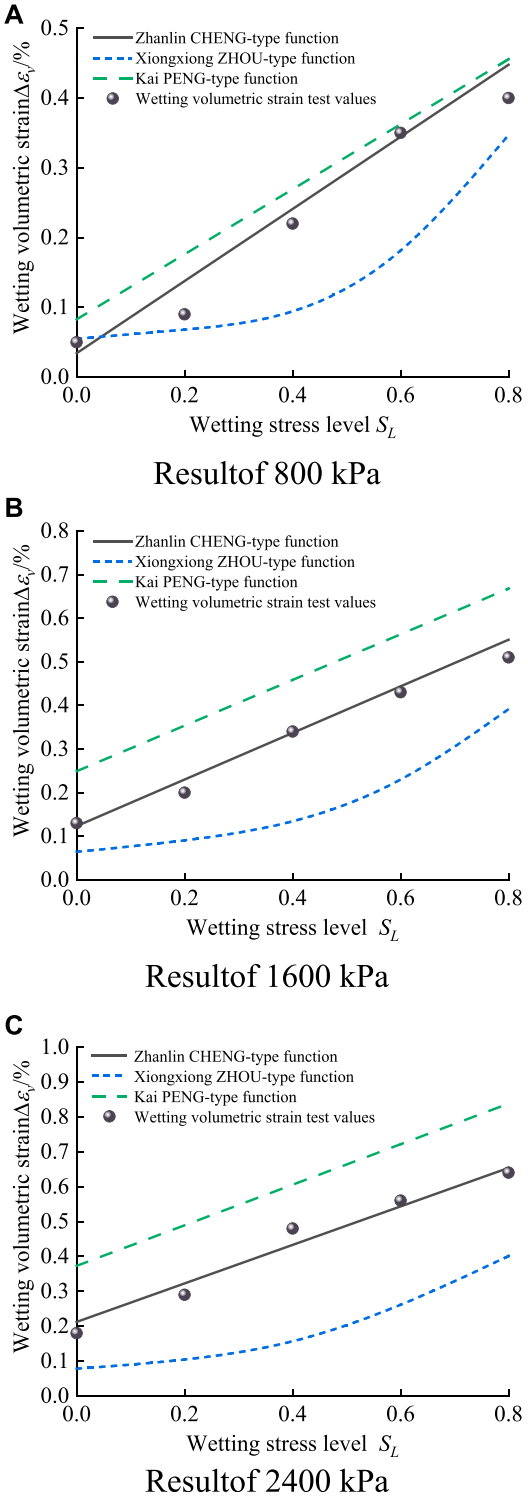

FIGURE 5
Comparison of simulation results and test results of three wetting volumetric strain models. **(A)** Result of 800 kPa **(B)** Result of 1,600 kPa **(C)** Result of 2,400 kPa.

grained materials. A cylindrical specimen with an internal diameter of 150 mm and a height of 300 mm was used in the triaxial wetting test. The finite element model of the specimen is shown in Figure 6, with a total of 1760 elements and 1983 nodes generated. Based on the P-Z wetting model, finite element simulations of triaxial compression tests are carried out on the

TABLE 10 Parameters of the P-Z constitutive model for coarse-grained materials.

Parameters	M_g	M_f	α_g	α_f	β_0	β_1
Numerical values	1.73	0.97	0.45	0.45	4.2	0.2
Parameters	H_0	γ_{DM}	γ_u/kPa	H_{u0}/kPa	K_{evo}/kPa	G_{eso}/kPa
Numerical values	34.83	0	0	0	5,581	18493.40

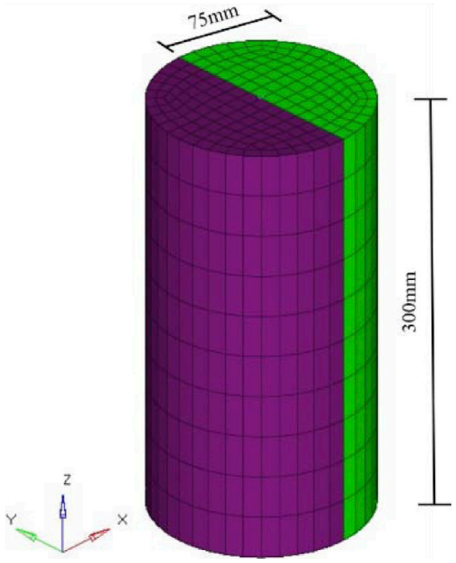

FIGURE 6
Simulation diagram of actual specimen for triaxial tests.

specimens. The simulation results are compared and analyzed with the triaxial test results to verify the rationality of the P-Z wetting procedure.

According to the standard for geotechnical test methods, when the axial strain of the specimen reaches 15% of the specimen height, it is considered a shear failure. The P-Z wetting program was used to numerically simulate three types of confining pressure conditions at 800kPa, 1600kPa, and 2400kPa, respectively. The calculated results of the simulated triaxial wetting test are shown in Figures 7, 8 shows the comparison between the triaxial wetting test and the numerical simulation results.

The comparison results show that the maximum axial strain error at 800 kPa is 9.5% and the maximum volumetric strain error is 8.6%; the maximum axial strain error at 1,600 kPa is 7.7%, and the maximum volumetric strain error is 9.1%; the maximum axial strain error at 2,400 kPa is 9.5%, and maximum volumetric strain error is 7.4%. With the increase of confining pressure, the error decreases gradually. The main reason is that before the axial strain reaches 10%, the deformation of the sample during the test is greatly affected by the factors such as rubber membrane embedding, which leads to the error of the data, but the error is in the range of 7.4%–9.5%, which is less than 10%. It shows that the P-Z model shows good adaptability to the stress-related properties of coarse-grained materials under complex stress paths and can better simulate the wetting deformation pattern of coarse-grained materials.

4.3 BP neural network wetted deformation prediction model

Based on the P-Z wetting model of coarse granular material, BP neural network is introduced to train the wetting test deformation and establish an artificial neural network (Zhang et al., 2021; Ju et al., 2005) wetting deformation model based on the P-Z model, which enables a better mapping of the non-linear relationship between wetting deformation of earth-rock dams and its influencing factors. It reduces the influence of systematic and chance errors in wetting deformation analysis. A three-layer BP neural network is selected, relying on increasing the number of nodes in the hidden layer to obtain a lower error. The input layer corresponds to the confining pressure and the wetting stress level, and the output layer corresponds to the wetting deformation. An empirical formula is used to determine the optimal number of nodes in the hidden layer, as shown in Formula (10). The topology and flow chart of the neural network wetting deformation model is shown in Figures 9, 10.

$$h = \sqrt{m+n} + a \tag{10}$$

Where:

h = the number of nodes in the hidden layer, m, n = the number of nodes in the input and output layers,

a = a regulation constant between 1 and 10.

Based on the P-Z wetting model, a total of 60 sets of wetting axial strain and wetting volumetric strain data at five wetting stress levels of 0,0.2,0.4,0.6 and 0.8 under 12 confining pressure conditions of 200 kPa, 400 kPa, 600 kPa, 800 kPa, 1,000 kPa, 1,200 kPa, 1,400 kPa, 1,600 kPa, 1800 kPa, 2000 kPa, 2,200 kPa and 2,400 kPa are used as training samples. The first 50 groups are used as the training set and the last 10 groups are used as the testing set. When the network training is iterated 95 and 98 times, the error cost function is satisfied, and the convergence process at the end of training is shown in Figure 11.

Figure 12 is the comparison between the experimental values and the predicted values of wetting deformation under five wetting stress levels with different confining pressures and the relative error of the prediction model. From Figure 12, it can be seen that the absolute error of the wetting axial strain prediction is in the range of

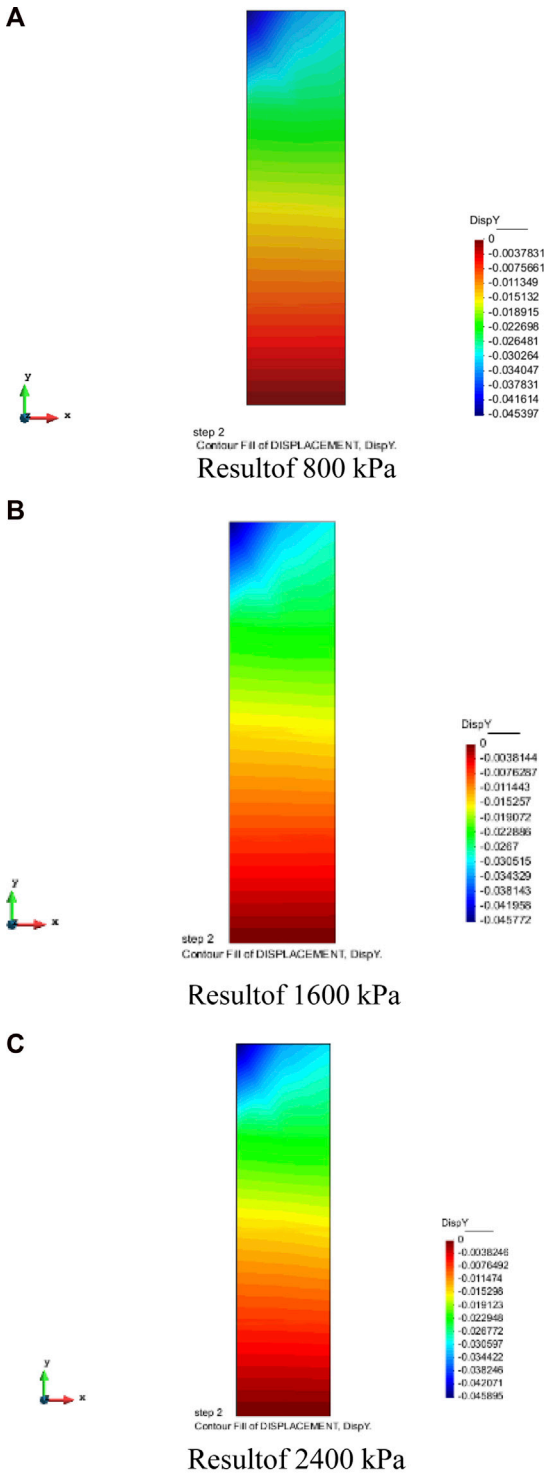

FIGURE 7
Simulation diagram of P-Z wetting model **(A)** Result of 800 kPa **(B)** Result of 1,600 kPa **(C)** Result of 2,400 kPa.

0.00086%–0.033%, with an average error of 0.011%, and the relative error is controlled within 1.041%–6.980%, with an average relative error of 4.094%, which are basically control within7%. The absolute error in the prediction of wetting volumetric strain ranged from 0.0029%–0.0115%, with an average error of 0.0122%, and the relative error is basically controlled within 0.5800%–5.872%, with an average relative error of 3.671%, which are basically controlled within 6%. This is due to the fact that the initial weights of the neural

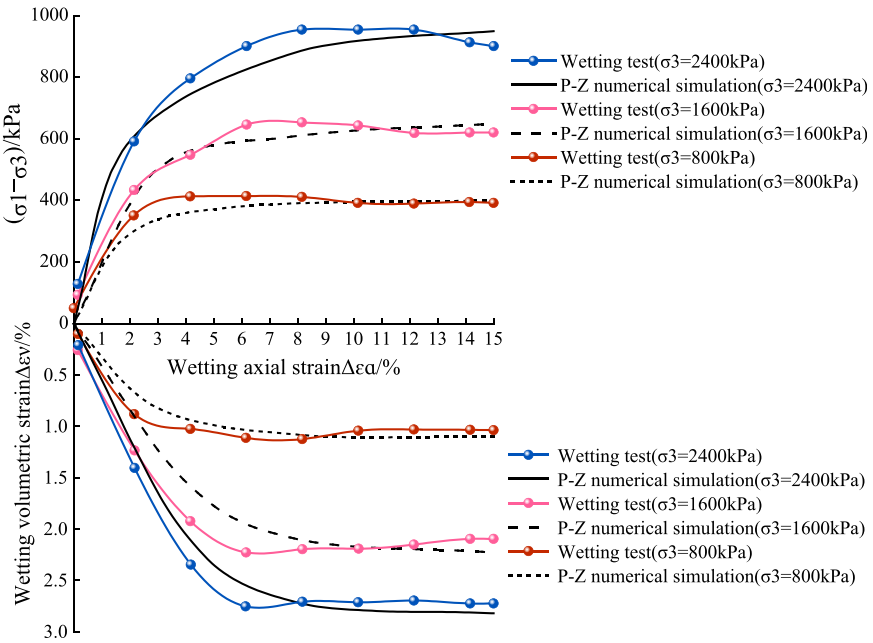

FIGURE 8
Comparison of simulation results and test results of the P-Z wetting Model.

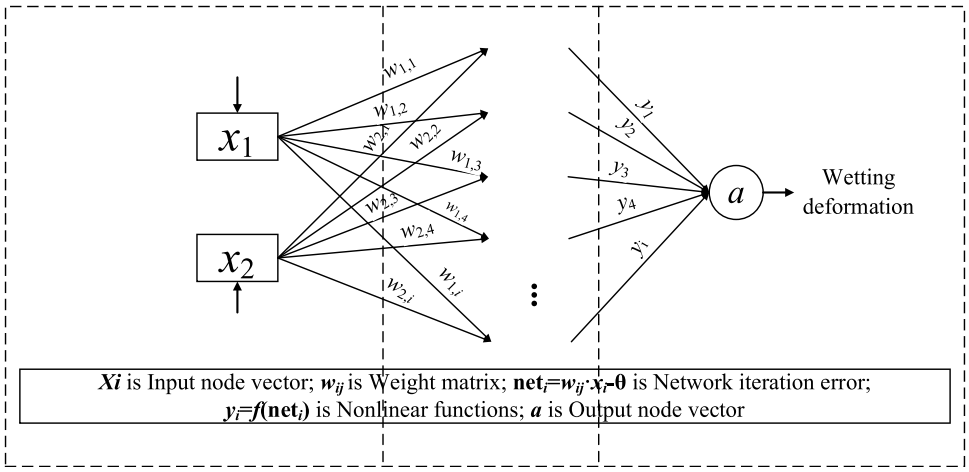

FIGURE 9
BP neural network topology.

network are randomly given, and the number of training sessions and the final weights will be slightly different each time, as well as the fact that there are human errors in the finite element numerical simulation and test conditions and test methods based on the P-Z model, resulting in differences between the prediction results and the test results. The relative error of the prediction model in this paper is basically controlled within 6%, so it can be considered that the neural network model is more reliable and accurate, which can meet the accuracy requirements for the prediction of wetting deformation.

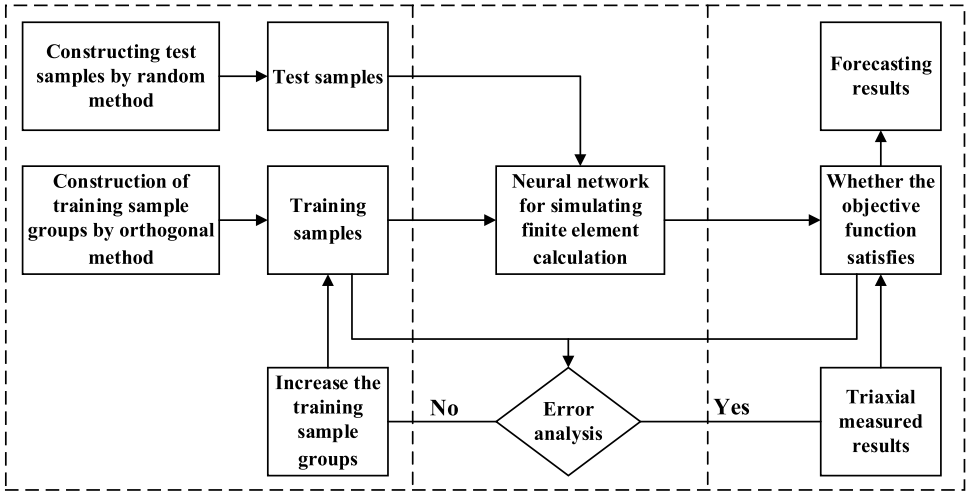

FIGURE 10
Analysis method of wetting deformation prediction model of BP neural network.

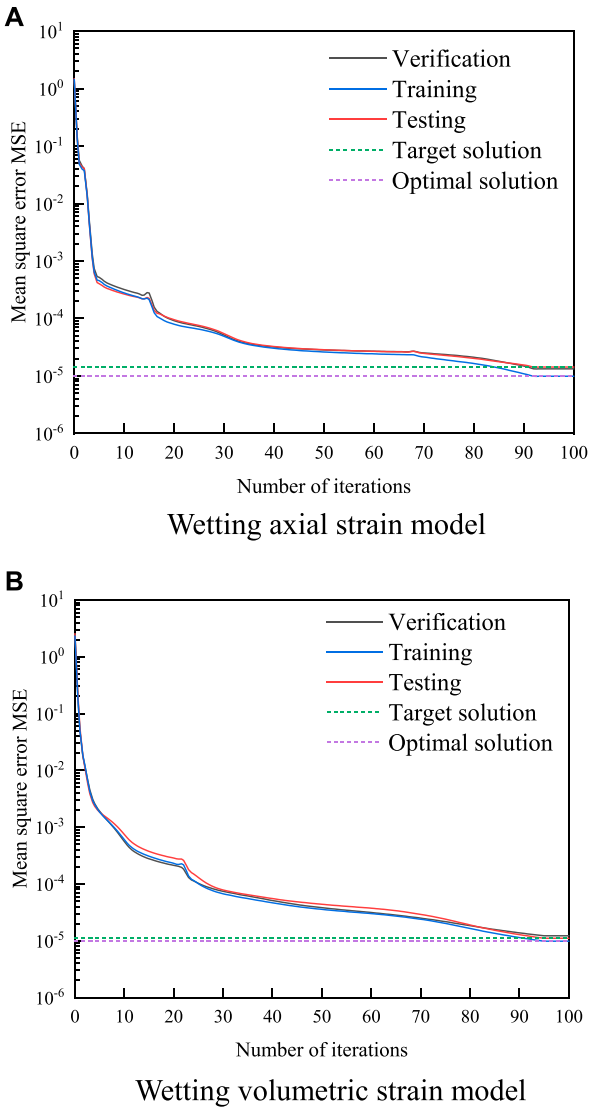

FIGURE 11
Iterative process of wetting prediction model. **(A)** Wetting axial strain model **(B)** Wetting volumetric strain model.

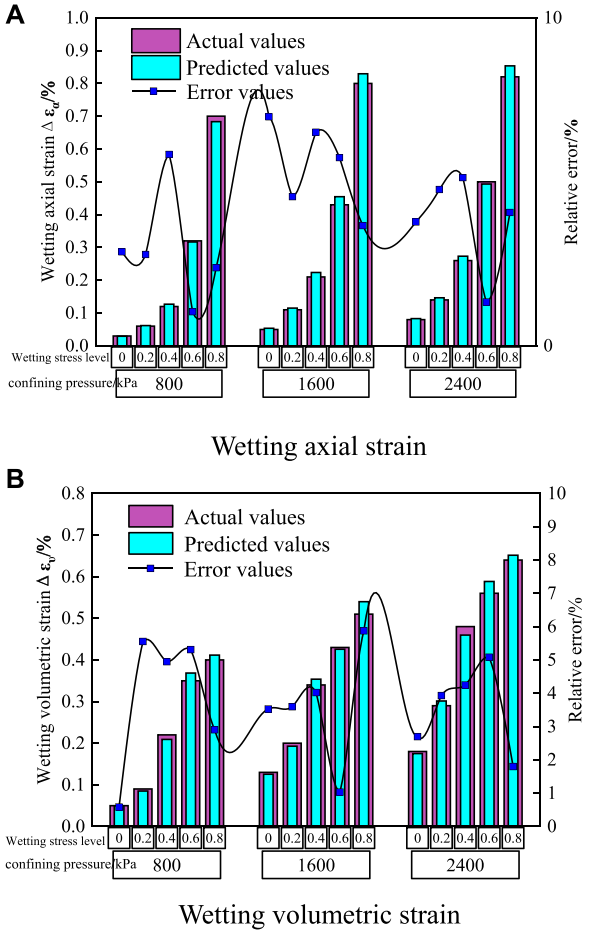

FIGURE 12
Comparison of predicted and measured values of wetting deformation. **(A)** Wetting axial strain **(B)** Wetting volumetric strain.

5 Conclusion

In this research, based on the previous research results of wetting deformation, the model parameters are fitted by triaxial wetting test data, and the wetting deformation of each model is calculated and compared with the test data. The proposed wetting axial strain model and wetting volumetric strain model are verified and analyzed. The P-Z model is improved by using the empirical formula of the wetting model. Based on the P-Z wetting model, the BP neural network is introduced to train the deformation of the wetting test, and the artificial neural network wetting deformation prediction model based on the P-Z model is established. Finally, the following conclusions are drawn.

(1) The experimental data are used to fit the parameters to the wetting model proposed by the previous authors and to calculate the wetting deformation, and the results showed that: The relationship between wetting axial strain and wetting stress level is best fitted by exponential function I (Formula 1); The relationship between the wetting volumetric strain and the wetting stress level is best fitted by the linear function expression of Cheng (Formula 5).

(2) The results of the finite element numerical simulation based on the P-Z wetting model are compared with the results of the triaxial wetting test to verify the accuracy of the P-Z wetting model in simulating the wetting deformation law of coarse-grained materials, indicating that the P-Z model can better reflect the wetting deformation characteristics of coarse-grained materials under complex stress paths, providing a basis for the application of the P-Z model in practical engineering.

(3) In the proposed BP neural network wetting deformation prediction model, the relative error between the predicted and tested values are controlled within 6%, indicating that the prediction model is more reliable and accurate, and can meet the accuracy requirements for wetting deformation prediction.

Data availability statement

The original contributions presented in the study are included in the article/supplementary material further inquiries can be directed to the corresponding author.

Author contributions

HZ: Funding acquisition, Investigation, Content conception, Data analysis and Resource; XL, PH, and YY: Experimental protocol design,Operation, Data processing; XL: Writing, Forming the first draft, and Further analysis. JL, ZD, and LH: Software, Supervision, and Validation; XZ and SW: Reviewed the text and revised the draft.

Funding

This study was supported by the National Natural Science Foundation of China (No. 51609087, 52079051), Key Scientific Research Projects of Colleges and Universities in Henan Province (No.21A570001, 22A570004, 23A570006) and Collaborative Innovation Center for Efficient Utilization of Water Resources in Yellow River Basin.

Conflict of interest

The authors declare that the research was conducted in the absence of any commercial or financial relationships that could be construed as a potential conflict of interest.

Publisher's note

All claims expressed in this article are solely those of the authors and do not necessarily represent those of their affiliated organizations, or those of the publisher, the editors and the reviewers. Any product that may be evaluated in this article, or claim that may be made by its manufacturer, is not guaranteed or endorsed by the publisher.

References

Chen, J. (2019). Study on wetting deformation characteristics of low permeability gravel soil core wall material. *J. Yangtze River Sci. Res. Inst.* 2019, 1. doi:10.26982/d.cnki.gcjky.2019.000001

Cheng, Z. L., Zuo, Y. Z., Ding, H. S., Jiang, J. S., and Kong, X. Y. (2010). Wetting characteristics of coarse-grained materials. Chin. J. Geotech. *Eng.* 32 (02), 243–247.

Chi, S. C., and Zhou, X. X. (2017). Slaking deformation model for rockfill materials. *Chin. J. Geotech. Eng.* 39 (01), 48–55. doi:10.11779/CJGE201701002

Ding, Y. H., and Qian, X. X. (2022). Study on the numerical model and computational method of wetting deformation of rockfill materials. *Water Resour Hydropower Eng* 53 (S1), 455–462. doi:10.13928/j.cnki.wrahe.2022.S1.076

Ge, W., Qin, Y. P., Li, Z. K., Zhang, H. X., Gao, W. X., Guo, X. Y., et al. (2020). Aninnovative methodology for establishing societal life risk criteria for dams: A case study to reservoir dam failure events in China. *Int. J. Disaster Risk Reduct.* 49, 101663. doi:10.1016/j.ijdrr.2020.101663

Ge, W., Jiao, Y. T., Wu, M. M., Li, Z. K., Wang, T., Li, W., et al. (2022). Estimating loss of life caused by dam breaches based on the simulation of floods routing and evacuation potential of population at risk. *J. Hydrol.* 612, 128059. doi:10.1016/j.jhydrol.2022.128059

Jia, Y. F., Xu, B., Desai, C. S., Chi, S. C., and Xiang, B. (2020). Rockfill particle breakage generated by wetting deformation under the complex stress path. *Int. J. Geomech.* 20(10), 4020166. doi:10.1061/(ASCE)GM.1943-5622.0001789

Jia, Y. F., Xu, B., Chi, S. C., Xiang, B., Xiao, D., and Zhou, Y. (2018). Joint back analysis of the creep deformation and wetting deformation parameters of soil used in the Guanyinyan composite dam. *Comput. Geotech.* 96, 167–177. doi:10.1016/j.compgeo.2017.10.018

Jia, Y. F., Xu, B., Chi, S. C., Xiang, B., Xiao, D., and Zhou, Y. (2019). Particle breakage of rockfill material during triaxial tests under complex stress paths. *Int. J. Geomech.* 19 (12), 04019124. doi:10.1061/(ASCE)GM.1943-5622.0001517

Jie, Y. X., Zhang, Y. Y., and Yang, G. H. (2019). Discussion on calculation method of wetting deformation of earth-rock materials. *Rock Soil Mech.* 40 (S1), 11–20. doi:10.16285/j.rsm.2019.0276

Ju, S. Q., Gu, C. S., and Hou, Y. C. (2005). Settlement model for earth-rock dams based on artificial neural networks. *Water Resour Power* 1 (01), 76–78+94. doi:10.3969/j.issn.1000-7709.2005.01.025

Lin, D. T., Zhu, S., Wu, M. K., Chen, X. H., and Ying, J. T. (2017). Cause analysis of crest cracking of Pubugou rockfill dam with a central gravelly soil core during first reservoir impounding. *Hydroelectr. Power* 43 (10), 56–61. doi:10.3969/j.issn.0559-9342.2017.10.015

Miao, L. Q. (2018). Experimental study on evaluation of loess subsidence in southern hebei area based on single and double-oedometer methods. *J. Hebei GEO Univ.* 41 (05), 44–47. doi:10.13937/j.cnki.hbdzdxxb.2018.05.006

Niu, A. (2020). *Experimental study on wet deformation of coarse-grained aggregates in earth-rock dams*. Zhengzhou: North China University of Water Resources and Electric Power.

Pastor, M., Zienkiewicz, O. C., and Chan, A. (1987). *A generalized plasticity continuous loading model for geomaterials*. State of New Jersey: Engineering, Theory and Application.

Pastor, M., Zienkiewicz, O. C., and Leung, K. H. (1985). Simple model for transient soil loading in earthquake analysis. II. Non-associative models for sands. *Int. J. Numer. Anal. Meth. Geomech.* 9, 477–498. doi:10.1002/nag.1610090506

Peng, K., Zhu, J. G., and Wang, G. Q. (2010). Study on slaking deformation of rockfill materials by triaxial test. *J. Cent. South Univ. Sci. Technol.)* 41 (05), 1953–1960. doi:10.3969/j.issn.1000-7598.2007.08.015

Sun, X. J., Pan, J. J., Zhou, Y. F., and Zuo, Y. Z. (2023). A comparative study of the wetting deformation model of the single-line method of damming coarse grain. *J. Yangtze River Sci. Res. Inst.* 40 (1), 146–152+160. doi:10.11988/ckyyb.20210869

Wang, T., Li, Z. K., Ge, W., Zhang, Y. D., Jiao, Y. T., Sun, H. Q., et al. (2022). Calculation of dam risk probability of cascade reservoirs considering risk transmission and superposition. *J. Hydrol.* 609, 127768. doi:10.1016/J.JHYDROL.2022.127768

Wang, T., Li, Z. K., Ge, W., Zhang, H., Zhang, Y. D., Sun, H. Q., et al. (2023). Risk consequence assessment of dam breach in cascade reservoirs considering risk transmission and superposition. *Energy* 265, 126315. doi:10.1016/J.ENERGY.2022.126315

Wei, S., and Zhu, J. G. (2007). Study on the wetting behavior of coarse-grained soil in triaxial test. *Rock Soil Mech.* 08, 1609–1614. doi:10.16285/j.rsm.2007.08.017

Wu, M. M., Wu, Z. N., Ge, W., Wang, H. L., Shen, Y. X., Jiang, M. M., et al. (2021). Identification of sensitivity indicators of urban rainstorm flood disasters: A case study in China. *J. Hydrol.* 599, 126393. doi:10.1016/J.JHYDROL.2021.126393

Xu, Z. P. (2018). Laos-preliminary analysis and thinking on the dam failure of sang nam nei hydropower station. *Express Water Resour. Hydropower Inf.* 39 (08), 6–10. doi:10.15974/j.cnki.slsdkb.2018.08.001

Zhang, H. Y., Han, P. J., He, Q., Sun, Y. D., Song, Z. Y., Ding, Z. L., et al. (2022). Research on wetting deformation model of coarse-grained materials of earthrock dam. *Arab. J. Geoscci* 15 (4), 350. doi:10.1007/s12517-022-09619-w

Zhang, H. Y., Song, Z. Y., Peng, P., Sun, Y. D., Ding, Z. L., and Zhang, X. Q. (2021). Research on seepage field of concrete dam foundation based on artificial neural network. *Alex Eng. J.* 60 (1), 1–14. doi:10.1016/j.aej.2020.03.041

Zhang, H. Y., Zhang, W. X., Ding, Z. L., Li, S., and Ge, W. (2019). Parameter optimization method for the pastor-zienkiewicz model based on empirical mode decomposition and cloud theory. *J. Eng. Sci. Technol. Rev.* 12 (6), 44–53. doi:10.25103/jestr.126.06

Zhou, X. X., Chi, S. C., and Jia, Y. F. (2019). Wetting deformation characteristics of coarse granular materials. *Chin. J. Geotech. Eng.* 41 (10), 1943–1948. doi:10.11779/CJGE201910020

Zou, D. G., Fu, M., Liu, J. M., and Kong, X. J. (2013). Study of adaptability of a generalized plastic model of coarse-grained soil under various stress paths. *J. Dalian Univ. Technol.* 53 (05), 702–709. doi:10.7511/dllgxb201305014

Zuo, Y. M., and Shen, Z. J. (1989). Determination of the deformation character of gravel sand due to wetting. *Hydro-Science Eng.* 1 (01), 107–113. doi:10.16198/j.cnki.1009-640x.1989.01.010

frontiers | Frontiers in Earth Science

TYPE Original Research
PUBLISHED 10 May 2023
DOI 10.3389/feart.2023.1196677

OPEN ACCESS

EDITED BY
Wei Ge,
Zhengzhou University, China

REVIEWED BY
Wei Li,
Zhengzhou Railway Vocational and Technical College, China
Xiangdong He,
Henan Provincial Water Conservancy Research Institute, China

*CORRESPONDENCE
Ming Chen,
chenming202205@126.com

RECEIVED 30 March 2023
ACCEPTED 25 April 2023
PUBLISHED 10 May 2023

CITATION
Han L, Chen M, Sun Z, Si J, Ma L, Ji W and Zhang H (2023), Stability analysis of slopes based on cloud model-Monte Carlo coupling.
Front. Earth Sci. 11:1196677.
doi: 10.3389/feart.2023.1196677

Stability analysis of slopes based on cloud model-Monte Carlo coupling

Liwei Han[1,2], Ming Chen[1]*, Zuozhuang Sun[1], Jiaxuan Si[1], Liyuan Ma[1], Wenhui Ji[1] and Hongyang Zhang[1]

[1]School of Water Conservancy, North China University of Water Resources and Electric Power, Zhengzhou, China, [2]Henan Key Laboratory of Water Environment Simulation and Treatment, Zhengzhou, China

Risk analysis of dam slopes is crucial for ensuring the safety and stability of hydraulic engineering. To improve the accuracy and reliability of risk analysis, we adopt the cloud theory approach and conduct a study on the distribution types of soil shear strength indicators based on indoor geotechnical tests. We propose a "cloud model-Monte Carlo" coupling model that uses the cloud model to describe the uncertainty of risk factors and determine the probability distribution types of shear strength parameters, while the Monte Carlo method is used to simulate random variables in the model. The effectiveness of the proposed model is validated through a risk analysis of a slope of an earth-rock dam, with results showing significantly greater accuracy and reliability compared to traditional methods. The calculation results show that the risk probability corresponding to the design flood level of the dam is 9.01×10^{-6}, exceeding its allowable risk standard of 0.5×10^{-6}, hence the need for reinforcement treatment. The proposed model can accurately evaluate the risk of dams and provide the scientific basis for decision-making in dam safety management.

KEYWORDS

shear strength index, probability distribution type, cloud theory, earth and rock dams, risk analysis

1 Introduction

In recent years, with the continuous acceleration of urbanization and the development of engineering construction, geological disasters have posed a serious threat to people's life and property safety (Tu et al., 2023). Among them, the slope stability problem has been a hot issue of great concern in geological engineering (Wen et al., 2022). In slope control, the soil shear strength parameter is one of the most important parameters for evaluating the safety of slope engineering. To analyze the risk of dam landslides, Monte Carlo simulation is a widely used method for dam slope risk analysis (Lu et al., 2022), which involves generating random samples of uncertain variables and simulating the dam behavior under different scenarios. However, traditional Monte Carlo simulations assume that the uncertain variables follow a specific probability distribution (Chorol and Gupta, 2023). In contrast, cloud modeling is a novel uncertainty modeling approach (Cheng et al., 2022) that captures the stochasticity and ambiguity in uncertain variables. Therefore, we propose a new approach combining cloud models and Monte Carlo simulations to analyze dam landslide risk. Specifically, we use the cloud model for solving

uncertainty problems and Monte Carlo simulation for generating stochastic samples and simulating dam behavior.

In previous studies, conventional methods (Rouzéa and Dattaa, 2016; Wang-Wang et al., 2018; Zhang et al., 2022a) have faced uncertainty issues in parameter selection under limited data conditions, leading to the simultaneous fitting of multiple distribution functions. In contrast, cloud theory can address the uncertainty problem in distribution types. Cloud theory was proposed by Professor Li (Li et al., 2009), which can effectively convert quantitative and qualitative information and visualize it through cloud maps (Ma and Zhang, 2020). Among them, the normal cloud model is the most important type of cloud model and has been widely used in prediction, comprehensive evaluation, data mining, intelligent control, and other fields (Liu et al., 2021; Ruan et al., 2021). Cloud theory has also been extensively applied in the assessment field (Chen et al., 2023; Guojiao et al., 2023). Monte Carlo simulation, as a classic random number simulation method, has been extended to various fields such as medicine (Santos et al., 2022), water conservancy (Vihola et al., 2020), and science and technology materials (Wang et al., 2020). Considering the scalability and reliability of cloud models in fuzzy decision-making fields (Mao et al., 2018; Mao et al., 2022; Yang et al., 2023), we developed a "cloud model-Monte Carlo" coupling model to calculate slope failure probability and perform risk assessment.

Risk analysis originated in the United States (Xie and Sun, 2009) and was first applied in nuclear power plant risk assessment. Risk analysis includes identifying potential hazards (Ge et al., 2020a), assessing their likelihood and consequences, and formulating mitigation measures to reduce risks (Wu et al., 2021; Zhang et al., 2022b). In terms of dam safety, hazardous situations include natural disasters such as floods or earthquakes, as well as human errors or equipment malfunctions. The consequences of these hazards can range from property and economic losses to loss of life and environmental degradation (Ge et al., 2020b; Wu et al., 2020; Ge et al., 2022; Zhang et al., 2023). Various methods such as probabilistic risk assessment and quantitative risk analysis (Li et al., 2018; Wang et al., 2022) can be used for risk assessment. These methods involve collecting design, location, and operation data of the dam, as well as external factors such as weather patterns and geological conditions. Based on these data, mathematical models are established to simulate the performance of the dam under different hazardous situations and estimate associated risks (Li et al., 2021; Wang et al., 2023).

In the past few decades, many studies have focused on developing probabilistic methods to analyze slope stability (Cai et al., 2021; Chakraborty and Dey, 2022) and have demonstrated their superiority in risk assessment. However, many factors need to be considered when evaluating slope stability (Raghuvanshi, 2019; Yang et al., 2021), and simple deterministic methods may not satisfy complex practical situations. This article aims to introduce a probabilistic-based method, where we propose a new approach for slope stability analysis based on the "cloud model-Monte Carlo". We demonstrate the effectiveness of this method by applying it to a case study of earth-rockfill dams. The proposed method provides an assessment of dam landslide risk and can provide a reference for decision-makers to formulate effective risk management strategies.

2 Materials and methods

2.1 Indoor tests

The experimental parameters employed in this study were derived exclusively from indoor geotechnical tests utilizing remolded soil samples. Sampling was conducted within a rectangular area located in the northeast of Tianshuihu, Pingyu County, China, with dimensions of approximately 500 m in length and 150 m in width. According to the geological profile of the region, the geological structure of the Tianshuihu area is characterized by homogeneous cohesive soils, mainly composed of fourth-quaternary loamy soil and clay. To mitigate uncertainties arising from spatial and temporal factors, sampling depth was limited between half a meter to 1 m, with the obtained soil samples being plastic loamy soil. After the sifting of soil samples, direct shear testing was performed, following the specific steps outlined in Figure 1.

In this study, 26 sets of powdered clay test data obtained from indoor direct shear tests were selected for the study, including the shear strength index c and the internal friction angle index φ. The specific values are shown in Table 1.

2.2 Research overview

The earth-rockfill dam (Yong, 2004) is a rolled clay core wall dam with a maximum dam height of 70 m, a crest width of 12 m, and a base width of 465 m. The normal water level is 185 m, the dead water level is 167 m, the total storage capacity is 1.13 billion m^3, and the effective storage capacity is 570 million m^3. The upstream slope is from bottom to top at a ratio of 1:4.0, 1:3.5, 1:3.0, 1:2.0, and the downstream slope is from bottom to top at a ratio of 1:4.0, 1:3.0, 1:2.0. Approximately 144 m below the dam base is a thick clay core wall, and the slope is 1:4.0, 1:0.5. Above 144 m, the slope is 1:0.1–1:0.2. The river length above the hub dam site is 120 km, the controlled drainage area is 2,000 square kilometers, the annual average flow rate is 37.8 m^3/s, and the annual average runoff volume is 1.2 billion m^3. The design flood peak flow rate corresponding to a once-in-a-millennium event is 6,640 m^3/s, and the corresponding flood level is 188.1 m. The verification flood peak flow rate corresponding to a once-in-a-ten-thousand-years event is 8,700 m^3/s, and the corresponding flood level is 189.5 m.

The analysis object is the unreinforced earth-rockfill dam with an upstream water level of 188.1 m, a downstream water level of 132.0 m, and a dam base elevation of 120.0 m. The non-stochastic mechanical parameters of the dam body are shown in Table 2. In recent years, the reservoir has had many safety hazards: the core wall narrows above the elevation of 144 m, and the slope decreases from the original ratio of 1:0.5 to 1:0.1; starting from an elevation of 150 m, gravelly soil has been used in the core wall, resulting in severe seepage of the dam body, the infiltration line overflows the dam slope, and large-scale mortification occurs on the downstream slope, which affects the stability and safety of the dam body.

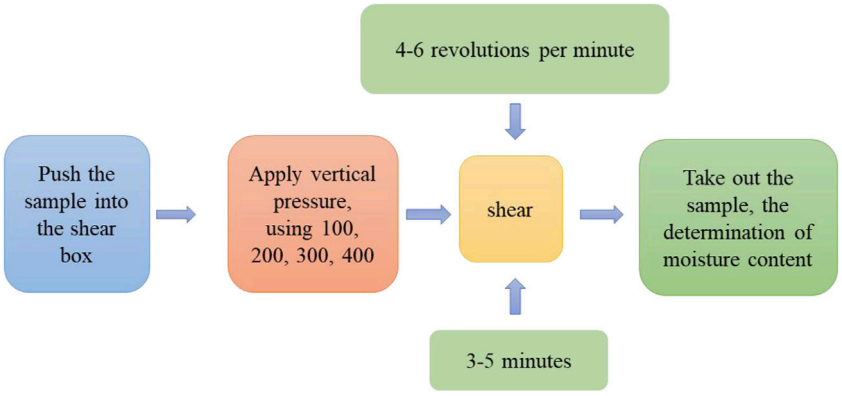

FIGURE 1
Shear test steps.

TABLE 1 Record sheet of direct shear test for soil samples (No. 1–26 soil).

Group	Cohesion (kPa)	Internal friction angle φ (°)	Group	Cohesion (kPa)	Internal friction angle φ (°)
1	12.2	10.4	14	18.9	15.8
2	15	11.6	15	16.3	16.8
3	15	12.2	16	16.4	17
4	15	12.4	17	17.2	17.2
5	19.7	13.5	18	17.3	17.2
6	15	14	19	17.3	18.8
7	15.5	14	20	21	18.8
8	21.8	14.6	21	17.7	19.5
9	15.8	15.1	22	17.7	19.5
10	15.8	15.4	23	18.3	20.9
11	15.8	15.6	24	18.3	21.5
12	18.8	15.6	25	18.3	24.6
13	16	15.7	26	18.4	25.9

TABLE 2 Non-random mechanical parameters of earth and rock dams.

Physical properties	Wet capacity	Dry capacity	Saturated capacity	Floating capacity
Unit	t/m^3	t/m^3	t/m^3	t/m^3
Quantity	1.995	1.730	2.090	1.090

2.3 Model construction

The "cloud theory-Monte Carlo" approach to analyzing the risk of earth and rock dams is shown in Figure 2.

The method proposed in this paper is a cloud model used to determine the type of probability distribution of shear strength parameters. Monte Carlo methods are used to simulate the random variables in the cloud model and to calculate the probability of dam slope failure based on the probability distribution of the random variables.

2.3.1 Basic principles of cloud model

The cloud model, based on fuzzy mathematics and statistical theory, is a powerful tool for describing the randomness and fuzziness between uncertain language and precise numerical values. It has been applied to several uncertain problems and

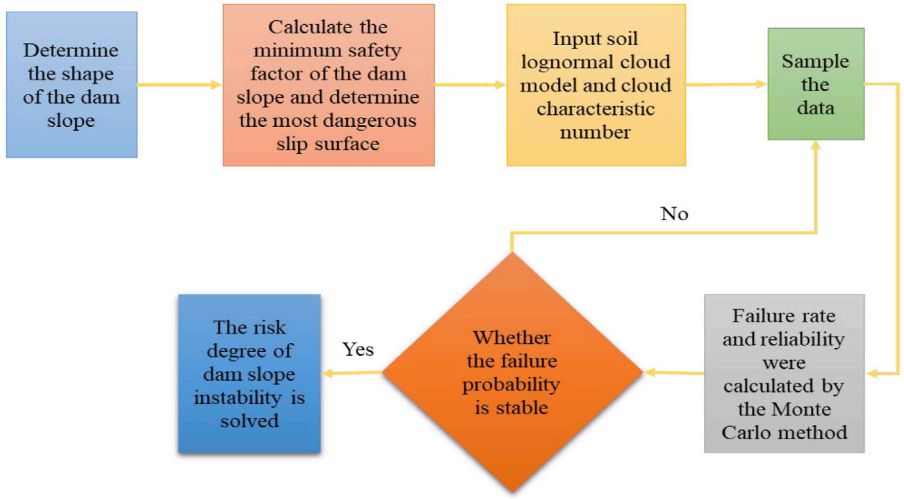

FIGURE 2
Flow chart of the "cloud theory—Monte Carlo" based dam slope instability calculation.

owing to its superiority in handling uncertainty issues, we have incorporated it into our study of inferred soil shear strength distribution indices.

Let U be a quantified domain represented by precise numerical values, and C be a qualitative concept defined on the domain U. If the quantitative value $x \in U$ is a random realization of the qualitative concept C, and satisfies $x \sim N(Ex, En'^2)$, where $En' \sim N(En, He^2)$, and the degree of certainty of x for C satisfies μ, then the distribution of x on the domain U is known as the normal cloud.

$$\mu = e^{-\frac{(x-Ex)^2}{2(En')^2}} \tag{1}$$

The cloud model no longer emphasizes precise function representation (Yangping et al., 2019), but instead employs three numerical features to represent the uncertainty of concepts: expectation "*Ex*", entropy "*En*", and hyper-entropy "*He*". "*Ex*" represents the central position of the concept in the domain and is the value that best represents this qualitative concept. "*En*" describes the level of discreteness of the qualitative concept, characterizing its randomness and fuzziness. The greater the entropy, the larger the range of acceptable numerical values for the concept, making the concept more macroscopic. "*He*" is a measure of uncertainty in entropy and is generally determined empirically. According to the 3"*En*" rule of statistics, the cloud droplets contributing to the concept are typically situated within the interval [*Ex*-3*En*, *Ex*+3*En*].

2.3.2 Inverse cloud algorithm optimization

The radiation fitting algorithm of the inverse cloud generator is based on the radiative digital characteristics of clouds and their corresponding radiative expectation functions. It expresses the probability distribution characteristics of cloud droplets' energy radiation over the entire numerical domain space. By following data radiation and improving the inverse cloud generator algorithm based on its fitting, the specific description of the algorithm is as follows:

Input: The coordinates *li* of each cloud droplet in the numerical domain space along with their respective degree of certainty $C_T(l)$ representing the concept.

Output: The values of *Ex*, *En*, and *He* for the concept, and the number of cloud droplets *N*.

The estimated value $\hat{E}x(l)$ of *Ex* is obtained by fitting the known cloud droplets using the cloud expectation curve $C_T(l)$.

$$C_T(l) = \frac{1}{\hat{f}(l)} e^{-\frac{\left[\hat{f}(l)(l-\hat{E}x)\right]^2}{2[\hat{E}n(l)]^2}} \tag{2}$$

$$\hat{E}x(l) = \frac{\sum_{i=1}^{n} \hat{f}(l_i) l_i}{\sum_{i=1}^{n} \hat{f}(l_i)} \tag{3}$$

The cloud droplets with $C_T(l) > 0.999$ are removed, leaving m droplets. We then calculate $\hat{E}n(l_i)$; as well as $\hat{E}n(l)$ and $\hat{H}e(l)$, the estimated values of *En* and *He* respectively.

$$\hat{E}n(l_i) = \frac{\left|f(l_i)\left(l_i - \hat{E}x\right)\right|}{\sqrt{-2\ln\left(f(l_i)C_T(l_i)\right)}} \tag{4}$$

$$\hat{E}n(l) = \sqrt{\frac{\sum_{i=1}^{m}\left[\hat{f}(En(l_i))En(l_i)\right]}{\sum_{i=1}^{m}\left[\hat{f}(En(l_i))\right]}} \tag{5}$$

$$\hat{H}e(l) = \sqrt{\frac{\sum_{i=1}^{n}\left[\hat{f}(En(l_i))(En(l_i) - \hat{E}n(En(l_i))\right]^2}{\sum_{i=1}^{n}\hat{f}(En(l_i))}} \tag{6}$$

2.3.3 Cloud model pervasiveness

The geometric shape of the normal cloud has distinct characteristics, with its expectation curve reflecting the shape of the normal cloud. It can be deduced that for any $0<\mu\leq 1$, as determined by μ.

$$X = Ex \pm \sqrt{-2\ln\mu}En' \tag{7}$$

As En' is a random variable, and x is a symmetrical random variable located on both sides of Ex. Therefore, it is sufficient to analyze only X_1, as the analysis of X_2 is entirely analogous.

$$X_1 = Ex + \sqrt{-2\ln\mu}En' \tag{8}$$

$$X_2 = Ex - \sqrt{-2\ln\mu}En' \tag{9}$$

From $En' \sim N(En, He^2)$, it can be deduced that X follows a normal distribution with an expectation of EX and a standard deviation of B. Therefore, according to this formula, the discreteness of cloud droplets is directly proportional to He and inversely proportional to y. This implies that as He increases, so does the discreteness of cloud droplets, while decreasing y (i.e., approaching the foot of the mountain) leads to more dispersed cloud droplets.

$$EX = Ex + \sqrt{-2\ln\mu}En' \tag{10}$$

$$B = \sqrt{DX} = \sqrt{-2\ln\mu}He \tag{11}$$

By solving for μ from EX, the expectation curve y of the normal cloud can be obtained.

$$\mu = e^{\frac{-(EX-Ex)^2}{2En^2}} \tag{12}$$

$$y = e^{\frac{-(x-Ex)^2}{2En^2}} \tag{13}$$

2.3.4 Calculation of the coefficient of safety for dam slope stability

Because most slope stability analysis problems are super-stationary, SL274-2001(SL274-2001, DAMS, 2002) (Chinese Standards) states that the equations of ultimate equilibrium must be established using the simplified Bishop bar method the Swedish bar method, and the Spencer method.

According to the simplified Bishop's bar method, the following limiting equation of state is established.

$$G(X) = \frac{1}{\cos\alpha_i + \tan\varphi_i \sin\alpha_i}\left[c_i l_i + (w_i - u_i b_i)\tan\varphi_i\right] - w_i \sin\alpha_i \tag{14}$$

Where, α_i is the angle between the gravity line of the soil strip and the radius in the bottom surface passing through this line; c_i is the cohesive force at the bottom surface of the strip and φ_i is the angle of internal friction at the bottom surface of the strip; w_i is the self-weight of the strip; b_i is the width of the strip; and u_i is the pore water stress.

2.3.5 Calculation of the risk level of the dam slope

2.3.5.1 Calculation of $\Delta F_0(h_i)$

The number of levels upstream of an earth and rock dam is considered a random variable. Its calculation can be statistically analyzed on a long series of observations of the reservoir water level, which in turn leads to a probability plot of the probability distribution characteristics of the water level. Given a certain water as Z_m, the value of $\Delta F_0(h_i)$ is calculated from the corresponding frequency value. Alternatively, the value of $\Delta F_0(h_i)$ can be found by applying the probabilistic algorithm for reservoir regulation calculations concerning the literature (Yaowu and Dongwei, 1994).

2.3.5.2 Calculation of $\bar{F_L}(h_i)$

According to the previous description, $\bar{F_L}(h_i)$ represents the average probability that the sliding moment is greater than the anti-slip moment at a certain water level h_i. The expressions are.

$$\bar{F_L}(h_i) = \int_r^{\infty} f(l/h)dl \tag{15}$$

The specific condition probability density function for the sliding moment L of a dam under a certain water level H, denoted as (l/h) in the formula, is extremely complex, and its solution is very difficult to obtain. Nevertheless, using the Monte Carlo method can yield high results. The solution process for $\bar{F_L}(h_i)$ is related to the form of the slip surface, and different slip surfaces will produce different values. Therefore, it is necessary to determine the maximum value of $\bar{F_L}(h_i)$. However, directly seeking the maximum value is not practical. Hence, we first calculate the minimum safety factor $K_{\min}$ (Zhang et al., 2006) for the landside dam slope and then use the corresponding most dangerous slip arc to obtain the maximum value of $\bar{F_L}(h_i)$.

2.3.6 Coupled "cloud model-Monte Carlo" model for dam slope instability risk analysis

The relationship between the sliding moment S and the anti-slip moment R is a key factor affecting the stability of the dam slope. When $S>R$, the dam slope becomes unstable, according to which, the following mathematical model of the risk of instability of the slope of an earth and rock dam can be established, setting the functional function as

$$g(\cdot) = g(L, R) = R - L \tag{16}$$

$$P_f = P(L > R) = \iint_{g(\cdot)<0} f_{R,L}(r, l)drdl \tag{17}$$

Where, $f_{R,L}(r,l)$ is the joint probability density distribution function of the sliding moment L and the anti-slip moment R of the earth and rock dam.

Due to the great difficulties in the practical application of the above equation, it is transformed into

$$P_f = \int_{-\infty}^{\infty}\int_0^l f_R(r)dr f_L(l)dl = \int_{-\infty}^{\infty} F_R(l) f_L dl \tag{18}$$

The problem of using probabilistic combinations to estimate P_f indirectly exists and can be solved perfectly. Thus, let the joint probability density function of the sliding moment L and the water level upstream of the dam H be

$$f_{HL}(h, l) = f(l/h) f_o(h) \tag{19}$$

Where, (l/h) is the conditional probability density function of the water level H for the sliding moment L under the given conditions and the probability density function $f_o(h)$ is for the water level upstream of the dam.

The probability density function for the sliding moment L of an earth and rock dam slope can be calculated by the full probability density formula, expressed as follows:

$$f(l) = \int_{-\infty}^{\infty} f(l/h) f_0(h) dh \tag{20}$$

Combining Eq. 18 with Eq. 19 yields

$$\begin{aligned} P_f = P(L>R) &= \int_r^{\infty} \left[\int_{-\infty}^{\infty} f(l/h) f_0(h) dh \right] dl \\ &= \int_0^{\infty} \left[\int_{-\infty}^{\infty} f(l/h) dl \right] f_0(h) dh \end{aligned} \tag{21}$$

If

$$F_l(h) = \int_r^{\infty} f(l/h) dl \tag{22}$$

What about there

$$P_f = P(L>R) = \int_{h_1}^{h_2} F_l(h) f_0(h) dh \tag{23}$$

where, h_1 is the minimum water level specified in the risk of instability calculation for the earth and rock dam slopes and h_2 is the maximum water level specified in the risk of instability calculation for the earth and rock dam slopes.

Eq. 23 is the formula for calculating the risk of instability in the slope of an earth and rock dam, but it is very difficult to solve the formula directly by integration. Therefore, in the actual calculation, it is necessary to apply the method of discrete numerical integration to solve it. After dividing the part of the load probability density distribution curve on $L \leq h2$ into N segments, the solution is given by the following equation.

$$P_f = P(L>R) = \int_{h_1}^{h_2} F_l(h) f_0(h) dh = \sum_{i=1}^{N} \Delta F_0(h_i) \bar{F}_L(h_i) \tag{24}$$

Where, $F_l(h)$ is the probability that the sliding moment corresponding to a certain water level h is greater than the anti-slip moment; N is the calculated number of segments of the water level frequency curve upstream of the earth and rock dam; $\Delta F_0(h_i)$ is the probability of the ith segment of the water level frequency curve upstream of the earth and rock dam; $\bar{F}_L(h_i)$ is the i-th segment of the sliding moment L is the mean value of the probability that L is greater than the anti-slip moment R.

In the process of slope risk analysis, the shear strength parameter cohesion and the internal friction coefficient $f = tan\,\varphi$ of the landslide material are analyzed as random variables and it is assumed that c and φ are statistically independent of each other and obey lognormal cloud distributions of $D(\mu_c = Ex_c, \sigma_c = En_c), D(\mu_f = Ex_f, \sigma_f = En_f)$ respectively. N cloud drops are generated for c and f to obtain a cloud distribution plot of the two.

When using the Monte Carlo method of calculation, the cloud distribution of the shear strength parameter is allowed to replace the distribution histogram, and the standard deviation of the factor of safety and the mean of the distribution are obtained from the cloud distribution as in Eqs. 25–(26).

$$En = \sigma_Y = \left[\ln\left(1 + V_X^2\right)\right]^{\frac{1}{2}} \tag{25}$$

$$Ex = \mu_Y = \ln \mu_X - \frac{1}{2}\sigma_{\ln x}^2 = \ln\left(\frac{\mu_X}{\sqrt{1+V_X^2}}\right) \tag{26}$$

$$x_i = e^{y_i} \tag{27}$$

Where, X is the lognormal cloud distribution (its mean is the expectation of the cloud Ex, the standard deviation is the entropy of the cloud En; and the coefficient of variation is Vx; $Y = lnx$ is the normal distribution (mean μ_Y and standard deviation σ_Y); x_i is the random number of variables X.

2.3.7 Steps for calculating the "cloud model—Monte Carlo" model

The "cloud model-Monte Carlo" model used in the calculation process of the failure probability P_f of the earth-rock dam slope can be summarized into several steps.

1) Input each random statistical characteristic and distribution model.
2) The uncertainty cloud model is used to generate cloud drops and sample uncertain quantities such as cohesion c and internal friction angle φ.
3) The random set of uniformly distributed random numbers is generated and the corresponding parameters are generated according to the distribution law of each variable.
4) Generated random numbers and parameters are substituted into the function of the Swedish strip division method for multiple calculations, the number of failures is recorded, and the failure probability P_f is calculated.
5) Solve for the risk of dam slope instability based on the failure probability P_f.

3 Results

3.1 Cloud distribution model for shear strength index

Based on the small sample data, the three numerical features of the shear strength parameter c were derived by the inverse cloud generator, and then the cloud distribution map was obtained by the forward cloud generator (φ values, c values log cloud distribution map of the same analysis path), and the basic parameters of the cloud model are shown in Table 3.

Through multiple cycles of the forward and reverse cloud generators, 1000 cloud drops were simulated, generating the cloud distribution shown in Figure 3.

According to Figure 3, it can be seen that the generalized normal distribution of clouds can effectively model the discrete nature of finite sample data. The cloud droplets generated based on the three characteristic figures are mainly distributed in the intervals [12,22] [0.75,1.75] [12.5,20], and [1.1,1.3], by the '3 days' rule in cloud theory. This indicates that the cohesion and internal friction angles obey both normal and lognormal cloud distributions. In order to determine the optimal probability distribution model for the shear strength index of the soil, a comparison was made. The results show that the tail cloud drops of the lognormal cloud distribution for cohesion and internal friction angle are 'lighter' than the normal cloud distribution and that the drops fluctuate less around the desired curve. This indicates that the variability between the sample data is reduced and the data is more concentrated after the logarithmic transformation. The log-transformed coefficient of variation for the soil parameters is calculated to be 0.043, which is

10.3389/feart.2023.1196677

TABLE 3 Basic parameters of the Cloud model.

Mechanical index	Possibility type	*Ex*	*En*	*He*	A first-order sample center distance	Variance	Coefficient of variation
cohesion	normal	17.116	2.075	0.317	1.656	4.404	0.121
	lognormal	1.230	0.053	0.008	0.042	0.029	0.043
internal friction angle φ	normal	16.677	3.623	1.037	2.89	14.201	0.226
	lognormal	1.209	0.090	0.016	0.071	0.024	0.128

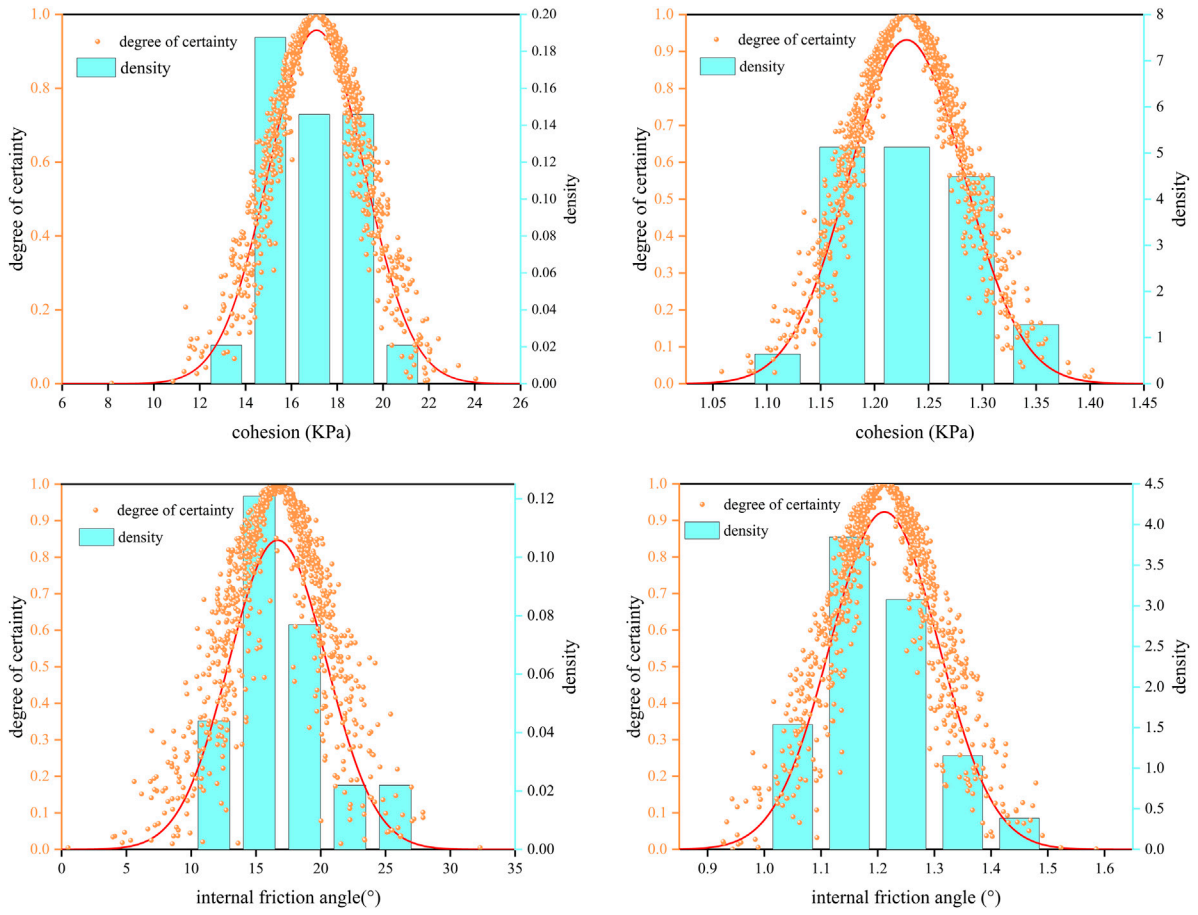

FIGURE 3
Sample parameter cloud distribution.

much smaller than the untransformed coefficient of 0.121 and is consistent with the inferred results for the cloud distribution. Therefore, the log-normal cloud distribution is considered to be the optimal probability distribution model for cohesion and internal friction angle.

In order to make full use of the sample information without over-relying on the sample data, this study adopts a cloud theory-based method for studying the distribution types of soil shear strength indicators. As can be seen from Figure 3, the thickness of the clouds is not strictly normally distributed but is a generalized normal cloud distribution. In contrast to the distribution histogram and its fitted curve, the pan-normal distribution of clouds describes the uncertainty of finite data by introducing the super entropy He. As shown in Figure 3C, the cloud thickness is large and the cloud droplet distribution is discrete appearing fogged in the internal friction angle cloud distribution plot, indicating a large uncertainty in the sample data for the internal friction angle, a property that is not

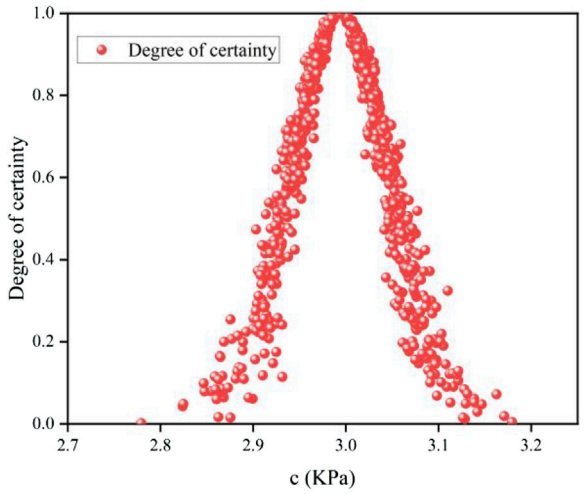

FIGURE 4
Cloud distribution of mean slope calculation results.

represented in the histogram of the internal friction angle distribution.

3.2 "Cloud Model-Monte Carlo" based slope stability risk analysis

3.2.1 Cloud simulation of shear strength parameters

The cohesive force c and the coefficient of internal friction f=tanφ of the landslide soil are considered random variables and are assumed to follow a log-normal cloud distribution. After 1000 simulations, the cloud distribution of the coefficient of safety is shown in Figure 4. The expected value Ex and variance En of the safety factor are shown in Table 4.

3.2.2 Determination of the minimum safety factor

3.2.2.1 Calculation assumptions

This calculation assumes a starting elevation of 160 m. The infiltration line of the earth and rock dam body is determined using the finite element method, which is not limited by irregular geometry and inhomogeneous materials, and the calculation results are highly reliable.

3.2.2.2 Calculation method

During the period of steady seepage, the Swedish strip division method was used to carry out the downstream slope stability analysis of the earth and rock dam, and the minimum safety factor and the location of the most dangerous slip surface were obtained through the calculation.

3.2.2.3 Calculation results

The minimum safety factors obtained using the Swedish arc method at each water level, together with the values specified in the code, are shown in Table 5 below.

3.2.3 Calculation of slope failure probability

3.2.3.1 Probability of failure $\bar{F_L}$ (h_i) calculation

After obtaining the minimum safety coefficient from the slope stability analysis, the calculation was carried out using the Monte Carlo method and the relevant electro-computing procedures. In general, the probability of failure was under 0.1% according to the number of solutions $N > \frac{100}{P_f}$, and to meet the requirements of calculation accuracy, the number of solutions was set to 200,000 times to calculate the probability of failure of the downstream dam slope, and the calculation results are shown in Table 6.

3.2.3.2 Calculation of the interval frequency $\Delta F_0\,(h_i)$

Based on the upstream flood level frequency curve of the earth and rock dam Figure 5, the interval frequency value $\Delta F_0\,(h_i)$ can be found as shown in Table 7.

3.2.4 Coupled "cloud Model-Monte Carlo" model for dam slope risk calculation

The degree of risk $\bar{R}$ can be calculated by the following equation.

$$\bar{R} = P_f = P(L > R) = \int_{h_1}^{h_2} F_L(h) f_0(h) dh = \sum_{i=1}^{N} \Delta F_0(h_i) \overline{F_L}(h_i) \tag{28}$$

The results of the calculation are shown in Table 8.

For a parameter F that fits the lognormal cloud distribution, let y fit the normal cloud distribution and have

$$y = lnF \tag{29}$$

or

$$F = e^y \tag{30}$$

Then F can be transformed into a normal cloud distribution.

The following transformation relationship exists between the expectation and entropy of F and y, i.e.,

$$En_y = \left[\ln\left(1 + V_F^2\right)\right]^{\frac{1}{2}} \tag{31}$$

$$Ex_y = \ln\left(\frac{Ex_x}{\sqrt{1 + V_F^2}}\right) \tag{32}$$

In the above equation: μ_Y and σ_Y are the standard deviation and mean of y respectively.

The coefficient of variation is obtained from Eqs. 31–(32) as

TABLE 4 Characteristic values of random mechanical parameters of earth and rock dams.

Variable name	Symbol	Distribution type	Mean	Variance	Coefficient of variation
Cohesion	c	log-normal cloud	3	0.29	0.5
Internal friction angle coefficient	f	log-normal cloud	0.5095	0.,24	0.2

10.3389/feart.2023.1196677

TABLE 5 Calculation of the slope stability factor of safety for the earth and rock dams.

Dam slope	Upstream water level/m	Coefficient of safety K_{min}	Range of specified values
Downstream	188.1	1.29	1.24
	186.0	1.32	
	185.0	1.34	
	184.0	1.36	
	182.0	1.40	
	180.0	1.49	
	178.0	1.54	
	176.0	1.60	
	174.0	1.67	
	172.0	1.68	
	170.0	1.70	
	168.0	1.76	
	166.0	1.76	
	164.0	1.85	
	162.0	1.89	
	160.0	1.92	

TABLE 6 Calculation of slope failure probability $\bar{F_L}\ (h_i)$ for earth and rock dams.

Dam slope	Safety factor K_{min}	Probability of failure $\bar{F_L}\ (h_i)$/%
Downstream	1.29	0.15101
	1.32	0.13526
	1.34	0.19311
	1.36	0.11174
	1.40	0.11876
	1.49	0.08711
	1.54	0.08701
	1.60	0.07515
	1.67	0.05250
	1.68	0.03825
	1.70	0.03450
	1.76	0.02525
	1.76	0.03350
	1.85	0.01920
	1.89	0.01635
	1.92	0.01715

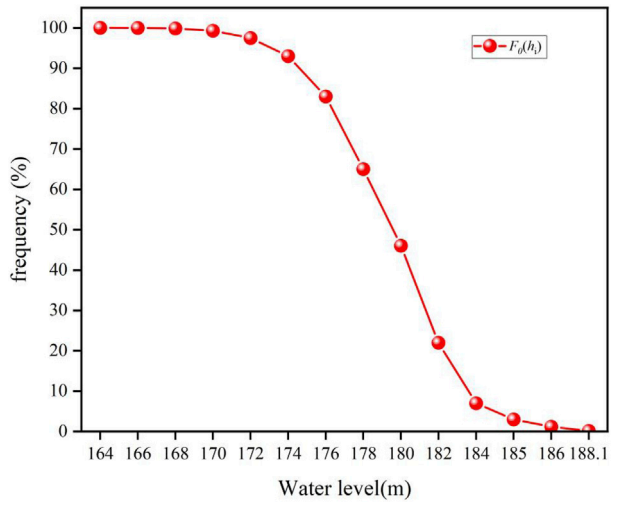

FIGURE 5
Water level frequency graph for earth and rock dams.

TABLE 7 Flood level frequency relationships upstream of earth and rock dams.

Water level/m	Frequency $F_0(h_i)$%	$\Delta F_0(h_i)$/%
164.0	99.999	
166.0	99.98	0.019
168.0	99.85	0.13
170.0	99.3	0.55
172.0	97.5	1.8
174.0	93	4.5
176.0	83	10
178.0	65	15
180.0	46	22
182.0	22	24
184.0	7	15
185.0	3	4
186.0	1.2	1.8
188.1	0.15	1.05

$$V_F = \frac{\sigma_F}{\mu_F} = \frac{En_F}{Ex_F} \tag{33}$$

Since y less than 0 is equivalent to F less than 0, the reliability index $\beta = Ex_y/En_y$ not only reflects the probability that $Y < 0$, but also represents the probability that probability of $F < 1$. For a normal cloud distribution, the variables y and β alike can be expressed in terms of Ex_F, En_F.

$$\beta = \frac{\mu_y}{\sigma_y} = \frac{Ex_y}{En_y} = \frac{\ln\left(\frac{Ex_x}{\sqrt{1+V_F^2}}\right)}{\left[\ln\left(1+V_F^2\right)\right]^{\frac{1}{2}}} \tag{34}$$

According to the above equation, for $\mu_F = Ex_y = 3$, $V_F = 9.7\%$, a review of the data shows that the probability of $F > 1$ is 99% and can be obtained by the following equation.

$$En_y = \left[\ln\left(1+0.097^2\right)\right]^{\frac{1}{2}} = 0.109 \tag{35}$$

$$Ex_y = \ln\left(\frac{3}{\sqrt{1+0.097^2}}\right) = 0.252 \tag{36}$$

$$\beta = \frac{0.251}{0.109} = 2.204 \tag{37}$$

The improved risk analysis method based on cloud theory yields a risk level of 879.01×10^{-6}, which is smaller and more accurate than the traditional method of 929.25×10^{-6}, proving that this method is more reliable.

3.2.5 Risk evaluation

In recent years, the main method of risk analysis has been based on parameters following a normal distribution. However, this may lead to negative values for certain parameters, particularly when analyzing slope engineering parameters such as cohesion. This can result in lower reliability as cohesion may have negative values. To address this issue, this paper analyzes parameters following a logarithmic normal cloud distribution, aligning the stability measurement standard of slope instability with the traditional analysis method of functional functions less than zero.

Traditional slope stability analysis uses deterministic models to obtain the safety factor F. However, risk analysis based on cloud theory uses two indicators, the expectation Ep and entropy En, to determine the failure probability of the slope by analyzing the variability characteristics of influencing factors, which is more reasonable. Studies have shown that the probability of dam collapse due to landslides in earth-rock dams is on the order of 10^{-5} per dam per year, therefore, we set the landslide probability of earth-rock dams at 10^{-5} per dam per year. Taking into account the safety factors, the statistical probability of landslides for each dam per year is set at 1×10^{-5}. Therefore, the safety reliability of earth-rock dams against landslides is above 99.999%.

However, determining the value of landslide risk for earth-rock dams is influenced by many factors. The process of determining risk standards requires repeated weighing between economic benefits, political risks, environmental assessments, and dam safety. Referring to relevant risk standards, this paper sets the allowable landslide risk standard at 0.5×10^{-6}, resulting in a safety reliability indicator of over 99.9995.

The calculation results show that the risk probability corresponding to the design flood level of the dam is 9.01×10^{-6}, exceeding the allowable risk standard of 0.5×10^{-6}, thus reinforcement treatment is necessary.

4 Discussion

This study proposes a “cloud model-Monte Carlo” coupling model and applies it to evaluate the risk of specific earth-rock dam landslides. The results show that the proposed model is effective in analyzing the risk of dam slope failure and provides a comprehensive assessment of potential risks related to the dam. The cloud model is used to determine the probability distribution

TABLE 8 Calculation of the risk of dam slope instability for earth and rock dams.

Water level/m	The factor of safety K_{min}	$F_L(h)$/%	$\bar{F}_L(h_i)$/%	$F_0(h_i)$/%	$\Delta F_0(h_i)$/%	Degree of risk R
164.0	1.85	0.151	99.999			
166.0	1.76	0.13525	0.0265	99.98	0.019	0.05
168.0	1.76	0.1931	0.0294	99.85	0.13	0.38
170.0	1.70	0.11175	0.0294	99.3	0.55	1.62
172.0	1.68	0.11875	0.0359	97.5	1.8	6.646
174.0	1.67	0.0871	0.0454	93	4.5	20.43
176.0	1.60	0.087	0.0634	83	10	62.4
178.0	1.54	0.07525	0.0807	65	15	121.05
180.0	1.49	0.0525	0.087	46	22	191.4
182.0	1.40	0.03825	0.1029	22	24	246.96
184.0	1.36	0.0345	0.1148	7	15	172.2
185.0	1.34	0.02525	0.1519	3	4	60.76
186.0	1.32	0.0335	0.1642	1.2	1.8	25.56
188.1	1.29	0.0192	0.1427	0.15	1.05	14.98
∑						879.11

type of uncertain shear strength parameters. Then, the Monte Carlo method is used to generate a large number of random samples based on the cloud model for simulating the probability of dam slope failure. In addition, the results of the risk assessment indicate that under normal conditions, the risk of dam slope failure is relatively low, but it significantly increases under extreme weather conditions (such as heavy rain). This suggests the need to take appropriate measures to reduce the risk of dam slope failure under extreme weather conditions, such as strengthening the dam structure or implementing emergency response plans.

Overall, the cloud model-Monte Carlo coupling model provides an effective approach for evaluating the risk of dam slope failure. The results of this study can provide valuable information to dam managers and decision-makers to make informed decisions under different weather conditions and ensure dam safety.

5 Conclusion

Firstly, this paper employs a research method based on cloud theory to study the distribution types of soil shear strength indicators. The optimal probability distribution model for cohesion and internal friction angle is found to be the logarithmic normal cloud distribution. Moreover, we propose a "cloud model-Monte Carlo" coupling model, which can effectively evaluate the risk of dam landslides. The cloud model can handle the uncertainty of shear strength parameters and determine their probability distribution models. The Monte Carlo method can simulate the random behavior of input variables and calculate the probability of output variables. The combination of these two methods can provide more accurate risk assessment results. In slope risk analysis, the "cloud theory-Monte Carlo" model can calculate failure probability and risk degree more accurately and reliably compared to traditional methods.

Secondly, referring to relevant risk standards, this paper sets the allowable landslide risk standard for earth-rock dams at 0.5×10^{-6}, with a safety reliability indicator of over 99.9995%. The calculation results show that the risk probability corresponding to the design flood level of the dam is $9.01\times10^{-6,}$ exceeding the allowable risk standard. Therefore, it is necessary to reinforce the earth-rock dam to reduce the risk of failure.

Finally, the proposed cloud model-Monte Carlo coupling model has broad application prospects in the field of dam risk assessment. It can be used to analyze the risks of various types of dams and provide accurate risk assessment results. In future research, the model can be further improved to enhance its accuracy and applicability, while being more widely applied and validated.

Data availability statement

The raw data supporting the conclusion of this article will be made available by the authors, without undue reservation.

Author contributions

Method: MC; Experiment: MC, JS, LM, and WJ; Data analysis: MC and ZS; Prepare the original manuscript: MC; Writing, reviewing and editing: MC and LH; Fund buy-out, LH; Guidance: LH and HZ

Funding

This work was supported by North China University of Water Resources and Electric Power and the National Natural Science Foundation of China (51509091).

Conflict of interest

The authors declare that the research was conducted in the absence of any commercial or financial relationships that could be construed as a potential conflict of interest.

Publisher's note

All claims expressed in this article are solely those of the authors and do not necessarily represent those of their affiliated organizations, or those of the publisher, the editors and the reviewers. Any product that may be evaluated in this article, or claim that may be made by its manufacturer, is not guaranteed or endorsed by the publisher.

References

Cai, J.-S., Yeh, T.-C. J., Yan, E.-C., Tang, R.-X., and Hao, Y.-H. (2021). Design of borehole deployments for slope stability analysis based on a probabilistic approach. *Comput. Geotechnics* 133, 103909. doi:10.1016/j.compgeo.2020.103909

Chakraborty, R., and Dey, A. (2022). Probabilistic slope stability analysis: State-of-the-art review and future prospects. *Innov. Infrastruct. Solutions* 7, 177. doi:10.1007/s41062-022-00784-1

Chen, H., Guo, Q., Wang, L., and Meng, X. (2023). Evaluation of slope stability within the influence of mining based on combined weighting and finite cloud model. *Energy Explor. Exploitation* 41, 636–655. doi:10.1177/01445987221134638

Cheng, W., Dong, F., Tang, R., Yin, H., Shi, L., Zhai, Y., et al. (2022). Improved combination weighted prediction model of aquifer water abundance based on a cloud model. *ACS Omega* 7, 35840–35850. doi:10.1021/acsomega.2c04162

Chorol, L., and Gupta, S. K. (2023). Evaluation of groundwater heavy metal pollution index through analytical hierarchy process and its health risk assessment via Monte Carlo simulation. *Process Saf. Environ. Prot.* 170, 855–864. doi:10.1016/j.psep.2022.12.063

DAMS (2002). *Code for Design of rolled earth-rock DAMS*. Beijing: Survey and Design Institute of Yellow River Water Conservancy Commission.

Ge, W., Jiao, Y., Wu, M., Li, Z., Wang, T., Li, W., et al. (2022). Estimating loss of life caused by dam breaches based on the simulation of floods routing and evacuation potential of population at risk. *J. Hydrology* 612, 128059. doi:10.1016/j.jhydrol.2022.128059

Ge, W., Li, Z., Li, W., Wu, M., Li, J., and Pan, Y. (2020a). Risk evaluation of dam-break environmental impacts based on the set pair analysis and cloud model. *Nat. Hazards* 104, 1641–1653. doi:10.1007/s11069-020-04237-9

Ge, W., Qin, Y., Li, Z., Zhang, H., Gao, W., Guo, X., et al. (2020b). An innovative methodology for establishing societal life risk criteria for dams: A case study to reservoir dam failure events in China. *Int. J. disaster risk Reduct.* 49, 101663. doi:10.1016/j.ijdrr.2020.101663

Guojiao, L., Baohui, M., and Lehao, W. (2023). Water quality assessment of wenyu river with variable weight cloud model. *Nat. Environ. Pollut. Technol.* 22, 63–72. doi:10.46488/NEPT.2023.v22i01.005

Li, D., Liu, C., and Gan, W. (2009). A new cognitive model: Cloud model. *Int. J. intelligent Syst.* 24, 357–375. doi:10.1002/int.20340

Li, Z., Li, W., and Ge, W. (2018). Weight analysis of influencing factors of dam break risk consequences. *Nat. Hazards Earth Syst. Sci.* 18, 3355–3362. doi:10.5194/nhess-18-3355-2018

Li, Z., Zhang, Y., Wang, J., Ge, W., Li, W., Song, H., et al. (2021). Impact evaluation of geomorphic changes caused by extreme floods on inundation area considering geomorphic variations and land use types. *Sci. Total Environ.* 754, 142424. doi:10.1016/j.scitotenv.2020.142424

Liu, J., Shi, H., Wang, R., Si, Y., Wei, D., and Wang, Y. (2021). Quantitative risk assessment for deep tunnel failure based on normal cloud model: A case study at the ASHELE copper mine, China. *Appl. Sci.* 11, 5208. doi:10.3390/app11115208

Lu, X., Chen, C., Li, Z., Chen, J., Pei, L., and He, K. (2022). Bayesian network safety risk analysis for the dam–foundation system using Monte Carlo simulation. *Appl. Soft Comput.* 126, 109229. doi:10.1016/j.asoc.2022.109229

Ma, Z., and Zhang, S. (2020). Risk-based multi-attribute decision-making for normal cloud model considering pre-evaluation information. *IEEE Access* 8, 153891–153904. doi:10.1109/ACCESS.2020.3018153

Mao, X.-B., Hu, S.-S., Dong, J.-Y., Wan, S.-P., and Xu, G.-L. (2018). Multi-attribute group decision making based on cloud aggregation operators under interval-valued hesitant fuzzy linguistic environment. *Int. J. Fuzzy Syst.* 20, 2273–2300. doi:10.1007/s40815-018-0495-2

Mao, X., Wu, H., and Wan, S. (2022). A personalized comprehensive cloud-based method for heterogeneous MAGDM and application in COVID-19. *CMES-Computer Model. Eng. Sci.* 131, 1751–1792. doi:10.32604/cmes.2022.019501

Raghuvanshi, T. K. (2019). Governing factors influence on rock slope stability–Statistical analysis for plane mode of failure. *J. King Saud University-Science.* 31, 1254–1263. doi:10.1016/j.jksus.2019.01.002

Rouzéa, C., and Dattaa, N. (2016). Analysis of finite sample size quantum hypothesis testing via martingale concentration inequalities. *arXiv preprint arXiv:1612.01464*.

Ruan, D., Bian, J., Wang, Q., Wu, J., Yu, Y., and Gu, Z. (2021). Application of modified cloud model-level eigenvalue method in water quality evaluation. *J. Hydrology* 603, 126980. doi:10.1016/j.jhydrol.2021.126980

Santos, C. J., De Almeida Ribeiro, M. C., Santos, W. S., Belinato, W., Neves, L. P., and Perini, A. P. (2022). Medical and occupational dosimetry during interventional pediatric cardiology procedures: A Monte Carlo approach. *Phys. Medica Eur. J. Med. Phys.* 104, S28. doi:10.1016/S1120-1797(22)02179-2

Tu, K., Ye, S., Zou, J., Hua, C., and Guo, J. (2023). InSAR displacement with high-resolution optical remote sensing for the early detection and deformation analysis of active landslides in the upper yellow river. *Water* 15, 769. doi:10.3390/w15040769

Vihola, M., Helske, J., and Franks, J. (2020). Importance sampling type estimators based on approximate marginal Markov chain Monte Carlo. *Scand. J. Statistics* 47, 1339–1376. doi:10.1111/sjos.12492

Wang, D., Xu, C., Yuan, P., and Huang, D. (2020). A revised Monte Carlo method for target location with uav. *J. Intelligent Robotic Syst.* 97, 373–386. doi:10.1007/s10846-019-01011-3

Wang, T., Li, Z., Ge, W., Zhang, H., Zhang, Y., Sun, H., et al. (2023). Risk consequence assessment of dam breach in cascade reservoirs considering risk transmission and superposition. *Energy* 265, 126315. doi:10.1016/j.energy.2022.126315

Wang, T., Li, Z., Ge, W., Zhang, Y., Jiao, Y., Sun, H., et al. (2022). Calculation of dam risk probability of cascade reservoirs considering risk transmission and superposition. *J. Hydrology* 609, 127768. doi:10.1016/j.jhydrol.2022.127768

Wang-Wang, C., Dian-Qing, L., Xiao-Song, T., and Zi-Jun, C. (2018). Probability distribution of shear strength parameters using maximum entropy principle for slope reliability analysis. *Rock Soil Mech.* 39, 1469–1478. doi:10.16285/j.rsm.2016.1062

Wen, T., Hu, Z., and Tang, H. (2022). The field survey and deformation characteristics of exit slope of Qingshuigou tunnel in the southwest of China. *Arabian J. Geosciences* 15, 1096. doi:10.1007/s12517-022-10327-8

Wu, M., Ge, W., Wu, Z., Guo, X., Di, D., and Huang, S. (2020). Evaluation of the benefits of urban water resource utilization based on the catastrophe and emergy methods. *Water Resour. Manag.* 34, 1843–1853. doi:10.1007/s11269-020-02530-7

Wu, M., Wu, Z., Ge, W., Wang, H., Shen, Y., and Jiang, M. (2021). Identification of sensitivity indicators of urban rainstorm flood disasters: A case study in China. *J. Hydrology* 599, 126393. doi:10.1016/j.jhydrol.2021.126393

Xie, J., and Sun, D. (2009). Statistics of dam failures in China and analysis on failure causations. *Water Resour. Hydropower Eng.* 40, 124–128.

Yang, L., Chen, Y., Lu, H., Qiao, Y., Peng, H., He, P., et al. (2023). Cloud model driven assessment of interregional water ecological carrying capacity and analysis of its spatial-

temporal collaborative relation. *J. Clean. Prod.* 384, 135562. doi:10.1016/j.jclepro.2022.135562

Yang, X., Hao, Z., Ma, G., and Li, G. (2021). Research on slope stability evaluation based on improved set pair analysis method: A case of tonglvshan open-pit mine. *Shock Vib.* 2021, 1–16. doi:10.1155/2021/6713581

Yangping, G., Wangyong, L., Lingling, W., and Linzhi, C. (2019). Parameter estimation of cloud model based on bayesian theory. *Statistics Decis.* 6.

Yaowu, Y., and Dongwei, C. (1994). Analysis of stability and reliability of soil slope. *Chin. J. Geotechnical Eng.* 16, 80–87.

Yong, M. R. (2004). *Risk analysis methods and applications for earth and rock dams.* Beijing: Science Press.

Zhang, H., Ge, W., Zhang, Y., Li, Z., Li, W., Zhu, J., et al. (2023). Risk management decision of reservoir dams based on the improved life quality index. *Water Resour. Manag.* 37, 1223–1239. doi:10.1007/s11269-023-03426-y

Zhang, M., Jin-Yong, L., and Jia-Xuan, M. (2006). Reliability analysis and design of slope stability of earth-rock dam. *J. Hydroelectr. Eng.* 25, 103–107.

Zhang, Y., Li, Z., Ge, W., Wang, J., Guo, X., Wang, T., et al. (2022b). Assessment of the impact of floods on terrestrial plant biodiversity. *J. Clean. Prod.* 339, 130722. doi:10.1016/j.jclepro.2022.130722

Zhang, Y., Yu, X., Liu, S., Dong, X., Li, D., Zang, H., et al. (2022a). Wind power interval prediction based on hybrid semi-cloud model and nonparametric kernel density estimation. *Energy Rep.* 8, 1068–1078. doi:10.1016/j.egyr.2022.02.094

frontiers | Frontiers in Earth Science

TYPE Original Research
PUBLISHED 18 May 2023
DOI 10.3389/feart.2023.1196903

OPEN ACCESS

EDITED BY
Xihui Gu,
China University of Geosciences Wuhan, China

REVIEWED BY
Keke Fan,
Henan Agricultural University, China
Dongdong Kong,
China University of Geosciences Wuhan, China

*CORRESPONDENCE
Zongzhi Wang,
wangzz77@163.com

RECEIVED 30 March 2023
ACCEPTED 02 May 2023
PUBLISHED 18 May 2023

CITATION
Du H, Wang Z and Yin J (2023), Analysis of flood control risk in floodwater utilization considering the uncertainty of flood volume and peak.
Front. Earth Sci. 11:1196903.
doi: 10.3389/feart.2023.1196903

Analysis of flood control risk in floodwater utilization considering the uncertainty of flood volume and peak

Huihua Du[1], Zongzhi Wang[1]* and Jun Yin[2]

[1]State Key Laboratory of Hydrology-Water Resources and Hydraulic Engineering, Nanjing Hydraulic Research Institute, Nanjing, China, [2]School of Hydrology and Water Resources, Nanjing University of Information Science and Technology, Nanjing, China

Introduction: A design flood is a hypothetical flood used for the design of reservoirs and other hydrologic engineering infrastructures. Among many hydrological properties of a design flood, flood volume and peak can significantly affect the safety of reservoir operation. However, the uncertainty of flood volume and peak has rarely been considered in the risk analysis of reservoir operation regarding floodwater utilization.

Methods: In this paper, a general risk analysis framework that integrates the Monte Carlo sampling method and the most likely event selection method is proposed to calculate the risk of operating a single reservoir. By generating a large amount of stochastic bivariate flood data, the most likely design values were selected for a given return period. The probability of the maximum water level exceeding the current design flood level was calculated based on the simulation of flood control operation under various floodwater utilization schemes.

Results: The model is applied to the Shagou reservoir in the Shuhe River basin, China. The results show that the design flood volume and flood peak obtained by the bivariate joint return are 7.59% and 8.22% higher than those from univariate frequency analysis, respectively; the joint return period of bivariate design value spans from 10a to 1000a compared to the historical data; and the flood control risk at Shagou reservoir is 0.29 under current flood control operations based on the uncertainty of flood volume and peak.

Discussion: Moreover, the marginal benefit may contain floodwater utilization and a transmission risk effect between different node projects in the flood control system.

KEYWORDS

flood control risk, uncertainty of flood volume and peak, floodwater utilization, Shagou reservoir, stochastic simulation

1 Introduction

With continuous economic development and population growth, the demand for water resources is becoming increasingly intense, and scarcity of water resources is among the major factors restricting social progress (Chen et al., 2016; Chang et al., 2017). To alleviate water resource shortages, various floodwater utilization models have been recently developed and demonstrated to be effective in many studies (Ding et al., 2017; Meng et al., 2018; Liu et al., 2019; Wang et al., 2019). According to the floodwater utilization concept (Wallington and Cai, 2020; Wang et al., 2020), floodwater utilization strategies can only be implemented if the risks

are controlled within an acceptable range. As one of the major and effective engineering measures for floodwater utilization, reservoirs are built for multiple purposes, including flood control, water supply, and other functions. Moreover, floods are among the most frequent, widespread, and devastating natural disasters in the context of climate change and human activities (Wu et al., 2020); thus, flood control risks are particularly important for reservoir flood control operations. Therefore, the scientific assessment of flood control risk in floodwater utilization operations is important for flood management in reservoirs.

The risk analysis of floodwater utilization is a fundamental issue in flood management, engineering design, and area planning. Because the uncertainty factors lead to deviations between the calculated deterministic results and the actual occurrence and the risks involved in flood control decision making (Xiong and Qi, 2010; Delenne et al., 2012; Simonovic and Arunkumar, 2016; Ocio et al., 2017; Chen et al., 2019), various uncertainties have been discussed in the estimations of floodwater utilization in past years, including meteorological and hydrological forecast uncertainties, hydraulic uncertainties and human operation uncertainty (Melching, 1992; Cloke and Pappenberger, 2009; Dong, 2009; Diao and Wang, 2010; Wu et al., 2011; Kriauciuniene et al., 2013; Tung and Wong, 2014; Yan et al., 2014; Ocio et al., 2017). Due to significant concerns regarding design flood estimation under a specific return period for reservoir flood management, the study of its uncertainty has received much research attention from hydrologists (Parkes and Demeritt, 2016; Nakamura and Oki, 2018; Brunner and Sikorska-Senoner, 2019; Guo et al., 2020). Notably, design floods are generally defined by several features that are correlated with uncertainty (Dung et al., 2015; Daneshkhah et al., 2016; Guo et al., 2020), such as flood peak, flood volume, and regional flood composition. Hence, analysis of bivariate design floods characterized by correlated flood volumes and peaks reveals its advantage over traditional analysis of univariate design floods. In recent years, numerous frameworks have been developed to estimate uncertainties in bivariate design floods in various flood control systems (Zhang and Singh, 2007c; Yan et al., 2014; Fan et al., 2016; Ozga-Zielinski et al., 2016; Yin et al., 2018b; Xiong et al., 2019; Guo et al., 2020; Huang et al., 2020). The application of the copula-based methodology has been of growing interest in bivariate design floods. Various uncertainties in copula-based design flood estimation are discussed (Malekmohammadi et al., 2009; Serinaldi, 2013; Michailidi and Bacchi, 2017; Liu et al., 2018; Guan et al., 2022), including model uncertainty, parameter uncertainty, and sampling uncertainty. In particular, the sampling uncertainty of flood volume and peak is high in bivariate design floods, influencing the selection of model structure and parameters. The floodwater utilization approach is devised based on the analysis of flood control risk caused by various uncertainties. Analyzing the frequency curve of flood control reservoir capacity is necessary to balance risks and benefits considering the uncertainty of flood volume and peaks in the selection of floodwater utilization schemes.

However, to the best of our knowledge, there are few studies on the flood control risk of floodwater utilization from a sampling uncertainty perspective. More importantly, apart from a few papers, flood volume and peak and their impacts on flood control risk have not been systematically estimated in the literature. Towards this goal, here we propose an integrated model that employs the Monte Carlo sampling method and the most likely event selection method to estimate the probability of the maximum water level exceeding the current design flood level.

The remainder of this paper is structured as follows. Section 2 describes the Shagou reservoir of the Shuhe River in the Huaihe River Basin in China, which is chosen as the study domain. Section 3 introduces the research framework. Section 4 presents the computational process and the results. Section 5 discusses the impacts of flood control operations on flood control risk. Section 6 provides the conclusions of this study.

2 Case study

2.1 Study area

The Shagou reservoir is located upstream of the Shuhe River in the Huaihe River Basin in China, with a control basin area of 164 km^2, as shown in Figure 1. The average annual precipitation is 745 mm, and flood season (from June to September) accounts for approximately 74% of the annual precipitation. In the current flood control operation, the flood-limited water level of the Shagou reservoir is 231.5 m, and the maximum control outflow is 500 m^3/s under the given return period T =20a. In this paper, the Shagou reservoir is taken as the research object to discuss the flood control risk in floodwater utilization considering the uncertainty of flood volume and peak.

2.2 Data

The annual maximum 72 h flood volume and corresponding flood peak observed in 1964–2013 are utilized to represent the flood characterization in the Shagou reservoir. The data are provided by the Yi-Shu-Si River Basin Administration, which is responsible for the unified management of major rivers (including the Shuhe River), lakes, hubs and other projects in the Yishusi Basin. The statistical results of flood volume and flood peak are shown in Table 1.

According to the statistics of historical flood data, the highest annual maximum flood volume is 3.115 $m^3 \times 10^7$ m^3, which is approximately 3.5 times the multiyear average, and the lowest annual maximum is 70.4 $m^3 \times 10^4$ m^3. Similarly, the highest annual maximum flood peak is 1,190 m^3/s, which is approximately 3.7 times the multiyear average, and the lowest annual maximum is 3.92 m^3/s. The annual flood change is dramatic, and floodwater utilization is necessary for local regional water management. When the range of flood volume is [2,070, 2,204] $\times 10^4$ m^3, the flood peak range is [315, 994] m^3/s. Obvious uncertainty exists between flood volume and peak, which may have an adverse effect on flood control operation. Estimating the flood control risk caused by the flood volume and peak uncertainty in the Shagou reservoir is important for flood control operation decision making in floodwater utilization management.

3 Materials and methods

3.1 Joint distribution of flood variables based on copulas

Multivariate distribution construction using copulas has been well developed in the past years (Sklar, 1959; Shaked and Joe, 1998; Sancetta and Satchell, 2004). A bivariate joint distribution can be

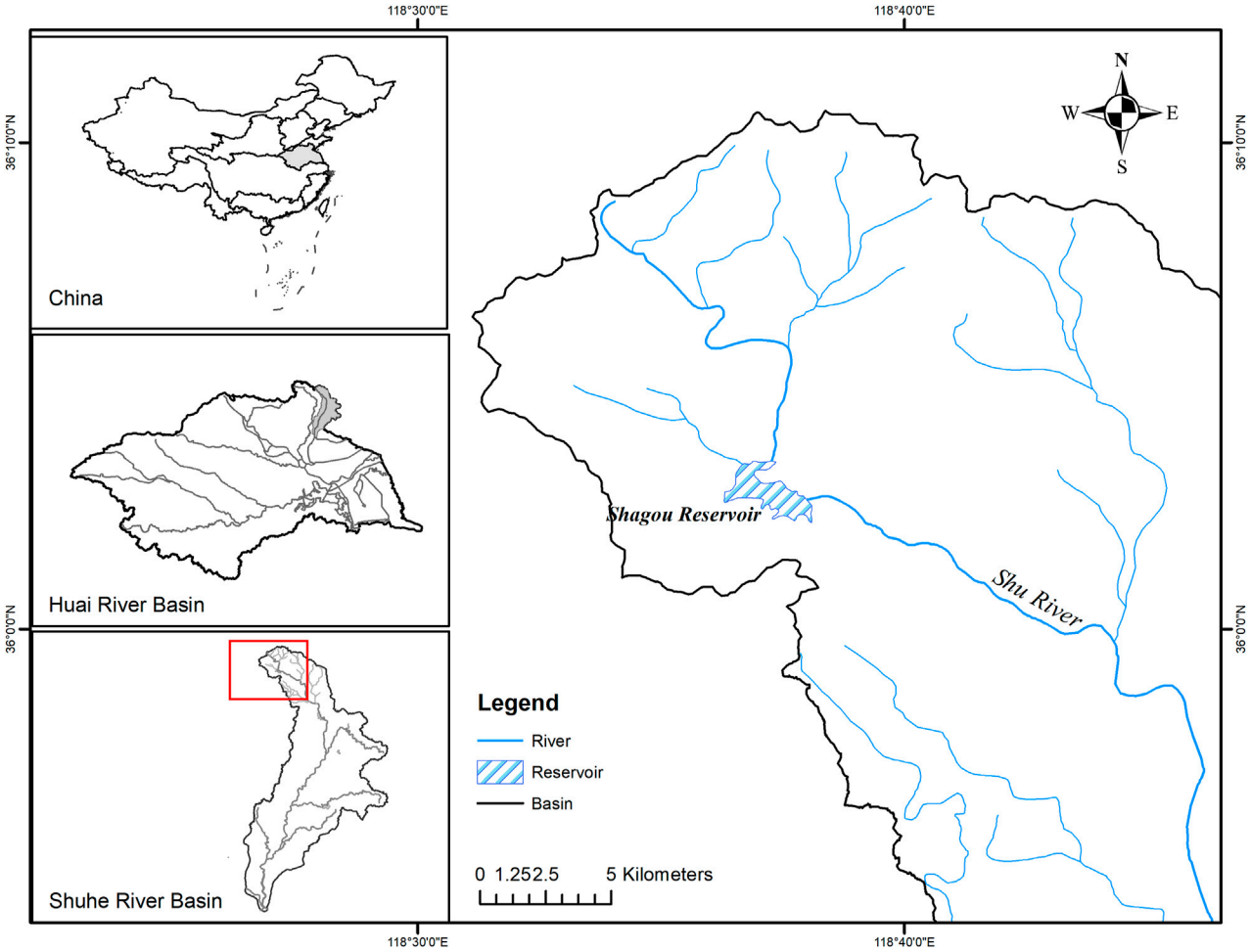

FIGURE 1
Sketch map of the Shagou reservoir in the Shu River basin, China.

TABLE 1 Statistical features of flood variables from 1964 to 2013.

Flood variables	Mean	Standard deviation	Skewness
Volume (10^4 m^3)	911.8	652.1	1.1287
Peak (m^3/s)	315.1	258.5	1.4355

expressed by a copula function and its corresponding marginal distributions. A copula is a function that links two marginal distribution functions to construct a multivariate distribution function. Sklar's theorem states that if $F_{XY}(x, y)$ is a bivariate distribution function of 2 correlated random variables X and Y the respective marginal distributions $F_X(x)$ and $F_Y(y)$, it is possible to write a cumulative distribution function (CDF) with two single marginal distributions as follows:

$$F_{XY}(x, y) = C_\theta[F_X(x), F_Y(y)] \quad (1)$$

where θ is the copula parameter. If these marginal distributions are continuous, a unique copula function $C(\cdot)$ exists (Sraj et al., 2015).

There are many classes of copula functions, such as Archimedean copulas, elliptical copulas and Plackett copulas (Plackett, 1965; Fang et al., 2002). Archimedean copulas are popular because they can be easily constructed and are capable of capturing a wide range of dependence structures with several desirable properties, such as symmetry and associativity (Nelson, 2006; Hofert, 2008). The widely used bivariate Archimedean family copulas include the Clayton Copula, Frank Copula, and Gumbel-Hougaard (GH) Copula, with a parameter θ, as shown in Table 2. The copula parameter θ is usually estimated by the maximum likelihood method (Strupczewski et al., 2001). Therefore, the joint distribution function based on the copula method can be derived when the marginal distribution functions of variables are determined (Zhang and Singh, 2007a).

In current studies, root mean square error (*RMSE*) (Zhang and Singh, 2006), Akaike's information criterion (*AIC*) (Zhang and Singh, 2007b) and Nash-Sutcliffe efficiency (E_{ns}) (Xu et al., 2017) are usually employed to measure the goodness of fit of the joint distribution.

3.2 Joint return period

In conventional univariate analysis, the return period is usually used to represent the average time interval of a specific design flood,

TABLE 2 Types of Clayton, Frank and GH copulas.

Archimedean copula	C_θ	Range of θ
Clayton	$(F_X(x)^{-\theta} + F_Y(y)^{-\theta} - 1)^{-1/\theta}$	$\theta > 0$
Frank	$-\frac{1}{\theta}\ln[1 + \frac{(e^{-\theta F_X(x)}-1)(e^{-\theta F_Y(y)}-1)}{e^{-\theta}-1}]$	$-\infty < \theta < \infty$
G-H	$\exp[-((-\ln F_X(x))^\theta + (-\ln F_Y(y))^\theta)^{1/\theta}]$	$\theta \geq 1$

which is also a method used to measure the magnitude of floods. Within the copula-based framework, various definitions of the joint return period have been proposed, such as OR, AND, Kendall, dynamic, and structure-based return periods (Shiau, 2003; De Michele et al., 2005; Salvadori et al., 2011; Yin et al., 2018a). In this paper, the OR case (T_{or}) is adopted to describe the flood occurrence and can be expressed as follows:

$$T_{or} = \frac{\mu}{1 - F(q,w)} = \frac{\mu}{1 - C_\theta[F_Q(q), F_W(w)]} \tag{2}$$

where μ is the mean interarrival time between two consecutive events (in the case of annual maxima μ =1 year), and $F(q,w) = P(q \geq Q, w \geq W)$ is depicted by a copula function $C_\theta[F_Q(q), F_W(w)]$; $F_Q(q)$ and $F_W(w)$ denote the marginal distribution functions Q and W, respectively.

3.3 Most-likely event selection

According to Eq. 2, in the bivariate case, infinite possible combinations of Q and W can be selected for a given joint return period T_{or}, which have the same joint probability. The different likelihood of each combination must be considered to select appropriate design scenarios (Salvadori et al., 2011; Xiong et al., 2020). Based on Sklar's theorem, all the possible compositions of flood volume and peak differ in terms of their probability of occurrence, which can be measured by the value of the joint PDF (Salvadori et al., 2011; Gräler et al., 2013; Guo et al., 2018). The most likely flood event $[q^*(t), w^*(t)]$ of all possible events at a given joint return period T_{or} can be obtained by the following formula:

$$\begin{cases} [q^*(t), w^*(t)] = \operatorname{argmax} f(q,w) = c_\theta[F_Q(q), F_W(w)] \cdot f_Q(q) \cdot f_W(w) \\ C_\theta[F_Q(q), F_W(w)] = 1 - \frac{1}{T_{or}} \end{cases} \tag{3}$$

where $f(q,w)$ is a nonstationary joint PDF of q and w; $C(\cdot)$ is the density function of the copula for nonstationary data series; and $f_Q(q)$ and $f_W(w)$ are the marginal PDFs.

3.4 Flood control risk

Generally, the risk is simplified and defined as the probability of occurrence of a risk event (Sun et al., 2018; Li et al., 2022). In this paper, the flood control risk for the reservoir is defined as the probability of the highest level over the design flood level and can be expressed as follows:

$$R = P(\mathrm{H}_m > \mathrm{H}_d) = \frac{m}{n} \tag{4}$$

where H_m is the highest reservoir level in the flood control operation, H_d is the design flood level of the reservoir, m is the number of times that the highest water level exceeds the design water level in stochastic simulations, and n is the total number of stochastic simulations.

3.5 General framework of risk estimation

In this research, the framework of estimating flood control risk with the flood uncertainty of flood volume and peak is proposed based on the Monte Carlo sampling method and the most likely event selection method. It can be divided into three steps, which are shown in Figure 2.

Step 1: Establish the joint distribution function. Based on the observed flood volume and peak data with k-samples, the marginal distributions $F_X(x)$ and $F_Y(y)$ and the probability density functions $f_X(x)$ and $f_Y(y)$ are established, respectively. The copula functions can be estimated by using the historical flood series. According to the goodness of fit of the joint distribution, the optimal copula function is selected to construct the joint distribution function of flood volume and peak.

Step 2: Stochastic simulation of the flood. Based on the multilevel Monte Carlo method (Giles, 2008; Brodie, 2013; Clare et al., 2022), n sets of bivariate data with k-samples are randomly generated. Based on the generated flood series, the joint distribution function is constructed for each set. The most likely method is employed to select the appropriate (q,w) under the given T_{or}.

Step 3: Calculate the risk. According to the engineering and hydrological characteristics, various design floodwater utilization schemes have been developed. The design flood hydrograph can be obtained by n sets of (q,w) and typical floods. Taking n sets of flood hydrographs as input data, the simulation of flood control operation is carried out, and the flood control risk can be calculated by Eq. 4.

4 Results

4.1 Parameter estimation for the marginal distributions

In this paper, the Pearson type III (P-III) distribution, which is recommended by the Chinese Ministry of Water Resources (Wang et al., 2015; Peng et al., 2017; Gao et al., 2018), was employed to obtain the single marginal distribution of flood volume and flood peak. The parameters of the P-III distribution were estimated by the moment method (Hosking, 1990) and are shown in Table 3. The K-S test (D_n) is employed to describe how well the distributions fit the flood data. With K-S's critical value $D_{0.05} = \frac{1.36}{\sqrt{50}} = 0.1923$, the D_n of flood volume and peak are both 0.0980. Therefore, flood volume data and flood peak data both failed to reject the P-III distribution.

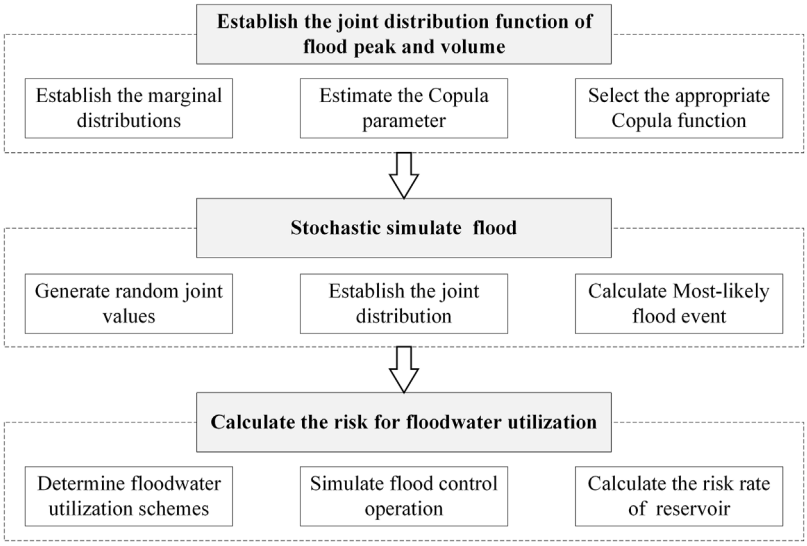

FIGURE 2
Flowchart of the proposed framework.

TABLE 3 Parameters of P-III in flood volume and peak.

Flood variables	α	β	δ	C_v	C_s	$\bar{x}$
Volume	0.95	0.0013	182	0.82	2.05	911.8
Peak	0.76	0.0030	63	0.92	2.30	315.1

TABLE 4 Results of copula parameter and goodness of fit.

Objects	Clayton copula	Frank copula	G-H copula
θ	0.1835	7.5897	1.8890
RMSE	0.0738	0.0424	0.0361
AIC	−258.5977	−313.9757	−330.2635
E_{ns}	0.9288	0.9763	0.9829

4.2 Joint distribution function based on the copula function

For the flood data, Clayton, Frank and G-H Copula were used to establish the joint distribution. *RMSE*, *AIC* and E_{ns} were obtained to measure the goodness of joint distribution as shown in Table 4. The empirical joint probabilities were estimated for the flood data by using the Gringorten formula (Gringorten, 1963; Du et al., 2019). The smaller the *RMSE* and *AIC* are, the better the joint distribution is. The larger E_{ns} is, the better the joint distribution is. Based on the above measurement principles, the results indicated that the best-fitted joint distribution is the G-H copula function with the parameter 1.8890 in the Shagou reservoir flood volume and peak. Then, the structure of the joint distribution function of the historical flood volume and peak was determined.

4.3 Most-likely design values

According to the bivariate joint distribution of historical flood data, the most likely method was employed to obtain the bivariate flood volume and peak for a given joint return period T_{or}. The comparison of design flood values under the bivariate joint return period and univariate return period is shown in Table 5.

The results show that the flood volume and peak obtained by the bivariate joint return for a given joint return period T_{or} are larger than the values obtained by the univariate return period. As shown

TABLE 5 Design flood values under different return periods.

T	Univariate return period		Bivariate joint return period	
	Volume (10^4m^3)	Peak (m^3/s)	Volume (10^4m^3)	Peak (m^3/s)
1,000	5,378	2,140	5,657	2,258
500	4,850	1917	5,129	2,035
200	4,153	1,624	4,431	1,741
100	3,626	1,403	3,904	1,519
50	3,100	1,184	3,377	1,299
20	2,406	897	2,678	1,009

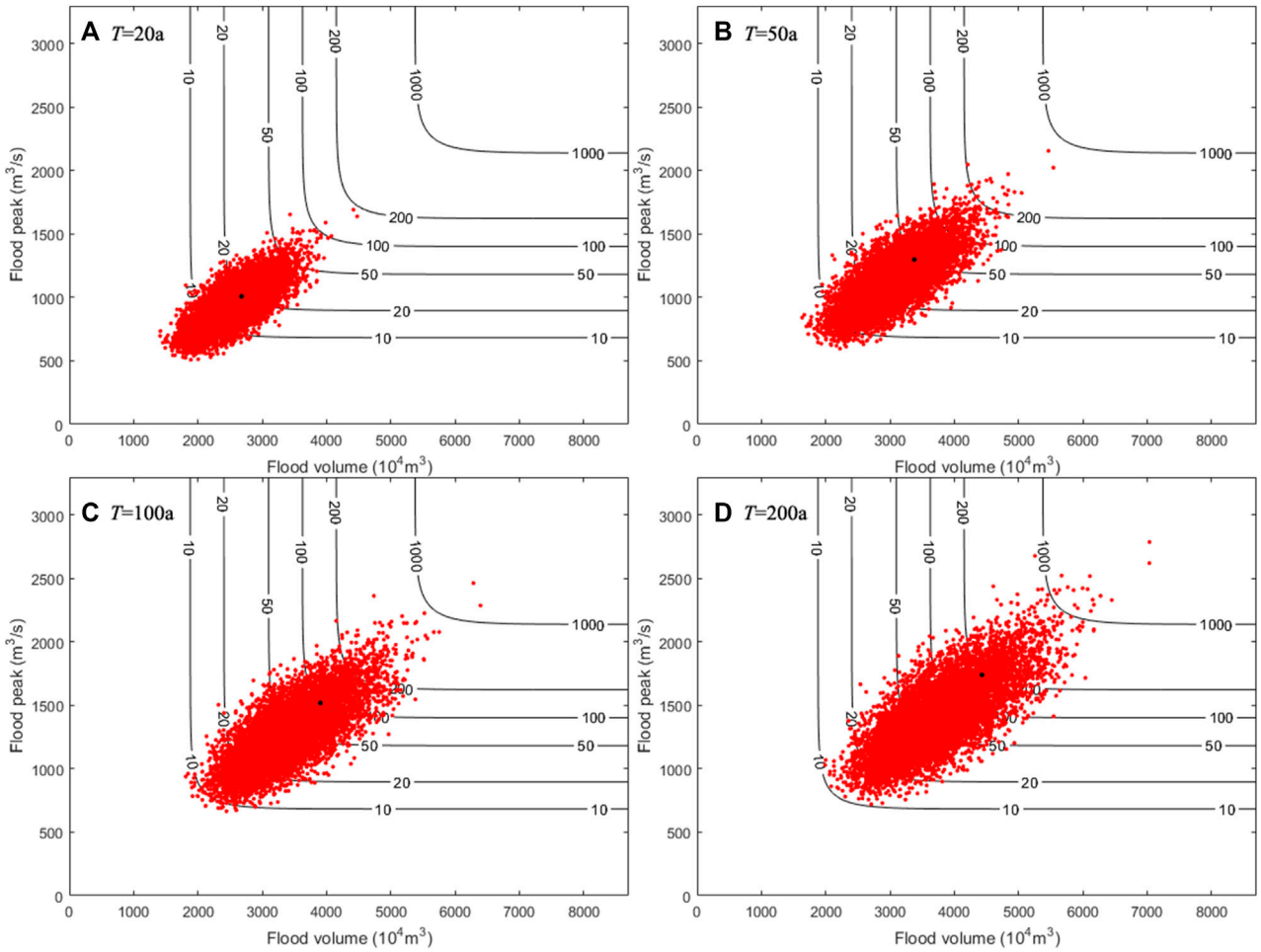

FIGURE 3
Design flood values under different stochastic simulations (the black point indicates that the value was obtained by historical data): **(A)** T = 20a; **(B)** T =50a; **(C)** T =100a; **(D)** T=200a.

in Table 5, the design flood volume for the univariate return period is 7.59% more than that for the bivariate joint return period, and the design flood peak for the univariate return period is 8.22% more than that for the bivariate joint return period. The value of flood volume and peak for joint return period T_{or} = 100a will make a larger return period in the respective univariate frequency analysis, which is nearly 144 a. Considering the correlation between flood volume and peak, multivariable flood events can be described more reasonably and may demonstrate a new theoretical basis for flood control operations.

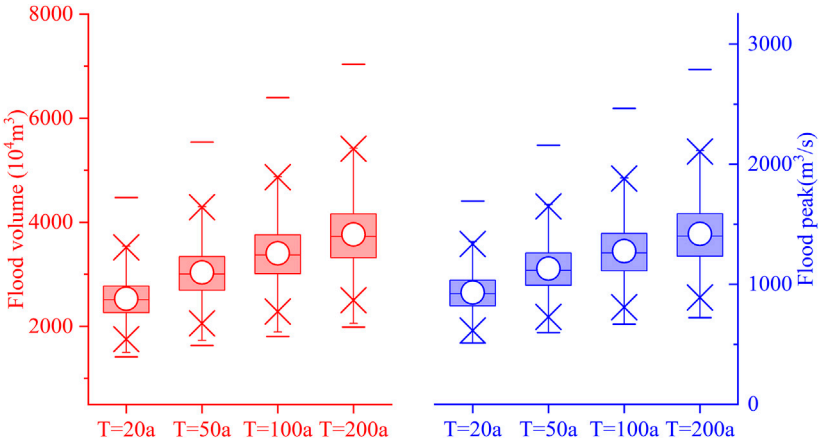

FIGURE 4
Box-plots of bivariate design data under different bivariate joint return periods.

4.4 Stochastic flood simulation

Based on the joint distribution function of flood volume and peak, the multilevel Monte Carlo method was employed to generate bivariate design data. Considering the number of historical flood data, 50 samples are randomly generated in each set. In the same way, the joint distribution was constructed, and the most likely design values were obtained. The number of stochastic simulation sets is 10,000 in this paper and the design flood values based on the stochastically simulated flood for given T_{or} are shown in Figure 3. The statistics of bivariate design data under different bivariate joint return periods are shown in Figure 4.

The results reveal that the generated design flood values are scattered around the most likely design value calculated based on historical flood data. As the bivariate joint return period increases, the generated design values also increase. For the T_{or} = 20a, the range of flood volume and flood peak is [1,412, 4,476] $\times 10^4$ m^3 and [509, 1,692] m^3/s, respectively. And for the T_{or} = 200a the range of flood volume and flood peak is [1990, 7,036] $\times 10^4$ m^3 and [721, 2,788] m^3/s, respectively. The Shagou reservoir is designed with the univariate return period T=100a, and the joint return period of the simulated joint design value spans from 10a to 1000a compared to the historical data under the same bivariate joint return period T_{or} = 100a. The joint design value is related to the economy of engineering construction and the reliability of flood control operation for reservoirs. If a small joint design value is adopted, the scale of the reservoir will be small, which is not conducive to providing its own benefits and may lead to a huge loss of life and property in flood control. The uncertainty of flood volume and peak should be given more attention in the field of floodwater utilization.

4.5 Flood control risk of reservoir

As mentioned in Section 2.1, the Shagou reservoir was designed with the standard T=100a, and the corresponding design flood water level is 233.13 m, which was obtained by univariate flood volume frequency analysis. In the current scheduling rules, the water level is limited to 231.5 m in the flood season. The essence of floodwater utilization is transferring more floodwater into ordinary water resources in the flood season for use in the non-flood season, where the flood-limited water level plays an important role. In recent years, numerous studies have been carried out to scientifically raise the flood-limited water level in the flood season without decreasing flood control standards or damaging the ecological environment of rivers (Li et al., 2010; Liu et al., 2015; Chang et al., 2017; Xie et al., 2018; Ye et al., 2019; Wang et al., 2020). In this paper, according to the current operation, the flood-limited water level is designed to be from 231.5 m to 232.0 m with an interval of 0.1 m to indicate various floodwater utilization schemes.

TABLE 6 Flood control risk statistics under different flood-limited water levels.

H_c (m)	H_s (m)	m_s	R_s
231.5	236.42	2,960	0.29
231.6	236.47	3,387	0.34
231.7	236.51	3,902	0.39
231.8	236.55	4,446	0.44
231.9	236.59	5,070	0.50
232.0	236.64	5,682	0.57

The flood in August 1974 was selected as a typical flood, and various flood hydrographs were obtained by using the design bivariate design value in Section 4.4. By simulating the current flood control operation, the maximum water level (H_s), the count of the maximum water level exceeding the current design water level (m_s), and the flood control risk (R_s) were calculated under different flood-limited water levels (H_c), which are shown in Table 6. The statistical results of the maximum water level are shown in Figure 5 under different flood-limited water levels.

In the flood control operation of a reservoir, the flood-limited water level is considered to be the initial water level in a flooding process. With the initial water level rise, the maximum water level in

TABLE 7 Flood control risk under different maximum control outflows.

Q_c (m^3/s)	H_s (m)	R_s
450	236.50	0.40
500	236.42	0.29
550	236.25	0.15

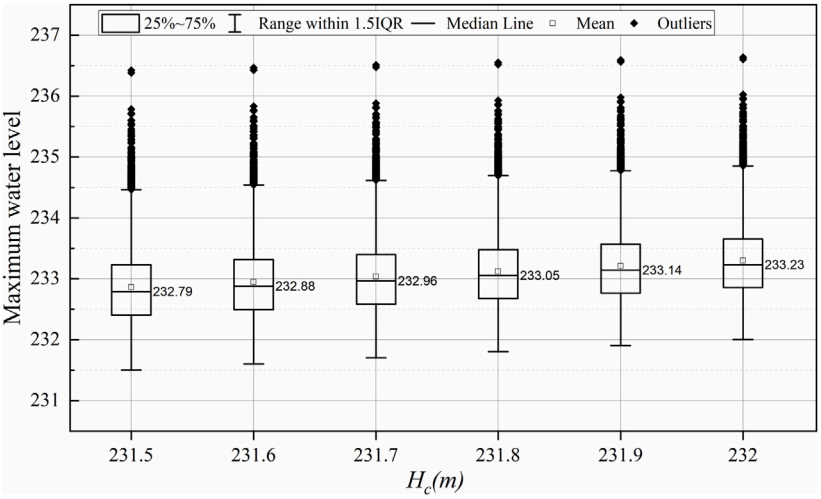

FIGURE 5
Statistical results of the maximum water level under various flood-limited water levels.

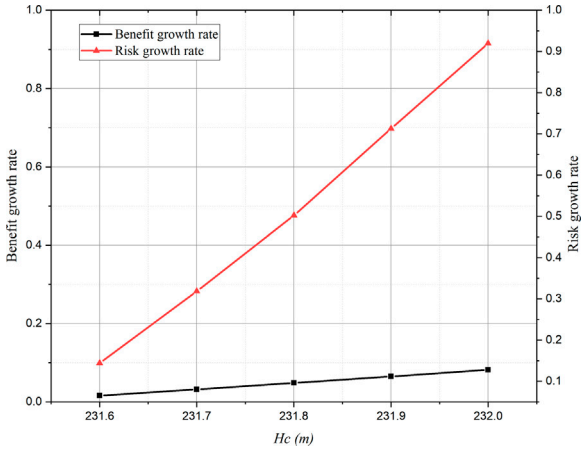

FIGURE 6
Increased water resources and flood control risk under various floodwater utilization schemes.

the flood control operation process will also increase accordingly. According to the statistical results, the averages of the maximum water levels are all less than the design water level of 233.13 m under flood utilization with flood-limited water levels of 231.5, 231.6, 231.7 and 231.8 m. With the increase in flood-limited water level, the counts of the maximum water level exceeding the current design water level similarly increased. When the flood-limited water level increased from 231.5 m to 232, H_c and R_s nearly doubled. The flood control risk increased with the rising flood-limited water level, and the benefit of floodwater utilization grew correspondingly. Assuming that the water level of the reservoir can be kept at the flood-limited water level when the flood season ends, the benefit

growth rate and risk growth rate can be calculated quantitatively compared to the current operation and are shown in Figure 6.

The results reveal that different increased rates occurred between benefit and risk with the same increased flood-limited water level. In particular, the growth rates of benefit and risk are 0.08% and 91% with H_c =232.0 compared to the current operation, respectively. Achieving a lower benefit increment brings a greater risk increment to water management, which shows that the marginal benefit may be contained in floodwater utilization.

5 Discussion

Flood control operations have a certain impact on reservoir flood control risk. As an important indicator of flood control operation, the maximum control outflow (Q_c) and the maximum water level in the flooding process are directly related (Ding et al., 2015; Moridi and Yazdi, 2017; Zhao et al., 2017). In this section, different maximum control outflows of the reservoir were set, representing the corresponding flood control operation, and the corresponding flood control risk was calculated based on the steps in Section 3. According to the current maximum control outflow of 500 m^3/s, flood control operations with maximum control outflows of 450 and 500 m^3/s were set, and the simulation of reservoir flood control was carried out with the design bivariate value in Section 4.4. Based on various flood control operations, the maximum water level of the reservoir was calculated, and the flood control risk was obtained, as shown in Table 7.

In flood operations, with the increase in the maximum control outflow of the reservoir, more floods are released downstream. For the upstream reservoir, the less flood control storage is needed, the lower the flood control risk is in flood control operation. In this paper, the maximum control outflow has a strong impact on flood control risk. In particular, with the maximum control outflow increasing to 550 from 500 m^3/s, the reduction in flood control risk will be 48%. In the field of floodwater utilization, many studies aim at risk decision-making for transforming some amount of floodwater into ordinary water resources without decreasing flood control standards (Li et al., 2010; Ye et al., 2019; Wang et al., 2022). The reduction of flood control risk is favorable for floodwater utilization, however, the flood control risk of the upstream reservoir affects the flood control risk of the downstream reservoir through changes in discharge control. In the flood control system, there is a risk transmission effect in different flood control projects.

6 Conclusion

Considering the influence of the uncertainty of flood volume and peak, the estimation of flood control risk is discussed in this paper. Taking the reservoir as the study object, the Monte Carlo sampling method and the most likely event selection method were employed to develop a general framework and then applied to the Shagou reservoir in the Shuhe River basin, China. The main conclusions can be summarized as follows:

(1) The proposed framework can estimate the flood control risk considering the uncertainty of flood volume and peak. For flood control risk with an uncertain distribution of random variables, the stochastic simulation has certain advantages. At present, the framework can be used with a single reservoir in the flood control risk of flood control systems. The calculation of flood control risk under cascade reservoirs and parallel reservoirs will continue to be studied in future work.

(2) The application of the framework to the Shagou reservoir in the Shuhe River basin showed that the flood control risk caused by the uncertainty of flood volume and peak is 0.29, which indicates that the design value obtained by the bivariate joint return is much greater than the value from univariate frequency analysis. Multivariable flood events can be described more reasonably and may provide a new theoretical basis for flood control operations.

(3) The flood control risk and the benefit of floodwater utilization increased with the rising flood-limited water level, and different rate increases occurred between the benefit and risk. The marginal benefit may be in floodwater utilization. The flood operation function, such as different maximum control outflows, also has a considerable impact on the flood control risk and may play an important role in floodwater utilization. The transmission effect of flood control risk is not quantitatively evaluated, which will be improved in future research.

Data availability statement

The raw data supporting the conclusion of this article will be made available by the authors, without undue reservation.

Author contributions

HD: conceptualization, methodology, writing original, and resources. ZW: review and editing, investigation, and resources. JY: review and provided advice for analyzing the data and figures. All authors contributed to the article and approved the submitted version.

Funding

This research was supported by the Natural Science Foundation of Jiangsu Province of China (No. BK20211023).

Conflict of interest

The authors declare that the research was conducted in the absence of any commercial or financial relationships that could be construed as a potential conflict of interest.

Publisher's note

References

Brodie, I. M. (2013). Rational Monte Carlo method for flood frequency analysis in urban catchments. *J. Hydrol.* 486, 306–314. doi:10.1016/j.jhydrol.2013.01.039

Brunner, M. I., and Sikorska-Senoner, A. E. (2019). Dependence of flood peaks and volumes in modeled discharge time series: Effect of different uncertainty sources. *J. Hydrol.* 572, 620–629. doi:10.1016/j.jhydrol.2019.03.024

Chang, J., Guo, A., Du, H., and Wang, Y. (2017). Floodwater utilization for cascade reservoirs based on dynamic control of seasonal flood control limit levels. *Environ. Earth Sci.* 76, 260. doi:10.1007/s12665-017-6522-z

Chen, J., Shi, H., Sivakumar, B., and Peart, M. R. (2016). Population, water, food, energy and dams. *Renew. Sustain. Energy Rev.* 56, 18–28. doi:10.1016/j.rser.2015.11.043

Chen, J., Zhong, P.-A., An, R., Zhu, F., and Xu, B. (2019). Risk analysis for real-time flood control operation of a multi-reservoir system using a dynamic Bayesian network. *Environ. Model. Softw.* 111, 409–420. doi:10.1016/j.envsoft.2018.10.007

Clare, M. C. A., Piggott, M. D., and Cotter, C. J. (2022). Assessing erosion and flood risk in the coastal zone through the application of multilevel Monte Carlo methods. *Coast. Eng.* 174, 104118. doi:10.1016/j.coastaleng.2022.104118

Cloke, H. L., and Pappenberger, F. (2009). Ensemble flood forecasting: A review. *J. Hydrol.* 375, 613–626. doi:10.1016/j.jhydrol.2009.06.005

Daneshkhah, A., Remesan, R., Chatrabgoun, O., and Holman, I. P. (2016). Probabilistic modeling of flood characterizations with parametric and minimum information pair-copula model. *J. Hydrol.* 540, 469–487. doi:10.1016/j.jhydrol.2016.06.044

De Michele, C., Salvadori, G., Canossi, M., Petaccia, A., and Rosso, R. (2005). Bivariate statistical approach to check adequacy of dam spillway. *J. Hydrol. Eng.* 10, 50–57. doi:10.1061/(asce)1084-0699(2005)10:1(50)

Delenne, C., Cappelaere, B., and Guinot, V. (2012). Uncertainty analysis of river flooding and dam failure risks using local sensitivity computations. *Reliab. Eng. Syst. Saf.* 107, 171–183. doi:10.1016/j.ress.2012.04.007

Diao, Y., and Wang, B. (2010). Risk analysis of flood control operation mode with forecast information based on a combination of risk sources. *Sci. China-technological Sci.* 53, 1949–1956. doi:10.1007/s11431-010-3124-3

Ding, W., Zhang, C., Cai, X., Li, Y., and Zhou, H. (2017). Multiobjective hedging rules for flood water conservation. *Water Resour. Res.* 53, 1963–1981. doi:10.1002/2016WR019452

Ding, W., Zhang, C., Peng, Y., Zeng, R., Zhou, H., and Cai, X. (2015). An analytical framework for flood water conservation considering forecast uncertainty and acceptable risk. *Water Resour. Res.* 51, 4702–4726. doi:10.1002/2015WR017127

Dong, W. (2009). Rethinking risk analysis: The risks of risk analysis in water issues as the case. *Hum. Ecol. Risk Assess. Int. J.* 15, 1079–1083. doi:10.1080/10807030903304690

Du, H., Wang, Y., Liu, K., and Cheng, L. (2019). Exceedance probability of precipitation for the Shuhe to futuan water transfer project in China. *Environ. Earth Sci.* 78, 240. doi:10.1007/s12665-019-8207-2

Dung, N. V., Merz, B., Bárdossy, A., and Apel, H. (2015). Handling uncertainty in bivariate quantile estimation – an application to flood hazard analysis in the Mekong Delta. *J. Hydrol.* 527, 704–717. doi:10.1016/j.jhydrol.2015.05.033

Fan, Y. R., Huang, W. W., Huang, G. H., Li, Y. P., Huang, K., and Li, Z. (2016). Hydrologic risk analysis in the Yangtze River basin through coupling Gaussian mixtures into copulas. *Adv. Water Resour.* 88, 170–185. doi:10.1016/j.advwatres.2015.12.017

Fang, H.-B., Fang, K.-T., and Kotz, S. (2002). The meta-elliptical distributions with given marginals. *J. Multivar. Anal.* 82, 1–16. doi:10.1006/jmva.2001.2017

Gao, S., Liu, P., Pan, Z., Ming, B., Guo, S., Cheng, L., et al. (2018). Incorporating reservoir impacts into flood frequency distribution functions. *J. Hydrol.* 568, 234–246. doi:10.1016/j.jhydrol.2018.10.061

Giles, M. B. (2008). Multilevel Monte Carlo path simulation. *Oper. Res.* 56, 607–617. doi:10.1287/opre.1070.0496

Gräler, B., van den Berg, M. J., Vandenberghe, S., Petroselli, A., Grimaldi, S., De Baets, B., et al. (2013). Multivariate return periods in hydrology: A critical and practical review focusing on synthetic design hydrograph estimation. *Hydrol. Earth Syst. Sci.* 17, 1281–1296. doi:10.5194/hess-17-1281-2013

Gringorten, I. I. (1963). A plotting rule for extreme probability paper. *J. Geophys. Res.* 68, 813–814. doi:10.1029/jz068i003p00813

Guan, X., Xia, C., Xu, H., Liang, Q., Ma, C., and Xu, S. (2022). Flood risk analysis integrating of Bayesian-based time-varying model and expected annual damage considering non-stationarity and uncertainty in the coastal city. *J. Hydrol.* 617, 129038. doi:10.1016/j.jhydrol.2022.129038

Guo, A., Chang, J., Wang, Y., Huang, Q., and Li, Y. (2020). Uncertainty quantification and propagation in bivariate design flood estimation using a Bayesian information-theoretic approach. *J. Hydrol.* 584, 124677. doi:10.1016/j.jhydrol.2020.124677

Guo, S., Muhammad, R., Liu, Z., Xiong, F., and Yin, J. (2018). Design flood estimation methods for cascade reservoirs based on copulas. *Water* 10, 560. doi:10.3390/w10050560

Hofert, M. (2008). Sampling archimedean copulas. *Comput. Stat. Data Anal.* 52, 5163–5174. doi:10.1016/j.csda.2008.05.019

Hosking, J. (1990). L-Moments: Analysis and estimation of distributions using linear combinations of order statistics. *J. R. Stat. Soc. Ser. B* 52, 105–124. doi:10.1111/j.2517-6161.1990.tb01775.x

Huang, Y., Liang, Z., Hu, Y., Li, B., and Wang, J. (2020). Theoretical derivation for the exceedance probability of corresponding flood volume of the equivalent frequency regional composition method in hydrology. *Hydrol. Res.* 51, 1274–1292. doi:10.2166/nh.2020.027

Kriauciuniene, J., Jakimavicius, D., Sarauskiene, D., and Kaliatka, T. (2013). Estimation of uncertainty sources in the projections of Lithuanian river runoff. *Stoch. Environ. Res. Risk Assess.* 27, 769–784. doi:10.1007/s00477-012-0608-7

Li, J., Zhong, P., Wang, Y., Yang, M., Fu, J., Liu, W., et al. (2022). Risk analysis for the multi-reservoir flood control operation considering model structure and hydrological uncertainties. *J. Hydrol.* 612, 128263. doi:10.1016/j.jhydrol.2022.128263

Li, X., Guo, S., Liu, P., and Chen, G. (2010). Dynamic control of flood limited water level for reservoir operation by considering inflow uncertainty. *J. Hydrol.* 391, 124–132. doi:10.1016/j.jhydrol.2010.07.011

Liu, K., Wang, Z., Cheng, L., Zhang, L., Du, H., and Tan, L. (2019). Optimal operation of interbasin water transfer multireservoir systems: An empirical analysis from China. *Environ. Earth Sci.* 78, 238. doi:10.1007/s12665-019-8242-z

Liu, P., Li, L., Guo, S., Xiong, L., Zhang, W., Zhang, J., et al. (2015). Optimal design of seasonal flood limited water levels and its application for the Three Gorges Reservoir. *J. Hydrol.* 527, 1045–1053. doi:10.1016/j.jhydrol.2015.05.055

Liu, Z., Xu, X., Cheng, J., Wen, T., and Niu, J. (2018). Hydrological risk analysis of dam overtopping using bivariate statistical approach: A case study from geheyan reservoir, China. *Stoch. Environ. Res. Risk Assess.* 32, 2515–2525. doi:10.1007/s00477-018-1550-0

Malekmohammadi, B., Kerachian, R., and Zahraie, B. (2009). Developing monthly operating rules for a cascade system of reservoirs: Application of Bayesian Networks. *Environ. Model. Softw.* 24, 1420–1432. doi:10.1016/j.envsoft.2009.06.008

Melching, C. S. (1992). An improved first-order reliability approach for assessing uncertainties in hydrologic modeling. *J. Hydrol.* 132, 157–177. doi:10.1016/0022-1694(92)90177-W

Meng, X., Chang, J., Wang, X., and Wang, Y. (2018). Multi-objective hydropower station operation using an improved cuckoo search algorithm. *Energy* 168, 425–439. doi:10.1016/j.energy.2018.11.096

Michailidi, E. M., and Bacchi, B. (2017). Dealing with uncertainty in the probability of overtopping of a flood mitigation dam. *Hydrol. Earth Syst. Sci.* 21, 2497–2507. doi:10.5194/hess-21-2497-2017

Moridi, A., and Yazdi, J. (2017). Optimal allocation of flood control capacity for multi-reservoir systems using multi-objective optimization approach. *Water Resour. Manag.* 31, 4521–4538. doi:10.1007/s11269-017-1763-x

Nakamura, S., and Oki, T. (2018). Paradigm shifts on flood risk management in Japan: Detecting triggers of design flood revisions in the modern era. *Water Resour. Res.* 54, 5504–5515. doi:10.1029/2017WR022509

Nelson, R. B. (2006). *An introduction to copulas*. New York, NY: Springer.

Ocio, D., Le Vine, N., Westerberg, I., Pappenberger, F., and Buytaert, W. (2017). The role of rating curve uncertainty in real-time flood forecasting. *Water Resour. Res.* 53, 4197–4213. doi:10.1002/2016WR020225

Ozga-Zielinski, B., Ciupak, M., Adamowski, J., Khalil, B., and Malard, J. (2016). Snow-melt flood frequency analysis by means of copula based 2D probability distributions for the Narew River in Poland. *J. Hydrol. Reg. Stud.* 6, 26–51. doi:10.1016/j.ejrh.2016.02.001

Parkes, B., and Demeritt, D. (2016). Defining the hundred year flood: A bayesian approach for using historic data to reduce uncertainty in flood frequency estimates. *J. Hydrol.* 540, 1189–1208. doi:10.1016/j.jhydrol.2016.07.025

Peng, Y., Chen, K., Yan, H., and Yu, X. (2017). Improving flood-risk analysis for confluence flooding control downstream using copula Monte Carlo method. *J. Hydrol. Eng.* 22, 04017018. doi:10.1061/(ASCE)HE.1943-5584.0001526

Plackett, R. L. (1965). A class of bivariate distributions. *J. Am. Stat. Assoc.* 60, 516–522. doi:10.1080/01621459.1965.10480807

Salvadori, G., De Michele, C., and Durante, F. (2011). On the return period and design in a multivariate framework. *Hydrol. Earth Syst. Sci.* 15, 3293–3305. doi:10.5194/hess-15-3293-2011

Sancetta, A., and Satchell, S. (2004). The bernstein copula and its applications to modeling and approximations of multivariate distributions. *Econom. Theory* 20, 535–562. doi:10.1017/s026646660420305x

Serinaldi, F. (2013). An uncertain journey around the tails of multivariate hydrological distributions. *Water Resour. Res.* 49, 6527–6547. doi:10.1002/wrcr.20531

Shaked, M., and Joe, H. (1998). Multivariate models and dependence concepts. *J. Am. Stat. Assoc.* 93, 1237. doi:10.2307/2669872

Shiau, J. T. (2003). Return period of bivariate distributed extreme hydrological events. *Stoch. Environ. Res. Risk Assess.* 17, 42–57. doi:10.1007/s00477-003-0125-9

Simonovic, S. P., and Arunkumar, R. (2016). Comparison of static and dynamic resilience for a multipurpose reservoir operation. *Water Resour. Res.* 52, 8630–8649. doi:10.1002/2016WR019551

Sklar, A. (1959). Fonctions de répartition à n dimensions et leurs marges. *Publ. Inst. Stat. Univ. Paris* 8, 229–231. doi:10.1007/978-3-642-33590-7

Sraj, M., Bezak, N., and Brilly, M. (2015). Bivariate flood frequency analysis using the copula function: A case study of the litija station on the sava river. *Hydrol. Process.* 29, 225–238. doi:10.1002/hyp.10145

Strupczewski, W. G., Singh, V. P., and Feluch, W. (2001). Non-stationary approach to at-site flood frequency modelling I. Maximum likelihood estimation. *J. Hydrol.* 248, 123–142. doi:10.1016/S0022-1694(01)00397-3

Sun, Y., Zhu, F., Chen, J., and Li, J. (2018). Risk analysis for reservoir real-time optimal operation using the scenario tree-based stochastic optimization method. *Water* 10, 606. doi:10.3390/w10050606

Tung, Y., and Wong, C. (2014). Assessment of design rainfall uncertainty for hydrologic engineering applications in Hong Kong. *Stoch. Environ. Res. Risk Assess.* 28, 583–592. doi:10.1007/s00477-013-0774-2

Wallington, K., and Cai, X. (2020). Feedback between reservoir operation and floodplain development: Implications for reservoir benefits and beneficiaries. *Water Resour. Res.* 56. doi:10.1029/2019WR026610

Wang, J., Liang, Z., Hu, Y., and Wang, D. (2015). Modified weighted function method with the incorporation of historical floods into systematic sample for parameter estimation of Pearson type three distribution. *J. Hydrol.* 527, 958–966. doi:10.1016/j.jhydrol.2015.05.023

Wang, K., Wang, Z., Liu, K., Du, H., Mo, Y., Wang, M., et al. (2022). Assessing the floodwater utilization potential in a reservoir-controlled watershed: A novel method considering engineering regulations and an empirical case from China. *Ecol. Inf.* 68, 101581. doi:10.1016/j.ecoinf.2022.101581

Wang, Z., Wang, K., Liu, K., Cheng, L., Wang, L., and Ye, A. (2019). Interactions between lake-level fluctuations and waterlogging disasters around a large-scale shallow lake: An empirical analysis from China. *Water* 11, 318. doi:10.3390/w11020318

Wang, Z., Zhang, L., Cheng, L., Liu, K., Ye, A., and Cai, X. (2020). Optimizing operating rules for a reservoir system in northern China considering ecological flow requirements and water use priorities. *J. Water Resour. Plan. Manag.* 146. doi:10.1061/(ASCE)WR.1943-5452.0001236

Wu, S.-J., Yang, J.-C., and Tung, Y.-K. (2011). Risk analysis for flood-control structure under consideration of uncertainties in design flood. *Nat. Hazards* 58, 117–140. doi:10.1007/s11069-010-9653-z

Wu, Z., Shen, Y., Wang, H., and Wu, M. (2020). Urban flood disaster risk evaluation based on ontology and Bayesian Network. *J. Hydrol.* 583, 124596. doi:10.1016/j.jhydrol.2020.124596

Xie, A., Liu, P., Guo, S., Zhang, X., Jiang, H., and Yang, G. (2018). Optimal design of seasonal flood limited water levels by jointing operation of the reservoir and floodplains. *Water Resour. Manag.* 32, 179–193. doi:10.1007/s11269-017-1802-7

Xiong, F., Guo, S., Liu, P., Xu, C.-Y., Zhong, Y., Yin, J., et al. (2019). A general framework of design flood estimation for cascade reservoirs in operation period. *J. Hydrol.* 577, 124003. doi:10.1016/j.jhydrol.2019.124003

Xiong, F., Guo, S., Yin, J., Tian, J., and Rizwan, M. (2020). Comparative study of flood regional composition methods for design flood estimation in cascade reservoir system. *J. Hydrol.* 590, 125530. doi:10.1016/j.jhydrol.2020.125530

Xiong, W., and Qi, H. (2010). "A extended TOPSIS method for the stochastic multi-criteria decision making problem through interval estimation," in 2010 2nd International Workshop on Intelligent Systems and Applications, China, 22-23 May 2010.

Xu, P., Wang, D., Singh, V. P., Wang, Y., Wu, J., Wang, L., et al. (2017). A two-phase copula entropy-based multiobjective optimization approach to hydrometeorological gauge network design. *J. Hydrol.* 555, 228–241. doi:10.1016/j.jhydrol.2017.09.046

Yan, B., Guo, S., and Chen, L. (2014). Estimation of reservoir flood control operation risks with considering inflow forecasting errors. *Stoch. Environ. Res. Risk Assess.* 28, 359–368. doi:10.1007/s00477-013-0756-4

Ye, A., Wang, Z., Zhang, L., Wang, L., and Wang, K. (2019). Assessment approach to the floodwater utilization potential of a basin and an empirical analysis from China. *Environ. Earth Sci.* 78, 52. doi:10.1007/s12665-019-8050-5

Yin, J., Guo, S., He, S., Guo, J., Hong, X., and Liu, Z. (2018a). A copula-based analysis of projected climate changes to bivariate flood quantiles. *J. Hydrol.* 566, 23–42. doi:10.1016/j.jhydrol.2018.08.053

Yin, J., Guo, S., Liu, Z., Yang, G., Zhong, Y., and Liu, D. (2018b). Uncertainty analysis of bivariate design flood estimation and its impacts on reservoir routing. *Water Resour. Manag.* 32, 1795–1809. doi:10.1007/s11269-018-1904-x

Zhang, L., and Singh, V. P. (2006). Bivariate flood frequency analysis using the copula method. *J. Hydrol. Eng.* 11, 150–164. doi:10.1061/(asce)1084-0699(2006)11:2(150)

Zhang, L., and Singh, V. P. (2007a). Bivariate rainfall frequency distributions using Archimedean copulas. *J. Hydrol.* 332, 93–109. doi:10.1016/j.jhydrol.2006.06.033

Zhang, L., and Singh, V. P. (2007b). Gumbel–hougaard copula for trivariate rainfall frequency analysis. *J. Hydrol. Eng.* 12, 409–419. doi:10.1061/(asce)1084-0699(2007)12:4(409)

Zhang, L., and Singh, V. P. (2007c). Trivariate flood frequency analysis using the gumbel–hougaard copula. *J. Hydrol. Eng.* 12, 431–439. doi:10.1061/(asce)1084-0699(2007)12:4(431)

Zhao, T., Zhao, J., Lei, X., Wang, X., and Wu, B. (2017). Improved dynamic programming for reservoir flood control operation. *Water Resour. Manag.* 31, 2047–2063. doi:10.1007/s11269-017-1599-4

frontiers | Frontiers in Earth Science

TYPE Original Research
PUBLISHED 30 May 2023
DOI 10.3389/feart.2023.1209868

OPEN ACCESS

EDITED BY
Wei Ge,
Zhengzhou University, China

REVIEWED BY
Wei Li,
Zhengzhou Railway Vocational and Technical College, China
Chaoning Lin,
Hohai University, China

*CORRESPONDENCE
Hanyu Zhu,
hanyu_zhu_ncwu@163.com

RECEIVED 21 April 2023
ACCEPTED 16 May 2023
PUBLISHED 30 May 2023

CITATION
Jiao H, Zhang J, Li Y, Cheng L, Chen Y and Zhu H (2023), Research on decision-making of water diversion supply chain considering both social welfare and water quality utility.
Front. Earth Sci. 11:1209868.
doi: 10.3389/feart.2023.1209868

Research on decision-making of water diversion supply chain considering both social welfare and water quality utility

Hongbo Jiao, Jiachao Zhang, Yinan Li, Liming Cheng, Yongrui Chen and Hanyu Zhu*

North China University of Water Resources and Electric Power, Zhengzhou, China

When water diversion projects become important part of the water network around the world, the effective operation and management of the projects play important roles in giving full play to the optimal allocation of water resources. For the operation and management of water transfer, the decision-making of water supply chain under the scenario of economic benefit, producer surplus, and water quality utility should be considered simultaneously. According to the idea of supply chain, this paper regards water transfer operation management as a water supply chain composed of water transfer companies, water supply companies, and consumers. From the perspective of social welfare and water quality utility, a comprehensive optimization and coordination decision model for water transfer is proposed. Taking the South-to-North Water Diversion Project as the research object, the cost-sharing contract is designed, and the Stackelberg game method is used to optimize the decision-making and coordination of the water supply chain. The results show that when the concern coefficient and the cost-sharing ratio are evaluated within a given feasible value region, the profits of both the water transfer company and the water supply company can be improved. The feasible value interval of the concern coefficient decreases with the increase in the cost-bearing proportion. When the concern coefficient increases, the profit of the water transfer company decreases, while profit of the water supply company, water quality, consumer surplus, water quality utility, and utility of the water transfer company increase gradually. The results provide valuable references for water transfer decision-making.

KEYWORDS

water division supply chain, decision-making research, social welfare, water quality utility, Stackelberg game

1 Introduction

Under the circumstances of global climate change, population growth, and uneven regional distribution of natural water resources, the construction and operation of large-scale inter-basin water transfer projects have alleviated the problems of water resource shortage and uneven spatial distribution. Among them, the most typical cross-basin water diversion projects include the California State Water Project, the Quebec Water Transfer Project in Canada, the Snowy Mountains Scheme in Australia, and the South-to-North Water Diversion Project (SNWDP) in China (Yang, 2003). SNWDP, as the largest water diversion project in China, is a systematic, quasi-public, and basic large-scale project,

involving various aspects such as economy, society, resources, and environment. The water transmission line of SNWDP is 4,350 km, crossing the four major river basins of the Yangtze River, Huaihe River, Yellow River, and Haihe River (Xu and Zeng, 2022). As of February 2023, the SNWDP has accumulatively transferred more than 60 billion cubic meters of water, directly benefiting more than 150 million people (Wang, 2023), effectively alleviating the water shortage problem in Beijing, Tianjin, and other cities (Guo et al., 2020; Niu et al., 2022). The main objectives and tasks of the project construction and operation are to achieve water supply and water saving, ecological security, and spiritual culture, and the government, enterprises, citizens, and other parties are jointly involved. As a large-scale and complex water diversion project across river basins, multi-subjects, and multi-objectives, it covers a wide range, involves many stakeholders, and has high operational and management complexity (Kattel et al., 2019). In operation and management practices, the management department often considers the economic benefits of the project as the primary factor when making decisions on issues, such as water price formulation, water volume scheduling, and water allocation. Although social factors, such as population migration, land requisition, and social welfare, and environmental factors, such as geological landforms, ecological environment, and water quality and quantity, are also taken into consideration, the influence of these factors on decision-making is still limited (Chen and Wang, 2019; Song et al., 2019). Therefore, how to consider social and environmental factors for the improvement of the operation management mechanism and decision-making efficiency is an urgent problem to be solved.

The operation of water diversion projects needs to realize the effective allocation of water resources on the basis of coordinating the interests of all parties, which can be analyzed by applying the theory of cost reduction and efficiency increase in supply chain management theory and the mechanism of interest negotiation. It is also of great practical significance to the SNWDP, a complex supply chain system with multiple basins, multiple water sources, multiple subjects, and environmental and social benefits. Many scholars have used supply chain theory to conduct research studies on the operation and management issues of SNWDP. The research topics involve the operational decision-making and applicability of the water resource supply chain (Sheng and Webber, 2018; Sheng et al., 2022), profit distribution (Sheng and Webber, 2021), policy research evaluation (Peng et al., 2018; Sheng and Qiu, 2022), benefit analysis (Yang et al., 2021), and many other aspects. It can be seen that the existing supply chain theory is mainly used in the analysis of economic goals. However, in fact, the SNWDP is not only a water resource allocation project but also a welfare project that guarantees social benefits and improves ecological benefits (Xu et al., 2021; Lu Q. et al., 2022; Liu et al., 2022). However, the existing research has limited discussions on its social and environmental dimensions and cannot fully match the needs of the SNWDP to achieve multiple goals (Koberg and Longoni, 2019). The sustainable supply chain theory focuses on the influence of "social and environmental" factors, which is highly consistent with the operational goals of SNWDP and also appropriately reflects the conflict of interests that urgently need to be resolved in the water transfer supply chain system (Chen and Wang, 2020). Therefore, it is quite necessary to introduce the theoretical model of sustainable supply chain and explore it from multiple dimensions of society and the environment.

Social needs and social interests exist widely in water conservancy projects, covering aspects such as daily life, agriculture, industry, flood control, ecological environment, and disaster management (Wang et al., 2022; Wang et al., 2023). Before the 1970s, international scholars' research on the impact of engineering projects mainly focused on economic aspects (He et al., 2018). As the social problems caused by engineering projects are receiving more and more attention, some scholars have proposed that in the impact research of engineering projects, both economic development and social impact should be emphasized (Ge et al., 2020b). Research on social factors related to hydraulic engineering includes social impact assessment, social risk assessment, and social welfare (De Nicolás, 2016; Liu et al., 2016). Water resources have the characteristics of quasi-public goods, and water conservancy projects have the characteristics of public welfare. In the operation of cross-basin water diversion projects, it is crucial to make better use of water resources to solve the water resource shortage problem and the contradiction between the supply and demand and promote economic development outside. Meanwhile, it is more essential to improve the ecological environment and achieve coordinated development among regions to improve public interests and social welfare (Chen and Chen, 2020).

The book American Dictionary of Social Work defines social welfare as a national system of programs, benefits, and services designed to assist people in meeting their social, economic, educational, and health needs (Barker, 2003). Its main function is to meet the needs of a better life, and it is also the most basic and important social institutional arrangement. The cross-basin water diversion project reduces the environmental capacity of the water source area and has an adverse impact on the ecological environment of the water source area. However, changes in the ecological environment along the water diversion project will have adverse effects on the interaction of stakeholders and policy formulation, which will inevitably affect social welfare (Mu, 2018). Studies chose game theory and coordination theory to study the cross-basin water transfer supply chain from a social welfare maximization perspective and provide theoretical advice for the improvement of business performance and social welfare optimization of supply chain participants (Chen and Pei, 2018; Chen et al., 2019a). One of the goals of the SNWDP is to fully guarantee the life, production, and ecological security of the people in the water source area and the water-receiving area (Xu and Zeng, 2022), which is the embodiment of social welfare when the government sets the project goals. Similarly, for enterprises, actively paying attention to social welfare undertakings and assuming corporate responsibilities are also necessary for the sustainable development of enterprises (Peng et al., 2022). Therefore, how does the government intervene in the realization of social welfare goals (such as planning capital investment, formulating social security and welfare policies, optimizing supervision and evaluation mechanisms), how do the enterprises play their social responsibility role to return to the society (such as sustainable management of water resources, cooperation with stakeholders, and promotion of social investment projects), and

more importantly how to coordinate and cooperate with various roles in the supply chain to ensure that the public benefits from the green operation of water transfer projects and maximize social welfare are urgent issues to be discussed (Li C. et al., 2022).

As a large-scale cross-basin water diversion project, the SNWDP will have a series of ecological and environmental impacts on the water ecosystem. Therefore, it is crucial to maintain the health of ecosystems while meeting human water demands (Guo et al., 2020). Guo et al. (2019) found that water diversion may have a chain reaction on fish communities, and more attention should be paid to the long-term ecological effects of future water diversion. Du et al. (2021) analyzed the changes in the water cycle, groundwater level, climatic factors, and subsidence patterns in the Beijing area after the implementation of the SNWDP Middle Route. Liu et al. (2020) proposed a comprehensive water footprint index and discussed the adverse impacts of water diversion projects on ecosystems and the environment. Feng and Zhao (2020) believed that, from the perspective of ecological footprint, organic agriculture can effectively promote the ecological security of the water source area of the SNWDP. Among many environmental factors, surface water quality plays a vital role in determining the ecological environment, public health, and socioeconomic development (Wu et al., 2020). Water diversion projects focus on ecological environmental factors during construction and operation and take measures to protect and maintain the health of the water ecosystem, ensuring good water quality effects. At the same time, the protection and improvement of water quality also help maintain and promote the health of the ecological environment. Apparently, water ecosystems and water quality are interdependent and jointly promote sustainable water use and ecological balance.

The water quality utility of the water diversion project refers to the management and control of the water quality during the water diversion process to ensure that the quality of the delivered water meets specific requirements and standards. The water quality utility of water diversion projects includes ensuring water quality safety, water quality maintenance, water quality adjustment, water quality monitoring and management, and water quality environmental protection. In the water transfer supply chain, water quality is a key factor that affects the demand for water resources and the benefits of enterprises along the route. Through effective water quality management, water diversion projects can provide water quality that meets requirements and standards and social needs and protect the health of the water environment and ecosystem. Water quality safety is a key factor related to the success or failure of long-distance water diversion projects. With the development of society and economy, the contradiction among population, resources, and environment has become increasingly prominent (Wu et al., 2021; Zhang et al., 2022). The shortage of water resources is increasingly manifested as new problems, such as shortage of water quality, shortage of projects, and shortage of institutions. Brouwer and De Blois (2008) gave an overview of sources of uncertainty in the analysis of least-cost approaches to improving water quality, and their findings showed that the interaction between environmental and economic uncertainties is complex. In the past, the traditional water resource allocation model that only considered water volume is no longer suitable for the needs of rapid social and economic development (Jin-yan et al., 2021; Shen et al., 2021). The rational and effective use of water resources must take into account the quantity and quality of water resources and implement joint scheduling and control from the source (Aiqing et al., 2020). Therefore, it is one of the key factors in the water quality investment and pricing decision-making process of each main enterprise in the water supply chain to study the dispatching and allocation of water resources by using water quality utility.

It can be seen from the aforementioned research results that social welfare and water quality are the key issues that should be considered in water diversion projects. Existing studies have investigated the management decision-making aspects of water diversion projects. For example, some studies have described in detail the challenges faced by the SNWDP in terms of water demand, water supply quality, and management policies when incorporated into water supply plans (Chen and Wang, 2012). There are also studies using multiple linear regression analysis (Nong et al., 2020), factor analysis (Kuo et al., 2019), multivariate statistical techniques (Guo et al., 2020), water quality index (WQI) (Qu et al., 2020), catastrophe theory (Wu et al., 2020), data envelopment analysis (Su and Chen, 2021), and other methods for water quality evaluation and decision-making research of water diversion projects and provide suggestions for policy formulation. However, most of these studies are only observed from a single perspective (Chen and Pei, 2018; Chen et al., 2019b), and there are few comprehensive multi-angle studies. Chen et al. (2023) explored the coordination mechanism of the SNWDP supply chain from two aspects of economic benefits and social responsibilities. The results showed that the overall profit and the profit of suppliers and distributors under the centralized decision-making situation are higher than those under the decentralized decision-making. Meanwhile, the profits from the dual perspectives are also higher than those from a single economic perspective. Studies have also shown better simulation (Li et al., 2021), or evaluation results are obtained by using comprehensive evaluation models (Ge et al., 2020a; Ge et al., 2022) or considering multiple perspectives (Zhang et al., 2023). The main participants in SNWDP are the government and enterprises (water source companies and water supply companies), in which the government is committed to maintaining social welfare and public interests while enterprises pursue economic interests. In the process of balancing the relationship between social welfare, public interests, and economic interests, social welfare and water quality utility are crucial factors in the decision-making of water diversion projects.

This paper attempts to discuss the optimal decision-making and coordination issues of the SNWD supply chain from the dual perspectives of social welfare and water quality utility, establishes the corresponding Stackelberg decentralized decision-making model and cost-sharing contract model, and discusses how to realize economic benefits under the premise of considering ecological benefits and social benefits. It also maximizes and provides decision-making reference for relevant decision-makers.

Based on the aforementioned discussion, the remainder of this paper is organized as follows: Section 2 describes the water transfer supply chain model, Stackelberg game model, and contract sharing model. Section 3 obtains the visualization results of the model through numerical simulation. Section 4 analyzes and discusses the results. Finally, conclusion of the paper is given in Section 5.

2 Research methodology

In order to reveal how enterprises of all parties to the water diversion supply chain maximize their profits under the premise of considering social welfare and water quality effectiveness, a model is designed and analyzed.

2.1 General engineering situation

The SNWDP (South-to-North Water Diversion Project) is a strategic water transfer project in China. It was conceived in 1952 when President Mao Zedong inspected the Yellow River to solve the water shortage problem in the northern part of China, especially in the Yellow, Huai, and Hai River basins. After numerous planning schemes, three water transfer lines are identified: East, Middle, and West, which are linked to the Yangtze River, Yellow River, Huai River, and Hai River, forming a general layout with "four horizontal and three vertical" to help realize a rational allocation pattern of China's water resources from north to south and from east to west. The starting point of the East Route Project is located at the Jiangdu Hydrojunction in Yangzhou, Jiangsu Province. The Middle Route Project starts from Danjiangkou Reservoir in the middle and upper reaches of the Han River, and the catchment areas are Henan, Hebei, Beijing, and Tianjin. The middle route of the SNWDP and the eastern route of the SNWDP (Phase 1) have been completed and will transfer water to the north, while the western route is still in the planning stage. The total length of the East, Middle and West trunk lines planned for the project is 4,350 km. The total length of the trunk line of the East and Middle Routes of the SNWDP (Phase 1) is 2,899 km, with approximately 2,700 km of complementary branch canals at the first level in six provinces and cities along the line. The SNWDP planning area involves a population of 438 million people and a water diversion scale of 44.8 billion cubic meters. South water has become the main source of water for more than 150 million people in more than 280 counties and urban areas in more than 40 large- and medium-sized cities, including Beijing and Tianjin, since its completion in 2014. The water resources brought by the SNWDP not only meet people's basic living needs but also provide important support for the agricultural development in North China and improve the social welfare benefits of the water-receiving areas. At the same time, it has established a complete water quality monitoring network at key locations such as river sources, reservoirs, water delivery channels, and water sources and adopted water purification measures to ensure the stability and safety of water quality.

2.2 Overall model construction

A supply chain is an integrated manufacturing process in which raw materials are transformed into final products, which are then delivered to customers (Beamon, 1998). Wang et al. (2005) first introduced supply chain theory and contract design into the operation and management of the SNWDP. From the perspective of the supply chain, the East Route Project of SNWDP was regarded as a supply chain composed of water suppliers and distributors, and its applicability and wide application prospects were discussed. In most studies on water transfer supply chains, supply chain participants are divided into "water supply-distribution" or "water transfer-water supply" structures, which is in line with the actual operation of SNWDP (Chen et al., 2019b; Lu Y. et al., 2022). Drawing on ideas from related articles, this paper divides the participants in the SNWDP water supply chain into three categories: water transfer companies, water supply companies, and consumers, taking into account the practical operation of the SNWDP in China and drawing on the idea of supply chain operation. Water transfer companies cover all participants in the supply of water resources at the source. Water transfer companies, which cover all participants in the supply of water resources at the source, are concerned about water quality utility, their own profits, and consumer surplus, and their decision variables are the price of water diversion, water quality, and the concern coefficient about water quality utility and consumer surplus. Water supply companies, which cover the organizational managers of water resource utilization in the catchment areas along the SNWDP, are concerned with their own profits and set market water prices based on water demand. Consumers cover all end-users of SNWDP water resources. The water transfer company transports water resources from the water source to the water supply company, and then the water supply company distributes the water resource products to consumers. The supply chain structure of water resources in the SNWDP is shown in Figure 1. Relevant symbols in the paper and their meanings are explained in Table 1.

Assuming that the water demand in the catchment area decreases as the water price increases and increases as the water quality increases, the water demand function is given as

$$Q = a - bp + rm, \tag{1}$$

where a, b, r are positive variables, while water demand Q, water price p, and water quality m are non-negative variables. Water transfer companies improve water quality, and the cost function is given as

$$C(m) = 0.5km^2, k > 0. \tag{2}$$

Using Eq. 1, it can be found that the consumer surplus generated by the consumer's purchase of water resources is

$$S = \int_p^{\frac{a+rm}{b}} (a - bp + rm)dp = \frac{(a - bp + rm)^2}{2b}. \tag{3}$$

Multiplying water quality utility H, water demand Q, and water quality m, we obtain

$$H = Qm = (a - bp + rm)m. \tag{4}$$

Furthermore, assuming that the unit water transfer cost of the water transfer company is c_1, the transfer price is w, and the unit water supply cost of the water supply company is c_2, then the profit function π_1 of the water transfer company and the profit function π_2 of the water supply company are

$$\pi_1 = (a - bp + rm)(w - c_1) - 0.5km^2, \tag{5}$$

$$\pi_2 = (a - bp + rm)(p - w - c_2). \tag{6}$$

Social welfare consists of producer surplus and consumer surplus, where the producer surplus is represented by the profit

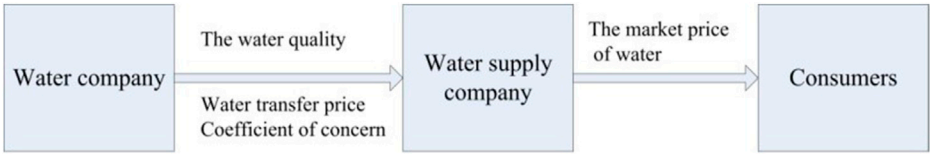

FIGURE 1
Illustration of the monitoring and assessment information system for reservoir resettlement.

TABLE 1 Symbol description table.

Symbol	Meaning description	Symbol	Meaning description
p	Market water price in the receiving area	a	Potential water demand
Q	Water demand in the receiving area	b	Water price preference coefficient
m	Water quality	r	Water quality preference coefficient
S	Consumer surplus	k	Water quality improvement cost coefficient
H	Water quality utility	c_1	Unit cost of water transfer
w	Water wholesale price	c_2	Unit cost of water supply
π_1	Water transfer company profits	λ	Concern coefficient of water diversion company
π_2	Water supply company profits	U	Utility of the water supply company

function of the water transfer company and the water supply company. Assuming that the water supply company only cares about its own profits, while the water transfer company cares about its own profits as well as consumer surplus and water quality utility, in the dual perspective of social welfare and water quality utility, the utility function of the water transfer company is designed as

$$U = \pi_1 + \lambda(S + H), \tag{7}$$

where λ denotes the concern coefficient of the water transfer company for water quality, utility, and consumer surplus, $\lambda \geq 0$. When $\lambda = 0$, the utility function degenerates the profit function of the water transfer company.

2.3 Stackelberg game model

The decision-making models currently used in the study of water transfer supply chains include the IDR model (Ouyang et al., 2019), differential game model (Sheng and Webber, 2021), and Stackelberg game model (Xin et al., 2022). The optimal allocation of water resources by the IDR model is affected by the selection of indicators. The calculation accuracy of the differential game model is slightly lower, while the Stackelberg game model has been relatively mature in the study of water transfer supply chain decision-making and has shown good results. Wang et al. (2008) first used the Stackelberg game to establish a pricing model for the supply chain on the eastern route of the SNWDP and obtained the Pareto optimality of the eastern route supply chain. Du et al. (2019) studied the production, operation, and management of water resources in SNWDP based on the two-stage Stackelberg game method, regarding the East Route Project and the Middle Route Project as two water resource supply chain systems, and explored the chain-to-chain competition model. The theory of supply under competition was expanded. Chain operation provides management enlightenment for the sustainable development of water resources. Related research also shows that the Stackelberg game model is very consistent with the dispatching research of power and water conservancy systems (Li Y. et al., 2022; Sun et al., 2023). It can be seen that it is appropriate and effective to apply the Stackelberg game model to the research of the water transfer supply chain.

Assuming that the water transfer company is the leader of the Stackelberg game and the water supply company is the follower, the reverse induction method is used for the solution. The optimal market water price reaction function is derived from the first-order condition $\frac{\partial \pi_2}{\partial p} = 0$ as follows:

$$p = \frac{(w + c_2)b + rm + a}{2b}. \tag{8}$$

Substituting the market water price response function 8 into the water transfer company utility function 7, the Hessian matrix of the utility function U concerning w and m is expressed as

$$\begin{pmatrix} \frac{\partial^2 U}{\partial w^2} & \frac{\partial^2 U}{\partial w \partial m} \\ \frac{\partial^2 U}{\partial m \partial w} & \frac{\partial^2 U}{\partial m^2} \end{pmatrix} = \begin{pmatrix} -b + \frac{1}{4}\lambda b & \frac{(-2b - r)\lambda}{4} + \frac{r}{2} \\ \frac{(-2b - r)\lambda}{4} + \frac{r}{2} & \frac{(4\lambda r - 4k)b + \lambda r^2}{4b} \end{pmatrix}. \tag{9}$$

Under the Hessian matrix negative definite condition, the first-order master equation is less than zero and the Hessian matrix determinant is greater than zero. The calculation yields

$$-b+\frac{1}{4}\lambda b<0, \tag{10}$$

$$-b^2\lambda^2+((-k-2r)\lambda+4k)b-r^2>0. \tag{11}$$

Under the Hessian matrix negative definite condition, the first order condition $\frac{\partial U}{\partial w}=0$ and $\frac{\partial U}{\partial m}=0$, by the water transfer company utility function can be solved for the optimal wholesale price w^* and the optimal water quality m^*. (The optimal result of the Stackelberg game model is indicated by the superscript *)

$$\begin{aligned}w^*=&\left(-b^2c_2\lambda^2+\left(a\lambda^2+(-kc_2+r(c_1-c_2))\lambda-2k(c_1-c_2)\right)b\right.\\&\left.+a(k+r)\lambda+c_1r^2-2ak\right)\Big/\left(b^2\lambda^2+((k+2r)\lambda-4k)b+r^2\right),\end{aligned} \tag{12}$$

$$m^*=\frac{((c_1+c_2)b-a)(\lambda b+r)}{b^2\lambda^2+((k+2r)\lambda-4k)b+r^2}. \tag{13}$$

Substituting w^* and m^* into Eq. 8 yields the optimal water price as

$$p^*=\frac{(a\quad\lambda^2+r(c_1+c_2)\lambda-k(c_1+c_2))b+a(k+r)\lambda+(c_1+c_2)r^2-3ak}{b^2\lambda^2+((k+2r)\lambda-4k)b+r^2}. \tag{14}$$

Substituting m^*, w^*, and p^* into Eqs 3–7, the optimal profits of the water transfer company and the water supply company, the optimal profits of the supply chain system, the optimal water quality utility, the optimal consumer surplus, and the optimal utility of the water transfer company can be derived as follows:

$$\pi_1^*=-\frac{3k\left(b^2\lambda^2+\left(\left(\frac{2k}{3}+\frac{4r}{3}\right)\lambda-\frac{4k}{3}\right)b+\frac{r^2}{3}\right)(a-(c_1+c_2)b)^2}{2\left(b^2\lambda^2+((k+2r)\lambda-4k)b+r^2\right)^2}, \tag{15}$$

$$\pi_2^*=\frac{k^2(a-(c_1+c_2)b)^2b}{\left(b^2\lambda^2+((k+2r)\lambda-4k)b+r^2\right)^2}, \tag{16}$$

$$\pi_1^*+\pi_2^*=-\frac{3k(a-(c_1+c_2)b)^2\left(b^2\lambda^2+\left(\left(\frac{2k}{3}+\frac{4r}{3}\right)\lambda-2k\right)b+\frac{r^2}{3}\right)}{2\left(b^2\lambda^2+((k+2r)\lambda-4k)b+r^2\right)^2}, \tag{17}$$

$$S^*=\frac{k^2((-c_1-c_2)b+a)^2b}{2\left(b^2\lambda^2+((k+2r)\lambda-4k)b+r^2\right)^2}, \tag{18}$$

$$H^*=\frac{(\lambda b+r)k(a-(c_1+c_2)b+a)^2b}{\left(b^2\lambda^2+((k+2r)\lambda-4k)b+r^2\right)^2}, \tag{19}$$

$$U^*=-\frac{k((-c_1-c_2)b+a)^2}{2b^2\lambda^2+((2k+4r)\lambda-8k)b+2r^2}. \tag{20}$$

2.4 Cost-sharing contract model

In the Stackelberg game model shown previously, the cost of improving water quality is borne entirely by the water transfer company. However, in the SNWDP practices, there is a basic cost-sharing model based on the principle of "who benefits, who bears costs" by dividing channels and levels. The ultimate goal of the water transfer supply chain is to improve competitiveness; hence, companies in the supply chain cannot develop their business without cooperation and cost-sharing (Stadtler, 2015). In order to stimulate the cooperation between the water transfer company and the water supply company, this article assumes that the water supply company shares a certain proportion of the cost of improving water quality, and the proportional coefficient is η $(0\le\eta\le1)$. When $\eta=0$, the water company does not bear the cost of improving water quality. When $\eta=1$, all the costs of improving water quality are fully borne by the water company. Therefore, the profit function of the water transfer company and the water supply company, together with the utility function of the water transfer company, is modified as

$$\pi_1=(a-bp+rm)(w-c_1)-\frac{1}{2}(1-\eta)km^2, \tag{21}$$

$$\pi_2=(a-bp+rm)(p-w-c_2)-\frac{1}{2}\eta km^2, \tag{22}$$

$$\begin{aligned}U=&(a-bp+rm)(w-c_1)-\frac{(1-\eta)k\quad m^2}{2}\\&+\lambda\left(\frac{(a-bp+rm)^2}{2b}+(a-bp+rm)m\right).\end{aligned} \tag{23}$$

Using Eq. 22, the market water price response function can be obtained from the first-order condition $\frac{\partial\pi_2}{\partial p}=0$ as

$$p=\frac{(w+c_2)b+rm+a}{2b}. \tag{24}$$

Substituting the water price response function 24 into the water transfer company utility function 23 , the Hessian matrix of utility U concerning w and m is given as

$$\begin{pmatrix}\frac{\partial^2U}{\partial w^2} & \frac{\partial^2U}{\partial w\partial m}\\ \frac{\partial^2U}{\partial m\partial w} & \frac{\partial^2U}{\partial m^2}\end{pmatrix}=\begin{pmatrix}-b+\frac{1}{4}\lambda b & \frac{(-2b-r)\lambda}{4}+\frac{r}{2}\\ \frac{(-2b-r)\lambda}{4}+\frac{r}{2} & \frac{(4\lambda r+4(-1+\eta)k)b+\lambda r^2}{4b}\end{pmatrix}. \tag{25}$$

The Hessian matrix 25 with negative definiteness is conditioned on

$$-b+\frac{1}{4}\lambda b<0, \tag{26}$$

$$-b^2\lambda^2+(((-1+\eta)k-2r)\lambda-4(-1+\eta)k)b-r^2>0. \tag{27}$$

In the Hessian matrix negative definite period, the optimal water transfer price w^{**} and the optimal water quality m^{**} can be solved by the first-order condition $\frac{\partial U}{\partial w}=0$ in conjunction with $\frac{\partial U}{\partial m}=0$ as follows (the optimal result of the cost-sharing contract model is denoted by the superscript **)

$$\begin{aligned}w^{**}=&\left(-b^2c_2\lambda^2+\left(2\left(\frac{1}{2}\lambda c_2+c_1-c_2\right)(-1+\eta)k\right.\right.\\&+\lambda(\lambda a+r(c_1-c_2)))b-a(\lambda-2)(-1+\eta)k\\&\left.+a\lambda r+c_1r^2\right)/\left(b^2\lambda^2+(-(-4+\lambda)(-1+\eta)k\right)\\&\left.+2\lambda r)b+r^2\right),\end{aligned} \tag{28}$$

$$m^{**}=-\frac{((-c_1-c_2)b+a)(\lambda b+r)}{b^2\lambda^2+((2r+(1-\eta)k)\lambda+4(-1+\eta)k)b+r^2}. \tag{29}$$

By substituting the optimal transfer price w^{**} and the optimal water quality m^{**} into the water price reaction function 24, the optimal water price can be obtained as

$$\begin{aligned}p^{**}=&\left(((-1+\eta)(c_1+c_2)k+\lambda(\lambda a+r(c_1+c_2)))b\right.\\&\left.-a(\lambda-3)(-1+\eta)k+r(\lambda a+r(c_1+c_2))\right)\\&\Big/\left(b^2\lambda^2+(-(-4+\lambda)(-1+\eta)k+2\lambda r)b+r^2\right).\end{aligned} \tag{30}$$

Furthermore, the water transfer company profit π_1^{**}, water supply company profit π_2^{**}, supply chain system profit $\pi_1^{**}+\pi_2^{**}$, consumer surplus S^{**}, water quality effect H^{**}, and water transfer company utility U^{**} in the cost-sharing contract situation are as follows:

$$\pi_1^{''}=\frac{3\left(\left(-c_1-c_2\right)b+a\right)^2\left(b^2\lambda^2+\left(-\frac{2(\lambda-2)\left(-1+\eta\right)k}{3}+\frac{4\lambda r}{3}\right)b+\frac{r^2}{3}\right)\left(-1+\eta\right)k}{2\left(b^2\lambda^2+\left(-\left(-4+\lambda\right)\left(-1+\eta\right)k+2\lambda r\right)b+r^2\right)^2}, \tag{31}$$

$$\pi_2^{**}=-\frac{\left(b^2\eta\lambda^2+\left(-2\left(-1+\eta\right)^2k+2r\eta\lambda\right)b+\eta r^2\right)\left(\left(-c_1-c_2\right)b+a\right)^2k}{2\left(b^2\lambda^2+\left(-\left(-4+\lambda\right)\left(-1+\eta\right)k+2\lambda r\right)b+r^2\right)^2}, \tag{32}$$

$$\begin{aligned}\pi_1^{**}+\pi_2^{**}=&\left(\left(\lambda^2\left(\eta-\frac{3}{2}\right)b^2+\left(\left(-\left(-1+\eta\right)^2k+r\left(\eta-2\right)\right)\lambda\right.\right.\right.\\&\left.\left.\left.+3\left(-1+\eta\right)^2k\right)b-\frac{r^2}{2}\right)\left(\left(-c_1-c_2\right)\left(b+a\right)^2k\right)/\left(\left(b^2\lambda^2\right.\right.\\&\left.\left.+\left(\left(2r+\left(1-\eta\right)k\right)\lambda+4\left(-1+\eta\right)k\right)\left(b+\eta^2\right)^2\right)\right),\end{aligned} \tag{33}$$

$$S^{**}=\frac{b\left(\left(-c_1-c_2\right)b+a\right)^2\left(-1+\eta\right)^2k^2}{2\left(b^2\lambda^2+\left(-\left(-4+\lambda\right)\left(-1+\eta\right)k+2\lambda r\right)b+r^2\right)^2}, \tag{34}$$

$$H^{**}=-\frac{b\left(\left(-c_1-c_2\right)b+a\right)^2\left(\lambda b+r\right)\left(-1+\eta\right)k}{\left(b^2\lambda^2+\left(\left(-k\eta+k+2r\right)\lambda+4\left(-1+\eta\right)k\right)b+r^2\right)^2}, \tag{35}$$

$$U^{**}=\frac{\left(\left(-c_1-c_2\right)b+a\right)^2\left(-1+\eta\right)k}{2b^2\lambda^2+\left(-2\left(-4+\lambda\right)\left(-1+\eta\right)k+4\lambda r\right)b+2r^2}. \tag{36}$$

Compared with the results of the Stackelberg game, the condition that the water transfer company and the water supply company can successfully and consciously achieve the cost-sharing contract is that both parties can improve their profits under the cost-sharing contract, which means $\pi_1^{**}>\pi_1^{*}$ and $\pi_2^{**}>\pi_2^{*}$, and the parameters and variables should be taken by the economic implication and should satisfy the Hessian matrix negative definite condition.

3 Results

Through numerical simulations, the Hessian matrix negative definite conditions, the conditions for the implementation of cost-sharing contracts for water quality improvement between the water transfer company and the water supply company, and the effect of the concern factor of the water transfer company on profits, producer surplus, and water quality effects are further explored. The parameters are taken as $a=400$, $b=2$, $c_1=6$, $c_2=4$, $k=4$, and $r=1$. From Eqs 10, 26 of the Hessian matrix negative definite condition and $\lambda\geq 0$, the parameter λ takes the value interval $[0,4)$. The water quality improvement cost-sharing ratio η takes the value interval $[0,1]$. Therefore, using the aforementioned parameter settings, the Hessian matrix negative definite condition in equalities Eqs 11, 27 and $\pi_1^{**}-\pi_1^{*}>0$, $\pi_2^{**}-\pi_2^{*}>0$ can be expressed as follows:

$$-4\lambda^2-12\lambda+31>0, \tag{37}$$

$$-\lambda^2+\frac{\left(-6+4\eta\right)\lambda}{2}+\frac{31}{4}-8\eta>0, \tag{38}$$

$$\begin{aligned}&\frac{866400\left(4\lambda^2-\frac{16(\lambda-2)\left(-1+\eta\right)}{3}+\frac{8\lambda}{3}+\frac{1}{3}\right)\left(-1+\eta\right)}{\left(4\lambda^2-8\left(\lambda-4\right)\left(-1+\eta\right)+4\lambda+1\right)^2}\\&-\frac{866400\left(4\lambda^2+8\lambda-\frac{31}{3}\right)}{\left(4\lambda^2+12\lambda-31\right)^2}>0,\end{aligned} \tag{39}$$

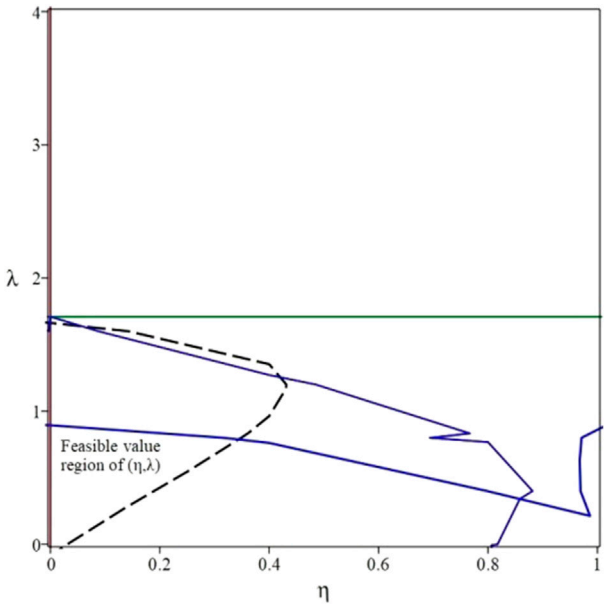

FIGURE 2
Feasible value region of (η,λ).

$$\frac{288800\left(-16\lambda^4+64\eta\quad\lambda^2-96\lambda^3+320\lambda\eta-24\lambda^2-1008\eta+360\lambda+31\right)\eta\left(2\lambda+1\right)^2}{\left(8\lambda\eta-4\lambda^2-32\eta-12\lambda+31\right)^2\left(4\lambda^2+12\lambda-31\right)^2}>0. \tag{40}$$

The feasible value area of (η,λ) that simultaneously satisfies in Eqs 37–40 in the parameter space $(\eta,\lambda)\in[0,1]\times[0,4)$ is shown Figure 2, and its local enlargement is shown in Figure 3. The intersection point coordinates of the black dashed line and the blue solid line in Figure 3 are (0.33,0.78). The maximum feasible value of the sharing ratio η is 0.33. As η increases in the interval (0, 0.33), the feasible value of the concern coefficient λ becomes smaller. When the value of (η,λ) is outside the feasible value area as shown in Figure 3, or the Hessian matrix negative definite condition is not satisfied, the optimal solution is invalid. When the water transfer company and the water supply company cannot make the profit both sides through the cost-sharing contract, the cost-sharing contract does not attract both parties to perform consciously. Compared to the results of the Stackelberg game, the surfaces of the increase in profit of the water transfer company $\pi_1^{**}-\pi_1^{*}$ and the increase in profit of the water supply company $\pi_2^{**}-\pi_2^{*}$ with the parameter (η,λ) under the cost-sharing contract are shown in Figures 4, 5. It is clear from Figures 4, 5 that when the parameter (η,λ) is taken in the feasible value region as shown in Figure 3, the difference between the profits of both the water transfer company and the water supply company in the cost-sharing contract model and the profits in the Stackelberg game model is more than 0, meaning that both the water transfer company and the water supply company achieve a Pareto improvement in their profits. For a given cost-sharing ratio η, compared with the results of the Stackelberg game, Figure 4 shows that the increase in profit $\pi_1^{**}-\pi_1^{*}$ for the water transfer company decreases as the concern factor λ increases, and Figure 5 shows that the profit $\pi_2^{**}-\pi_2^{*}$ increases for the water supply company as the concern factor λ increases.

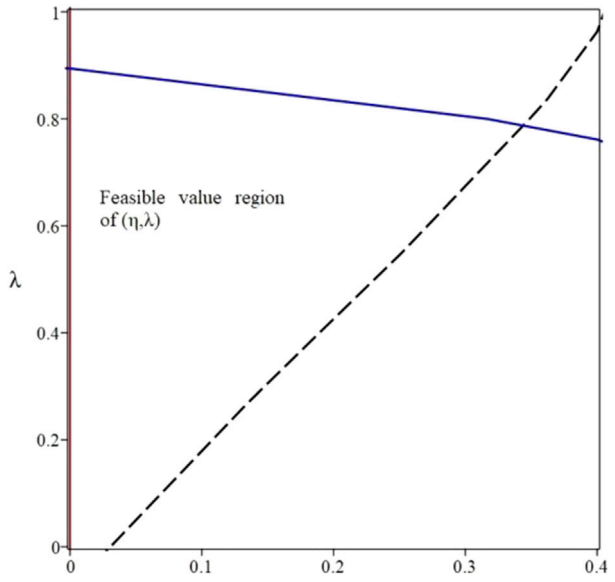

FIGURE 3
Local enlargement of the feasible value region of (η, λ).

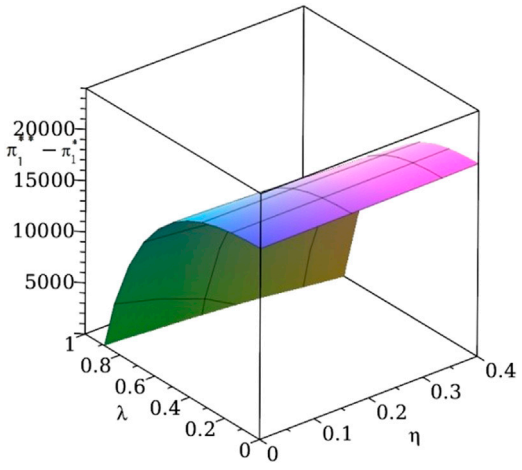

FIGURE 4
Pareto improvement surface of the water transfer company's profit.

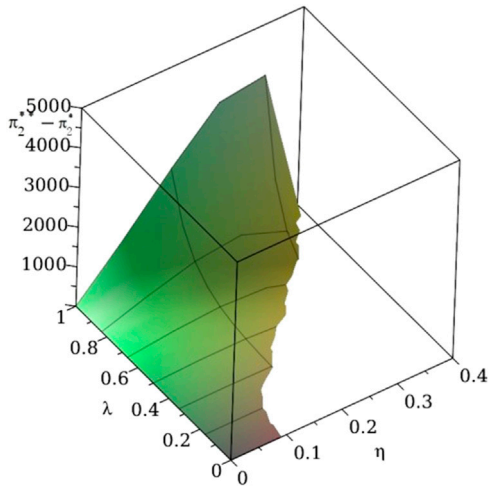

FIGURE 5
Pareto improvement surface of the water supply company's profit.

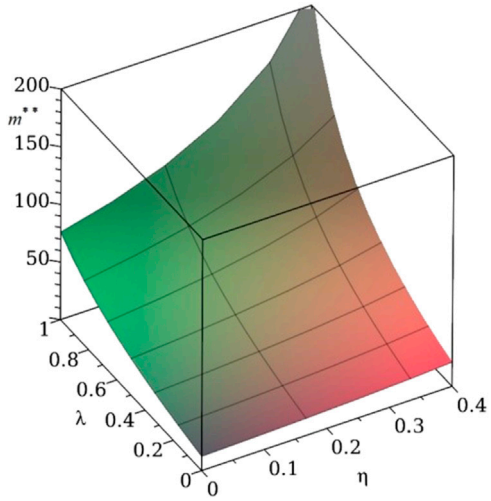

FIGURE 6
Water quality variation surface of (η, λ).

Under the aforementioned parameter conditions, the optimal water quality, consumer surplus, water quality effect, and utility of the water transfer company in the cost-sharing contract model as a function of parameter (η, λ) are given as follows:

$$m^{**} = -\frac{380(2\lambda + 1)}{4\lambda^2 + 2(-4\eta + 6)\lambda - 31 + 32\eta}, \tag{41}$$

$$S^{**} = \frac{2310400(-1 + \eta)^2}{(4\lambda^2 - 8(\lambda - 4)(-1 + \eta) + 4\lambda + 1)^2}, \tag{42}$$

$$H^{**} = -\frac{1155200(-1 + \eta)(2\lambda + 1)}{(4\lambda^2 + 2(-4\eta + 6)\lambda - 31 + 32\eta)^2}, \tag{43}$$

$$U^{**} = \frac{-577600 + 577600\eta}{8\lambda^2 - 16(\lambda - 4)(-1 + \eta) + 8\lambda + 2}. \tag{44}$$

Using Eqs 41–44, the surfaces of variation in water quality, consumer surplus, water quality effect, and water transfer company utility concerning parameters (η, λ) are plotted in Figures 6–9, respectively. It is evident from Figures 6–9 that for a given cost-bearing ratio η, water quality, consumer surplus, water quality effect, and water transfer company utility all increase with the increase in the concern factor λ.

4 Discussion

(1) According to Figures 2, 3, in the concern factor λ and water quality improvement cost-sharing ratio η taking the value

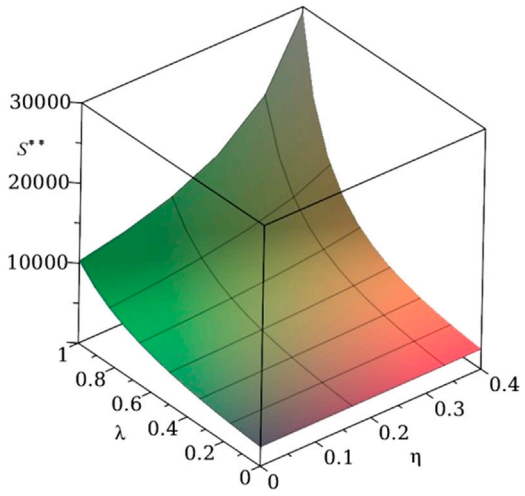

FIGURE 7
Consumer surplus variation surface of (η, λ).

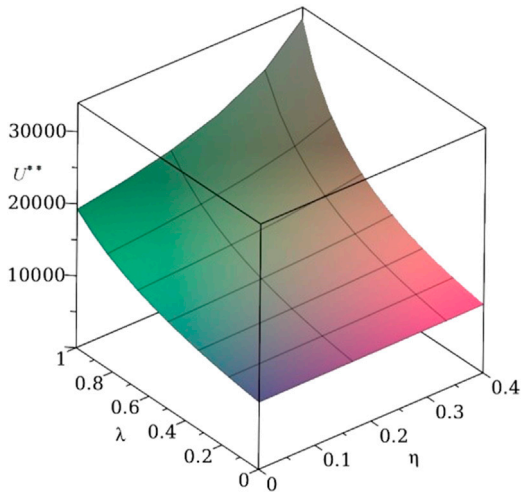

FIGURE 9
Water transfer company variation surface of (η, λ).

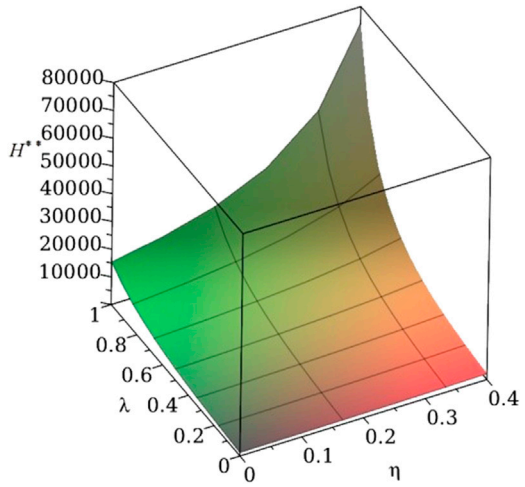

FIGURE 8
Water quality variation surface of (η, λ).

plane, there is a large feasible value region (η, λ), so that the water transfer company and the water supply company in the cost-sharing contract model can both obtain more profit than in the Stackelberg game model. In order to make the water diversion supply chain more profitable, the proportion η of water supply company's responsibility for water quality improvement should be less than 0.33. At present, the ratio of the water transfer company to the water supply company to bear the cost of water quality improvement in the actual project is not clear yet. Government management departments such as the South-to-North Water Diversion Office and provincial water conservancy departments need to encourage and supervise all participants in project operation and management (water transfer companies and water supply companies) to sign cost-sharing contracts for cooperation and cost-sharing.

(2) According to Figures 4–9, the concern factor and cost-sharing ratio have a complex effect on the game outcome, and both vary in dependence. For the optimal outcome of the cost-sharing contract model, when the cost-sharing ratio or concern factor is fixed, the optimal water quality, consumer surplus, water quality utility, and the total utility of the water transfer company all increase with the other party. Each interested individual will seek to maximize their own interests, but the state of each party's lack of cooperation will eventually lead to a reduction in operational efficiency [40]. Therefore, balancing the cost-sharing ratio under the cooperation between the two sides and jointly pursuing social welfare and water quality utility are a favorable means to improve the profits of water transfer and water supply companies and to achieve optimal coordination of the water transfer supply chain. Therefore, the water source companies on the eastern middle line of the SNWDP should actively strengthen information communication and information sharing with water supply companies in various regions, balance the cost-sharing ratio, and achieve Pareto improvement in the performance of the SNWD supply chain.

(3) Within the range of feasible parameters, the water transfer company shows an increase in concern coefficient to increase its total utility of interest, including economic benefits, water quality utility, and consumer surplus, but a decrease in its own profit, while there is an increase in the profit of the water supply company. This indicates that the water transfer company has to sacrifice some of its own profits to increase the total utility of concern while the water supply company's profits increase, which has a "free-rider" effect. This provides an incentive for the water transfer company to share some of its profits with the water supply company, thus allowing the water transfer company to increase its concern coefficient even further and indirectly increasing the profit level of the water supply

company. Therefore, in the SNWDP, in order to avoid the "free-ride" effect of destroying the benefits of each participant and affecting the realization of the company's own profits and social welfare, it is possible to coordinate and improve the interests of all participants in the supply chain by signing a revenue-sharing contract. The profit-sharing contract design of the water transfer supply chain is one of the future research directions.

(4) This paper introduces water quality utility and consumer surplus into the decision model, and the results of the study reflect not only the economic interests of the water supply company and the water transfer company but also the concern for ecological benefits and social welfare. The Stackelberg game is studied in a non-cooperative scenario between the water supply company and the water transfer company, and the optimal solution of the game is given. The conditions for cost-sharing contracts to improve the profits of both water suppliers and water transfer companies are also explored. However, numerical calculation of specific values in this paper is related to the parameter settings given in the text. For different parameter settings, the specific results should be further subjected to specific analysis.

5 Conclusion

The operation and management of water transfer projects play an important role in giving full play to the optimal allocation of water resources. From the perspective of both social welfare and water quality utility, based on supply chain and game theory, this paper proposes a management decision model considering a comprehensive objective of economic efficiency, producer surplus, and water quality utility. Taking the South-North water transfer as an example, the impact of designing a cost-sharing contract for water quality improvement on the decision outcome is explained through numerical simulation.

Within the feasible value region of (η, λ), as the proportion η of water quality improvement cost that is borne by the water supply company increases, the feasible value interval of concern coefficient λ of the water transfer company becomes smaller. As the concern coefficient increases, optimal water quality, consumer surplus, water quality utility, and the profit of the water supply company all increase, while the profit of the water transfer company decreases.

The results provide valuable references for water resources operation and management decisions of SNWDP and similar projects.

Data availability statement

The original contributions presented in the study are included in the article/Supplementary Material; further inquiries can be directed to the corresponding author.

Author contributions

Conceptualization and methodology: HJ and HZ; writing—original draft preparation: HJ, JZ, and HZ; software and visualization: JZ, YL, LC, and YC; investigation: LC and YC; writing—review and editing: JZ, YL, and HZ; supervision: HJ and HZ. All authors contributed to the article and approved the submitted version.

Funding

This project was financed by the Henan Province Science and Technology Project of Water Conservancy Project (GG202261), Henan Provincial Philosophy and Social Science Planning Project (2022BZX006), Henan Province Soft Science Research Project (232400411111), Henan Province Soft Science Research Project (232400410146), and Excellent Teaching Case Project for Professional Degree Postgraduates in Henan Province (YJS2023AL008).

Conflict of interest

The authors declare that the research was conducted in the absence of any commercial or financial relationships that could be construed as a potential conflict of interest.

Publisher's note

All claims expressed in this article are solely those of the authors and do not necessarily represent those of their affiliated organizations, or those of the publisher, the editors, and the reviewers. Any product that may be evaluated in this article, or claim that may be made by its manufacturer, is not guaranteed or endorsed by the publisher.

References

Aiqing, K., Li, J., Lei, X., and Ye, M. (2020). Optimal allocation of water resources considering water quality and the absorbing pollution capacity of water. *Water Resour.* 47, 336–347. doi:10.1134/S0097807820020074

Barker, R. L. (2003). *The social work dictionary*. Washington, DC, USA: NASW Press.

Beamon, B. M. (1998). Supply chain design and analysis:. *Int. J. Prod. Econ.* 55, 281–294. doi:10.1016/S0925-5273(98)00079-6

Brouwer, R., and De Blois, C. (2008). Integrated modelling of risk and uncertainty underlying the cost and effectiveness of water quality measures. *Environ. Model. Softw.* 23, 922–937. doi:10.1016/j.envsoft.2007.10.006

Chen, J., Zhang, X., and Wang, Q. (2023). Contract coordination of water supply chain of South-to-North Water Diversion Project from the perspective of economic benefits and water quality improvement. *Control decision-making* 38, 825–833. doi:10.13195/j.k.zyjc.2021.1573

Chen, X., and Chen, Z. (2020). Joint pricing and inventory management of interbasin water transfer supply chain. *Complexity* 2020, 1–16. doi:10.1155/2020/3954084

Chen, Z., Cheung, K. C. K., and Tan, M. (2019a). Inter-Basin water transfer supply chain coordination with ramsey pricing. *Int. J. Environ. Res. Public Health* 16, 3651. doi:10.3390/ijerph16193651

Chen, Z., and Pei, L. (2018). Inter-Basin water transfer green supply chain equilibrium and coordination under social welfare maximization. *Sustainability* 10, 1229. doi:10.3390/su10041229

Chen, Z., Su, S.-I. I., and Wang, H. (2019b). Inter-Basin water transfer supply chain equilibrium and coordination: A social welfare maximization perspective. *Water Resour. Manag.* 33, 2577–2598. doi:10.1007/s11269-019-02269-w

Chen, Z., and Wang, H. (2012). Asymmetric Nash bargaining model for the eastern route of south-to-north water diversion supply chain cooperative operations. *J. Chin. Inst. Industrial Eng.* 29, 365–374. doi:10.1080/10170669.2012.710878

Chen, Z., and Wang, H. (2020). Inter-basin water transfer green supply chain coordination with partial backlogging under random precipitation. *J. Water Clim. Change* 12, 296–310. doi:10.2166/wcc.2020.104

Chen, Z., and Wang, H. (2019). Water-saving service supply chain cooperation under social welfare maximization. *J. Water Clim. Change* 11, 703–721. doi:10.2166/wcc.2019.188

De Nicolás, V. L. (2016). Towards a transformational hydraulic engineering project for the territory: A focus on the working with people (WWP) model. *Land Use Policy* 54, 246–252. doi:10.1016/j.landusepol.2016.02.010

Du, W., Fan, Y., Liu, X., Park, S. C., and Tang, X. (2019). A game-based production operation model for water resource management: An analysis of the South-to-North Water Transfer Project in China. *J. Clean. Prod.* 228, 1482–1493. doi:10.1016/j.jclepro.2019.04.351

Du, Z., Ge, L., Ng, A. H.-M., Lian, X., Zhu, Q., Horgan, F. G., et al. (2021). Analysis of the impact of the South-to-North water diversion project on water balance and land subsidence in Beijing, China between 2007 and 2020. *J. Hydrology* 603, 126990. doi:10.1016/j.jhydrol.2021.126990

Feng, D., and Zhao, G. (2020). Footprint assessments on organic farming to improve ecological safety in the water source areas of the South-to-North Water Diversion project. *J. Clean. Prod.* 254, 120130. doi:10.1016/j.jclepro.2020.120130

Ge, W., Jiao, Y., Wu, M., Li, Z., Wang, T., Li, W., et al. (2022). Estimating loss of life caused by dam breaches based on the simulation of floods routing and evacuation potential of population at risk. *J. Hydrology* 612, 128059. doi:10.1016/j.jhydrol.2022.128059

Ge, W., Li, Z., Li, W., Wu, M., Li, J., and Pan, Y. (2020a). Risk evaluation of dam-break environmental impacts based on the set pair analysis and cloud model. *Nat. Hazards* 104, 1641–1653. doi:10.1007/s11069-020-04237-9

Ge, W., Qin, Y., Li, Z., Zhang, H., Gao, W., Guo, X., et al. (2020b). An innovative methodology for establishing societal life risk criteria for dams: A case study to reservoir dam failure events in China. *Int. J. Disaster Risk Reduct.* 49, 101663. doi:10.1016/j.ijdrr.2020.101663

Guo, C., Chen, Y., Gozlan, R. E., Liu, H., Lu, Y., Qu, X., et al. (2020). Patterns of fish communities and water quality in impounded lakes of China's south-to-north water diversion project. *Sci. Total Environ.* 713, 136515. doi:10.1016/j.scitotenv.2020.136515

Guo, C., Chen, Y., Liu, H., Lu, Y., Qu, X., Yuan, H., et al. (2019). Modelling fish communities in relation to water quality in the impounded lakes of China's South-to-North Water Diversion Project. *Ecol. Model.* 397, 25–35. doi:10.1016/j.ecolmodel.2019.01.014

He, Z., Huang, D., Zhang, C., and Fang, J. (2018). Toward a stakeholder perspective on social stability risk of large hydraulic engineering projects in China: A social network analysis. *Sustainability* 10, 1223. doi:10.3390/su10041223

Jin-yan, L., Lan-bo, C., Miao, D., and Ali, A. (2021). Water resources allocation model based on ecological priority in the arid region. *Environ. Res.* 199, 111201. doi:10.1016/j.envres.2021.111201

Kattel, G. R., Shang, W., Wang, Z., and Langford, J. (2019). China's South-to-North water diversion project empowers sustainable water resources system in the north. *Sustainability* 11, 3735. doi:10.3390/su11133735

Koberg, E., and Longoni, A. (2019). A systematic review of sustainable supply chain management in global supply chains. *J. Clean. Prod.* 207, 1084–1098. doi:10.1016/j.jclepro.2018.10.033

Kuo, Y.-M., Liu, W.-W., Zhao, E., Li, R., and Muñoz-Carpena, R. (2019). Water quality variability in the middle and down streams of Han River under the influence of the Middle Route of South-North Water diversion project, China. *J. Hydrology* 569, 218–229. doi:10.1016/j.jhydrol.2018.12.001

Li, C., Wang, J., and Shi, Y. (2022a). The impact of government intervention and cap-and-trade on green innovation in supply chains: A social welfare perspective. *Sustainability* 14, 7941. doi:10.3390/su14137941

Li, Y., Wang, B., Yang, Z., Li, J., and Chen, C. (2022b). Hierarchical stochastic scheduling of multi-community integrated energy systems in uncertain environments via Stackelberg game. *Appl. Energy* 308, 118392. doi:10.1016/j.apenergy.2021.118392

Li, Z., Zhang, Y., Wang, J., Ge, W., Li, W., Song, H., et al. (2021). Impact evaluation of geomorphic changes caused by extreme floods on inundation area considering geomorphic variations and land use types. *Sci. Total Environ.* 754, 142424. doi:10.1016/j.scitotenv.2020.142424

Liu, J., Li, M., Wu, M., Luan, X., Wang, W., and Yu, Z. (2020). Influences of the south–to-north water diversion project and virtual water flows on regional water resources considering both water quantity and quality. *J. Clean. Prod.* 244, 118920. doi:10.1016/j.jclepro.2019.118920

Liu, M., Ding, W., and Lu, Y. (2022). Collaborative management of a sustainable supply chain in a water diversion project. *Water Resour. Manag.* 36, 2665–2683. doi:10.1007/s11269-022-03168-3

Liu, Z., Zhu, Z., Wang, H., and Huang, J. (2016). Handling social risks in government-driven mega project: An empirical case study from West China. *Int. J. Proj. Manag.* 34, 202–218. doi:10.1016/j.ijproman.2015.11.003

Lu, Q., Hua, D., Li, Y., and Wang, D. (2022a). Estimation of water resource ecosystem service value inTarim river basin—from a full value chain perspective. *Water* 14, 2355. doi:10.3390/w14152355

Lu, Y., Ding, W., and Liu, M. (2022b). Study on the evaluation model of collaborative governance capacity of sustainable supply chain in water diversion projects. *Water Policy* 24, 1366–1382. doi:10.2166/wp.2022.200

Mu, Y. (2018). Stackelberg–Nash equilibrium, social welfare and optimal structure in hierarchical continuous Public Goods game. *Syst. Control Lett.* 112, 1–8. doi:10.1016/j.sysconle.2017.12.001

Niu, P., Zhang, E., Feng, Y., and Peng, P. (2022). Spatial-temporal pattern analysis of land use and water yield in water source region of middle route of South-to-North water transfer project based on google Earth engine. *Water* 14, 2535. doi:10.3390/w14162535

Nong, X., Shao, D., Zhong, H., and Liang, J. (2020). Evaluation of water quality in the South-to-North Water Diversion Project of China using the water quality index (WQI) method. *Water Res.* 178, 115781. doi:10.1016/j.watres.2020.115781

Ouyang, S., Qin, H., Shao, J., Lu, J., Bing, J., Wang, X., et al. (2019). Multi-objective optimal water supply scheduling model for an inter-basin water transfer system: the SouthSouth-to-North water diversion middle route project, China. *Water Supply* 20, 550–564. doi:10.2166/ws.2019.187

Peng, W., Xin, B., and Xie, L. (2022). Optimal strategies for product price, customer environmental volunteering, and corporate environmental responsibility. *J. Clean. Prod.* 364, 132635. doi:10.1016/j.jclepro.2022.132635

Peng, Z., Zhang, L., Yin, J., and Wang, H. (2018). Study of impact factors of willingness to pay regarding water reserve of South-to-North Water Diversion Project in Beijing based on Bayesian network model. *J. Clean. Prod.* 184, 569–578. doi:10.1016/j.jclepro.2018.02.263

Qu, X., Chen, Y., Liu, H., Xia, W., Lu, Y., Gang, D.-D., et al. (2020). A holistic assessment of water quality condition and spatiotemporal patterns in impounded lakes along the eastern route of China's South-to-North water diversion project. *Water Res.* 185, 116275. doi:10.1016/j.watres.2020.116275

Shen, X., Wu, X., Xie, X., Wei, C., Li, L., and Zhang, J. (2021). Synergetic theory-based water resource allocation model. *Water Resour. Manag.* 35, 2053–2078. doi:10.1007/s11269-021-02766-x

Sheng, J., and Qiu, W. (2022). Inter-basin water transfer policies and water-use technical efficiency: China's South-North water transfer project. *Socio-Economic Plan. Sci.* 85, 101432. doi:10.1016/j.seps.2022.101432

Sheng, J., Wang, H., and Qiu, W. (2022). Water quality and incentive coordination in water markets: The eastern route of China's South-North Water Transfer Project. *J. Hydrology* 607, 127526. doi:10.1016/j.jhydrol.2022.127526

Sheng, J., and Webber, M. (2021). Incentive coordination for transboundary water pollution control: The case of the middle route of China's South-North water Transfer Project. *J. Hydrology* 598, 125705. doi:10.1016/j.jhydrol.2020.125705

Sheng, J., and Webber, M. (2018). Using incentives to coordinate responses to a system of payments for watershed services: The middle route of South–North Water Transfer Project, China. *Ecosyst. Serv.* 32, 1–8. doi:10.1016/j.ecoser.2018.05.005

Song, X., Li, W., and Tian, M. J. (2019). Research overview on public-private partnership (PPP) project supervision in the field of hydraulic engineering. *IOP Conf. Ser. Earth Environ. Sci.* 330, 022019. doi:10.1088/1755-1315/330/2/022019

Stadtler, H. (2015). "Supply chain management: An overview," in *Supply chain management and advanced planning: Concepts, models, software, and Case studies*. Editors H. STADTLER, C. KILGER, and H. MEYR (Berlin, Germany: Springer).

Su, Q., and Chen, X. (2021). Efficiency analysis of metacoupling of water transfer based on the parallel data envelopment analysis model: A case of the South–North Water transfer project-middle route in China. *J. Clean. Prod.* 313, 127952. doi:10.1016/j.jclepro.2021.127952

Sun, B., Li, M., Wang, F., and Xie, J. (2023). An incentive mechanism to promote residential renewable energy consumption in China's electricity retail market: A two-level Stackelberg game approach. *Energy* 269, 126861. doi:10.1016/j.energy.2023.126861

Wang, H., and Hu, Z. (2005). Several issues on south-to-north water transfer project supply chain operations management. *Adv. Water Sci.* 6, 864–869. doi:10.14042/j.cnki.32.1309.2005.06.01

Wang, H., Zhang, L., and Yang, W. (2008). Pricing model of water resources supply chain for east-route south-to-north water transfer project. *J. hydraulic Eng.* 6, 758–762. doi:10.13243/j.cnki.slxb.2008.06.02

Wang, T., Li, Z., Ge, W., Zhang, Y., Jiao, Y., Sun, H., et al. (2022). Calculation of dam risk probability of cascade reservoirs considering risk transmission and superposition. *J. Hydrology* 609, 127768. doi:10.1016/j.jhydrol.2022.127768

Wang, H. (2023). More than 60 billion cubic meters of water has been transferred to the East and Middle routes of the South-to-North Water Diversion Project. Available: http://paper.people.com.cn/rmrb/html/2023-02/06/nw.D110000renmrb_20230206_1-01.htm (Accessed May 13, 2023).

Wang, T., Li, Z., Ge, W., Zhang, H., Zhang, Y., Sun, H., et al. (2023). Risk consequence assessment of dam breach in cascade reservoirs considering risk transmission and superposition. *Energy* 265, 126315. doi:10.1016/j.energy.2022.126315

Wu, M., Ge, W., Wu, Z., Guo, X., Di, D., and Huang, S. (2020). Evaluation of the benefits of urban water resource utilization based on the catastrophe and emergy methods. *Water Resour. Manag.* 34, 1843–1853. doi:10.1007/s11269-020-02530-7

Wu, M., Wu, Z., Ge, W., Wang, H., Shen, Y., and Jiang, M. (2021). Identification of sensitivity indicators of urban rainstorm flood disasters: A case study in China. *J. Hydrology* 599, 126393. doi:10.1016/j.jhydrol.2021.126393

Xin, B., Zhang, L., and Xie, L. (2022). Pricing decision of a dual-channel supply chain with different payment, corporate social responsibility and service level. *RAIRO-Oper. Res.* 56, 49–75. doi:10.1051/ro/2021187

Xu, W., Zhong, Z., Proverbs, D., Xiong, S., and Zhang, Y. (2021). Enhancing the resilience of the management of water resources in the agricultural supply chain. *Water* 13. doi:10.3390/w13121619

Xu, J., and Zeng, Z. (2022). Water resources allocation of South-to-North Water Diversion Project adapting to high quality development and countermeasures. Available at: https://www.waterinfo.com.cn/xsyj/tszs/202203/t20220317_33904.html (Accessed: May 13, 2023).

Yang, L. X. (2003). *Foreign projects of water diversion*. Beijing, China: China Water and Power Press.

Yang, Z., Huang, X., Fang, G., Ye, J., and Lu, C. (2021). Benefit evaluation of East Route project of south to North Water transfer based on trapezoid cloud model. *Agric. Water Manag.* 254, 106960. doi:10.1016/j.agwat.2021.106960

Zhang, H., Ge, W., Zhang, Y., Li, Z., Li, W., Zhu, J., et al. (2023). Risk management decision of reservoir dams based on the improved life quality index. *Water Resour. Manag.* 37, 1223–1239. doi:10.1007/s11269-023-03426-y

Zhang, Y., Li, Z., Ge, W., Wang, J., Guo, X., Wang, T., et al. (2022). Assessment of the impact of floods on terrestrial plant biodiversity. *J. Clean. Prod.* 339, 130722. doi:10.1016/j.jclepro.2022.130722

frontiers | Frontiers in Earth Science

TYPE Original Research
PUBLISHED 01 June 2023
DOI 10.3389/feart.2023.1214713

OPEN ACCESS

EDITED BY
Wei Ge,
Zhengzhou University, China

REVIEWED BY
Yi Ji,
Northeast Agricultural University, China
Xinzhou Zhang,
Nanjing Hydraulic Research Institute, China

*CORRESPONDENCE
Yuzhou Zhang,
zhangyzh@zjweu.edu.cn

RECEIVED 30 April 2023
ACCEPTED 22 May 2023
PUBLISHED 01 June 2023

CITATION
Hu J, Yang C, Zhang Y, Song H, Lu M, Meng Z and Zhang J (2023), Effect of bubble volume on the sweeping velocity of air bubbles in horizontal pipelines in water supply system.
Front. Earth Sci. 11:1214713.
doi: 10.3389/feart.2023.1214713

Effect of bubble volume on the sweeping velocity of air bubbles in horizontal pipelines in water supply system

Jianyong Hu[1,2], Chengzhi Yang[3], Yuzhou Zhang[1,2]*, Hongge Song[4], Miao Lu[1,2], Zhenzhu Meng[2,5] and Jinxin Zhang[2,5]

[1]School of Geomatics and Municipal Engineering, Zhejiang University of Water Resources and Electric Power, Hangzhou, China, [2]Engineering Research Center of Digital Twin Basin of Zhejiang Province, Hangzhou, China, [3]Henan Water and Power Engineering Consulting Co., Ltd., Zhengzhou, China, [4]College of Energy and Power Engineering, North China University of Water Resources and Hydropower, Zhengzhou, China, [5]School of Water Conservancy and Environmental Engineering, Zhejiang University of Water Resources and Electric Power, Hangzhou, China

Trapped air bubbles in pipelines significantly affect the safety and efficiency of water supply systems, potentially inducing water hammer and leading to pipeline explosions and interruptions. This study investigates the sweeping velocity of air bubbles in horizontal pipelines by analyzing the forces acting on a single air bubble and deriving a theoretical expression for calculating the sweeping velocity. Physical model experiments and numerical simulations are conducted to examine the variations in sweeping velocity with respect to bubble volume and dimensionless bubble volume. Results indicate that the sweeping velocity increases with bubble volume, and the diameter of the pipeline significantly affects the movement of air bubbles. These findings contribute to a better understanding of air bubble behavior in horizontal pipelines and can inform strategies for mitigating risks associated with trapped air bubbles, ultimately improving the safety and reliability of water supply systems.

KEYWORDS

bubble volume, pipe diameter, force analysis, horizontal pipeline, air bubbles, water supply system, sweeping velocity

1 Introduction

Constructing long-distance water supply projects is one of the most direct methods to ensure the optimal allocation of water resources, and has become the main means of water supply for water-deficient cities and regions around the world (Zhang et al., 2015; Li et al., 2018; Ge et al., 2022). These projects require complicated fluid transportation systems which equipped with long pipelines with large flow, high pressure, many branches, wide range, and complex terrain conditions. Their operational safety requirements are extremely high (Leila et al., 2016; Wang et al., 2022; Zhang et al., 2023). Trapped air is a dominant factor which may induce pipeline burst in pressured pipeline transportation systems, and it has been one of the major potential risks that threaten the safe operation of water supply projects. The sweeping velocity of air bubbles reflects the ability of the fluid in the pipeline to carry air pockets,

which can be used as a measure to estimate the movement and retention of air pockets in water pipelines.

Numbers of researches have been conducted to study the moving status, morphological variations, and physical processes of air bubbles in water pipelines. Benjamin T, 1968 determined the Fred number corresponding to the sweeping velocity of air bubbles in horizontal pipelines based on theoretical analysis. Bendiksen (1984) conducted physical model experiments using horizontal pipelines with the diameters ranged from 0.02 to 0.05 m, and proved the existing of the slip velocity. Escarameia et al. (2005) found that the velocity of bubbles in closed pipelines is directly proportional to the diameter of the pipe. The velocity of the air bubbles increase with the increasing of the diameters of pipeline. Yang et al. (2007) demonstrated that pressure affects the physical mechanism governing the gas-liquid interaction, and accordingly influences the dynamics of air bubbles. The dynamics of air bubbles plays a key role in dictating the transport phenomena in gas—liquid fluidization systems. Pothof (2011) deemed that the dimensionless velocity of air bubbles in an outlet pipe n is related to the bubble volume and pipe diameter. Previous researchers have linked the bubble sweeping velocity with the pipe diameter, pipe inclination, and gravity acceleration. However, there is a gap in the effect of bubble volume, surface tension, and other parameters on the bubble sweeping velocity. Ni et al. (2008) believed that bubbles are merely affected by surface tension and buoyancy force. Liu et al. (2008) proposed the correction relation of the friction coefficient between the air phase and water phase using theoretical and experimental analysis. Wang et al. (2019) conducted air-water two-phase flow experiments using a horizontal pipeline, and deduced the friction coefficient between the air phase and water phase.

A numbers of numerical simulation methods also have been proposed to study the law of movement of air bubbles in pipelines. The interface tracking methods (Jafari and Okutucu-Özyurt, 2016; Wu et al., 2021; Wang et al., 2023) such as, MAC (marker and cell technology) model (Santos et al., 2012), etc., have been introduced. The interface capture methods such as the level-set (Zhang et al., 2013; Zhai et al., 2021; Amin and Majid Eshagh, 2020), VOF (volume of fluid) (Ye et al., 2020; Mohammad et al., 2020; Li et al., 2021), and CLSVOF models also have been widely used. Song (2011) proved that when computing the sweeping velocity of air bubbles using convection transport equation, the precision of air–liquid two-phase flow using the CLSVOF model is much more accurate than that of the level-set model and the VOF model. The CLSVOF model is also used to simulate the bubble rising process. This model can not only overcome the shortcomings of the level-set and VOF methods, but also benefits from the advantages of the two methods (Shang et al., 2017; Ge et al., 2020).

Researchers have used machine learning methods to analyze the velocity and shape of air bubbles obtained from physical model experiments. The precision of these methods are more accurate comparing with that of the empirical equations (Deng et al., 2019). Bak et al. (2020) proposed a semi-theoretical correlation developed from a steady-state bubble number density transport equation for predicting the distribution of local bubble size. To obtain physical mechanism governing the air-water interaction, a new method to determine the bubble velocity magnitude was proposed (Qu et al., 2020). Giorgio et al. (2016) provided an experimental method to observe the motion of air bubbles by using a light-field camera, and then analyzed the flow properties and distribution of the air bubbles. Himr (2015) observed the trapped air in the pipeline using a high-speed camera and workbench, and determined the relevant movement laws of trapped air. In order to describe the gas—liquid two-phase flow; Baranivignesh et al. (2019) proposed a new observation method that can locally measure the gas—liquid two-phase flow using particle image velocimetry (PIV) technique, and they verified that the measured bubble size error was small. The optical flow method is a technical method used to detect underwater gas (Sandsten and Andersson, 2012). Xu et al., 2020 designed an automatic detection method for underwater gas, and predicted the motion of underwater gas by using the Farneback optical flow method. The systematical error analysis of the optical flow method in velocity measurements was valid by comparing with the cross-correlation method using in PIV technique (Liu et al., 2015).

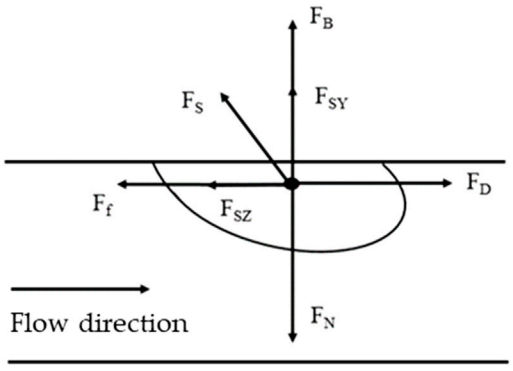

FIGURE 1
Force analysis of a single air bubble in a horizontal pipeline.

The sweeping velocity of the air bubbles is an important index to estimate the carrying capacity of the water supply system. At present, the understanding of the sweeping velocity is still not sufficient. Also, the conclusions obtained from different studies are lack of consistency. This paper studies the motion of bubbles in horizontal water pipelines experimentally and numerically, and deduces the formula of bubble sweeping velocity on the basis of forces analysis. Then, the effect of bubble volume and pipe diameter on the bubble sweeping velocity is discussed.

2 Theoretical analysis

In practical engineering, the pipes can be horizontal or with certain slopes depending on actual construction conditions. To simplify the complexity of practical engineering, we only considered horizontal pipeline in this study. We first define the dimensionless bubble volume as:

$$n = \frac{4V_b}{\pi D^3} \tag{1}$$

where n is the dimensionless bubble volume, V_b is the volume of the bubble, and D is the diameter of the water pipeline.

For the situation of $n > 0.8$, the air in the pipeline is mainly in the form of air pocket, i.e., the bubbles gathers together, and the sweeping velocity of the air pocket is mainly affected by the diameter and inclination of the pipeline. For the situation of $n < 0.8$, the air is mainly in the state of dispersive bubbles. The universal movement law of air bubbles is still lacking. In this section, the forces and sweeping velocity of air bubbles in a horizontal pipeline is analyzed.

When $n < 0.8$, the air bubbles in the horizontal pipeline are mainly affected by the buoyancy force, the support force of the side wall of the pipeline, the drag force of the water flow, the friction resistance of the side wall of the pipeline, and the surface tension. When the fluid velocity in the horizontal pipe is small, the resultant force acts on the bubbles in the horizontal direction is zero, and the bubbles remain still close to the upper wall of the pipe. Figure 1 illustrates the force analysis of a single air bubble in a horizontal pipeline. F_D is the drag force, F_f is the frictional resistance of the side wall of the pipeline to the bubble, F_N is the support force of the side wall of the pipeline on the bubble, F_B is the buoyancy force, F_S is the surface tension of the bubble with F_{SY} the vertical component of surface tension and F_{SZ} the horizontal component of surface tension. If the resultant force in the vertical and horizontal directions is zero, the bubble will adhere to the pipe wall.

For the horizontal direction:

$$F_B + F_{SY} = F_N \tag{2}$$

For the vertical direction:

$$F_f + F_{SZ} = F_D \tag{3}$$

The expressions of the drag force F_D are as follows:

$$F_D = \frac{1}{2} C_D \rho_\omega \bar{u}^2 \pi \frac{ab}{4} \tag{4}$$

$$C_D = \frac{24}{R_{e_b}}\left(1 + 0.173 R_{e_b}^{0.657}\right) + \frac{0.413}{1 + 16300 R_{e_b}^{-1.09}} \tag{5}$$

$$R_{e_b} = \frac{\rho_\omega \bar{u} c}{2\mu} \tag{6}$$

$$u = 1.235 V\left(\frac{d}{D/2}\right) \tag{7}$$

$$\bar{u} = \frac{2}{c}\int_{y=0}^{y=\frac{c}{2}} u\, dy = 1.3173 V \frac{\left(\frac{c}{4}\right)^{1/7}}{D^{1/7}} \tag{8}$$

where a is the length of the long axis of the bubble, b is the length of the central axis of the bubble, c is the length of the short axis of the bubble, $\bar{u}$ is the average velocity of the bubble, Re_b is the Reynolds number of the bubble, μ is the dynamic viscosity coefficient of the water, u is the velocity of the bubble, V is the average flow velocity of the water, and d is the distance from the bubble to the pipe wall. The direction of the buoyancy force is vertically upward, and the buoyancy force is proportional to the volume of the bubble. The buoyancy force F_B can be written as:

$$F_B = V_B(\rho_\omega - \rho_a)g \tag{9}$$

$$V_B = \frac{1}{12}\pi abc \tag{10}$$

where V_B is the volume of the bubble in the pipeline, ρ_w is the density of water, and ρ_a is the density of air. The surface tension of the bubble in the horizontal direction F_{SZ} and vertical direction F_{SY} are calculated as follows:

$$F_{SZ} = -\int_0^\pi a\sigma \cos\gamma \cos\varnothing d\varnothing \tag{11}$$

$$F_{SY} = -\int_0^\pi a\sigma \sin\gamma d\varnothing \tag{12}$$

where σ is the liquid stress tensor acting on the surface of the bubble, γ is the contact angle between the bubble and the tube wall, and $\varnothing$ is the circumferential angle of the contact surface between the tube wall and the bubble. The frictional resistance of the side wall of acts on the air bubble F_f is as follows:

$$F_f = \mu_P F_N \tag{13}$$

where μ_P is the friction coefficient of the side wall of the pipeline. The sweeping velocity of the air bubble in the horizontal water pipeline v_c can be deduced from the above analysis.

$$v_c = \sqrt{\left(\frac{8(\mu_P((F_B + F_{SY}) + F_{SZ})}{C_D \rho_\omega \left(1.3173\left(\frac{c}{4D}\right)^{1/7}\right)^2}\right)} \tag{14}$$

3 Physical model experiment

3.1 Experimental facilities

Figure 2 illustrates the experimental facilities used in the physical model experiments of this study. The experiments were conducted in constant temperature and pressure environment. The temperature was 25°C and the temperature was the standard atmospheric pressure. Figure 2A shows the panorama Gram of the facilities which mainly include three parts: an air—water two-phase flow test platform, a data acquisition system, and an image acquisition system. The air—water two-phase flow test platform mainly included a water supply module, an air transmission module, and a bubble movement observation module. The pipe material commonly used in practical engineering is concrete. In our experiments, we used transparent plastic pipe to visualize the motion of bubble inside the pipeline. The material of the pipe may affect the dynamic of the fluid via influencing the resistance of the side wall. However, we do not enter the errors result from difference of side wall materials in this study. The data acquisition system can not only collect the characteristics of the flow such as velocity, but also controls the velocity of flow and volume of air bubbles. The image acquisition system mainly includes a high-speed camera. In order to improve the quality and accuracy of images, the experimental setup was equipped with a high-precision and high-speed camera with a built-in 12bit CMOS sensor. The resolution of the camera includes 1920 × 1,080, 1,280 × 1,024, and 800 × 600, with a minimum pixel of 5 × 5 μm. In this experiment, we have used a camera with a resolution of 1920 × 1,080 with a minimum pixel of 5 × 5 μm. The sensitivity is 12,000–3000 ISO monochrome, 4,800–1200 ISO color, shutter speed 3 μs to 41.667 ms. The velocity and state of bubble initiation were recorded using the

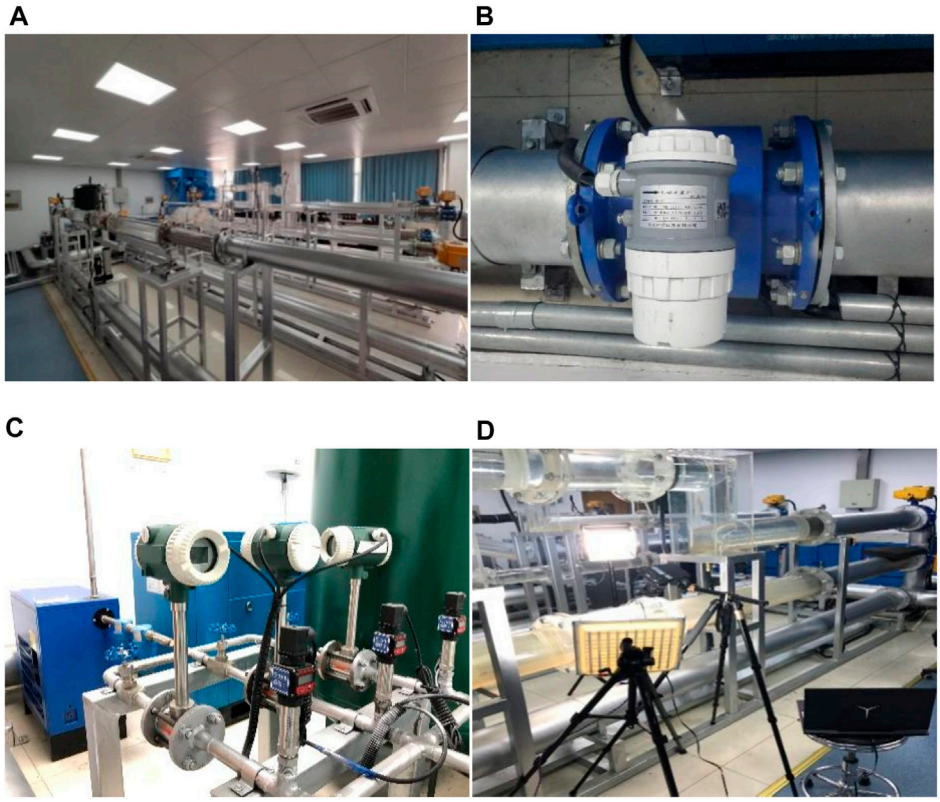

FIGURE 2
Experimental facilities: **(A)** the panoramagram of the facilities, **(B)** the electromagnetic flowmeter, **(C)** the air flow measurement assembly, **(D)** image acquisition system.

high speed camera. The image acquisition system is shown in Figure 2D. An electromagnetic flowmeter was used to measure the real time velocity of fluid. The measurement range of the electromagnetic flowmeter is 0–15 m/s, and the flow velocity accuracy was 0.005 m/s. The layout of the electromagnetic flowmeter is shown in Figure 2B. The air flow measurement assembly is shown in Figure 2C. These facilities are used to explore the dynamic of air bubbles in horizontal pipelines with different inclinations and diameters.

The high-speed camera collected images with a frequency of 500 frames per second. The velocity of air bubbles can be determined by using the distance and time interval between different frames of images, where the difference between the bubble and water flow velocity is the slip velocity v_s, and the ratio of bubble velocity to water flow velocity is the slip velocity ratio K_s.

$$\boldsymbol{v_s = v_\omega - v_b} \tag{15}$$

$$\boldsymbol{K_s = \frac{v_b}{v_\omega}} \tag{16}$$

where v_s is the slip velocity (m/s), v_w is the water velocity in the pipe (m/s), v_b is the bubble velocity (m/s), and K_s is the slip ratio.

In addition, to study the effect of the diameter of pipeline on the sweeping velocity of air bubbles, the DN100 and DN200 pipelines were used. Both of them are horizontal pipelines with a length of 2 m. The diameter of the DN200 pipeline is 0.2 m, and the diameter of the DN100 pipeline is 0.1 m.

3.2 Experimental results

This experiment mainly investigated the sweeping velocity of bubbles in horizontal water pipelines. Using different pipe diameters (DN100 and DN200), horizontally arranged pipes, and bubbles of different sizes, we collected data using the image acquisition system and data acquisition system, and explored the sweeping velocity of air bubbles under different conditions. We then analyzed the sweeping velocity of air bubbles and influence of trapped air in combination with the theoretical analysis, and determined the pressure, flow rate, and other data in the pipeline. In the numerical simulation and theoretical analysis, the case of one bubble was studied. However, in the experimental part, due to the limitation of the experimental facility, several bubbles were produced in the pipe. We neglected the potential errors result from the interaction among bubbles.

For the DN100 and DN200 horizontal pipelines, the bubble sweeping velocity tests under different working conditions were carried out by controlling the parameters including the long axis of the bubble, the bubble volume, the dimensionless bubble volume, the bubble velocity, the slip velocity, and the slip ratio Table 1 shows the results of experiments conducted using the DN100 pipeline. The results of experiments conducted using the DN200 pipeline are listed in Table 2.

The variations of the sweeping velocity of air bubbles to the bubble volume and dimensionless bubble volume n under two

10.3389/feart.2023.1214713

TABLE 1 The results of experiments conducted using the DN100 horizontal pipeline.

Long axis (m)	Bubble volume (m^3)	Dimensionless number n	Sweeping velocity (m/s)	Bubble velocity (m/s)	Slip velocity (m/s)	Ks
0.005	3.27×10^{-8}	4.17×10^{-5}	0.054	0.039	0.015	0.72
0.01	2.61×10^{-7}	3.33×10^{-4}	0.117	0.096	0.021	0.82
0.015	5.61×10^{-7}	7.15×10^{-4}	0.14	0.12	0.02	0.86
0.033	3.61×10^{-6}	4.59×10^{-3}	0.173	0.138	0.035	0.80
0.049	6.15×10^{-6}	7.84×10^{-3}	0.192	0.141	0.051	0.73
0.06	8.24×10^{-6}	1.05×10^{-2}	0.201	0.152	0.049	0.76
0.075	1.08×10^{-5}	1.36×10^{-2}	0.218	0.159	0.059	0.73
0.092	1.27×10^{-5}	1.62×10^{-2}	0.227	0.153	0.074	0.67
0.13	1.79×10^{-5}	2.28×10^{-2}	0.241	0.166	0.075	0.69
0.174	2.62×10^{-5}	3.34×10^{-2}	0.239	0.158	0.081	0.66

different pipeline diameters (DN100 and DN200) are shown in Figure 3. In this study, the bubble volume varies within the range of 0 to 3.5×10^{-5} m^3, and the dimensionless bubble volume ranges within 0 to 5.0×10^{-5}. Accordingly, the sweeping velocity varies from 0.05 to 0.30 m/s. It is obvious that the sweeping velocity of air bubbles in horizontal pipeline increase with the increasing of bubble volume. In addition, the sweeping velocity of air bubbles in a large diameter pipeline is significantly higher than that in a small diameter pipeline. As shown in Figure 3B, estimating using the dimensionless bubble volume, the sweeping velocity of air bubbles in the DN200 pipeline is also higher than that in the DN100 pipeline.

4 Numerical simulation

We established a three-dimensional horizontal pipeline numerical model using the same parameters as physical model experiments, including the velocity of water in the pipeline, the parameters of air bubbles, etc. The schematic diagram of the three-dimensional numerical model is shown in Figure 4. Same as the experimental part of this study, the diameter of the pipeline is 0.2 m for DN200 and 0.1 m for DN100.

By processing the calculation results of the numerical simulation, the bubble sweeping velocity, bubble moving pattern, and bubble shape changes with different pipe diameters and bubble parameters in the horizontal pipeline were analyzed. The fluid dynamics at the cross-section of the pipeline were obtained from the three-dimensional numerical model. Figure 5 shows the motion of the air bubble obtained from the numerical simulation, where the blue part indicates the water phase, and the red part indicates the air phase.

Figure 5A shows the initiation process of air bubbles in the DN200 horizontal pipeline under the conditions of long axis is 0.012 m, middle axis is 0.012 m, and short axis is 0.008 m. At the initial stage, the fraction of the water-phase volume is 1, and the velocity of water is 0.05 m/s. A bubble was introduced into the front end of the observation section. At this time, the bubble was mainly affected by the buoyancy force and the drag force. The bubble moves to the vicinity of the side wall of the pipeline, and then approaches the side wall under the influence of the surface tension and the friction resistance of pipeline. Henceforth, the bubble tended to be stable. After the bubble was stable, we increased the water flow rate gradually, with the increase rate not exceeding 0.02 m/s each time. After the water flow became steady, we increased the flow rate again until the bubble moved. When the velocity of water reaches 0.196 m/s, the bubble was sweeping slowly, and the bubble slip velocity was slow in the initial stage before increasing slowly until it was washed out of the observation section by the water flow. The bubbles moved close to the side wall of the pipeline throughout the whole process.

Figure 5B shows the start of the bubbles' movement process in the DN200 horizontal pipeline, under the conditions of long axis is 0.067 m, middle axis is 0.026 m, and short axis is 0.024 m. When the flow rate increased to 0.274 m/s, two bubbles (after bubble splitting) were washed out of the observation section by the water flow at different flow velocities and accelerations.

10.3389/feart.2023.1214713

TABLE 2 The experimental results of the bubbles starting to move in the DN200 horizontal pipeline.

Long axis (m)	Bubble volume (m^3)	Dimensionless number n	Sweeping velocity (m/s)	Bubble velocity (m/s)	Slip velocity (m/s)	Ks
0.0064	6.86×10^{-8}	1.09×10^{-5}	0.064	0.047	0.017	0.73
0.012	3.01×10^{-7}	4.8×10^{-5}	0.13	0.096	0.034	0.74
0.024	2.14×10^{-6}	3.4×10^{-4}	0.183	0.136	0.047	0.74
0.035	3.85×10^{-6}	6.13×10^{-4}	0.22	0.159	0.061	0.72
0.056	7.08×10^{-6}	1.13×10^{-3}	0.241	0.155	0.086	0.64
0.067	1.09×10^{-5}	1.74×10^{-3}	0.261	0.162	0.099	0.62
0.095	1.67×10^{-5}	2.7×10^{-3}	0.29	0.169	0.121	0.58
0.15	3.04×10^{-5}	4.8×10^{-3}	0.286	0.157	0.129	0.55

Figure 6 shows the streamline of the DN200 horizontal pipeline under the conditions of long axis is 0.024 m, middle axis is 0.026 m, and short axis is 0.024 m, where the blue part is the water phase, the red part is the air phase, and black is the streamline. After the initiation of the bubble, the flow field around the bubble changes, and the water flows around and through the bubble. The streamline above the bubble's front end is sparse, and the streamline below the bubble's front end has a high density. We think the reason is that the overflow section area is hindered when the bubble is close to the wall, resulting in the sparse streamline above the bubble's front end and the dense streamline below the bubble's front end. Then, the water flow bypasses the bubble, and the back end of the bubble gradually returns to a uniform flow field. When the bubble is washed out of the observation section by the water flow, the whole flow field returns to a uniform flow field, and the flow field under other working conditions is similar to that under this working condition.

In order to simplify the observation of the air bubble, the shape of moving air bubbles under different working conditions as shown in Figure 7, where the black part is the bubble and the light blue part is the water phase. After the bubble is filled into the pipe, it becomes oval due to the influence of surface tension and other forces. During the period near the pipe wall, the shape is constantly changing; the short axis becomes longer and the long axis becomes shorter. Near the pipe wall, the bubble profile changes from oval to semi-oval. During the forward movement of the air bubbles adsorbed on the pipe wall, the long axis of the air bubbles changes slightly, but the overall shape remains semi-oval until it rushes out of the observation section.

In Figure 7, the initial section shape of the bubble adsorbed on the pipe wall after filling the pipe is semi-elliptical. When adsorbed on the pipe wall, the long axis is continuously elongated and the short axis is continuously shortened under the action of surface tension and buoyancy. With the increase in the drag force, the bubble gradually splits into two semi-elliptical bubbles and rushes out of the observation section at different movement rates.

For the DN100 and DN200 horizontal pipelines, numerical simulations of the bubble sweeping velocity under different working conditions were carried out. The simulation results are shown in Tables 3, 4. It can be seen from the velocity data in Tables 3, 4 that in the horizontal pipeline, the sweeping velocity of the bubbles is affected by factors such as bubble volume and pipe diameter. In the horizontal pipeline with the same diameter, the sweeping velocity of the bubbles increases with the increase in the bubble volume. When it reaches a certain critical value, the change in the bubbles' sweeping velocity tends to be gentle.

Figure 8 shows the variations of the sweeping velocity of air bubbles to the bubble volume and dimensionless bubble volume obtained from numerical simulation conducted with DN100 and DN200 pipelines. The results are quite similar with those obtained from physical model experiments. The sweeping velocity of air bubbles in horizontal pipeline increase with the increasing of bubble volume. In addition, the sweeping velocity of air bubbles in a large diameter pipeline is significantly higher than that in a small diameter pipeline. Estimating using the dimensionless bubble volume, the sweeping velocity of air bubbles in the DN200 pipeline is also higher than that in the DN100 pipeline.

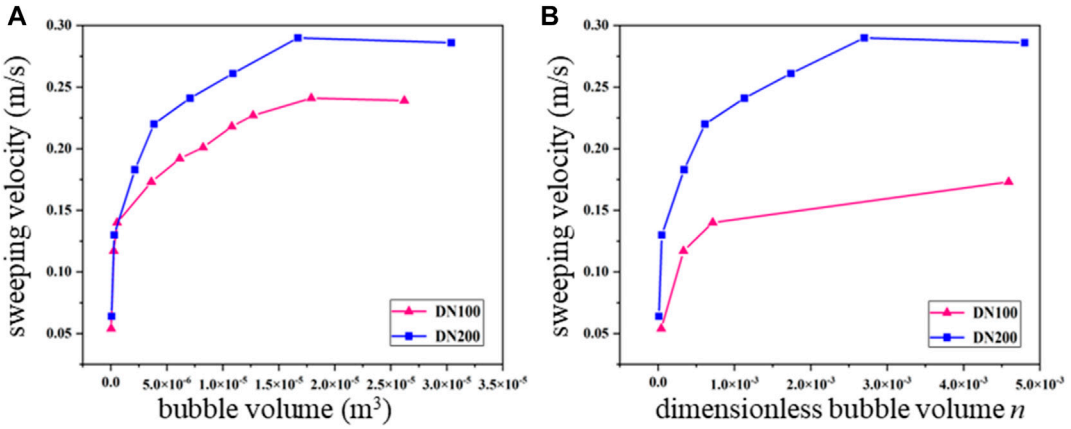

FIGURE 3
Variations of the sweeping velocity of air bubbles to the **(A)** bubble volume and **(B)** dimensionless bubble volume obtained from experiments conducted using DN100 and DN200 pipelines.

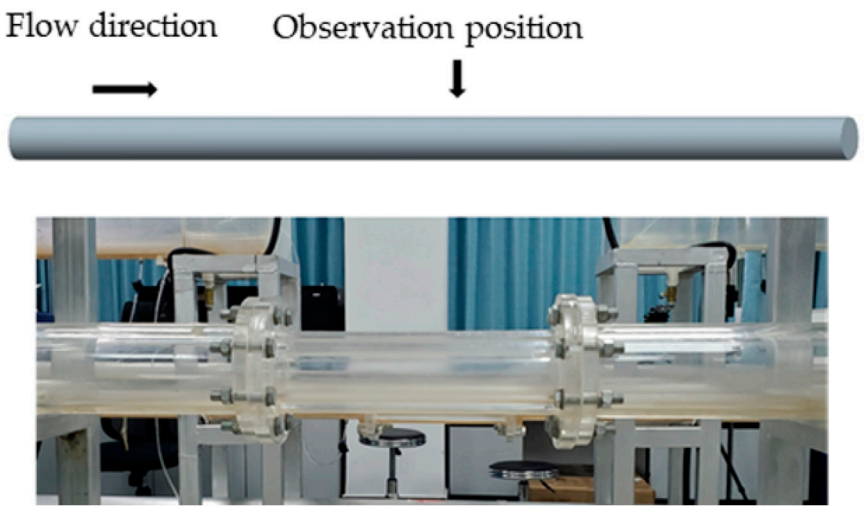

FIGURE 4
Schematic diagram of the three dimensional numerical model.

5 Discussions

The numerical simulation results of the sweeping velocity of air bubbles in horizontal pipelines with different pipe diameters were compared with the results of theoretical calculation proposed in Section 2. Figures 9, 10 show the comparison of the theoretical calculation and numerical simulation results for the sweeping velocity of air bubbles in the DN100 pipeline and DN200 pipeline, respectively.

As can be perceived from Figure 9, in the DN100 horizontal pipeline, when the bubble volume is less than 1.25×10^{-5}, the theoretical calculation value is greater than the numerical simulation result. When the bubble volume is greater than 1.25×10^{-5}, the theoretical calculation value is less than the numerical simulation result. When the n is less than 1.5×10^{-2}, the theoretical calculation value is greater than the numerical simulation result. When n is greater than 1.5×10^{-2}, the theoretical calculation values are less than the numerical simulation results. As shown in Figure 10, in the DN200 horizontal pipeline, when the bubble volume is less than 1×10^{-5}, the numerical simulation results of the bubble sweeping velocity fit the theoretical calculation value; when the bubble volume is greater than 1×10^{-5}, the bubble sweeping velocity in the numerical simulation is slightly larger than the theoretical calculation value, and the average error rate is less than 3%; when the n is less than 1.5×10^{-3}, the numerical simulation results fit the theoretical calculation value; and when the n is greater than 1.5×10^{-3}, the theoretical calculation value is less than the numerical simulation result.

The formula deduced above was used to calculate the sweeping velocity of the bubbles, which was then compared with the results

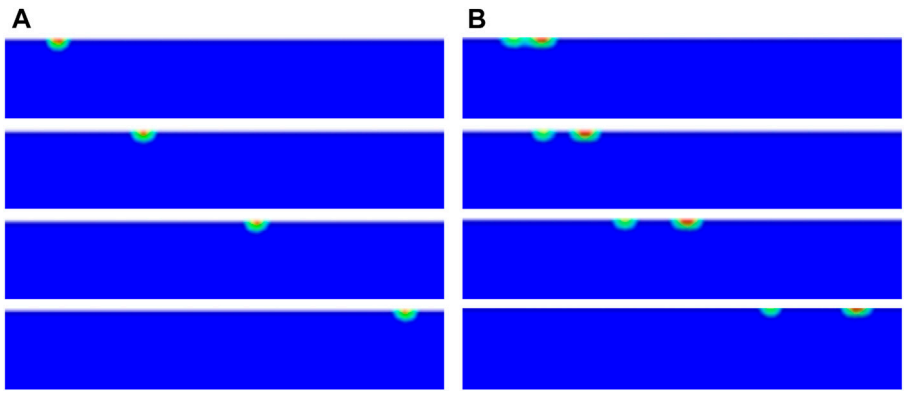

FIGURE 5
Process diagram of bubbles starting to move in the DN200 pipeline diagram. **(A)** under the conditions of long axis is 0.012 m, middle axis is 0.012 m, and short axis is 0.008 m; **(B)** under the conditions of long axis is 0.067 m, middle axis is 0.026 m, and short axis is 0.024 m.

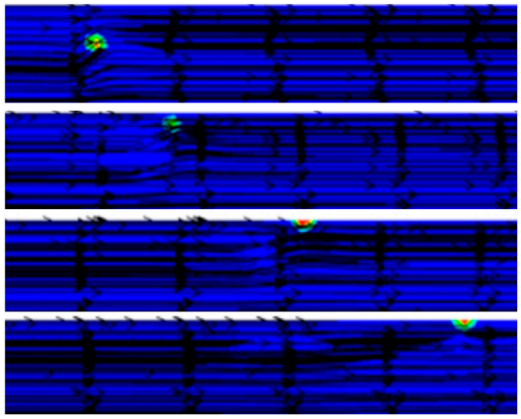

FIGURE 6
The flow line of bubbles starting to move in the DN200 horizontal pipeline.

measured by the physical experiments to verify the reliability of the formula. Figures 11, 12 show the comparison of experimental results and theoretical calculation results for the sweeping velocity of air bubbles in the DN100 pipeline and DN200 pipeline, respectively.

It can be perceived from Figures 11, 12 that in the DN100 horizontal pipeline, when the bubble volume is less than 1×10^{-5}, the experimental result is greater than the theoretical calculation value; when the bubble volume is greater than 1×10^{-5}, the experimental results are in excellent agreement with the theoretical calculation values. When the dimensionless bubble volume n is less than 2×10^{-2}, the experimental results are less than the theoretical calculation value. When n is greater than 2×10^{-2}, the experimental result is in excellent agreement with the numerical simulation results. In the DN200 horizontal pipeline, when the bubble volume is less than 1.25×10^{-5}, the experimental results are less than the theoretical calculation results. When the bubble volume is greater than 1.25×10^{-5}, the experimental results are greater than the theoretical calculation results. When n is less than 2.2×10^{-2}, the experimental results are greater than the theoretical calculation results; and when n is greater than 2.2×10^{-2}, the experimental results are less than the theoretical calculation results.

The numerical simulation results in horizontal pipelines with different diameters were compared with the bubble sweeping velocity measured by experiments under the same working conditions. Figures 13, 14 show the comparison of physical experiment and numerical simulation results for the sweeping velocity of air bubbles in the DN200 horizontal pipeline, respectively. In the DN100 horizontal pipeline, when the bubble volume is less than 5×10^{-6}, the experimental results are greater than the numerical simulation results; when the bubble volume is greater than 5×10^{-6}, the physical experimental results are less than the numerical simulation results. When n is less than 5×10^{-3}, the experimental results are greater than the numerical simulation results; and when n is greater than 5×10^{-3}, the experimental results are less than the numerical simulation results. In the DN200 horizontal pipeline, when the bubble volume is less than 1.25×10^{-5}, the experimental results are less than the numerical simulation results; when the bubble volume is greater than 1.25×10^{-5}, the experimental results are greater than the numerical simulation results. When n is less than 2.3×10^{-3}, the experimental results are less than the numerical simulation results; and when n is greater than 2.3×10^{-3}, the experimental results are greater than the numerical simulation results.

In general, the results of the numerical simulations fit well with the results of physical model experiments. The sweeping velocity obtained from the numerical simulations is higher than that of experimental results. In addition, the error of numerical simulation is smaller comparing with that of experiments. In general, the sweeping velocity of bubbles in pipeline increase with the increasing of the diameter of the pipeline and the dimensionless bubble volume. The results confirms the finding of previous studies that the velocity is influenced by these two factors. In addition, by comparing the theoretical results with the experimental and numerical results, the theoretical expression proposed in this study can be validate, which provide a simple way to estimate the sweeping velocity of bubbles in pipeline.

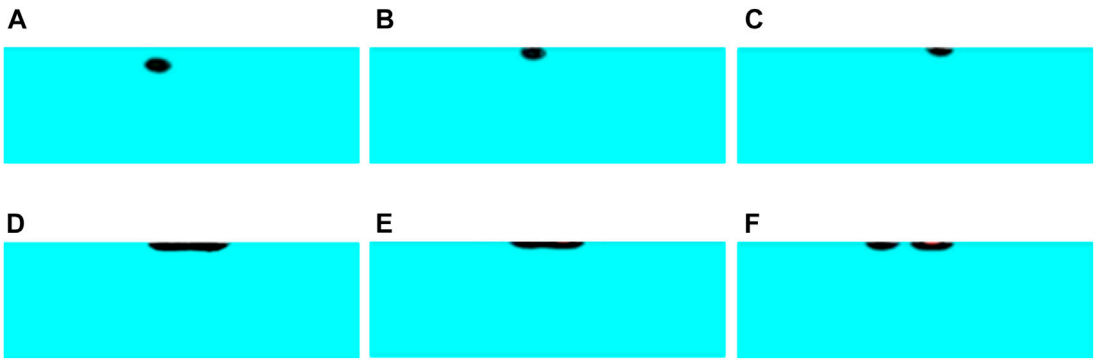

FIGURE 7
The shape of moving air bubbles in the DN200 horizontal pipeline. **(A)** under the conditions of long axis is 0.064 m, middle axis is 0.064 m, and short axis is 0.064 m; **(B)** under the conditions of long axis is 0.012 m, middle axis is 0.012 m, and short axis is 0.008 m; **(C)** under the conditions of long axis is 0.024 m, middle axis is 0.02 m, and short axis is 0.017 m; **(D)** under the conditions of long axis is 0.067 m, middle axis is 0.026 m, and short axis is 0.024 m; **(E)** under the conditions of long axis is 0.095 m, middle axis is 0.028 m, and short axis is 0.024 m; **(F)** under the conditions of long axis is 0.15 m, middle axis is 0.031 m, and short axis is 0.025 m.

TABLE 3 The numerical simulation results of the bubbles starting to move in the DN100 horizontal pipeline.

Long axis (m)	Middle axis (m)	Short axis (m)	Bubble volume (m^3)	Dimensionless number n	Sweeping velocity (m/s)
0.005	0.005	0.005	3.27×10^{-8}	4.17×10^{-5}	0.073
0.01	0.01	0.01	2.61×10^{-7}	3.33×10^{-4}	0.102
0.015	0.013	0.011	5.61×10^{-7}	7.15×10^{-4}	0.134
0.033	0.019	0.022	3.61×10^{-6}	4.59×10^{-3}	0.165
0.049	0.02	0.024	6.15×10^{-6}	7.84×10^{-3}	0.212
0.06	0.021	0.025	8.24×10^{-6}	1.05×10^{-2}	0.223
0.075	0.022	0.025	1.08×10^{-5}	1.36×10^{-2}	0.234
0.092	0.022	0.024	1.27×10^{-5}	1.62×10^{-2}	0.244
0.13	0.021	0.025	1.79×10^{-5}	2.28×10^{-2}	0.256
0.174	0.024	0.024	2.62×10^{-5}	3.34×10^{-2}	0.260

TABLE 4 The numerical simulation results of the bubbles starting to move in the DN200 horizontal pipeline.

Long axis (m)	Middle axis (m)	Short axis (m)	Bubble volume (m^3)	Dimensionless number n	Sweeping velocity (m/s)
0.0064	0.0064	0.0064	6.86×10^{-8}	1.09×10^{-5}	0.092
0.012	0.012	0.008	3.01×10^{-7}	4.8×10^{-5}	0.134
0.024	0.02	0.017	2.14×10^{-6}	3.4×10^{-4}	0.196
0.035	0.02	0.021	3.85×10^{-6}	6.13×10^{-4}	0.262
0.056	0.021	0.023	7.08×10^{-6}	1.13×10^{-3}	0.270
0.067	0.026	0.024	1.09×10^{-5}	1.74×10^{-3}	0.274
0.095	0.028	0.024	1.67×10^{-5}	2.7×10^{-3}	0.284
0.15	0.031	0.025	3.04×10^{-5}	4.8×10^{-3}	0.282

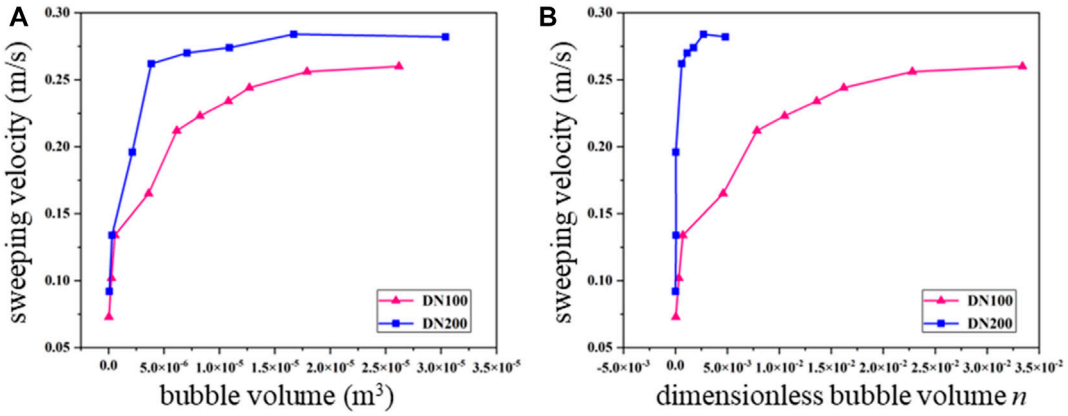

FIGURE 8
Variations of the sweeping velocity of air bubbles to the **(A)** bubble volume and **(B)** dimensionless bubble volume obtained from numerical simulation conducted with DN100 and DN200 pipelines.

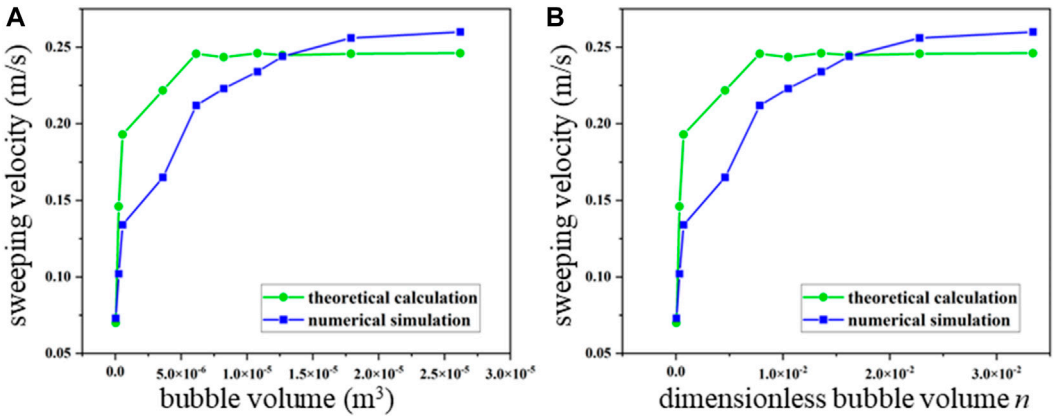

FIGURE 9
Comparison of the sweeping velocity of air bubbles to the **(A)** bubble volume and **(B)** dimensionless bubble volume obtained from DN100 horizontal pipelines conducted with theoretical calculation and numerical simulation.

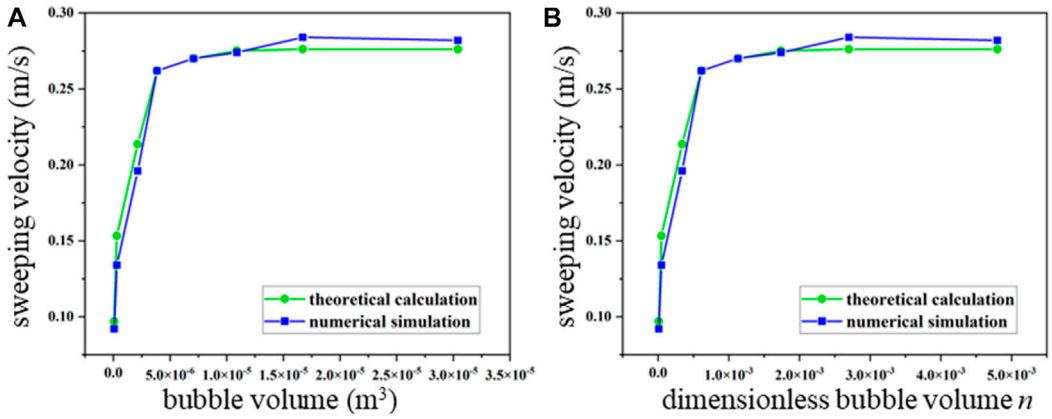

FIGURE 10
Comparison of the sweeping velocity of air bubbles to the **(A)** bubble volume and **(B)** dimensionless bubble volume obtained from DN200 horizontal pipelines conducted with theoretical calculation and numerical simulation.

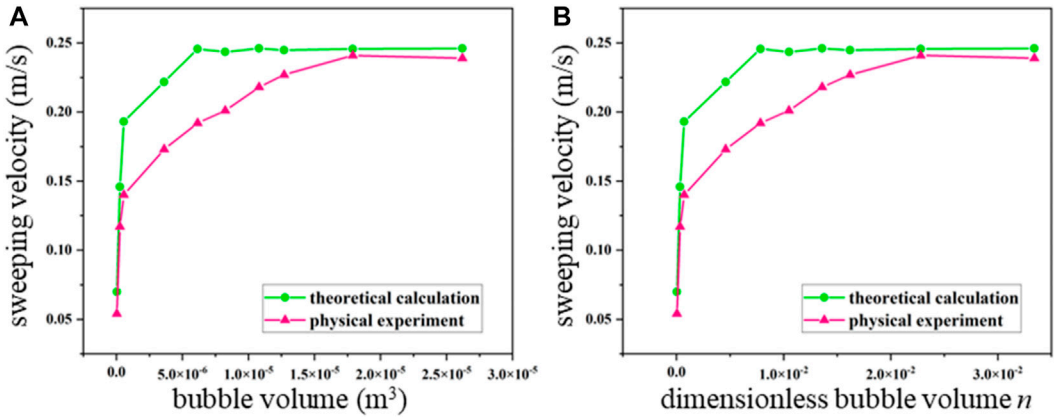

FIGURE 11
Comparison of the sweeping velocity of air bubbles to the **(A)** bubble volume and **(B)** dimensionless bubble volume obtained from DN100 horizontal pipelines conducted with physical experiment and theoretical calculation results.

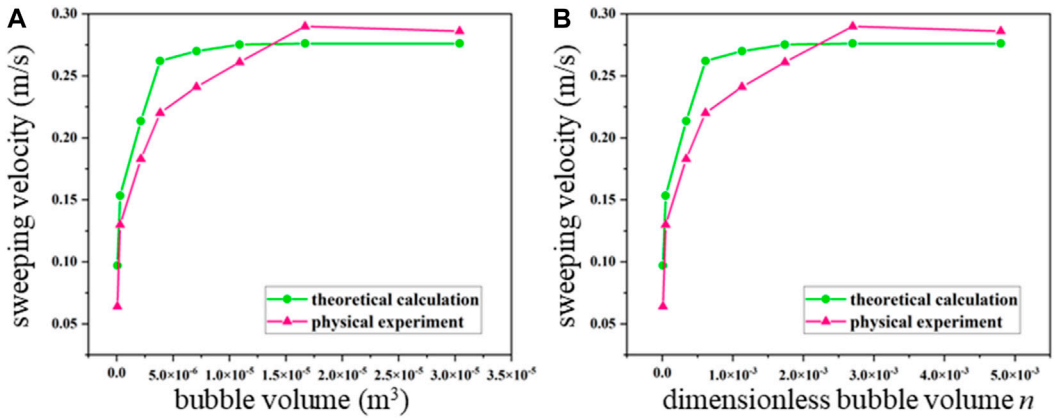

FIGURE 12
Comparison of the sweeping velocity of air bubbles to the **(A)** bubble volume and **(B)** dimensionless bubble volume obtained from DN200 horizontal pipelines conducted with physical experiment and theoretical calculation results.

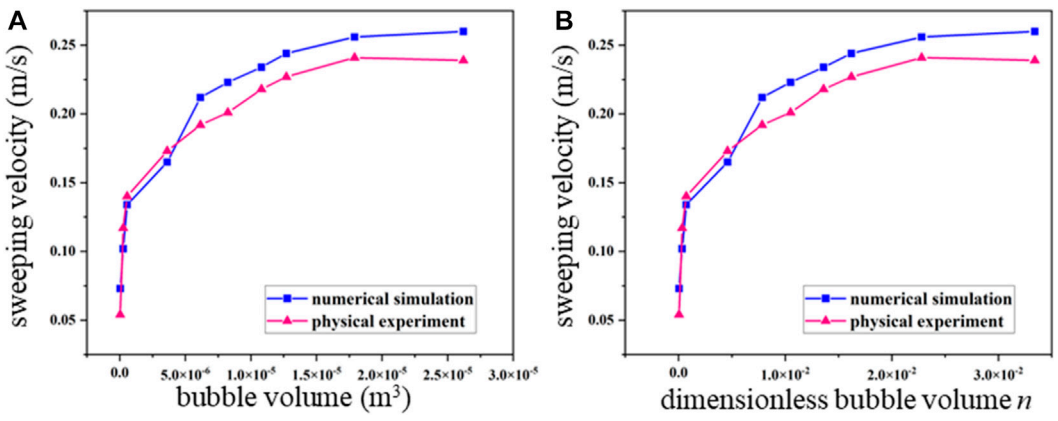

FIGURE 13
Comparison of the sweeping velocity of air bubbles to the **(A)** bubble volume and **(B)** dimensionless bubble volume obtained from DN100 horizontal pipelines conducted with physical experiment and numerical simulation results.

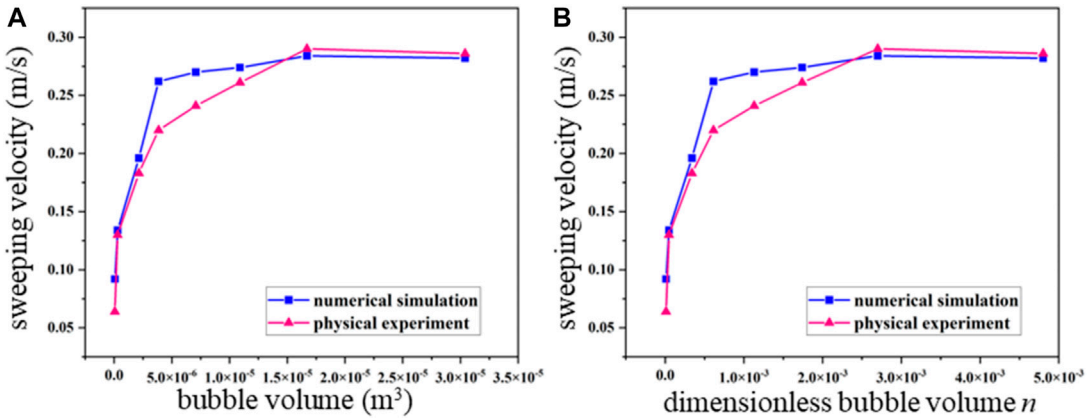

FIGURE 14
Comparison of the sweeping velocity of air bubbles to the **(A)** bubble volume and **(B)** dimensionless bubble volume obtained from DN200 horizontal pipelines conducted with physical experiment and numerical simulation results.

6 Conclusion

This paper gives insights to the sweeping velocity of air bubbles in horizontal pipelines in water supply system. We first analyze the forces act on a single air bubble in a horizontal pipeline, and provide a theoretical expression for calculating the sweeping velocity of the air bubble. Physical model experiments are conducted with different parameters of air bubbles and pipelines. The variations of the sweeping velocity to the bubble volume and dimensionless bubble volume are determined experimentally. We then carry out numerical simulations with the same initial settings as experiments and analyze the flow line, velocity field, as well as the sweeping velocity of the bubbles. The conclusions are as follows:

First, the sweeping velocity of air bubbles in horizontal pipelines obtained from theoretical calculation, simulated simulation, and experiments fit quite well. The results indicate that the sweeping velocity of air bubbles increases with the increase of bubble volume. When the bubble volume is less than 2.8×10^{-5} the sweeping velocity of air bubbles in the DN100 pipeline varies from 0.05 m/s to 0.23 m/s; when the bubble volume is greater than 1.8×10^{-5}, the sweeping velocity reaches a steady state at 0.23 m/s. When the bubble volume is less than 3.1×10^{-5}, the sweeping velocity of air bubbles in the DN200 pipeline increases from 0.06 m/s to 0.28 m/s; when the bubble volume is greater than 1.7×10^{-5}, the sweeping velocity reaches a steady state at 0.28 m/s.

In addition, the moving process of air bubbles can be divided into four stages: bubble attachment, bubble sweeping, bubble slip, and bubbles breaking away from the wall. When the water velocity is low, the bubbles remain in their original shape under the multiple action of several forces. When the velocity of water increases to reach the sweeping velocity of the air bubble, the bubble shape changes, the bubble deforms significantly, and then splits into two bubbles. The mechanical equilibrium of the bubble is broken, and the bubble enters a sliding state. At this time, the bubble moves close to the up-side wall of the pipeline, and the bubble velocity is lower than water velocity. After a period of time, the bubble may break away from the wall. With the bubble velocity increasing, the bubble is washed out of the observation section by the water flow.

Data availability statement

The original contributions presented in the study are included in the article/supplementary material, further inquiries can be directed to the corresponding author.

Author contributions

Conceptualization, JH, CY, and YZ; methodology, JH, CY, and YZ; writing—original draft, JH and YZ; writing—review and editing, ZM, ML, and JZ; supervision, HS; project administration, HS; funding acquisition, JH. All authors contributed to the article and approved the submitted version.

Funding

This work was supported by the Key Joint Funds of the Zhejiang Provincial Natural Science Foundation of China (No. LZJWZ22E090004).

Acknowledgments

We are very grateful to the reviewers for their constructive comments and suggestions.

Conflict of interest

Author CY was employed by Henan Water and Power Engineering Consulting Co, Ltd.

The remaining authors declare that the research was conducted in the absence of any commercial or financial relationships that could be construed as a potential conflict of interest.

Publisher's note

References

Amin, H., and Majid Eshagh, N. (2020). A geometric mass control approach in level set method to simulate multiphase flows with complex interface topologies, case study: Oblique coalescence of gas bubbles in a liquid. *P. I. Mech. Eng. E-J. Pro.* 234, 56–69. doi:10.1177/0954408919883729

Bak, J., Kim, H., Jeong, J. J., Euh, D., and Yun, B. (2020). Development of bubble size correlation for adiabatic forced convective bubbly flow in low pressure condition using CFD code. *Appl. Sci.* 10, 5443. doi:10.3390/app10165443

Baranivignesh, P., Harisinh, P., Milinkumar, T. Shah., Vishnu, K. Pareek., Lefebvre, A., and Ranjeet, P. U. (2019). Simultaneous measurements of two phases using an optical probe. *ECMF* 1, 233–241. doi:10.1007/s42757-019-0025-y

Bendiksen, K. H. (1984). An experimental investigation of the motion of long bubbles in inclined tubes. *Int. J. Multiphas Flow.* 10, 467–483. doi:10.1016/0301-9322(84)90057-0

Benjamin T, B. (1968). Gravity currents and related phenomena. *J. Fluid Mech.* 31, 209–248. doi:10.1017/s0022112068000133

Deng, B., Chin, R. J., Tang, Y., Jiang, C., and Sai, H. L. (2019). New approach to predict the motion characteristics of single bubbles in still water. *Appl. Sci.* 9, 3981. doi:10.3390/app9193981

Escarameia, M., Rwp, M., Burrows, R., and Gahan, C. (2005). *Air in pipelines – a literature review*. Oxfordshire, BA, UK: HR Wallingford Limited, 15–25.

Ge, W., Jiao, Y., Wu, M., Li, Z., Wang, T., Li, W., et al. (2022). Estimating loss of life caused by dam breaches based on the simulation of floods routing and evacuation potential of population at risk. *J. Hydrology* 612, 128059. doi:10.1016/j.jhydrol.2022.128059

Ge, W., Qin, Y., Li, Z., Zhang, H., Gao, W., Guo, X., et al. (2020). An innovative methodology for establishing societal life risk criteria for dams: A case study to reservoir dam failure events in China. *Int. J. Disaster Risk Reduct.* 49, 101663. doi:10.1016/j.ijdrr.2020.101663

Giorgio, B., Pietro, B., Alberto, F., and Fabio, I. (2016). Estimation of bubble size distributions and shapes in two-phase bubble column using image analysis and optical probes. *Flow. Meas. Instrum.* 52, 190–207. doi:10.1016/j.flowmeasinst.2016.10.008

Himr, D. (2015). Investigation and numerical simulation of a water hammer with column separation. *J. Hydra. Eng.* 141, 04014080. doi:10.1061/(ASCE)HY.1943-7900.0000967

Jafari, R., and Okutucu-Özyurt, T. (2016). 3D numerical modeling of boiling in a microchannel by arbitrary Lagrangian-Eulerian (ALE) method. *Appl. Math. Comput.* 272, 593–603. doi:10.1016/j.amc.2015.03.042

Leila, R., Bryan, K., and Ahmad, M. (2016). Encouraging effective air management in water pipelines: A critical review. *J. Water Res. Plan. Man.* 142, 04016055. doi:10.1061/(ASCE)WR.1943-5452.0000695

Li, Z., Li, W., and Ge, W. (2018). Weight analysis of influencing factors of dam break risk consequences. *Nat. Hazards Earth Syst. Sci.* 18 (12), 3355–3362. doi:10.5194/nhess-18-3355-2018

Li, Z., Zhang, Y., Wang, J., Ge, W., Li, W., Song, H., et al. (2021). Impact evaluation of geomorphic changes caused by extreme floods on inundation area considering geomorphic variations and land use types. *Sci. Total Environ.* 754, 142424. doi:10.1016/j.scitotenv.2020.142424

Liu, Y., Zhang, H., Wang, S., and Wang, J. (2008). Gas–liquid interfacial friction factor for the transition from stratified to slug flow. *Microgravity Sci. Technol.* 20, 299–305. doi:10.1007/s12217-008-9078-4

Liu, T., Merat, A., Makhmalbaf, M. H. M., Claudia, F., and Parviz, M. (2015). Comparison between optical flow and cross-correlation methods for extraction of velocity fields from particle images. *Exp. Fluids* 56, 166. doi:10.1007/s00348-015-2036-1

Mohammad, A., Morteza, T., and Nowrouz Mohammad, N. (2020). Study of intermittent flow characteristics experimentally and numerically in a horizontal pipeline. *J. Nat. Gas. Sci. Eng.* 79, 103326. doi:10.1016/j.jngse.2020.103326

Ni, B., Luo, Z., and Zou, Z. (2008). "Thermodynamics analysis on bubble attachment to solid wall in liquid," in *Proceedings of the national symposium on physical chemistry of metallurgy* (Guiyang, China), 1–4.

Pothof, I. W. M. (2011). *Co-current air-water flow in downward sloping pipes*. Enschede, Netherlands: Gildeprint Drukkerijen BV.

Qu, X., Guo, Q., Zhang, Y., Qi, X., and Liu, L. (2020). A new vector-based signal processing method of four-sensor probe for measuring local gas–liquid two-phase flow parameters together with its assessment against one bubbly flow. *Appl. Sci.* 10, 5463. doi:10.3390/app10165463

Sandsten, J., and Andersson, M. (2012). Volume flow calculations on gas leaks imaged with infrared gas-correlation. *Opt. Express* 20, 20318–20329. doi:10.1364/OE.20.020318

Santos, F. L. P., Ferreira, V. G., Tomé, M. F., Castelo, A., Mangiavacchi, N., and McKee, S. (2012). A marker-and-cell approach to free surface 2-D multiphase flows. *Int. J. Numer. Methods. Fluids* 70, 1543–1557. doi:10.1002/fld.3641

Shang, Z., Luo, J., and Li, H. (2017). Simulations of flow transitions in a vertical pipe using coupled level set and VOF method. *Int. J. Comp. Meth-Sing* 14, 1750013. doi:10.1142/S021987621750013X

Song, Y., Wang, C., and Ning, Z. (2011). Computation of incompressible two-phase flows by using CLSVOF method. *Trans. Chin. Soc. Agric. Mach.* 42, 26–31. doi:10.3969/j.issn.1000-1298.2011.07.006

Wang, Y., Liu, Z., Chang, Y., Zhao, X., and Guo, Z. (2019). Experimental study of gas-liquid two-phase wavy stratified flow in horizontal pipe at high pressure. *Int. J. Heat. Mass Transf.* 143, 118537. doi:10.1016/j.ijheatmasstransfer.2019.118537

Wang, T., Li, Z., Ge, W., Zhang, H., Zhang, Y., Sun, H., et al. (2023). Risk consequence assessment of dam breach in cascade reservoirs considering risk transmission and superposition. *Energy* 265, 126315. doi:10.1016/j.energy.2022.126315

Wang, T., Li, Z., Ge, W., Zhang, Y., Jiao, Y., Sun, H., et al. (2022). Calculation of dam risk probability of cascade reservoirs considering risk transmission and superposition. *J. Hydrology* 609, 127768. doi:10.1016/j.jhydrol.2022.127768

Wu, M., Wu, Z., Ge, W., Wang, H., Shen, Y., and Jiang, M. (2021). Identification of sensitivity indicators of urban rainstorm flood disasters: A case study in China. *J. Hydrology* 599, 126393. doi:10.1016/j.jhydrol.2021.126393

Xu, C., Wu, M., Zhou, T., Li, J., Du, W., Zhang, W., et al. (2020). Optical flow-based detection of gas leaks from pipelines using multibeam water column images. *Remote Sens.* 12, 119. doi:10.3390/rs12010119

Yang, G. Q., Bing, D., and Fan, L. S. (2007). Bubble formation and dynamics in gas–liquid–solid fluidization—a review. *Chem. Eng. Sci.* 62, 2–27. doi:10.1016/j.ces.2006.08.021

Ye, H., Chen, Y., and Kevin, M. (2020). A discrete-forcing immersed boundary method for moving bodies in air–water two-phase flows. *J. Mar. Sci. Eng.* 8, 809. doi:10.3390/jmse8100809

Zhai, S., Geng, S., and Jing, M. (2021). Numerical simulation of gas-water two-phase seepage flow based on level set method. *IOP Conf. Ser. Earth Environ. Sci.* 781, 022041. doi:10.1088/1755-1315/781/2/022041

Zhang, Y., Ge, S., and Ni, J. (2013). Study on dynamic behavior of single bubble in wedge-shaped channel. *Chin. J. Hydro.* 28, 307–316. doi:10.3969/j.issn1000-4874.2013.03.008

Zhang, L., Li, S., Loáiciga, H. A., Zhuang, Y., and Du, Y. (2015). Opportunities and challenges of interbasin water transfers: A literature review with bibliometric analysis. *Scientometrics* 105, 279–294. doi:10.1007/s11192-015-1656-9

Zhang, H., Ge, W., Zhang, Y., Li, Z., Li, W., Zhu, J., et al. (2023). Risk management decision of reservoir dams based on the improved life quality index. *Water Resour. Manag.* 37, 1223–1239. doi:10.1007/s11269-023-03426-y

frontiers | Frontiers in Earth Science

TYPE Brief Research Report
PUBLISHED 13 June 2023
DOI 10.3389/feart.2023.1211775

OPEN ACCESS

EDITED BY
Wei Ge,
Zhengzhou University, China

REVIEWED BY
Dongli She,
Hohai University, China
Menghua Xiao,
Zhejiang Institute of Hydraulics and Estuary, China

*CORRESPONDENCE
Xun Zou,
17754806021@163.com

RECEIVED 25 April 2023
ACCEPTED 30 May 2023
PUBLISHED 13 June 2023

CITATION
Hu X, Zou X and Fan H (2023), Analysis of landscape influencing factors of urban waterfront greenways based on the scenic beauty estimation method, taking Tongjian Lake in Hangzhou as an example.
Front. Earth Sci. 11:1211775.
doi: 10.3389/feart.2023.1211775

Analysis of landscape influencing factors of urban waterfront greenways based on the scenic beauty estimation method, taking Tongjian Lake in Hangzhou as an example

Xiujun Hu[1,2], Xun Zou[3]* and Haiyan Fan[4]

[1]Zhejiang Institute of Water Resources and Ocean Engineering, Zhejiang University of Water Resources and Electric Power, Hangzhou, China, [2]Key Laboratory for Technology in Rural Water Management of Zhejiang Province, Hangzhou, China, [3]College of Civil Engineering, Anhui Jianzhu University, Hefei, China, [4]Beijing Water Science and Technology Institute, Beijing, China

In order to assess the unique beauty of Tongjian Lake in Hangzhou, 80 sample photographs were selected for landscape beauty degree assessment using the Scenic Beauty Estimation method. The 14 characteristic influencing factors of landscape photos were extracted according to the Scenic Beauty Estimation value, and the influencing factors with insignificant differences and small bias correlation coefficients were eliminated through multiple linear regression analysis. The results showed that the main factors affecting the expression of the beauty of Tongjian Lake were water ecology, greenway morphology, landscape openness, water area ratio, vegetation color richness, and vignette matching. Combining the abovementioned analysis results, the two-dimensional plan, isometric map, and three-dimensional space are combined to show the main factors in a visual way, and on this basis, the corresponding optimization strategy is proposed. It provides a reference for future urban waterfront greenway landscape creation.

KEYWORDS

urban waterfront greenway, Scenic Beauty Estimation method, landscape expression factor, Tongjian Lake, multi-dimensional presentation

1 Introduction

China's cities have grown quickly in recent years, with an increased focus on the advancement of ecological civilization. This growth emphasizes how peacefully nature and man can interact. In this trend, urban greenways are becoming more and more popular as a result of rising ecological concerns and frequent recreational trips among city dwellers. The waterfront greenway landscape is not only a crucial component of the system of urban green spaces; it also contributes to the establishment and improvement of the ecology between urban water bodies and land areas. Additionally, it can successfully control the interaction of people with urban avenues, water bodies, and landscaped green spaces, enhancing the aesthetic appeal of the city. As a result, the waterfront greenway should not only be practical but also pay attention to its aesthetics and coordination with the surrounding area because it is an essential component of the urban water landscape.

There are various landscape evaluation methods, divided into comparative evaluation methods: the Analytic Hierarchy Process (AHP) method, the Geographic Information System (GIS) method, the Scenic Beauty Estimation (SBE) method, and the Semantic Difference (SD) method. Among these, the Scenic Beauty Estimation method is a practical method commonly used in the evaluation of landscapes such as urban parks, urban green spaces, and scenic areas (Liu et al., 2016). Through the Scenic Beauty Estimation method, the aesthetic preference of the public for the study target is assessed and decomposed into quantifiable elements so as to establish a correlation model with the quantitative values of landscape elements.

Both local and international academics have conducted a significant amount of research on the appraisal of water landscapes. The study primarily assesses the ecological role, aesthetic value, and humanistic expression of water landscapes in various regions, illuminating the relationships and rules between them (Yang, 2014; Cao, 2016; Lu et al., 2016; Huang et al., 2019; Sun et al., 2021; Ye et al., 2021; Xu et al., 2022; Wang et al., 2023). The waterfront greenway is a type of water landscape, and it is crucial to investigate how water bodies, buildings, and plants interact in space (Luo et al., 2023; Ren et al., 2023) as well as their ecological and humanistic benefits in order to support the development of spiritual civilization. (Wei, 2017; Li, 2020; Wang, 2021a; Yang et al., 2021; Fang and Liu, 2022). The SBE method was employed by Xue Ren et al. (Ren and Liu, 2023b) to assess the aesthetic value of plant landscapes and investigate the connection between parks and plant spaces. Shi et al. (2020) evaluated urban park landscapes using evaluation indices combining the SBE technique and the AHP method; Li et al. (2022) evaluated landscapes in water using the SBE method and suggested low-cost methods for enhancing aesthetic qualities; Xu (2023) employed the landscape evaluation method to assess the public's aesthetic preferences for the waterfront greenway in the park and to create a sample of multiple regressions.

Studies on the combination of lakefront regions and greenways are now less common. In order to provide a solid scientific foundation and workable strategies for improving the natural landscape and realizing the sustainable development of the urban waterfront greenway landscape space, this paper presents a thorough analysis of the visual quality of the waterfront greenway in Tongjian Lake, West Lake District, Hangzhou. The city's life and atmosphere improved.

2 Research method

2.1 Study area

Tongjian Lake is a 4.35-square-kilometer lake on the bank of the Qianjiang River in the West Lake area of Hangzhou, with a main lake area of 1.35 square kilometers, a total reservoir capacity of 5 million cubic meters, and a storage capacity of 3.2 million cubic meters. Among them, the Tongjian Lake Greenway is particularly outstanding and was named the "Most Beautiful Greenway in Hangzhou" in 2022. The Tongjian Lake Greenway is a high-quality greenway built by West Lake District, with a length of 31.5 km. The greenway sets up road widths, materials, stations, and signage systems according to local conditions and displays local history, culture, and folklore with the help of sculptures, cultural relic protection, and science popularization, so as to build a green space for visitors to rest, leisure, travel, and fitness.

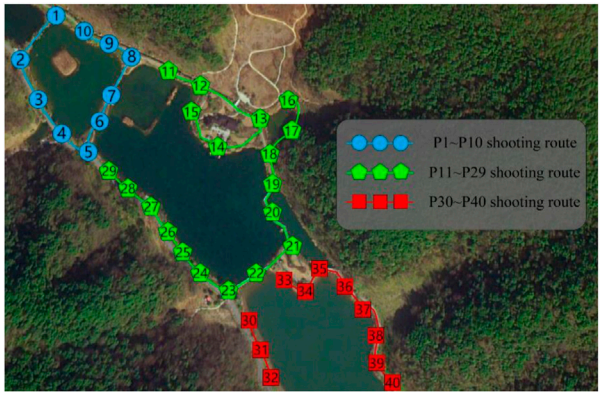

FIGURE 1
Landscape sample photo collection points.

2.2 Scenic beauty estimation method

The Scenic Beauty Estimation method (hereinafter referred to as the SBE method) transforms the relationship of landscape aesthetics into a stimulus-response relationship in evaluation by combining the physical characteristics of the landscape with the respondents' landscape perceptions and preferences. The general aesthetic feeling of the group is used as the standard for measuring the merits of the waterfront greenway, thus better reflecting the diversity and richness of the landscape. According to the evaluation process of the SBE method, the landscape nodes of the Tongjian Lake Greenway were selected for field photography, while the participants were invited to score the photo samples to derive the SBE values to reflect the public's preferences. Also, the waterfront greenway landscape factors were decomposed to construct a relationship model between the public's preferences and each landscape factor.

The SBE method is based on the premise that, while there are some variances in how people see things, there are also some similarities. The second assumption made by the SBE method is that the measured landscape values are normally distributed, with the mean value of this distribution serving as the most accurate representation of the observed landscape. The true quantitative value of the measured landscape attributes can be most accurately represented by the average value of this distribution. Both domestic and international experts have fully endorsed the method's scientific nature, sensitivity, accuracy, and other qualities, and it has been extensively applied to the study of plant landscapes.

2.3 Photo acquisition and selection

To ensure the quality and diversity of the photo samples and to enhance the colorfulness of the color images, a windy and sunny season was chosen for the shooting of the greenway landscape. The

shooting was carried out by using the same camera on 28 June 2022, with 40 landscape nodes on the waterfront greenway, from 8:30 a.m. to 11:00 a.m. and from 14:30 p.m. to 16:00 p.m. The shots were taken from different angles and positions, and the preferred locations for filming were scenic locations with a fixed horizon of 1.6 m. The shots included close-up, medium, and long-range views, and a total of 332 photos were taken in one shot. Each landscape node selected the two most representative photos as sample photos. Finally, 80 sample photos were obtained. The distribution of landscape nodes is shown in Figure 1.

2.4 Selection of evaluators

Due to the differences in individual aesthetics, different judges will have different evaluations of the same waterfront greenway photos. In order to ensure the objectivity of the evaluation results, three groups of judges with different professional types were selected in this research study, totaling forty-two people. Among them, the expert group consisted of four experts, mainly engaged in landscape planting research. The gardening group consisted of fourteen university students majoring in gardening-related disciplines, and the other fourteen non-gardening groups consisted of social workers.

2.5 Landscape scoring

We made 80 slides from 80 photos and classified the beauty of the waterfront greenway into seven levels: extremely dislike, very dislike, relatively dislike, general, relatively like, very like, and extremely like, corresponding to scores of 1, 2, 3, 4, 5, 6, and 7, respectively, gathered the judges together, and projected the landscape slides on a large screen using a projector. It is shown three times: the first time at a rate of 2 s to give the judges a comprehensive perception of the entire landscape; the second time at a rate of 4 s to allow the judges to notice the stunning photos; and the third time for the official judging, which is shown at a rate of 10 s. The judges were asked to give a complete review within 10–20 s. After the live scoring by forty-two judges, there were no invalid questionnaires, and forty-two valid questionnaires were received in the end.

2.6 Data processing

Using the standardization method in the SBE method, the differences between the data were removed, thus obtaining a more accurate scenic beauty evaluation value with the following formula:

$$Z_{ij} = \frac{\left(R_{ij} - \bar{R}_j\right)}{S_j}, \tag{1}$$

$$Z_i = \sum_j Z_{ij} \Big/ N_j, \tag{2}$$

where Z_{ij} denotes the standardized score of the ith greenway photo by the jth reviewer; R_{ij} denotes the rating value of the ith greenway photo by the jth reviewer; $\bar{R}_j$ denotes the mean of the ratings of all greenway photos by the jth reviewer; S_j denotes the standard deviation of the ratings of all greenway photos by the jth reviewer; N_j denotes the total number of reviewers for the jth greenway photo; Z_i denotes the final standardized score of the ith greenway photo, i.e., the Scenic Beauty Estimation value (hereinafter referred to as the SBE value).

The SBE value is a measure of the aesthetic quality of the landscape and reflects the aesthetic preferences of each reviewer. Therefore, the SBE value needs to be analyzed in depth to explore the aesthetic differences of each group of people and identify the relevant elements that affect the score. If the SBE value is greater than 0, the landscape is of high quality. If the ecological configuration and aesthetic effects are at the desired level, then the quality of the waterfront greenway will be enhanced rather than below zero.

2.7 Decomposition of landscape factors

Quantitative analysis is to express some unclear and ambiguous factors with actual concrete data, which can be more convenient and intuitive to see the changing trend of each factor. According to the experimental purpose and the performance characteristics reflected by the landscape photos, the main factors affecting the waterfront greenway landscape are divided into 14 quantitative factors, namely: water ecology, greenway width, greenway material, greenway form, landscape openness, water area ratio, green percentage, vegetation species, vegetation distribution, vegetation color richness, waterfront architecture, sense of spatial extension, waterfront distance, and other supporting scenery. The elements are decomposed into different categories according to the unified standard, and the specific quantification methods are shown in Table 1. Through the image processing software, the proportion of landscape openness, water area ratio, green percentage, and waterfront architecture in the photos can be calculated, comparisons are shown as A and B in Figure 2.

3 Analysis and conclusion nomenclature

3.1 Waterfront greenway landscape SBE value analysis

The SBE values of each sample were calculated according to the standardized formula as shown in Table 2 and Figure 3. From the figure and table, it can be seen that the number of sample photos with extremely high or low SBE values was low; 75% of the SBE values were distributed between −0.5 and 0.5, and there were more photos with negative SBE values. The sample with the lowest SBE value is photo P54 (see Figure 4), with a score of only −1.40244; the sample with the highest SBE value is photo P30 (see Figure 5), with a score of 1.73117. Further analysis of photos P30 and P54 was conducted. The close-up view of photo P30 shows a trestle bridge, which is neat and clean, with the white body of the bridge reflecting green plants and the reflection in the water being clear and translucent like a mirror. The middle and far views are composed of mountains towering into the clouds,

TABLE 1 Quantification and assignment table of landscape factors.

Number	Landscape factors	Assigning a score					Quantification methods
		1	2	3	4	5	
F1	Water ecology	Muddy and unclear	With impurities	Clear bottom	-	-	Yes/no
F2	Greenway material	Cement	Marble	Asphalt	Pebbles	Combination form	Yes/no
F3	Greenway width	<1.5 m	1.5–2.5 m	2.5–3 m	>3 m	-	Measure
F4	Greenway form	Straight and sheltered	Straight and open	Curved and sheltered	Curved and open	-	Yes/no
F5	Landscape openness	<30%	30%–60%	60%–90%	≥90	-	Software analysis
F6	Water area ratio	<30%	30%–60%	60%–90%	≥90	-	Software analysis
F7	Green percentage	<30%	30%–50%	50%–70%	70%–90%	≥90	Software analysis
F8	Vegetation species	1 kind	2 kinds	3 kinds	4 kinds	More than 4 kinds	Count
F9	Vegetation distribution	Centralized distribution	Dispersed distribution	Both of them	-	-	Subjective judgment
F10	Vegetation color richness	1 kind	2 kinds	3 kinds	4 kinds	More than 4 kinds	Count
F11	Waterfront architecture	<30%	30%–50%	50%–70%	70%–90%	≥90%	Software analysis
F12	Sense of spatial extension	<2 m	2m–5 m	5m–8 m	>8 m	-	Measure
F13	Waterfront distance	<0.5 m	0.5m–1 m	1m–1.5 m	1.5m–2 m	>2 m	Measure
F14	Other supporting scenery	Hardly	Propaganda board	Stone scape	Pavilion	All inclusive	Count

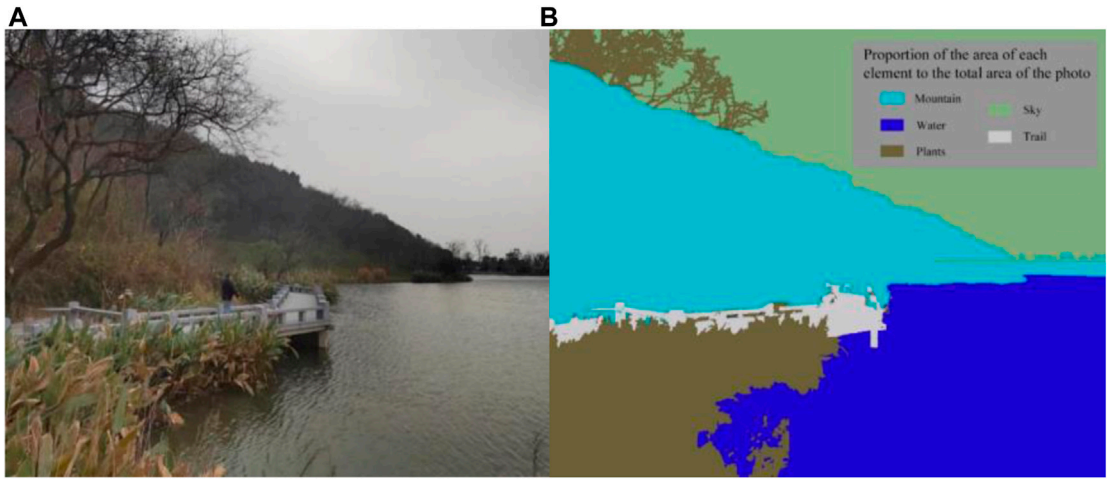

FIGURE 2
Image processing example diagram. **(A)** Sample, **(B)** Sample photo analysis images.

which are lush and green, with different shades of color and order, forming a natural waterfront greenway. The P54 photo shows that the greenway is short and slightly abrupt in color, with an obvious sense of border contrast with the surrounding environment, and the close-up shot is a completely hard landscape, lacking vegetation. Although the water is open, the overall color is single, giving the viewer a negative feeling.

By observing the sample pictures and their SBE values, it can be found that the high-scoring samples have richer landscape elements and more layered colors, with winding waterfront greenways, a

TABLE 2 SBE values of landscape sample photos.

No.	SBE value	No.	SBE value	No.	SBE value	No.	SBE value
P1	−0.00622	P21	0.56381	P41	−0.36425	P61	0.63794
P2	−0.5118	P22	−1.29275	P42	0.92856	P62	−0.41723
P3	−0.21621	P23	−0.24102	P43	−0.44983	P63	1.09132
P4	−0.58435	P24	−0.37621	P44	0.01586	P64	1.61799
P5	−0.35568	P25	−0.05924	P45	0.15881	P65	1.15195
P6	−0.54862	P26	0.8315	P46	0.43851	P66	0.18476
P7	−0.102	P27	−0.68214	P47	0.46203	P67	−0.04744
P8	−0.63615	P28	−0.51793	P48	−0.21449	P68	0.76517
P9	0.46516	P29	−0.15604	P49	1.48513	P69	−1.32938
P10	0.15881	P30	1.73117	P50	−0.16833	P70	1.45109
P11	−0.6772	P31	−0.1324	P51	−0.62419	P71	0.48942
P12	0.36688	P32	−0.51609	P52	0.39028	P72	−0.16737
P13	−0.84394	P33	0.23908	P53	−0.52421	P73	−0.16459
P14	−0.13669	P34	0.00188	P54	−1.40244	P74	0.4549
P15	−0.61466	P35	−0.56431	P55	−0.1593	P75	1.60543
P16	0.55345	P36	0.80908	P56	−0.16769	P76	−0.88621
P17	−0.32793	P37	−0.18002	P57	0.87018	P77	0.33156
P18	0.83884	P38	1.01408	P58	0.64045	P78	−1.22661
P19	−0.5096	P39	−0.59591	P59	−0.48917	P79	−0.51306
P20	−0.35714	P40	−0.21791	P60	−0.67296	P80	−0.47857

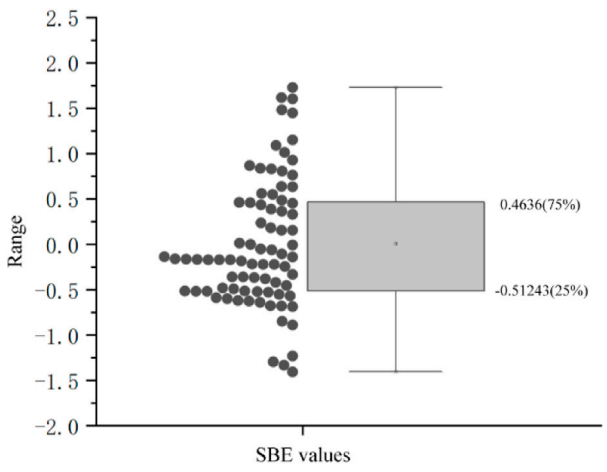

FIGURE 3
Distribution of SBE values.

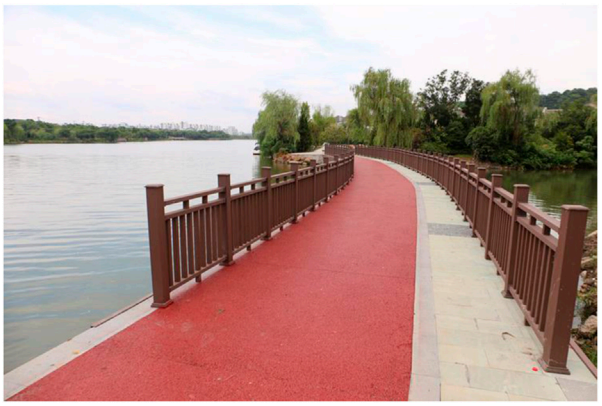

FIGURE 4
No. P54 sample photo.

certain amount of artificial or natural supporting scenery around the greenways, wide and layered water views, and strong seasonal changes, showing good natural scenery. The low-scoring samples, on the other hand, showed monotonous views, poor environmental coordination, and poor sightline permeability, and these problems limited the assessment of SBE values. Therefore, in the creation of the waterfront greenway landscape space, appropriate transformation strategies should be adopted according to the local characteristics in order to enhance the landscape's beauty and make it harmonize with the overall landscape of the real environment.

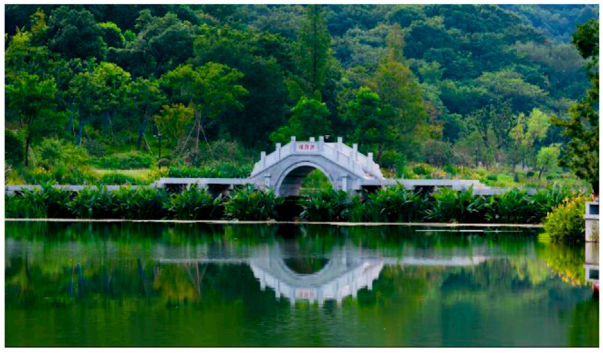

FIGURE 5
No. P30 sample photo.

3.2 Quantitative analysis of landscape factors

With the SBE value of the waterfront greenway as the dependent variable and 14 landscape factors as independent variables to establish the model and conduct multiple linear regression analysis, the results are shown in Table 3. Six main factors influencing the SBE value of urban waterfront greenway landscapes were identified, namely,: water ecology, greenway form, landscape openness, water area ratio, vegetation color richness, and other supporting scenery. The six main factors were substituted into the regression equation to establish the landscape evaluation model:

$$SBE = 1.675 + 0.269*F1 + 0.065F4 + 0.148*F5 + 0.101*F6 + 0.107*F10 + 0.191*F14. \quad (3)$$

All six factors in the formula are positively correlated with the SBE value. According to the ANOVA table, the model shown in Table 3 passed the F-test at a confidence level of 0.05 ($F=12.894, p=0.001^{e}<0.05$) and had an R^2 value of 0.625, thus allowing a specific analysis of the relationship between the influence of the independent variables on the dependent variable. The fit was more appropriate. Based on this result, ways to enhance the beauty of the waterfront trail were further explored.

In order to evaluate the landscape factors screened by the regression model from more perspectives, eight sample photos with SBE values ≥1 were selected, and experts engaged in landscape architecture, municipal landscape, and water ecology were invited to analyze the degree of influence of the six main factors on the landscape of the waterfront greenway. The results are shown in Figure 6.

As can be seen from Figure 6, after the expert evaluation weighting analysis, the priority ranking of the waterfront trail landscape factor is water ecological, landscape openness, other supporting scenery, water area ratio, greenway form, and vegetation color richness. Among them, water ecology is the most important factor; vegetation color richness is also an important factor affecting the waterfront greenway landscape as the natural shape and color give people a rich aesthetic interest; the creation of vignettes with scenery is also an important factor, which can bring people closer to nature, and the space with complete facilities can reflect this more.

Combining SBE values and quantitative evaluation of factors, it can be found that in those landscape nodes with high SBE values, the greenway morphology, water area ratio, and landscape openness are more coordinated, while the water ecology, vegetation color richness, and other supporting scenery of the waterfront greenway are the key factors affecting the waterfront greenway landscape score. Therefore, when constructing the waterfront greenway, focusing on the overall layout, local spatial integrity, and the improvement of individual basic elements can enhance the overall landscape quality.

3.3 Realistic simulation of major factors

According to the findings of this paper, combined with literature (Wang, 2021b) and field research, the area of the Tongjian Lake Waterfront Greenway mainly includes the areas of water bodies, heritage areas, trail areas, green areas, building areas, mountain areas, and recreational areas.

In order to present the quantitative factors of the waterfront greenway more accurately, the 2D plan view, isometric map, and 3D modeling were combined to show the real-world factors in a visual way.

TABLE 3 Coefficient decomposition table of linear regression analysis.

Impact factor	*Non-standardized factor*		*Standardization factor*	*T-test value*	p_{Sig}	*CS*	
	B	*SD*	*Beta*			*Tolerances*	*VIF*
(Constant)	1.675	0.472		−3.552	0.001		
Water ecology (F1)	0.269	0.074	0.271	3.651	0.001	0.225	1.436
Greenway form (F4)	0.065	0.037	0.106	1.782	0.039	0.353	1.830
Landscape openness (F5)	0.148	0.056	0.201	2.670	0.010	0.220	1.548
Water area ratio (F6)	0.101	0.056	0.159	1.811	0.045	0.161	1.210
Vegetation color richness (F10)	0.107	0.050	0.014	1.130	0.049	0.102	1.761
Other supporting scenery (F14)	0.191	0.055	0.358	3.490	0.001	0.118	1.471

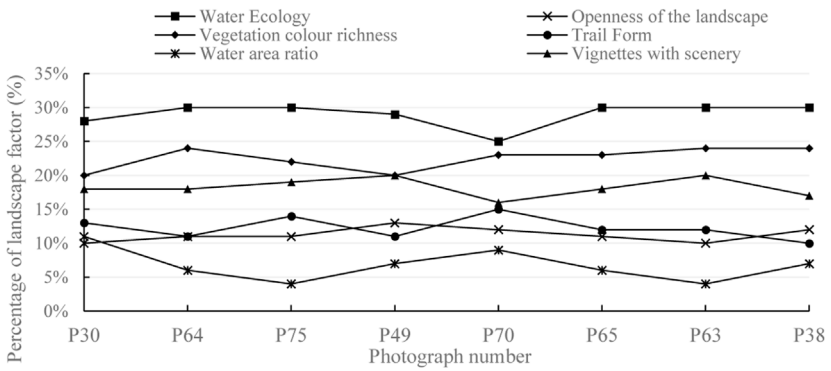

FIGURE 6
Evaluation of six factors in photos with SBE value ≥1.

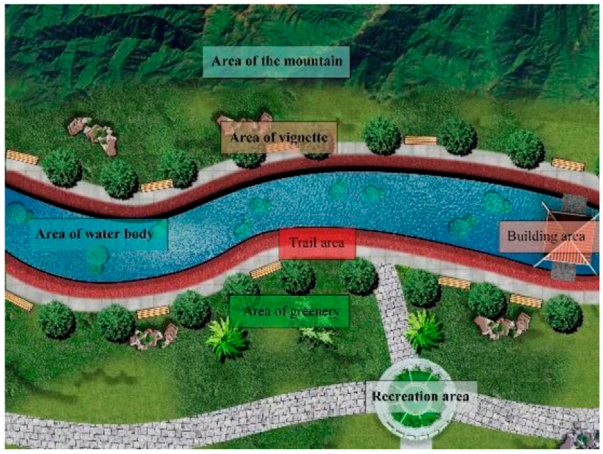

FIGURE 7
Plan view of the sample.

The 2D plan view is the landscape plan of the sample photo from the overhead perspective, and the proportional size of the area of each factor of the waterfront greenway to the total area of the photo plan was measured by using the image software. The corresponding landscape patterns as well as colors were filled in, as shown in Figure 7.

The isometric map is closer to human vision compared with the plan view, making the image realistic and three dimensional. First, the isometric map of the landscape area is drawn using the board drawing software, and then, the landscape elements in the map are classified by the image processing software, and the proportion and size of each element in the plane photo are calculated. The weights of vignette matching, greenway morphology, water ecology, vegetation color richness, landscape openness, and water area ratio were analyzed, as shown in Figure 8.

Through 3D Max software, the landscape factors in the waterfront greenway photos can be modeled and decomposed into various types of factors such as distant view, medium view, close view, plant angle, and plant color to achieve the purpose of coordinating the water ecology and spatial environment, and according to the characteristics of each factor, the materials are adjusted and finally imported into Lumion rendering to obtain the distribution map of the waterfront greenway landscape factors and realize the 3D spatial expression, as shown in Figure 9.

3.4 Urban waterfront greenway landscape optimization strategy

3.4.1 Optimizing the view of the greenway

It is recommended that the openness of the view of the waterfront greenway of Tongjian Lake be increased to provide enough space for visitors to rest within the beautiful scenery and that a viewing platform be set up so visitors can enjoy the scenery. The focus of these changes should be on the continuous flow of the greenway and the guidance of the line of sight, and enhancing the extension of the greenway space through vegetation or other landscape elements. When designing the waterfront greenway, the principle of proximity should be followed to minimize detours so that nearby residents can reach it quickly and easily. The size of the greenway should also be scientific and reasonable, with the flexible treatment of the twists and turns of the channel based on the sparseness of the surrounding air. The spatial distribution should consider the integration of open space and private space as much as possible, so that the surrounding environment, vignettes, grass, trees, and other elements together form a private space, thus increasing the attractiveness of the waterfront greenway.

3.4.2 Enhancement of the green vision ratio

It is recommended that the greening of the waterfront greenway should be strengthened to cover the entire trail, including the area on both sides of the trail and the surrounding area. Lawns, shrubs and flowers and trees should be reasonably matched with height levels; the water can be planted with some aquatic plants, such as lotus and reeds, to increase the beauty and ecological function of the ecological environment; the surrounding vignette buildings should be covered with vines to increase the greening area and beautify the environment. In this way, the colourful combination of colours

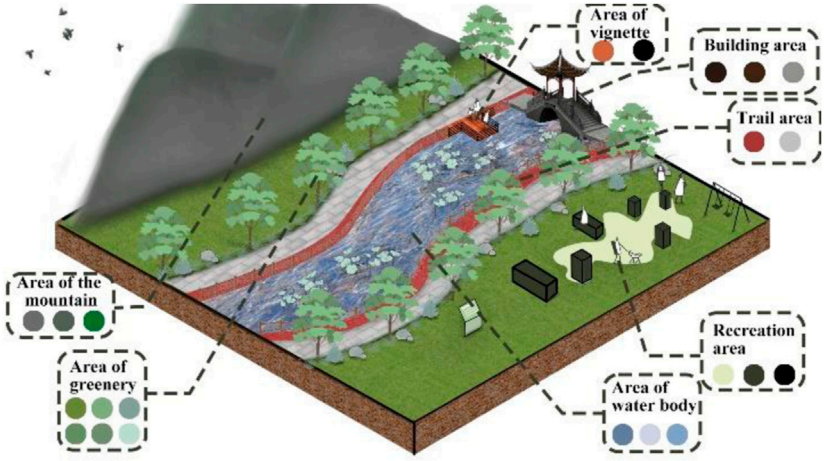

FIGURE 8
Isometric effect of the sample.

FIGURE 9
3D spatial effect of the sample.

can also enhance the visual impact of the landscape. The water surface in the view is static, and the grass and trees are moving. The plants are sparse in the near view but cascading in the far view, which is a collection of dynamic and sparse transformations and brings a rich visual experience to people. The types of vegetation use vines, bamboo, flowers, shrubs, etc., to create a multi-layered and multi-colored flora that has high aesthetic and ecological value. Green plants can not only improve the quality of the landscape but also effectively reduce noise and pollution, having a positive impact on the ecological environment.

3.4.3 Control of the architectural style

The architectural style and environment surrounding Tongjian Lake are mainly Chinese, supplemented by modern minimalist and natural styles. It is suggested that the exterior of the historic district be flexibly combined with flower boxes and planted with evergreen shrubs or flowering plants to enrich the stores along the river. Other neighborhood facades use evergreen shrubs and fast-growing vine plants to enrich the sense of spatial hierarchy and ecological diversity of plant landscapes. At the same time, with the increase of leisure and entertainment places beside Tongjian Lake, the color and location should be integrated with the natural scenery and surrounding buildings, which will make the overall appearance of the entire Tongjian Lake waterfront greenway more harmonious and beautiful.

3.4.4 Adding ecological berms

The scenic area of Tongjian Lake is rich in natural resources and lush vegetation, and the original berm can be seen everywhere. However, the survey shows that as some of the berms have not been designed and transformed, the grass and trees are more disorganized; therefore, it is especially necessary to beautify the berm area to achieve a more perfect landscape effect under the premise of meeting the safety function of flood prevention and flood control. First, the ecological berm should consider the important factor of porosity so that the berm can grow plants and improve the stability of the raised bank structure with the help of plant action. Second, the berms should use flexible materials to adapt to the complex and tortuous lines of the waterfront greenway. The arrangement and spacing of the seats along the lakefront greenway should consider the comfort and privacy of the public; the design of the waterfront platform needs to have enough space for activities; the trestle bridge and others should also have a reasonable form, color adaptation, and solid structure. These leisure facilities can soften the borders of the berm, and while regulating the vegetation structure and beautifying the environment, they can also allow visitors to get close to nature and show a beautiful picture of man and nature living in harmony.

4 Conclusion and suggestions

1) This study employs the urban waterfront greenway as its research subject and scores the landscape's aesthetics according to the SBE method. Six key factors influencing the expression of the scenic

beauty degree of the Tongjian Lake waterfront greenway were derived using multiple linear regression analysis and expert evaluation analysis, and based on this, a comparable optimization technique is suggested as a guide for creating future urban waterfront greenways.

2) Regarding the study of the beauty of the urban river and lake landscapes, the method of deriving landscape factors mostly relies on regression models (Sun et al., 2021; Xu, 2023), which are standard but not comprehensive enough. This paper combines the regression model with professional human evaluation to make a comprehensive judgment and comes up with the weight ranking of landscape factors, which fully considers the aesthetic judgment and subjective consciousness feelings. The area is allocated according to the ranking of the landscape factors, and each landscape factor is reflected in the plan according to its area share to obtain a scientific and reasonable area distribution. Furthermore, isometric and three-dimensional maps are depicted, spatial analysis is carried out, and optimization strategies are proposed. Therefore, this paper innovates a new evaluation method for urban river and lake landscapes that is more scientific and intuitive.
3) The findings of this paper discuss the main factors that create a beautiful scenic landscape surrounding urban rivers and lakes, which could guide the landscape design of urban rivers. For rural rivers and large-scale composite rivers, we need to conduct targeted research on the factors influencing scenic landscapes. Additionally, we recommend that the "Beautiful River and Lake" satisfaction survey be updated to include the SEB score to improve the evaluation of the site.

Data availability statement

The raw data supporting the conclusion of this article will be made available by the authors, without undue reservation.

Author contributions

XH, XZ, and HF contributed to the conception and design of the study. XH organized the database. XH and XZ performed the statistical analysis. XH and XZ wrote the first draft of the manuscript. HF wrote sections of the manuscript. All authors contributed to the article and approved the submitted version.

Funding

This research was funded by the Key R&D Program of Zhejiang (2022C02035) and the Joint Funds of the Zhejiang Provincial Natural Science Foundation of China (LZJWZ22E090004).

Acknowledgments

The authors are very grateful to the reviewers for their constructive comments and suggestions.

Conflict of interest

The authors declare that the research was conducted in the absence of any commercial or financial relationships that could be construed as a potential conflict of interest.

Publisher's note

References

Cao, B. (2016). Shenyang city river waterfront green space plant landscape evaluation. *For. Sci. Technol. Inf.* 48 (2), 84–87. doi:10.3969/j.issn.1009-3303.2016.02.032

Fang, P. L., and Liu, X. (2022). Research on landscape construction of urban riverside walkway under micro-intervention design strategy. *Chongqing Archit.* 21 (S1), 157–160. doi:10.3969/j.issn.1671-9107.2022.S1.157

Huang, Y.-L., Pan, H., Lv, L., et al. (2019). Landscape evaluation of waterfront plants in the campus based on AHP method with guangyin lake of fujian agriculture and forestry university as an example. *Southeast Hortic.* 7 (04), 49–55.

Li, X. J. (2020). Assessment of the service value of the ecosystem of the Meixiang River as a provincial wetland park. *Heilongjiang Hydraulic Sci. Technol.* 48 (03), 221–225. doi:10.3969/j.issn.1007-7596.2020.03.063

Li, X., Wang, X., Han, J., Wu, D., Lin, Q., Zhou, J., et al. (2022). Effects of river scale on the aesthetic quality of urban on-water sightseeing. *Sustainability* 14 (19), 12543. doi:10.3390/su141912543

Liu, L., Liu, Z.-C., Yang, R.-Y., Zhang, R.-F., Li, H., Xu, X.-M., et al. (2016). Quantitative classification and diversity characteristics of plant communities in the river corridor of the dry section of Yongding River (Luliang section). *J. Ecol.* 40 (24), 9129–9137. doi:10.5846/stxb202003050419

Lu, M.-H., Zhang, T., and Ma, C.-C. (2016). Landscape evaluation of recreational road green space plant communities in Nanjing. *Jiangsu Agric. Sci.* 44 (12), 239–243. doi:10.15889/j.issn.1002-1302.2016.12.073

Luo, Y., He, J., Long, Y., Xu, L., Zhang, L., Tang, Z., et al. (2023). The relationship between the color landscape characteristics of autumn plant communities and public aesthetics in urban parks in changsha, China. *Sustainability* 15 (4), 3119. doi:10.3390/su15043119

Ren, X., and Liu, J. P. (2023). Landscape evaluation of plants in nanchong city north lake park based on SBE method. *Contemp. Hortic.* 46 (7), 50–52. doi:10.3969/j.issn.1006-4958.2023.07.019

Shi, Y., Lv, D., and He, J. (2020). Landscape evaluation of urban parks based on SBE and AHP: A case study of kunming city. *IOP Conf. Ser. Earth Environ. Sci.* 580 (1), 012016. doi:10.1088/1755-1315/580/1/012016

Sun, D., Li, Q., Gao, W., Huang, G., Tang, N., Lyu, M., et al. (2021). On the relation between visual quality and landscape characteristics: A case study application to the waterfront linear parks in shenyang, China. *Environ. Res. Commun.* 3 (11), 115013. doi:10.1088/2515-7620/ac34c7

Tan, X., Li, X., and Peng, Y. (2021). Aesthetic evaluation of plant landscape based on principal factor analysis and SBE in wetland park–a case study of Jinlong lake wetland park (China). *J. Environ. Eng. Landsc. Manag.* 29 (1), 40–47. doi:10.3846/jeelm.2021.14367

Wang, C. (2021). Waterfront park plant configuration analysis--take quanzhou jiangbin north road xinhua dry lock transformation waterfront park as an example. *Contemp. Hortic.* 44 (24), 48–50. doi:10.3969/j.issn.1006-4958.2021.24.019

Wang, Y.-M., Li, S., and Jiang, J.-Y. (2023). Plantscape assessment of comprehensive parks in wuhan. *J. Chin. Urban For. Endocrinol*, 1–10. doi:10.12169/zgcsly.2021.04.22.0001

Wei, L. (2017). Spatial interface characteristics of urban waterfront trails. *Contemp. Hortic.* 344 (20), 114. doi:10.14051/j.cnki.xdyy.2017.20.091

Xu, C. R. (2023). The evaluation and analysis of scenic beauty estimation on the waterfront walkway: A case of the north garden of minjiang park in fuzhou. *Urbanism Archit.* 20 (2), 189–193. doi:10.19892/j.cnki.csjz.2023.02.51

Xu, H., Ou, D.-Y., Du, C.-Y., Lian, Y.-Q., et al. (2022). Evaluation and comparative analysis of day-night audio-visual land scape of sea plank roa. *J Huaqiao Univ. Sci.* 43 (06), 736–742. doi:10.11830/ISSN.1000-5013.202111015

Yang, F., Li, C. K., Yang, Y. M., Hang, Q.-T., et al. (2021). Study on the influence of waterfront footpath in Minjiang Park on visitors' physical and mental health. *J. Hebei For. Sci. Technol.* 230 (3), 28–34. doi:10.16449/j.cnki.issn1002-3356.2021.03.009

Yang, X. (2014). Structural quality in waterfront green space of shaoyang city by scenic beauty evaluation. *Asian J. Chem.* 26 (17), 5644–5648. doi:10.14233/ajchem.2014.18181

Ye, X. J., Fang, X. L., Chu, X., Gu, Y.-Q., et al. (2021). Analysis on the strategy of enhancing the vitality of the grand canal waterfront space in canglang new town section of suzhou city. *Archit. Cult.* 211 (10), 165–166. doi:10.19875/j.cnki.jzywh.2021.10.062

frontiers | Frontiers in Earth Science

TYPE Original Research
PUBLISHED 29 June 2023
DOI 10.3389/feart.2023.1220842

OPEN ACCESS

EDITED BY
Wei Ge,
Zhengzhou University, China

REVIEWED BY
Kan Kan,
College of Energy and Electrical Engineering, China
Jiachun Liu,
Ningbo University, China

*CORRESPONDENCE
Jiahua Mao,
maojh@zjweu.edu.cn

RECEIVED 11 May 2023
ACCEPTED 12 June 2023
PUBLISHED 29 June 2023

CITATION
Hu J, Wang Q, Song H and Mao J (2023), Effect of wave disturbance on the fluid dynamics of the pump turbine in a seawater pumped storage hydroplant. *Front. Earth Sci.* 11:1220842. doi: 10.3389/feart.2023.1220842

Effect of wave disturbance on the fluid dynamics of the pump turbine in a seawater pumped storage hydroplant

Jianyong Hu[1,2], Qingbo Wang[2,3], Hongge Song[2,3] and Jiahua Mao[1,2]*

[1]School of Geomatics and Municipal Engineering, Zhejiang University of Water Resources and Electric Power, Hangzhou, China, [2]Engineering Research Center of Digital Twin Basin of Zhejiang Province, Hangzhou, China, [3]College of Energy and Power Engineering, North China University of Water Resources and Hydropower, Zhengzhou, China

Compared with conventional pumped-storage hydroplants, seawater pumped-storage hydroplants are constructed in a complex marine environment. The wave disturbance may affect the safety operation of the pump turbine in the seawater pumped hydroplant via affecting the level of the free water surface. To explore the effect of wave disturbance on the operation of the pump turbine in a seawater pumped-storage hydroplant, assuming that the wave disturbance follows a sine function, on the basis of Airy's micro-amplitude wave theory and the comprehensive characteristic curve of a pump turbine, we use sliding grid technology and the SST $k-\omega$ turbulence model to simulate the dynamics of fluid in a full-flow channel. In this study, the unsteady flow field, Q-criterion vorticity, relative pressure pulsation amplitude, and frequency of pressure pulsation are analyzed to determine the internal flow field and pressure pulsation under different wave disturbance conditions and operating loads. The results show that both the pressure pulsation in the pump turbine and its frequency domain are affected by the wave disturbance. In addition, the turbulent flow with a large flow rate tends to produce higher relative pressure pulsation under wave disturbance. Due to the large flow rate and strong static and dynamic interference in the vaneless area, the relative amplitude of the pressure pulsation is significantly affected by wave disturbance. Furthermore, the low-frequency pressure pulsation of the draft tube is superimposed with the wave disturbance frequency.

KEYWORDS

wave disturbance, frequency domain, pump turbine, static and dynamic interference, pressure pulsation, seawater pumped-storage hydroplant

1 Introduction

A seawater pumped-storage hydroplant can not only form a stable power supply system with the support of wind and solar energy but also solve the water supply problems in ocean islands through seawater desalination. Compared with a conventional pumped-storage hydroplant, the lower reservoir of the seawater pumped-storage power station is constructed in a marine environment, whose operation is significantly affected by typhoons, extreme waves, and ocean currents (Fujihara et al., 1998; Ramos et al., 2014; Shi et al., 2015). The pump turbine is the core component of a pumped-storage hydroplant, and its hydraulic

characteristics directly affect the safety operation of the pumped-storage hydroplant. Therefore, investigating the effect of wave disturbance on the fluid dynamics of the pump turbine is of significant importance for the management of the seawater pumped-storage hydroplant (Fernández et al., 2009; Yao et al., 2011).

Previous studies have demonstrated that the main factors affecting the hydraulic characteristics of a pump turbine include three parts: the dynamic and static interference, the rotating stall, and the vortex rope of the draft tube (Tanaka, 2011). The mechanism governing the dynamic and static interference is the periodic variation in the pressure and velocity of the flow channel due to the rotating turbine. Periodic changes are also present in the flow regime of the stationary guide vane zone. The dynamic and static interference is the periodic disturbances of the flow field between the rotor and the stationary guide vane. It may lead to high-amplitude pressure pulsations in the vaneless space (Xu et al., 2018). The rotating stall occurs mainly in the pump turbine under off-design pump conditions. With the decrease in the flow rate and increase in the impulse angle of the guide vane, serious flow separation occurs between the runner blades and backflow in the runner flow path gradually evolves into rotating stall masses. The stall mass also propagates downstream, causing more deliquescent vortices and secondary flows in the overflow components, such as the guide vanes and worm gear (Liu et al., 2015). The vortex rope of the draft tube often occurs when the operating conditions of the pump turbine deviate from the optimal operating conditions. In addition, the pressure pulsation caused by the vortex rope of the draft tube usually belongs to low-frequency pressure pulsation (Zhong et al., 2018). These unstable flows not only significantly reduce the pump turbine operating efficiency but also cause pump turbine fatigue damage and hydraulic resonance (Zuo and Liu., 2017).

In recent years, many research studies have been conducted on the characteristics of a pump turbine. Li et al. (2021) carried out non-constant numerical simulations of the "S"-zone operating condition of the medium specific-speed pump turbine model and found that the pressure pulsation increases gradually from the turbine operating condition to the braking condition. Under the turbine operating condition, the turbine backflow occurs mainly on the lower-ring side, while the runaway operating status backflow occurs mainly from the middle of the turbine to the lower-ring side. Under the braking condition, a rotational stall occurs, and the flow in the turbine has significant asymmetry. Hu et al. (2022) found that the pressure fluctuation is the highest in the vaneless space. Zhou et al. (2018) carried out a full-flow channel three-dimensional numerical simulation for the load rejection transition process of a pump turbine model. They found that during the load rejection transition, the rapid development of inlet reverse flow in the vane wheel increases the turbulent kinetic energy in the vaneless space, leading to dynamic and static interference between the guide vane and the vane wheel. Furthermore, the inlet reverse flow in the vane wheel led to an imbalance in the flow pattern distribution in the vane, which results in low-frequency rotational-stall pressure fluctuation. Ardizzon et al. (2016) simulated the low-frequency components caused by the rotating stall phenomenon at low flow rates and found that the draft tube flow-state change is significant when the operating load is small. The vortex rope rotation frequency is generally 1/3–1/5 of the rotation frequency (Wang et al., 2017; Yang et al., 2021). Guo et al. (2021) found that the smaller the guide vane opening, the more disordered the vortex generated in the mixed-flow turbine, thus affecting the efficient and stable operation of the turbine. Gao et al. (2021) explored the internal flow characteristics of the same tidal turbine with the guide vane opening of the crossflow unit, which showed that the rotating water flow in the draft tube at low pressure is not necessarily caused by the vortex rope. It may be caused by air masses and hydraulic imbalances at the runner outlet. Zhou et al. (2013) numerically simulated the operating characteristics of a low-head turbine by setting the inlet pressure varying cyclically. The runner speed was found to lag the inlet pressure by 1/4-cycle. By simulating the boundary conditions of the pump turbine load rejection transition process, Fu et al. (2018) found that the interstitial flow between the runner and the stationary components significantly affects the accurate simulation of the pulsating performance characteristics and non-constant vortex of the pump turbine. In addition, the effect of the interstitial flow becomes more severe when it moves closer to the low-flow conditions. Li et al. (2019) carried out numerical simulations of the full-flow channel for seven different guide vane openings of the pump turbine and found that when the guide vane opening is small, the morphology of the draft tube vortex rope is more obvious and reconfigured. When the guide vane opening is large, the circumferential velocity near the wall of the draft tube vortex rope is large, which is the main reason for turbulent kinetic energy loss at the wall of the straight cone section.

However, at present, the relevant research direction mainly focuses on the transition process and partial load operation of the pump turbine. There is a gap on investigating the operating conditions where the inlet and outlet pressures of the pump turbine vary periodically (Dewan et al., 2017; Nam et al., 2018; Zheng et al., 2018; Peng et al., 2020). Seawater pumped-storage hydroplants mainly use high-water-head and large-capacity vertical mixed-flow pump turbines, which are more likely to encounter hydraulic instability problems when the hydroplant is disturbed by high-amplitude periodic waves. The objective of this study is to investigate the flow field and pressure fluctuation in pump turbines so as to reveal how the periodic wave disturbances affect the hydraulic characteristics of the pump turbine under different operating loads. To explore the effect of wave disturbance on the operation of the pump turbine in a seawater pumped-storage hydroplant, assuming that the wave disturbance follows a sine function, on the basis of Airy's micro-amplitude wave theory and the comprehensive characteristic curve of a pump turbine, we use sliding grid technology and the SST k–ω turbulence model to simulate the dynamics of fluid in a full-flow channel.

2 Mathematical details of the numerical scheme

2.1 Governing equations

For three-dimensional numerical simulation of unsteady flow in a pump turbine under wave disturbance, the governing equations involve the mass and momentum conservation equations.

The mass conservation equation is

$$\frac{\partial \rho}{\partial t} + \frac{\partial}{\partial x_i}(\rho u_i) = 0. \tag{1}$$

The momentum conservation equation is

$$\frac{\partial}{\partial t}(\rho u_i) + \frac{\partial}{\partial x_j}(\rho u_i u_j) = -\frac{\partial p}{\partial x_i} + \frac{\partial^2 \tau_{ij}}{\partial x_j} + S_{mi}, \tag{2}$$

where u_i and u_j are velocity vectors, t is the flow time, ρ is the fluid density, p is the static pressure, τ_{ij} is the stress tensor, and S_{mi} is a generalized source term of the momentum equation.

Previous studies have demonstrated the high accuracy and stability of the SST k–ω turbulence model in the numerical simulation of turbomachinery (Menter, 2009). The SST k–ω turbulence model has the advantages of both the k–ε model and k–ω model. It adopts different functions according to the characteristics of fluid at different regions; for instance, it uses the k–ω model for simulating fluid in the regions with a low Reynolds number near the side wall and uses the k–ε model for simulating fluid in the regions with a high Reynolds number in the central part of the flume, which makes it possible to simulate the characteristics of fluid under complex conditions. The SST k–ω turbulence model involves two transport equations, namely, the k-transport equation and the ω-transport equation.

The k-transport equation can be written as

$$\frac{\partial(\rho k)}{\partial t} + \frac{\partial(\rho k u_i)}{\partial x_i} = \frac{\partial}{\partial x_i}\left[(\mu + \sigma_k \mu_t)\frac{\partial k}{\partial x_i}\right] + \tilde{P}_k - \beta' \rho k \omega. \tag{3}$$

The ω-transport equation can be written as

$$\frac{\partial(\rho \omega)}{\partial t} + \frac{\partial(\rho \omega u_i)}{\partial x_i} = \alpha \rho S^2 - \beta \rho \omega^2 + \frac{\partial}{\partial x_i}\left[\frac{(\mu + \sigma_\omega \mu_t)\partial \omega}{\partial x_i}\right] + 2(1 - F_1)\frac{\rho \sigma_{\omega 2}}{\omega}\frac{\partial k}{\partial x_i}\frac{\partial \omega}{\partial x_i}, \tag{4}$$

where P_k is the production term of turbulent kinetic energy, S is the invariant measure of the strain rate, μ is the dynamic viscosity, F_1 is the blending function, μ_t is the turbulent eddy viscosity, and β, β', σ_k, and σ_ω are the constants of the turbulence model.

2.2 Airy's micro-amplitude wave theory

Airy's micro-amplitude wave theory is one of the most basic and widely used linearization theories to solve partial differential equations in wave problems (Janssen, 2008). It assumes that the wave amplitude is significantly smaller than the wavelength and water depth and considers the wave as a linearity wave. According to Airy's micro-amplitude wave theory (Huang, 2011), the pressure p can be expressed by the linearized Bernoulli equation as follows:

$$p = -\rho g z - \rho \frac{\partial \Phi}{\partial t}. \tag{5}$$

Substituting the velocity of the micro-amplitude wave into Eq. 5, the pressure of a micro-amplitude wave can be expressed as

$$p = -\rho g z + \rho g \frac{H}{2}\frac{\cosh k(z+d)}{\cosh kd}\cos(kx - \omega t). \tag{6}$$

Eq. 6 shows that the pressure consists of two parts: the hydrostatic pressure and hydrodynamic pressure. Considering

$$K_Z = \frac{\cosh k(z+d)}{\cosh kd},\ \eta_k = \rho g \frac{H}{2}\cos(kx - \omega t), \tag{7}$$

we can obtain

$$p = \rho g(\eta_k K_Z - Z), \tag{8}$$

where p is the pressure, ρ is the fluid density, η_k is the vertical distance between the instant free water surface and the average water surface, K_Z is the pressure sensitivity coefficient, which decreases with the increase in the distance between the particle position and the still water surface, and Z is the elevation of the free water surface. For small-amplitude sinusoidal waves, the hydrostatic and hydrodynamic pressures follow sinusoidal or cosine function, and the amplitude depends on the water depth (Sullivan et al., 2007).

2.3 Q-criterion vortex identification method

In this study, the Q-criterion (Lu et al., 2021) is used to identify the strength and structure of the vortex, which has high efficiency in vortex identification. The equation of the velocity gradient tensor is as follows:

$$\lambda^3 - P\lambda^2 + Q\lambda - R = 0, \tag{9}$$

where λ is the eigenvalue of the characteristic equation and P, Q, and R are three invariants of the velocity gradient tensor. Q can be expressed as

$$Q = \frac{1}{2}(\Omega^2 - S^2), \tag{10}$$

where Ω is the vorticity tensor and S is the strain rate tensor. When $Q>0$, the vorticity dominates the dynamics of the fluid, and when $Q<0$, it indicates that the strain rate or viscous stress dominates the dynamics of the fluid. The expression of Q can be written as

$$Q = -\frac{1}{2}\left[\left(\frac{\partial u}{\partial x}\right)^2 + \left(\frac{\partial v}{\partial y}\right)^2 + \left(\frac{\partial w}{\partial z}\right)^2\right] - \left(\frac{\partial u}{\partial y}\right)\left(\frac{\partial v}{\partial x}\right) - \left(\frac{\partial u}{\partial z}\right)\left(\frac{\partial w}{\partial x}\right) - \left(\frac{\partial v}{\partial z}\right)\left(\frac{\partial w}{\partial y}\right). \tag{11}$$

3 Model development

3.1 Initial settings and grid division

Figure 1 shows the three-dimensional model of the pump turbine, which mainly includes five regions: spiral case, stay vanes, guide vanes, runner, and draft tube. The initial settings of the pump turbine are as follows: rated head H = 40 m, rated speed n = 760 r/min, rated flow Q_r = 0.28 m^3/s, runner inlet diameter D_1 = 0.55 m, runner outlet diameter D_2 = 0.25 m, number of runner blades Z = 7, number of stay vanes Z_s = 20, and number of guide vanes Z_0 = 20.

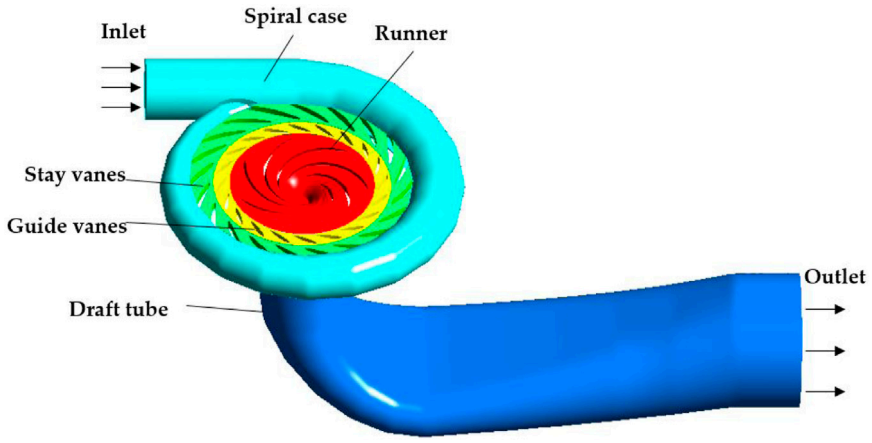

FIGURE 1
Three-dimensional model of the full-flow channel of the pump turbine.

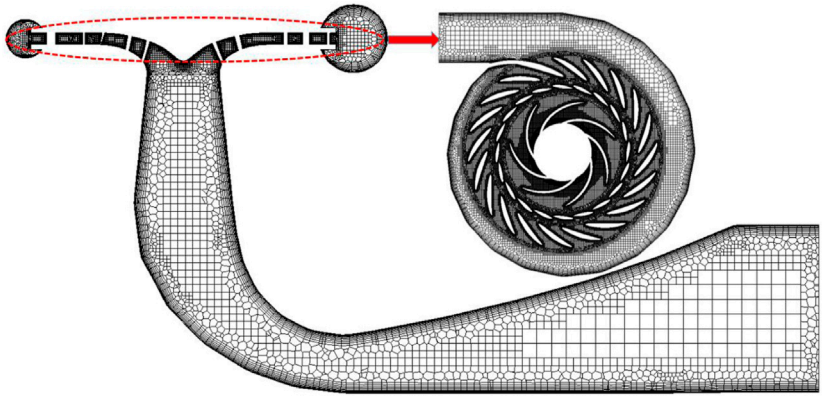

FIGURE 2
Grid division of the full-flow channel of the pump turbine.

Figure 2 shows the sketch of the grid division of the pump turbine. The grid division was conducted using Fluent Meshing software. To ensure the computing accuracy, unstructured grids are used to divide the model, and boundary-layer infilling is carried out on the walls of the runner blades, spiral case, and guide vanes. Considering the complexity of the flow pattern evolution in the runner, to accurately simulate the flow separation of the runner, the boundary-layer grid in the runner area is set with 18 layers with a minimum thickness of 0.02 mm, and the average y^+ value of the whole runner wall is less than 5. To avoid the number of grids affecting the simulation results, the independence of the number of total grids to the Q_r hydraulic turbine is verified (See Figure 3). When the number of grids is larger than 6 million, the calculation results tend to be stable. In addition, reducing the number of grids could decrease the calculation time. Here, the total number of grids is set to 7 million, and the minimum orthogonal quality of the grids is 0.3. Sliding grid technology is used to cope with the dynamic static interface of the runner, and data exchange is carried out between the calculation domains and the interface. The equations for calculating the head and efficiency of the turbine are shown in Eq. 12 and Eq. 13, respectively.

$$H = \frac{(P_{in} - P_{out})}{\rho g}, \tag{12}$$

$$\eta = \frac{M\omega}{9.81QH} \times 100\%, \tag{13}$$

where P_{in} is the inlet pressure, P_{out} is the outlet pressure, M is the runner torque, ω is the angular velocity, and Q is the water flow.

The operating point is determined based on the characteristic curve and similarity criterion of the pump turbine. As shown in Figure 4, this study provides insights into the working condition of the first quadrant of the pump turbine. Under the condition of rated head H = 40 m, the flow rate is adjusted by changing the guide vane opening so as to obtain different loads and outputs. As wind energy and solar energy are unstable and intermittent, it is

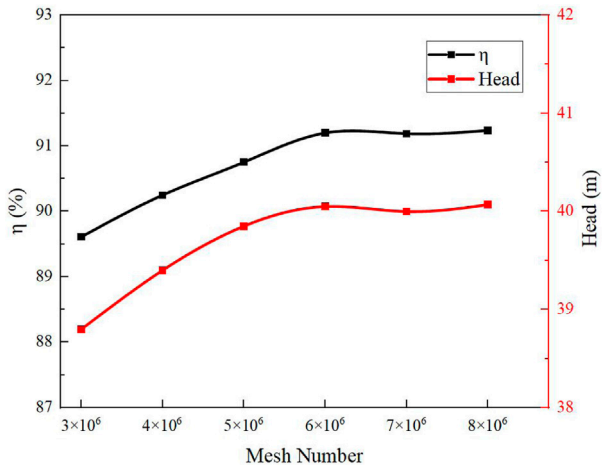

FIGURE 3
Variation in the mesh number to the head and the efficiency of the turbine.

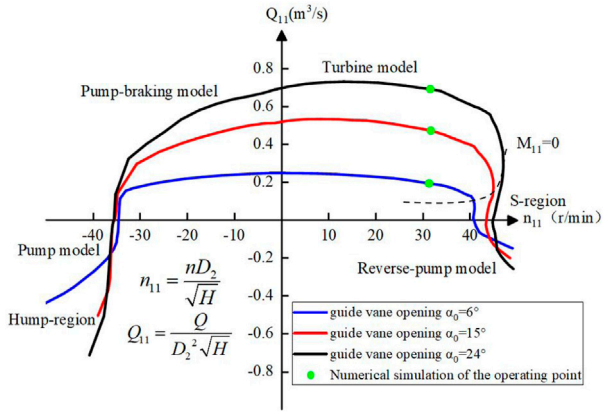

FIGURE 4
Characteristic curve of the pump turbine and the operating point of the numerical simulation.

necessary to operate the pumped-storage units under unbalanced load conditions to balance the power grid parameters. In order to compare the influence of wave disturbance on the operating status of the pump under different operating loads, this study selects three levels of guide vane openings, namely, small opening $\alpha_0 = 6^\circ$, medium opening $\alpha_0 = 15^\circ$, and rated opening $\alpha_0 = 24^\circ$. The corresponding flows are 0.3 Q_r, 0.7 Q_r, and rated flow Q_r, respectively.

For the wave disturbance, we select the characteristics of waves near an island in the East China Sea during the last 10 years as an example. To simplify the complexity of natural waves and quantify the effect of each influencing factor of natural waves, we assume the wave as a regular wave based on the characteristics of natural waves rather than using monitoring data of natural waves directly. According to the micro-amplitude wave theory, hydrostatic pressure and hydrodynamic pressure can be considered following sine or cosine functions. That is, the waveform basically follows a sine function, the maximum effective wave height is 10 m, and the wave period is 6 s (Yu et al., 2020). According to the relevant literature (Nanjing Hydraulic Research Institute, 2002), the pressure scale and frequency scale can be expressed as follows:

$$\lambda_p = \lambda_k = \frac{l_p}{l_m}, \tag{14}$$

$$\lambda_f = \lambda_k^{-\frac{1}{2}}, \tag{15}$$

where λ_k is the wavelength scale, l_p is the wavelength of the wave in the real world, l_m is the wavelength of the model, λ_p is the pressure scale, and λ_f is the frequency scale. In this study, the wavelength scale λ_k is set to 10.

After a scale conversion between the modeled wave and real wave, the tail water level disturbance caused by wave disturbance in the pump turbine model is $\Delta H = 1 \times \sin \frac{2\pi t}{T}$, and the pressure fluctuation at the outlet of the draft tube can be calculated using the formula $\Delta P = 10000 \sin \frac{\sqrt{10}\pi t}{3}$. When the wave period is 1.9 s, the wave frequency is 0.527 Hz. This pressure fluctuation is the boundary condition for the operation under the wave disturbance. The initial settings of the selected working conditions are shown in Table 1.

3.2 Boundary conditions and layout of monitoring points

In this study, Fluent 2020 R2 was used in numerical simulation. The boundary conditions of the proposed model are as follows: the spiral case inlet is set as the mass flow inlet, and the draft tube outlet is set as the pressure outlet. Based on the coupling of pressure and velocity, the SIMPLEC algorithm is used for steady calculation, and the PISO algorithm is used for unsteady calculation. The second-order upwind format is used to discretize the momentum and turbulent kinetic energy dissipation rate. All over-current components are connected through an interface. The solid wall is set as a non-slip wall condition, and the residual convergence accuracy is set to 10^{-5}.

We first assume that the fluid has a steady flow and the result of steady-flow calculation is the initial conditions of the model. The rotating speed of the runner is 760 r/min, and the fixed time step is set to 6.579×10^{-4} s (rotate 3° for each time step). The maximum number of iteration steps is set to 500, and the iterative convergence is stable in 50 steps. For the situation without wave disturbance, 15 rotor rotation periods are calculated. A total of 10 rotor rotation periods are calculated for analyzing the dynamics of fluid after being stable. Under the situation with the wave disturbance, two wave disturbance periods are calculated, and the results of the second wave disturbance period are analyzed.

In order to explore how the pressure pulsation varies with the flow field in the pump turbine, monitoring points are arranged every 45° in the circumferential direction of the axial cross section of the spiral case, every 30° in the vaneless space between the guide vane and the runner, and every 0.1 m in the center of the axial plane of the draft tube. The sketch of the positions of the monitoring points is shown in Figure 5.

TABLE 1 Initial settings of the selected working conditions.

Working condition	Guide vane opening α_0 (degree)	Unit speed n_{11} (r/min)	Unit flow Q_{11} (m^3/s)	Outlet pressure P_{out} (Pa)
Case 1	6	760	0.084	0
Case 2	15	760	0.193	0
Case 3	24	760	0.280	0
Case 4 (wave disturbance)	6	760	0.084	$10000 \sin \frac{\sqrt{10}\pi t}{3}$
Case 5 (wave disturbance)	15	760	0.193	$10000 \sin \frac{\sqrt{10}\pi t}{3}$
Case 6 (wave disturbance)	24	760	0.280	$10000 \sin \frac{\sqrt{10}\pi t}{3}$

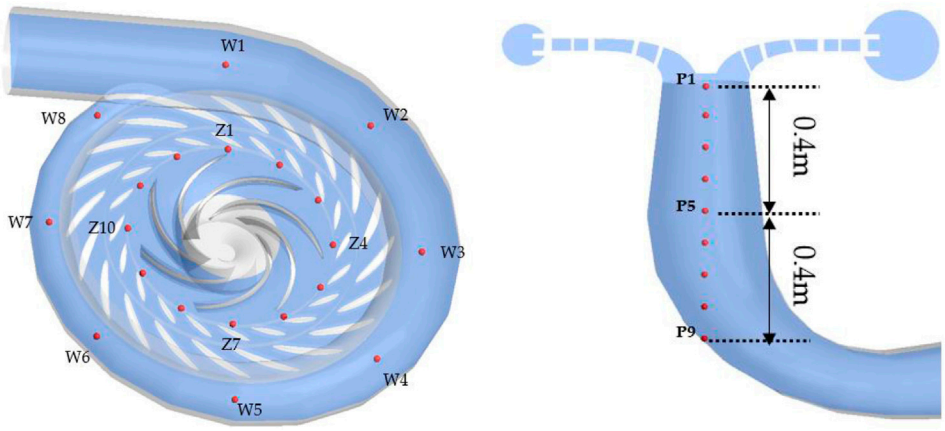

FIGURE 5
Sketch of the positions of the monitoring points in the pump turbine.

4 Results and discussion

4.1 Variation in internal flow characteristics of the pump turbine

Figure 6 shows the streamline in the guide vanes, runner, and draft tube under different operating conditions without wave disturbance. The velocity triangle corresponds to the position of the red dot in the streamline diagram, where U is the circumferential velocity, W is the relative velocity, and V is the absolute velocity. Figure 7 shows the vortex distribution in the draft tube under different operating conditions without wave disturbance.

As shown in Figure 6A and Figure 7A, under the operating condition of 0.3 Q_r, due to the small inlet flow and velocity, the inlet attack angle of the runner is large, and the water flow forms a high-speed water-retaining ring under the influence of the static and dynamic interference when it flows through the vaneless space. The generation of the high-speed water-retaining ring makes the fluid that should have flowed into the original runner rotate at high-speed flow into other runners. At this time, the circumferential velocity of the water flow on the inner wall of the draft tube is important, a rotating downward-flow state is formed on the wall of the draft tube, and a large amount of backflow is generated along the axial direction of the draft tube center. This flow state creates a high-intensity spiral vortex that almost fills the straight cone section of the draft tube. A high level of vortex in the draft tube may lead to hydraulic resonance. Therefore, the low-load operating condition should be avoided during the operation of the turbine.

As shown in Figure 6B and Figure 7B, under the operating condition of 0.7 Q_r, with the increase in the guide vane opening, the high-speed water ring in the vaneless space obviously weakens, and the maximum velocity decreases obviously, which is obviously improved compared with the low-flow operating condition. However, as the water flow at the inlet of the runner cannot maintain the best angle with the runner blades, the vortex and backflow remain on the water-facing surface of the runner blades. Although the water flow in the draft tube is inclined to the axial direction, it still maintains a large circumferential velocity component, and the flow field at the bottom of the straight cone section of the draft tube is chaotic. A significant vortex is observed, while the strength of the vortex is reduced.

As shown in Figure 6C and Figure 7C, under the operating load of Q_r, the water flow rate is increased, and the velocity of the fluid between the guide vane and the runner is uniform. There is no high-speed water ring in the vaneless space. In addition, the water enters the runner evenly and stably. The streamline in the draft tube is modeled with mainly axial flow, with a small circumferential velocity component. A small draft tube vortex area and low vortex strength are observed, which means that the unit runs smoothly under this operating condition.

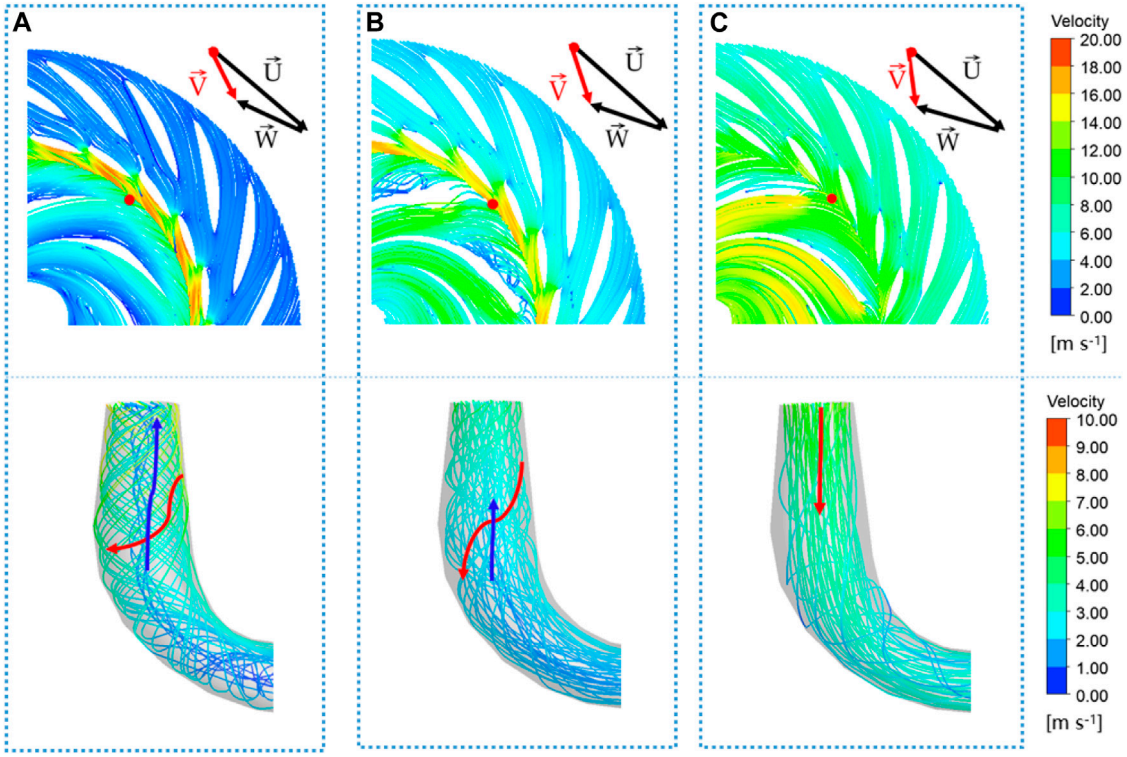

FIGURE 6
Streamline in the guide vanes, runner, and draft tube under different operating conditions without wave disturbance: **(A)** Case 1, 0.3 Q_r; **(B)** Case 2, 0.7 Q_r; and **(C)** Case 3, Q_r.

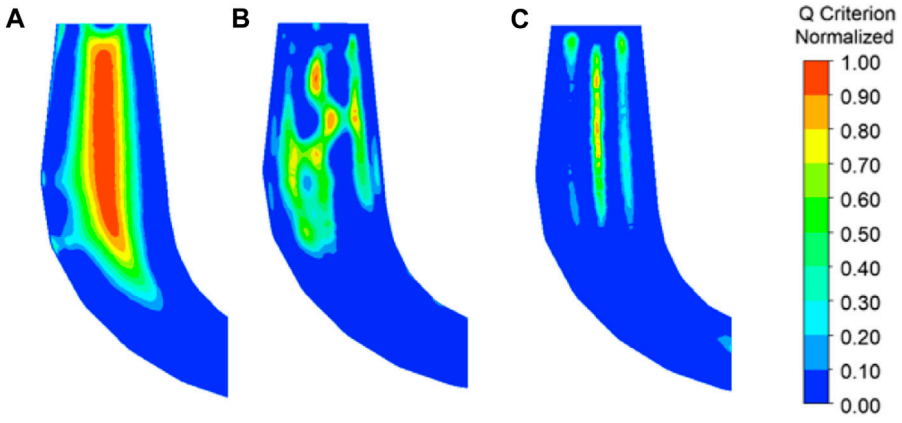

FIGURE 7
Vorticity of the draft tube under different operating conditions without wave disturbance: **(A)** Case 1, 0.3 Q_r; **(B)** Case 2, 0.7 Q_r; and **(C)** Case 3, Q_r.

Figure 8 shows pressure distribution in the pump turbine without wave disturbance under different operating conditions. The pressure in each working condition gradually decreases from the spiral case to the runner in the centripetal direction. In addition, the pressure gradient changes in the vaneless space. With the increase in the opening of the guide vane, the variation in pressure in the vaneless space gradually becomes stable. As the blades of the runner convert the kinetic energy of the water flow into the rotating mechanical energy of the runner, the pressure gradient in the runner is obvious, and the pressure on the water surface of the blade is generally higher than that on the back surface. The pressure on the waterfront surface of the blade is generally higher than that on the back surface, and the blade pressure gradually decreases

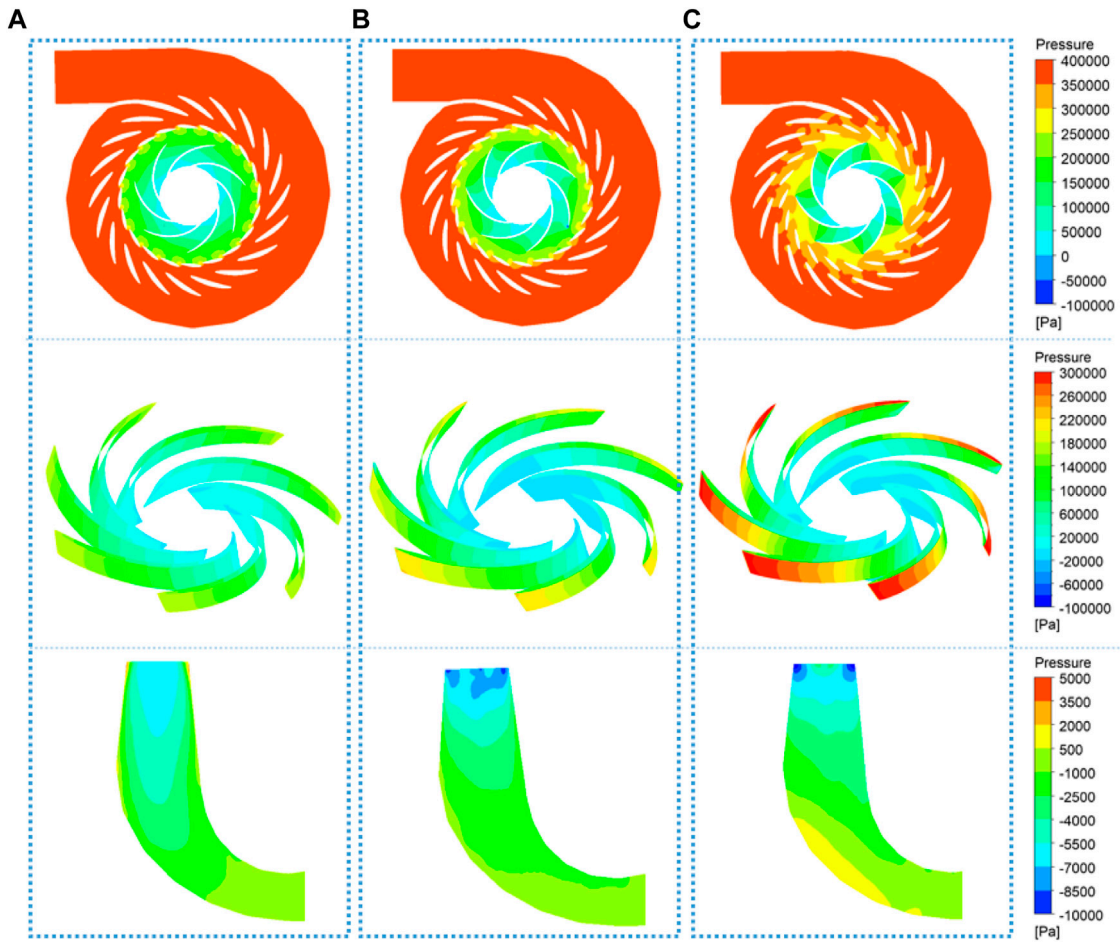

FIGURE 8
Pressure distribution of the pump turbine under different operating conditions without wave disturbance: **(A)** Case 1, 0.3 Q_r; **(B)** Case 2, 0.7 Q_r; and **(C)** Case 3, Q_r.

from the inlet to the outlet, forming a negative pressure area at the blade outlet. The influence of the guide vane opening on the surface pressure of the blade is obviously less than that under the operating condition of a large opening. Under the operating condition of 0.3 Q_r, as the flow rate is low and the circumferential speed is high, the water flow clings to the draft tube wall in a rotating downward-flow state. The maximum pressure area can be observed on both sides of the draft tube inlet wall, and the straight tapered section of the draft tube presents an obvious conical pressure gradient. With the increase in the guide vane opening, the flow rate increases, the conical pressure gradient of the draft tube gradually stabilizes, and both sides of the draft tube inlet wall become the minimum pressure area.

Figure 9, Figure 10, and Figure 11 show the influence of wave disturbance on the internal flow pattern of the pump turbine under the operating condition of Q_r, allowing us to analyze the streamline, pressure, and vortex of the draft tube in channels with wave disturbance. The effect of wave disturbance on the water head is relatively small. Furthermore, the wave disturbance has no obvious influence on the flow direction, velocity, and vortex distribution of the draft tube. However, the pressure at different times is obviously different. The maximum pressure occurs at T/4 and the minimum pressure occurs at 3 T/4, which confirms the sinusoidal functions of wave disturbance. Therefore, the wave disturbance only affects the pressure in the pump turbine. Its influence on the streamline, draft tube vortex rope, and pressure distribution can be neglected.

4.2 Quantitative analysis of the pressure pulsation

To analyze the main characteristics of the pressure pulsation, two dimensionless numbers, the relative pressure pulsation amplitude $\Delta H'$ and the pressure pulsation coefficient C_p, are introduced to characterize the pressure pulsation (Xu et al., 2022).

$$\Delta H' = \frac{\Delta H}{H} = \frac{P_{i\max} - P_{i\min}}{\rho g H} \times 100\%, \tag{16}$$

$$C_p = \frac{P_i - \bar{P}}{\rho g H} \times 100\%, \tag{17}$$

where ΔH is the peak value of pressure pulsation, H is the water head, P_{imax} and P_{imin} are the maximum and minimum pressures at point i, respectively, C_p is the dimensionless pressure pulsation

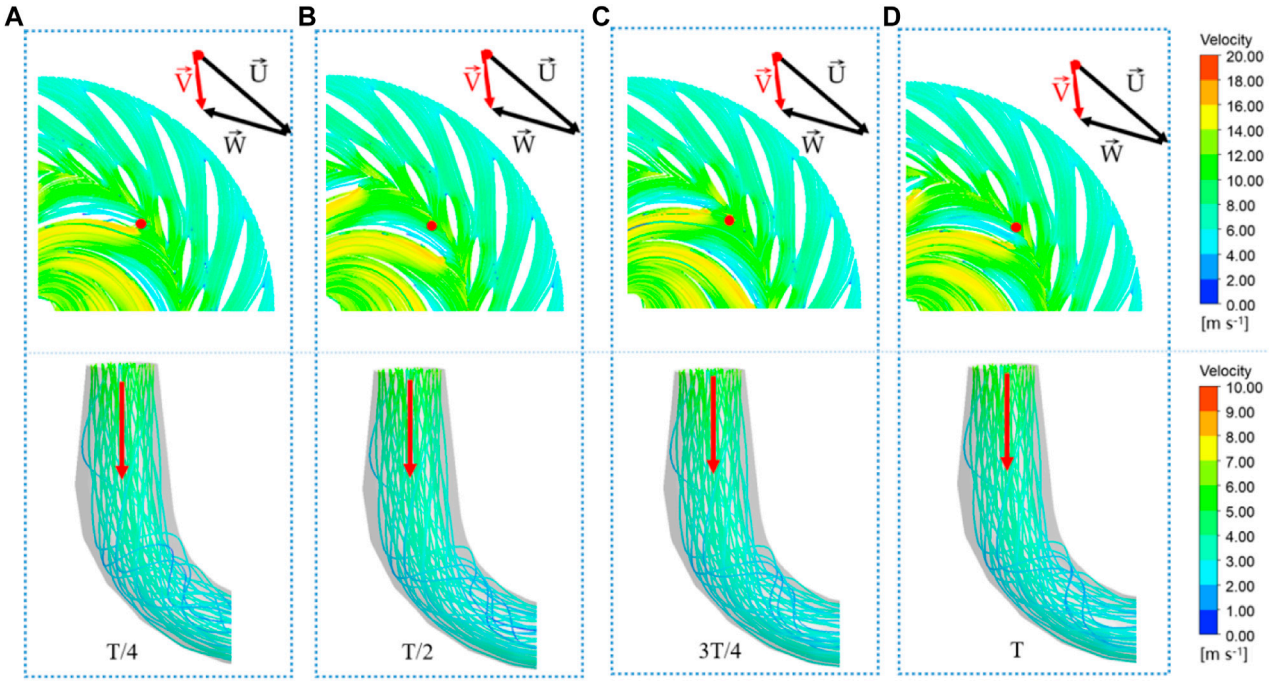

FIGURE 9
Streamline of guide vanes, runner, and draft tube under the operating condition of Q_r with wave disturbance: **(A)** T/4, **(B)** T/2, **(C)** 3T/4, and **(D)** T.

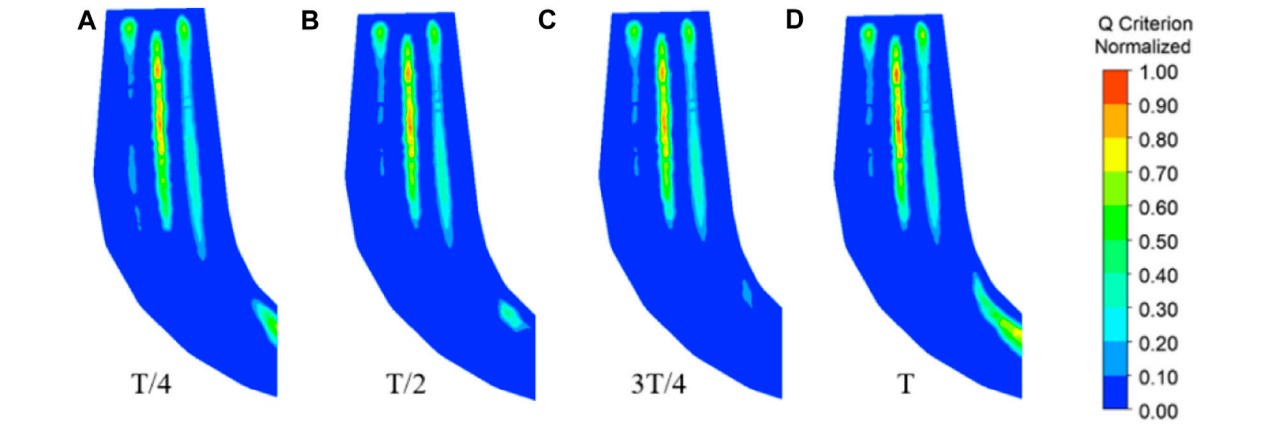

FIGURE 10
Vorticity of the draft tube under the operating condition of Q_r with wave disturbance: **(A)** T/4, **(B)** T/2, **(C)** 3T/4, and **(D)** T.

coefficient, P_i is the corresponding pressure at point i, and $\bar{P}$ is the average pressure over time.

Figure 12 shows the relative pressure pulsation at the monitoring points in the spiral case. For the condition without wave disturbance, the relative pressure pulsation amplitude increases with the increase in load, and the maximum value of Q_r is 1.40% under the rated working condition. For the condition with wave disturbance, the relative pressure pulsation amplitude of each working condition generally increases. However, the 0.7-Q_r working condition is affected by wave disturbance, and its relative pressure pulsation amplitude is almost the same as the rated working condition, which means that the relative pressure pulsation amplitude is related not only to the flow rate but also to the turbulent flow pattern.

Figure 13 shows the relative pressure pulsation amplitude at the monitoring points in the vaneless space. With the strong dynamic and static interference caused by the rotation of the runner blades, the relative pressure pulsation amplitude of the measuring points in the vaneless space is higher than that in other areas. For the condition

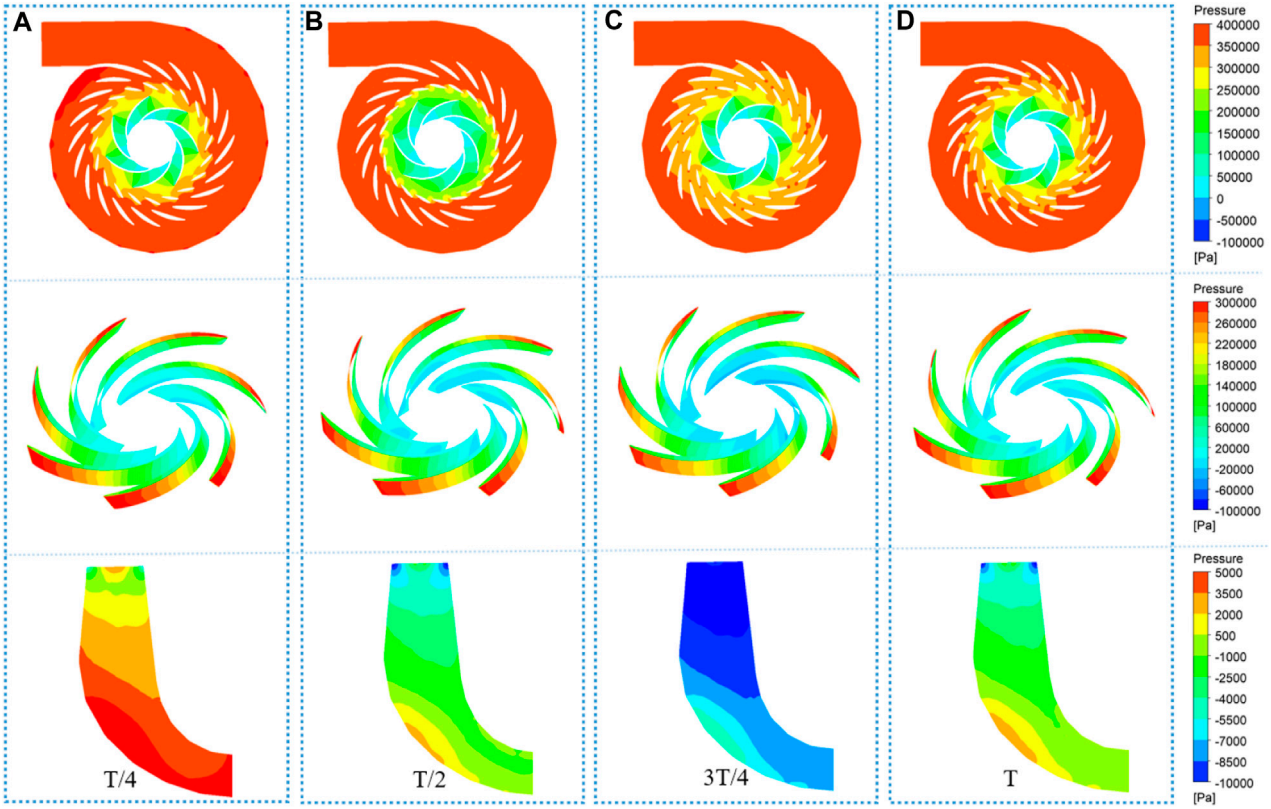

FIGURE 11
Pressure distribution of the pump turbine under the operating condition of Q_r with wave disturbance: **(A)** T/4, **(B)** T/2, **(C)** 3T/4, and **(D)** T.

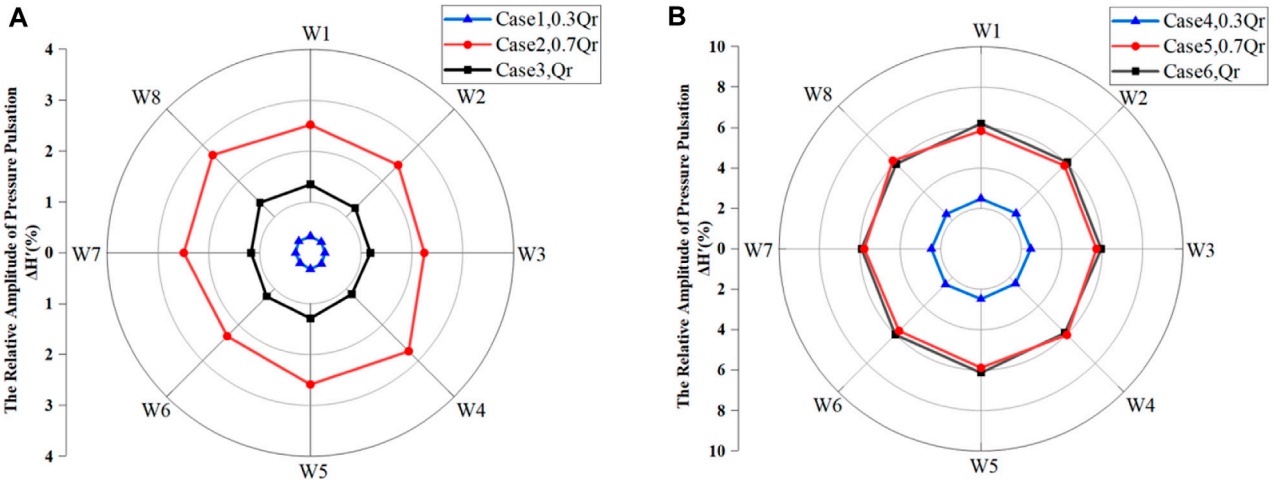

FIGURE 12
Relative pressure pulsation amplitude at the monitoring points in the spiral case: **(A)** without wave disturbance; **(B)** with wave disturbance.

without wave disturbance, the relative pressure pulsation amplitude increases with the increase in the load, and the maximum value is 16.55% under the rated working condition Q_r. For the condition with the wave disturbance, the relative pressure pulsation amplitude of each working condition generally increases, and the maximum value is 21.93% under the 0.7-Q_r working condition. However, due to the

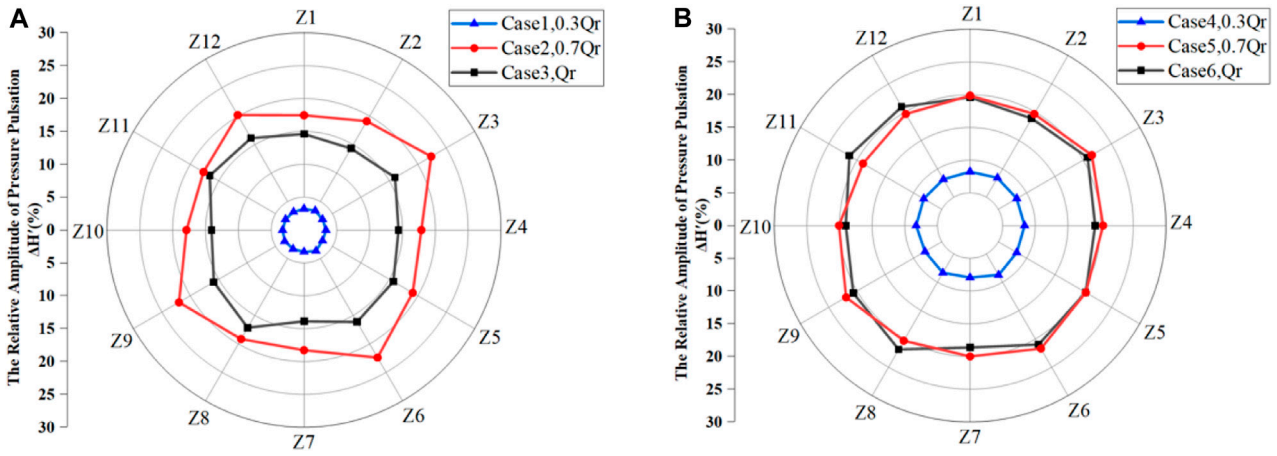

FIGURE 13
Relative pressure pulsation amplitude of the monitoring points in the vaneless space: **(A)** without wave disturbance; **(B)** with wave disturbance.

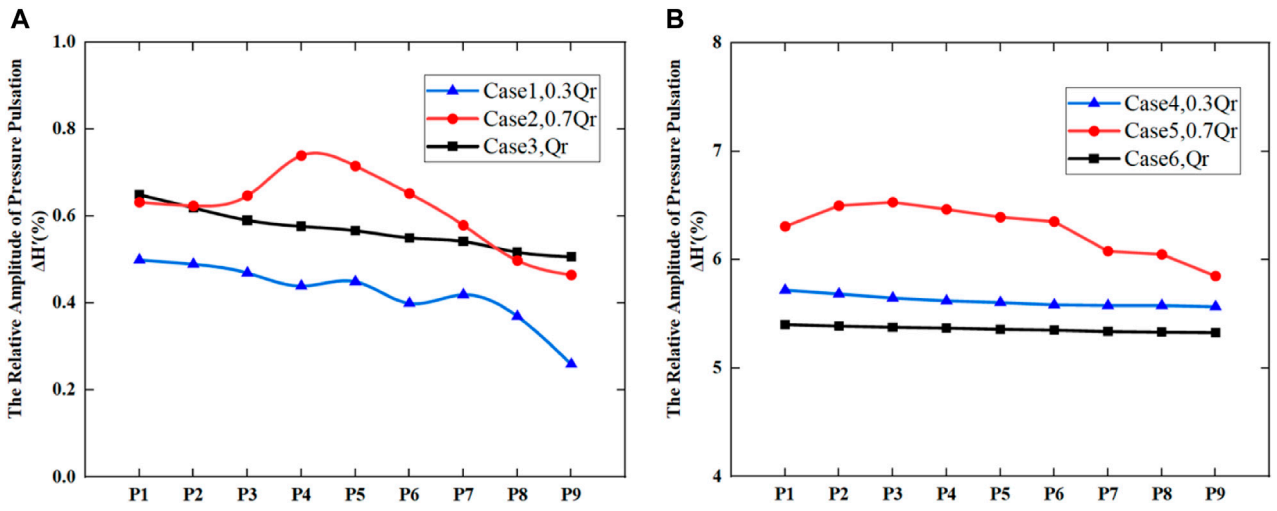

FIGURE 14
Relative pressure pulsation amplitude at the monitoring points in the draft tube: **(A)** without wave disturbance; **(B)** with wave disturbance.

large relative pressure pulsation amplitude of the vaneless space under the large-flow working condition, the amplitude variation caused by wave disturbance is not significant under the rated working condition Q_r. Under the 0.7-Q_r working condition, part of the fluid flows with a high-speed water-retaining ring in the vaneless space, and the flow field is turbulent, which means that the pressure pulsation is obviously affected by wave disturbance.

Figures 14A, B show the relative pressure pulsation amplitude at the monitoring points in the draft tube for the conditions without and with wave disturbance, respectively. Compared with other areas, the relative pressure pulsation amplitude in this area is the smallest. For the situation without wave disturbance, the relative pressure pulsation amplitude in this area is related not only to the load but also to the strength of the eccentric vortex in the draft tube. The relative pressure pulsation amplitude has a positive correlation with the strength of the eccentric vortex in the draft tube, so the maximum relative amplitude of pressure pulsation is observed at the P4 measuring point with a value of 0.75% under the working condition of 0.7 Q_r. For the situation with wave disturbance, the relative amplitude of the pressure pulsation increases with the increase in load under different operating conditions, which shows that the eccentric vortex intensity of the draft tube is the main factor affecting the relative amplitude of the pressure pulsation for the case without wave disturbance.

4.3 The frequency domain of pressure pulsation

As the frequency domain of the pressure pulsation at the monitoring points in the same area is highly similar, the

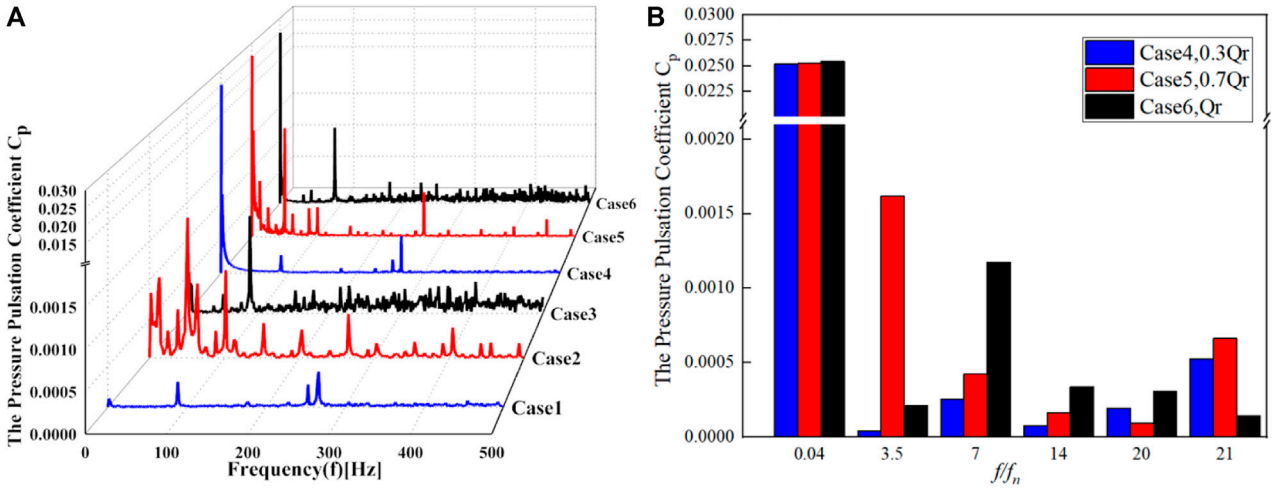

FIGURE 15
Variation in the pressure pulsation coefficient to **(A)** the frequency and **(B)** main frequency types under different operating conditions at the W1 monitoring point in the spiral case.

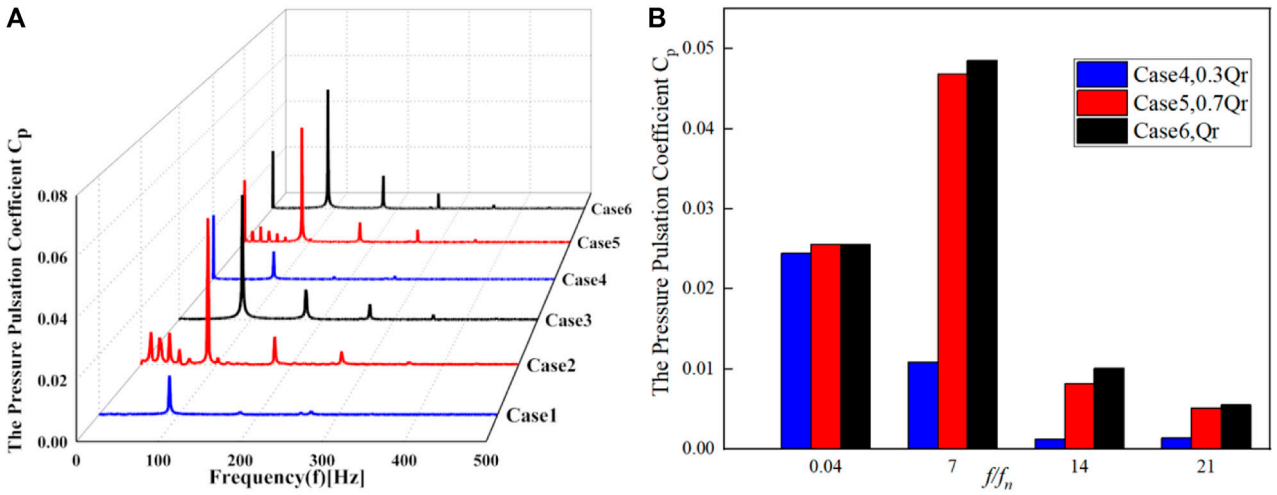

FIGURE 16
Variation in the pressure pulsation coefficient to **(A)** the frequency and **(B)** main frequency types under different operating conditions at the Z1 monitoring point in the spiral case.

representative monitoring points are selected for analyzing the frequency domain of the pressure pulsation, based on the internal flow characteristics of the pump turbine and the relative amplitude of the pressure pulsation. The W1 monitoring point is selected in the spiral case, and the Z1 monitoring point is selected in the vaneless space. Due to the influence of the vortex rope on the draft tube, the draft tube flow pattern changes are more complicated, and the relative amplitude of the pressure pulsation is more obviously affected by the wave disturbance. Three representative monitoring points, P1 at the draft tube inlet, P5 at the center of the straight cone section, and P9 at the bottom of the elbow section, are selected to analyze the pressure fluctuation in the frequency domain.

Figure 15 shows the relationship between the pressure pulsation factor and the frequency domain at monitoring point W1 in the spiral case area. f_n is the frequency conversion factor of the runner (approximately 12.7 Hz), and 0.04 f_n is the wave disturbance frequency (approximately 0.527 Hz). For the situation without wave disturbance, the pressure pulsation increases with the increase in load. This is because the frequency components are complicated and numerous, and there are more low-frequency and high-amplitude pressure pulsations under the operating condition

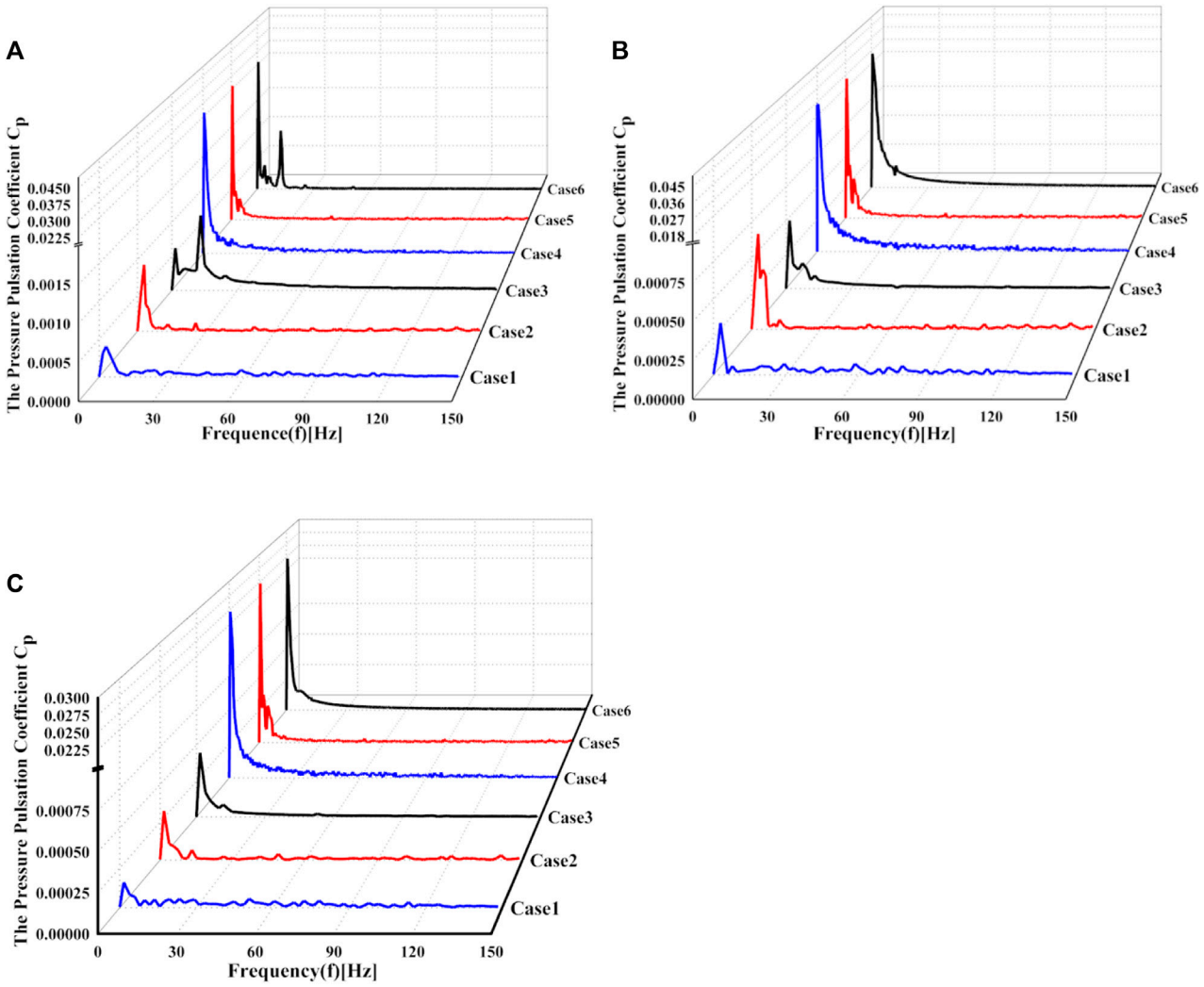

FIGURE 17
Variation in the pressure pulsation coefficient to frequency at **(A)** P1, **(B)** P5, and **(C)** P9 monitoring points.

of 0.7 Q_r (Case 2). For the situation with wave disturbance, the pressure pulsation has an additional wave disturbance frequency. However, the other main frequency characteristics did not change obviously. Thus, we only analyze the main frequency components under the wave disturbance (see Figure 15B). Here, the frequency of the wave disturbance is 0.04 f_n, which is caused by the wave pressure propagating from the downstream to the spiral case. Furthermore, the blade frequencies 7 f_n, 14 f_n, and 21 f_n and their multiples are mainly caused by static and dynamic interference. However, under different loads, the alternating hydraulic components acting on the runner blades are different, resulting in different amplitudes of pressure pulsation. In general, with the increase in the load, the frequency of the pressure pulsation increases. Moreover, 20 f_n is the number of guide vanes multiplied by the rotation frequency. This frequency type is mainly affected by the thickness of the guide vanes and the runner blades crowding out the water flow. Thus, the water flow pressure fluctuates periodically, which is particularly obvious under the light-load condition (Cases 1 and 4). Due to the high flow rate and the influence of the high-speed water-retaining ring on the vaneless space under the working condition of Cases 2 and 5, there are more vortices and secondary flows in the spiral case area, resulting in more high-amplitude pressure pulsations similar to 3.5 f_n.

Figure 16A shows the frequency domain results of pressure pulsation at monitoring point Z1 in the vaneless space, and Figure 16B shows the main frequency components of pressure pulsation under wave disturbance at this monitoring point. The pressure pulsation amplitude in the vaneless space is high, mostly due to the blade frequency and its frequency multiples, indicating that the pressure pulsation in the vaneless space is mainly caused by static and dynamic interference, and the higher the load, the higher the pressure pulsation amplitude caused by the static and dynamic interference. At 0.7 Q_r (Cases 2 and 5), there are many low-frequency and high-amplitude pressure pulsations; however, the other conditions do not appear, indicating that the occurrence of low-frequency and high-amplitude pressure pulsations in the vaneless space is related to the chaotic flow pattern. Due to the large pressure pulsation caused by the static and dynamic

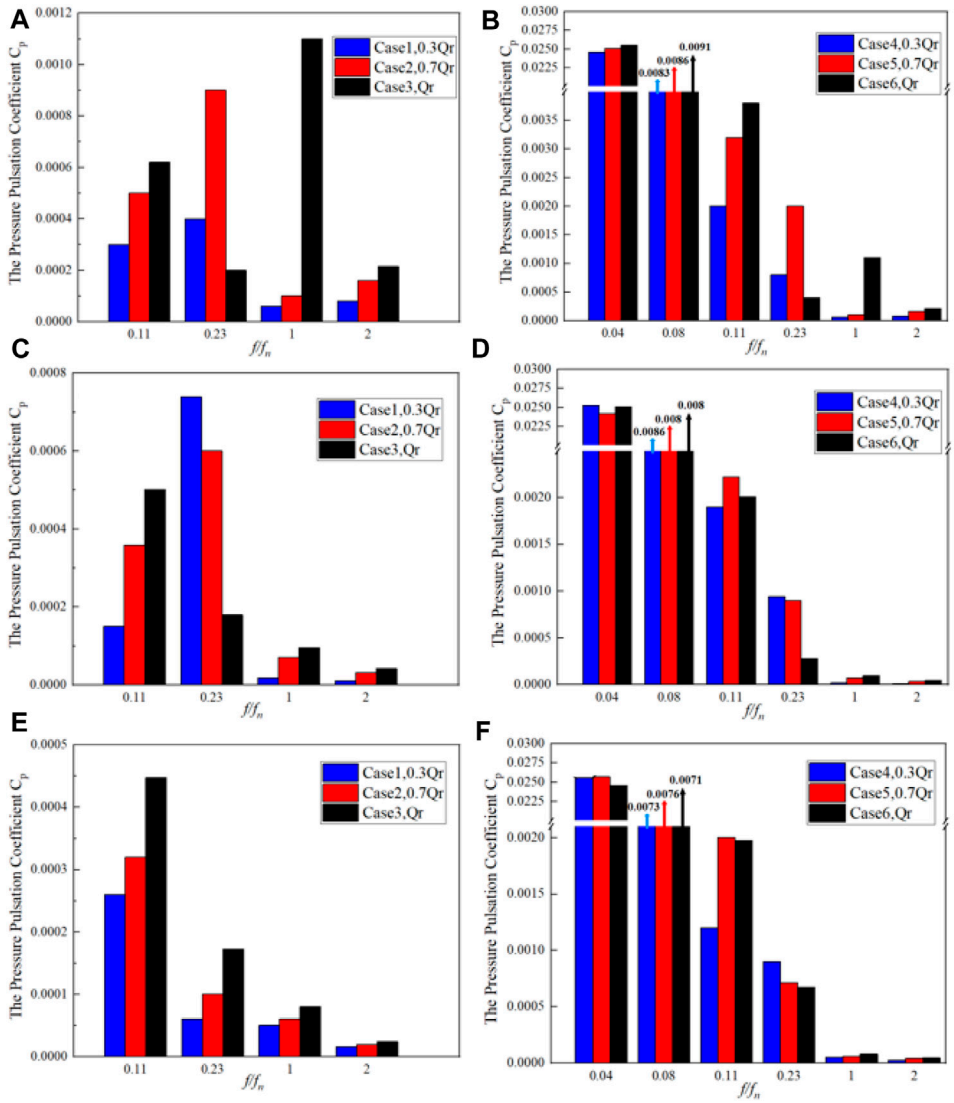

FIGURE 18
Variation in the pressure pulsation coefficient to the main frequency types at P1, P5, and P9 monitoring points under different operating conditions: **(A)** P1, without wave disturbance; **(B)** P1, with wave disturbance; **(C)** P5, without wave disturbance; **(D)** P5, with wave disturbance; **(E)** P9, without wave disturbance; and **(F)** P9, with wave disturbance.

interference in the vaneless space, the main frequencies of the other two working conditions have not changed under the wave disturbance, except for the low load 0.3 Q_r (Cases 1 and 4), which is still 7 f_n.

Figure 17 shows the variation in the pressure pulsation coefficient to the frequency at the monitoring points P1, P5, and P9 in the draft tube. Due to the low-frequency and high-amplitude characteristics of the pressure pulsation in the draft tube, the pressure pulsation under wave disturbance is superimposed with the original pressure pulsation in the draft tube, resulting in more low-frequency and high-amplitude pressure pulsation. Therefore, the main frequency components for the two cases with and without wave disturbance are analyzed, respectively.

Figures 18A, C, E show the main frequency components of pressure pulsation in the draft tube without wave disturbance. There is a large amplitude of pressure pulsation of 0.11 f_n for all operating conditions. As a similar unsteady pressure phenomenon, many scholars have confirmed that the main frequency of the draft tube pressure pulsation of the pump turbine is approximately 0.11 f_n. Under the working conditions of 0.3 Q_r (Case 1) and 0.7 Q_r (Case 2), the upstream monitoring points P1 and P5 have a maximum amplitude of pressure pulsation at 0.23 f_n. However, under the working conditions of Q_r (Case 3), the pressure amplitude corresponds to 0.23 f_n, and the rotation frequency of the vortex rope is generally 1/3–1/5 of the rotation frequency, so 0.23 f_n is the main frequency of the draft tube vortex rope. The runner rotating frequency is 1 f_n, which is caused by the hydraulic imbalance in the runner components. This pressure pulsation has an impact on the whole draft tube. The closer to the runner, the higher the amplitude of pressure pulsation of 1 f_n, and the frequency of the maximum pressure amplitude at P1 point at the draft tube inlet is 1 f_n. For the frequency of 2 f_n, this type of frequency is formed by the

vortex and secondary flow passing through the runner, and its corresponding amplitude of pressure pulsation is small.

Figures 18B, D, F show the main frequency components of pressure pulsation for the condition with wave disturbance. Under the working conditions of 0.3 Q_r (Case 4) and 0.7 Q_r (Case 5), the main frequency of the draft tube vortex rope is 0.23 f_n, and the pressure pulsation amplitude is still high. As the monitoring point P1 is close to the runner, it is influenced by the dynamic and static interference of the runner. Hence, it has a high-pressure amplitude at the rotating frequency of 1 f_n. Compared with the condition without wave disturbance, the main frequency of the pressure pulsation at each monitoring point is close to 0.527 Hz, which is the frequency of the wave disturbance. In addition, there are several high-amplitude pressure pulsations with a frequency doubling of 0.527 Hz, such as 0.08 f_n. In this case, the frequency is superimposed with the original low-frequency pressure pulsation of the draft tube. Therefore, the frequency spectrum of the pressure pulsation becomes complicated. The amplitude of the high-frequency pressure pulsation above 1 f_n shows no obvious variation, but the pressure amplitudes of 0.11 f_n and 0.23 f_n generally increase by 2–15 times. The wave disturbance has an impact on the low-frequency pressure pulsation of the draft tube.

5 Conclusion

Taking the characteristics of waves in an island in the East China Sea as an example, we carried out a numerical simulation of a pump turbine with and without wave disturbance based on the micro-amplitude wave theory and the characteristic curve of the pump turbine. The hydraulic stability of the pump turbine under three different operating conditions was compared and analyzed. The main conclusions are as follows.

(1) For the internal dynamics of the pump turbine, the high-speed water-retaining ring in the vaneless space and the strength of the draft tube vortex rope are mainly related to the inlet flow. With the inlet flow approaching the rated flow, the high-speed water-retaining ring in the vaneless space gradually disappears, and the strength of the draft tube vortex gradually decreases. With the wave disturbance, the variation in the pressure depends on the wave disturbance.

(2) For the relative pressure pulsation, the maximum value of rated working condition Q_r in the vaneless space is 16.55% for the case without wave disturbance, and the maximum value of 0.7 Q_r in the vaneless space is 21.93% for the case with wave disturbance. The turbulent flow with a large flow rate tends to produce a higher relative pressure pulsation for the case with wave disturbance than for the case without wave disturbance. Under the working condition of 0.7 Q_r, due to the large flow and the strong static and dynamic interference in the vaneless space, the relative pressure pulsation is mostly affected by wave disturbance. For the case with wave disturbance, the strength of the eccentric vortex of the draft tube is the main factor affecting the relative pressure pulsation.

(3) For the frequency variation in the pressure pulsation, the main frequencies of the spiral case and vaneless space are the runner rotating frequency of 1 f_n, the blade frequency and its frequency multiples of 7 f_n, 14 f_n, and 21 f_n, and the secondary flow frequency of 3.5 f_n. The draft tube exhibits typical characteristics of low frequency and high amplitude, with the main frequencies of the draft tube being 0.11 f_n, the draft tube vortex rope being 0.23 f_n, and the runner rotating frequency being 1 f_n. Under the wave disturbance conditions, due to the superposition of the low-frequency pressure pulsation in the draft tube and the frequency doubling of the wave disturbance, the frequency spectrum of the pressure pulsation becomes complicated, and the amplitude of the low-frequency pressure generally increases by 2–15 times.

Data availability statement

The original contributions presented in the study are included in the article/Supplementary Material; further inquiries can be directed to the corresponding author.

Author contributions

Conceptualization: JH, QW, and JM; methodology: JH, QW, and JM; writing—original draft: JH and QW; writing—review and editing: JH, HS, and JM; supervision: HS; project administration: HS; funding acquisition: JH. All authors contributed to the article and approved the submitted version.

Funding

This work was supported by the Joint Funds of the Zhejiang Provincial Natural Science Foundation of China (No. LZJWZ22E090004).

Acknowledgments

The authors thank the reviewers for their constructive comments and suggestions.

Conflict of interest

The authors declare that the research was conducted in the absence of any commercial or financial relationships that could be construed as a potential conflict of interest.

Publisher's note

References

Ardizzon, G., Giovanna, C., Covi, A., and Giorgio, P. (2016). Analysis of the unstable behavior of a pump-turbine in turbine mode: Fluid-dynamical and spectral characterization of the S-shape characteristic. *J. Fluids Eng.* 138 (2), 021105. doi:10.1115/1.4031368

Dewan, Y., Custer, C., and Ivashchenko, A. (2017). Simulation of the francis-99 hydro turbine during steady and transient operation. *J. Phys. Conf.* 782 (1), 012003. doi:10.1088/1742-6596/782/1/012003

Fernández Oro, J. M., González, J., Argüelles Díaz, K. M., and Guerras Colón, F. I. "Deterministic interaction between the impeller flow and both the inlet and outlet volute tongues for a double suction centrifugal pump," in Proceedings of the ASME Fluids Engineering Division Summer Conference 2009, Vail, Colorado USA, August 2009.

Fu, X., Li, D., Wang, H., Zhang, G., Li, Z., and Wei, X. (2018). Influence of the clearance flow on the load rejection process in a pump-turbine. *Renew. Energy* 127, 310–321. doi:10.1016/j.renene.2018.04.054

Fujihara, T., Imano, H., and Oshima, K. (1998). Development of pump turbine for seawater pumped-storage power plant. *Hitachi Rev.* 47 (5), 199–202. doi:10.1061/40440(1999)67

Gao, X. (2019). Study of flow characteristics of draft tube of tidal power station. *Eng. J. Wuhan. Univ.* 52 (7), 594–599. doi:10.14188/j.1671-8844.2019-07-005

Guo, T., Xu, L., and Wang, W. (2021). Influence of upstream disturbances on the vortex structure of francis turbine based on the criteria of identification of various vortexes. *Energies* 14, 7626. doi:10.3390/en14227626

Hu, D. L., Cheng, Y. G., Zhang, P. C., Wang, X., Ding, J. H., and Zhang, X. X. (2022). Distribution features of flow patterns and pressure pulsations of pump-turbine in five operating modes on the four-quadrant plane. *Front. Energy. Res.* 10. doi:10.3389/FENRG.2022.880293

Huang, D. B. (2011). *Fundamentals of water wave theory*. Beijing, China: National Defense Industry Press.

Janssen, P. (2008). Progress in ocean wave forecasting. *J. Com. Phy.* 227 (7), 3572–3594. doi:10.1016/j.jcp.2007.04.029

Li, J. H., Zhang, W. W., Zhu, B. S., Li, Z. G., and Zhang, F. (2021). Study on pressure pulsation in vaneless space of pump turbine. *J. Eng. Therm.* 42 (5), 1213–1223.

Li, Q. F., Zhao, C. B., Long, S. C., and Quan, H. (2019). Study on the evolution of draft tube vortex rope under the runaway condition of pump turbine. *Vib. Impact* 38 (4), 222–228. doi:10.13465/j.cnki.jvs.2019.04.033

Liu, T., Zhang, Y. N., and Du, X. Z. (2015). Antibacterial effects and action modes of asiatic acid. *J. Hydro. Power.* 34 (11), 16–24. doi:10.7603/s40681-015-0016-7

Lu, J., Qian, Z., and Lee, Y. H. (2021). Numerical investigation of unsteady characteristics of a pump turbine under runaway condition. *Renew. Energy.* 169, 905–924. doi:10.1016/j.renene.2021.01.063

Menter, F. R. (2009). Review of the shear-stress transport turbulence model experience from an industrial perspective. *Int. J. Com. Fl. Dyn.* 23 (4), 305–316. doi:10.1080/10618560902773387

Nam, M. C., De, C. B., Yue, X. G., and Jin, M. R. (2018). Design optimization of hydraulic turbine draft tube based on CFD and DOE method. *Environ. Sci.* 136, 012019. doi:10.1088/1755-1315/136/1/012019

Nanjing Hydraulic Research Institute (2002). *JTJ/T 234-2001; wave model test regulation*. Nanjing, China: Nanjing Hydraulic Research Institute.

Peng, S. Y., Li, Z. G., Li, X. R., Chai, X., Liu, D. Y., Zhao, Y. Z., et al. (2020). Flow analysis of tubular turbine draft tube based on vortex analysis. *Eng. J. Wuhan. Univ.* 53 (8), 679–685. doi:10.14188/j.1671-8844.2020-08-004

Ramos, H. M., Amaral, M. P., and Covas, D. I. C. (2014). Pumped-storage solution towards energy efficiency and sustainability: Portugal contribution and real case studies. *J. Water Resour. Prote.* 06 (12), 1099–1111. doi:10.4236/jwarp.2014.612103

Shi, W. H., Cha, H., Luo, H., and Wang, K. Y. (2015). Preliminary study on development of seawater pumped storage power station in China. *China Energy* 37 (12), 36–40.

Sullivan, P. P., Mcwilliams, J. C., and Melville, W. K. (2007). Surface gravity wave effects in the oceanic boundary layer: Large-eddy simulation with vortex force and stochastic breakers. *J. Fl. Mech.* 593, 405–452. doi:10.1017/S002211200700897X

Tanaka, H. (2011). Vibration behavior and dynamic stress of runners of very high head reversible pump-turbines. *Int. J. Fluid Mach. Syst.* 4 (2), 289–306. doi:10.5293/IJFMS.2011.4.2.289

Wang, Z., Zhu, B., Wang, X., and Qin, D. (2017). Pressure fluctuations in the S-shaped region of a reversible pump-turbine. *Energies* 10, 96. doi:10.3390/en10010096

Xu, H. Q., Lu, L., Wang, W. P., and Zhao, L. C. (2018). Study on the mechanism of pressure pulsation in the vaneless space of pump turbine. *J. China Aca. Water. Res. Hydro. Res.* (4), 248–256. doi:10.13244/j.cnki.jiwhr.20180217

Xu, L. C., Peng, Y. J., Tang, W., Liu, D. M., and Liu, X. B. (2022). Flow characteristics and pressure pulsation in the S characteristic area of model pump turbine. *Chin. J. Hydro.* 37 (2), 213–225. doi:10.16076/j.cnki.cjhd.2022.02.009

Yang, J., Lv, Y., Liu, D., and Wang, Z. (2021). Pressure analysis in the draft tube of a pump-turbine under steady and transient conditions. *Energies* 14, 4732. doi:10.3390/en14164732

Yao, Z., Wang, F., Qu, L., Xiao, R., He, C., and Wang, M. (2011). Experimental investigation of time-frequency characteristics of pressure fluctuations in a double-suction centrifugal pump. *J. Fl. Eng. Trans. ASME.* 133 (10). doi:10.1115/1.4004959

Yu, J. M., Ji, Q. Y., Zheng, H., Yang, L. Y., Wang, R. Q., and Chen, C. J. (2020). The investigation of wave energy in zhoushan coastal area based on SWAN model. *Mar. Fore.* 37 (4), 38–49. doi:10.11737/j.issn.1003-0239.2020.04.005

Zheng, Y., Jiang, W. Q., Chen, Y. J., and Sun, O. R. (2018). Investigation on low frequency pulsating and draft tube vortex of tubular turbine. *J. Trans. Chin. Soc. Agric. Mach.* 49 (4), 165–171. doi:10.6041/j.issn.1000-1298.2018.04.019

Zhong, L. T., Lai, X. D., Liao, G. L., and Zhang, X. (2018). Analysis of the relationship between outlet swirl of francis turbine and draft tube vortex rope. *J. Hydro.* 37 (9), 7. doi:10.11660/slfdxb.20180905

Zhou, D. Q., Chen, S. F., and Li, C. (2013). Numerical simulation of operation characteristics of low-head tubular turbine. *J. Irr. Dra. Mac. Eng.* 2013 (10), 6. doi:10.3969/j.issn.1674-8530.2013.10.006

Zhou, Q., Xia, L., Zhang, C., Yuan, Y., and Zhu, Z. (2018). Transient pressure fluctuations and runner loadings of a model pump-turbine during a load rejection process. *J. Hydraulic Eng.* 49 (11), 1429–1438. doi:10.13243/j.cnki.slxb.20180706

Zuo, Z. G., and Liu, S. H. (2017). Study on flow instability of pump turbine in China. *Engineering* 3 (4), 162–178. doi:10.1016/J.ENG.2017.04.010

Appendix: The nomenclature

C_p	Coefficient of pressure fluctuation
D_1	Inlet diameter of the runner (m)
D_2	Outlet diameter of the runner (m)
f	Frequency (Hz)
f_n	Rotation frequency (Hz)
F_1	Blending function
g	Acceleration of gravity (m/s^2)
H	Head (m)
$\mathrm{H_r}$	Rated hydraulic head (m)
K_z	Pressure sensitivity coefficient
l_p	Prototype length (m)
l_m	Model length (m)
M	Torque of impeller blades (N·m)
n	Rotational speed (r/min)
n_{11}	Specific speed (r/min)
p	Static pressure (Pa)
P_k	Production term of turbulent kinetic energy
$\mathrm{Q_r}$	Design discharge (m^3/s)
Q_{11}	Specific flow rate (m^3/s)
S	Invariant measure of the strain rate
S_{mi}	Generalized source term of the momentum equation
U	Circumferential velocity (m/s)
V	Absolute velocity (m/s)
W	Relative speed (m/s)
Z	Elevation of the free surface (m)
α_0	Guide vane opening (degree)
β	Constant of the turbulence model
β'	Constant of the turbulence model
σ_k	Constant of the turbulence model
σ_ω	Constant of the turbulence model
ρ	Density (kg/m^3)
μ	Dynamic viscosity (Pa·s)
τ	Fluid shear stress (Pa)
τ_{ij}	Reynolds stress (Pa)
λ	Eigenvalue of the characteristic equation
Ω	Vorticity tensor
η	Efficiency (%)
ω	Angular velocity (rad/s)
λ_k	Scale length of the wave model
λ_p	Scale of wave pressure
λ_f	Scale of wave frequency
ΔH	Peak value of pressure pulsation (m)
$\Delta H'$	Relative pressure pulsation amplitude (%)
CFD	Computational fluid dynamics
FFT	Fast Fourier transform
SST	Shear stress transport
SIMPLEC	Semi-Implicit Method for Pressure-Linked Equations-Consistent

frontiers | Frontiers in Earth Science

TYPE Original Research
PUBLISHED 06 July 2023
DOI 10.3389/feart.2023.1226451

OPEN ACCESS

EDITED BY
Wei Ge,
Zhengzhou University, China

REVIEWED BY
Huiliang Wang,
Zhengzhou University, China
Anyuan Xiong,
China Meteorological Administration, China

*CORRESPONDENCE
Fan Deng,
dengfan@yangtzeu.edu.cn

RECEIVED 21 May 2023
ACCEPTED 26 June 2023
PUBLISHED 06 July 2023

CITATION
Gong J, Wang Y, Liu M and Deng F (2023), Snow identification from unattended automatic weather stations images using DANet.
Front. Earth Sci. 11:1226451.
doi: 10.3389/feart.2023.1226451

Snow identification from unattended automatic weather stations images using DANet

Jie Gong[1,2], Yonghua Wang[2], Min Liu[1,3] and Fan Deng[2,4]*

[1]Institute of Geological Survey, China University of Geosciences, Wuhan, China, [2]Wuhan Huaxin Lianchuang Technology Engineering Co., Ltd., Wuhan, China, [3]Wuhan Natural Resources and Planning Information Center, Wuhan, China, [4]School of Geosciences, Yangtze University, Wuhan, China

Identifying snow phenomena in images from automatic weather station (AWS) is crucial for live weather monitoring. In this paper, we propose a convolutional neural network (CNN) based model for snow identification using images from AWS cameras. The model combines the attention mechanism of the DANet model with the classical residual network ResNet-34 to better extract the features of snow cover in camera images. To improve the generalizability of the model, we also use images from public datasets in addition to images taken by cameras from unmanned weather stations. Our results show that the proposed model achieved a POD of 91.65%, a FAR of 7.34% and a TS score of 85.45%, demonstrating its effectiveness in snow identification. This study has the potential to facilitate more efficient and effective weather monitoring in a variety of locations.

KEYWORDS

snow identification, automatic weather station (AWS), attention mechanism, DANet model, weather monitoring

1 Introduction

The formation of snow is a complex process influenced by various meteorological factors at the ground level (Yang et al., 2019). Snow is a major winter disaster that can result in extensive accumulation, which can damage crops and disrupt transportation (Andrey et al., 2003). However, the occurrence and intensity of snow vary greatly at a local level, making it difficult to predict using traditional statistical methods (Strle and Ogrin, 2022). Therefore, accurate identification of snow weather from images is crucial for understanding these variations and improving real-time weather monitoring.

Satellite observations from space provide a major data source for identifying different types of weather, including rain, clouds, and snow. Many image processing and recognition algorithms have been developed based on different satellite and ground radar remote sensing data to identify snow surface cover or weather phenomena such as snow or rain. For multispectral satellite images, the Normalized Difference Snow Index (NDSI) is often used to identify snow because it is sensitive to snow signals in the image (Song et al., 2011). Satellite-borne passive microwave radiometers have been used to retrieve snow depth on Arctic sea ice using lower frequencies and artificial neural networks (Rostosky et al., 2018) (Zaerpour et al., 2020). Although satellite images are useful for weather monitoring at regional, continental, and global scales, they have relatively coarse spatial resolutions and are not suitable for real-time weather identification (Liang et al., 2008; Jiang et al., 2014; Getirana et al., 2020).

Compared to satellite sensors, AWS provide a different method for weather identification in local areas. AWS have become essential infrastructure for urban

meteorological forecasting, disaster prevention, and mitigation in many countries (Lu et al., 2020). They are usually equipped with video and meteorological equipment, making them more suitable for monitoring real-time weather at a local scale (Munandar et al., 2017). While meteorological equipment captures meteorological parameters such as temperature and humidity, video captures sequence images of the surroundings, enabling the identification of different types of weather (Kumari et al., 2020).

Traditional manual identification methods suffer from low efficiency and are not conducive to conducting large-scale data analysis. Consequently, automatically identifying snow weather from video images is valuable but challenging for real-time weather identification. Many image classification methods, such as supervised support vector machines, have been used to identify local weather phenomena (Roser and Moosmann, 2008). The NDSI is widely used for ice and snow identification, and some studies have also developed a similar RGBNDSI index for snow identification in RGB images (Hinkler et al., 2002). However, these methods often require a specially designed camera system and careful arrangement of the camera position and shooting angle to observe specific targets. There is also the use of blue channel thresholding for snow and non-snow recognition in RGB images, which is based on the digital number value of blue channel component histogram (Salvatori et al., 2011). This method is sensitive to lighting conditions, surface roughness, and the distance from the camera (Härer et al., 2013).

The identification of snow in video images obtained by meteorologists is a challenging task due to issues such as deformation, illumination, and blur. In recent years, deep learning methods, particularly convolutional neural networks (CNNs), have emerged as effective alternatives to traditional machine learning algorithms for extracting semantic information from images (Ibrahim et al., 2019). One example of a CNN-based method is the Faster R-CNN approach, which uses a region generation network to directly determine the region for image identification (Ren et al., 2017). The Inception V3 model of Google Inception has also been applied to CNNs for snow cover identification from video images taken by weather stations (Huang et al., 2019). Despite their effectiveness, there is still room for improvement in CNN models. In recent years, attention mechanisms have gained significant attention in the deep learning community. These modules allow CNNs to focus on relevant regions or features, leading to improved performance (Li et al., 2020). The limitation of insufficient training data poses a challenge in CNN applications, as models may struggle to generalize well (Alzubaidi et al., 2021).

However, there are still challenges to be addressed in this field. For instance, current methods do not fully exploit local snow cover information, and the incorporation of attention modules into different features may be necessary as CNNs continue to evolve. Additionally, the construction of CNNs for snow identification should consider the use of various open-source images containing different weather phenomena, as the limited images captured by each AWS camera at a fixed angle, height, and view may not be representative of the full range of snow and other weather phenomena.

This paper presents a novel CNN-based approach for snow identification in AWS images. The proposed method has two main advantages compared to previous models. Firstly, it utilizes an attention convolutional neural network model, specifically a double attention network (DANet), to enhance the accuracy of snow identification. By incorporating both channel attention and spatial attention, the DANet can focus on the target area of snow in the global image and suppress irrelevant information. Secondly, the proposed method is based on open-source weather images, rather than video images from a single camera, as in previous studies. The performance of the DANet was evaluated using a dataset of more than 20,000 images and compared to traditional CNN models. The results demonstrate the effectiveness of the proposed approach in accurately identifying snow in unattended AWS images.

2 Study area and data

2.1 Study area

The study area is located in Wuhan, China, which is situated in the middle reaches of the Yangtze River. Wuhan has a subtropical monsoon climate with four distinct seasons, and experiences frequent occurrences of snow and rime in the winter months. The research utilized video images of snow captured by a weather station located in the Dongxihu district of Wuhan (30°60′ N, 114°05′ E). The station's camera, which has a fixed shooting angle and a shooting distance of approximately 50 m, was used to provide the images for snow identification.

2.2 Data

The video images used for snow identification in this study were obtained from the camera of an automatic meteorological observation station at the Wuhan weather station. The snow images were collected between Beijing local time 11:00 and 15:30, and from 18:00 to 21:00 on 29 December 2020, when there was snow in Wuhan. The non-snow images were from 14 December 2020, and were also taken from the same camera at the Wuhan weather station. Images of the ground covered in snow or experiencing ongoing snowfall are manually labeled as snow images. A total of 1,000 images with or without snow labels were extracted from the video data by automatically selecting every 10th frame, forming the test dataset for this study. The images have a resolution of 2,048 × 1,536 pixels and were resized to 600 × 400 pixels for computation efficiency.

The location and climatic conditions of Wuhan Station are particularly distinctive, with a scarcity of significant snowfall events, making it challenging to acquire a comprehensive dataset of snow-related images. Consequently, this study aims to address this limitation by selecting publicly available weather datasets as the training data and leveraging real-time observational data for testing and precision evaluation purposes. Among them, the positive samples consist of 10,000 images depicting snowy weather conditions, while the negative samples encompass

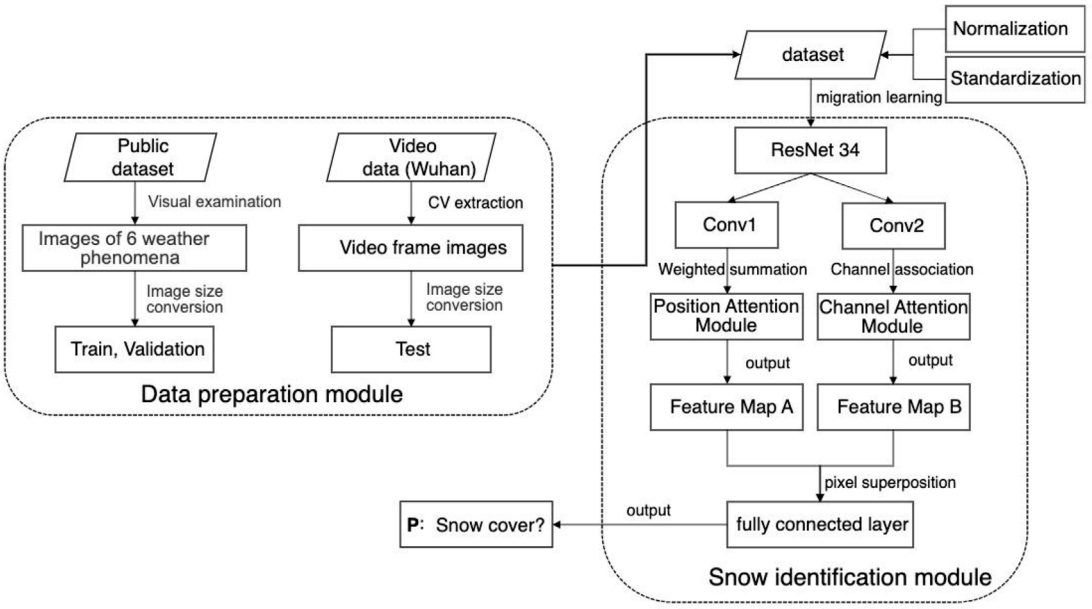

FIGURE 1
Snow identification network based on attention convolutional neural network.

2,000 images each of clear, rainy, foggy, cloudy, and thunderstorm weather phenomena.

3 Snow identification network based on DANet

The flowchart of the proposed snow identification network based on the attention convolutional neural network is shown in Figure 1. It can be divided into a data preparation module and a snow identification module. In the data preparation module, the open-source weather image set is used to construct the training and validation sets for neural network training. The total sample is split into a training set and a validation set in a 4:1 ratio. The images are normalized and standardized to improve numerical stability during backpropagation and accelerate the convergence of the neural network. In the snow identification module, the residual network model (ResNet-34) is used for image convolution and deep semantic feature extraction to obtain the convolutional snow feature map. ResNet-34 consists of 34 layers, with the majority being 3 × 3 convolutional layers. It incorporates residual learning and skip connections to address the degradation problem in deep networks. Then, the attention module, including position and channel attention, is used to focus on the snow feature for snow identification. The position attention module performs position-weighted summation on the convolutional layer, while the channel attention module performs channel-dependent correlation on the same convolutional layer. Both pixel feature maps obtained from these processes are superimposed pixel-wise, focusing simultaneously on the most salient position and channel characteristics in the image. Finally, the fully connected layer is used for snow identification. An image with a probability greater than 0.5 is identified as a snow image, while an image with a probability less than 0.5 is identified as a non-snow image. The details of the various modules are described in the following sections.

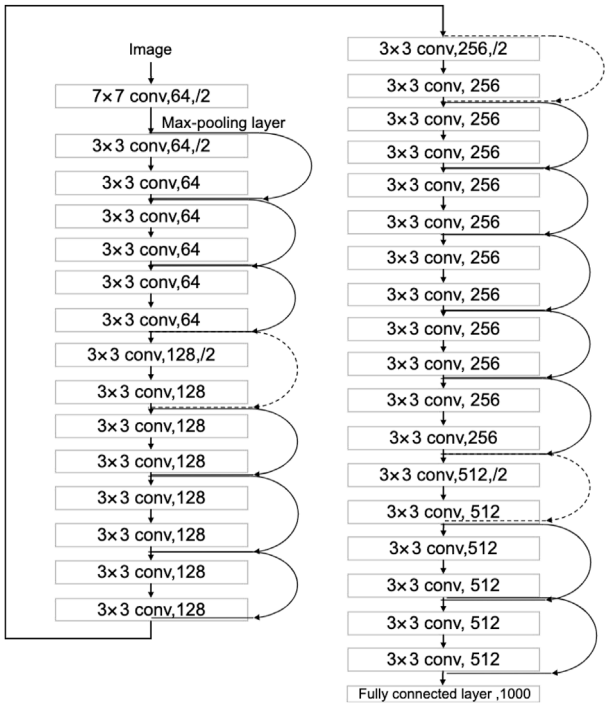

FIGURE 2
ResNet-34 network structure.

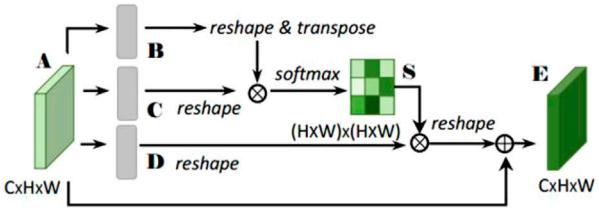

FIGURE 3
Position attention module.

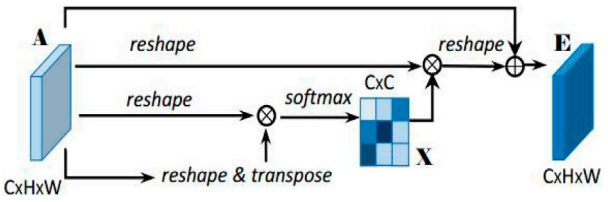

FIGURE 4
Channel attention module.

3.1 Snow feature extraction module based on CNN

The residual network (ResNet) is a convolutional neural network that addresses the problem of gradient explosion and network recession in the Visual Geometry Group (VGG) algorithm by adding residual units to the deep neural network. ResNets have been shown to improve identification accuracy and are well-suited for practical scenarios (Glorot et al., 2011; He et al., 2016). ResNets are a popular choice for feature extraction and classification, and can be divided into various structures based on their convolutional depth, including ResNet-18, ResNet-34, ResNet-50, ResNet-101, and ResNet-152. In this paper, the ResNet-34 structure is adopted, which consists of a 7 × 7 × 64 convolutional layer, 16 blocks of residual modules each composed of two convolutional layers, and a fully connected layer. The network structure of ResNet-34 is shown in Figure 2.

3.2 Snow feature enhancement based on attention module

The DANet model, introduced in CVPR 2019 (Xue et al., 2019), uses deep semantic information about snow extracted by ResNet-34 to adaptively integrate local and global features. This is achieved through the use of two modules: a position attention module and a channel attention module. The position attention module allows the network to selectively focus on the features of individual positions by using weighted summation. The channel attention module emphasizes the interrelated channel graph by combining relevant features from all channel graphs. The feature graphs produced by these two modules are combined to enhance the representation of snow cover features.

3.2.1 Position attention module

To address the issue of lacking sensitivity in detecting local features of snow due to CNN convolution and pooling, a position attention module is used to extract more context information about these local features. This allows the network to more efficiently focus on and better detect both large- and small-scale features of snow. The position attention module is illustrated in Figure 3. It takes in a local feature map (A) with dimensions of C × H × W. The module then generates two feature maps (B and C) through a convolution layer, which have dimensions of C × H × W. The dimensions of B and C are changed to C × N, where N is the number of pixels (N = H × W). B is transposed and multiplied with C, and the softmax function is used to calculate the spatial attention map (S) (Eq. 1) with dimensions of N × N (Liu et al., 2016). The map helps the network focus on specific parts of the feature map, which has dimensions of C × H × W.

$$S_{ji} = \frac{exp\left(B_i \cdot C_j\right)}{\sum_{i=1}^{N} exp\left(B_i \cdot C_j\right)} \tag{1}$$

where S_{ji} denotes the influence of i^{th} position on j^{th}. The more similar the characteristics of the two positions, the higher correlation between them.

The feature map D is created in a similar way to feature maps B and C, through a convolution and a change in dimensions. It has dimensions of C × H × W. Then, D and S are multiplied and transformed through transposition and a change in dimensions. The resulting map is multiplied by a scale parameter (α) and added to the original feature map A, resulting in the final output feature map E (Eq. 2) with dimensions of C × H × W.

$$E_j = \alpha \sum_{i=1}^{N} (S_{ji} D_i) + A_j \tag{2}$$

where the scale parameter (α) is initially set to 0 and gradually learns to assign more weight to certain features. In Eq. 2, all the points on the E feature map are the weighted sum of features from all positions and the original features, allowing the network to obtain a large amount of global information and selectively focus on local features according to the spatial attention map. This helps to better express similar features, leading to increased compactness and semantic consistency within the class.

3.2.2 Channel attention module

Each high-dimensional feature channel mapping can be thought of as a specific response to a particular class, and there should be a relationship between the information between classes. To better understand this interdependence and emphasize interdependent feature mappings, a channel attention module is used to explicitly model the relationship between channels in order to improve the representation of original features. This module is shown in Figure 4.

Unlike the position attention module, the channel attention module directly calculates feature map X with dimensions of C × C from feature map A with dimensions of C × H × W. To do this, the dimensions of A are transformed and multiplied with a matrix of A,

TABLE 1 DANet model parameter change table.

Layers	Outsize	Operation
Conv1	112 × 112	7 × 7, 64, stride2
Conv2_x	56 × 56	3 × 3 max pool, stride2
		$\begin{bmatrix} 3\times3 & 64 \\ 3\times3 & 64 \end{bmatrix} \times 3$
Conv3_x	28 × 28	$\begin{bmatrix} 3\times3 & 128 \\ 3\times3 & 128 \end{bmatrix} \times 4$
Conv4_x	14 × 14	$\begin{bmatrix} 3\times3 & 256 \\ 3\times3 & 256 \end{bmatrix} \times 6$
Conv5_x	7 × 7	$\begin{bmatrix} 3\times3 & 512 \\ 3\times3 & 512 \end{bmatrix} \times 3$
	7 × 7	PAM_Module
	7 × 7	CAM_Module
	1 × 1	Average pool, 1000-d fc, softmax
FLOPs		3.6×10^9

and the resulting map is passed through the softmax function (Eq. 3) to generate the final feature map X.

$$x_{ji} = \frac{exp\left(A_i \cdot A_j\right)}{\sum_{i=1}^{C} exp\left(A_i \cdot A_j\right)} \tag{3}$$

where x_{ji} denotes the effect of the i^{th} channel on j^{th}.

In addition, matrix multiplication is used to transform feature map X and multiply it with the transpose of feature map A. The resulting map has dimensions of C × H × W, similar to the scale parameter α. A new scale parameter (β) is introduced for this multiplication, and the result is added to the pixels of feature map A to produce the final feature map E (Eq. 4) with dimensions of C × H × W.

$$E_j = \beta \sum_{i=1}^{C} (x_{ji} A_i) + A_j \tag{4}$$

In Eq. 4, the final feature of each channel is the weighted sum of all channel features and original features, using a scale parameter (β) that starts at zero and gradually learns to assign more weight. This helps to strengthen the relationship between different channel feature maps and improve the representation of distinctive features of snow by emphasizing the rich semantic dependence between channels.

3.3 Snow identification module based on DANet

To fully incorporate information about spatial context, local details, and class information, this paper combines the features from the location and channel attention modules. The output of these two modules is mapped to the same feature map through a convolution layer and then combined by adding their respective pixels. Finally, the snow is identified through a fully connected layer, namely:

TABLE 2 Distribution of snow and non-snow images in datasets.

Dataset	Snow	Non-snow	Total
Training set	8,000	8,000	16,000
Validation set	2,000	2,000	4,000
Test set (Wuhan)	1,000	1,000	2,000
Total	11,000	11,000	22,000

TABLE 3 Comparison of verification accuracy between ResNet and DANet models.

	POD (%)	FAR (%)	TS (%)
ResNet34	85.73	4.93	82.08
DANet	94.68	6.63	88.71

TABLE 4 Accuracy evaluation of the DANet model.

	POD (%)	FAR (%)	TS (%)
Validation	94.68	6.63	88.71
Test (Wuhan)	91.65	7.34	85.45

$$\text{Loss} = -\frac{1}{N}\sum_{i=0}^{N-1} \mathcal{Y}_i \log p_i \tag{5}$$

where $\mathcal{Y}$ is the true label of the sample, N is the number of samples in a batch, and p_i is the prediction probability of the sample.

4 Experiments

4.1 Hyper-parameter settings

The hyperparameters for the DANet model, including the number and size of layers, convolution kernel size and step length, pooling window size and step length, regularization weight, learning rate, node loss rate, and batch size, are listed in Table 1. The network is constructed using Linear, ReLU, Normalization, and Dropout layers. The Adam optimization algorithm and a learning rate attenuation technique are used to speed up the convergence of the model. The learning rate is continuously adjusted during training to reduce and stabilize the loss value. Specifically, the model is trained in 80 batches, with a learning rate of 10–2 for the first 20 batches, 10–3 for batches 21–40, 10–4 for batches 41–60, and 10–5 for batches 61–80.

4.2 Accuracy assessment

This paper used a total of 8,000 snow images and 8,000 non-snow images to train the proposed DANet model, and 2,000 snow images and 2,000 non-snow images were used for validation. 2,000 images from the AWS were used for model testing

FIGURE 5
Missing judgment images and false alarm images at Wuhan station at night.

(Table 2). The performance of the model was evaluated using the Probability of Detection (POD) (Eq. 6), False Alarm Rate (FAR) (Eq. 7), and Threat Score (TS) (Eq. 8).

$$POD = TP\,(TP + FN)^{-1} \tag{6}$$

$$FAR = FP\,(TP + FP)^{-1} \tag{7}$$

$$TS = TP\,(TP + FN + FP)^{-1} \tag{8}$$

where TP (true positive) is the number of forecasts and observations that are both true, FN (false negative) is the number of false forecasts and true observations, and FP(false positive) is the number of true forecasts and false observations.

5 Results

This paper evaluated the trained DANet model using a validation image set and a separate test image set. Images were classified as snow if they had a probability of higher than 50% and classified as non-snow if they had a probability of less than 50%. The addition of the attention module led to significant improvements in the overall TS and POD of the model, as indicated by the results (Table 3). However, it is worth noting that FAR also increased with the inclusion of the attention module. The FAR increased because the model occasionally recognized fuzzy features similar to snow as actual snow, leading to false positive judgments (Figure 5).

The accuracy metrics for the proposed DANet model are shown in Table 4. According to the test data, POD is 91.65%, FAR is 7.34%, the TS score is 85.45%. These high accuracy scores demonstrate the efficiency of the proposed model in snow identification. The majority of the missing alarm errors occurred at night, with 75.6% of the 84 mission alarm images being captured during the night. Similarly, 69.1% of the 73 false alarm images were also captured at night. This is likely due to the strong contrast between night and daytime, as well as the camera shake in windy conditions causing some images to be unclear.

According to the test results at the Wuhan station, the TS score was higher than 85%. The trained model was able to effectively extract the features of snow and positively impact snow identification. However, the winter weather in Wuhan can be unstable, so it is recommended to increase the observation time in the modelling process to ensure continuous snow weather phenomena and improve accuracy. In cases where sufficient data is available, it is recommended to use a "one station one model" approach, which involves creating a separate model for each station. This can help to better capture the unique characteristics of the snow at each station.

6 Conclusion

In order to improve real-time weather monitoring, it is important to develop methods for accurately identifying snow in local areas. AWS equipped with video offers one potential approach to this problem. In this paper, we address the problem of recognizing weather phenomena from images at meteorological stations, and propose improvements through the use of open-source weather images and double attention mechanisms.

The result shows that using an attention convolutional neural network (CNN) with channel and position attention modules can improve the accuracy of snow identification. When compared to a traditional CNN model, the attention module CNN resulted in a 6.63% increase in the TS score and a 8.95% increase in the POD. The attention module is able to focus on specific areas and extract relevant details while ignoring unnecessary information, leading to better classification performance. Additionally, our proposed method simplifies the process of training the CNN by using an open-source weather image set rather than relying on a large amount of video camera images, which can be difficult to obtain and time-consuming. This proposed DANet model has demonstrated the ability to handle images from various AWS cameras with different viewing angles and heights, making it a potentially suitable tool for identifying weather phenomena globally. The proposed improvements in this study have not only advanced the field of meteorological image and video analysis, but also have practical value for widespread use and implementation at meteorological stations.

Further research could explore the application of this model to other types of weather phenomena and in different environments, as

well as investigate ways to optimize and refine the model for improved performance.

Data availability statement

The raw data supporting the conclusion of this article will be made available by the authors, without undue reservation.

Author contributions

JG: conceptualization and writing-original draft. FD: conceptualization, writing-review and editing and funding acquisition. YW: data curation. ML: data curation. All authors contributed to the article and approved the submitted version.

Funding

The project is supported by the Open Fund of Key Laboratory of Urban Land Resources Monitoring and Simulation, Ministry of Natural Resources.

Acknowledgments

We thank Li Xiaodong for help in reviewing and editing the English language and grammar.

Conflict of interest

Authors JG, YW, and FD were employed by Wuhan Huaxin Lianchuang Technology Engineering Co., Ltd.

The remaining author declares that the research was conducted in the absence of any commercial or financial relationships that could be construed as a potential conflict of interest.

Publisher's note

References

Alzubaidi, L., Zhang, J., Humaidi, A. J., Al-Dujaili, A., Duan, Y., Al-Shamma, O., et al. (2021). Review of deep learning: Concepts, CNN architectures, challenges, applications, future directions. *J. big Data* 8, 53–74. doi:10.1186/s40537-021-00444-8

Andrey, J., Mills, B., Leahy, M., and Suggett, J. (2003). Weather as a chronic hazard for road transportation in Canadian cities. *Nat. hazards* 28 (2), 319–343. doi:10.1023/a:1022934225431

Getirana, A., Kirschbaum, D., Mandarino, F., Ottoni, M., Khan, S., and Arsenault, K. (2020). Potential of GPM IMERG precipitation estimates to monitor natural disaster triggers in urban areas: The case of rio de Janeiro, Brazil. *Remote Sens.* 12 (24), 4095. doi:10.3390/rs12244095

Glorot, X., Bordes, A., and Bengio, Y. "Deep sparse rectifier neural networks," in Proceedings of the fourteenth international conference on artificial intelligence and statistics, Fort Lauderdale, FL, USA, April 2011, 315–323.*JMLR Workshop Conf. Proc.*

Härer, S., Bernhardt, M., Corripio, J. G., and Schulz, K. (2013). Practise–photo rectification and classification software (v. 1.0). *Geosci. Model Dev.* 6 (3), 837–848. doi:10.5194/gmd-6-837-2013

He, K., Zhang, X., and Ren, S., "Deep residual learning for image recognition," in Proceedings of the IEEE conference on computer vision and pattern recognition, Las Vegas, NV, USA, June 2016, 770–778.

Hinkler, J., Pedersen, S. B., Rasch, M., and Hansen, B. U. (2002). Automatic snow cover monitoring at high temporal and spatial resolution, using images taken by a standard digital camera. *Int. J. Remote Sens.* 23 (21), 4669–4682. doi:10.1080/01431160110113881

Huang, X. Y., Zhang, Y., and Ye, C. Z. (2019). Research on artificial intelligence observation and identification of snow cover weather phenomenon on surface. *Meteor Mon.* 45 (9), 1189–1198. doi:10.7519/j.issn.1000-0526.2019.09.001

Ibrahim, M. R., Haworth, J., and Cheng, T. (2019). WeatherNet: Recognising weather and visual conditions from street-level images using deep residual learning. *ISPRS Int. J. Geo-Information* 8 (12), 549. doi:10.3390/ijgi8120549

Jiang, L. M., Wang, P., Zhang, L. X., Yang, H., and Yang, J. (2014). Improvement of snow depth retrieval for FY3B-MWRI in China. *Sci. China Earth Sci.* 57 (6), 1278–1292. doi:10.1007/s11430-013-4798-8

Kumari, N., Gosavi, S., and Nagre, S. S. "Real-time cloud based weather monitoring system," in Proceedings of the 2020 2nd International Conference on Innovative Mechanisms for Industry Applications (ICIMIA), Bangalore, India, March 2020, 25–29.

Li, W., Liu, K., Zhang, L., and Cheng, F. (2020). Object detection based on an adaptive attention mechanism. *Sci. Rep.* 10 (1), 11307. doi:10.1038/s41598-020-67529-x

Liang, T. G., Huang, X. D., Wu, C. X., Liu, X., Li, W., Guo, Z., et al. (2008). An application of modis data to snow cover monitoring in a pastoral area: A case study in northern xinjiang, China. *Remote Sens. Environ.* 112 (4), 1514–1526. doi:10.1016/j.rse.2007.06.001

Liu, W., Wen, Y., Yu, Z., et al. "Large-margin softmax loss for convolutional neural networks," in Proceedings of the International Conference on Machine Learning. PMLR, New York NY USA, June 2016, 507–516.

Lu, Z., Peng, B., Zhao, C., and Liu, Z. (2020). Research on unattended implementation of surface meteorological observation and its guarantee method. *Meteorological Hydrological Mar. Instrum.* 37 (02), 14–18. doi:10.3969/j.issn.1006-009X.2020.02.004

Munandar, A., Fakhrurroja, H., and Rizqyawan, M. I."Design of real-time weather monitoring system based on mobile application using automatic weather station," in Proceedings of the 2017 2nd International Conference on Automation, Cognitive Science, Optics, Micro Electro-Mechanical System, and Information Technology (ICACOMIT), Jakarta, Indonesia, October 2017, 44–47.

Ren, S., He, K., Girshick, R., and Sun, J. (2017). Faster R-CNN: Towards real-time object detection with region proposal networks. *IEEE Trans. Pattern Analysis Mach. Intell.* 39 (06), 1137–1149. doi:10.1109/tpami.2016.2577031

Roser, M., and Moosmann, F. "Classification of weather situations on single color images," in Proceedings of the 2008 IEEE intelligent vehicles symposium, Eindhoven, Netherlands, June 2008, 798–803.

Rostosky, P., Spreen, G., Farrell, S. L., Frost, T., Heygster, G., and Melsheimer, C. (2018). Snow depth retrieval on Arctic sea ice from passive microwave radiometers—improvements and extensions to multiyear ice using lower frequencies. *J. Geophys. Res. Oceans* 123 (10), 7120–7138. doi:10.1029/2018jc014028

Salvatori, R., Plini, P., Giusto, M., Valt, M., Salzano, R., Montagnoli, M., et al. (2011). Snow cover monitoring with images from digital camera systems. *Ital. J. Remote Sens.* 43 (6), 137–145. doi:10.5721/itjrs201143211

Song, Z., Chen, X., Liu, H., Tian, L., and Wu, W. (2011). Snow cover extraction based on the HJ-1A/1B satellite data. *Resour. Environ. Yangtze Basin* 20 (5), 553–558.

Strle, D., and Ogrin, M. (2022). Five different types of lowered snow line in alpine valleys. *J. Mt. Sci.* 19, 73–84. doi:10.1007/s11629-020-6237-6

Xue, H., Liu, C., and Wan, F."Danet: Divergent activation for weakly supervised object localization," in Proceedings of the IEEE/CVF International Conference on Computer Vision, Seoul, Korea (South), October 2019, 6589–6598.

Yang, C., Liu, C., Sun, T., Zhang, A., Ouyang, D., Deng, S., et al. (2019). High breakdown voltage and low dynamic ON-resistance AlGaN/GaN HEMT with fluorine ion implantation in SiN_x passivation layer. *Meteorol. Mon.* 45 (2), 191–202. doi:10.1186/s11671-019-3025-8

Zaerpour, A., Adib, A., and Motamedi, A. (2020). Snow depth retrieval from passive microwave imagery using different artificial neural networks. *Arabian J. Geosciences* 13, 696–716. doi:10.1007/s12517-020-05642-x

frontiers | Frontiers in Earth Science

TYPE Review
PUBLISHED 21 July 2023
DOI 10.3389/feart.2023.1238203

OPEN ACCESS

EDITED BY
Xihui Gu,
China University of Geosciences Wuhan, China

REVIEWED BY
Wei Si,
Hohai University, China
Ting Zhang,
Tianjin University, China
Yun Chen,
China Three Gorges University, China

*CORRESPONDENCE
Leizhi Wang,
wanglz@nhri.cn

RECEIVED 11 June 2023
ACCEPTED 13 July 2023
PUBLISHED 21 July 2023

CITATION
Shang S, Wang L, Wang Y, Su X, Li L and Xia X (2023), Exploration of sponge city construction in China from the perspective of typical cases. *Front. Earth Sci.* 11:1238203. doi: 10.3389/feart.2023.1238203

Exploration of sponge city construction in China from the perspective of typical cases

Shouwei Shang[1], Leizhi Wang[1]*, Yintang Wang[1], Xin Su[1], Lingjie Li[1] and Xiaohan Xia[2]

[1]Key Laboratory of Flood and Drought Disaster Defense, The Ministry of Water Resources, Nanjing Hydraulic Research Institute, Nanjing, China, [2]School of Foreign Languages, Sun Yat-sen University, Guangzhou, China

Night years have witnessed the construction of sponge city in China. In recent years, more frequent extreme rainstorm has put more pressure on urban flood control and waterlogging elimination, and the construction of sponge city has been facing many controversies. In response, this study discusses the concept, connotation, evaluation indexes, construction objectives, investment and benefits of sponge city construction. The key point is that the concept of the sponge city has expanded from the construction of low-impact development to a new model of urban development and construction, with an emphasis on improving the overall function of the city and enhancing the comprehensive response to urban water issues. Its construction benefits cannot be measured only in terms of flood control and waterlogging prevention. Besides, the biggest problem faced by cities is still flooding. The priority of building a sponge city is the prevention of waterlogging. Meanwhile, the integrity and systematic construction which integrates multiple sectors, industries and fields should be considered. The government should focus on the combination of ecological methods and engineering facilities, and scientifically promote the systematic management of urban water.

KEYWORDS

sponge city, urban water issue, construction objectives, construction benefits, rainstorm waterlogging

1 Introduction

Rapid urbanization in China has led to a series of "urban diseases", such as urban heat island effect, water environment pollution and water ecological degradation (Yoshikoshi et al., 2009; Park et al., 2020). Moreover, climate change and human activities have brought frequent extreme hydrometeorological events, contributing to the worsening urban water situation in China. In particular, rainstorm waterlogging is quite serious, resulting in frequent "urban sea-watching phenomenon" (Jia, 2017) and tremendous economic losses in events such as the Beijing "7.21" flood in 2012, the Wuhan "7.6" flood in 2016, the Jinan "7.18" flood in 2016, the Nanning "3.25" flood in 2020 (Yuan et al., 2018), and the Zhengzhou "7.20" flood in 2021 (Li et al., 2022). For this reason, a large number of scholars have carried out continuous research on urban waterlogging panoramic simulation and risk management (Wu et al., 2021; Ge et al., 2022; Zhang H et al., 2023). However, the numbers of cities and people affected by floods in China are predicted to increase with climate change (Tellman et al., 2021). Hence, issues of flood control and drainage have become the focus of the management of urban water systems.

TABLE 1 Comparison of sponge city concepts.

Scholars/Resources	Date	Concepts
The MOHURD	November 2014	The city is constructed like a sponge, with good "resilience" in adapting to environmental changes and coping with natural disasters, which can absorb, store, seep and purify water during precipitation. It is ready for use, and is of low-impact
Qiu	January 2015	The essence is to change the traditional concept of urban construction and follow a low-impact development model, that is, in harmony with nature. Sponge city construction is also known as low-impact design and low-impact development (Qiu, 2015)
Che et al	April 2015	The "grey" and "green" infrastructures should be constructed as resilient infrastructures for rainwater. It can use water efficiently and enable cities to handle extreme rainstorm as well as climate change, maintaining urban ecosystems (Che et al., 2015)
Yu et al	June 2015	The "sponge city", as an ecological approach of urban water management, is to construct multi-scale hydro-ecological infrastructures (Yu et al., 2015)
The MOHURD	October 2015	The sponge city construction should take the measures of "infiltration, detention, retention, purification, utilization and discharge" to minimize the impact of urban development and construction activities on the ecological environment
Wang	September 2017	In the sponge city, there is no waterlogging, and the rainstorm-related pollution is under control. Rainwater can be reused. The fundamental philosophy is matching the sky area with the ground area, that is, absorbing rainwater over the local area, which emphasizes local adaptation (Wang et al., 2017)
Ren	July 2017	As a new urban development construction concept and model, the sponge city is part of the comprehensive improvement of urban water resources and water environment, focusing on solving urban waterlogging and urban water environment deterioration (Ren et al., 2017)
Xia	October 2017	The construction of sponge city requires a unified planning, clear interconnection and coordination of sponge measures and relationships among different departments (Xia et al., 2017)
The MOHURD	December 2018	The sponge city construction follows the concept of "source reduction, process control and systematic remediation", emphasizes the roles of urban water ecology and water environment function, and highlights the overall improvement of urban area function
The Ministry of Finance, jointly with the MOHURD and the Ministry of Water Resources of China	April 2021	The sponge city coordinates the construction of drainage and flood control facilities, urban water environment improvement, urban ecological restoration, green space construction*etc.*

In recent years, thirty pilot cities have pumped more than 160 billion into sponge city construction (Ren et al., 2020); however, most pilot cities still suffer from serious urban waterlogging after extreme rainstorms, such as Zhengzhou, Nanning, and Wuhan. It is indicated that sponge city construction has achieved little in urban flood control and waterlogging elimination. At the same time, the construction of sponge city involves multiple sectors, industries and disciplines, while different industries and disciplines have different definitions of the sponge city. It triggered a series of debates and disagreements, mainly on the construction objectives, models and cost-benefit of sponge city (Hou et al., 2020).

Over the past decade, the connotation of sponge city has changed from the low-impact development to the comprehensive enhancement of the fundamental functions of the urban ecological system. Meanwhile, the main goal of sponge city has also been developed from urban flood management to the comprehensive management of water environment, water ecology, water resources and water security. Sponge facilities can mitigate urban flooding and store storm water to some extent, but they cannot assume the main role of flood control and drainage (Xu et al., 2020). Therefore, this study identifies the concept in Section 2, discusses the objectives and evaluation indexes of sponge city in Section 3, and makes a statistical analysis of sponge city planning, construction and financial investment in each city in Section 4. As this study elaborates on the construction objectives, connotations and functions of sponge city, it is of great importance to the scientific understanding and effective construction of sponge city.

2 Concept of sponge city

Highly urbanized cities may face aggravated urban water issues. Since the 1970s, western countries have tried to systematically solve a series of water issues concerning water resources and water environment in these cities. After nearly 50 years, a control system centered on urban stormwater management has been developed (Eckart et al., 2018).

With the increasingly prominent urban waterlogging in China, the concept of sponge city was put forward with the experience of foreign cities in urban rainwater management as a reference. In December 2013, China proposed to "build a sponge city with natural accumulation, natural infiltration and natural purification". That was the first time that the concept of sponge

TABLE 2 Changes in sponge city evaluation indexes.

Documents	Categories	Evaluation indexes	Differences
Sponge City Development Technical Guideline: Low Impact Development		Total annual runoff volume capture ratio, peak runoff and runoff pollution control targets, rainwater utilization	
Measures for Performance Evaluation and Assessment of Sponge City Development (Trial)	Water ecology	Total annual runoff volume capture ratio, ecological shoreline restoration, groundwater level, urban heat island effect	The 18 evaluation indexes of the sponge city are subdivided into six categories, focusing on the water environment and water ecology
	Water environment	Water environment quality, urban surface source pollution control	
	Water resources	Wastewater recycling rate, rainwater resource utilization rate, pipe network leakage control	
	Water security	Urban rainstorm water-logging disaster prevention and control, drinking water safety	
	System construction and implementation	Planning and construction control system, blue and green line delineation and protection, technical specifications and standards construction, investment and financing mechanism construction, performance assessment and incentive mechanism, industrialization	
	Effect	Multi-regional demonstration effect, more than 60% areas meeting the standard	
Guideline of the Ministry of Water Resources on Promoting the Water Conservancy Construction in Sponge City		Flood control standard, rainfall retention rate, water area rate, surface water quality standard-reaching rate, rainwater resource utilization rate, recycled water utilization rate, levee standard-reaching rate, flood discharge standard-reaching rate, river and lake ecological protection ratio, groundwater depth, soil erosion control rate	Two new indexes have been added, which are soil erosion control rate and flood control standard
Assessment Standard for Sponge City Development Effect	Total annual runoff capture ratio	New construction and alterations: shall not be lower than the lower limit in the area on the total annual runoff control zoning map	Based on the water Provisions of water ecology, water environment, and water security are made clear in the *Measures for Performance Evaluation and Assessment of Sponge City Construction (Trial)*
	Source reduction	Total annual runoff pollutants (Suspended solids) abatement rate ≥70% for new buildings, complexes, roads and squares, and ≥40% for reconstruction; total park runoff volume capture ratio ≥90% for green spaces	
	Waterlogging and flood control	Reasonable connection of grey and green infrastructures, no ponding or waterlogging with respect to precipitation under the design return period	
	Ecological shoreline protection of water bodies	Water area should not be reduced, and the proportion of ecological shoreline is no less than 70%	
	Environmental quality of urban water bodies	There is no direct discharge of sewage or wastewater in dry days. The annual overflow volume control rate of the combined sewer overflow discharge outlet in rainy days is ≥50%, and the water body is not black or odorous	
		Trends in groundwater burial depth, urban heat island effect mitigation	
Notice on Systematic and Territorial Demonstration of Sponge City Construction	Display of effect	Successful construction of each area	Emphasis on the successful construction of each area

city appeared in the national documents. In November 2014, the Ministry of Housing and Urban-Rural Development (MOHURD) of China issued the *Sponge City Development Technical Guideline: Low Impact Development* (hereinafter referred to as the *Guideline*). It can be seen that the concept of the sponge city was first associated with low-impact development. Subsequently, scholars from different disciplines and fields have explained this concept (Table 1). Since then, the connotations of the sponge city have been continuously expanded.

TABLE 3 Distribution of pilot sponge cities.

Classification	Grading	Number of pilot cities	Number of demonstration cities promoting construction in the whole region
Climate zone	Humid	18	13
	Semi-humid	12	7
City scale	Large cities	14	4
	Medium cities	9	10
	Small cities	7	6

In October 2015, the General Office of the State Council of China issued the *Guiding Opinions on Promoting the Development of Sponge City* (hereinafter referred to as the *Opinion*), presenting the comprehensive technical measures of "infiltration, detention, retention, purification, utilization and discharge" to minimize the impacts of urban development and construction activities on the ecological environment. The *Opinion* explicitly proposed to update the concept of urban planning and construction, and insisted on the combination of ecological methods and engineering facilities. In 2018, the MOHURD of China issued the *Assessment Standard for Sponge City Development Effect* (hereinafter referred to as the *Standard*), which put forward the sponge city concept of "source reduction, process control and systematic remediation". It emphasizes the role and function of urban water ecology and water environment, and highlights the overall function improvement of urban areas. In April 2021, the Ministry of Finance, jointly with the MOHURD and the Ministry of Water Resources of China, issued the *Notice on Systematic and Territorial Demonstration of Sponge City Construction* (hereinafter referred to as the *Notice*). It clearly proposed that the construction of new urban areas should be goal-oriented, and that of the old urban areas should be problem-oriented to coordinate the construction of drainage and flood control facilities, urban water environment improvement, urban ecological restoration and green space construction.

Therefore, the concept of sponge city has been constantly developing based on practice, evolving from "building a comprehensive rainwater management system with low-impact development" (building a low-impact development rainwater system) to "changing the concept of urban construction and development" (improving the overall function of urban areas). In essence, it consists of three aspects. First, the sponge city concerns the harmonious relationship between urbanization and the ecological environment. Second, the sponge city construction aims to make cities more resilient in adapting to environmental changes and coping with natural disasters. Third, it shifts the way to deal with flood prevention and control and advocates building a low-impact system of rainfall and flood management (Zhang, 2015). Therefore, at this stage, sponge city is essentially a change in the model of urban planning and construction.

3 Objectives and content of sponge city construction

While the connotation of a sponge city is expanding, the evaluation indexes of sponge city construction in China are also being constantly improved. Table 2 presents the changes in the development of evaluation indexes of the sponge city in China. The *Guideline* issued by the MOHURD in 2014 marked the first time that China proposed a sponge city control index system at the government level. The *Guideline* emphasized the principles of low-impact development and ecological priority, and it pointed out that sponge city in China take urban rainwater and flood management as the control objectives, including planning control indexes of runoff volume, peak runoff and runoff pollution, and rainwater utilization. The *Guideline* divided China into five regions and clarified the application scope of indexes. However, these indexes are simple and imprecise, and they lack consideration of local conditions. In 2015, the MOHURD issued the *Measures for Performance Evaluation and Assessment of Sponge City Development (Trial)* (hereinafter referred to as the *Measure*), where the eighteen indexes fall into six categories covering water ecology, water environment, water resources, water security and display of effect. The *Measure* is used to systematically assess the effectiveness of sponge city construction. However, urban stormwater management is mainly judged by the total annual runoff volume capture ratio, rainwater resource utilization and urban stormwater flood control. The indexes in *Measure* are more specific than the *Guideline*, while the focus has changed, with more emphasis on water ecology and water environment. In August 2015, the Ministry of Water Resources issued the *Guideline of the Ministry of Water Resources on Promoting the Water Conservancy Construction in Sponge City*, which put forward the main indexes for water conservancy construction in sponge city. Compared with the *Measure,* it includes two new indexes of soil erosion control rate and flood control standards. The *Standard* promulgated by the MOHURD in 2018 is the first national standard on sponge city construction in China. It further described the indexes, clearly subdivided the annual runoff volume disposal into old urban built-up areas and newly-built areas, and made detailed provisions for the total annual runoff volume in different areas and places. The actual concentration abatement target was added to the water environment evaluation. Compared with the *Measure*, the *Standard* further improves and strengthens the control indexes, takes into account the differences in the urgency of different cities to achieve the central objectives, and emphasizes the localization and precision of the measures. The *Notice* issued in 2021 further stressed the display of effect and explicitly stated that every construction of an area should be effective, with an emphasis on the overall effect of sponge city construction.

The changes in evaluation indexes show that the construction of sponge city in China is not limited to low-impact development, and it emphasizes more on the improvement of overall urban functions.

TABLE 4 Main controlling indicators of typical cities.

City scale	City	Water ecology	Water security			Water environment	Water resources
		Total annual runoff volume capture rate	Flood control standard	Stormwater drainage design standard	Flood control standard (central city area)	Surface source pollution control	Rainwater resource utilization
Large Cities	Shanghai	≥75%	Once in 100 years	≥5 years in the main urban area, 30 years for sunken buildings	Meeting planning requirements	≥75%	≥5%
	Shenzhen	70%	Once in 50 years	3–5 years, ≥10 years for especially important areas	Once in 200 years	100%	Short-term: 1.5%
							Long-term: 3%
	Guangzhou	70%	Once in 50 or more years	5–10 years, 30–50 years for sunken buildings	Once in 200 years	New construction areas: >50%	>3%
						Rebuilding areas: >40%	
	Zhengzhou	75%	Once in 20–50 years	3–5 years, 30 years for sunken buildings	Once in 200 years	>50%	>5%
	Shijiazhuang	Old urban areas: 70%	Once in 20–50 years	3–5 years	Once in 200 years	≥50%	7.5%
		In new urban areas: 75%					
	Wuhan	60%–85%	Once in 50–100 years	10 years for trunk roads, 20 years for expressways*etc.*	Once in 200 years	≥50%	≥5%
	Qingdao	75%	Once in 50 years		Once in 100 years	2020: 50%	2020: 5%
						2030: 65%	2030: 8%
	Nanjing	Built-up areas: 70%–75%	Once in 50 years	3–10 years, 30–50 years for sunken buildings	Once in 200 years	50%	2020: 2%
		New construction areas: 80%–85%					2030: 5%
	Beijing	72.6%	Once in 50–100 years	20–100 years	Once in 200 or more years	≥60%	2020: 8%
							2035: 10%
	Chongqing	≥70%	Once in 50 years	5–10 years, 50 years for sunken buildings	Once in 100 years	≥50%	localization
Medium cities	Xining	≥85%	Once in 50 years	2–5 years	Once in 50–100 years	≥60%	≥2%
	Huai'an	70%	Once in 30 years	3–5 years	Once in 100 years	≥45%	≥3%
	Suqian	70%	Once in 30 years	2–5 years, 20 years for sunken buildings	Once in 100 years	40%	≥3%
	Qinzhou	70%	Once in 50 years		Once in 100 years	40%	0.9%
	Xiangtan	75%	Once in 30 years	2–5 years, 20–30 years for sunken buildings	Once in 100 years	55%	
	Zhuhai	80%	Once in 30–50 years	3–5 years, 20 years for sunken buildings	Once in 100 years	Short-term: 35%	Short-term: 5%
						Long-term: 40%	Long-term: 10%
	Zhuzhou	80%	Once in 30 years	3–10 years, 20–30 years for underground buildings	Once in 100 years	Short-term: 45%	≥4%
						Long-term: 60%	
Small cities	Pingxiang	75%			Once in 50 years	2017: 50%	2017: 12%
						2030: 75%	2030: 15%

(Continued on following page)

TABLE 4 (*Continued*) **Main controlling indicators of typical cities.**

City scale	City	Water ecology	Water security			Water environment	Water resources
		Total annual runoff volume capture rate	Flood control standard	Stormwater drainage design standard	Flood control standard (central city area)	Surface source pollution control	Rainwater resource utilization
	Hebi	70%	Once in 30 years	≥2 years	Once in 20–100 years	70%	1.1%
	Yiyang	Short-term: ≥75%	Once in 30 years	2–5 years, 20 years for sunken buildings	Once in 50–100 years	45%	Short-term: 1%
		Long-term: ≥80%					Long-term: 3%

It is clear that these evaluation indexes have been improved. However, there are still some problems, such as the disconnection among multiple disciplines and fields, lack of correspondence between objectives and indexes, insufficient display of effect, and fragmented construction.

4 Typical cases of sponge city planning and construction

4.1 Construction objectives and targets of typical cities

In 2015 and 2016, a total of thirty cities including Qian'an, Baicheng, Fuzhou, Beijing and Xining were selected as pilot sponge cities in China, and another 20 cities including Guangzhou, Wuxi, and Suqian were selected as national demonstration cities in 2021 to systematically promote the whole construction of sponge city. Table 3 shows the distribution of these cities. The climate zone and city scale of pilot cities show that the construction of sponge city is not limited to the highly urbanized areas in East China, and they are also distributed in the arid areas in the hinterland of China. In addition to these pilot cities, more than three hundred cities, such as Nanjing, Zhongshan, Chengdu, and Zhuzhou, are also constructing sponge city, and China has entered a period that the construction of sponge city is undergoing throughout the country.

Table 4 presents the control indexes of sponge city planning for large, medium and small cities in China in four aspects: water ecology, water security, water environment and water resources. The indexes include total annual runoff volume capture ratio, waterlogging prevention and control standard, rainwater pipe and drainage design standard, flood control standard, surface source pollution control and rainwater resource utilization rate, *etc.* Among the cities in the statistics, four are coastal cities; five are northern cities; four are inland cities; five are southern cities. Nine of the above cities are national pilot cities and two are national demonstrations, so these cities are represented in terms of spatial distribution.

From the main control indexes of each city, the construction of the sponge city in different cities focuses on water security, water ecology, water environment and the function of water resources. Besides, some cities take into account the water sight and water culture, such as Zhengzhou, Guangzhou, Yiyang, Zhuhai, Zhuzhou, and Pingxiang. Among the nineteen cities in the statistics, seven cities, including Shenzhen, Beijing, Pingxiang, and Zhuhai, have proposed detailed near-term and long-term implementation targets, while Shijiazhuang, Nanjing and Guangzhou have further proposed construction targets for different areas on this basis, considering the differences between new and old urban areas. In addition, each city's *Special Plan* has proposed a clear time node, that is, the total annual runoff in 20% (80%) of the built-up area should meet the control rate requirements by 2020 (2030). In short, at this stage, the sponge city constructions have not yet formed a whole. Sponge infrastructure is scattered, and the fragmented construction is serious. Therefore, the construction cannot play the overall effect of sponge infrastructure, and the effect of sponge city construction is not as expected.

From the main control indexes of each city mentioned above, we can find that sponge city construction has different focuses in different cities, and each city considers regional differences in terms of control indexes as well as construction objectives. At the same time, water culture-related content is further incorporated into sponge city planning, so the connotation of the sponge city is constantly expanded during the construction.

4.2 Construction content of typical sponge cities

The construction programs for water security, water resources, water ecology and water environment in the *Special Plan* of each city are shown in Table 5. For water security, the sponge city construction in each city contains three major approaches of ecological protection, ecological restoration, and low-impact development. The construction of rainwater drainage channels and the improvement of urban drainage systems are the priorities of construction. Meanwhile, the integration of gray and green infrastructures is emphasized. Zhengzhou and Xiangtan proposed to build flood protection dikes and consolidate river embankments based on their needs. Guangzhou, Zhuhai, and Yiyang focus on the management of waterlogging-prone spots in urban area. At the same time, these cities are restoring inland water systems, building natural water storage systems in wetland parks, and enhancing rainwater use and control as non-engineering measures to ensure water security. For water resources,

TABLE 5 Engineering and non-engineering measures for the construction of the typical sponge cities.

City	Water security		Water resources		Water ecology		Water environment	
	Engineering measures	Non-engineering measures	Engineering measures	Non-engineering measures	Engineering measures	Non-engineering measures	Engineering measures	Non-engineering measures
Shenzhen	Floodway construction	River cross-section regulation, rainwater drainage system construction	New storm sewers and reservoirs	Unconventional water resources utilization, adjustment of water source structure	Construction of ecological river cross-sections	Conservation of green space systems and water system protection	Construction of drainage pipelines, diversion of rain and sewage	Wetland purification and runoff control
Zhengzhou	Strengthening river embankments, building flood storage and detention areas and building drainage facilities	191 floodways are planned	Construction of water supply pipe network	Optimization of the allocation of water resources and the use of unconventional water resources	\	\	Rainwater reservoirs, sewage treatment plants	Comprehensive river course regulation and revitalized water flow project
Shijiazhuang	Construction of flood control facilities and improvement of drainage systems	Restoration of inland water systems, optimization of drainage zoning, and strengthening of Blue Line management	\	\	Construction of ecological river cross-sections	Regional runoff control, water system protection	Storm sewage diversion project	Malodorous black water treatment
Guangzhou	Construction of drainage facilities and treatment of waterlogging-prone spots	Sponge and wetland park construction	Renovation and expansion of water plants and reclaimed water plants	Ecological wetlands, ecological corridors	\	River ecological remediation	Construction or expansion of a sewage treatment plant	River remediation, constructed wetlands
Xicheng District, Beijing	Permeable pavement renovation, renovation and expansion of drainage systems	Stormwater control and utilization	Renovation of water supply pipe network and improvement of reclaimed water system	Optimization of the allocation of water resources	Shoreline landscape construction	Strengthening the management of blue lines of rivers and lakes, preventing and controlling soil erosion	comprehensive improvement of old residential areas, renovation of shanty towns	Control of non-point source pollution
Huai'an	Construction of flood control and drainage facilities	Strengthening the rainwater regulation and storage, and restoring the inland river system	Construction of rainwater harvesting facilities	Improving the utilization of unconventional water resources	Construction of ecological river cross-sections	Strengthening the water system protection and regional runoff control	Construction of rainwater sewage diversion system and sewage pipeline network	Smooth flow of running water, malodorous and black water treatment
Xiangtan	Construction of flood control dikes, drainage facilities, and floodway construction	Adjusting floodways and inland river connecting and dredging	Construction of sewage treatment plants and rainwater utilization facilities	\	Building ecological barges and sunken green spaces	Comprehensive improvement of river courses and restoration of bank zones	New rainwater sewage diversion pipe network and sewage pipe network	Ecological restoration, comprehensive improvement of river courses
Zhuhai	Construction of embankments and waterlogged spot treatment, and renovation of the drainage pipe network	Establishing water source protection zones and building coastal ecological coastlines	Renovation and expansion of green space systems and rainwater harvesting systems	Utilization of unconventional water resources	New reservoirs and regulating ponds	Construction of forest for water source conservation and restoration of wetlands	Construction of sewage interception ditches	River system dredging, malodorous and black water body remediation

(Continued on following page)

10.3389/feart.2023.1238203

TABLE 5 (*Continued*) Engineering and non-engineering measures for the construction of the typical sponge cities.

City	Water security		Water resources		Water ecology		Water environment	
	Engineering measures	Non-engineering measures	Engineering measures	Non-engineering measures	Engineering measures	Non-engineering measures	Engineering measures	Non-engineering measures
Zhuzhou	waterlogging-prone spots rectification, pipe network upgrading, 34 sewage pump stations construction	Comprehensive treatment of flood control water system	Construction of reclaimed water facilities and rainwater storage facilities	Utilization of unconventional water resources	Sunken green space, permeable paving, storage facilities	\	Storm sewage diversion retrofit	Remediation of malodorous and black water body, whole-process control of rainwater pollution
Lishui	Construction of the drainage system and rainwater runoff drainage system exceeding the standard	Multi-level rainwater storage and source regulation	Water supply pipe network, secondary water supply renovation	Unconventional water utilization, control of pipe network leakage, strengthening the technical archives management	Construction of urban artificial lakes and dredging of river courses	Returning fishing to lakes, returning farmland to lakes and transforming ecological shorelines	Construction of rainwater sewage diversion, sewage treatment facilities, and rainwater storage tanks	Street dredging, ecological restoration, water diversion, and replenishment
Yiyang	Floodway construction, renovation of drainage systems, and treatment of waterlogging points	River course rehabilitation	Construction of a reclaimed water reuse system	Establishing water source protection areas and emergency water source areas	\	\	Construction of sewage treatment plants, rainwater and sewage diversion	Remediation of malodorous and black water body, wetland construction

engineering measures (such as improving and expanding the urban water supply system and building rainwater storage tanks) and non-engineering measures (such as adjusting the water source structure and optimizing water resource allocation) are the main construction content, aiming to improve the urban water resource security rate. For water ecology, the cities focus on the "integration of gray and green infrastructures". Shenzhen, Shijiazhuang, Beijing and other cities combine the construction of ecological riverbanks and sunken green areas with the strengthening of water system protection, regional runoff control and the construction of green space systems to jointly safeguard urban water ecology. The eleven cities in the statistics have taken measures to improve the quality of the urban water environment and achieve the water environment construction objectives by using rainwater and sewage diversion renovation, building and expanding sewage recycling and treatment systems, conducting water treatment, restoring ecological wetlands and replenishing ecological water.

The above analyses and practices show that the current measures of sponge city construction focus on green infrastructures like ecological restoration and water environment management, and very few engineering measures such as drainage system construction are involved. Therefore, the construction of sponge city deviates from the original objective of flood control and waterlogging elimination, and is more inclined to restore the urban water environment and water ecology. However, the urgent issue that needs to be tackled in the current urban development process is the urban flooding issue. The "urban sea-watching" is essentially a failure of the urban flood control and drainage system (ZHANG C et al., 2023). The current sponge city construction focuses on the source control system. Most of these constructions are "green infrastructure", while urban drainage and de-risking rely more on the construction of "gray infrastructure" such as drainage networks. In addition, the flood control capacity of the source control system is limited (Feng et al., 2021), and the construction of sponge city in part area (with the old urban areas focusing on the management of waterlogging points) leads to the fragmentation of sponge city construction and planning (Ren, 2018). The overall urban flood control and drainage system cannot be changed. Thus, the current sponge city construction can only solve the waterlogging caused by poor drainage in local areas, while it is difficult to cope with the urban flooding under extreme rainfall. Therefore, at this stage, we should steadily and scientifically promote the construction of sponge city, reasonably plan the construction content and continuously optimize the configuration of "sponge infrastructures".

The investment in sponge city mainly involves seven aspects, including road traffic system, urban water system, building district renovation, garden and green space system, water supply and drainage system, capacity building and related projects outside the built-up areas. The investment of each city is shown in Table 6. It is found that except for Shijiazhuang, other cities mainly invest in road traffic system, urban water system and garden and green space system, accounting for more than 75% of the total investment. The proportion of investment in road traffic system exceeds 50% in Jinan and exceeds 25% in Zhengzhou, indicating that the sponge city construction of these two cities is mainly in urban infrastructure construction. Shijiazhuang's investment is mainly concentrated in the renovation of building

TABLE 6 Sponge city construction investment (Unit: 100 million yuan).

Cities	Road traffic system	Urban water system	Building district renovation	Garden and green space system	Capacity building	Related projects outside the built-up areas	Water supply and drainage system	Total
Jinan	76.40	35.00	8.00	2.80	2.60	16.00		140.80
Zhengzhou	137.10	138.10	57.50	139.90	1.00		61.20	534.80
Shijiazhuang	5.70	2.87	30.63	2.88	0.54		11.71	54.33
Xicheng District, Beijing				62.08	0.60		4.10	66.78
Wuhan	24.90	85.60	27.80	8.50			13.00	159.80
Suqian	7.31	81.64		24.96		0.89	21.13	135.93

districts and water supply and drainage facilities, accounting for 69.3% of the total investment. Then, the investment in sponge city construction is mainly concentrated in "sponge facilities", while the investment in disaster prevention and mitigation capabilities such as monitoring and early warning accounts for less than 1% of the total funds. At the same time, the "sponge facilities" are mainly concentrated in three aspects of green space square, urban roads and urban water system, where 48 of the 68 sponge projects in Hebi and 38 of 58 projects in Xixian New Area are green space, roads, and urban water systems. There is basically no project related to capability building. Therefore, the proportion of investment in sponge city construction is unbalanced, and there is a lack of financial support in the forecasting and early-warning operation and the urban hydrological system research that facilitate the development and construction of sponge city, which is precisely the basis for understanding the urban hydrological cycle and enhancing source control (Bell et al., 2016; Pande and Sivapalan, 2016).

The construction of sponge city is mainly based on water environment governance and water ecological restoration. Its content, such as water system management and green park construction, is mainly to improve the overall function of the city, and the construction of urban flood control and waterlogging elimination system (drainage facilities) accounts for a very low proportion of investment. Therefore, the effectiveness of sponge city construction cannot be assessed only from urban waterlogging elimination. In addition, sponge city construction overlaps with other urban planning. Most of the investment in current urban construction is categorized as the investment in sponge city construction. For example, the road traffic system investment accounts for more than 50% in Jinan and more than 25% in Zhengzhou, and the renovation of old residential areas in Wuhan accounts for more than 50%. Whether the construction of all these infrastructures can be counted as an investment in sponge city remains controversial. Therefore, we cannot just consider the investment in sponge city and a specific aspect when assessing the benefits of sponge city. Sponge infrastructure and ecological rivers play an important role in building new urban water systems, and sponge facilities and ecological restoration involve benefits from environmental, economic as well as social aspects. Therefore, when measuring the effectiveness of sponge city, we cannot just consider flood control and waterlogging elimination or deny the benefits of sponge city just because waterlogging occurs in the city.

5 Conclusion and suggestions

5.1 Conclusion

By reviewing the development history of sponge city concept in China and combining the construction content, measures and investment of typical sponge city, this paper expounds on the essence of sponge city in China, and draws the following two conclusions:

First, a scientific understanding of the sponge city is essential. Sponge city is not the same as low-impact development, and its concept has developed from low-impact rainwater system construction into new urban construction. It is a new model of integrated urban water system management, which is designed to

promote the harmonious development of urbanization, water resources and water ecology, aiming to further enhance the overall function of the city and make the city "resilient" to coping with natural disasters.

Second, the construction of sponge city is to systematically tackle the water issues in China's cities and to integrate rainwater management into the whole urban development and construction. And it can effectively combine flood and waterlogging control, water resources utilization, water environment protection and water ecological restoration to further enhance the comprehensive response to urban water issues.

5.2 Suggestions

Throughout the development of China's sponge city, the construction of sponge city has achieved remarkable results in the urban water ecological environment. However, there are still some problems in urban waterlogging control, multi-department and multi-level coordinated promotion. Based on this, two suggestions are put forward on promoting sponge city.

First, at the current stage, the construction goals, indexes, content and investment in sponge city are relatively broad, and are easily confused with other municipal construction content, thus leading to the "fragmentation" of sponge city system construction. Hence, we should scientifically promote the construction of sponge city, give priority to solving urban flooding, reasonably lay out the "sponge facilities" and give full play to their overall advantages.

Second, the fundamental problem of sponge city construction is the systematic governance of water. It not only involves the city itself, but also the watershed and the region. Therefore, in sponge city construction, we should emphasize the overall concept, coordinate different sectors,

Author contributions

SS: Information collecting, Writing—original draft. LW: Conceptualization, resources, writing—original draft, research design. YW: Resources, writing—review and editing. XS: Writing—review and editing. LL: Writing—review and editing. XX: Writing—review and editing. All authors contributed to the article and approved the submitted version.

Funding

The research was funded by National Key R&D Program of China (2021YF3000101-02), the National Natural Science Foundation of China (52109028, 52239008), the Natural Science Foundation of Jiangsu Province (BK20210042).

Conflict of interest

The authors declare that the research was conducted in the absence of any commercial or financial relationships that could be construed as a potential conflict of interest.

Publisher's note

References

Bell, C. D., Mcmillan, S. K., Clinton, S. M., and Jefferson, A. J. (2016). Hydrologic response to stormwater control measures in urban watersheds. *J. Hydrology* 541, 1488–1500. doi:10.1016/j.jhydrol.2016.08.049

Che, W., Zhao, Y., Li, J., Wang, W., Wang, J., Wang, S., et al. (2015). Explanation of sponge city development technical guide: Basic concepts and comprehensive goals. *China Water &Wastewater* 31 (08), 1–5. (in Chinese). doi:10.19853/j.zgjsps.1000-4602.2015.08.001

Eckart, K., Mcphee, Z., and Bolisetti, T. (2018). Multiobjective optimization of low impact development stormwater controls. *J. Hydrology* 562, 564–576. doi:10.1016/j.jhydrol.2018.04.068

Feng, C., Zhang, N., Habiyakare, T., Yan, Y., and Zhang, H. (2021). Prospects of eco-hydrological model for sponge city construction. *Ecosyst. Health Sustain.* 7. doi:10.1080/20964129.2021.1994885

Ge, W., Jiao, Y., Wu, M., Li, Z., Wang, T., Li, W., et al. (2022). Estimating loss of life caused by dam breaches based on the simulation of floods routing and evacuation potential of population at risk. *J. Hydrology* 612, 128059. doi:10.1016/j.jhydrol.2022.128059

Hou, X., Guo, H., Wang, F., Li, M., Xue, X., Liu, X., et al. (2020). Is the sponge city construction sufficiently adaptable for the future stormwater management under climate change? *J. Hydrology* 588, 125055. doi:10.1016/j.jhydrol.2020.125055

Jia, S. (2017). China should prioritize waterlogging prevention for recent urban storm water management. *Water Resour. Prot.* 33 (02), 13–15. (in Chinese). doi:10.3880/j.issn.1004-6933.2017.02.003

Li, W., Ma, H., Fu, R., Han, H., and Wang, X. (2022). Development and maintenance mechanisms of a long-lived mesoscale vortex which governed the earlier stage of the "21.7" henan torrential rainfall event. *Front. Earth Sci.* 10. doi:10.3389/feart.2022.909662

Pande, S., and Sivapalan, M. (2016). Progress in socio-hydrology: A meta-analysis of challenges and opportunities. *WIREs Water* 4. doi:10.1002/wat2.1193

Park, H., Paterson, R., Zigmund, S., Shin, H., Jang, Y., and Jung, J. (2020). The effect of coastal city development on flood damage in South Korea. *Sustainability* 12, 1854. doi:10.3390/su12051854

Qiu, B. (2015). Connotation, approach and prospect of sponge city (LID). *Constr. Sci. Technol.* 01, 11–18. (in Chinese). doi:10.16116/j.cnki.jskj.2015.01.003

Ren, N. (2018). *Don't fall into a misunderstanding about the construction of sponge city*. Beijing: Green Living, 78. (in Chinese).

Ren, N., Wang, Q., Wang, Q., Huang, H., and Wang, X. (2017). Upgrading to urban water system 3.0 through sponge city construction. *Front. Environ. Sci. Eng.* 11, 9. doi:10.1007/s11783-017-0960-4

Ren, N., Zhang, J., and Wang, X. (2020). Promoting the sponge city construction widely to eliminate urban waterlogging and create livable environment. *Acta Sci. Circumstantiae* 40 (10), 3481–3483. (in Chinese). doi:10.13671/j.hjkxxb.2020.0423

Tellman, B., Sullivan, J. A., Kuhn, C., Kettner, A. J., Doyle, C. S., Brakenridge, G. R., et al. (2021). Satellite imaging reveals increased proportion of population exposed to floods. *Nature* 596, 80–86. doi:10.1038/s41586-021-03695-w

Wang, H., Mei, C., and Liu, J. (2017). Systematic construction pattern of the sponge city. *J. Hydraulic Eng.* 48 (09), 1009–1014+1022. (in Chinese). doi:10.13243/j.cnki.slxb.20170308

Wu, M., Wu, Z., Ge, W., Wang, H., Shen, Y., and Jiang, M. (2021). Identification of sensitivity indicators of urban rainstorm flood disasters: A case study in China. *J. Hydrology* 599, 126393. doi:10.1016/j.jhydrol.2021.126393

Xia, J., Zhang, Y., Zhang, Y., Zou, L., and Wang, Q. (2017). Research and prospects of water problems in construction of sponge city in China. *Yangtze River* 48 (20), 1–5+27. (in Chinese). doi:10.16232/j.cnki.1001-4179.2017.20.001

Xu, Z., Ren, M., Cheng, T., and Chen, H. (2020). Treating non-responders: Pitfalls and implications for cancer immunotherapy trial design. *China Flood Drought Manag.* 30 (04), 20–24. (in Chinese). doi:10.1186/s13045-020-0847-x

Yoshikoshi, A., Adachi, I., Taniguchi, T., Kagawa, Y., Kato, M., Yamashita, A., et al. (2009). Hydro-environmental changes and their influence on the subsurface environment in the context of urban development. *Sci. Total Environ.* 407, 3105–3111. doi:10.1016/j.scitotenv.2008.11.030

Yu, K., Li, D., Yuan, H., Fu, W., Qiao, Q., Wang, S., et al. (2015). Sponge city: Theory and practice. *City Plan. Rev.* 39 (06), 26–33. (in Chinese). doi:10.1016/j.cbi.2015.06.010

Yuan, X., Wang, S., and Hu, Z.-Z. (2018). Do climate change and el niño increase likelihood of yangtze river extreme rainfall? *Bull. Am. Meteorological Soc.* 99, S113–S117. doi:10.1175/bams-d-17-0089.1

Zhang, C., Xu, T., Wang, T., and Zhao, Y. (2023). Spatial-temporal evolution of influencing mechanism of urban flooding in the Guangdong Hong Kong Macao greater bay area, China. *Front. Earth Sci.* 10. doi:10.3389/feart.2022.1113997

Zhang, H., Ge, W., Zhang, Y., Li, Z., Li, W., Zhu, J., et al. (2023). Risk management decision of reservoir dams based on the improved life quality index. *Water Resour. Manag.* 37, 1223–1239. doi:10.1007/s11269-023-03426-y

Zhang, L., Zhu, X., Kashima, H., Li, J., Ye, D. D., Liao, Q., et al. (2015). Anolyte recirculation effects in buffered and unbuffered single-chamber air-cathode microbial fuel cells. *Water & Wastewater Eng.* 51 (06), 26–34. (in Chinese). doi:10.1016/j.biortech.2014.11.106

frontiers | Frontiers in Earth Science

TYPE Original Research
PUBLISHED 21 July 2023
DOI 10.3389/feart.2023.1198431

OPEN ACCESS

EDITED BY
Wei Ge,
Zhengzhou University, China

REVIEWED BY
Bai Tao,
Xi'an University of Technology, China
Yuan Wenlin,
Zhengzhou University, China

*CORRESPONDENCE
Wenhao Han,
han0617521@163.com

RECEIVED 01 April 2023
ACCEPTED 17 April 2023
PUBLISHED 21 July 2023

CITATION
Chai Q, Han W, Wan F, Ding Z and Wu F (2023), Study on coordinated allocation of conventional and unconventional water resources in typical regions of North China.
Front. Earth Sci. 11:1198431.
doi: 10.3389/feart.2023.1198431

Study on coordinated allocation of conventional and unconventional water resources in typical regions of North China

Qihui Chai[1,2], Wenhao Han[1,2]*, Fang Wan[1,2], Zelin Ding[1,2] and Feng Wu[1,2]

[1]School of Water Resources, North China University of Water Resources and Electric Power, Zhengzhou, China, [2]Henan Key Laboratory of Water Resources Conservation and Intensive Utilization in the Yellow River Basin, North China University of Water Resources and Electric Power, Zhengzhou, China

Introduction: The North China Plain is an important production base of grain, cotton, and fruits in China. However, the climate is dry and rainless, and thus, water resources are scarce. The combination of water resources, population, and cultivated land is extremely unbalanced, making the region a serious water shortage area in China. In addition to long-term groundwater over-exploitation, water shortage has become an important bottleneck, restricting the economic and social development of the North China Plain and national food security. Therefore, making full use of unconventional water resources and reducing the proportion of conventional water resources will alleviate the shortage of water resources and improve the utilization of water resources.

Methods: Taking Hengshui City as an example, this paper establishes an optimal allocation model of water resources with the minimum relative water shortage rate as the objective function, the coordinated allocation of water resources between conventional and unconventional water resources is studied, and various available water sources are effectively allocated between regions and water use departments. The genetic algorithm is used to study the model, by taking 2020 as the starting year, and optimize the allocation of water resources in Hengshui City between 2020 and 2025.

Results and Discussion: The results show that the water demand of each county in Hengshui City will be guaranteed in 2025, and there will be no water shortage. In the 2025 level year, the total amount of unconventional water resources in Hengshui City will increase compared with that in 2020, with an increase of 21.9144 million m^3. Among them, there will be an increase in brackish water consumption, 11.3244 million m^3, and an increase in sewage reuse water consumption, 10.59 million m^3, which will effectively alleviate the contradiction between supply and demand of water resources in Hengshui City.

KEYWORDS

coordinate allocation of water resources, unconventional water resources, genetic algorithm, typical area of Hebei, Hengshui City

1 Introduction

The North China Plain is an important production base of grain, cotton, and fruits in China. However, the climate in this area is dry and rainy, and water resources are scarce. The *per capita* water resources are 523 m^3, and the average water resources are 309 m^3, which are 1/4 and 1/5 of the national average, respectively. The combination of water resources, population, and cultivated land is extremely unbalanced, making the region a serious water shortage area in China. Long-term groundwater over-exploitation has formed a groundwater "funnel group" consisting of a series of funnels with an area of 40, 000 km^2 in the Hebei Plain, causing a series of ecological and geological hazards, such as land subsidence and collapse. The shortage of water resources has become an important bottleneck, restricting the economic and social development of the North China Plain and national food security (Li et al., 2021).

The utilization of unconventional water resources in northern China is relatively low, and it is necessary to increase the proportion of unconventional water supply, which is also an important measure to alleviate the current water shortage (Li et al., 2022; Huang et al., 2021; Wu et al., 2020). It is of great significance to develop unconventional water resources according to local conditions to alleviate the shortage of water resources in the North China Plain. In the North China Plain, except for Beijing, underground salt water with salinity greater than 2 g/L is widely distributed, and its distribution area is 7.11×10^4 km^2, accounting for 51.48% of the total area of 13.81×10^4 km^2. The recoverable resources of salt water with TDS<5 g/L in the North China Plain are approximately 30×10^8 m^3, and there are still 13.51×10^8 m^3 of salt water resources that have not been developed and utilized. The shallow salt water has the characteristics of easy exploitation, fast supply, and low energy consumption. The utilization potential of shallow salt water should be fully explored (Zhang D. et al., 2022; Ma et al., 2020). The North China Plain is densely populated. With the acceleration of urbanization, reclaimed water, as a product of daily urban operation, has a low utilization rate and great potential for excavation (Zhang, 2013). In order to solve the increasingly acute contradiction between supply and demand of water resources, it is imperative to increase the development and utilization of unconventional water resources (Zhu, 2020; Wu X. et al., 2021; Wang et al., 2023). With the economic development, population growth, and urban expansion, the demand for water resources in cities is increasing year by year, and the contradiction between supply and demand is prominent. Under the background of global traditional water shortage, making full use of unconventional water resources has become an important means to alleviate urban water pressure (Liu, 2017; Morante-Carballo et al., 2022; Zhang et al., 2023).

This paper chooses Hengshui City to carry out the optimal allocation of unconventional and conventional water resources. Hengshui City belongs to the Heilongjiang area, and the distribution area of salt water is 91.8%, which belongs to the typical salt water distribution area of the North China Plain. At the same time, Hengshui is a large agricultural city, and agricultural irrigation water accounts for approximately 83% of the city's water supply. Water resources are over-exploited, groundwater over-exploitation is serious, and food production is not effectively guaranteed. It is crucial to incorporate the development and utilization of unconventional water resources into the water resource management system (Liang and Zuo, 2012; Hu and Wu, 2018). Therefore, Hengshui is considered a strong representative of the unconventional water resource in the arid middle and lower reaches of the plains in northern China. This research can provide some experience and reference for the coordinated allocation of water resources in other arid middle and lower reaches of the plains in northern China.

2 Present situation of water resource development and utilization in Hengshui City

The data on the utilization status of conventional water resources and unconventional water resources in this part are derived from "Hengshui City Water Resources Planning."

2.1 Conventional water resource utilization status

Hengshui City, in 2015, had a total water supply of 1.539 billion m^3. From the perspective of water supply, surface water supply is 265 million m^3, groundwater supply is 1.273 billion m^3, and sewage treatment and reuse water supply is 590, 000 m^3, accounting for 17.2%, 82.7%, and 0.1% of the total water supply, respectively. From the perspective of water consumption, agricultural water consumption is 1.31 billion m^3, industrial water consumption is 108 million m^3, domestic water consumption is 105 million m^3, and ecological environment water consumption is 9 million m^3, accounting for 85%, 7%, 7%, and 1% of the total water consumption, respectively. In 2015, Hengshui City's overdraft deep groundwater was 900 million m^3. Conventional water resources still account for the vast majority of water supply, and the main source of water consumption is agricultural water. Therefore, making full use of unconventional water resources and reducing the proportion of conventional water resources will alleviate the shortage of water resources and improve the utilization of water resources (Feng, 2015).

2.2 Status of unconventional water resource utilization

2.2.1 Development and utilization of salt water resources

The natural resources of shallow groundwater in the brackish water area of Hengshui City are 767.0694 million m^3/a, of which the natural resources of shallow freshwater are 19.7963 million m^3/a, and the natural resources of shallow brackish water are approximately 747.2731 million m^3/a (the natural resources of salinity 1~2 g/L, 2~3 g/L, 3~5 g/L, and > 5 g/L are 119.5131 million m^3/a, 285.4454 million m^3/a, 238.4545 million m^3/a, and 123.6564 million m^3/a, respectively).

The exploitable resources of shallow groundwater in the saline water area of Hengshui City are 415.9866 million m^3/a, of which the

exploitable resources of shallow fresh water are 14.8664 million m^3/a, and the exploitable resources of shallow saline water are approximately 401.1202 million m^3/a (the exploitable resources of salinity 1~2 g/L, 2~3 g/L, 3~5 g/L, and >5 g/L are 59.547 million m^3/a, 174.0753 million m^3/a, 144.4893 million m^3/a, and 23.0086 million m^3/a, respectively).

2.2.2 Development and utilization of reclaimed water resources

Since 2014, Hengshui City reclaimed the water treatment capacity will usher in a new peak of growth. However, at present, the utilization of reclaimed water is less and the utilization method is relatively single. Taking the Hengshui sewage treatment plant as an example, the annual main pollutant emission reductions amount to COD 6558 tons, BOD 2218 tons, SS 4417 tons, TN 948 tons, and TP 119 tons, and the effluent is finally discharged into the Fuyang River. The reclaimed water utilization mainly includes more than 20, 000 tons of landscape water.

2.3 Problems in development and utilization of water resources

At present, the main problems of water resource development and utilization in Hengshui City are as follows.

2.3.1 Shortage of water resources

Hengshui City is located in the south of the Haihe River Basin. Since the origin of the People's Republic of China, after years of construction and development, the average annual water supply in the Haihe River Basin has been increased to 37.2 billion m^3, the development and utilization rate has reached 81%, the actual water use has reached 43.2 billion m^3, and the total local water resources have reached 37.2 billion m^3. Due to the over-exploitation of water resources, upstream reservoir construction, and interception of runoff, it resulted in a sharp reduction in downstream rivers or cut off, which seriously affected the downstream areas of domestic, industrial, and agricultural water usage.

2.3.2 Serious over-exploitation of groundwater

The domestic and agricultural water in Hengshui City is dominated by groundwater. After years of exploitation, the groundwater level continues to decline, the salt–fresh water interface moves down, and the groundwater quality deteriorates.

2.3.3 Low utilization of water resources: an imperfect water-saving mechanism

Hengshui City is a large agricultural city, and agricultural irrigation water accounts for approximately 83% of the city's water supply. Its traditional agricultural planting structure is mainly wheat, corn, and other crops with high water consumption and low efficiency. Field irrigation is mainly flood irrigation, and the utilization rate of flood irrigation water is only approximately 45%.

2.3.4 Low utilization rate of unconventional water resources

The utilization rate of reclaimed water, such as the water used for farmland irrigation, urban ecology, family life, and urban landscaping, in Hengshui is still very low. It is mainly used in urban landscaping and shows great potential for excavation. The overall utilization of rainwater in Hengshui is in the early stages of development. In addition to the demonstration collection and utilization projects built by individual units in Hengshui City, most of them are still in the blank stage, and the understanding of rainwater as a resource is not enough. With the development of urban construction, the city's hardening area is increasing and the city's permeable area is shrinking, so surface water cannot infiltrate into the ground to increase the groundwater composition. Underground pipe network construction is seriously lagging behind. Most of the pipe network construction still follows the traditional direct discharge and dredging mode, resulting in the loss of rainwater resources. The city lacks systematic rainwater utilization planning, and there are no relevant laws and regulations to provide support and guarantee for the systematic utilization of rainwater (Shadeed et al., 2020; Ge et al., 2022; Wang et al., 2022; Wu M et al., 2021). The use of brackish water in Hengshui City is relatively extensive, but it is mainly used for direct irrigation with 2~3 g/L brackish water, and 3–10 g/L brackish water and salt water still show great development potential.

3 Co-ordinated allocation of conventional and unconventional water resources in Hengshui City

In order to make use of the limited unconventional and conventional water resources, both the water resources can be scientifically allocated between different water use sectors of agriculture, industry, construction, tertiary industry, domestic usage, and ecological usage. This chapter uses the basic connotation of the coordinated allocation of unconventional and conventional water resources, comprehensively considering the economic development status and planning of the study area, and focuses on the following principles when incorporating unconventional water resources into the unified allocation of water resources.

3.1 Principles of collaborative optimal allocation of water resources

3.1.1 Principles of water supply by quality

Although it is currently technically feasible to purify unconventional water resources to drinking water, considering other issues, such as production costs, potential risks, and social acceptance, unconventional water resources need to be used for other purposes other than drinking water, such as urban ecology, industry, and agriculture (Jodar-Abellan et al., 2019; Ge et al., 2020a; Zhang Y et al., 2022). Therefore, according to the water demand of different users, it is necessary to carry out targeted quality water supply, high quality and excellent use.

3.1.2 Principles of water safety

The water security principle is mainly reflected in two aspects: one is to give priority to meet the domestic and ecological water demands, on this basis, considering the rational allocation of

construction, tertiary industry, and industrial and agricultural water. Second, considering the stability and efficiency of the water supply guarantee rate, surface water is preferentially supplied for domestic, industrial, and agricultural usage, followed by the exploitation of groundwater (Ge et al., 2020b). The treatment cost of unconventional water resources is also much smaller than the corresponding water transfer cost. Therefore, the principle of controlling groundwater exploitation and expanding the scale of unconventional water resource utilization is adhered to, and the water supply order of each water source is defined as follows: reclaimed water, mine drainage water, surface water, and groundwater (Kim et al., 2022; Mu and Wang, 2020).

3.2 Establishment of the collaborative optimal allocation model of water resources

3.2.1 Objective function

For optimal allocation of water resources, the minimum relative water shortage rate is generally selected as the objective function, but the objective is a cumulative value, which cannot reflect the depth of water supply damage and the quality of the water supply process. According to the uniformity of water distribution in time and space, the storage capacity of water conservancy projects can be fully exerted. In the calculation period T, the water supply process with time and space uniformity is selected as the objective function of water supply scheduling, that is, the maximum water shortage rate in a certain period of the water supply process is the minimum. The objective function is

$$f(x) = \min \max_t \left[(Q_t - G_{0,t} - X_t)/Q_t \right]. \tag{1}$$

In the formula, Q_t is the water demand of the water supply area in the period t; $G_{0,\ t}$ is the conventional water supply of the water supply area in the period t; X_t is the water supply of unconventional water in the period t; $t = 1, 2, \ldots,$ T, where T is the number of water supply periods.

The model of the minimum–maximum water shortage rate can make the water supply process and water shortage loss in the water supply area uniform so that the water shortage in a certain period is not very serious in order to meet the water demand of the previous period, which can reduce the damage depth of water shortage, improve the uniformity of the water supply process, and effectively reduce the maximum damage depth (Li et al., 2018).

3.2.2 Constraint conditions

3.2.2.1 Water supply condition constraints

The supply of water resources shall not exceed the total supply of water resources; the expressible formula is

$$\sum_{k=1}^{\sigma}\sum_{i=1}^{m}\sum_{j=1}^{n} x_{ij}^{k} \le W_S. \tag{2}$$

In this formula, W_S is the total supply of water resources, 10,000 m^3; x^k_{ij} is the water supply of the i water source to j users in k area; k is the water supply area, a total of σ; i is the source of water supply, including surface water, groundwater, reclaimed water, mine drainage water, and brackish water, a total of m; j for different users, including life, tertiary industry, industry, agriculture, construction, and ecology, a total of n. Because the surface water and groundwater in the available water resources are conventional water resources, it is necessary to pay attention to conservation. The total amount of available surface water and groundwater cannot exceed the red line of the total amount control of surface water and groundwater in Hengshui while not exceeding the calculated available water.

3.2.2.2 Unconventional water supply constraints

$$h^k \le \frac{x_{3j}^k + x_{4j}^k + x_{5j}^k}{\sum_{i=1}^{m} x_{ij}^k} \le H^k. \tag{3}$$

In this formula, x^k_{3j}, x^k_{4j}, and x^k_{5j} are the water supply of reclaimed water, mine drainage water, and brackish water to j users, respectively. Taking into account the principle of water supply and water supply network constraints, domestic water and tertiary industry water do not consider unconventional water; h^k and H^k are the minimum and maximum water supply ratios of unconventional water resources of j users in k area, respectively.

3.2.2.3 Contamination carrying capacity constraints

COD emissions should not be greater than the regional *COD* capacity; the expressible formula is

$$\sum_{j=1}^{n} 0.01 d_j p_j \sum_{i=1}^{m} x_{ij}^k \le \theta^k COD. \tag{4}$$

In this formula, $\theta^k COD$ is the maximum *COD* capacity in k region, t.

3.2.2.4 Effective irrigation area constraint

The water consumption of the irrigation area in the same level year should be higher than the predicted water consumption of the low scheme but lower than the predicted water consumption of high scheme; the expressible formula is

$$N_1^k C^k \le x_g^k \le N_2^k C^k. \tag{5}$$

In this formula, N^k_1 and N^k_2 are the predicted values of the effective irrigation area of low scheme and high scheme in the k region, respectively, km^2; C^k is the water requirement per unit effective irrigation area in the k region, 0.01m, referencing to the Gansu Province water quota value; x^k_g is the irrigation water consumption to k area, 10,000 m^3, and x^k_g is contained in agricultural water.

3.2.2.5 Tertiary industry output value constraint

The output value of the tertiary industry in the planning year should be greater than the planning value target; the expressible formula is

$$\sum_{k=1}^{\sigma}\sum_{k=1}^{m} x_{i3}^k \cdot \alpha_{i3}^k \ge 10^4 Z_3. \tag{6}$$

In this formula, x^k_{i3} is the water supply of the tertiary industry in the k region, 10000 m^3; α^k_{i3} is the economic output value of unit water resources of the tertiary industry in the k region, yuan/m^3; Z_3 is the tertiary industry output value planning target, 100 million yuan.

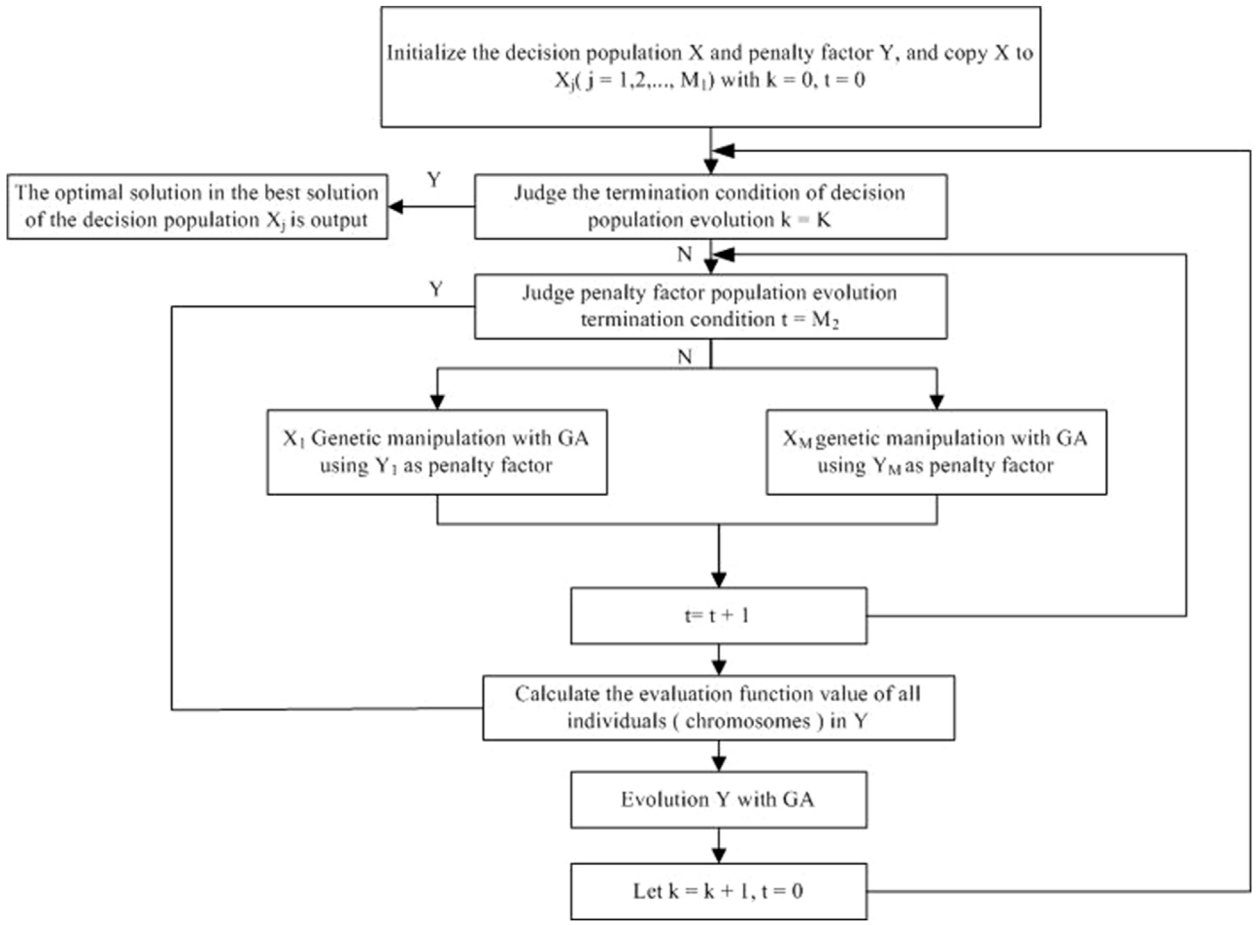

FIGURE 1
Solution flow chart based on genetic algorithm.

3.2.2.6 Non-negative constraint

Water supply is non-negative; the expressible formula is

$$x_{ij}^{k} \geq 0. \tag{7}$$

4 Model solution of collaborative optimal allocation of water resources

The genetic algorithm (GA) was first proposed by Professor Holland of Michigan University in 1975. The basic idea was based on Darwin's theory of evolution and Mendel's theory of genetics. The recombination and mutation operators were the two most important components of GA, and they were repeatedly applied to the chromosomes formed by encoding the solution of the problem. This is a new global optimization search algorithm, simple and universal, robust, and suitable for parallel processing; based on the fitness function, the genetic operation is applied to the individuals in the group to realize the reorganization of the individual structure in the group so that the individuals in the group can be optimized and gradually approach the global optimal solution. It can calculate multidimensional problems in optimal allocation of water resources.

In this paper, a set of basic feasible decoding of the problem is expressed as a set of binary strings. Each string contains multiple substrings. The combination of one or more bits of each substring is called a gene, also known as a chromosome. Then, some operations are carried out on these genes (chromosomes) to gradually realize parameter optimization and achieve the purpose of optimal allocation of water resources.

At the beginning of the genetic algorithm, some individuals (initial solutions) are randomly generated; each individual is evaluated according to the predetermined objective function (1), and the fitness value of the individual is given. Based on the fitness value, the individual is selected to copy the next generation. The selection operation embodies the "survival of the fittest" principle, in which "good" individuals are selected for replication and "bad" ones are eliminated. Then, the selected individuals are recombined by exchange and mutation operators to generate a new generation. This new group of individuals inherits some of the good traits of the previous generation and is therefore superior in performance. The genetic algorithm realizes the process of optimal allocation of water resources by simulating the three ways of replication, exchange, and mutation of biological genes. The specific process is shown in Figure 1. The specific steps are as follows:

TABLE 1 Statistics on water supply in counties and districts of the Hengshui City in 2020 unit: 10^4 m^3.

County name	Groundwater				Surface water				External water diversion	Waste water reuse	Total
	Deep well	Shallow well	Brackish water	Subtotal	Water diversion project	Electro mechanical site	Water storage project	Subtotal			
Taocheng District	1762.15	73.05	78.49	1913.69	1549.84	0.00	1778.17	3328.01	7221.13	306.32	12769.15
Jizhou City	2461.57	319.58	89.09	2870.24	2239.46	3951.40	982.04	7172.90	2434.12	334.27	12811.52
Zaoqiang County	3550.94	1934.27	0.00	5485.21	5741.55	0.00	0.00	5741.55	3702.11	0.00	14928.87
Wuyi County	3446.85	761.19	152.96	4361.00	1411.98	0.00	5660.63	7072.61	991.39	727.11	13152.11
Shenzhou City	3931.07	1950.99	0.00	5882.06	24302.7	0.00	0.00	24302.71	811.33	323.97	31320.07
Wuqiang County	3667.01	0.00	0.00	3667.01	1493.24	0.00	4195.47	5688.71	293.19	88.74	9737.65
Raoyang County	3167.32	667.83	0.00	3835.15	5456.48	0.00	653.24	6109.72	351.66	169.04	10465.57
Anping County	3019.41	2732.15	59.69	5811.25	77.56	0.00	5191.62	5269.18	310.37	0.00	11390.81
Gucheng County	1622.96	1598.84	308.47	3530.27	4573.24	0.00	1239.99	5813.23	1842.97	1016.76	12203.23
Jing County	5251.99	874.29	0.00	6126.28	5949.23	0.00	0.00	5949.23	5367.03	1010.61	18453.15
Fucheng County	5860.25	493.47	0.00	6353.72	7825.15	0.00	1243.85	9069.00	1776.72	605.69	17805.13
New industrial district	85.27	22.65	21.97	129.89	0.00	0.00	0.00	0.00	1745.02	901.49	2776.40
Lakeside new district	385.82	19.68	11.01	416.51	0.00	165.80	189.80	355.60	735.76	0.00	1507.87
Whole city	38212.60	11447.9	721.68	50382.26	60620.4	4117.20	21134.8	85872.45	27582.79	5484.00	169321.50

10.3389/feart.2023.1198431

TABLE 2 Statistical table of water supply in counties and districts of Hengshui City in 2022 unit: 10^4 m^3.

County name	Groundwater				Surface water				External water diversion	Waste water reuse	Total
	Deep well	Shallow well	Brackish water	Subtotal	Water diversion project	Electro mechanical site	Water storage project	Subtotal			
Taocheng District	2321.88	71.27	262.70	2655.85	2570.03	0.00	2078.16	4648.19	9448.26	365.35	17117.6
Jizhou City	1584.46	274.28	271.40	2130.14	2637.53	4511.66	800.83	7950.02	4583.22	398.69	15062.1
Zaoqiang County	2285.66	1660.06	0.00	3945.72	5534.36	0.00	0.00	5534.36	9021.24	0.00	18501.3
Wuyi County	2211.76	636.12	449.75	3297.63	6861.26	0.00	2629.96	9491.22	1835.78	867.17	15491.8
Shenzhou City	1530.41	1686.64	0.00	3217.05	21054.12	0.00	876.45	21930.57	9227.59	388.88	34764.1
Wuqiang County	2060.38	0.00	0.00	2060.38	1985.22	0.00	6066.78	8052.00	875.12	105.83	11093.3
Raoyang County	2038.73	573.15	0.00	2611.88	7513.17	0.00	868.46	8381.63	688.83	201.60	11883.9
Anping County	784.91	2173.18	0.00	2958.09	6941.12	0.00	2482.28	9423.40	607.96	0.00	12989.4
Gucheng County	1044.66	1372.18	643.90	3060.74	6079.98	0.00	775.19	6855.17	4317.84	1212.65	15446.3
Jing County	3380.59	750.35	0.00	4130.94	7254.04	0.00	0.00	7254.04	10512.99	1205.32	23103.3
Fucheng County	4093.95	423.51	0.00	4517.46	8475.56	0.00	3522.06	11997.62	3480.26	722.36	20717.7
New industrial district	376.72	19.44	184.22	580.38	226.91	0.00	0.00	226.91	1570.71	1075.16	3453.16
Lakeside new district	248.34	16.89	42.15	307.38	0.00	189.32	900.01	1089.33	695.10	0.00	2091.82
Whole city	23962.47	9657.08	1854.12	35473.67	77133.29	4700.98	21000.2	102834.4	56864.89	6543.00	201716

10.3389/feart.2023.1198431

TABLE 3 List of unconventional water resource growth in 2025 unit: 10^4 m^3.

	Year 2020	Year 2025	Increment
Brackish water	721.68	1854.12	1132.44
Sewage reuse	5484	6543	1059
Total	6205.68	8397.12	2191.44

Step 1: Individual coding: Taking the amount of water distributed to each user as the decision variable Z, the decision variables are coded and a feasible solution set is formed.

Step 2: Initializing the decision population and penalty factor population: The algorithm parameters are assigned, several sets of initial water resources pre-allocation schemes are randomly generated, and some relatively better allocation schemes are selected as the initial scheme set for the next optimization. The population size is L_1, and L_2 copies are M populations. Taking w_1 and w_2 as penalty factors, the population Y with L_2 penalty factors is randomly generated, where $Y_J = (w_{1J}, w_{2J})(J = 1, 2, \ldots, L_2)$.

Step 3: Formula (1) is used as the fitness function to evaluate the advantages and disadvantages of each individual in the population.

Step 4: Genetic operations of decision population and penalty factor population: For each sub-population Z in the decision population M, the individuals with the same number in the population Y are used as penalty factors, and the GA algorithm is used to evolve until the number of iterations is set. The GA algorithm is used to evolve the next generation of population Y so as to obtain a new penalty factor population Y.

Step 5: Iterations of the algorithm: After the end of the first generation co-evolution, Step 4 is repeated, until the convergence criterion of the algorithm is reached.

Step 6: Output of the optimal solution. By comparing all the historically best solutions obtained in the population M, the optimal solution is output as the final solution and the optimal individual in the population Y is the optimal penalty factor.

5 Calculation results and analysis

Based on the present situation of water resource development and utilization in counties and cities of Hengshui City, the conventional and unconventional water resources between 2020 and 2025 are allocated accordingly. Among them, the water supply situation of counties and districts in Hengshui City in 2020 is as shown in Table 1; the water supply of each county in Hengshui in 2025 is shown in Table 2. Among them, the basic data from 2020 are derived from the "Hengshui City Water Resources Bulletin," and the basic data for 2025 are predicted based on a large amount of data. Due to the limited space, this paper does not elaborate on the prediction model.

The growth of unconventional water resources in 2025 is shown in Table 3; the proportion of conventional and unconventional water resources between 2020 and 2025 level years is shown in Figures 2, 3.

Analysis of water supply and water use in counties and cities of Hengshui City in the 2025 level year shows that according to the configuration results in Table 2, from the perspective of each user, it can be seen that the water supply and demand in counties and cities of Hengshui City in the 2025 level year is relatively balanced. Compared with other water use sectors, the agricultural sector has the largest water demand. In order to avoid the contradiction between supply and demand of water resources, strengthening agricultural water conservation will be the focus of future work.

From the perspective of water supply sources, the water supply ratio of groundwater, surface water, external water transfer, and unconventional water will be 29%, 51%, 16%, and 4% after the allocation of counties and districts in Hengshui City in 2020 (Figure 2); In 2025, the proportion of groundwater, surface water, external water transfer, and unconventional water supply in each county of Hengshui City is 17%, 51%, 28%, and 4%, respectively (Figure 3). Compared with the 2020 level year, surface water will still remain the largest source of water supply in Hengshui City; by 2025, groundwater consumption will continue to decrease, and the amount of water supply for external water transfer will increase. According to Table 3, compared with the 2020 level year, the total amount of unconventional water resources in Hengshui City will increase by the 2025 level year, with an

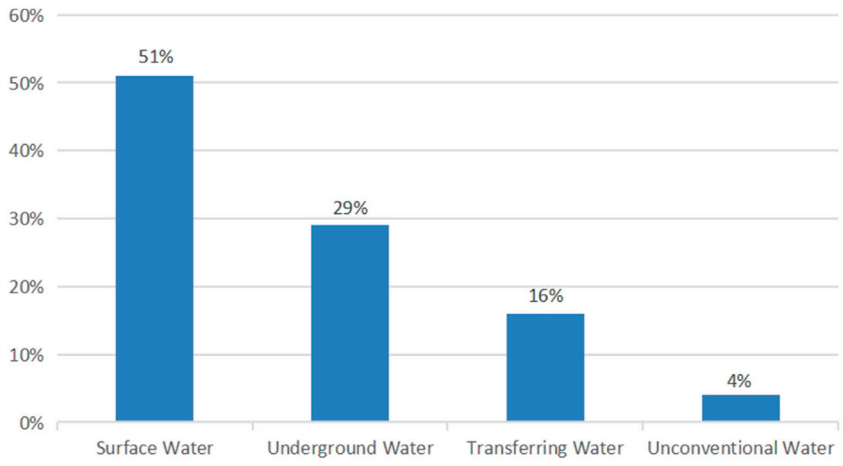

FIGURE 2
Proportion of water resources allocation in Hengshui City in 2020.

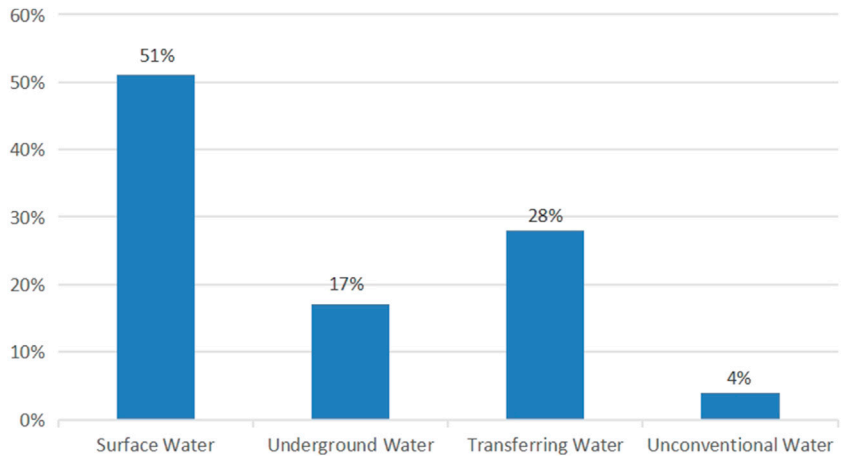

FIGURE 3
Proportion of water resources allocation in Hengshui City in 2025 level year.

increase of 21.9144 million m^3, of which the increase in brackish water consumption would be 11.3244 million m^3, and the increase in sewage reuse water consumption will be 10.59 million m^3.

6 Conclusion

The North China Plain is an important grain, cotton, fruit, and vegetable production base in China. The grain production accounts for 29.6% of the total grain production in the country, and the vegetable production accounts for 42.7% of the national vegetable production. The area uses less than 1/2 of its total arable land to produce 80% of vegetables, 65% of grain, and 60% of economic crops. However, the climate in this area is dry and rainy, and the water resources are scarce. The *per capita* water resources are 523 m^3, and the average water resources are 309 m^3, which are 1/4 and 1/5 of the national average, respectively. The combination of water resources, population, and cultivated land is extremely unbalanced, making this area a serious water shortage area in China. Long-term groundwater over-exploitation has formed a groundwater "funnel group" consisting of a series of funnels with an area of 40, 000 km^2 in the Hebei Plain, causing a series of ecological and geological hazards, such as land subsidence and collapse. The shortage of water resources has become an important bottleneck, restricting the economic and social development of the North China Plain and national food security. Therefore, this study takes Hengshui City as an example to study the coordinated allocation of water resources between conventional and unconventional water resources. The results show that from the perspective of each user, the water demand of each county and city in Hengshui City will be guaranteed in 2025, and there will be no water shortage. From the perspective of each user, the water supply and demand of each county and city in Hengshui City will be relatively balanced by 2025. Compared with other water use sectors, the agricultural sector has the largest water demand. In order to avoid the contradiction between supply and demand of water resources, strengthening agricultural water saving and inhibiting water demand will be the focus of future work. The planned use of unconventional water resources, such as reclaimed water and rainwater, is a good way to turn waste water and sewage into resources, which is a feasible way to effectively alleviate the imbalance between supply and demand of water resources; the coordinated allocation of conventional water and unconventional water resources can maximize the comprehensive benefits of society, economy, and ecological environment.

Data availability statement

The original contributions presented in the study are included in the article/Supplementary Material; further inquiries can be directed to the corresponding author.

Author contributions

Conceptualization: QC and WH; methodology: QC; software, WH; validation: WH, ZD, and FW; formal analysis: ZD; investigation: FW and ZD; data curation and writing—original draft preparation: FWu; writing—review and editing: WH; supervision: FWu. All authors contributed to the article and approved the submitted version.

Funding

This research was funded by the General Project of Science Foundation in the Henan Province (222300420491) and the Major Science and Technology Special Projects in the Henan Province (201300311400).

Conflict of interest

The authors declare that the research was conducted in the absence of any commercial or financial relationships that could be construed as a potential conflict of interest.

Publisher's note

References

Feng, J. D. (2015). Research on the utilization of urban unconventional water resources [J]. *Innovation Appl. Sci. Technol.*, (23), 178.

Ge, W., Jiao, Y., Wu, M., Li, Z., Wang, T., Li, W., et al. (2022). Estimating loss of life caused by dam breaches based on the simulation of floods routing and evacuation potential of population at risk. *J. Hydrology* 612, 128059. doi:10.1016/j.jhydrol.2022.128059

Ge, W., Li, Z., Li, W., Wu, M., Li, J., and Pan, Y. (2020a). Risk evaluation of dam-break environmental impacts based on the set pair analysis and cloud model. *Nat. Hazards* 104, 1641–1653. doi:10.1007/s11069-020-04237-9

Ge, W., Qin, Y., Li, Z., Zhang, H., Gao, W., Guo, X., et al. (2020b). An innovative methodology for establishing societal life risk criteria for dams: A case study to reservoir dam failure events in China. *Int. J. Disaster Risk Reduct.* 49, 101663. doi:10.1016/j.ijdrr.2020.101663

Hu, Y. Q., and Wu, W. Y. (2018). Current situation and development strategy of agricultural unconventional water resources irrigation in China [J]. *China Eng. Sci.* 20 (05), 69–76. doi:10.15302/J-SSCAE-2018.05.011

Huang, Y. Q., Yu, D. S., Shen, C. S., et al. (2021). Utilization status and countermeasures of unconventional water resources in guiyang city [J]. *Compr. Util. Resour. China* 39 (1), 83–85. doi:10.3969/j.issn.1008-9500.2021.01.025

Jodar-Abellan, A., López-Ortiz, M. I., and Melgarejo-Moreno, J. (2019). Wastewater treatment and water reuse in Spain. Current situation and perspectives. *Water* 11 (8), 1551. doi:10.3390/w11081551

Kim, B. R., Lee, S.-I., and Yu, S. M. (2022). Conjunctive operation of sand dam and groundwater well for reliable water supply during drought conditions. *Water* 14, 2249. doi:10.3390/w14142249

Li, J., Song, S. B., Wang, X. J., et al. (2022). Coordinated allocation model of regional conventional and unconventional water resources considering different stakeholders [J]. *Appl. J. Fundam. Eng. Sci.* 30 (1), 50–63. doi:10.16058/j.issn.1005-0930.2022.01.005

Li, Z., Li, W., and Ge, W. (2018). Weight analysis of influencing factors of dam break risk consequences. *Nat. Hazards Earth Syst. Sci.* 18 (12), 3355–3362. doi:10.5194/nhess-18-3355-2018

Li, Z., Zhang, Y., Wang, J., Ge, W., Li, W., Song, H., et al. (2021). Impact evaluation of geomorphic changes caused by extreme floods on inundation area considering geomorphic variations and land use types. *Sci. Total Environ.* 754, 142424. doi:10.1016/j.scitotenv.2020.142424

Liang, S. k., and Zuo, Q. T. (2012). Discussion on key issues of unconventional water resources utilization-A case study of xinmi city [J]. *South-to-North Water Divers. Water Conservancy Technol.* 10 (03), 109–112. + 153. doi:10.3724/SP.J.1201.2012.03109

Liu, F. (2017). *Utilization strategy and safeguard measures of unconventional water resources in Xiamen [D]*. Xiamen University.

Ma, T., Liu, J. F., Peng, A. B., et al. (2020). Advances in unconventional water resources development and utilization in China [J]. *Adv. water Sci.* 31 (06), 960–969. doi:10.14042/j.cnki.32.1309.2020.06.015

Morante-Carballo, F., Montalván-Burbano, N., Quiñonez-Barzola, X., Jaya-Montalvo, M., and Carrión-Mero, P. (2022). What do we know about water scarcity in semi-arid zones? A global analysis and research trends. *Water* 14 (17), 2685. doi:10.3390/w14172685

Mu, Y., and Wang, J. L. (2020). The application status and utilization prospects of several unconventional water resources [J]. *Sci. Technol. horizon* (11), 222–224. doi:10.19694/j.cnki.issn2095-2457.2020.11.083

Shadeed, S., Judeh, T., and Riksen, M. (2020). Rainwater harvesting for sustainable agriculture in high water-poor areas in the west bank, Palestine. *Water* 12 (2), 380. doi:10.3390/w12020380

Wang, T., Li, Z., Ge, W., Zhang, H., Zhang, Y., Sun, H., et al. (2023). Risk consequence assessment of dam breach in cascade reservoirs considering risk transmission and superposition. *Energy* 265, 126315. doi:10.1016/j.energy.2022.126315

Wang, T., Li, Z., Ge, W., Zhang, Y., Jiao, Y., Sun, H., et al. (2022). Calculation of dam risk probability of cascade reservoirs considering risk transmission and superposition. *J. Hydrology* 609, 127768. doi:10.1016/j.jhydrol.2022.127768

Wu, M., Ge, W., Wu, Z., Guo, X., Di, D., and Huang, S. (2020). Evaluation of the benefits of urban water resource utilization based on the catastrophe and emergy methods. *Water Resour. Manag.* 34, 1843–1853. doi:10.1007/s11269-020-02530-7

Wu, M., Wu, Z., Ge, W., Wang, H., Shen, Y., and Jiang, M. (2021). Identification of sensitivity indicators of urban rainstorm flood disasters: A case study in China. *J. Hydrology* 599, 126393. doi:10.1016/j.jhydrol.2021.126393

Wu, X., Chen, Z. X., Wen, Q. B., et al. (2021). Optimal allocation model of unconventional water resources based on reinforcement learning [J]. *J. Hydropower* 40 (7), 23–31. doi:10.11660/slfdxb.20210703

Zhang, D., Xie, X., Wang, T., Wang, B., and Pei, S. (2022). Research on water resources allocation system based on rational utilization of brackish water. *Water* 14 (6), 948. doi:10.3390/w14060948

Zhang, H., Ge, W., Zhang, Y., Li, Z., Li, W., Zhu, J., et al. (2023). Risk management decision of reservoir dams based on the improved life quality index. *Water Resour. Manag.* 37, 1223–1239. doi:10.1007/s11269-023-03426-y

Zhang, Y. (2013). Accelerating the development and utilization of unconventional water resources [J]. *Water Dev. Res.* 13 (01), 13–16. + 68. doi:10.13928/j.cnki.wrdr.2013.01.002

Zhang, Y., Li, Z., Ge, W., Wang, J., Guo, X., Wang, T., et al. (2022). Assessment of the impact of floods on terrestrial plant biodiversity. *J. Clean. Prod.* 339, 130722. doi:10.1016/j.jclepro.2022.130722

Zhu, S. Y. (2020). *Research on the collaborative allocation model of unconventional water resources and conventional water resources in Yulin City [D]*. Northwest A and F University. doi:10.27409/d.cnki.gxbnu.2020.001283

frontiers | Frontiers in Earth Science

TYPE Original Research
PUBLISHED 17 August 2023
DOI 10.3389/feart.2023.1234319

OPEN ACCESS

EDITED BY
Wei Ge,
Zhengzhou University, China

REVIEWED BY
Yun Chen,
China Three Gorges University, China
少华 胡,
武汉理工大学, China
Ali Moridi,
Shahid Beheshti University, Iran
Chaoning Lin,
Hohai University, China
Huaping Sun,
Jiangsu University, China

*CORRESPONDENCE
Liang Liu,
liuliang@ncwu.edu.cn

RECEIVED 04 June 2023
ACCEPTED 04 August 2023
PUBLISHED 17 August 2023

CITATION
Liu D, Liu L and Tan X (2023), Risk sharing in quasi-public-welfare water conservancy (PPP) public-private participation projects: an integrated application of Shapley value and utility theory.
Front. Earth Sci. 11:1234319.
doi: 10.3389/feart.2023.1234319

Risk sharing in quasi-public-welfare water conservancy (PPP) public-private participation projects: an integrated application of Shapley value and utility theory

Dawei Liu[1], Liang Liu[2]* and Xin Tan[3]

[1]College of Teacher Education, Hubei University of Education, Wuhan, China, [2]College of Geosciences and Engineering, North China University of Water Resources and Electric Power, Zhengzhou, China, [3]College of Mathematics and Statistics, Hubei University of Education, Wuhan, China

Introduction: Quasi-public water conservancy PPP (Public-private participation) projects are closely related to people's livelihoods and involve multiple participating stakeholders. Previous research on risk sharing in such projects has primarily focused on qualitative analysis of risk factors. Due to self-interest considerations, the collaborating parties tend to deflect and transfer risks to each other as much as possible in the risk sharing process. Additionally, some quantitative analysis methods have been predominantly based on a unilateral perspective.

Methods: Therefore, the present study proposed a new model, which is based on the Shapley Value and the Utility Theory, encompassing a comprehensive analysis of multiple factors such as the proportion of capital contribution, bargaining position, risk management capabilities, and risk-taking willingness of heterogeneous subjects. Firstly, the relationship between the risk losses of different stakeholders and their corresponding value scales and utility attributes is comprehensively analysed, and the transformation characteristics and links of their risk preferences on spatial and temporal scales are summarised. Secondly, The utility values of heterogeneous subjects are employed as quantitative indicators to evaluate utility, leading to the construction of a comprehensive utility objective function for these subjects. Finally, The Shapley Value is then applied to modify the risk-sharing ratio based on the Utility Theory.

Results: The research results show that the risk sharing ratio obtained by single use of shapley value theory or utility theory will be biased toward one side, while the result calculated by using the combination of the two methods is 57.35% for the government to share the risk ratio, and 42.65% for the social capital side, which is a more balanced result.

Discussion: The proposed model enriches the risk management method and theory of quasi public welfare water conservancy PPP projects.

KEYWORDS

quasi-public water conservancy project, PPP, risk sharing, Shapley value, utility theory

1 Introduction

Water conservancy is closely related to people's livelihoods and function as a key factor in promoting regional economic development, ensuring industrial production, and improving living standards. While water conservancy projects hold a pivotal position in the realm of infrastructure development, they also encounter numerous risks and challenges throughout their preparatory, construction, and operational stages (Wu et al., 2021; Ge et al., 2022). In recent years, the adoption of the Public-Private Partnership (PPP) model has gained significant traction in the realm of water conservancy projects (Zhang, 2014; Li, 2017; Qiu et al., 2018). As of the end of September 2018, according to the data from the project database of the China Public Private Partnerships Center, there are 538 water conservancy engineering PPP (Public-private participation) projects in China, with an investment amount of up to more than 400 billion yuan. Among them, water conservancy construction PPP projects account for 60.78% of all projects, with a total of 327 projects and a total project investment of more than 260 billion yuan. Quasi-public-welfare water conservancy projects play an indispensable role in the field of water supply and other social livelihoods and public services. Since quasi-public-welfare water projects are not intended to make a profit, the pricing of products and services set under the guidance of the government cannot affect the purchase and use of the public for over-high prices. Therefore, the project fees are difficult to cover the cost, resulting in low economic benefits, lack of attractiveness to investors, and difficulty in financing. At the same time, quasi-public-welfare water conservancy projects are

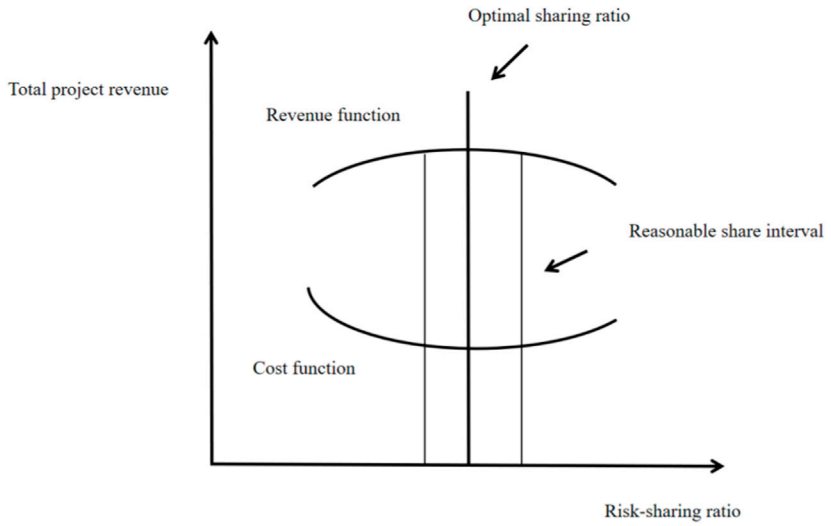

FIGURE 1
Relationship between project benefits and risk-control costs.

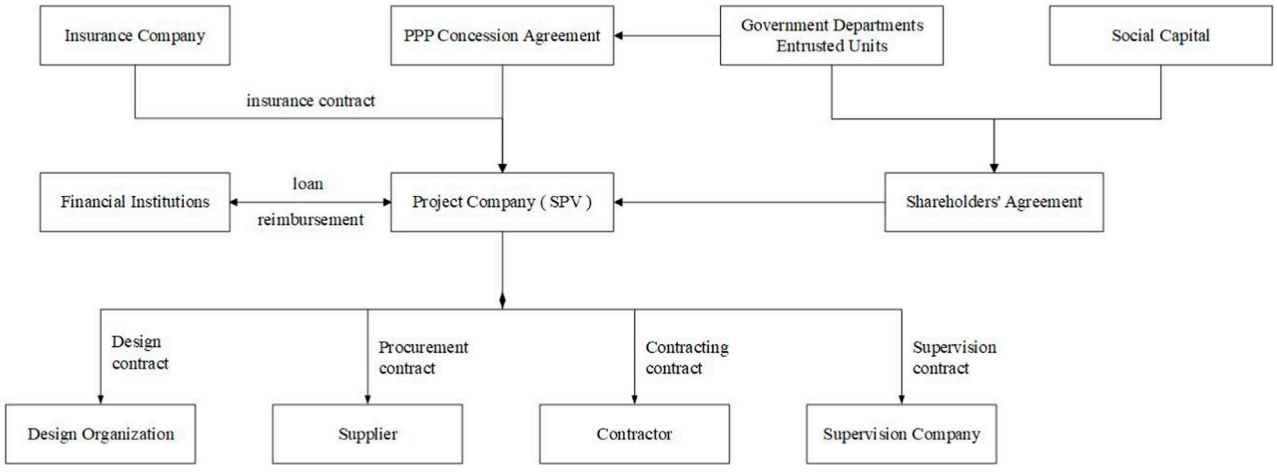

FIGURE 2
PPP project participant-relationship map.

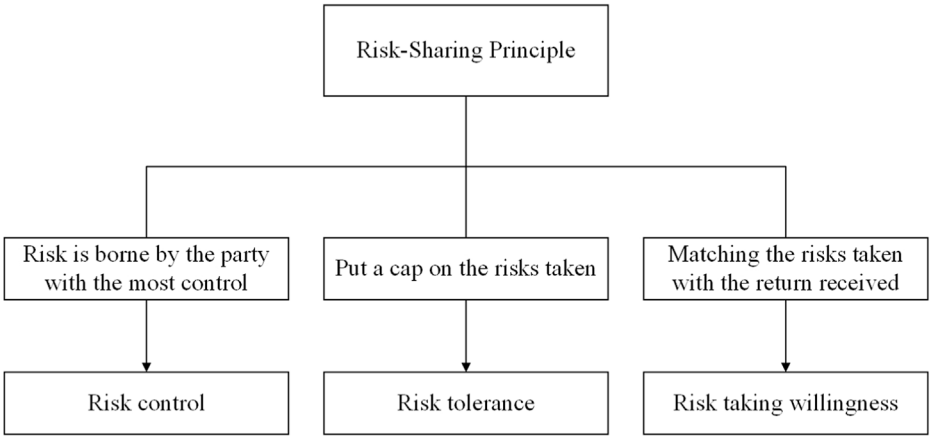

FIGURE 3
Risk-sharing principles for quasi-public-welfare water PPP projects.

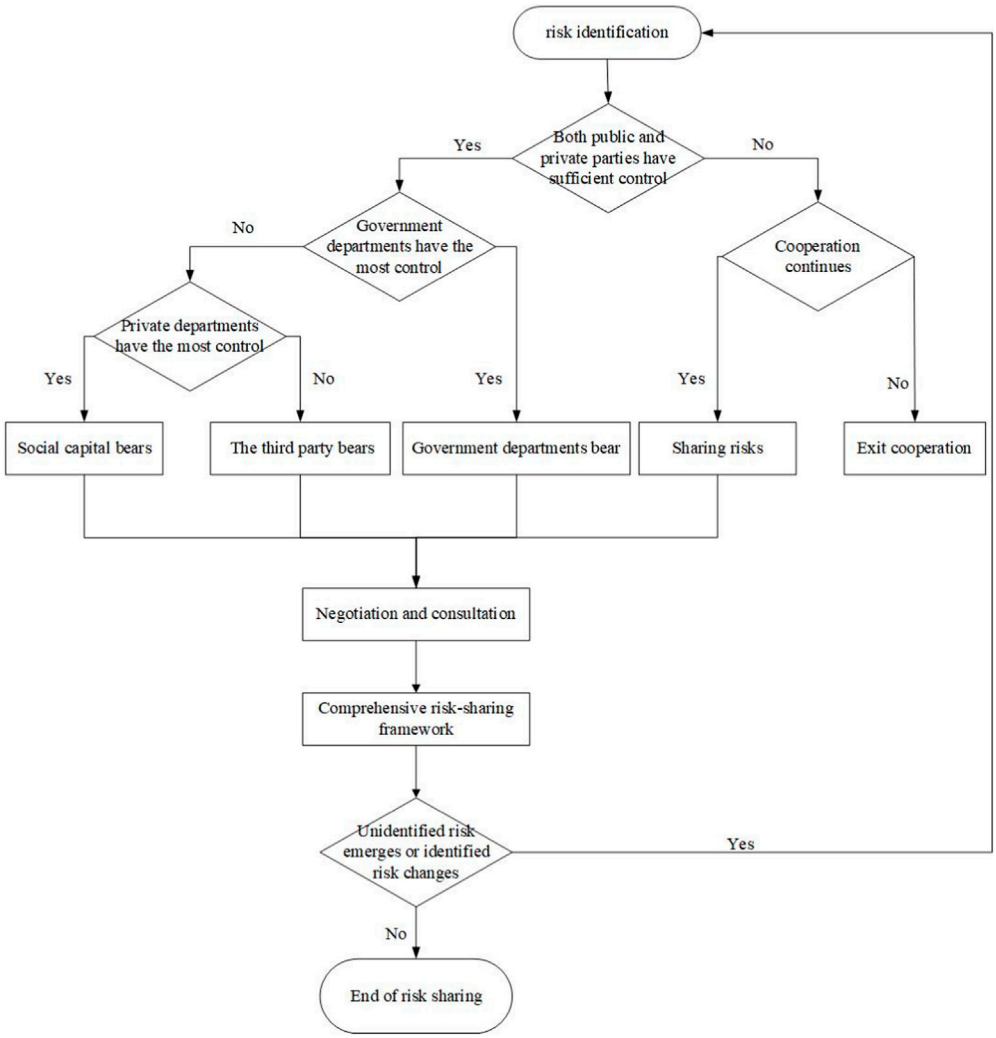

FIGURE 4
Risk-sharing flow chart for quasi-public-welfare water PPP projects.

TABLE 1 Risk sharing program.

Risk factor	The most risk-control force		Risk sharing method		
	Government department	Social capital	Government department	Social capital	Shared
Construction cost overrun		√		√	
Financing		√		√	
Engineering change					√
Operation cost overrun		√		√	
Operating revenue		√		√	
Residual value					√
Government officials corruption	√		√		
Charge change		√		√	
Cost payment	√		√		
Interest rate	√		√		
Exchange	√		√		
Inflation	√		√		
Operating cost overruns		√		√	
Tax adjustment	√		√		
Changes in social capital investors		√		√	
Project measurement method subjective		√		√	
Insufficient financial supervision of the project		√		√	
Duration					√
Construction safety					√
Completion					√
Lack of practical experience		√		√	
Unclear definition of responsibility					√
Construction site pollution					√
Waste pollution					√
Climate/geological conditions					√

difficult to implement due to high technical requirements and strict project management requirements, and require coordination of multiple units to collaborate in the meantime during the actual construction process. Given China lacks experience in managing quasi-public-welfare water conservancy PPP projects, many problems occur in the practical application (Ding, 2005; Li et al., 2013; Bi et al., 2016; Gao, 2018).

Quasi-public-welfare water PPP projects are characterized by their large scale, involvement of numerous stakeholders, and long cooperation periods that can span several years or even decades. These projects are susceptible to various uncertainties throughout their life cycle, such as changes in the economic environment, which may result in complex and diverse project risks. In order to safeguard their own interests, both partners in PPP projects aim to transfer as many risks as possible to the other party, which often leads to prolonged negotiation time and increased agreement costs. Furthermore, even after a cooperation agreement is successfully signed, instances of mutual shirking of responsibilities may arise out of project implementation, further exacerbating overall project risks and costs. Therefore, risk allocation is one of the key considerations in research on risk management measures.

Risk sharing, as an important means to control economic risks, is aimed at determining a reasonable allocation of risks that can incentivize the participants in PPP projects, leverage their respective strengths to enhance operational efficiency, reduce the likelihood of risk occurrence or loss, and maximize the overall project benefits. Although the theoretical model of risk sharing is relatively mature, the relevant research mainly focuses on the risk sharing of simple projects. Such projects are often dominated by one party and from a unilateral viewpoint. This traditional risk sharing method is not

TABLE 2 Common risk-sharing model approaches.

Risk sharing model	Feature	Application cases
Principal-agent model	Assuming that both the principal and the agent are strictly risk-averse, the optimal risk-sharing scheme is that each party bears a certain amount of risk	
Game model	The assumptions of the game model are numerous and the parameter settings that determine the calculation results are mainly based on experience and approximate estimates	The Comprehensive Improvement PPP Project for the Luoyang River reach at Luojiang District
Utility Theory model	High efficiency of risk sharing is made possible by taking into account the ratio of proportion of capital contribution, bargaining position, willingness to take risks, and other factors	The first phase of eastern and middle routes of the South-North Water Diversion Project
Gray relational analysis method	Based on the similarity of development trends among factors. The magnitude of the correlation coefficient can be used to measure the proximity of the evaluated party to the ideal risk taker	A sewage treatment plant PPP project, an Olympic sports center PPP project
Bargaining theory	In response to the respective proposed allocation schemes, the other party will again be caught in a long bargaining process, where the government department and the social capital party share the risk loss	A highway PPP project
Monte carlo simulation	It overcomes the shortcomings of traditional risk-analysis methods such as qualitative estimation of a single risk, and enables a more comprehensive and systematic analysis of project risk sharing	
The theory of Shapley Value	The Shapley method reflects the ' average ' contribution to the distribution of benefits for each participant. It also takes into account the degree of contribution of each participant to the total project revenue and its ability to manage risk	Heishanxia river reach water conservancy PPP project

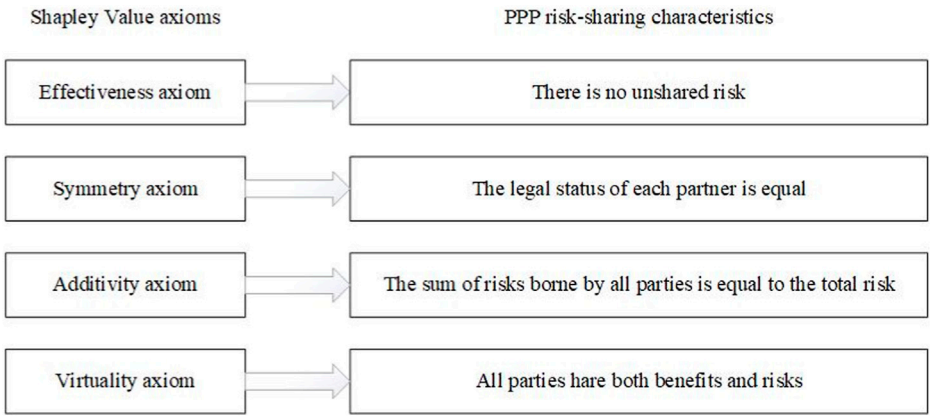

FIGURE 5
The theory of shapley value and PPP risk-sharing applicability.

suitable for PPP projects with multi-party participation and equal status. Because of the complexity of the project structure and the specific nature of the water conservancy industry, the research threshold of quasi-public welfare water conservancy PPP projects has increased, coupled with the fact that there are fewer completed projects of this type, the risk sharing research of quasi-public welfare water conservancy PPP projects both is lagging behind the social demand. Therefore, it is necessary to carry out research on quantitative risk-sharing methods for quasi-public welfare PPP projects based on multi-party perspectives to meet the interests of all parties and reduce the overall risk of the project, so as to improve the enthusiasm of social capital invested in quasi-public welfare water projects and create more water projects that benefit society.

2 Research status quo

In the field of project management, the decision-making process regarding risk sharing is of great importance. As a basis for risk sharing decision, Xu (Xu et al., 2022) constructed the risk evaluation index system and the DEMATEL-ANP-FUZZY risk evaluation model of the water conservancy PPP project. Jin, (2010) conducted a study utilizing dealing cost economics and resource organization ability to identify five key characteristics that influence risk sharing in projects. Jin, (2011) further developed a predictive model by combining fuzzy logic and artificial neural networks to accurately forecast effective risk-sharing strategies in dynamic business environments. The proposed Fuzzy TOPSIS decision model aids organizations in determining the optimal risk taker

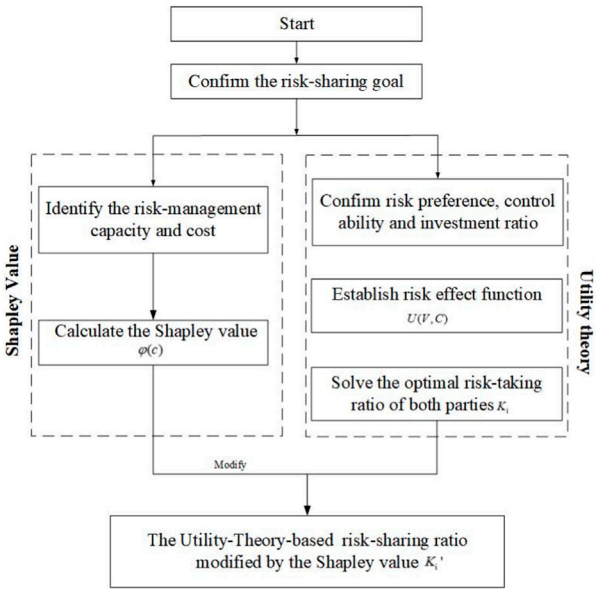

FIGURE 6
Flow chart of risk-sharing based on Shapley Value and Utility Theory.

throughout the risk-sharing process (Khazaeni et al., 2012). Zhao (Zhao et al., 2020) determines the risk factors to be shared among participants through the method of combining GCA method and TOPSIS method. And build a model based on the utility theory to determine the proportion of risks shared among participants. In the context of contract-based projects, Xu et al. (2018) explained how risk-sharing mechanisms in contracts incentivize contractors to collaborate with project owners through a parallel mediating mechanism. Tembo-Silungwe and Khatleli, (2018) introduced the structuration theory to identify the constraints and facilitators of risk sharing. They conducted interviews with practitioners in the Zambian construction industry for finding ways to optimize risk-sharing practices. Li (Li and Wang, 2023) studied the risk sharing problem in the public-private partnership model and constructed a game model of PPP risk sharing dynamic government regulation. Shi et al. (2021) argued against the effect of the Principal-Agent Theory in designing risk-sharing rules for construction projects involving risk-neutral contractors. They highlighted the potential bias in incentive structures and proposed the analysis of risk sharing between owners and risk-neutral contractors to address this issue.

Studies on risk sharing in PPP projects can be categorized into three main groups. The first category involves questionnaire-based studies that aim to determine the allocation of risks between the public and private sectors. Zhao et al. (2020) employed the Delphi method to identify key risk factors. Meanwhile, in order to achieve rational risk sharing, he determined the risk factors that participants were willing to assume and subsequently calculated the risk sharing ratio by combining the GCA method and TOPSIS method. Shrestha et al. (2018), based on the expertise of 32 practitioners, investigated the risk allocation in PPP water projects in China. They found that poor risk management was often brought about by the misallocation of risk between the two primary actors in the PPP. The second category comprises empirical analyses. Huang et al. (2022) conducted an empirical analysis with the Risk Mechanism Information Integration System (RMIS) and took the Chengdu Metro Rail Transit Line 17 Phase I PPP project as a case study. They established a risk-sharing decision-making model to evaluate different risk allocation options, and determined the optimal decision for each risk factor between social capital and the government. Nguyen et al. (2018) studied 31 risk allocation schemes for 21 road PPP contracts in the U.S. and discovered that the majority of risks were transferred to the private sector. Heravi and Hajihosseini, (2012) analyzed the contract organization of the Tehran-Chalus toll road PPP project and proposed suggestions on the improvements of the risk-sharing schemes for better project performance. The third category combines different methodologies to build models for risk allocation. Wang et al. (Wang, Zhou, Jin, Zhao, and Sun, 2022) developed risk assessment models, including the optimal-worst multi-criteria decision-making method and fuzzy comprehensive evaluation method, to achieve effective risk sharing and benefit allocation among different stakeholders. Their objective was to promote win-win outcomes. Mazher et al. (2019) proposed a multi-attribute risk allocation decision-making method based on non-additive fuzzy integration. In this method, the risk management capabilities of each stakeholder could be effectively aggregated and the acceptable principles for risk allocation could be evaluated. Some scholars have conducted quantitative research on the proportion of risk sharing based on a unilateral perspective: Zhao et al. (2020) based on the model of utility theory to determine the proportion of risk shared among participants from the government's perspective, and validated it with the PPP project of sponge city in Qingshan District, Wuhan City. Wang et al. (2022) combined the capital investment, contribution, and project participation to revise the Shapley value income distribution model to obtain a more fair and reasonable income distribution and risk sharing system.

Through the analysis of the existing literature, the previous research on risk sharing by scholars at home and abroad focuses on the qualitative analysis of risk factors, i.e., to determine which risks

TABLE 3 Risk-sharing ratio.

Sharing ratio calculation method	Risk-sharing ratio	
	Government department (%)	Social capital (%)
Utility Theory	34.62	65.38
Shapley Value	69.57	30.43
Utility-Theory and Shapley Value	57.35	42.65

are shared by both public and private parties, which risks are borne by each party, and lacks quantitative judgment on the proportion of shared risks; a small number of scholars have made a quantitative study on the proportion of risk sharing in PPP projects, but the majority of them are concentrated in the operational PPP projects with strong profitability, and they focus on considering some factors such as the risk disposal capacity or risk appetite, or they are based on a unilateral viewpoint of the governmental departments or the social capitalists, which is one-sided, and the assumption of conditions are many, and the computation process is complex.

In view of this, in order to ensure that the risk sharing scheme is scientific, fair and effective, combined with the characteristics of quasi-public welfare water conservancy PPP projects, this study taking into account the proportion of capital contribution, bargaining position, and the differences in the ability of both parties to deal with risks. The Shapley value is coupled with the utility theory, the quasi public welfare water conservancy PPP project in the government sector and the social capital party risk sharing ratio to carry out research, and combined with the Chongqing Fengsheng Reservoir Project examples to carry out The risk sharing ratio is calculated with the example of Chongqing Fengsheng Reservoir Project.

3 Principles and process of PPP project risk management

In a PPP project, risk sharing plays a crucial role in distributing various risk elements among the participants. It is a strategy that can be employed to manage the relationship between stakeholders in risk management. Given the complexity of risks, the multiplicity of participants, and the severity of implications brought by risks, risk sharing has always been a challenging and pivotal aspect of project risk management (Xu et al., 2010; Tian, 2014).

Achieving the most reasonable balance of benefit sharing and risk sharing between social capitalists and government departments is essential for reducing project costs, enhancing operational efficiency, and maximizing overall benefits (Xu et al., 2010; Ranjith et al., 2016). Insufficient risks shared with the private sector may lead to decreased efficiency and increased project costs, while excessive risks shared may also diminish the private sector's enthusiasm and inflate the overall project cost likewise. Therefore, identifying the optimal risk-sharing ratio is crucial to maximizing project revenue and minimizing the total cost of risk control, as depicted in Figure 1.

A clear definition of risk-sharing subjects is essential in PPP projects, considering the multitude of participating parties, including government departments, social capital parties, project companies, financiers, contractors and operators, and the rights and obligations of each subject are different (Li, 2017; Wu, 2017; Li, 2018). The scientificity and effectiveness of the risk-sharing scheme can be ensured only when the risk-sharing subjects are precisely identified (Zhao, 2018). Throughout the entire life cycle of PPP projects, government departments, and social capitalists serve as the primary risk-bearing parties. Together, they establish the project company as the project's operating entity, responsible for financing, design, construction, and operation, among other specific tasks. The relationships are presented in Figure 2.

The risk-sharing scheme should be developed by initially identifying and analyzing potential risks at each stage of the project. Subsequently, the risk preferences, risk tolerance, and risk-control abilities of each participant are further examined to formulate an appropriate risk-sharing plan (Jin et al., 2011; Lang et al., 2017).

The fundamental principle of the PPP model lies in the sharing of benefits and risks, with the primary risk bearers being government departments and private investors. As the core participants, they play indispensable roles in quasi-public-welfare PPP projects. This chapter focuses on social capitalists and government departments as the key stakeholders and places emphasis on investigating the risk-sharing mechanisms between them.

In the realm of risk sharing, numerous scholars such as Lam, Li, and others have conducted research on the subject. They have put forth a risk-sharing principle as depicted in Figure 3 (Arndt, 1998; Wang et al., 2022; Li et al., 2005; Ng and Loosemore, 2007; Lam et al., 2008).

(1) Risk is borne by the party with the most control

When a participant in a project has the highest level of control, they possess an advantage in terms of reducing the likelihood of risk occurrence and mitigating risk losses.

(2) Put a cap on the risks taken

In situations where a project incurs substantial risk losses that surpass the capacity of the responsible party, it becomes necessary to prevent project insolvency by stipulating that the risk cannot be solely borne by one party or continued to be shared according to the previously agreed risk-sharing ratio.

(3) Matching the risks taken with the return received

Effective risk sharing should be grounded in comprehensive risk identification and analysis, which entails taking factors such as the probability of risk occurrence, potential losses, costs associated with risk retention, and the expenses associated with risk transfer into consideration. By comparing these elements with the project returns, a well-aligned risk-sharing arrangement can be established.

Within the risk management process of PPP projects, a sound design of procedures serves as a crucial assurance for the implementation of risk sharing (Jin, 2011; Wang, 2017). Following the completion of effective risk identification for the project, the risk-sharing procedures for quasi-public-welfare water PPP projects can be established under the aforementioned risk-sharing principles, as depicted in Figure 4.

In the development of quasi-public-welfare water PPP projects, the risk-allocation process is dynamic and complex. During the project's decision-making phase, a comprehensive analysis is conducted to examine the unique advantages, status disparities, investment and revenue objectives, as well as the risk appetite and control capabilities of both government departments and social capitalists involved in the PPP project. This analysis provides insights into the specific characteristics and circumstances of each party. Following this analysis, suitable risk identification methods are employed to thoroughly explore and analyze

potential sources of risk throughout the project's lifecycle, so as to assess whether these risks fall within controllable limits. The subsequent stage comes to the actual risk sharing when, government departments and social capitalists collaborate to determine the allocation of risks, specifying which risks will be borne by the government, which borne by the social capitalists, and which shared jointly. Once the shared risks are identified, it becomes necessary to establish the risk-sharing ratio for each party involved in order to determine their respective responsibilities and obligations for the shared risks.

The scheme on risk identification and preliminary risk sharing for quasi-public-welfare water conservancy PPP projects, as demonstrated in Table 1, is developed based on the risk-sharing principles put forth by Liu Xinping and others (Liu and Wang, 2006; Wang, 2017). Additionally, the research conducted by Li Yang et al. on risk-sharing schemes for relevant PPP engineering cases (Li, 2018; Xu et al., 2022) has been referred to as well.

4 Risk-sharing model

The success of PPP projects hinges on the effective sharing of project risks among the participants. The most notable distinction between PPP and other models lies in the establishment of a reasonable sharing ratio that aims to stimulate the enthusiasm of all parties involved and leverage their respective advantages. If government departments assume an excessive amount of risk, it may lead to financial strain on the government and undermine the original intent of introducing social capitalists through PPP projects. On the other hand, if social capitalists shoulder an excessive amount of risk, it may deter their participation in PPP projects, ultimately impeding their contributions in terms of capital and expertise. Thus, risk sharing in PPP projects must adhere to the principle of achieving mutual benefits and a win-win situation for all parties involved.

The current research on risk sharing in PPP projects can be broadly classified into two categories. The first category involves using questionnaires to gather information and derive a project risk-sharing matrix, which provides decision support for risk sharing. This approach aims to capture the perspectives and insights of project participants to determine an appropriate risk-sharing arrangement. The second category of research focuses on quantitative methods for risk sharing in PPP projects. These methods employ techniques such as Linear Programming and Game Theory to analyze and optimize the outcomes of risk sharing. By means of mathematical models and computational approaches, these methods aim to achieve an objective and efficient allocation of risks among project participants.

Table 2 displays some common quantitative research methods employed in studying risk sharing in PPP projects (Wang and Yang, 2013; Wang, 2017; Zhang, 2017). These methods offer valuable tools for analyzing and evaluating risk-sharing strategies in PPP projects.

The theoretical model of risk sharing has matured, with the relevant research primarily concentrated on risk sharing in simple projects. However, limited attention has been given to the risk-haring aspects of quasi-public-welfare water conservancy PPP projects. Consequently, this paper aims to address this gap by focusing on risk sharing in quasi-public water PPP projects. It takes into consideration the unique characteristics of such projects and seeks to implement practical risk-sharing principles and methods.

The theory of Shapley Value mainly focuses on the disparity in risk-management capabilities between the two parties involved to determine the allocation of risk-sharing ratios. The results from applying the theory primarily reflect the risk-management abilities of both parties and highlight the differences between them. Hence, this paper seeks to combine the Shapley Value approach with the Utility Theory with the latter used to calculate the risk-sharing ratio, and the former employed to adjust the risk-sharing ratio derived from Utility Theory. The risk-sharing model established based on the two theories provides a more comprehensive and rational approach to determining the risk-sharing ratio and proves to be more reasonable than those solely relying on the Utility Theory or the Shapley Value Theory for calculating the risk-sharing ratio.

4.1 The theory of shapley value

In economic activities, when multiple actors join forces through alliances or partnerships, they have the potential to achieve greater gains or minimize losses compared to working individually, thereby creating a win-win or multi-win situation. The theory of Shapley Value focuses on the distribution of benefits or sharing of risks among the members of an alliance. It takes into account the level of contribution made by each member towards the overall goals of the alliance and reflects the interactive process of cooperation among alliance members. The theory of Shapley Value is primarily applied to address issues related to the distribution of cooperation costs and benefits among alliance members (Yu et al., 2014; Xu et al., 2016).

In recent years, the application of the Shapley Value Theory has extended to various areas such as investment analysis, compensation allocation, risk allocation, and burden apportionment. In the water sector, the Shapley Value has emerged as a prominent method for solving cooperative game problems. It provides a quantitative allocation ratio that is practical and straightforward to apply (Yang, 2016; Wang et al., 2018).

The calculation of the Shapley value is made in view of the costs and capabilities of both parties involved in managing a particular risk. Its results can reflect the disparity in risk management abilities between the parties. However, some factors such as the ratio of proportion of capital contributions and bargaining positions of the parties are not taken into account. Given the theoretical limitations of the Shapley Value and the unique characteristics of PPP projects, it is necessary to revise the index system of the Shapley Value method. This revision allows for a more comprehensive analysis, considering factors specific to PPP projects (Fan, 2014; Sheng and An, 2019).

Pinpointing the optimal allocation scheme or "solution" is indeed the most challenging aspect of the Cooperative Game Theory. The Shapley Value method, as a type of cooperative game, presents a straightforward calculation process and allocates benefits based on the partners' marginal benefit to the alliance, which aligns with Adams' equity theory. The latter theory suggests that distributing benefits based on the contribution rate can enhance team cooperation and output, in line with the principles of benefit

sharing and risk sharing in PPP projects. It can also help emphasize each partner's importance within the alliance.

Let N be the set of alliances consisting of n cooperating parties, and $N = 1, 2, ..., n$. The cooperating parties within the alliance are non-antagonistic and the overall cooperation gains increase in step with participating parties. Let S be a subset of N, representing a cooperative alliance formed among the parties, such that $S \subseteq N$. $v(S)$ denotes the profit of the cooperative alliance S, and $[N, V]$ represents an n-person cooperative game with the characteristic function v. Specifically, $v(\varphi) = 0$, $v(S_1 \cup S_2) \geq v(S_1) + v(S_2)$, where $S_1 \cap S_2 = \varphi$ and φ represents the empty set. By applying the Shapley Value method to evaluate the marginal contributions of each party to the overall cooperation, a fair and reasonable allocation of interests for each party can be obtained.

The total benefits obtained by the cooperative alliance surpass the sum of the individual benefits obtained by each party working alone, i.e.,

$$v(S_1) > \sum_{i \in S} v(i) \tag{1}$$

Here, v (i) represents the profits obtained by participant i when working alone.

Let X_i represent the distribution of benefits obtained by member i from the cooperative alliance. $X = (X_1, X_2, ..., X_n)$ indicates that the cooperative participants' benefits in the alliance are no less than the benefits obtained by independently completing the project, where $i = 1, 2, ..., n$.

$$X_i \geq v(i) \tag{2}$$

$$\sum_{i \in S} X_i \geq v(s) \tag{3}$$

Assuming that the members of the cooperative alliance join the alliance N in a random order, there are a total of n! possible orderings. Each ordering has an equal probability of occurrence, which is $\frac{1}{n!}$. When party i forms an alliance S with the preceding $(s-1)$ individuals, the marginal contribution of party i to the alliance $S \in N/i$ is $v(S) - v(S\backslash i)$. Since there are $(|S|-1)!$ permutations of the preceding $(s-1)$ parties and $(n-s)!$ permutations of the remaining $(n-s)$ parties, the total number of permutations for the alliance S formed is $(n-1)!(|S|-1)!$. The probability of forming the alliance S is $\frac{(n-|S|)!(|S|-1)!}{n!}$. Therefore, the expected value of the marginal contribution of participant i in alliance S is precisely the Shapley value.

The calculation formula for the Shapley value $\varphi(v) = (\varphi_1(v), \varphi_2(v), ..., \varphi_n(v))$ is as follows:

$$\varphi_i(v) = \sum_{S \in S_i} W(|S|)[v(S) - v(S\backslash i)] \tag{4}$$

Substituting $W(|S|) = \frac{(n-|S|)!(|S|-1)!}{n!}$, we have:

$$\varphi_i(v) = \frac{(n-|S|)!(|S|-1)!}{n!}(v(S) - v(S\backslash i)) \tag{5}$$

Here, $i = 1, 2, ..., n$, $|S|$ represents the number of cooperating parties in the alliance; $S\backslash i$ represents all subsets of set N that contain i; $W(|S|)$ is the weighting factor; $v(S\backslash i)$ represents the overall benefit obtained by the alliance S when party i is excluded; and $v(S) - v(S\backslash i)$ represents the marginal contribution of party i to the alliance S.

The research in this paper focuses on the risk sharing of quasi-public-welfare water conservancy PPP projects, which involves the allocation of costs within a cooperative alliance. To derive cost sharing, the term "revenue" in the previous formulas needs to be replaced with "cost". The specific calculation formulas are as follows:

$$\varphi_i(c) = \sum_{S \in S_i} W(|S|)[c(S) - c(S\backslash i)] \tag{6}$$

$$\varphi_i(c) = \frac{(n-|S|)!(|S|-1)!}{n!}(c(S) - c(S\backslash i)) \tag{7}$$

But before that we need to explore the four axioms of the Shapley Value to determine its suitability for risk-sharing studies in PPP projects. The study of risk sharing in PPP projects is grounded on the principle that benefit sharing is premised on risk sharing, and both parties voluntarily cooperate for mutual benefit. Figure 5 demonstrates the analysis of risk sharing in PPP projects based on the four axioms of the Shapley Value:

First, all partners share all the risks of the project, without any risk being left unshared, which aligns with the effectiveness axiom of the Shapley Value. Secondly, although the government department is the initiator of a PPP project and the social capital party plays a dominant role in the PPP project company, the risk-sharing results only take into account factors such as risk-control ability, risk-bearing ability, and risk willingness of each party and the legal equality of each partner is not considered during risk sharing. This satisfies the axiom of symmetry. Thirdly, sum of the risks respectively borne by each party is amount to the total risks of the PPP project, in line with the axiom of additivity. Finally, there is a clear division of work and responsibilities among the participants with each being required to share both project benefits and risks. As a result, no partner solely bears risks without enjoying benefits or solely enjoys benefits without bearing risks, aligning with the axiom of virtuality.

In conclusion, PPP projects, including quasi-public-welfare water PPP projects, align with the four axioms of the Shapley Value method. Consequently, the Shapley Value Theory can be effectively applied to analyze and study the risk-sharing dynamics in quasi-public-welfare water PPP projects. This approach provides a solid foundation for understanding the fair distribution of risks and benefits among the project stakeholders, promoting the overall effectiveness and success of such projects.

4.2 Utility theory

The Utility Theory, originally proposed by mathematician D. Bernoulli (1954), is a decision-making theory widely used in economics. It provides a framework for decision-makers to make choices by considering their individual utility or satisfaction levels. Since different decision-makers may have different utility preferences, even when presented with the same information, they still have diverse perceptions and evaluations.

In the context of risk-sharing decisions, the Utility Theory employs utility values as quantitative indicators. Higher utility values represent higher satisfaction with the expected returns, while lower utility values indicate lower satisfaction. The Utility Theory takes into account various factors such as the proportion of capital contributions of the parties involved and their bargaining positions. It enables the measurement of evaluations, preferences, and attitudes of different individuals toward risks and other factors.

Through the risk-sharing game that considers expected benefits and costs, the utility theory model enables the determination of a reasonable risk-sharing ratio., which provides valuable insights and references for decision-makers involved in the project. By utilizing this model, decision-makers can make more well-grounded and strategic choices, leading to optimized risk management and maximized project revenue.

In quasi-public-welfare water conservancy PPP projects, the utility functions U of the government department and the social capital party can be represented as functions of project benefits V and the cost of project risk control C, i.e., $U = U(V, C)$. Considering that PPP projects usually involve risk sharing and co-operation between multiple participants, each participant has a different sensitivity and preference for risk. With a fixed total investment, each party's perception of risk taking has a non-linear characteristic, i.e., a higher risk control cost leads to a greater loss of utility, while a lower risk control cost has a lesser impact on the increase of utility, and as a quasi-public welfare projects the contribution of economic returns to utility is linear. Therefore, this paper adopts a quadratic utility function for quasi-public welfare PPP projects can comparatively describe this nonlinear relationship, the formula is:

$$U = -\frac{1}{a}C^2 + V + 1 \tag{8}$$

The parameter $a > 0$ is estimated or adjusted according to individual preferences and risk attitudes. Larger values of a imply that individuals are more resistant to the cost of taking risks, and government departments are more sensitive to costs than social capitalists in Quasi-Public-Welfare Water Conservancy PPP Projects.

The optimization model for minimizing project risk-control costs is represented as follows:

$$Max\left[U_1(V_1, C_1) + U_2(V_2, C_2)\right] \tag{9}$$

$$MinCr(C_1, C_2) \tag{10}$$

Here, U_1, V_1, and C_1 represent the utility function, benefits, and risk-bearing cost of the government department, respectively. U_2, V_2, and C_2 represent the utility function, benefits, and risk-bearing cost of the social capital party.

Assuming the expected total risk cost is C_e, where K_e represents the proportion of risk shared by the government department (with $0 \le K \le 1$) and the proportion of risk shared by the social capital party is $1 - K$. The actual cost required for risk control is represented as C_r.

$$C_e = C_{eg} + C_{es} \tag{11}$$

$$C_r = C_{rg} + C_{rs} \tag{12}$$

$$C_{eg} = KC_e, C_{es} = (1 - K)C_e \tag{13}$$

$$C_{rg} = KC_r, C_{rs} = (1 - K)C_r \tag{14}$$

Here, C_{eg} and C_{rg} represent the expected risk cost borne by the government department and the actual risk cost, respectively. C_{es} and C_{rs} represent the expected risk cost borne by the social capital party and the actual risk cost, respectively.

The actual cost of risk is a function of the effectiveness of risk control and management, as well as the shared estimated risk cost. The actual risk cost is determined by the effectiveness function of risk control and the function of shared expected risk costs, represented as:

$$C_{rg} = F\left(K, C_{eg}\right) \tag{15}$$

$$C_{rs} = G(1 - K, C_{es}) \tag{16}$$

Here, F and G are the effectiveness functions of risk control for both the public and private sectors. The spillover benefits respectively obtained by the public and private sectors from effective risk control are as follows:

$$V_1 = C_{eg}C_{rg} = K(C_eC_r) \tag{17}$$

$$V_2 = C_{es}C_{rs} = (1 - K)(C_eC_r) \tag{18}$$

Furthermore, the maximum utility function can be derived as:

$$max\left[U_1(K(C_eC_r), KC_r) + U_2(1 - K)(C_eC_r), (1 - K)C_r\right] \tag{19}$$

$$min\, C_r \tag{20}$$

To maximize the overall efficiency of the quasi-public-welfare water conservancy PPP project, a comprehensive utility objective function is constructed for the government and the social capital:

$$f(U_1, U_2) = a_1\left(U_1 \cdot \left(U_1^0\right)\right) + a_2\left(U_2 \cdot \left(U_2^0\right)\right) \tag{21}$$

Here, a_1 and a_2 are the weighting coefficients of the negotiation between the government and the social capital, and $a_1 + a_2 = 1$. Generally, a is inversely proportional to the risk-sharing ratio. U_1^0 and U_2^0 are the initial utility values for the government and the social capital without risk impact, and $U_1 \cdot (U_1^0)$ and $U_2 \cdot (U_2^0)$ represent the spillover utilities obtained by the government and the social capital due to risk assumption. Since the overall objective is to maximize the comprehensive benefits, the spillover utilities are positive values, i.e., $U_1 \cdot (U_1^0) > 0$ and $U_2 \cdot (U_2^0) > 0$.

Due to the long cooperation period and complex risks involved in the quasi-public-welfare water conservancy PPP project, it is challenging to determine the total risk cost. The minimum risk cost represents the joint expected cost of risk for both the government and the social capital, which can be expressed as:

$$C_r = \overline{EC} \tag{22}$$

The optimization model for risk-sharing is as follows:

$$\begin{aligned} max\, f(U_1, U_2) = max\,\{&a_1\left(U_1(K(C_e - C_r), K \cdot C_r) - U_1^0\right) + \\ &a_2(U_2(1 - K) \cdot (C_e - C_r), (1 - K) \cdot C_r) - U_2^0\} \end{aligned} \tag{23}$$

$$s.t. \quad C_r = \overline{EC}$$

In this model, the objective is to maximize the function $f(U_1, U_2)$, which represents the comprehensive utility of the government and the social capital. The constraint ensures that the actual risk cost C_r is equal to the expected cost $\overline{EC}$, which represents the desired level of risk control.

To solve for the optimal risk cost-sharing ratio for the government, we can take the partial derivative of $f(U_1, U_2)$ with respect to K. Given that C_r is a function of K and C_e is constant, we obtain:

$$\begin{aligned} \frac{\partial f}{\partial K} = a_1&\left[(C_e - C_r)\frac{\partial U_1}{\partial V_1} - K\frac{\partial U_1}{\partial V_1}\frac{\partial C_r}{\partial K} + C_r\frac{\partial U_1}{\partial C_1} + K\frac{\partial U_1}{\partial C_1}\frac{\partial C_r}{\partial K}\right] + \\ a_2&\left[(\partial C_e - C_r)\frac{\partial U_2}{\partial V_2} - K\frac{\partial U_2}{\partial V_2}\frac{\partial C_r}{\partial K} + C_r\frac{\partial U_2}{\partial C_2} + K\frac{\partial U_2}{\partial C_2}\frac{\partial C_r}{\partial K}\right] \end{aligned} \tag{24}$$

By applying the Lagrange multiplier method to find the optimal solution, we let $a_1 = a$ and denote the optimal risk cost-sharing ratio as $K_0 = u \cdot a$. Thus, we have:

$$\begin{aligned} L &= f(U_1, U_2) + \lambda(\overline{EC} - C_r) \\ &= a[U_1(K_0(C_e - C_r), K_0 \cdot C_r) - {U_1}^0] + \\ &\quad (1-a)[U_2((1-K_0)(C_e - C_r), (1-K_0) \cdot C_r) - {U_2}^0] \\ &\quad + \lambda(\overline{EC} - C_r) \end{aligned} \tag{25}$$

Taking $\frac{\partial L}{\partial a} = 0$ and $\frac{\partial L}{\partial \lambda} = 0$, we obtain:

$$\begin{aligned} \frac{\partial L}{\partial a} &= a\left[(C_e - C_r)\frac{\partial U_1}{\partial V_1}u'(a) + C_r\frac{\partial U_1}{\partial C_1}u'(a)\right] \\ &\quad + [U_1(K_0(C_e - C_r), K_0 \cdot C_r) - {U_1}^0] - (1-a) \\ &\quad \left[(C_e - C_r)\frac{\partial U_2}{\partial V_2}u'(a) + C_r\frac{\partial U_2}{\partial C_2}u'(a)\right] \\ &\quad - [U_2((1-K_0) \cdot (C_e - C_r), (1-K_0) \cdot C_r) - {U_2}^0] \\ &\quad = 0 \end{aligned} \tag{26}$$

$$\frac{\partial L}{\partial \lambda} = \overline{EC} - C_r = 0 \tag{27}$$

By Eq. 27, can be determined. Substituting C_r into Eq. 25 yields the value of a, which allows the determination of K. Consequently, the risk allocation between the parties involved will be established. The determined risk allocation not only effectively motivates the cooperation of all participants, enabling risk sharing, but also reduces the overall project risk cost.

The application of the Utility Theory for quasi-public-welfare water PPP projects assumes that the following conditions are all satisfied.

(1) Cost minimization and benefit maximization as key performance indicators for both partners;
(2) Independent existence of each risk;
(3) Transparent communication and symmetric information about risks among partners;
(4) The cost of risk can be estimated and the shared risk can be identified;
(5) Both government departments and private institutions are groups with bounded rationality to pursue their own interests.

4.3 Risk sharing calculation

Though taking into account factors such as the proportion of capital contributions and bargaining position of both parties, the Utility Theory neglects the disparity in the parties' risk-management abilities. On the other hand, the Shapley values calculation is based on the cost and ability of the parties to handle a specific risk, providing insights into their differing risk-management capabilities. To address these considerations comprehensively, a combined approach of the Shapley Value and the Utility Theory is employed. The Shapley value is calculated for different sharing agents, reflecting their respective abilities in risk handling. Meanwhile, the Utility Theory is used to calculate the risk-sharing ratio based on the preferences and evaluations of the sharing parties. The Shapley value is then adopted to modify the risk-sharing ratio. By integrating these two approaches, a risk-sharing model based on the Shapley Value and the Utility Theory is established. Firstly, the relationship between the risk loss of heterogeneous subjects and the corresponding value scale and utility attribute is calibrated by comprehensively analyzing the factors such as the proportion of capital contribution, negotiation status and risk disposal ability of heterogeneous subjects, and the transformation characteristics and relationship of risk preference of heterogeneous subjects on time and space scale are summarized. Secondly, the utility value of the heterogeneous subject to the evaluation utility is used as the quantitative index to construct the comprehensive utility objective function of the heterogeneous subject. Finally, The Shapley Value is then applied to modify the risk-sharing ratio based on the Utility Theory. The risk-sharing process based on the two theories is depicted in Figure 6, illustrating the comprehensive and balanced consideration of these factors.

The steps are as follows.

The first step: Determining risk-sharing parties.

During the risk management process, it is essential to establish the allocation of risks between government departments and the social capital party provided that those mutually shared risks have also been identified. Since the objective of risk-sharing is to address the risks that both parties are responsible for, before initiating the sharing process, it is crucial to establish a clear understanding of which risks fall under the shared responsibility of both parties.

The second step: Calculating the share of risk based on Utility Theory.

Provided that the risk-sharing objectives are determined, based on the risk preference, control ability, and proportion of capital contribution of the government and social capital towards the risk, the expected loss brought by risk disposal and negotiation weighting coefficients are determined. The utility functions of the government and social capital in quasi-public-welfare water conservancy PPP projects can be expressed as a function of project returns V and the cost of project risk control C, that is, $U = U(V, C)$.

Based on Eqs 8–20, we construct the comprehensive utility objective function for the government and social capital as follows:

$$f(U_1, U_2) = a_1\left(U_1{U_1}^0\right) + a_2\left(U_2{U_2}^0\right) \tag{28}$$

where a_1 and a_2 represent the weighting coefficients of the negotiation between the government and social capital, respectively, and $a_1 + a_2 = 1$. In general, a is inversely proportional to the risk-sharing ratio. ${U_1}^0$ and ${U_2}^0$ denote the initial utility values of the government and social capital respectively, in the absence of risk influence.

The optimization model for risk-sharing can be formulated as follows:

$$\begin{aligned} max\, f(U_1, U_2) = max\{&a_1\left(U_1(K(C_eC_r), K \cdot C_r){U_1}^0\right) + \\ &a_2\left(U_2((1-K) \cdot (C_eC_r), (1-K) \cdot C_r){U_2}^0\right)\} \\ s.t. \quad & C_r = \overline{EC} \end{aligned} \tag{29}$$

Taking partial derivatives of K with respect to $f(U_1, U_2)$, where C_r is a function of K and C_e is a constant, we can derive the optimal risk-cost sharing ratio K_1 for the government sector and the optimal risk-cost sharing ratio $K_2 = 1 - K_1$ for the private capital sector.

The third step: Calculate the Shapley values of risk sharing parties.

In order to quantify the cost of risk disposal in consideration of the differences in risk-management capabilities between government departments and social capital partners, the cost of individual risk disposal and the cost of collaborative risk disposal are evaluated. The Shapley values calculation formula, as shown in Eq. 30, is used to calculate the Shapley values for both government departments and social capital partners.

$$\varphi_i(c) = \frac{(n-|S|)!\,(|S|-1)!}{n!}\,(c(S) - c(S\backslash i)) \tag{30}$$

Where: i represents the subject sharing the risk and can take values from 1 to n. n is the total number of risk-sharing subjects, with $n = 2$. $c(S)$ denotes the cost saved when both parties collaborate in risk management. $c(S\backslash i)$ represents the cost saved by the subject sharing the risk. $\varphi_i(c)$ indicates the Shapley values of the risk-sharing subject.

The last step: By modifying the sharing ratio calculated in the Utility Theory with the Shapley values, the desired sharing ratio and sharing amounts of risks for both parties are obtained.

Based on the calculation results of Steps (2) and (3), the revised risk-sharing amounts and sharing ratios are obtained with Eqs 31, 32:

$$\varphi_i(c) = \varphi_i(c) + (K_i - 1/n) \times c(S\backslash i) \tag{31}$$

$$K_i = \varphi_i(c) \Big/ \sum_{i=1}^{n} \varphi_i(c) \tag{32}$$

In the above equations, i represents the risk-sharing subject and can take values of $i = 1, 2, ..., n$; n represents the number of risk-sharing subjects; K_i is the risk-sharing ratio of the risk-sharing party i calculated by the Utility Theory; K_i is the risk-sharing ratio of the risk-sharing party i modified with the Shapley Value; $\varphi_i(c)$ is the Shapley value of the risk-sharing party i; $\varphi_i(c)$ is the revised risk-sharing amount of the risk-sharing party i; and $c(S\backslash i)$ is the contribution of risk sharing in the alliance S after excluding i.

5 Example analysis

5.1 Project funding

The Chongqing Fengsheng Reservoir project construction-and-operation company has a registered capital of 10 million yuan. Social investors who have won the bidding hold a 75% stake, while the PPP project implementation agencies hold the rest 25% stake. The construction of the reservoir constitutes a significant portion of the overall investment, with a preliminary estimated budget of 574.74 million yuan. The project construction will be carried out based on the total amount of investment determined through the bidding process.

To support the project, the successful social investors will contribute 114.94 million yuan, which accounts for 20% of the total project investment. This amount will be injected as a one-time cash investment into the project construction-and-operation company, specifically for expenses related to land acquisition, resettlement, and construction costs. Additionally, the central and municipal governments will provide investment subsidies amounting to 459.8 million yuan.

5.2 Risk-sharing ratio calculation

The Chongqing Fengsheng Reservoir project involves the participation of two entities: the government departments and the social capital party. A preliminary risk-sharing scheme for the project is outlined in Table 1. Among the various risks associated with the project, those that can be controlled by both the public and private parties will be managed through individual risk-control methods, with each party independently bearing the losses incurred by such risks.

For risks that require shared responsibility, it is essential to establish a scientifically and reasonably determined risk-sharing ratio. For the present analysis, a typical example of a risk shared by both parties within the sharing scheme is examined and the risk-sharing ratio between the two entities is analyzed.

A scenario is now assumed where a risk occurs, resulting in a loss cost of 12 million yuan for the government department and 20 million yuan for the social capital party, with the total loss cost of the project amounting to 32 million yuan. If the government department handles the risk independently, due to its special position and power in risk management, it would need to spend 20 million yuan while saving 12 million yuan.

On the other hand, if the social capital party handles the risk independently, leveraging its extensive experience and high management efficiency, it would need to spend 12 million yuan while saving 20 million yuan.

Alternatively, if both parties collaborate and jointly address the risk, they would need to spend 10 million yuan while saving 22 million yuan. These figures illustrate the potential costs and savings respectively associated with each party's independent risk-management efforts as well as their collaborative approach.

(1) Calculating the sharing ratio obtained from the Utility Theory

During the risk-control negotiation process, due to the differences in contribution between the two parties, the weighting coefficients for the government department, representing the advantaged party, and the social capital side, representing the disadvantaged party, are 0.75 and 0.25 respectively. Assuming utility function of the risk for the government department is:

$$U_1 = -\frac{1}{580}{C_1}^2 + V_1 + 1 \tag{33}$$

And assuming utility function of the risk for the social capital side is:

$$U_2 = -\frac{1}{400}{C_2}^2 + V_2 + 1 \tag{34}$$

Here, U_1, V_1, and C_1 represent the utility function, benefits, and risk-bearing cost of the government department, respectively. U_2, V_2, and C_2 represent the utility function, benefits, and risk-bearing cost of the social capital party. The values of a are assumed to be 580 and 400 in U_1 and U_2, respectively.

The actual cost of this risk is C million yuan ($C \geq 0$), and the initial utility values for the government department and social capital side, excluding risk impact, are ${U_1}^0 = 1$ and ${U_2}^0 = 1$ respectively.

Based on Eq. 22 in the risk-sharing model, the average expected cost for both parties is 16 million RMB. Assuming the risk-sharing ratio for the government department is denoted as K, by substituting $a_1 = 0.75$ and $a_2 = 0.25$ into Eq. 23 and performing rearrangements. We obtain the following expression:

$$\begin{aligned}\max f(U_1, U_2) = \max \{&0.75[U_1(K \cdot (1200 - 1600), K \cdot 1600) - 1] + \\ &0.25[U_2((1 - K) \cdot (2000 - 1600), (1 - K) \cdot 1600) - 1]\}\end{aligned} \tag{35}$$

By substituting the risk utility function and by setting $\frac{\partial F}{\partial K} = 0$, we can solve for K as follows:

$$\frac{\partial F}{\partial K} = \frac{186200}{29} - \frac{284800K}{29} = 0 \tag{36}$$

Solving this equation yields $K = 0.3462$. Consequently, the risk-sharing ratio for the social capital side is given by $1 - K = 1 - 0.3462 = 0.6538$. Hence, the project's risk will be shared with the government department assuming 34.62% of the risk, while the social capital side will bear 65.38% of the risk.

(2) Calculating the Shapley values

In the calculation of risk sharing in PPP projects, controlling risks in a reasonable manner can lead to a reduction in project losses, which turns into the increase of project returns. The initial Shapley values calculation formula for the Fengsheng Reservoir PPP project in Chongqing is as follows:

$$\varphi_i(c) = \sum_{s \subseteq N} \frac{(n - |S|)!(|S| - 1)!}{n!} \tag{37}$$

Where: $i = 1$ represents the government side; $i = 2$ represents the social capital side; $n = 2$; $c(S) = 22$ million RMB; $c(S\backslash 1) = 12$ million RMB; $v(S\backslash 2) = 20$ million RMB. we can solve for Shapley value as follows:

$$\begin{aligned}\varphi_1 &= \frac{(2-2)!(1-1)!}{2!}(2000 - 0) + \frac{(2-2)!(2-1)!}{2!}(2200 - 1000) \\ &= 16\,\text{million}\end{aligned} \tag{38}$$

$$\begin{aligned}\varphi_2 &= \frac{(2-1)!(1-1)!}{2!}(1200 - 0) + \frac{(2-2)!(2-1)!}{2!}(2200 - 2000) \\ &= 7\,\text{million}\end{aligned} \tag{39}$$

Therefore, the initial Shapley value for the government side of the Fengsheng Reservoir PPP project in Chongqing is 16 million RMB, and the initial Shapley value for the social capital side is 7 million RMB.

(3) Modify the Utility-Theory-based sharing ratio with the Shapley Value

Integration of the Shapley Value and the Utility Theory can provide a more comprehensive approach to determining the risk-sharing ratio. While the Utility Theory considers factors like proportion of capital contribution and bargaining positions, it may not account for the varying abilities of the parties to handle risks. On the other hand, the Shapley values calculation precisely considers the costs and abilities of each party in managing specific risks, thereby reflecting their differential risk-management capabilities.

By combining the two theories, the risk-sharing ratio can be adjusted. The Shapley Value can help modify the Utility-Theory-based ratio by considering the parties' abilities to handle risks. This approach provides a more nuanced perspective that incorporates both the overall contribution and bargaining positions of the involved parties, as well as their risk-management capabilities.

According to the above Utility-Theory formula (23), it is calculated that the government department of the Chongqing Fengsheng Reservoir PPP project bears the proportion $K_1 = 0.3462$ and the social capital party bears the proportion $K_2 = 1 - K_1 = 1 - 0.3462 = 0.6538$.

From the Shapley value Eq. 30, we calculate that Initial Shapley value $\varphi_1 = 16$ million for the government side and $\varphi_2 = 7$ million for the social capital side.

Calculations are performed according to Eqs 31, 32 to derive the final risk-sharing amount and sharing ratio of each party K'.

$$\varphi_1(c) = 1600 + (0.3462 - 0.5) \times 2200 = 12.6164\,\text{million} \tag{40}$$

$$\varphi_2(c) = 700 + (0.6538 - 0.5) \times 2200 = 9.3836\,\text{million} \tag{41}$$

$$K_1' = \varphi_1(c)' \Big/ (\varphi_1(c)' + \varphi_2(c)') = 0.5735 \tag{42}$$

$$K_2' = \varphi_2(c)' \Big/ (\varphi_1(c)' + \varphi_2(c)') = 0.4265 \tag{43}$$

The calculation results are shown in Table 3, the government department bears the amount $\varphi_1(c) = 12.6164$ million RMB, the social capital party bears the amount $\varphi_2(c) = 9.3836$ million RMB, the government department bears the risk ratio of 0.5735, and the social capital party bears the ratio of 0.4265.

5.3 Analysis of risk-sharing results

As the expected loss of the government sector to the risk is smaller than the social capital party, the government's contribution ratio in the project is larger than that of the social capital party, the government sector as a management organization often occupies an advantageous position in the negotiation on risk sharing, while the utility theory mainly takes into account the two sides of the capital contribution ratio, negotiation position and other factors, so when a single use of the utility theory of the Chongqing Fengsheng Reservoir PPP project, both sides of the risk-sharing ratio When calculating, the results are often favorable to the government sector. As can be seen in Table 4.3, the proportion of the risk loss borne by the government sector calculated using the utility theory is 34.62%, and the proportion borne by the social capital party is 65.38%, and the proportion of the risk borne by the government sector is much smaller than that borne by the social capital party. Consistent with the previously expected results, this result is unfair to the social capital side, and the use of a single utility theory to calculate the risk-sharing ratio will hinder the enthusiasm of social capital to participate in the quasi-public welfare water conservancy PPP project.

On the contrary, when government departments deal with risks, their processing capacity is often weaker than that of social capital,

and for various reasons, their cost is larger than that of social capital, while Shapley value theory considers more factors such as the cost and ability of both parties to deal with a certain risk. Therefore, when Shapley value theory is used alone to calculate the risk-sharing ratio of both parties in Chongqing Fengsheng Reservoir PPP project, the results are often beneficial to social capital. It can be seen from Figure 4 that the proportion of government departments to bear the risk loss calculated by Shapley value theory is 69.57%, and the proportion of social capital is 30.43%. The proportion of government departments to bear the risk is much higher than that of social capital. Consistent with the previous expected results, this result is unfair to government departments. Using a single Shapley value theory to calculate the risk-sharing ratio will lead to excessive burden on government departments and cannot give full play to the advantages of the PPP model.

However, the introduction of the PPP model for quasi-public welfare water projects can bring the advantages of financial support, professional management, risk sharing, technological innovation and other aspects, which can help promote the smooth implementation and long-term development of the project. Facilitating quasi-public welfare water PPP projects requires full consideration of the responsibilities and interests of the partners to ensure that the cooperation is fair and equitable in order to achieve a win-win situation. A single risk-sharing calculation method using utility theory or Shapley value theory cannot ensure fairness for all parties.

Therefore, in order to improve the enthusiasm of the partners of Chongqing Fengsheng Reservoir PPP project and reduce the overall risk of the project, this study is based on a multi-party perspective, coupling the Shapley value with the utility theory, amending the risk sharing ratio of the utility theory with the Shapley value, and taking into account the differences in the proportion of the parties' contributions, negotiation status, risk disposal ability, etc. The Shapley value is used to modify the risk sharing ratio of utility theory, and the risk sharing calculation is carried out by taking into account the contribution ratio, negotiation status, risk disposal ability difference and other factors of each party. The results of the study show that: when the risk sharing model based on Shapley value and utility theory is used, the proportion of risk borne by the government is 57.35%, which is slightly higher than that of the social capital party (42.65%), and the calculation result is in between the results of the single utility theory or the Shapley value theory. The risk sharing model demonstrates significant advantages over the single method in considering various factors among all parties, which supports the previously proposed hypothesis. The derived risk sharing ratio is shown to be fairer and more reasonable, effectively mitigating the issue of unfairness arising from the use of a single method to calculate results. The model thoroughly accounts for the distinct characteristics and strengths of government departments and social capital parties, leading to a more rational and widely accepted risk-sharing approach. Consequently, it successfully mobilizes the enthusiasm and benefits of all involved parties, thereby reducing overall project risk.

The risk sharing model brings various benefits to quasi-public water resources PPP projects. Firstly, a fair and reasonable risk sharing ratio facilitates the formation of cooperation consensus among PPP project stakeholders. During the initial stages of project collaboration, mutual recognition of the fairness in risk sharing serves as the foundation for establishing cooperation consensus. Consequently, acceptance of the equitable risk allocation reduces cooperation concerns and promotes successful project implementation.

Secondly, it encourages active participation of both social capital parties and government departments in quasi-public water resources PPP projects. The risk sharing model takes into account the characteristics and advantages of both parties, balancing their interests to derive a more equitable and acceptable risk sharing proportion.

Lastly, the model enhances the success rate of quasi-public water resources PPP projects. The fair and reasonable risk sharing mechanism reduces disputes and dissatisfaction over risk allocation, consequently improving the project's success rate. When all parties are satisfied with and perceive the risk sharing ratio as reasonable, they are more likely to fully commit to project implementation, thus reducing potential risks and uncertainties and increasing the likelihood of project success.

The successful application of this model provides robust support for the sustainable development of quasi-public water resources PPP projects and offers new research ideas and approaches for risk sharing in similar collaborative projects. By promoting active participation of all stakeholders through equitable risk sharing, the model achieves the dual objectives of risk reduction and project success. Hence, this model holds significant applicability value for future projects with similar characteristics.

6 Conclusion

In the context of quasi-public-welfare water conservancy PPP projects, both government departments and social capital parties encounter significant risks during the project implementation phase. This chapter aims to analyze the fundamental risk-sharing principles and evaluate the advantages and disadvantages of various risk-sharing methods. Furthermore, it establishes a risk-sharing model based on the Shapley Value and the Utility Theory, considering factors such as the involved parties' proportion of capital contributions, bargaining positions, and disparities in their risk management capacities. A risk study was conducted using the Chongqing Fengsheng Reservoir PPP project as a case study to analyze the risk sharing scheme. In light of a particular shared risk existed in the project, utility theory was employed to calculate the risk sharing ratio and Shapley values for different stakeholders. The Shapley values were then used to modify the utility theory-based risk sharing ratio. Based on these analyses, the following conclusions were drawn:

First, compared with the traditional cooperation model and risk sharing mechanism dominated by one party, this study proposes a fairer risk sharing mechanism in line with the characteristics of PPP projects for quasi-public welfare water conservancy PPP projects, in which all participants are on equal footing and need to take into account the interests of all parties and risk preferences at the same time.

Secondly, a quasi-public welfare water conservancy PPP project risk sharing model based on Shapley value theory and utility theory is constructed. Compared with the single use of shapley value theory, the government department bears 69.57% of the risk loss, and the single use of utility theory, the government department bears 34.62% of the risk loss. The calculation result of the coupling of Shapley value theory and utility theory is 57.35% of the risk loss borne by the

government department, which is between the results of the single method, and the result is more fair and reasonable. It enriches the risk management methods and theories of quasi-public welfare water conservancy PPP projects.

The research in this paper also has limitations and shortcomings. First of all, the parameter a in the risk utility function is only assumed to be brought into the calculation. In practical engineering applications, it is necessary to fit the actual observed utility data into the risk utility function by constructing mathematical models and optimization algorithms based on empirical research and specific problems. Otherwise, Risk sharing is based on risk identification, due to the lack of experience in quasi-public welfare water conservancy PPP projects, the construction of the risk evaluation index system has not yet been perfected, and the field should be further supplemented and improved in the next research. In addition, the research in this paper is a further optimization of the quantitative methods of risk sharing based on Shapley value theory and utility theory proposed by previous scholars, and the conclusions obtained are only superior to the single use of a particular method. If other new risk sharing methods emerge, it is necessary to conduct a comparative study of risk sharing methods.

Data availability statement

The original contributions presented in the study are included in the article/supplementary material, further inquiries can be directed to the corresponding author.

Author contributions

DL: methodology, writing original, and resources. LL: review and editing, investigation, and funding acquisition. XT: review and provided advice for analyzing the data and figures. All authors contributed to the article and approved the submitted version.

Funding

This work was supported by Key Water Conservancy Research Project in Hubei Province (HBSLKY202311).

Conflict of interest

The authors declare that the research was conducted in the absence of any commercial or financial relationships that could be construed as a potential conflict of interest.

Publisher's note

References

Appuhami, R., and Perera, S. (2016). Management controls for minimising risk in public-private partnerships in a developing country: evidence from Sri Lanka. *J. Account. Organ. Change* 12, 408–431. doi:10.1108/jaoc-10-2013-0075

Bi, X., Guo, H., and Fan, J. (2016). Operation mode of social capital invested in major water conservancy projects. *J. Econ. Water Resour.* 34 (1), 28–30. doi:10.3880/j.issn.1003-9511.2016.01.008

Ding, Y. (2005). *A study on the main problems of introducing BOT investment in China in the process of project financing and its countermeasures*. China: Southwestern University of Finance and Economics.

Fan, L. (2014). *A study on stakeholder benefit distribution of PPP projects based on the shapley value correction*. Tianjin: Tianjin University.

Gao, F. (2018). *Study on problems and countermeasures of PPP model in sewage treatment at the operation stage*. Beijing: Beijing University Of Civil Engineering And Architecture.

Ge, W., Jiao, Y., Wu, M., Li, Z., Wang, T., Li, W., et al. (2022). Estimating loss of life caused by dam breaches based on the simulation of floods routing and evacuation potential of population at risk. *J. Hydrology* 612, 128059. doi:10.1016/j.jhydrol.2022.128059

Heravi, G., and Hajihosseini, Z. (2012). Risk allocation in public–private partnership infrastructure projects in developing countries: case study of the tehran–chalus toll road. *J. Infrastructure Syst.* 18 (3), 210–217. doi:10.1061/(asce)is.1943-555x.0000090

Huang, Y., Xu, W., and Li, C. (2022). Information integration framework for a public–private partnership system of an urban railway transit project (Part B: an empirical application). *J. Industrial Inf. Integration* 25, 100245. doi:10.1016/j.jii.2021.100245

Jin, X. H. (2010). Determinants of efficient risk allocation in privately financed public infrastructure projects in Australia. *J. Constr. Eng. Manag.* 136 (2), 138–150. doi:10.1061/(asce)co.1943-7862.0000118

Jin, X. H. (2011). Model for efficient risk allocation in privately financed public infrastructure projects using neuro-fuzzy techniques. *J. Constr. Eng. Manag.* 137 (11), 1003–1014. doi:10.1061/(asce)co.1943-7862.0000365

Jin, X. H. (2011). Model for efficient risk allocation in privately financed public infrastructure projects using neuro-fuzzy techniques. *J. Constr. Eng. Manag.* 137 (11), 1003–1014. doi:10.1061/(asce)co.1943-7862.0000365

Khazaeni, G., Khanzadi, M., and Afshar, A. (2012). Optimum risk allocation model for construction contracts: fuzzy TOPSIS approach. *Can. J. Civ. Eng.* 39 (7), 789–800. doi:10.1139/l2012-038

Lambovska, M. (2016). A concept of decision-making in times of crisis and uncertainty. *KSI Trans. Knowl. Soc.* 9.

Lang, Q., Xu, D., and Li, L. (2017). Study on risk sharing mechanism of sponge city PPP projects. *Manag. Adm.* (11), 141–144. doi:10.16517/j.cnki.cn12-1034/f.2017.11.039

Li, B., Akintoye, A., Edwards, P. J., and Hardcastle, C. (2005). Critical success factors for PPP/PFI projects in the UK construction industry. *Constr. Manag. Econ.* 23 (5), 459–471. doi:10.1080/01446190500041537

Li, X. (2017). Application of PPP model in ecological water conservancy project. *Value Eng.* 36 (5), 250–251. doi:10.14018/j.cnki.cn13-1085/n.2017.05.099

Li, Y. (2017). *Research on risk allocation of infrastructure PPP mode based on game theory*. China: China University of Mining and Technology.

Li, Y. (2018). *Research on risk identification and sharing of PPP project in water conservancy infrastructure*. China: Fujian Agriculture and Forestry University.

Li, Y., and Wang, X. (2023). Game analysis of social capital violations and government regulation in public–private partnership risk sharing. *Syst. Eng.* 26, 305–316. doi:10.1002/sys.21657

Liu, X., and Wang, S. (2006). Experimenting with risk allocation principles and frameworks for PPP projects. *Constr. Econ.* (02), 59–63.

Mazher, K. M., Chan, A. P. C., Zahoor, H., Ameyaw, E. E., Edwards, D. J., and Osei-Kyei, R. (2019). Modelling capability-based risk allocation in PPPs using fuzzy integral approach. *Can. J. Civ. Eng.* 46 (9), 777–788. doi:10.1139/cjce-2018-0373

Nguyen, D. A., Garvin, M. J., and Gonzalez, E. E. (2018). Risk allocation in U.S. Public-private partnership highway project contracts. *J. Constr. Eng. Manag.* 144–5. doi:10.1061/(asce)co.1943-7862.0001465

Qiu, Y., Xu, Y., and Niu, Z. (2018). The application of PPP mode in water conservancy project construction. *Shandong Water Resour.* 2, 1. doi:10.16114/j.cnki.sdsl.2018.02.005

Sheng, S., and An, Y. (2019). Study on income distribution of PPP projects in water conservancy projects based on AHP-Shapley Value method. *Water Resour. Hydropower Eng.* 50 (2), 161–167. doi:10.13928/j.cnki.wrahe.2019.02.023

Shi, L., He, Y., Onishi, M., and Kobayashi, K. (2021). Double moral hazard and risk-sharing in construction projects. *IEEE Trans. Eng. Manag.* 68 (6), 1919–1929. doi:10.1109/tem.2019.2938261

Shrestha, A., Chan, T. K., Aibinu, A. A., Chen, C., and Martek, I. (2018). Risk allocation inefficiencies in Chinese PPP water projects. *J. Constr. Eng. Manag.* 144, 4. doi:10.1061/(asce)co.1943-7862.0001457

Tembo-Silungwe, C. K., and Khatleli, N. (2018). Identification of enablers and constraints of risk allocation using structuration theory in the construction industry. *J. Constr. Eng. Manag.* 144, 5. doi:10.1061/(asce)co.1943-7862.0001471

Tian, Y. (2014). *The research of sharing the risk in quasi-operating infrastructure projects under the PPP mode*. China: Chongqing University.

Wang, J. Q., and Yang, W. E. (2013). Multiple criteria group decision making method based on intuitionistic normal cloud by Monte Carlo simulation. *Syst. Eng. Theory Pract.* 33 (11), 2859–2865. doi:10.1515/ijeeps-2015-0077

Wang, J. S. (2017). Research on the market demand risk and sharing mechanism of PPP projects. *J. Railw. Eng. Soc.* 34 (11), 95–98.

Wang, J., You, W., Liu, F., Zhang, S., and Peng, L. (2018). Research on income distribution of PPP project in urban public parking lot based on Shapley Value method. *J. Qingdao Univ. Technol.* 39 (04), 100–106+126.

Wang, S. Q., Tiong, R. L. K., Ting, S. K., and Ashley, D. (2000). Evaluation and management of political risks in China's BOT projects. *J. Constr. Eng. Manag.* 126 (3), 242–250. doi:10.1061/(asce)0733-9364(2000)126:3(242)

Wang, Y. (2017). *Risk allocation and incentive mechanisms of PPP projects by using risk and social preferences theories*. China: Southwest Jiaotong University.

Wang, Z., Zhou, Y., Jin, X., Zhao, N., and Sun, J. (2022). Risk allocation and benefit distribution of PPP projects for construction waste recycling: a case study of China. *Eng. Constr. Archit. Manag.* doi:10.1108/ecam-10-2021-0855

Wang, Z., Zhou, Y., et al. (2022). *Risk allocation and benefit distribution of PPP projects for construction waste recycling: A case study of China*. Engineering: Construction and Architectural Management.

Wu, M., Wu, Z., Ge, W., Wang, H., Shen, Y., and Jiang, M. (2021). Identification of sensitivity indicators of urban rainstorm flood disasters: a case study in China. *J. Hydrology* 599, 126393. doi:10.1016/j.jhydrol.2021.126393

Wu, S., Huang, Y. J., Bao, B., Wu, L. M., Dong, J., Liu, X. H., et al. (2017). miR-508-5p acts as an anti-oncogene by targeting MESDC1 in hepatocellular carcinoma. *Constr. Sci. Technol.* 64 (11), 40–47. doi:10.4149/neo_2017_105

Xu, S., and Liu, L. (2018). Research on income distribution of hydropower PPP project based on modified interval shapley value method. *Water Resour. Power* 36 (05), 122–126.

Xu, X., Zhao, M., Li, X., and Song, C. (2022). A study on the risk assessment of water conservancy scenic spot PPP projects. *Sustainability* 14 (24), 16625. doi:10.3390/su142416625

Xu, Y., Chan, A. P. C., and Yeung, J. F. Y. (2010). Developing a fuzzy risk allocation model for PPP projects in China. *J. Constr. Eng. Manag.* 136 (8), 894–903. doi:10.1061/(asce)co.1943-7862.0000189

Xu, Y., Skibniewski, M. J., Zhang, Y., Chan, A. P. C., and Yeung, J. F. Y. (2016). Developing a concession pricing model for PPP highway projects. *Int. J. strategic Prop. Manag.* 16 (2), 201–217. doi:10.3846/1648715x.2012.688071

Xu, Z., Yin, Y., Li, D., and Browne, G. J. (2018). Owner's risk allocation and contractor's role behavior in a project: a parallel-mediation model. *Eng. Manag. J.* 30 (1), 14–23. doi:10.1080/10429247.2017.1408388

Yang, J. (2016). *Research on distribution of benefits of the railway PPP project Stakeholders' Interests based on AHP -Shapley value method*. Lanzhou: Lanzhou Jiaotong University.

Zhang, L. (2017). *Research on PPP project risk sharing model of urban rail transit based on game theory*. Beijing, Beijing Jiaotong University.

Zhang, M., Wang, F., Hong, H., Wang, A., Wang, J., et al. (2014). Membrane fouling in a submerged membrane bioreactor: effect of pH and its implications. *Innovation Sci. Technol.* 000 (021), 7–14. doi:10.1016/j.biortech.2013.10.096

Zhao, H., Ma, S., and Bu, Z. (2020). Constructing a risk-sharing framework for Sponge City PPP projects from the perspective of the individual participant. *Adv. Civ. Eng.* 2020, 1–16. doi:10.1155/2020/8832664

Zhao, M. (2018). *Rearch on risk sharing of urban rail transit PPP projects*. Xi'an: Xi'an University Of Technology.

frontiers | Frontiers in Earth Science

TYPE Brief Research Report
PUBLISHED 24 August 2023
DOI 10.3389/feart.2023.1232481

OPEN ACCESS

EDITED BY
Zongkun Li,
Zhengzhou University, China

REVIEWED BY
Shaowei Wang,
Changzhou University, China
Ziyang Li,
Nanjing Hydraulic Research Institute, China

*CORRESPONDENCE
Jeremy D. Bricker,
jeremydb@umich.edu

RECEIVED 31 May 2023
ACCEPTED 05 July 2023
PUBLISHED 24 August 2023

CITATION
Liu L, Bricker JD and Hu C (2023), Late-stage diversion risk assessment for high dams considering early initial impoundment: a case study of Lianghekou Station, China.
Front. Earth Sci. 11:1232481.
doi: 10.3389/feart.2023.1232481

Late-stage diversion risk assessment for high dams considering early initial impoundment: a case study of Lianghekou Station, China

Lian Liu[1], Jeremy D. Bricker[2,3]* and Chao Hu[4]

[1]Hubei Key Laboratory of Construction and Management in Hydropower Engineering, College of Hydraulic and Environmental Engineering, China Three Gorges University, Yichang, China, [2]Department of Civil and Environmental Engineering, University of Michigan, Ann Arbor, MI, United States, [3]Faculty of Civil Engineering and Geosciences, Delft University of Technology, Delft, Netherlands, [4]China Renewable Energy Engineering Institute, Beijing, China

Early initial impoundment can generate additional revenue but bring more flood risk in late-stage construction diversion. In view of the possible flood risk and catastrophic consequences caused by high dam failures induced by early impoundment, a comprehensive assessment is proposed. Taking the Lianghekou high rockfill dam on the Yalong River, southwest China, as an example, this study established the late-stage diversion risk model and predicted the failure probabilities for the original, 15 days ahead, and 30 days ahead schemes varied with the initial impoundment time using the Monte Carlo method. Then, considering overtopping-induced gradual breaking of rockfill dams, the NWS dam-break flood forecasting model (DAMBRK) was used to estimate the break development and the outflow hydrograph. Due to no significant differences being found in the outflow hydrographs of the three schemes, life loss was used an index for the consequences of inundation. Combining the failure probability, life loss, and early impoundment revenues brought by earlier power generation, a satisfied initial impoundment scheme was acquired using the multi-objective decision model. The results revealed this method can find a reasonable initial impoundment time in view of the late-stage diversion risk assessment.

KEYWORDS

late stage diversion, diversion risk assessment, initial impoundment, MC method, Lianghekou Station

1 Introduction

It is generally believed that a large-scale flood is not likely to occur within the dam construction period (Marengo et al, 2017), but a high dam's longer construction period makes flood risks more possible. Since 1930, half of all failures and most relevant fatalities for dams higher than 30 m have been due to overtopping during construction (Lempérière, 2017). Available hydrologic evidence demonstrates this (e.g., at Kariba, Oros, Aldedavilla, Akosombo, Cahora Bassa, Tarbela, and Aguamilpa). For high dams of a 200 m level, river diversion failure probability, as well as its consequences, may be amplified by high

impounded water levels, uncertain construction progress, and multiple construction flood seasons.

In the past 5 years, an increasing number of super high dams have been built or are being built in China, such as Xiluodu Station (285.5 m), Baihetan Station (289.0 m), Wudongde Station (270.0 m), Changheba Station (240.0 m), and Shuangjiangkou Station (305.0 m). Many of them choose to impound water ahead of schedule to generate more revenue in late-stage diversions. Compared with two other typical diversion processes—the initial and mid stage diversions—storage and discharge capacity are limited at the late stage. Once overtopping flood events happen, the water level rises rapidly and the unbuilt dam overtopping risk increases greatly. In this case, early initial impoundment will bring potential safety hazards if the late diversion system does not work well. In August 2018, an overtopping flood occurred at the Hidroituango rockfill dam (225 m) in Colombia, induced by the heavy rainfall during the late-stage diversion. Nevertheless, researchers believed that closing two diversion tunnels to impound water before the time when the dam height was sufficient and the intermediate discharge structure not being finished yet were the factors that produced the overtopping (Guillermo, 2018). This failure cost at least 1 billion dollars, including a 3-year delay in power sales loss, plus clean-up and reconstruction costs. Hence, a late-stage diversion risk assessment is desirable before taking early initial impoundment.

Present risk assessment-related research about river diversions during dam construction has mainly focused on the initial and mid stages. Diversion risk probability is predicted well if the probabilistic distribution functions for uncertainties are known based on the Monte Carlo Simulation method (Hu et al, 2006; Song et al, 2018; Liu et al, 2019; Zhang et al, 2019). Generally, the curve between tunnel discharge and the upstream water level is relatively simple, but more constraints have to be considered about tunnel discharge in late-stage diversions, such as the water level rising speed rate, the ecological flow requirement, and maintenance days, and previous diversion risk models have not yet reflected these. As for the risk consequences, the flood inundation damage commonly represents it with velocity of flow, water depth, and inundation duration (Moel et al, 2011; McGrath et al, 2015), while high dam (200 m–300 m) failures will bring catastrophic consequences and make water depth much higher than a common dam, which means the depth or duration-damage functions are not adopted in this situation, as the downstream cities or towns are nearly completely inundated.

Taking the Lianhekou high rockfill dam as the case study, this article aims to estimate the late-stage diversion failure probability and risk consequences due to overtopping varied with initial impoundment times. Considering the constraints of initial impoundment, the late-stage diversion risk model is established, and the uncertainties are simulated using the Monte Carlo method to calculate the risk probability. Combining the risk probability, inundation loss by empirical formulas, and early impoundment revenues brought by earlier power generation, a comprehensive assessment is made using a multi-attribute decision-making method.

FIGURE 1
Location of Lianghekou Station.

2 Study area

Lianghekou Station is situated at a section about 2 km downstream from the junction of the Yalong River and its tributary, the Xianshu River. It is 25 km north of Yajiang County and 640 km north of Panzhihua City along the Yalong River in Sichuan Province, southwest China. The Yalong River is one of tributaries of the Yangtze River. The Jinsha River, the upper main reach of the Yangtze River, and the Yalong River are both nearly parallel to the Lancang River, an international river in the junction of Xizang Province and Yunnan Province. A map indicating the study area is shown in Figure 1.

The Lianghekou earth core wall rockfill dam has a maximum height of 295 m, and the reservoir capacity is about 10.15 billion m^3. Average annual discharge is 666 m^3/s. Its construction started in 2014 and is ongoing in 2023 with the main purpose of energy generation, and the total generation capacity is 3,000 MW. As the layout of the diversion system of Lianghekou Station (Figure 2) shows, five diversion tunnels are at the construction site, three higher elevation tunnels (#3, #4, and #5) and two lower tunnels (#1 and #2) are on the left and right bank, respectively. At the end of February 2018, the mid stage diversion began, when the dam height was 2,658 m in elevation. When it comes to the late-stage diversion, the height should be at 2,775 m elevation. Table 1 provides the detailed original late-stage diversion procedure.

The power generation water level for the first unit (2,785 m) needs to go through two impoundment stages. The monthly average flood discharge is more than 550 m^3/s in September and October every year, when the water level exceeds the closed-gate standard. Accordingly, only stage II has the early impoundment opportunity but the possibility of overtopping still exists. Hence, two early schemes are implemented to compare with the original scheme as shown in Table 2, 15 days ahead and 30 days ahead, respectively.

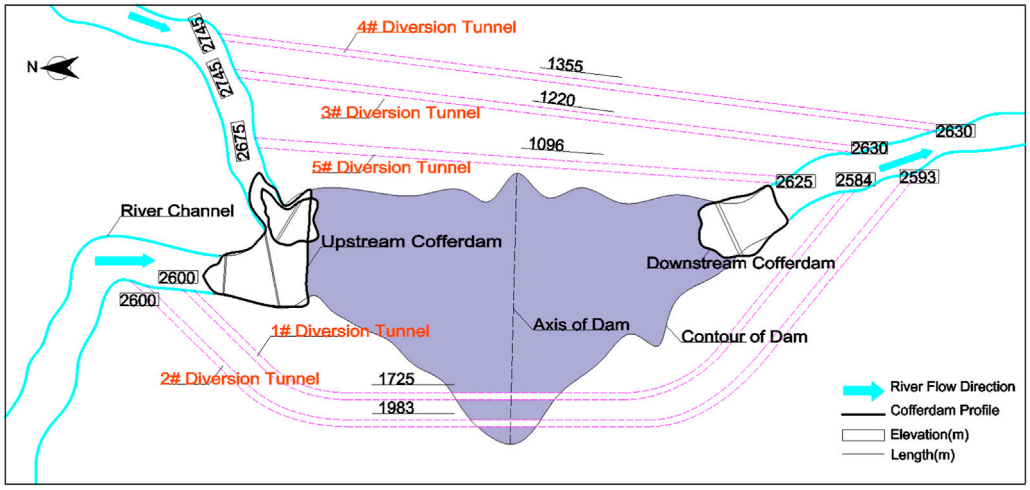

FIGURE 2
Layout of diversion system of Lianghekou Station.

TABLE 1 The original late-stage diversion procedure of Lianghekou Station.

Diversion procedure	Stage	Impoundment date	Discharge tunnels	Dam elevation (m)
Close/plug #1, #2	I	Nov. of the 8th year/Nov. of the 8th year—Mar. of the 9th year	#5	2,780
Retain water		Nov. of the 8th year—Mar. of the 9th year		2,800
Close/plug #5	II	Jun. of the 9th year/Jun—Oct. of the 9th year	#3, #4	2,808
Retain water		May of the 9th year—Oct. of the 10th year	#3, #4	
Close/plug #3		Nov. of the 10th year/Nov. of the 10th year—Mar. of the 11th year	#4	2,875

TABLE 2 Early impoundment schemes.

Scheme	Impoundment date	Dam elevation (m)	Dam width (m)
Original	1st June 2021	2,805.00	481.70
15 days ahead	15th May 2021	2,802.70	473.70
30 days ahead	1st May 2021	2,800.00	465.90

3 Materials and methods

3.1 Uncertainty analysis

Uncertainty refers to a condition or variable which is not able to be quantified exactly and it has random characteristics (Liu et al, 2017). Uncertainty analysis arises from our inability to assess the outcome of a system failure due to its inherent random characteristics in complex and non-linear models, and incomplete historical recorded data, or both. For a river diversion system risk assessment, hydrologic and hydraulic uncertainties are two main uncertain variables, which are described by flood inflow and diversion structure discharge, respectively (Afshar et al, 2009). One problem regarding these two variables under some predicable conditions is selecting their probabilistic distribution functions (PDF) to sample enough data with appropriate accuracy. The Pearson type III (P-III) distribution is widely accepted as the best PDF to fit hydrological variables like flood inflow series at different time scales in China (Wu et al, 2012; Hong et al, 2015), and it has also been generally adopted in river diversion risk analysis (Marengoa et al, 2013) and recommended to be used for frequency distributions for hydrological stochastic variables according to standard specifications in China (MWR, 2017a).

Another uncertainty is the discharge capacity of diversion structures, which is related to the river diversion system itself. Designed discharge that is inconsistent with the actual one often happens in practical construction due to design errors of hydraulic parameters or some unforeseen situations. Empirical formulas are

commonly used to calculate diversion structure discharge capacity, such as the Manning formula (Najafi et al, 2012; Andersson et al, 2019) being applied in open channels and the pressure flow formula in pressure tunnels. As the roughness highly correlates with the discharge value, its uncertainty can well describe the tunnel discharge uncertainty. Previous work (Johnson, 1996) has proved the roughness random variables approximate the normal distribution or triangular distribution, so it is reasonable and feasible that triangular distribution is assumed for diversion discharge variability (Liu et al, 2019; Zhang et al, 2019). Additionally, impoundment for high dams commonly uses tunnels at different elevations to discharge water in stages, and even adopts joint discharge, which makes the discharge capacity more random.

3.2 Upstream water level determination

These two uncertainties combined with the relationship between the reservoir discharge capacity q and reservoir water level Z jointly determine the highest upstream water level of the dam through the method of water balance calculation. In late-stage diversions, the reservoir capacity V is determined by the temporary dam section during construction, and its V-q and V-Z relation are generally obtained by measurement and hydrological observation. Hence, the flood regulating calculation can be expressed by the equation of water balance, V-q, and V-Z relations as Formula 1:

$$\begin{cases} \frac{1}{2}(Q_1 + Q_2)t - \frac{1}{2}(q_1 + q_2)t = V_2 - V_1 \\ q = f_1(V) \\ V = f_2(Z) \end{cases} \tag{1}$$

where Q_1 and Q_2 are the initial and end reservoir inflow in time interval t; q_1 and q_2 are the initial and end reservoir discharge in time interval t; V_1 and V_2 are the initial and end storage capacity in time interval t; f_1 is the functional relationship between q and V; and f_2 is the functional relationship between V and Z.

3.3 Late-stage diversion risk simulation

3.3.1 Risk model

Diversion risk is considered the failure probability of diversion works, which derives from uncertainties throughout the service life. For rockfill dams, overtopping is our most concerning and easily observed failure during the diversion period; therefore, this article defined overtopping probability as diversion risk. Compared with the initial- and mid-stage diversion risk definitions in previous studies (Zhang et al, 2014; Liu et al, 2019; Zhang et al, 2019), the late-stage diversion risk model with more constraints is as Formula 2:

$$R_t = P\left[(Z_m \geq H_d) \mid t, m, q, v, H_r, H_c\right] \tag{2}$$

$$s.t. \quad \begin{cases} q_{min} \leq q \leq q_{max} \\ 0 \leq v \leq v_{max} \\ H_r \leq h_{rmax} \\ H_c \leq h_{cmax} \end{cases}$$

where R_t is the diversion risk probability at time t; Z_m is the highest upstream water level of the dam; H_d is the dam elevation; $P(\ )$ is the probability that Z_m exceeds H_d under some constraints; m is the stages of impoundment; q is the discharge capacity of the diversion structures; q_{min} and q_{max} are the lower and upper limits of q; $v(\ )$ is the rising rate of the water level; v_{max} is the upper limit of v before the overtopping flood event occurs; H_r is the water head for the retaining of the tunnel gate; h_{rmax} is the upper limit of H_r; H_c is the water head for closing tunnel gate; and h_{cmax} is the upper limit of H_c.

3.3.2 Simulation method

Monte Carlo Simulation (MCS) is an effective approach to perform risk simulation which can replicate stochastic variables according to their distribution functions. It simplifies some complex mathematical analyses into a probabilistic model which is easily to implement. If the distribution functions are chosen reasonably, the problem of insufficient observation data can be solved. Therefore, MCS is widely applied in quantitative risk analyses involving uncertainties.

In the model above, R_t is obtained by the frequency statistics of sampling that Z_m is higher than H_d by MCS. H_d can be gained from the dam construction schedule, while Z_m cannot be calculated by the simulation-based sampling directly, as the measured highest upstream water level data sequence is too short during construction to fit a reliable distribution function. Therefore, the indirect access to credible samples of Z_m is the water balance calculation as described in 3.1 after generating random samples of flood inflow Q and discharge capacity q, which follow the P-III distribution and triangular distribution, respectively.

Each simulation generates one random flood inflow and one discharge of diversion structures, then outputs a single water level value at a time. The total simulation time is set as M. If the times that water level values are larger than the dam elevation H_d is N, the risk probability at time t is N/M.

3.4 Consequence

Besides the risk probability, consequence is also a significant quantitative index for risk assessment. The diversion risk assessment is separately defined as the product of overtopping probability and inundation loss downstream caused by overtopping. Compared with concrete dams and other dams with cementitious materials, rockfill dams have weaker flood resistance ability, especially when they are under construction. Hence, the extreme flood overtopping for the temporary dam section is highly likely to induce a dam break. The dam breach outflow and the river course characteristics both affect the downstream flood routing. Therefore, the numerical simulation for dam breach and flood routing can serve to risk assessment for dam failure and inundation.

3.4.1 Dam breach model

Overtopping breaking of rockfill dams in most cases is a kind of gradual breaking and is affected by overtopping flow, dam materials and structural type, and various other factors (Luo et al, 2014). The two modeling tasks of computing a dam breach outflow hydrograph and the flood routing through the downstream valley can be

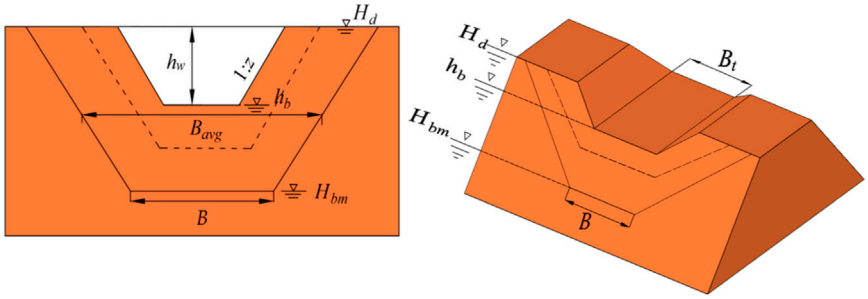

FIGURE 3
Geometric representation of breach parameters.

considered separately, and the breach outflow hydrograph can be further divided into a breach simulation and outflow hydrograph computation (Wurbs, 1987):

(1) The DAMBRK model (Fread, 1984) was used to predict the breach characteristics since breach outflow is largely by the geometry of the breach and the development of the breach with time. Figure 3 shows the breach parameter for a trapezoidal shape geometry required in the DAMBRK model. The final breach bottom width B can be determined using this relation:

$$B = B_{avg} - zh_w \tag{3}$$

where B_{avg} is the average breach width, and it can be deduced by empirical formula proposed by the Bureau of Reclamation (USBR, 1988); h_w is the water height above the breach bottom; and z is the breach side slope. Its value is deduced by the dam material and can refer to Formula 4:

$$z = \tan\left(45° + \frac{\varphi}{2}\right) \tag{4}$$

where φ is the internal friction angle of dam material, and 38° is reasonable since the main material of the dam is gravelly soil after rolling.

The development of the breach bottom elevation h_b and breach bottom width B_t can be seen as the functions of time in Formula 5:

$$\begin{cases} h_b = H_d - (H_d - H_{bm})\left(\frac{t_b}{T_k}\right)^{\rho} \\ B_t = B\left(\frac{t_b}{T_k}\right)^{\rho} \end{cases} \quad 1 < t_b < T_k \tag{5}$$

where H_d is the elevation of the dam; H_{bm} is the final breach bottom height; T_k is the dam break duration deduced by empirical formula proposed by the Bureau of Reclamation (USBR, 1988); t_b is the time that has elapsed since the beginning of the breach; and ρ is the parameter representing the breach non-linearity. In this paper, it is set as 1, assuming that the development of h_b and B_t follow a linear growth rate.

(2) The breach outflow Q_k is calculated using the broad crested weir equation shown in Formula 6–8. It can be seen as the upstream boundary for the flood routing model.

$$Q_k = V_c K_s \left[3.1 B_t (h_z - h_b)^{1.5} + 2.45 z (h_z - h_b)^{2.5}\right] \tag{6}$$

$$K_s \begin{cases} = 1 \quad \frac{h_f - h_b}{h_z - h_b} < 0.67 \\ = 1 - 27.8\left(\frac{h_f - h_b}{h_z - h_b} - 0.67\right)^3 \quad \frac{h_f - h_b}{h_z - h_b} \geq 0.67 \end{cases} \tag{7}$$

$$V_c = 1 + 0.023 \frac{{Q_p}^2}{{B_d}^2 (h_z - H_{bm})^2 (h_z - h_b)} \tag{8}$$

where V_c is the correction coefficient of the discharge; h_z is the reservoir water level by flood routing; h_f is the tail water level; and K_s is the coefficient considering the backwater effect of tailwater level. If K_s is 1, this effect is not considered; B_d is the dam width varied with impoundment time.

3.4.2 Inundation loss

Inundation loss mainly involves life loss and economic loss from damage caused by dam breaches. An approximation for loss of life derived from the historical record of dam failure and flash flood cases is put forward in Formula 7, and it was applied in the "Chinese risk assessment code for flood control on construction of hydropower and water resources project" issued by the National Energy Administration.

$$N_p = 0.075 P_T^{0.56} \exp[-0.759 T_w + (3.790 - 2.223 T_w) C_F] \tag{9}$$

where N_p is the number of lives lost; P_T is population of the at risk region; T_w is the number of hours warning; and C_F is the flooding forcefulness. If P_T is located on a plain, where flood water is likely to be shallow and slow, C_F is 0; if P_T is located in a canyon, where flood water is likely to be very deep and swift, C_F is 1.

It is reasonable to think human life value can be used as a statistical term to enable the numerical relation of life loss and economic loss to be established (Ge et al, 2017), although putting an economic value on human life can lead to strong criticism and opposition for ethical reasons.

The Chinese government, based on the economic data collected from prior accidents, believes that each individual death caused by an accident is roughly equivalent to 3.3 million to 5 million Yuan of direct economic loss. Thus, a ratio of 1 person to 4 million Yuan is recommended for the determination of economic risk criteria for dams in China (Li et al, 2018; Ge et al, 2022). Therefore, if the inundation areas are determined by numerical model, P_T and N_p will be used to estimate the direct economic losses.

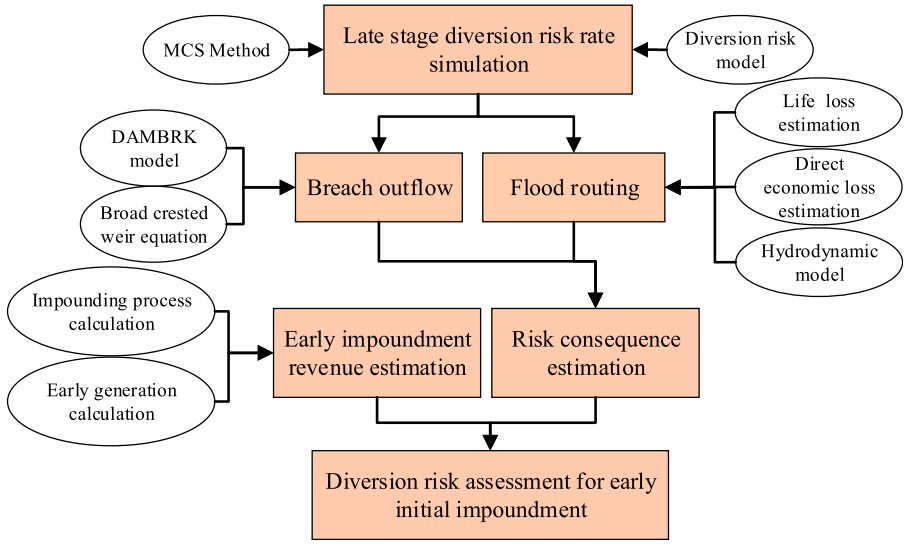

FIGURE 4
The technical route for late-stage diversion risk assessment.

TABLE 3 P-III distribution parameters of flood flow in the Yalong River.

Series	Mean value	Variation coefficient	Deviation coefficient
Flood peak (m^3/s)	3,050	0.29	1.16
7-day flood volume (10^8m^3)	15.4	0.29	1.16

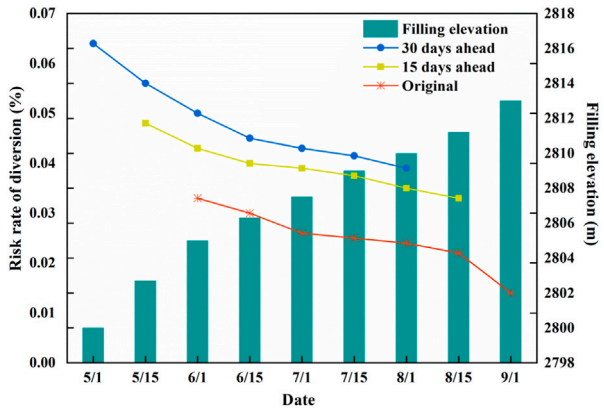

FIGURE 5
Diversion risk along with the impoundment time and filling elevation.

3.5 Generation revenue

Generation revenue comes from generation ahead of schedule, and is needed to predict how long the early impoundment will take compared with the original scheme. The early impoundment process calculation is as follows.

TABLE 4 Unbuilt dam parameters for the three schemes.

Scheme	G_t (m)	H_{bm}	H_d	B_{avg}	h_{bm}
Original	2,805	225.00	142.50	450.00	75.00
15 days ahead	2,802.7	222.70	141.04	445.40	74.23
30 days ahead	2,800	220.00	139.33	440.00	73.33

3.5.1 Inflow frequency analysis

The reservoir inflow data can be directly extracted from the annual runoff series during the impoundment period every year, and frequency analysis can be conducted.

3.5.2 Inflow hydrograph determination

According to "Chinese specification on water conservancy computation of hydroelectric projects", the inflow guarantee frequency for the initial impoundment calculation requires 75%–80%. Therefore, the inflow frequency which is closest to the guarantee frequency is selected as the inflow for the reservoir impoundment process calculation.

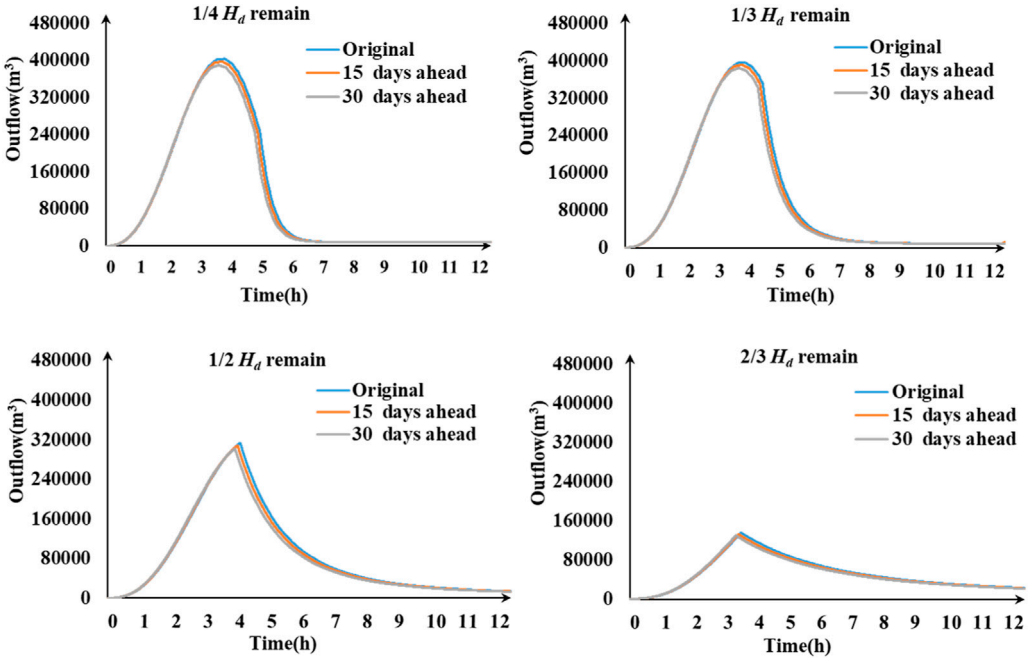

FIGURE 6
Breach outflow hydrographs of the three early impoundment schemes.

TABLE 5 The parameters and the result for loss of life in the 30 days ahead scheme.

Remains	Number of inundated villages	P_T (P)	T_w (h)	C_F	N_p
1/4	16	18,174	1.10	1	47.79
1/3	15	17,507	1.13	1	44.44
1/2	15	17,507	1.16	1	29.38
2/3	14	16,577	1.20	1	21.37

TABLE 6 The increased generation revenues for early impoundment schemes.

Impoundment schemes	B_i (million yuan)
15 days ahead	226.026
30 days ahead	334.949

Since impoundment and power generation is a gradual and continuous process, 1 day was selected for the generation calculation time step for accuracy requirements. The power generation calculation was described as follows:

Based on Bernoulli's equation and the energy conservation, the hydraulic turbine output power P and the daily generation w can be expressed as Formula 8

$$\begin{cases} P = 9.81 \times \eta_t \times \eta_g \times h \times q \\ w = T_o \times P \end{cases} \tag{10}$$

where h is the daily average net water head. It is equal to the difference between the impoundment water level and the downstream water level. η_t is the efficiency coefficient for the turbines; η_g is the efficiency coefficient for the generators; and q is the daily average water flow through the hydraulic turbines. It is equal to the reservoir inflow minus the outflow of the discharge structures and other water consumption, like ecological flow. T_o is the operation time.

The generation revenue B_g is given in Formula 9:

$$B_g = \sum_{i=1}^{T_c} w_i c \tag{11}$$

where T_c is the accumulated days; c is the electricity price; and w_i is the generation on the ith day.

Combining the failure probability, life loss, and early impoundment revenues brought by earlier power generation, a technical route for late-stage diversion risk assessment for high dams considering early initial impoundment is shown in Figure 4.

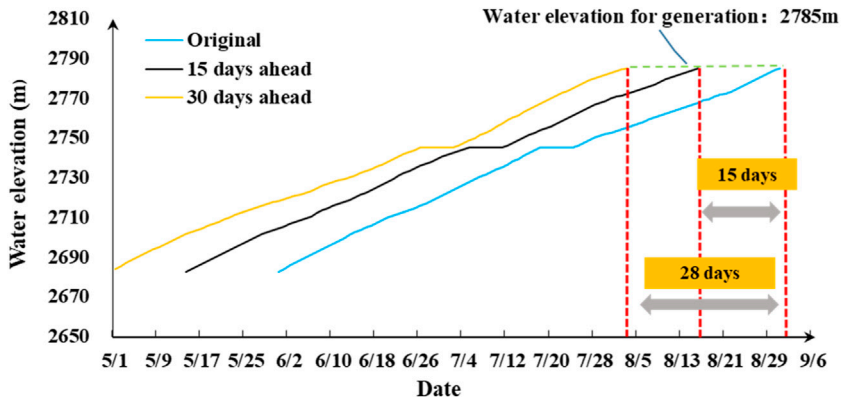

FIGURE 7
Days to reach generating water elevation in advance.

TABLE 7 Three indexes of the risk assessment for early initial impoundment.

Impoundment schemes	Risk probability (%)	N_p (P)	B_i (million yuan)
Original	0.023	45.010	0.000
15 days ahead	0.039	45.280	226.026
30 days ahead	0.048	47.790	334.949

TABLE 8 Three indexes expressed in unified dimensionless form.

Impoundment schemes	Risk probability	N_p	B_i
Original	0.209	0.326	0.000
15 days ahead	0.355	0.328	0.403
30 days ahead	0.436	0.346	0.597

4 Results

4.1 Risk probability

4.1.1 Hydrological parameters

Based on data from 1952 to 2012 from Yajiang hydrological station, the parameters of the Yalong River's P-III distribution are in Table 3. The random flood peak series were used to simulate flood hydrographs using the varied ratio amplification method (Xiao et al, 2007) deduced from a local typical flood hydrograph. The 2012 flood hydrograph was selected as the typical flood hydrograph. If the simulation time M was 10, the simulated flood hydrographs are in Supplementary Appendix SA.

4.1.2 Hydraulic parameter

In the second impoundment stage, tunnels #3 and #4 discharged jointly from November 2020 to March 2021. The discharge ability appeared in the triangular distribution and its parameters of maximum, median, and minimum were set as 0.98, 1.00, and 1.02, respectively. The relationship between reservoir discharge capacity q and reservoir water level Z in Formula 1 are given in the form of the relationship between reservoir capacity V and Z, as well as Z and q in Supplementary Appendix SB.

4.1.3 Other

The initial calculation water level is set 2,745 m as it is the starting level of the second impoundment stage; the ecological flow is 10% of the annual average flow, which is 67 m^3/s; the maximum flow is 6,387.5 m^3/s; The highest gate static water head is 70 m.

With all the data provided above, the upstream water level series and the highest upstream water level for each series can be calculated. Early impoundment makes the dam elevation for water retaining lower than that of the orginal scheme, so the risk simulation results using the MCS vary with the impoundment time advanced from May 31st to May 1st, as shown in Figure 5. To ensure accuracy and stability, the MCS should be conducted enough times to collect stable results. For this case, 100,000 times is enough. Figure 5 also reveals the tendency change of the diversion risk probability along with the impoundment time, and the filling elevation of the dam.

4.2 Overtopping break consequence

Since complete dam failures are rare, some remain parts of the dam will exist. Therefore, the breach bottom elevations are set 1/4 H_d, 1/3 H_d, 1/2 H_d, and 2/3 H_d. Table 4 gives the unbuilt dam parameters for the three schemes. The dam-break flood is set 5000-year flood to meet the worst condition. Breach failure time is predicted according to the

TABLE 9 The positive and negative ideal solutions and relative closeness of each scheme.

Impoundment schemes	Positive ideal solution	Negative ideal solution	Relative closeness
Original	0.304	0.057	0.441
15 days ahead	0.108	0.210	0.809
30 days ahead	0.443	0.051	0.337

empirical formula proposed by the Bureau of Reclamation (BR). The breach bottom elevation and breach bottom width vary linearly with time, and breach side slope z is 2.05.

The outflow hydrograph results in Figure 6 for the three impoundment schemes shows the outflow hydrographs have no significant difference.

The outflow hydrographs also indicate the flood routing and inundation loss of the three schemes are no different. The results of the hydrodynamic numerical calculations prove that all downstream villages with densely populated settlements along the river are totally under the water at a depth of 50–140 m. The consequences are catastrophic and homogeneous. Hence, the economic loss may not be considered as a risk assessment index in this case.

Since the downstream counties are all quite remote mountainous areas, the value of C_f is 1 in Formula 7. When the distance from the dam site is more than 50 km, people have sufficient evacuation time. Thus, the population at risk is in the Yajiang County region. The life losses are shown in Table 5. T_w is the duration from the time when the breach is observed to the outflow spread to the nearest village downstream. Through computing the flood routing, the number of inundated villages and the corresponding population P_T can be derived from the inundated water depth.

4.3 Early impoundment revenue

After frequency analyzing for runoff series from June to August at the dam site, the inflow of 1987 was selected as the reservoir impoundment inflow (the monthly average flow was 1,015.7 m^3/s) due to its 75.9% frequency, which is in the range of 75%–80%. During the impoundment period, the ecological water supply needs to be guaranteed. Generally, the ecological water demand for downstream rivers is about 10%–20% of the average annual flow. Therefore, the minimum ecological water outflow is 10% of the average flow, approximately 67 m^3/s below 2,745 m and 96 m^3/s above 2,745 m.

From June to August, the inflow is relatively large, so it has little effect on the guaranteed output of the downstream cascade power stations. Therefore, this paper does not consider the downstream station's generation requirement, and assumes that no surplus water can be realized by reasonable reservoir operation, which means the early generation capacity is the effective energy that can be absorbed by the grid system.

The water level control principle while rising is: at 2,685–2,745 m, the rising rate is not more than 1.5 m per day, and the monthly total rising height is within 40 m; when reaching 2,745 m, the water level must to be maintained at 2,745 m for 7 days due to the requirement for tunnel #5 closure; at 2,745–2,785 m, the rising rate is not more than 1.6 m per day, and the monthly total rising height is within 50 m. The dates of reaching the 2,745 m level of early impoundment are in Figure 7. The original scheme's date is from 1 June to 1 September. The other two schemes' dates are from 15 May to 16 August and 1 May to 3 August, respectively, and the time to reach 2,785 m has been advanced by 28 and 15 days, respectively.

The electricity price in the grid is set 0.343 yuan/KWh according to the Sichuan Provincial Development and Reform Commission. Hence, the increased generation revenues for early impoundment B_i are predicted by Formula 8 in Table 6.

4.4 Risk assessment

Three indexes of the risk assessment for early initial impoundment of the Lianghekou dam are in Table 7. They are expressed in unified dimensionless form in Table 8. By combining the subjective and objective weights with linear calculation, the weight vector for indexes w is obtained as {0.267, 0.201, and 0.532}. Based on the TOPISI multi-attribute decision-making method, the positive and negative ideal solutions and relative closeness of each scheme are in Table 9.

The highest value of relative closeness is the most satisfactory scheme in Table 9. Hence, 15 days ahead is the best initial impoundment scheme, and the existing scheme comes next MWR—Ministry of Water Resources, 2017b.

5 Conclusion

In this research, a late-stage diversion risk assessment for high dams considering early initial impoundment has been applied to the Lianghekou Station, and used to find a reasonable impound time for early generation. In the proposed approach, the Monte Carlo method is employed for risk simulation to obtain the dam overtopping probability for one assessment index. Considering overtopping-induced gradual breaking, the DAMBRK model and empirical formulas of life loss can serve as the inundation consequence estimation, which is selected as the second index. The days to reach 2,785 m in advance are predicted through impoundment process calculations, and used for assessing the increase of generation revenue, and is the third index. The three indexes are introduced in a multi-objective decision model for risk assessment. After comparing the three schemes, the 15 days ahead initial impoundment scheme is the best considering the three indexes. Generally, the major conclusions of this research are highlighted as follows.

(1) The tendency change of the late-stage diversion risk probability along with the impoundment time and corresponding dam elevation are significant. The equivalent return period of each late-stage diversion scheme is higher than the 500-return-year flood period, which means all three schemes meet the engineering design requirement.

(2) The breach outflow for high rockfill dam breaches induced by overtopping failure is extremely large. The economic loss brought about by high dam breaches is not sensitive to the impact of impoundment time. Hence, the economic loss of inundation may not be considered as an assessment index.
(3) The good performance of the 15 days ahead scheme indicates that it is feasible and scientific to take early initial impoundment for the Lianghekou dam.

Data availability statement

The original contributions presented in the study are included in the article/Supplementary Material, further inquiries can be directed to the corresponding author.

Author contributions

LL: writing, content conception, data processing, and funding acquisition; JB: software and formal analysis; CH: data resource and subject selection. All authors contributed to the article and approved the submitted version.

Funding

This work was supported by the Open Foundation of Hubei Key Laboratory of Construction and Management in Hydropower Engineering (2020KSD12) and the National Natural Science Foundation of China (No.51879147).

Acknowledgments

The authors would like to thank Hu Zhigen and Liu Quan at Wuhan University for their help with the diversion risk model. We also thank the Faculty of Civil Engineering and Geosciences, Delft University of Technology, which provided us with a high-performance server for parallel computing.

Conflict of interest

The authors declare that the research was conducted in the absence of any commercial or financial relationships that could be construed as a potential conflict of interest.

Publisher's note

All claims expressed in this article are solely those of the authors and do not necessarily represent those of their affiliated organizations, or those of the publisher, the editors and the reviewers. Any product that may be evaluated in this article, or claim that may be made by its manufacturer, is not guaranteed or endorsed by the publisher.

Supplementary material

The Supplementary Material for this article can be found online at: https://www.frontiersin.org/articles/10.3389/feart.2023.1232481/full#supplementary-material

References

Afshar, A., Rasekh, A., and Afshar, M. H. (2009). Risk-based optimization of large flood-diversion systems using genetic algorithms. *Optim. Eng.* 41 (3), 259–273. doi:10.1080/03052150802433213

Andersson, L. R., Hellström, J., Gunnar, I., Andreasson, P., and Lundström, T. S. (2019). Numerical investigation of a hydropower tunnel: Estimating localised head-loss using the Manning equation. *Water* 11 (8), 1562. doi:10.3390/w11081562

Ávila, Guillermo (2018). "Risk conditions for possible failure of HidroItuango dam in Colombia," in Proceedings of 2018 IPL Symposium on Landslides, Kyoto, Japan, December 3, 2018.

Fread, D. L. (1984). *Dambrk: The NWS dam-break flood forecasting model*. MA, United States: National Weather Service (NWS) Report, NOAA, Silver Spring.

Ge, W., Jiao, Y., Wu, M., Li, Z., Wang, T., Li, W., et al. (2022). Estimating loss of life caused by dam breaches based on the simulation of floods routing and evacuation potential of population at risk. *J. Hydrology* 612, 128059. doi:10.1016/j.jhydrol.2022.128059

Ge, W., Li, Z. K., Liang, R. Y., Li, W., and Cai, Y. C. (2017). Methodology for establishing risk criteria for dams in developing countries, case study of China. *Water Resour. Manag.* 31 (13), 4063–4074. doi:10.1007/s11269-017-1728-0

Hong, X. J., Guo, S. L., Zhou, Y. L., and Xiong, L. H. (2015). Uncertainties in assessing hydrological drought using streamflow drought index for the upper Yangtze River basin. *Stoch. Environ. Res. Risk Assess.* 29 (4), 1235–1247. doi:10.1007/s00477-014-0949-5

Hu, Z. G., Fan, X. E., Liu, Q., and Huang, H. (2006). Design of integrated risk distribution mechanism of construction diversion system. *J. Hydraulic Eng.* 37 (10), 1270–1277. doi:10.3321/j.issn:0559-9350.2006.10.020

Johnson, P. A. (1996). *Uncertainty* of hydraulic parameters. *J. Hydraulic Eng.* 122 (2), 112–114. doi:10.1061/(asce)0733-9429(1996)122:2(112)

Lempérière, F. (2017). Dams and floods. *Engineering* 3 (1), 144–149. doi:10.1016/J.ENG.2017.01.018

Li, Z., Li, W., and Ge, W. (2018). Weight analysis of influencing factors of dam break risk consequences. *Nat. Hazards Earth Syst. Sci.* 18 (12), 3355–3362. doi:10.5194/nhess-18-3355-2018

Liu, L., Luo, S., Zhao, C. J., Zhou, Y. H., Wang, J., He, J., et al. (2019). Choice of surgical procedure - lobectomy, segmentectomy, or wedge resection - for patients with stage T1-2N0M0 small cell lung cancer: A population-based study. *Eng. Lett.* 27 (3), 593–600. doi:10.1111/1759-7714.12943

Liu, Q., Hu, Z. G., Qi, Z. J., and Min, R. (2017). Risk feature analysis of river diversion for dam reconstruction on the original site. *Adv. Eng. Sci.* 49 (5), 35–41. doi:10.15961/j.jsuese.201700079

Luo, Y., Chen, L., Xu, M., and Huang, J. (2014). Breaking mode of cohesive homogeneous earth-rock-fill dam by overtopping flow. *Nat. Hazards* 74 (2), 527–540. doi:10.1007/s11069-014-1202-8

Marengo, H., Arreguin, F. I., Aldama, A. A., and Morales, V. (2017). Case study: Risk analysis by overtopping of diversion works during dam construction: The La Yesca hydroelectric project, Mexico. *Engineering* 42 (3), 26–34. doi:10.1016/j.strusafe.2013.01.005

Marengoa, H. H., Arreguin, F. I., Aldama, A. A., and Morales, V. (2013). Case study: Risk analysis by overtopping of diversion works during dam construction: The La Yesca hydroelectric project, Mexico. *Struct. Saf.* 42, 26–34. doi:10.1016/j.strusafe.2013.01.005

McGrath, H., Stefanakis, E., and Nastev, M. (2015). Sensitivity analysis of flood damage estimates: A case study in fredericton, new brunswick. *Int. J. Disaster Risk Reduct.* 14, 379–387. doi:10.1016/j.ijdrr.2015.09.003

Moel, H. D., and Aerts, J. C. (2011). Effect of uncertainty in land use, damage models and inundation depth on flood damage estimates. Nat. Hazards 58, 407–425. doi:10.1007/s11069-010-9675-6

MWR—Ministry of Water Resources (2017b). *Regulation for hydrologic computation of water resources and hydropower projects; sl278-2002*. Beijing, China: The Ministry of Water Resources of the People's Republic of China.

MWR—Ministry of Water Resources (2017a). *Specifications for construction planning of water resources and hydropower projects; sl303-2017*. Beijing, China: The Ministry of Water Resources of the People's Republic of China.

Najafi, M. R., and Nabipour, M. (2012). The effect of step on the hydraulic characteristics of the subcritical free surface flow in conveyance tunnel. *Tunn. Undergr. Space Technol.* 28 (1), 212–217. doi:10.1016/j.tust.2011.10.013

Song, Z. D., Liu, Q., Hu, Z. G., Li, H. A., and Xiong, J. Q. (2018). Assessment of sediment impact on the risk of river diversion during dam construction: A simulation-based project study on the jing river, China. *Water* 10 (2), 217. doi:10.3390/w10020217

USBR (1988). *Bureau of Reclamation, Downstream hazard classification guidelines*. Denver: U.S. Dept. of the Interior, Bureau of Reclamation. ACER Tech. Memorandum Rep. No. 11.

Wu, Y. C., Liou, J. J., Su, Y. F., and Cheng, K. S. (2012). Establishing acceptance regions for L-moments based goodness-of-fit tests by stochastic simulation. *Stoch. Environ. Res. Risk Assess.* 26 (6), 49–62. doi:10.1016/j.jhydrol.2008.02.023

Wurbs, R. A. (1987). Dam-breach flood wave models. *J. Hydraulic Eng.* 113 (1), 29–46. doi:10.1061/(asce)0733-9429(1987)113:1(29)

Xiao, Y., Guo, S. L., and Xiong, L. H. (2007). A new random simulation method for constructing synthetic flood hydrographs. *J. Sichuan Univ. Eng. Sci. Ed.* 39 (2), 55–60. doi:10.3969/j.issn.1009-3087.2007.02.010

Zhang, C., and Hu, Z. G. (2019). Risk model of flow diversion in the initial through middle stages for high arch dam construction and its application. *Adv. Water Sci* 30 (1), 102–111. doi:10.14042/j.cnki.32.1309.2019.01.011

Zhang, C., and Hu, Z. G. (2014). Water containment risk estimation during interim flooding for high rock-fill dams. *Adv. Water Sci.* 25 (6), 102–111. doi:10.14042/j.cnki.32.1309.2014.06.015

frontiers | Frontiers in Earth Science

TYPE Methods
PUBLISHED 28 August 2023
DOI 10.3389/feart.2023.1238394

OPEN ACCESS

EDITED BY
Xihui Gu,
China University of Geosciences Wuhan, China

REVIEWED BY
Yanhui Pan,
Huanghuai University, China
Lingjie Zhang,
Henan Vocational College of Water Conservancy and Environment, China
Yongqiang Zhou,
Chinese Academy of Sciences (CAS), China

*CORRESPONDENCE
Wei Li,
liwei@zzrvtc.edu.cn

RECEIVED 11 June 2023
ACCEPTED 08 August 2023
PUBLISHED 28 August 2023

CITATION
Li W, Yi J, Liu J, Zhang H and Jiao Y (2023), Dam failure environmental standards in China based on ecosystem service value. *Front. Earth Sci.* 11:1238394. doi: 10.3389/feart.2023.1238394

Dam failure environmental standards in China based on ecosystem service value

Wei Li[1,2]*, Jianni Yi[1], Jie Liu[1], Hexiang Zhang[2] and Yutie Jiao[2]

[1]Henan Engineering Research Center of Rail Transit Intelligent Security, Zhengzhou, China, [2]School of Water Conservancy and Environment, Zhengzhou University, Zhengzhou, China

Dam failure risk standards are the foundation of risk decision-making for dam managers. However, as an important component of dam failure risk standards, there are currently no unified environmental risk standards. Drawing on research ideas of ecological economics on ecosystem service values and equivalent factor methods, this study quantified environmental values and effectively connected environmental standards with existing standards using the ALARP principle and the F-N curve. Considering the differences in environmental and economic conditions in different regions, a risk preference matrix was constructed to determine the risk preference of each region and formulate the dam failure environmental risk standards for China. This study presents a preliminary exploration of the formulation of dam failure environmental risk standards, providing new methods and ideas for subsequent research.

KEYWORDS

dam failure, environmental risk standards, equivalent factor method, risk preference, ecosystem service (ES) values

1 Introduction

Recently, owing to frequent extreme weather events and the increasing occurrence of flood events exceeding standards, and problems such as design defects, poor construction quality, and inadequate operation and management of many reservoir dams in China, dam collapses occur occasionally (Chen Junfei et al., 2020; Xu et al., 2022). With continuous social and economic development, people are paying attention to the quality of their living environments (Tu et al., 2023). Environmental standards for dam collapse form the basis for environmental risk assessments and decision-making. Developing reasonable ecological environment risk standards is conducive to helping decision makers fully understand the risk level of dams to ensure scientific risk decisions, and has important significance for improving the evaluation system for the consequences of dam collapse risks and the theoretical management of dam risks (He et al., 2020).

Currently, there is no unified environmental standard for dam collapses (Li et al., 2019; Ge Wei. et al., 2020). This is primarily because the environmental scope of a dam collapse is wide, and there are many influencing factors. Furthermore, there is no unified dimensionality, making it difficult to quantify environmental values. Compared with the loss of life and economic losses caused by dam collapse, little attention has been paid to the environmental impact of dam collapse in previous studies. Therefore, most current research focuses on the construction of dam collapse indicator systems and mathematical method analysis. For example, Wang et al. (2006) believed that common environmental impacts refer to changes in environmental conditions caused by developmental activities or the formation of new environmental conditions. The environmental impacts of dam collapses mainly

include those on river morphology, loss of habitats for organisms and their growth, destruction of human landscapes, and industrial impacts that are susceptible to or cause considerable environmental effects or pollution, and define an impact index to evaluate risk size. He et al. (2008) believed that environmental impact refers to changes in environmental conditions in the area near the reservoir caused by dam collapses, which are specifically reflected in the impact on water, soil, ecology, and human habitats; they applied the Analytic Hierarchy Process and fuzzy mathematics to evaluate risk size. Francisco and Gallardo Izquierdo (2008) believed that environmental risk is primarily related to the erosion of the underlying surface of the dam, seepage, and pollution load, and defined the environmental safety index of the dam to calculate environmental risk. Cheng and Zhou (2013) believed that environmental impact refers to the effects of human activities, including economic and social activities, on the environment, and the resulting changes in the environment. Seven factors–river morphology, water environment, soil environment, vegetation cover, biodiversity, human environment, and pollution industry–were selected for analyzing the environmental impact of dam collapses, and the fuzzy mathematics theory was applied for environmental risk assessment. Xu et al. (2013) analyzed the environmental impact based on factors such as land-carrying capacity, water quality, reservoir siltation, downstream riverbed erosion, and earthquake geological hazards. These studies determined the factors of environmental impact and provide an important research basis for environmental assessment.

The above mentioned methods can be effectively used to rank the severity of environmental impacts caused by dam failures. However, they cannot provide specific representations of the consequences (typically categorized into 3–5 levels of severity), and are therefore semi-quantitative evaluations that may not be universally applicable. To achieve a quantitative representation of the environmental value of dam failures, the energy footprint method was introduced for the risk assessment of the environmental impacts of dam failure. This method is commonly used in ecological impact assessments (Binod et al., 2019; Chen Shurui et al., 2020; Yang et al., 2020). However, the scientific validity and accuracy of the energy conversion rate and energy conversion coefficients still require improvement. Meanwhile, the quantification of Ecosystem Service Value (ESV) based on the equivalent factor method is intuitive, widely used, and requires little data, making it suitable for regional- or global-scale environmental value assessments (Chen et al., 2023; Yang et al., 2023; Zhang et al., 2023).

The essence of the environmental impact is the change in the natural environment and ecological conditions of areas near the reservoir, caused by dam failure. Natural and ecological environments are composed of two parts, biotic and abiotic. Natural ecosystems provide various raw materials or products directly for survival (food, water, oxygen, wood, fibers, etc.) and regulate the climate, purify pollution, retain water sources, maintain soil and water, prevent wind and sand, reduce disasters, and protect biodiversity on a large scale (Enes and Ibrahim, 2022). Through its functions, the natural ecosystem continuously provides environmental conditions and material foundations for humans, creating service value (similar to the GDP created by human labor) (Langill Jennifer et al., 2022). Therefore, from the human perspective, the concept of environmental impact caused by dam failures can be defined as the destruction of the natural ecosystem service supply, resulting in a reduction in the output of ecosystem service value.

Based on the equivalent factor method for quantifying environmental values, this study explored the preliminary construction of China's regional dam break environmental risk standards using the ALARP principle, F-N curve method, and risk matrix, providing a new approach and method for subsequent research.

2 Methods

2.1 As low as reasonably practicable (ALARP) principle

No system carries risks that cannot be eliminated completely through preventive measures. Although the lower the risk of a system the higher the level of security, it is increasingly difficult and costly to further reduce the risk level. Given China's economic and social development level and the public's willingness to accept risks, a trade-off can be made between the risk level and the cost of a system. Therefore, the ALARP principle was selected to establish risk standards in China.

This principle stands divides risks into three zones: intolerable, ALARP, and broadly acceptable (Langdalen et al., 2020). If the risk falls into an intolerable zone, measures must be taken to reduce the risk. If it falls into the ALARP zone, taking risk control measures depends on whether risk reduction is feasible and whether the benefits outweigh the costs. If a risk falls into the broadly acceptable zone, no risk-control measures are required. This principle is illustrated in Figure 1.

2.2 F-N curve method

In 1967, Farmer proposed a limit curve for the acceptable risk of various accident types using probability theory, known as the famous F-N curve (Pei et al., 2018). The F-N curve is a limiting curve based on probability theory that allows various accidents to occur. It is based on probabilistic analysis and expected benefits, and takes into account the current state of risk in which it is located as well as people's aversion to risk, and it is highly scientific and versatile. It was first used for risk assessment in nuclear power plants and was later widely applied in the construction of social life risk standards for dam engineering. The expression for this curve is as follows:

$$1 - FN(x) < \frac{C}{x^n} \tag{1}$$

where $F_N(x)$ is the distribution function of the annual mortality rate, representing the probability of x deaths; $1-F_N(x)$ is the probability of $\leq N$ deaths; C is a constant that determines the position of the risk control line; and n is the slope that represents the degree of aversion to risk, with a larger slope indicating greater ecosystem to risk and less acceptability.

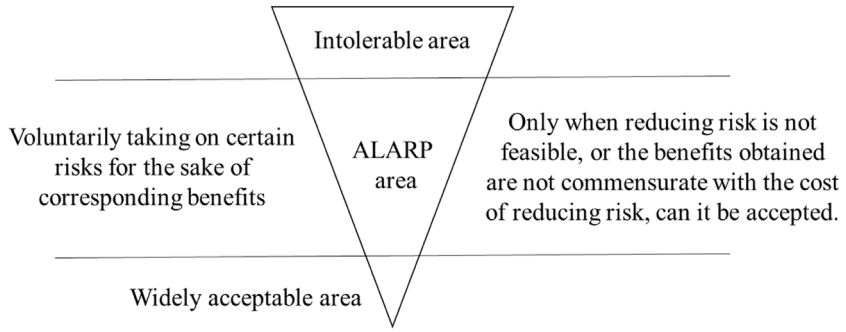

FIGURE 1
ALARP guidelines.

According to the Chinese State Council's "Regulations on Reporting and Investigating Production Safety Accidents," one death is equivalent to a direct economic loss of 3.3–5 million RMB (Li et al., 2015). Therefore, it is suggested to construct China's economic risk standards for reservoir dams based on a ratio of 4 million RMB per person. Although measuring human life values in economic terms is often considered inhumane and has gained strong criticism and opposition, it is reasonable to use life risk standards as a basis for constructing economic risk standards under the premise of controlling life risks at socially acceptable levels.

Constructing the environmental risk criteria for dam failure on the basis of the life and economic risk criteria avoids over-complicating the criteria on the one hand, and on the other hand allows for a strong correlation between the different criteria. Therefore, it is proposed to analyze the economic perspective by simplifying the environmental loss to the money needed to compensate the environmental risk, then the relationship between the loss of environmental value and its exceeding probability is as follows:

$$1 - FN'(x) < \frac{C}{x^n} \tag{2}$$

where $FN'(x)$ is the probability distribution function in which the funds needed to compensate for ecological and environmental risks $<x$, C is a constant, and n is the slope of the standard line

3 Estimation of environmental value

The Equivalent Factor Method is quantitative and based on expert knowledge. It is used to estimate the Ecosystem Service Value (ESV) (Zhang et al., 2022). One standard ecological value equivalent factor is defined as the economic value of natural food production per hectare of farmland with a national average yield (Cao et al., 2021). This reflects the potential contribution of ecosystems to ecological services. Food production reflects the value of the agricultural ecosystem, and the economic value of food production is primarily calculated based on three major grain crops: rice, wheat, and maize. The formula is as follows:

$$D = Sr \times Fr + Sw \times Fw + Sm \times Fm \tag{3}$$

Where D represents the environmental value of one standard equivalent factor (in yuan per hectare); Sr, Sw, and Sm represent the percentage of the planting area of rice, wheat, and maize, respectively, in the total planting area of the three crops; and Fr, Fw, and Fm represent the average net profit per hectare of rice, wheat, and maize, respectively, in China. The basic equivalent factor was determined to be 1482.67 yuan based on the data from China Statistical Yearbook 2017, 2018, and 2019 (National Bureau of statistics of the people's Republic of China, 2019), and the Compilation of National Agricultural Cost and Benefit Data (National Development Planning Commission, 2019).

Based on previous research results and expert experience, we constructed basic equivalent factors for different types of ecosystems and different types of environmental values, as shown in Table 1. Land-use remote sensing data were used to correspond farmland ecosystems to agricultural land types and wetland ecosystems to swamp land types. The average equivalent factors for forest, grassland, water, and desert ecosystems in the second level of classification were used as the calculation factors for the forest, grassland, water, and unused land (excluding swamp land) types in the remote sensing data. Based on Table 1, the ESV for each region in China in 2020 were calculated as shown in Figure 2.

4 Construction of environmental risk standards for dam failure based on ESV

4.1 Principles for constructing risk standards

Owing to substantial differences in politics, economics, culture, and other aspects among different countries (Li et al., 2018; Ge et al., 2020b), foreign risk standards cannot be directly applied to China (Ge et al., 2017; Ge et al., 2020c). Based on relevant domestic and foreign achievements and China's national conditions, the following principles were used to construct risk standards for dams:

(1) Compliance with the safety status of Chinese dams. Several of China's active reservoir dams were built from the 1950s to the 1970s. They were limited by economic and technological levels at that time, and several have hidden safety hazards. If standards

TABLE 1 Equivalent value of ecosystem services per unit area.

Ecosystem classification		Supply services			Conditioning services			Support services			Cultural services		Total
First-level	Secondary classification	Food production	Raw material production	Water supply	Air regulation	Climate regulation	Environmental purification	Hydrological regulation	Soil conservation	Maintenance of nutrient cycling	Biodiversity	Aesthetic landscape	
Farmland	Dry land	0.85	0.40	0.02	0.67	0.36	0.10	0.27	1.03	0.12	0.13	0.06	4.01
	Paddy field	1.36	0.09	−2.63	1.11	0.57	0.17	2.72	0.01	0.19	0.21	0.09	3.89
Forest	Coniferous	0.22	0.52	0.27	1.70	5.07	1.49	3.34	2.06	0.16	1.88	0.82	17.53
	Coniferous broadleaf hybrid	0.31	0.71	0.37	2.35	7.03	1.99	3.51	2.86	0.22	2.60	1.14	23.09
	Broadleaves	0.29	0.66	0.34	2.17	6.50	1.93	4.74	2.65	0.20	2.41	1.06	22.95
	Shrub	0.19	0.43	0.22	1.41	4.23	1.28	3.35	1.72	0.13	1.57	0.69	15.22
Grassland	Grassland	0.10	0.14	0.08	0.51	1.34	0.44	0.98	0.62	0.05	0.56	0.25	5.07
	Thicket	0.38	0.56	0.31	1.97	5.21	1.72	3.82	2.40	0.18	2.18	0.96	19.69
	Meadow	0.22	0.33	0.18	1.14	3.02	1.00	2.21	1.39	0.11	1.27	0.56	11.43
Wetland	Wetland	0.51	0.50	2.59	1.90	3.60	3.60	24.23	2.31	0.18	7.87	4.73	52.02
Desert	Desert	0.01	0.03	0.02	0.11	0.10	0.31	0.21	0.13	0.01	0.12	0.05	1.1
	Bare ground	0.00	0.00	0.00	0.02	0.00	0.10	0.03	0.02	0.00	0.02	0.01	0.2
Waters	Water system	0.80	0.23	8.29	0.77	2.29	5.55	102.24	0.93	0.07	2.55	1.89	125.61
	Glacial snow	0.00	0.00	2.16	0.18	0.54	0.16	7.13	0.00	0.00	0.01	0.09	10.27

10.3389/feart.2023.1238394

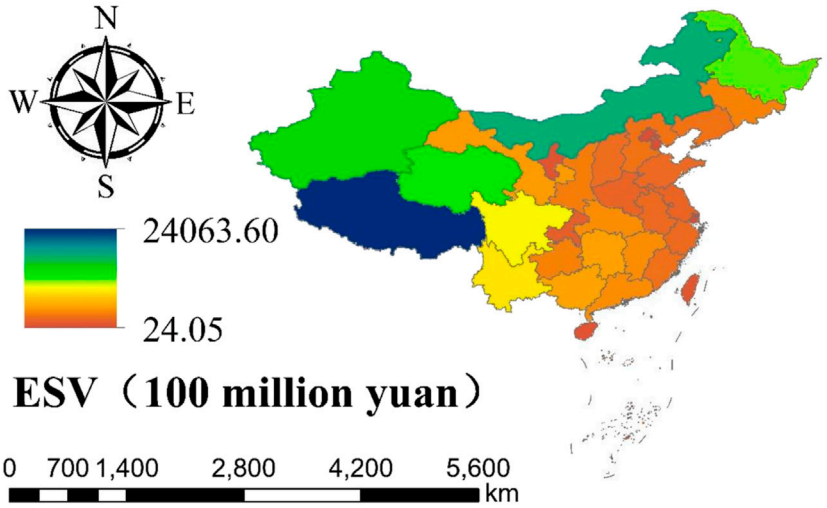

FIGURE 2
Distribution of ESV in each province.

TABLE 2 Values of *C* adopted by some countries or institutions.

Country/Region/Agency	*C* value	Country/Region/Agency	*C* value
Hong Kong, China (GEO)	10^{-3}	Brazil (Rio de Janeiro)	10^{-2}
United Kingdom (HSE)	10^{-2}	Brazil (Sao Paulo)	10^{-3}
Australia (AGS)	Newly built 10^{-4}	Netherlands (VROM)	10^{-3}
	Existing 10^{-3}	United States (Santa Barbara)	10^{-3}
Australia (Victoria)	10^{-2}	Canada (CDA)	10^{-3}
Australia (New South Wales)	3×10^{-3}	Denmark	10^{-2}

are too strict, more reservoirs will be classified as "dangerous or sick." In the current situation, where funding is relatively tight, several reservoirs will not be able to receive timely reinforcement against risks and will be forced to change operating conditions or stop operating, which will degrade the local economic development environment. It is also not conducive to effectively distinguish the degree of danger between "dangerous and sick" reservoirs.

(2) Compliance with the latest public acceptance of risks. With the increasing need for a better life for people, risk awareness is continuously increasing; in the event of equally serious accidents, the concern of the public will grow. Therefore, when formulating risk standards, both the engineering and the public's acceptance of risks should be considered.

4.2 Determination of the C value

C is a constant that determines the starting position of the standard line. The acceptable risk C values adopted by some countries and institutions are listed in Table 2. As seen from table, the value of *C* is primarily 10^{-3}/year. The values of *C* in Table 2 include various application categories such as nuclear power plants, hazardous chemicals, factories, all types of buildings (hospitals, schools, and residential buildings), slopes, and dams. Considering that accidents involving hazardous chemicals, factories, and buildings during new construction, reconstruction, expansion, and in-service production and storage processes are primarily caused by human factors, natural factors beyond human control are also important components of uncertainty during the construction and operation of reservoir dams. Therefore, according to the suggestion of Li et al. (2015), the standard for dam safety can be appropriately lowered to $C = 10^{-2}$. The acceptable risk standard can be one order of magnitude smaller than this; thus $C = 10^{-3}$.

4.3 Determination of the *n* value

The value of *n* represents the degree of risk preference. Considering the vast territory of China, there may be considerable differences in economic development, ecological environment quality, and social and cultural backgrounds among the different regions. Therefore, the degree of risk preference varies across the regions; thus, a risk matrix was introduced. This method

TABLE 3 Average ESV *per capita* GDP and unit area of each province in 2020.

Province (district)	Population (residential)/10,000	GDP *per capita*/ 10,000 yuan	ESV/ 100 million	Area (land only)/km^2	Average ESV/(yuan/m^2) per unit area
Anhui	6102.72	6.34	2282.98	140,100	16.30
Macau	68.32	24.63	0.38	33	11.60
Beijing	2189.31	16.49	295.51	16,410	18.01
Chongqing	3205.42	7.80	1451.82	82,402	17.62
Fujian	3973.00	10.57	2742.24	124,000	22.11
Gansu	2501.98	3.60	4797.57	425,800	11.27
Guangdong	12601.25	8.79	4059.66	179,725	22.59
Guangxi	5012.68	4.42	5308.27	237,600	22.34
Guizhou	3622.95	4.62	3678.02	176,167	20.88
Jiangsu	8474.80	12.12	1969.40	107,200	18.37
Hainan	1008.12	5.49	704.38	35,400	19.90
Hebei	7461.02	4.85	2794.48	188,800	14.80
Henan	9936.55	5.53	1974.39	167,000	11.82
Heilongjiang	3185.01	4.30	11614.27	473,000	24.55
Hubei	5775.00	7.52	4057.06	185,900	21.82
Hunan	6644.48	6.29	4997.21	211,800	23.59
Jilin	2690.73	5.11	3670.75	187,400	19.59
Jiangxi	4518.86	5.69	4109.97	166,900	24.63
Liaoning	4259.14	5.90	2874.17	148,600	19.34
Inner Mongolia	2404.92	7.22	17678.74	1,183,000	14.94
Ningxia	720.27	5.44	711.47	66,400	10.71
Qinghai	592.40	5.07	13065.77	722,300	18.09
Shandong	10152.75	7.20	2039.32	157,900	12.92
Shanxi	3491.56	5.06	2554.02	156,700	16.30
Shaanxi	3952.90	6.22	3360.46	205,600	16.34
Shanghai	2487.09	15.56	137.54	6,341	21.69
Sichuan	8367.49	5.81	9464.28	486,000	19.47
Taiwan	2356.12	18.20	946.47	36,014	26.28
Tianjin	1386.60	10.16	246.62	11,966	20.61
Tibet	364.81	5.22	24063.58	1,228,400	19.59
Hong Kong	747.42	32.30	24.05	1,107	21.74
Xinjiang	2585.23	5.34	14638.28	1,660,000	8.82
Yunnan	4858.30	5.19	8584.68	394,100	21.78
Zhejiang	6456.76	10.01	2362.88	105,500	22.40

was proposed by the US Air Force Electronic Systems Center in the mid-to-late 1990s, and has been widely used in US military weapon system development projects as a structural method for identifying the importance of project risks. It can evaluate the potential risks of projects and is currently widely used in research fields, such as project risk assessment and safety risk rating (Koulinas Georgios et al., 2021).

The higher the *per capita* GDP in a region, the higher the demand for quality of life; and the more emphasis it places on the surrounding ecological environment, the more averse it is to risk

TABLE 4 Risk appetite matrix.

Per capita GDP/10,000 yuan	Average ESV per unit area/(yuan/m^2)		
	(8, 14)	(14, 21)	(21, 28)
(2.58, 5.29)	X	X	Y
(5.29, 8.00)	X	Y	Y
>8.00	Y	Y	Z

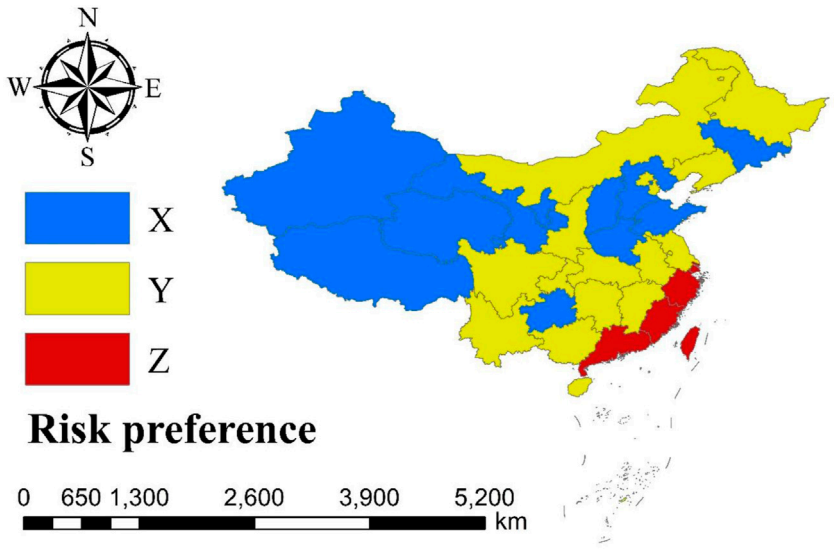

FIGURE 3
Risk appetite of each province.

(Francis et al., 2022). The higher the quality of the ecological environment, the higher the losses caused by disasters, and the more averse they are to risk. The per-unit area average ESV and the *per capita* ecological environment value reflect the ecological environment quality of a region from different perspectives. The higher the *per capita* ESV, the stronger sustainable development capability of the region. However, this does not necessarily mean that the ecological damage caused by disasters is more severe. For example, in areas with poor land quality, floods may not cause considerable ecological damage; however, the *per capita* ESV may still be relatively high because of low population density (Peter et al., 2022). Therefore, the average ESV per unit area is a better indicator of the importance of a region's ecological environment. The higher the average ESV per unit area, the greater are the losses caused by floods. Therefore, *per capita* GDP and per unit area average ESV were selected to construct a risk preference matrix. Based on statistical data released by the National Bureau of Statistics in 2020 (National Bureau of statistics of the people's Republic of China, 2020), the *per capita* GDP and per unit area average ESV of each province are shown in Table 3.

According to the 2020 income classification standard of the World Bank, most provinces in China have an annual *per capita* income in the middle-to high-income range, whereas the remaining provinces have a *per capita* income in the high-income range (Shah et al., 2022). To differentiate the *per capita* GDP income of each province more precisely, the middle-to high-income range was evenly divided into three categories: 2.58–5.29, 5.29–8, and >8 yuan *per capita* GDP. The average ecological service value per unit area (ESV) for each province was determined by setting the highest and lowest values as the upper and lower limits of the range and equally dividing the range into three categories: 8–14, 14–21, and 21–28 yuan per unit area. The resulting risk-preference matrices are presented in Table 4.

When falling into zone Z, n = 2 is assigned, indicating risk aversion; when falling into zone Y, n = 1.5 is assigned, indicating slight risk aversion; and when falling into zone X, n = 1 is assigned, indicating risk neutrality. Based on the *per capita* GDP and average ESV per unit area of each province in 2020, the risk preference of each province was determined using a risk matrix, as shown in Figure 3.

As shown in Figure 3, the regions with risk preference X primarily include some western and central provinces of China and Jilin Province. Western regions, such as Xinjiang, Tibet, Qinghai, Gansu, and Ningxia, have relatively underdeveloped economies. People in these areas tend to focus more on economic development than on the ecological environment, resulting in a risk preference of X. In central provinces, such as Hebei, Henan, Shanxi, and Shandong, although the total economic

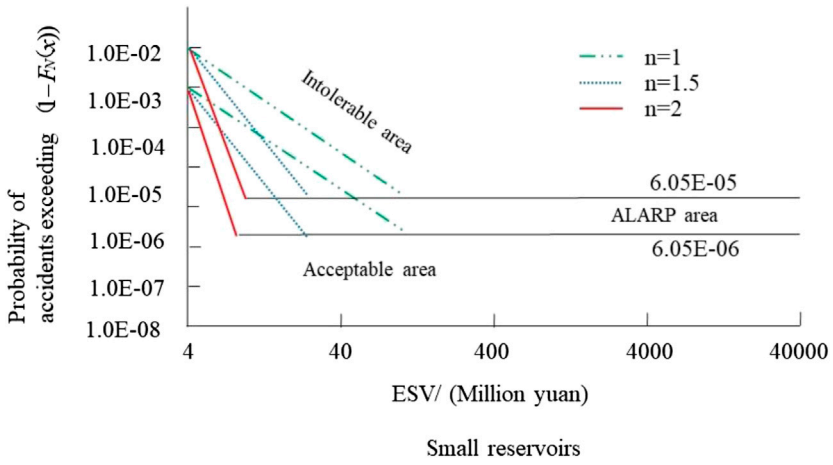

FIGURE 4
Risk standards for environmental losses caused by dam failure in large- and medium-sized reservoirs.

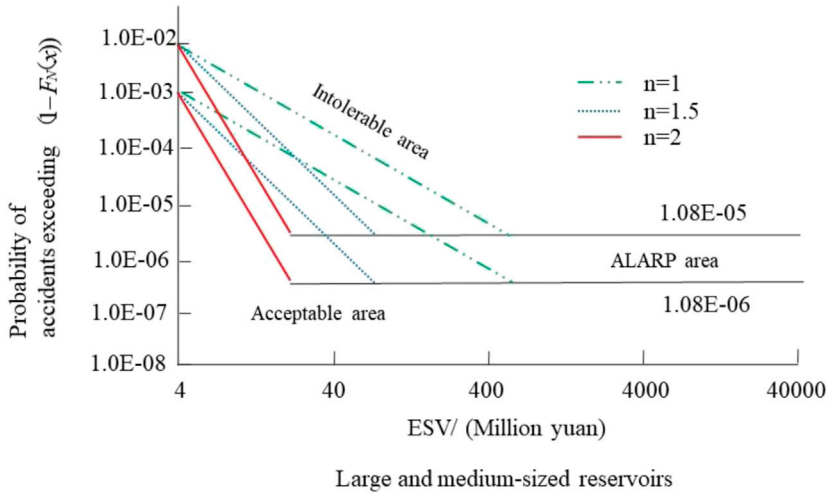

FIGURE 5
Risk criteria for environmental losses caused by dam failure in small reservoirs.

output is large, the population is large, and the *per capita* GDP is relatively small, resulting in a risk preference of X. Among the three northeastern provinces, only Jilin Province has a risk preference of X. Upon comparison, although Jilin's *per capita* GDP is higher than that of Heilongjiang, Heilongjiang has important ecological protection areas, such as the Greater and Lesser Khingan Mountains, with higher ecological value and lower risk tolerance. Therefore, among the three northeastern provinces, only Jilin Province has a risk preference of X.

The risk preference of most provinces in China is Y, where some areas have high ecological environment quality despite being economically underdeveloped, whereas others have moderate ecological environment quality despite being economically developed (i.e., Beijing). Additionally, some regions, such as Hunan, have good overall economic development and ecological environment quality; however, a large population means that their *per capita* GDP has not reached the high-income range, resulting in a Y risk preference.

Only Shanghai, Hong Kong, Guangdong, Fujian, Zhejiang, and Taiwan have a Z-risk preference and are concentrated in the southeastern coastal region of China. These areas are economically developed and have a high ecological environment quality, resulting in a lower tolerance for risk.

4.4 Determination of extreme value lines

Most countries or regions have set extreme value lines for the risk standards of the two types. First, the probability extreme value line set by Australia indicates that there is no need to consider the consequences of an accident if its probability is below a certain value (ANCOLD Australia National Committee on Large Dams, 2003).

The other, such as the loss extreme value line set by Hong Kong, indicates that if the accident loss exceeds a certain value, then the risk is intolerable. Considering the safety status of Chinese dams, management levels, and levels of economic and social development, it is currently not feasible to set extreme accident value lines (Li et al., 2015). Therefore, the following two points should be considered when setting the accident probability extreme value line:

(1) Probability of dam accidents in China. According to (Li et al., 2015; Fan and Jiang, 2005), the annual average probability of dam failure can be considered as 10% for the tolerable risk extreme value line and 1% for the acceptable risk extreme value line. From 1954 to 2018, 3,541 dam failures occurred in China, with an annual failure rate of 6.29×10^{-4}. Therefore, the tolerable and acceptable extreme value lines were 6.29×10^{-5} and 6.29×10^{-6}, respectively.
(2) Reliability standards in China. Reference (China Planning Press, 2013) stipulates the values of reliability indicators in China: 4.2 for large (I) reservoirs, 3.7 for large (II) and medium-sized reservoirs, and 3.2 for small reservoirs. According to the reliability theory, reliability indicators can evaluate or measure the level of structural reliability, as a quantitative basis for expressed symbolically, its relationship with failure probability P_f is as follows:

$$Pf = 1 - \Phi(\beta) \tag{4}$$

Where $\Phi(\cdot)$ represents the standard normal distribution function.

Assuming that the reliability function is a random variable following a normal distribution (Wilde and Johansson, 2013; Li S. et al., 2015; Ge et al., 2017). The current reliability standards in China are relatively consistent with the dam safety situation, so 10% of P_f can also be used as the tolerable risk extreme line and 1% as the acceptable risk extreme line.

As people's concern for the ecological losses caused by dam failures is significantly lower than that for the loss of life and economic losses, these requirements can be appropriately reduced. Moreover, the funding guarantees and management levels of large reservoirs were better than those of medium and small reservoirs. Among the 84 dam failures from 2000 to 2018, there were no failures in large reservoirs, 7 in medium-sized reservoirs, and the remainder in small reservoirs (Li H. et al., 2021). Therefore, to avoid excessive complexity in standards, large (I) reservoirs can adopt the same standards as large (II) and medium reservoirs. Thus, for large- and medium-sized reservoirs, the tolerable and acceptable risk probability extreme value lines are 1.08×10^{-5} and 1.08×10^{-6}, respectively, whereas for small reservoirs, the tolerable and acceptable risk probability extreme value lines are 7×10^{-5} and 6.29×10^{-6}, respectively.

To simultaneously meet the extreme value lines determined according to the safety level of the dam and current reliability standards, a smaller value was considered as the risk standard. Finally, the tolerable and acceptable risk probability extreme value lines for medium-sized reservoirs are 1.08×10^{-5} and 1.08×10^{-6}, respectively, whereas the tolerable and acceptable risk probability extreme value lines for small reservoirs are 6.29×10^{-5} and 6.29×10^{-6}, respectively.

5 Results

Based on the determination of the C value, n value, and limit line, environmental risk standards for Chinese reservoir dams were established, as shown in Figures 4, 5.

6 Conclusion

Reasonable dam-failure risk standards form the foundation for accurate risk assessment and management. There are difficult to define issues regarding the environment and its impacts, this study introduced ESV as a practical and operational method for determining environmental standards. The different provinces in China were divided into regions with distinctive characteristics, and the risk matrix method was used to determine the risk standards for these regions and established more targeted risk standards. This study determined the tolerable and acceptable standard values C of China's environmental impact risk standards, respectively. According to the GDP and environmental conditions of different provinces in China, a risk matrix is introduced to determine the risk appetite of each province. Finally, after the extreme value line has been determined, environmental loss risk criteria for reservoir dams of different sizes have been developed. These results were consistent with reality. The results can effectively help decision makers fully understand the level of dam risk management, promote further development of environmental risk research, and provide references and guidance for subsequent studies on environmental risks of dam failure.

Data availability statement

The datasets presented in this study can be found in online repositories. The names of the repository/repositories and accession number(s) can be found in the article/Supplementary Material.

Author contributions

Conceptualization, WL and JY; methodology, JL and JY; validation WL and HZ; formal analysis, WL and HZ; investigation, WL and JL; writing—original draft preparation, WL; writing—review and editing, WL and YJ; supervision, WL; funding acquisition, WL. All authors contributed to the article and approved the submitted version.

Funding

This work was supported by the National Natural Science Foundation of China (Grant Nos. 52179144, 52079127, and U2243244), Henan Science and Technology Research Project (Grant Nos. 202102310316 and 202102310394).

Conflict of interest

The authors declare that the research was conducted in the absence of any commercial or financial relationships that could be construed as a potential conflict of interest.

Publisher's note

References

ANCOLD (Australia National Committee on Large Dams) (2003). *Guideline on risk assessment*. Hobart, Tasmania: ANCOLD.

Binod, Baniya, Tang, Qiuhong, Yadu, Pokhrel, and Xu, X. (2019). Vegetation dynamics and ecosystem service values changes at national and provincial scales in Nepal from 2000 to 2017. *Environ. Dev.* 32, 100464. doi:10.1016/j.envdev.2019.100464

Cao, Gang, Liu, Yanzhong, Song, Xiangxiang, Chen, Y., Zhang, Z., and Wu, D. (2021). Study on the response mechanism of ecosystem services to urban land expansion by dynamic equivalent factor method: A case of wuhan, China. *IOP Conf. Ser. Earth Environ. Sci.* 651, 042039. doi:10.1088/1755-1315/651/4/042039

Chen, Junfei, Chen, Mengchen, and Zhou, Pei (2020a). Using multiple index comprehensive method to assess urban rainstorm disaster risk in jiangsu province, China. *Math. Problems Eng.* 2020, 1–10. doi:10.1155/2020/8973025

Chen, Shulin, Liu, Xiaotong, Yang, Li, and Zhu, Z. (2023). Variations in ecosystem service value and its driving factors in the nanjing metropolitan area of China. *Forests* 14 (1), 113. doi:10.3390/f14010113

Chen, Shurui, Yongjiu, Feng, and Tong, Xiaohua, (2020b). Modeling ESV losses caused by urban expansion using cellular automata and geographically weighted regression. *Sci. Total Environ.* 712, 13609. doi:10.1016/j.scitotenv.2020.136509

Cheng, Li, and Zhou, Jing (2013). Environmental impact analysis of dam failure based on fuzzy mathematical theory. *Value Eng.* 32 (15), 290–292. doi:10.14018/j.cnki.cn13-1085/n.2013.15.011

China Planning Press (2013). *Unified standard for reliability design of water conservancy and hydropower engineering structures:GB 50199—2013*. Beijing, China: China Planning Press.

Enes, Yildirim, and Ibrahim, Demir (2022). Agricultural flood vulnerability assessment and risk quantification in Iowa. *Sci. Total Environ.* 826, 154165. doi:10.1016/j.scitotenv.2022.154165

Fan, ziwu, and Jiang, shuhai (2005). Application of tolerance risk analysis method in decision-making of flood prevention. *J. Hydraulic Eng.* 36 (5). doi:10.13243/j.cnki.slxb.200505019

Francis, Duhamel, Daniel, Germain, and Guillaume, Fortin (2022). Flood risk quantification and mapping: an integrated vulnerability-based approach at the local scale in new brunswick, canada. *Int. J. Disaster Risk Reduct.* 83, 103403. doi:10.1016/j.ijdrr.2022.103403

Francisco, J., and Gallardo Izquierdo, A. (2008). Environmental risk index: A tool to assess the safety of dams for leachate. *J. Hazard. Mater.* 162 (1), 1–9. doi:10.1016/j.jhazmat.2008.05.018

Ge, Wei, Li, Zongkun, Liang Robert, Y., and Cai, Y. (2017). Methodology for establishing risk criteria for dams in developing countries, case study of China. *Water Resour. Manag.* 31 (13), 4063–4074. doi:10.1007/s11269-017-1728-0

Ge, Wei, Qin, Yupan, Li, Zongkun, Zhang, H., Gao, W., Guo, X., et al. (2020c). An innovative methodology for establishing societal life risk criteria for dams: A case study to reservoir dam failure events in China. *Int. J. Disaster Risk Reduct.* 49, 101663. doi:10.1016/j.ijdrr.2020.101663

Ge, Wei, Sun, Heqiang, Zhang, Hexiang, Li, Z., Guo, X., Wang, X., et al. (2020b). Economic risk criteria for dams considering the relative level of economy and industrial economic contribution. *Sci. Total Environ.* 725, 138139. doi:10.1016/j.scitotenv.2020.138139

Ge, Wei., Li, Zongkun, Li, Wei, Wu, M., Li, J., and Pan, Y. (2020a). Risk evaluation of dam-break environmental impacts based on the set pair analysis and cloud model. *Nat. Hazards* 104, 1641–1653. doi:10.1007/s11069-020-04237-9

He, Guanjie, Chai, Junrui, Qin, Yuan, Xu, Z., and Li, S. (2020). Coupled model of variable fuzzy sets and the analytic hierarchy process and its application to the social and environmental impact evaluation of dam breaks. *Water Resour. Manag.* 34, 2677–2697. doi:10.1007/s11269-020-02556-x

He, Xiaoyan, Sun, Dandan, and Huang, Jinchi (2008). Assessment on social and environmental impacts of dam break. *Chin. J. Geotechnical Eng.* 30 (11), 1752–1757.

Koulinas Georgios, K., Demesouka Olympia, E., Sidas Konstantinos, A., and Koulouriotis, D. E. (2021). A topsis—risk matrix and Monte Carlo expert system for risk assessment in engineering projects. *Sustainability* 13 (20), 11277. doi:10.3390/su132011277

Langdalen, Henrik, Abrahamsen, Eirik Bjorheim, and Selvik, Jon Tømmerås (2020). On the importance of systems thinking when using the ALARP principle for risk management. *Reliab. Eng. Syst. Saf.* 204, 107222. doi:10.1016/j.ress.2020.107222

Langill Jennifer, C., Christian, Abizaid, Yoshito, Takasaki, and Coomes, O. T. (2022). Integrated multi-scalar analysis of vulnerability to environmental hazards: assessing extreme flooding in western amazonia. *Glob. Environ. Change* 76, 102585. doi:10.1016/j.gloenvcha.2022.102585

Li, H., Ma, G., Wang, F., Rong, W., and He, Y. (2021). Analysis of dam failure trend of China from 2000 to 2018 and improvement suggestions. *Hydro-science Eng.* 2021 (5), 101–111. doi:10.12170/20201119001

Li, S., Zhou, X., Wang, Y., Zhou, J., Du, X., and Chen, Z. (2015a). Study of risk acceptance criteria for dams. *Sci. China Technol. Sc.* 58 (7), 1263–1271. doi:10.1007/s11431-015-5864-6

Li, Zongkun, Ge, Wei, and Wang, Juan, (2015). Risk criteria and application on reservoir dams in China. *J. Hydraulic Eng.* 46 (05), 567573+583. doi:10.13243/j.cnki.slxb.20141359

Li, Zongkun, Li, Wei, and Ge, Wei, (2019). Dam breach environmental impact evaluation based on set pair analysis-variable fuzzy set coupling model. *J. Tianjin Univ. Sci. Technol.* 52 (3), 269–276. doi:10.11784/tdxbz201807030

Li, Zonkun, Li, Wei, and Ge, Wei (2018). Weight analysis of influencing factors of dam break risk consequences. *Nat. Hazards Earth Syst. Sci.* 18 (12), 3355–3362. doi:10.5194/nhess-18-3355-2018

National Bureau of statistics of the people's Republic of China (2019). *China statistical Yearbook*. Beijing, China: China Statistics Press.

National Bureau of statistics of the people's Republic of China (2020). *China statistical Yearbook*. Beijing, China: China Statistics Press.

National Development Planning Commission (2019). *Compilation of national agricultural product cost-benefit data*. Beijing, China: China price Publishing House.

Pei, Jingjing, Wang, Guantao, Luo, Sida, and Luo, Y. (2018). Societal risk acceptance criteria for pressure pipelines in China. *Saf. Sci.* 109, 20–26. doi:10.1016/j.ssci.2018.05.006

Peter, Oyedele, Edinam, Kola, Felix, Olorunfemi, and Walz, Y. (2022). Understanding flood vulnerability in local communities of kogi state, Nigeria, using an index-based approach. *Water* 14 (17), 2746. doi:10.3390/w14172746

Shah, Muhammad. I., Muhammad Shehu, Shuaibu, AbdulKareem Hauwah, K. K., Khan, Z., and Abbas, S. (2022). Inequality consequences of natural resources, environmental vulnerability, and monetary-fiscal stability: A global evidence. *Environ. Sci. Pollut. Res. Int.* 30 (4), 10329–10345. doi:10.1007/s11356-022-22788-1

Tu, Yan., Shi, Han., Zhou, Xiaoyang, Liu, L., and Lev, B. (2023). Flood risk assessment of metro stations based on the SMAA-2-FFS-H method: A case study of the "7$$\cdot$$20" rainstorm in zhengzhou, China. *Stoch. Environ. Res. Risk Assess.* 37, 2849–2868. doi:10.1007/s00477-023-02422-3

Wang, Renzhong, Lei, Li, and Sheng, Jinbao (2006). On criterion of social and environmental risk of reservoir dams. *J. Saf. Environ.* (6), 8–11. doi:10.3969/j.issn.1009-6094.2006.01.003

Wilde, M., and Johansson, F. (2013). System reliability of concrete dams with respect to foundation stability: application to a spillway. *J. Geotech. Geoenviron.* 139 (2), 308–319. doi:10.1061/(ASCE)GT.1943-5606.0000761

Xu, Wu, Shen, Xiaojing, and Li, Jianshe (2022). Flood risk assessment model combining hierarchy process and variable fuzzy set theory: A case study in Zhejiang province, China. *Arabian J. Geosciences* 15, 188. doi:10.1007/s12517-022-09440-5

Xu, Xibao., Tan, Yan, and Yang, Guishan (2013). Environmental impact assessments of the three gorges project in China: issues and interventions. *Earth-science Rev.* 124, 115–125. doi:10.1016/j.earscirev.2013.05.007

Yang, Haijiang, Gou, Xiaohua, Xue, Bing, Ma, W., Kuang, W., Tu, Z., et al. (2023). Research on the change of alpine ecosystem service value and its sustainable development path. *Ecol. Indic.* 146, 109893. doi:10.1016/j.ecolind.2023.109893

Yang, Yijia, Song, Ge, and Lu, Shuai (2020). Study on the ecological protection redline (epr) demarcation process and the ecosystem service value (ESV) of the epr zone: A case study on the city of qiqihaer in China. *Ecol. Indic.* 109, 105754. doi:10.1016/j.ecolind.2019.105754

Zhang, Shuai, Wang, Yin, Wang, Yang, Li, Z., and Hou, Y. (2023). Spatiotemporal evolution and influencing mechanisms of ecosystem service value in the tarim river basin, northwest China. *Remote Sens.* 15 (3), 591. doi:10.3390/rs15030591

Zhang, Xiaoyan, Shen, Juqin, Sun, Fuhua, and Wang, S. (2022). Spatial-temporal evolution and influencing factors analysis of ecosystem services value: A case study in sunan canal basin of jiangsu province, eastern China. *Remote Sens.* 15 (1), 112. doi:10.3390/rs15010112

frontiers | Frontiers in Earth Science

TYPE Original Research
PUBLISHED 30 August 2023
DOI 10.3389/feart.2023.1237884

OPEN ACCESS

EDITED BY
Wei Ge,
Zhengzhou University, China

REVIEWED BY
Tao Yu,
Harbin Institute of Technology, China
Xi Guo,
Zhengzhou University, China
Yanlin Zhao,
Hunan University of Science and Technology, China

*CORRESPONDENCE
JunKe Xu,
1180711014@stu.xaut.edu.cn

RECEIVED 10 June 2023
ACCEPTED 14 August 2023
PUBLISHED 30 August 2023

CITATION
Xu J, Zhu J and Xie J (2023), Risk evolution and mitigation of the urban river ecological governance project based on social network analysis. *Front. Earth Sci.* 11:1237884. doi: 10.3389/feart.2023.1237884

Risk evolution and mitigation of the urban river ecological governance project based on social network analysis

JunKe Xu[1,2,3]*, Jiwei Zhu[1,2,3] and JianCang Xie[1,2]

[1]State Key Laboratory of Eco-hydraulics in Northwest Arid Region, Xi'an University of Technology, Xi'an, China, [2]Research Center of Eco-hydraulics and Sustainable Development, The New Style Think Tank of Shaanxi Universities, Xi'an, China, [3]School of Civil Engineering and Architecture, Xi'an University of Technology, Xi'an, China

This study aims to utilize complex network theory and network immune strategies to identify relevant risks in urban river ecological governance projects and develop corresponding risk response strategies. By constructing a risk evolution network with 53 nodes and 255 edges, we analyzed the network's degree centrality, betweenness centrality, closeness centrality, and composite value parameters, confirming the network's scale-free characteristics. Based on this, we used network global efficiency as a metric to assess the network's robustness under random and targeted attacks. The results revealed that under targeted attack scenarios, the degree value attack immune strategy performed optimally, while random immune strategies were less effective than targeted immune strategies. Moreover, this model offers various advantages in early risk response decision-making and establishing a forward-looking risk warning framework, providing an effective tool for risk management in urban river ecological governance projects.

KEYWORDS

SNA, engineering project risk, robustness, urban rivers, manage

1 Introduction

With the continuous acceleration of urbanization, the urban ecological environment faces increasingly severe challenges (Deng et al., 2022; Luo et al., 2022). Urban rivers are an essential part of the urban ecosystem and have significant implications for the quality of the urban ecological environment and its sustainable development (Liu et al., 2022; Zhao and Huang, 2022). The risk characteristics of urban river ecological governance projects encompass ecosystem restoration risk, water quality improvement risk, engineering safety risk, and social participation risk. To address these risk features, urban river ecological management projects need to take a comprehensive approach, considering ecological, engineering, and social factors, and implementing appropriate measures and governance strategies. Urban river ecological governance projects are essential for ecological and environmental governance. Through the extensive use of multidisciplinary knowledge and technological means such as ecology, engineering, and environmental science, urban rivers are comprehensively managed to achieve the purification of the water environment, restoration of ecological systems, and improvement of the ecological environment. However, urban river ecological governance projects involve multiple stakeholders, including governments, enterprises, and social organizations. The technologies and knowledge

involved are also relatively complex and diverse, so the project's risks and uncertainties are significant.

Risk studies for urban river ecological governance projects are an important way to ensure successful project implementation and sustainability. Various methods and tools such as qualitative analysis, quantitative modeling and expert judgment have been used to identify and assess potential risk factors and risk events (Yu et al., 2017; Zhu et al., 2022). In past studies, extensive research has been conducted on risk studies in urban river ecological governance projects (Ullah et al., 2021). Some researchers have assessed the impact of different stakeholders on the implementation of urban river ecological governance projects by applying social network analysis methodology. They found that cooperation and information flow among stakeholders play an important role in the successful implementation of a project, which provides a useful reference for the development of risk management strategies (Lienert et al., 2013). Xu et al. (2023a) conducted an in-depth study on risk management strategies for urban river ecological governance projects. They explored the effectiveness of implementing strategies such as risk avoidance, risk transfer, risk mitigation, and risk acceptance, and made recommendations to optimize risk management to improve the success and sustainability of the project (Xu et al., 2023a). Notably, in terms of technology, the researchers explored the application of emerging technologies in risk studies for urban river ecological governance projects. They focused on the application of technologies such as intelligent technologies, remote sensing, and big data analysis to improve the efficiency and accuracy of project monitoring and management, thereby better-supporting risk identification, assessment, and decision-making. Risk research on urban river ecological management projects involves many aspects, from social network analysis to risk management strategies to technology applications, and these studies will help provide comprehensive risk perception and management strategies for the implementation of urban river ecological governance projects. However, the field still faces challenges and opportunities, and further research is needed to address the complexity of urban environments and socio-economic factors to achieve sustainable development of ecological governance projects for urban rivers.

Based on this, this paper applies the social network theory (Valeri and Baggio, 2021) to the characteristics and evolutionary features of urban river ecological governance projects. Based on existing research, it constructs a directional weighted network model for the evolution of urban river ecological governance project risks. The network's degree centrality, mediator centrality, proximity centrality, and the ranking of key risk factors for a combined value scenario of the three have been analyzed. The scale-free characteristics of the network are pointed out. MATLAB programming simulations are used to analyze the changes in the proportion of randomly and deliberately attacked nodes under the structural stability and performance stability of the network and to compare and analyze the robustness effects of the degree value attacks, meso-value attacks, proximity centrality attacks, and combined value attacks. The method of identifying the key risk factors of the network is selected to clarify the critical risk factors of the network and propose a chain-breaking control strategy to theoretically enrich the relevant research on the risk of urban river ecological governance projects, make up for the shortcomings of existing research, and practically providing new ideas for the correct understanding, governance, and control of the risk network of urban river ecological governance projects.

2 Review of SNA research

Domestic and international academics have conducted preliminary studies on the interrelationship between risks, and some of the more common approaches include explanatory structural models (Soti et al., 2010; Karmaker et al., 2021; Abbas et al., 2022) and Bayesian network analysis (Leoni et al., 2019; Huang et al., 2021; Mohamed and Tran, 2021). These approaches explore the interrelationships between risks from different perspectives and provide some basis for decision-makers to manage risks scientifically. Still, none of them can provide a quantitative analysis of the position of risk factors in the risk network. For this reason, this paper introduces Social Network Analysis (SNA). The method is a research orientation based on graph theory to examine the connected relationships between social entities, their structural features, and the characteristics of relationships and networks through systematically analyzing relational data (Valente, 2012). Applying this method makes it possible to quantitatively analyze the virtual nodes in the risk network in terms of network density and centrality, thus deepening managers' understanding of project risks and improving risk management.

Research by many experts and scholars has shown that risk factors in engineering projects interact with each other rather than independently of each other (Teller and Kock, 2013; Xie et al., 2019). Therefore, effective risk response strategies emerge from risk research. Methods of risk association analysis can be classified as qualitative and quantitative. Qualitative methods: Quantifying qualitative evaluation results using these methods presents unpredictable information loss, especially when using linguistic variables (Wirba et al., 1996), design structure matrixes (Marle et al., 2013), and Delphi methods (Aloini et al., 2012). Quantitative methods: Bayesian network analysis is representative (Marcot and Penman, 2019), and Wang and Chen (2017) used Bayesian network analysis to assess risk in a tunneling project. They have developed a Bayesian network model to identify and evaluate the relationships between various risk factors and to predict the probability of successful project implementation. Ghasemi et al. (2018) used Bayesian network analysis to develop a network of engineering project risk relationships to identify and quantify the relationships between engineering project risk factors and predict the probability of successful project implementation. The findings suggest that Bayesian network models can help managers better identify and control project risks. The abstract mathematical tools and complex mathematical calculations involved in quantitative methods make them inapplicable to engineering practice, despite being theoretically powerful (Yang et al., 2021). Complex network theory appears more appropriate for risk-related analysis of complex projects given its simplicity and visibility. For example, Desavelle (2015) used complex network theory to analyze nuclear power engineering risks, constructing a complex network including various risk factors and identifying key risk factors and the relationships between them by analyzing the network structure

and characteristics. Fang et al. (2012) considered risk factors as nodes and constructed a complex network model by measuring the correlation and influence between nodes, and they used complex network theory to analyze the network structure and characteristics to identify key risk factors. Zhang et al. (2021) constructed a complex network model based on complex network theory. It treats risk factors and their degree of influence as nodes and edges, identifies critical risk factors and their relationships through network analysis methods, and proposes corresponding risk management strategies. However, they still use traditional numerical ranking and comparison methods of generic parameter values to determine key risks and interactions. After the risk has been resolved, the network is not updated because this is a static, one-time, global network process.

Yang et al. (2021) proposed an engineering risk management method combining SNA and immune network algorithms, which modeled a complex engineering risk problem as a multi-level network structure and used the SNA method to analyze the characteristics of the nodes and edges in the risk network. The risk nodes are then optimally selected and eliminated through a network immunity algorithm, thus enabling effective risk management. The method has been applied in a hydropower project, and good results have been achieved. Zhou et al. (2018) Propose an engineering risk assessment method combining SNA and immune network algorithms. The technique models the engineering risk problem as a complex network. It uses the SNA method to analyze the importance of the nodes and edges in the risk network-the network immunity algorithm eliminated and patched the risk nodes, resulting in an effective risk assessment scheme. The method was applied in a highway engineering project and achieved good results. Ma et al. (2022) In this paper, a complex network-based engineering risk management method is proposed, which models the engineering risk problem as a complex network and uses the SNA method to analyze the relationship between nodes and edges in the network. Then, the risk nodes are optimally selected and excluded by a network immunity algorithm, and finally, an effective risk management scheme is obtained. The method has been applied in a construction project with good results.

Among the network immunization methods (Subramanian et al., 2015) are random immunization (RI), targeted immunization (TI), and acquaintance immunization (AI) (Lanaridis and Stafylopatis, 2014). RI completely randomly selects some nodes for immunization (Wu et al., 2018), inconsistent with risk management principles. TI specifies a small number of immune nodes with blocking properties based on global information about the network (García-Pedrajas and Fyfe, 2007). AI (Cao, 2021) represents a compromise between immunization cost and effectiveness by randomly selecting certain nodes as immune nodes and subsequently immunizing one neighboring node for each of the immune nodes. In other words, it aims to strike a balance between the cost and effectiveness of the immunization process. Based on the above analysis, given the simplicity and operability of risk management requirements in engineering practice, this paper proposes a TI method oriented to the network characteristic parameters combined with RI to analyze risk models. In this study, we explore the difficulties involved in identifying key risks and developing risk response strategies.

3 Research design and methodology

3.1 Study design

In this study, a risk immune response strategy research method based on complex networks is developed to identify critical risks in urban river ecological governance projects and to analyze the propagation pathways affecting the abnormal degree of risk association in urban river ecological governance projects. The logical framework of the technique, as shown in Figure 1, involves five distinct steps. Firstly, we reviewed relevant research and tabulated the list of risks for complex projects. Secondly, the risk correlation data was taken from a brainstorming session. Then, we used the visualization software to build the model. Finally, the analysis is based on network immunity. As a result, we can develop risk response strategies based on key risks and significant abnormal risk transmissions.

3.2 Risk identification

The risk identification for this study is based primarily on literature research (Thorne et al., 2015; Damnjanovic and Reinschmidt, 2020; Erol et al., 2020; Gondia et al., 2020), combined with actual project risk research and the Ministry of Water Resources Supervision Department's Notice on the Issuance of a List of Common Problems in the Inspection of Water Construction Projects (for Trial Implementation). The system of risk indicators is derived from the authors' published research papers (Xu et al., 2023b), as shown in Table 1.

In the construction process of urban river ecological governance projects, economic relations or a network of responsibilities and rights are formed between the participants, with financial contracts as the link. Different participants play different roles and bear additional responsibilities in this network. This study divided the project into four stages and listed the composition of the participants in each step in Table 2. The study systematically identified and screened the risk factors of urban river ecological governance projects using relevant questionnaires to prepare the groundwork for subsequent research work.

3.3 Risk data linkage

The risk evolution of urban river ecological governance projects can be viewed as a process of complex networks, in which there are complex interconnections between different risk factors. Complex network theory provides a powerful tool for analyzing the network topology and relationships between nodes. By constructing a risk evolution network, the risk factors in an urban river ecological governance project can be taken as nodes, and the influence relationships between different risk factors can be taken as edges to form a complex network, to reveal the laws and characteristics of risk evolution.

To develop a reasonable and effective risk response strategy for urban river ecological governance projects, the entire risk system needs to be quantitatively analyzed and visualized. This study used 53 risk nodes, plus risk-associated edges, for modeling. Figure 2

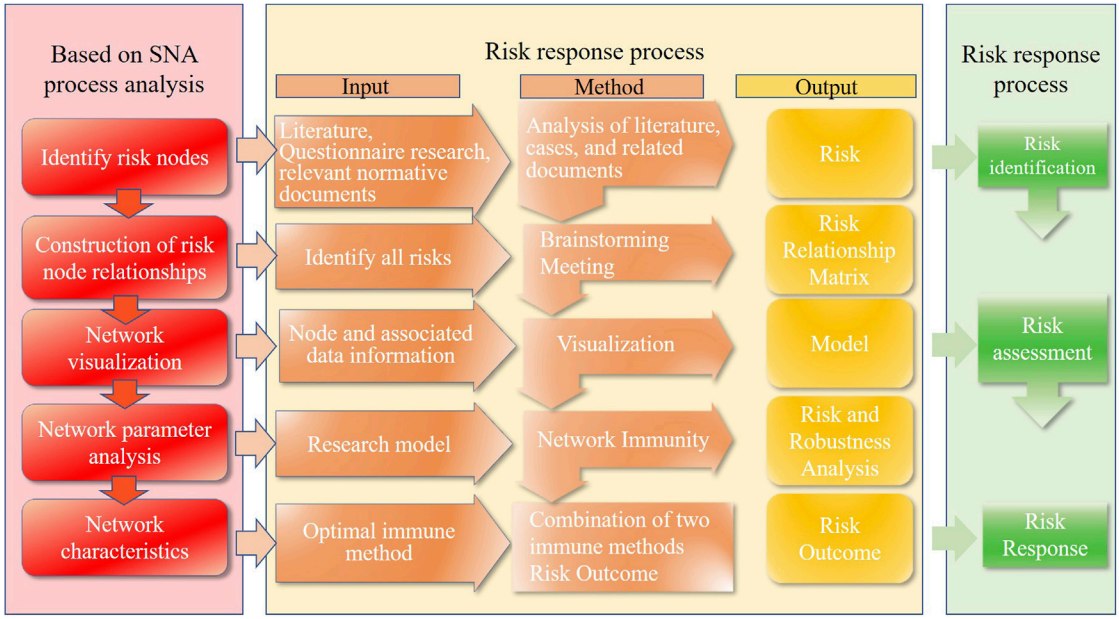

FIGURE 1
The logical framework of the risk immune response strategy research methodology.

presents the visual model of the generated network (Xu et al., 2023b).

The foundation of this study relies on a risk factor relationship data matrix (Table 3). In this matrix, columns represent the causers (emitters) of the relationship, while rows represent the effectors (affected parties) of the relationship. The presence of a relationship is denoted by "1," whereas the absence of a relationship is denoted by "0." Let there be n risk nodes in the risk element set A, $A_h = \cdot(R_1, R_2, \ldots, \cdot R_h)$ be the set of row risk elements, $A_m = \cdot(R_1, \cdot R_2, \ldots, \cdot R_m)$ be the set of column risk elements, and b_{ij} be the binary relational data in a matrix with row i and column $j, i = 1, 2, 3. \ldots, n, j = 1, 2, 3, \ldots, n$.

$b_{ij} = 1$ means: the risk element in row i affects the risk element in column j.

$b_{ij} = 0$ means the risk element in row i does not affect the risk element in column j.

We refer to the existing methods in the relevant literature, and the risk-associated data b_{ij} for urban river ecological governance projects were determined by 10 experts who have been involved in urban river ecological governance projects in the past 10 years through a brainstorming session with purposeful sampling (Yang et al., 2021). We invited 10 experts who have been involved in urban river ecological governance projects over the past decade to participate in a purposive sampling brainstorming session. These 10 experts included 2 personnel from government water departments, 1 project owner representative, 1 researcher from a scientific institution, 1 personnel from a survey and design unit, 1 from a construction contracting unit, 1 from a supervision company, 1 from a project consulting agency, 1 material supplier, and 1 subcontractor. In the first round of assessment, all 10 participants anonymously provided their evaluation results, and then a plenary meeting was convened to discuss the outcomes. Subsequently, a second round of scoring and discussion was conducted to obtain more consistent results. The data collected in the third round closely resembled the information obtained in the previous rounds, signifying the conclusion of the brainstorming session. Following three complete rounds of discussions, the participants' final opinions were compiled into the corresponding risk association adjacency matrix. We used the "0, 1"judging method to determine the existence of relationships between risks. When judging the risk relationships, we selected the answers with the highest frequency to maximize the determination of risk relationships and obtain the judgment results for risk association elements.

To validate the risk association data matrix constructed by the 10 experts, we established an independent validation focus group consisting of 20 individuals who were directly involved in urban river ecological governance projects on the front lines (Yang et al., 2021). Ten of the participants were practitioners from the same organization as the experts in the brainstorming session, with no knowledge of the experts' identities. The remaining ten participants were scholars specializing in engineering management. After extensive discussions, a consensus was reached that all the risk association data in the matrix were deemed reasonable and did not require retesting. As a result, the binary values of risk associations were considered both reliable and effective.

4 Network model characteristics and analysis of immunization results

4.1 Network characteristics

The network model was analyzed using software (Mandell, 1984; Lee et al., 2018), and the parameters of the overall network were obtained, as shown in Table 4 (Xu et al., 2023b).

TABLE 1 Risk table factors of river ecological management project.

Stage	Level 1 risk	Level 2 risk
1 Project concept stage	1 Political Risk	A1 Policy risk
		A2 Legal and regulatory risks
	2 Economic Risks	A3 Inflation risks
		A4 Risk of interest rate changes
		A5 Financing risk
	3 Natural environmental risks	A6 Hydrological and geological risks
		A7 Risk of meteorological conditions
		A8 Ecological environment risk
	4 Social Risks	A9 Sociocultural risk
		A10 Resident negotiated land acquisition risk
		A11 Social Security situation
		A12 Public opinion
2 Project decision stage	5 Project decision risk	A13 Project approval risk
		A14 Basic acceptance risk before implementation
		A15 Risk of decision-making error
		A16 Risk of land change
		A17 Risk of incomplete collection of primary data
3 Project preparation phase	6 Bidding risks	A18 Risk of document loss
		A19 Risk of improper competition
		A20 Information leakage risk
		A21 Bid evaluation risk
		A22 Normative risk of the bidding process
	7 Plan and design risks	A23 Risk of qualification of design unit
		A24 design schedule lag
		A25 The design has defects, errors, omissions, and frequent design plan changes
		A26 Survey accuracy risk
	8 Prepare for risks before construction	A27 Construction site layout and technical preparation risk
		A28 Project contract risks
		A29 Risk of insufficient supply of substances (materials) and materials
		A30 Risk of illegal start
4 Project implementation phase	9 Construction personnel risk	A31 Technical water risk
		A32 Weak security awareness
		A33 Employee qualification risk
		A34 Risk of construction personnel slowing down
	10 Construction technical risks	A35 (construction) drawings improper design risk
		A36 Engineering and technical risks
		A37 Construction machinery and equipment condition risk
		A38 Cross operation condition risk

(Continued on following page)

TABLE 1 (*Continued*) Risk table factors of river ecological management project.

Stage	Level 1 risk	Level 2 risk
		A39 Risk of construction accidents
	11 Construction management risks	A40 Safety management risks
		A41 Coordination risks of participating parties (including technical disclosure)
		A42 Rationality of construction organization design
		A43 Plan Adjustment and engineering change risk
		A44 Contract management and enforcement risks
		A45 Risk of organizational structure setup confusion
		A46 Manage permission risk
	12 Construction duration factor risk	A47 Certification period
		A48 Construction period
		A49 Risk of construction delay
	13 Completion acceptance risk	A50 Risk of file transfer not in place
		A51 Quality assessment risk
		A52 Audit risk
		A53 Risk of cost overruns

TABLE 2 Composition of parties involved in each phase of the project.

Stakeholders	Project Concept phase	Project decision phase	Project preparation phase	Project implementation phase
Project owner	√	√	√	√
Scientific Research Unit	√	√	√	√
Survey and design units	√	-	√	√
Construction Contractors	-	-	√	√
Government Agencies	√	√	-	√
Supervision companies	-	-	√	√
Project consultancy	√	√	√	√
Material suppliers	-	-	√	√
Subcontractors	-	-	√	√

As can be seen from Table 4, the density of the network is 0.0925, indicating that the risk evolution network of the urban river ecological governance project is less tight, the evolution path of risk factors is single, and the interaction relationship between them is general; The average degree value of the network is 9.6226, which indicates that each risk factor in the network is directly related to nine other risk factors on average, a result consistent with the small-world nature of complex networks; The average path length of a risk network is 2.5287, indicating that a risk factor only needs to pass through a unit length of 2.5287 to influence other risk factors; the maximum distance (i.e., network diameter) in this network is 7, indicating that a risk factor in the network needs to pass through a maximum of 7 steps to influence the risks in the network; The clustering coefficient of the network is 0.2977, indicating that the interactions between risk events in the network are not apparent and that risks are passed between risk events, which in turn leads to changes in take-off and landing safety risks; the global efficiency value of the network is 0.5281, a parameter that reflects the speed of transfer of threats in the network, and the connectivity of the network. Other parameters of the network are characterized as follows.

4.1.1 Node degree and degree distribution

Node degree is one of the indicators of network centrality, reflecting the influence of a node in the network. In a directed network, degrees can be categorized into in-degree, out-degree, and total degrees. In the urban river ecological governance project, the degrees of all network nodes were obtained using the anaconda3 software, as shown in Figure 3. Nodes with higher out-degree imply a greater number of risk factors generated under their influence. In the study, node (A25) has the highest

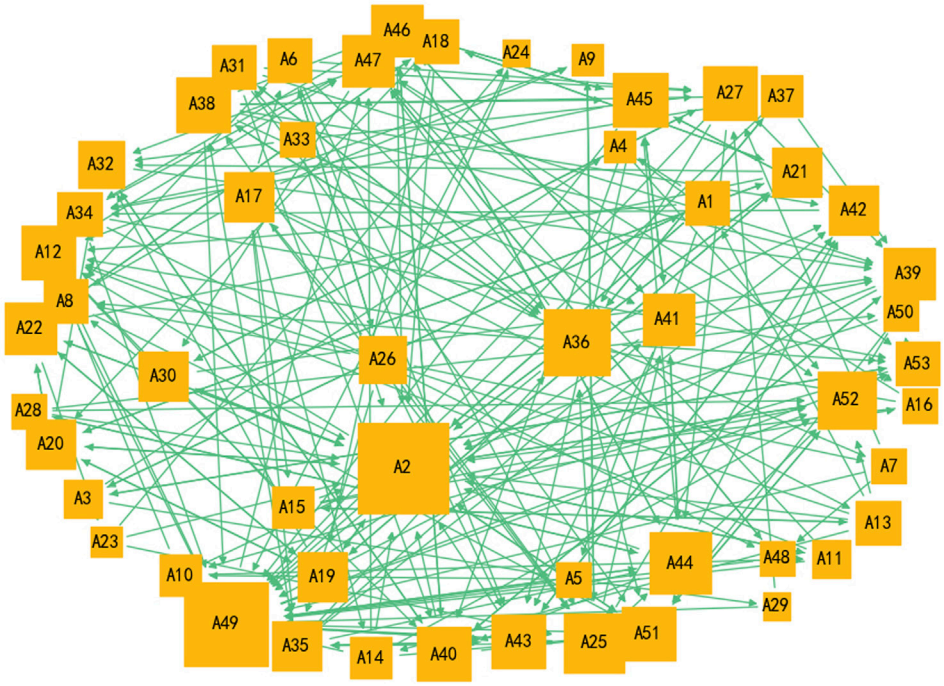

FIGURE 2
A complex network of risks for urban river ecological governance projects.

TABLE 3 Risk relationship matrix for urban river ecological management projects.

Risk factors	A_1	A_2	A_3	...	A_n
A_1	0	b_{12}	b_{13}	...	b_{1n}
A_2	b_{21}	0	b_{23}	...	b_{2n}
A_3	b_{31}	b_{32}	0	...	b_{3n}
⋮	⋮	⋮	⋮	0	b_{4n}
A_n	b_{n1}	b_{n2}	b_{n3}	b_{n4}	0

out-degree, and node (A2) has the highest in-degree. The total degree value of the node (A2) is 34, ranking first in the network. This indicates that (A25) has the greatest influence on other nodes in the network, and (A2) is most affected by other nodes, which aligns with the actual situation.

According to Figure 3, the nodes with larger degree values are, in order, A2, A49, A36, A44, A25, A52, A12, A27, A38, A40, A43, A45, A51, A22, A39, A41, A46, A47, A17, A19, A20, A21, A30, A35, A42, A26, A32, A1, A6, A8, A13, A18, A31, A34, A53, A10, A14, A15, A37, A3, A11, A5, A7, A16, A28, A33, A48, A50, A4, A9, A23, A24, A29.

4.1.2 The intermediation centrality of nodes

Software was used to calculate the meso-centrality of the nodes in the network. Then, the meso-number of each node was calculated, and the nodes were ranked according to the magnitude of the meso-number, as shown in Figure 4.

A node's intermediation centrality indicates its transport capacity, and the higher the intermediation centrality, the more influential it is. It is therefore believed that nodes with high intermediation centrality values in the project risk network are capable of effectively transmitting risk. As can be seen from Figure 4, A2 has the highest betweenness centrality, indicating that legal and regulatory risks are passed through multiple shortest paths in the entire network and play an essential role in risk transmission throughout the network. In practical work, many risk factors can affect risk generation by influencing A2. Nodes with

TABLE 4 Overall network parameter characteristics.

Parameter name	Overall network	Parameter name	Overall network
Number of nodes	53	Network diameter	7
Number of network edges	255	Average aggregation factor of the network	0.2977
Network Density	0.0925	Intermediate centrality	0.0331
Average network path	2.5287	Proximity centrality	0.3015
Network average degree	9.6226	Network global efficiency	0.5281

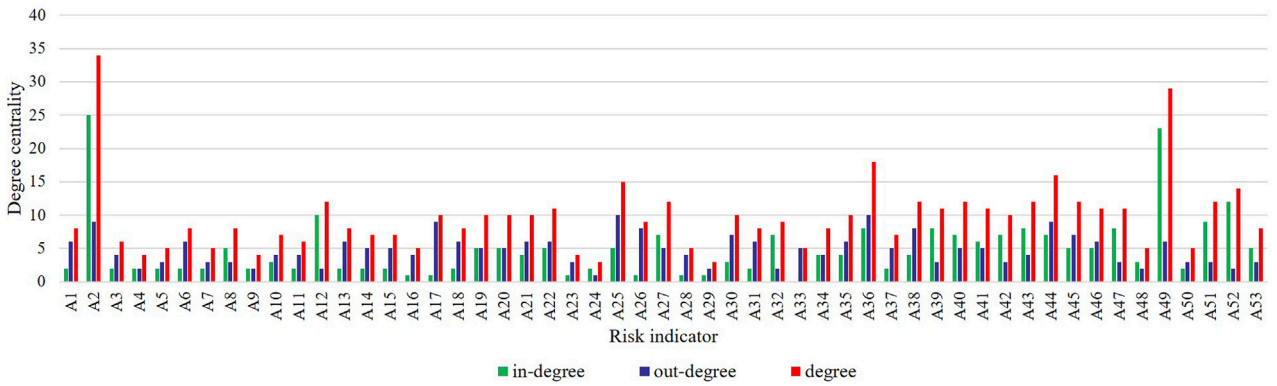

FIGURE 3
Map of riskiness values for urban river ecological governance projects.

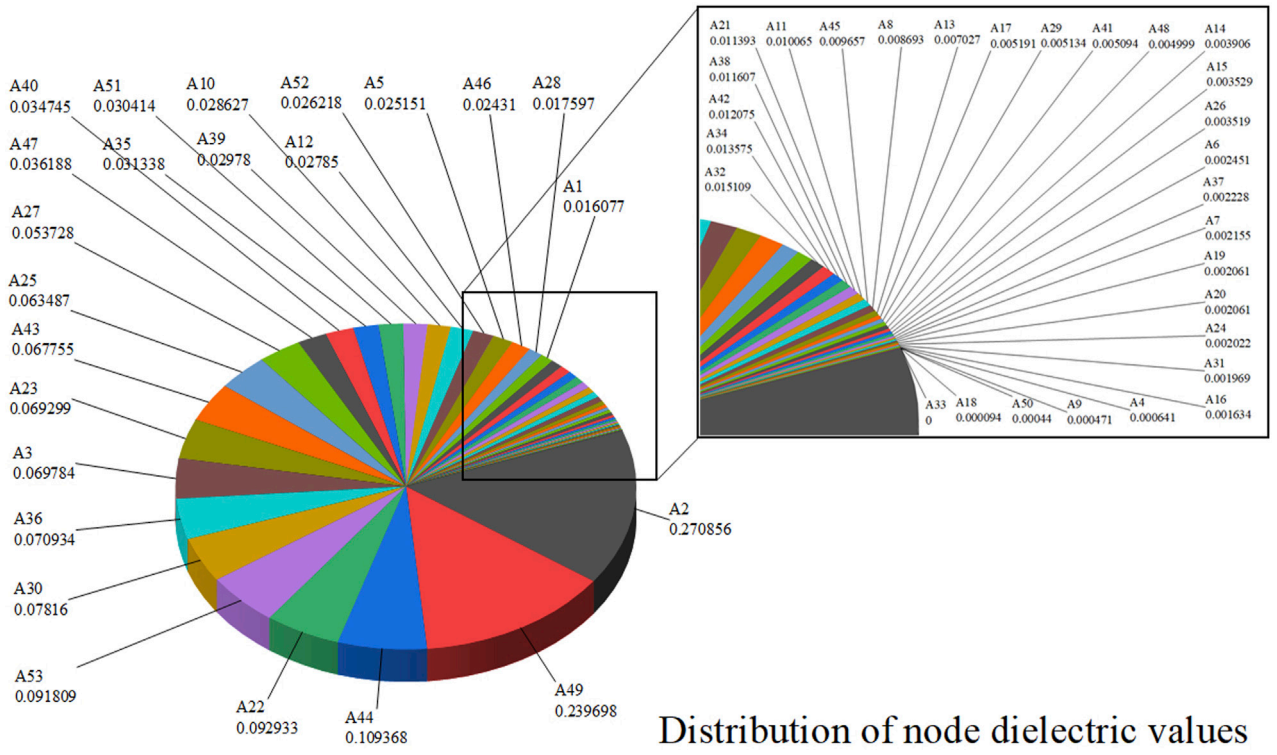

FIGURE 4
The intermediation centrality of nodes.

high betweenness centrality have an important position in the risk network.

4.1.3 Closeness centrality of nodes

Closeness centrality is defined as the reciprocal of the average distance from a node to all other nodes in the network, reflecting the importance of the node's position in the model. The closeness centrality of each node, calculated using software, is shown in Table 5. The distribution and ranking of closeness centrality of each node in the risk network were obtained through analysis using software, as shown in Figure 5.

In a network, a higher closeness centrality value indicates fewer paths between nodes, indicating the node is nearer the center. To determine whether a node is a central node in the overall project risk network, the closeness centrality is used. According to Figure 5, the top 10 nodes ranked by the closeness centrality index are A2, A, A52, A51, A12, A47, A30, A44, A43, and A53. Located closest to the network center, these nodes are extremely important. Therefore,

TABLE 5 Node proximity centrality values.

Nodes	Proximity to centrality	Nodes	Proximity to centrality	Nodes	Proximity to centrality
A1	0.245283	A19	0.390977	A37	0.244131
A2	0.604651	A20	0.390977	A38	0.285714
A3	0.307692	A21	0.38806	A39	0.40625
A4	0.242991	A22	0.390977	A40	0.409449
A5	0.244131	A23	0.284153	A41	0.356164
A6	0.038462	A24	0.235294	A42	0.358621
A7	0.043269	A25	0.242991	A43	0.42623
A8	0.356164	A26	0.025641	A44	0.436975
A9	0.19697	A27	0.363636	A45	0.339869
A10	0.393939	A28	0.305882	A46	0.361111
A11	0.409449	A29	0.199234	A47	0.464286
A12	0.481481	A30	0.448276	A48	0.342105
A13	0.043956	A31	0.244131	A49	0.597701
A14	0.053419	A32	0.348993	A50	0.25
A15	0.043956	A33	0	A51	0.495238
A16	0.040064	A34	0.295455	A52	0.536082
A17	0.025641	A35	0.320988	A53	0.419355
A18	0.284153	A36	0.319018	-	-

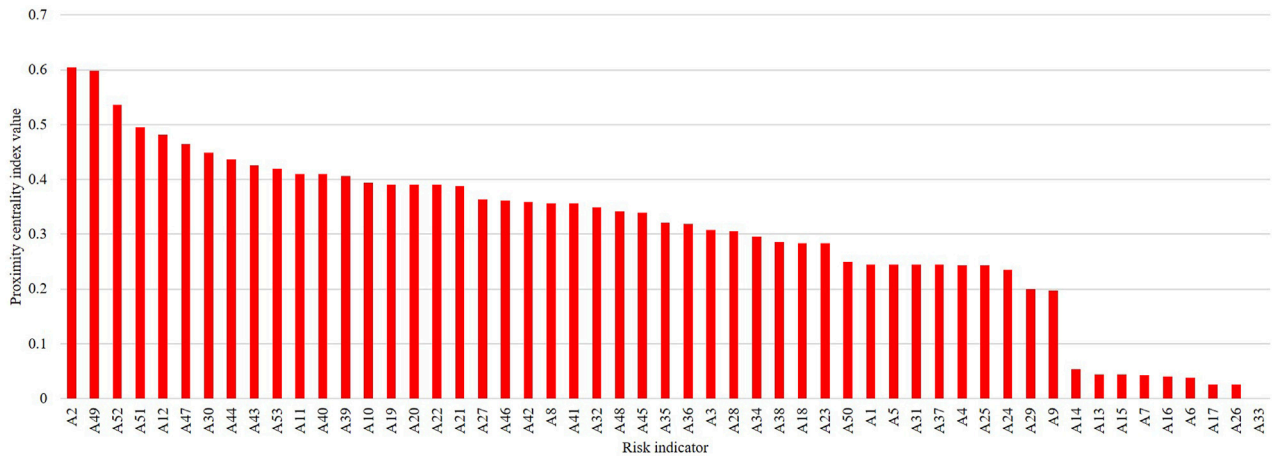

FIGURE 5
Ranking of the Node proximity centrality.

when developing risk management plans, it is necessary to consider targeted control measures for the above risk factors.

4.1.4 Combined value of nodes

Different parameter measurements may have other effects on the overall network. A single measurement parameter cannot often determine the importance of a risk factor in a network. To determine the final key risk factor, different parameters must be considered and compared comprehensively. In this study, network measurement indicators such as node degree centrality, betweenness centrality, and closeness centrality were analyzed. The average value of these indicators can be calculated to obtain the total value of each node, and their sizes are ranked, as indicated in Table 6.

According to the rankings of the total values of each node in Figure 6, it can be seen that node A2 has the most significant complete value, indicating that legal and regulatory risks are the

TABLE 6 Parameters for the combined value of risk nodes.

Risk name	General	Risk name	General	Risk name	General
A2	0.509784	A19	0.195115	A31	0.133315
A49	0.465031	A20	0.195115	A37	0.126992
A44	0.284678	A45	0.193432	A5	0.121812
A52	0.277177	A41	0.190932	A50	0.115531
A51	0.25214	A42	0.187668	A4	0.106852
A12	0.2467	A10	0.185727	A24	0.098336
A36	0.245369	A35	0.181544	A9	0.091455
A43	0.241585	A32	0.17906	A29	0.087354
A30	0.239581	A11	0.1783	A17	0.07438
A47	0.237337	A38	0.17603	A13	0.068277
A22	0.231816	A8	0.172901	A26	0.067412
A40	0.224988	A3	0.164287	A6	0.06492
A53	0.22167	A34	0.154292	A14	0.06398
A27	0.216044	A48	0.147753	A15	0.0607
A39	0.215856	A18	0.146031	A7	0.047193
A46	0.198986	A23	0.143458	A16	0.045951
A25	0.198313	A28	0.139878	A33	0.032051
A21	0.197254	A1	0.138402	-	-

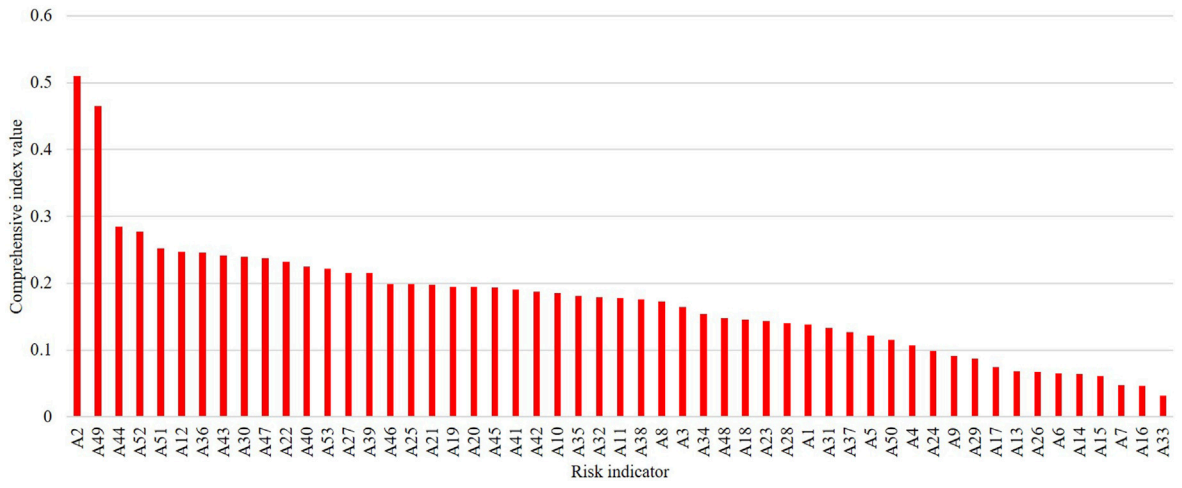

FIGURE 6
Ranking of the combined values of the risk nodes.

most critical node in the network. Meanwhile, in the rankings of degree centrality, closeness centrality, and betweenness centrality, legal and regulatory risks rank first in all three centrality measures, indicating that legal and regulatory risks have the highest importance in the risk network. When evaluating the importance of risk factors, the evaluation results of a single metric may be biased, and the judgment based on the total value is more accurate.

4.2 Immunological analysis

4.2.1 Nodal importance principle

The principle of node importance refers to the relationship between the importance of a node in a network and its position, connectivity, and other relevant factors in the network. Generally, the more a node is connected to other nodes in the network, the

TABLE 7 Four immunization strategies and characteristics.

Abbreviations	Parameters	Definition	Features
DC	Point Degree Centrality	The degree is the number of edges associated with a node and is determined by the outgoing and incoming degrees in a directed network	A high degree of exit means that the risk may lead to many further risks; at a high level, it means that many other risks may cause the risk itself
BC	Median centrality	Intermediate centrality is the frequency with which a node passes two other nodes on the shortest path	High BC nodes are more likely to be associated with other nodes and more likely to cause macro incidents
CC	Proximity centrality	Refers to the closeness of a node to other nodes	Based on the average distance of the node from other nodes
CV	Combined values	Average of modality, mesoscopic centrality, and proximity centrality	Ability to synthesize the importance of nodes

more critical it is. Additionally, node importance is also related to other factors such as its degree centrality, betweenness centrality, and closeness centrality. Analyzing and evaluating the significance of nodes can help identify critical nodes and main influencing factors in the network, thereby developing risk management strategies and measures in a targeted manner. Network robustness refers to the ability of a network to maintain connectivity in the event of an attack or failure of one or more nodes in the network. Network robustness reflects the impact of partial structural loss on the overall structure and functionality of a network when one or more nodes in the network are attacked or fail. Recently, it has become a hot research topic in complex networks. Scholars have conducted related research on the robustness of networks, and the leading indicators used to analyze the robustness of networks are average path length, size of the most significant connected component, and global efficiency. This study builds upon previous research and selects global efficiency as the indicator to investigate the performance robustness of the network.

4.2.2 Selection of parameters

The choice of which indicator to use for intentional attacks is also crucial. In this section, based on the above analysis and careful consideration, we propose four immune strategies, focusing on the immunity of nodes and the evaluation of network efficiency to reflect node importance, as shown in Table 7.

According to multi-attribute decision-making, the commonly used indicators of node importance in the risk evolution network were obtained through software. The importance of 53 risk points was ranked. Based on the four importance indicators listed earlier, the results of node importance were shown in Figures 3–6 in descending order of importance values.

4.2.3 Analysis of results

The selection of nodes for random immunity is entirely arbitrary. In this paper, the 53 nodes were sorted randomly using the random function in Excel. On the other hand, deliberate impunity is carried out by simulating immunity by targeting different node indicators one by one. To make the comparison more objective, this study added a control group of random immunity (RI) in this section and the four targeted immunity (TI) strategies to achieve a more straightforward comparison. For the risk network of urban river ecological governance projects, ND reflects the overall scale of the project risk system after the risks have been fully transmitted. Thus, the primary objective of the subsequent immunization process is to decrease the ND value. This study used the TI method to identify the key risks that determine the project's final scale. A degree-targeted immunity program (DTI), a betweenness centrality-targeted immunity program (BCTI), a closeness centrality-targeted immunity program (CCTI), and a comprehensive value-targeted immunity program (CVTI) are all part of it. In TI, the optimal immunized node represents the critical risk of the project, which can provide a basis for developing risk response strategies for the project.

According to Figure 7, the initial size of the network's most significant connected component (structural robustness) is close to 1. Under both attack modes, the structural robustness of the network decreases as the number of removed nodes increases, and the decrease in robustness is faster under deliberate attacks than random attacks. After randomly attacking 49% of the nodes on the network, the structural robustness of the network decreased to 0.5094. Similarly, attacking the same number of network nodes using the degree attack method reduced the network's structural robustness to 0.3396, the betweenness centrality attack method decreased it to 0.2452, the closeness centrality attack method reduced it to 0.4906, and the comprehensive value attack method reduced it to 0.4716. This indicates that the urban river ecological governance project risk evolution network is more robust and fault tolerant in the random attack mode and less robust in the deliberate attack mode. The degree value attack method is most effective in the intentional attack, i.e., the least robust. Under a random attack, the structural robustness of the network drops to zero only when the removal of nodes approaches 100%, suggesting that only effective control of the vast majority of risk factors in the network can bring down the entire network. However, in reality, risk factors exist objectively, and the probability of completely controlling all risk factors is small, so the urban river ecological governance project risk evolution network is highly robust to random attacks. Under deliberate attacks, the structural robustness of the network decreases faster when some of the nodes are attacked, indicating that these nodes are the core nodes of the network, and once these core nodes are attacked, the whole network is paralyzed. Thus, the urban river ecological governance project risk evolution network has poor robustness against deliberate attacks.

As can be seen from Figure 8, the line for the random attack is above the deliberate attack. Although some areas of contrast exist, the overall global efficiency decreases to a lesser extent than the intended attack. The reason for the poor effectiveness of the intentional attack is that when using the proximity centrality

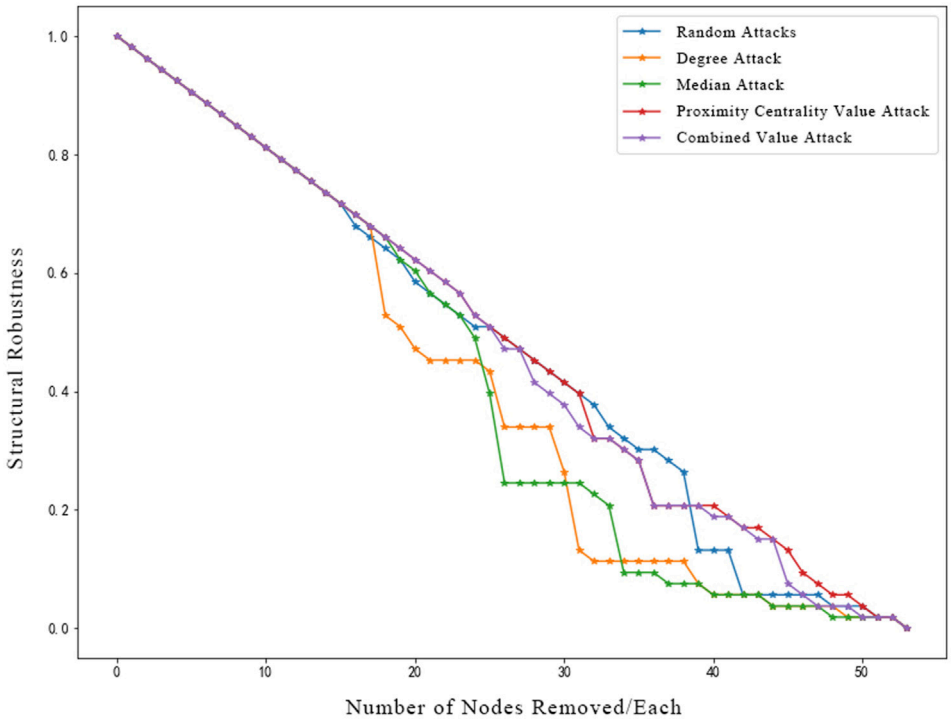

FIGURE 7
Structural robustness analysis diagram.

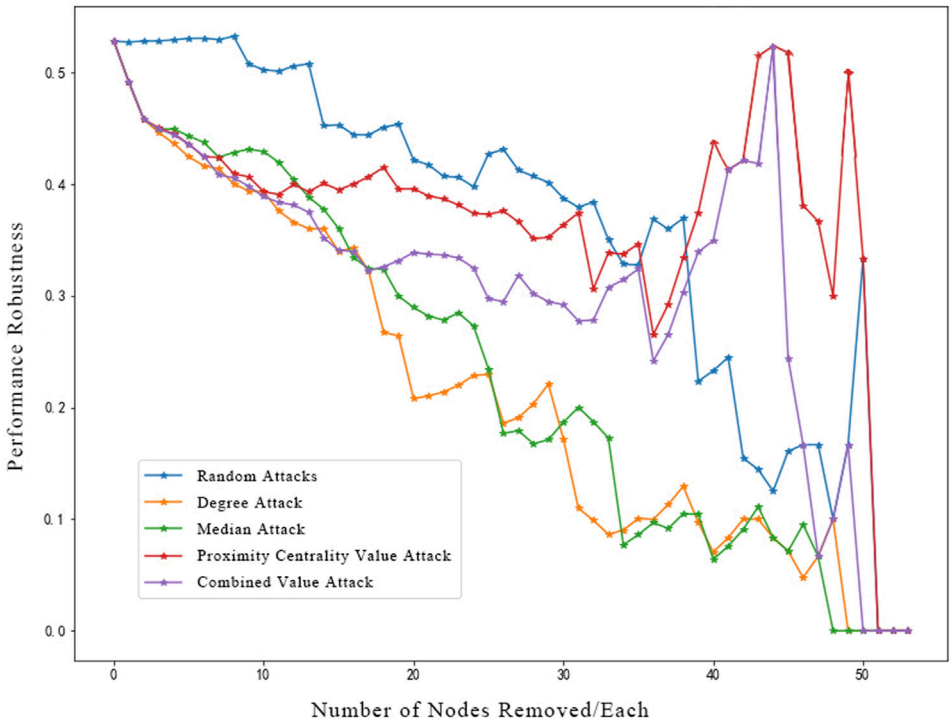

FIGURE 8
Performance robustness analysis chart.

attack and the combined value attack, some of the edge nodes in the network may have been removed, making the network more efficient instead, resulting in a short-lived contrast. The initial global efficiency (performance robustness) of the network was 0.5281, and a random attack on 38% of the nodes in the network resulted in a global efficiency of 0.5297; the same deliberate attack on 38% of the nodes reduced the global efficiency of the degree value attack to 0.2079, the global efficiency of the median value attack to 0.2896, and the global efficiency of the proximity centrality value attack to 0.9359. Among deliberate attacks, the metric attack makes the fastest and most effective reduction in global efficiency, i.e., the network is most vulnerable under this attack. The order of the nodes deliberately attacked shows that attacking the critical nodes first will cause a rapid change in the topology of the network, creating many isolated nodes relatively quickly and causing the network to go down quickly. In contrast, the probability of attacking exactly these critical nodes in a random attack is small, and only if enough nodes are attacked at random will the network go down.

1) The random immunization strategy was significantly less effective than the TI immunization strategy. According to the network performance robustness and structural robustness analysis, the overall effect of the random immunization strategy was considerably worse than that of the deliberate immunization strategy after removing the same nodes. In the intentional immunization strategy, the network efficiency of degree, mesh number, and near-center degree are worse than in random immunization. Therefore, it can be proved that focused management of critical nodes is an essential and effective means of risk management for urban river ecological governance projects.
2) Of the immunization strategies, near-center value attacks are the least effective, median value immunity is slightly more effective, and degree value immunity attacks are the most effective.
3) For risk management with urban river ecological governance projects, as nodal degree value immunity is the most effective, prevention solutions for risks are more preferred, and important nodes corresponding to nodal degree value immunity should be considered for prevention and control, i.e., nodes A2, A49, A36, A44, A25, A5, A12, etc.

In summary, the structural robustness and performance robustness of the network both decrease as the number of attacks (number of nodes removed) increases. In addition, the impact of deliberate attacks on robustness is more significant. For the risk evolution network of the urban river ecological governance project, robustness is poorer in the intentional attack mode. In contrast, robustness and fault tolerance are more robust in the random attack mode.

5 Discussion

By identifying the risks associated with urban river ecological governance projects, a risk network model was developed, visualized, and analyzed in this study. The risk response strategy for urban river ecological governance projects is explored through the perspective of network immunity. The results of the model parameter analysis demonstrate the applicability of this study to the risk of urban river ecological governance projects and the feasibility of a risk response strategy for urban river ecological governance projects developed based on the network immunity approach.

Firstly, the model parameter analysis results can be further explained and validated through complex network theory. In a risk network, DTI has a clear advantage as it can effectively control the spread effectiveness of the entire network. Therefore, identifying key risks and controlling abnormal risk-associated network immune strategies are not only more effective and reliable in assessing the importance of risks in the project but also more effective and reliable in subsequent risk-sharing tasks. Secondly, the model has several advantages, such as facilitating early risk response decisions and building a future-proof risk warning framework. To enhance the applicability of the model in urban river ecological governance projects, this study conducted a complete literature and case study and brainstorming sessions with 10 experienced experts to clarify risk relationships. Therefore, the risk list and 53-risk network developed in this study may be more effective and prospective. In addition, the accuracy of the network analysis process can be improved by simulating the analysis of different decision scenarios. This paper also develops and visualizes the entire risk network and filters out the accurate network through a simple statistical process. Finally, the evolution of landing and take-off safety risks for urban river ecological governance projects can be effectively controlled by disconnecting key risk factors in the network or effectively reducing the position of these key risk factors. The risk evolution of nodes can be prevented by disconnecting these risk factors or by reducing the risk level of these factor nodes and the intensity of the interaction between these factors using corresponding means. The way to reduce the level of risk at these factor nodes and the power of action between these factors using appropriate means is more suitable to prevent the evolution of risk in urban river ecological governance projects.

The impact of changing project conditions on the assessment of risk networks is a critical step in ensuring the stability and reliability of the results. The interactions between risk factors can vary significantly when dealing with different projects, hence the analytical methods that can be used when targeting different project-specific risk studies. 1) Validation based on historical data: If relevant data from previous projects are available, it can be used to validate the accuracy and stability of risk network assessment. By incorporating historical project data into the current project's risk network and comparing actual results with predicted results, the applicability and accuracy of risk network assessment across different projects can be evaluated. 2) Analyzing different scenarios: In risk network assessment, considering different scenarios of risks can be beneficial. For example, constructing separate risk networks for different project conditions or risk assumptions and conducting comparative analysis. This approach helps understand the interactions and influences of risk factors under different conditions. 3) Expert discussions and validation: During the assessment process, seeking expert opinions and validation is crucial. Engaging in discussions and validation with experts in relevant fields can lead to more comprehensive and accurate evaluation results, thereby reducing the impact of project condition changes on the assessment. By applying a combination of these methods, the stability and reliability of risk

network assessment can be improved, reducing the influence of project condition changes on the evaluation results. This, in turn, provides decision-makers with more reliable risk management strategies and decision-making foundations.

To investigate the advantages of social network-based analysis by comparing it with traditional methods and to highlight the unique value of the method in risk studies of urban river ecological governance projects. In terms of accuracy: Compare the accuracy of methods based on social network analyses with traditional methods in identifying key risk factors, risk relationships, risk propagation paths, and so on. Which method more accurately reflects the actual risk situation can be verified by some case studies or field surveys. In terms of efficiency: compare the efficiency of methods based on social network analysis with traditional methods in analyzing large-scale complex networks. Whether social network analysis produces results more quickly and handles large amounts of data better can be used as a basis for comparison. In terms of predictability: methods based on social network analysis are better at predicting future risk evolution and potential risks of a project. By comparing the performance of the two approaches in terms of risk prediction, it is possible to see whether the approach based on social network analysis is more forward-looking. At the same time whether the method based on social network analysis can provide clearer and more intuitive visualization results. Thus, the application of the method of social network analysis in the risk research of urban river ecological governance projects has greater advantages. It can further enhance its application value in the field of risk research.

6 Conclusion

Based on the causal pathways among risk factors, a complex network topology of 53 nodes and 255 edges was constructed for the risk evolution of urban river ecological governance projects. The risk factors were ranked based on degree centrality, betweenness centrality, closeness centrality, and composite value in the weighted directed network. The analysis demonstrated the scale-free property of the network. The application of complex network theory in analyzing the risk system for urban river ecological governance projects can effectively identify the critical factors of the entire risk system, determine the risk relationships, and then take targeted measures to reduce the risk of water engineering systems. The global efficiency of the network was used as an indicator to analyze the robustness of the risk evolution network under random and intentional attacks, revealing the changing patterns of performance stability and structural stability of the scale-free network. Based on the robustness analysis, the critical risk factors of the network were identified using degree centrality ranking. Based on this, corresponding network disconnect strategies were developed, which provides a theoretical basis for effectively preventing risk evolution.

The methodology used in this study is influenced to some extent by the subjectivity and experience of the individual experts. To address this limitation more comprehensively, future research could consider adopting more objective and reliable data sources, such as analyses based on actual observational data or large-scale datasets, to reduce reliance on expert subjective judgment. Additionally, combining quantitative and qualitative methods for a comprehensive analysis could enhance the objectivity and reliability of the research. Further studies can explore more comprehensive and objective approaches to fill this research gap and promote the advancement of related fields.

Data availability statement

The original contributions presented in the study are included in the article/supplementary material, further inquiries can be directed to the corresponding author.

Author contributions

Conceptualization: JKX; methodology: JKX; validation: JCX and JZ; formal analysis: JCX and JZ; data curation: JKX; writing—original draft preparation, JKX; writing—review and editing, JCX and JZ; funding acquisition, JZ. All authors contributed to the article and approved the submitted version.

Funding

This research was supported by Jinghe New City Jinghe Flood Control and Ecological Governance Engineering Consulting Research Project (No. 107-441220098).

Conflict of interest

The authors declare that the research was conducted in the absence of any commercial or financial relationships that could be construed as a potential conflict of interest.

Publisher's note

All claims expressed in this article are solely those of the authors and do not necessarily represent those of their affiliated organizations, or those of the publisher, the editors and the reviewers. Any product that may be evaluated in this article, or claim that may be made by its manufacturer, is not guaranteed or endorsed by the publisher.

References

Abbas, H., Asim, Z., Ahmed, Z., and Moosa, S. (2022). Exploring and establishing the barriers to sustainable humanitarian supply chains using fuzzy interpretive structural modeling and fuzzy MICMAC analysis. *Soc. Responsib. J.* 18 (8), 1463–1484. doi:10.1108/srj-12-2020-0485

Aloini, D., Dulmin, R., and Mininno, V. (2012). Modelling and assessing erp project risks: a petri net approach. *Eur. J. operational Res.* 220 (2), 484–495. doi:10.1016/j.ejor.2012.01.062

Cao, H., Duan, L., Zhang, Y., Cao, J., and Zhang, K. (2021). Current hydrogel advances in physicochemical and biological response-driven biomedical application diversity. *J. Inf. Process. Syst.* 17 (2), 426–439. doi:10.1038/s41392-021-00830-x

Damnjanovic, I., and Reinschmidt, K. (2020). *Data analytics for engineering and construction project risk management*. Germany: Springer.

Deng, Q., Qin, Y., and Ahmad, N. (2022). Relationship between environmental pollution, environmental regulation and resident health in the urban agglomeration in the middle reaches of yangtze river, China: spatial effect and regulating effect. *Sustainability* 14 (13), 7801. doi:10.3390/su14137801

Desavelle, J. (2015). *A risk management strategy for effective planning and budgeting for new build nuclear power plant construction: research methodology and implementation of the olkiluoto 3 project*. Master's thesis. Finland: Satakunta University of Applied Sciences. Available at: http://www.theseus.fi/handle/10024/95636.

Erol, H., Dikmen, I., Atasoy, G., and Birgonul, M. T. (2020). Exploring the relationship between complexity and risk in megaconstruction projects. *J. Constr. Eng. Manag.* 146 (12), 04020138. doi:10.1061/(asce)co.1943-7862.0001946

Fang, C., Marle, F., Zio, E., and Bocquet, J.-C. (2012). Network theory-based analysis of risk interactions in large engineering projects. *Reliab. Eng. Syst. Saf.* 106, 1–10. doi:10.1016/j.ress.2012.04.005

García-Pedrajas, N., and Fyfe, C. (2007). Immune network based ensembles. *Neurocomputing* 70 (7-9), 1155–1166. doi:10.1016/j.neucom.2006.11.005

Ghasemi, F., Sari, M. H. M., Yousefi, V., Falsafi, R., and Tamošaitienė, J. (2018). Project portfolio risk identification and analysis, considering project risk interactions and using Bayesian networks. *Sustainability* 10 (5), 1609. doi:10.3390/su10051609

Gondia, A., Siam, A., El-Dakhakhni, W., and Nassar, A. H. (2020). Machine learning algorithms for construction projects delay risk prediction. *J. Constr. Eng. Manag.* 146 (1), 04019085. doi:10.1061/(asce)co.1943-7862.0001736

Huang, S., Wang, H., Xu, Y., She, J., and Huang, J. (2021). Key disaster-causing factors chains on urban flood risk based on bayesian network. *Land* 10 (2), 210. doi:10.3390/land10020210

Karmaker, C. L., Ahmed, T., Ahmed, S., Ali, S. M., Moktadir, M. A., and Kabir, G. (2021). Improving supply chain sustainability in the context of COVID-19 pandemic in an emerging economy: exploring drivers using an integrated model. *Sustain. Prod. Consum.* 26, 411–427. doi:10.1016/j.spc.2020.09.019

Lanaridis, A., and Stafylopatis, A. (2014). An artificial immune network for multiobjective optimization problems. *Eng. Optim.* 46 (8), 1008–1031. doi:10.1080/0305215x.2013.823193

Lee, C.-Y., Chong, H.-Y., Liao, P.-C., and Wang, X. (2018). Critical review of social network analysis applications in complex project management. *J. Manag. Eng.* 34 (2), 04017061. doi:10.1061/(asce)me.1943-5479.0000579

Leoni, L., BahooToroody, A., De Carlo, F., and Paltrinieri, N. (2019). Developing a risk-based maintenance model for a natural gas regulating and metering station using bayesian network. *J. Loss Prev. Process industries* 57, 17–24. doi:10.1016/j.jlp.2018.11.003

Lienert, J., Schnetzer, F., and Ingold, K. (2013). Stakeholder analysis combined with social network analysis provides fine-grained insights into water infrastructure planning processes. *J. Environ. Manag.* 125, 134–148. doi:10.1016/j.jenvman.2013.03.052

Liu, K., Yang, S., Zhou, Q., and Qiao, Y. (2022). Spatiotemporal evolution and spatial network analysis of the urban ecological carrying capacity in the Yellow River Basin. *Int. J. Environ. Res. Public Health* 19 (1), 229. doi:10.3390/ijerph19010229

Luo, W., Deng, Z., Zhong, S., and Deng, M. (2022). Trends, issues and future directions of urban health impact assessment research: a systematic review and bibliometric analysis. *Int. J. Environ. Res. Public Health* 19 (10), 5957. doi:10.3390/ijerph19105957

Ma, X., Deng, W., Qiao, W., and Luo, H. (2022). *A novel methodology concentrating on risk propagation to conduct a risk analysis based on a directed complex network.Risk Anal.*

Mandell, M. (1984). Application of network analysis to the implementation of a complex project. *Hum. Relat.* 37 (8), 659–679. doi:10.1177/001872678403700806

Marcot, B. G., and Penman, T. D. (2019). Advances in bayesian network modelling: integration of modelling technologies. *Environ. Model. Softw.* 111, 386–393. doi:10.1016/j.envsoft.2018.09.016

Marle, F., Vidal, L.-A., and Bocquet, J.-C. (2013). Interactions-based risk clustering methodologies and algorithms for complex project management. *Int. J. Prod. Econ.* 142 (2), 225–234. doi:10.1016/j.ijpe.2010.11.022

Mohamed, M., and Tran, D. Q. (2021). Risk-based inspection for concrete pavement construction using fuzzy sets and bayesian networks. *Automation Constr.* 128, 103761. doi:10.1016/j.autcon.2021.103761

Soti, A., Shankar, R., and Kaushal, O. (2010). Modeling the enablers of Six Sigma using interpreting structural modeling. *J. Model. Manag.* 5 (2), 124–141. doi:10.1108/17465661011060989

Subramanian, N., Torabi-Parizi, P., Gottschalk, R. A., Germain, R. N., and Dutta, B. (2015). Network representations of immune system complexity. *Wiley Interdiscip. Rev. Syst. Biol. Med.* 7 (1), 13–38. doi:10.1002/wsbm.1288

Teller, J., and Kock, A. (2013). An empirical investigation on how portfolio risk management influences project portfolio success. *Int. J. Proj. Manag.* 31 (6), 817–829. doi:10.1016/j.ijproman.2012.11.012

Thorne, C., Castro, J., Cluer, B., Skidmore, P., and Shea, C. (2015). Project risk screening matrix for river management and restoration. *River Res. Appl.* 31 (5), 611–626. doi:10.1002/rra.2753

Ullah, F., Qayyum, S., Thaheem, M. J., Al-Turjman, F., and Sepasgozar, S. M. (2021). Risk management in sustainable smart cities governance: a toe framework. *Technol. Forecast. Soc. Change* 167, 120743. doi:10.1016/j.techfore.2021.120743

Valente, T. W. (2012). Network interventions. *science* 337 (6090), 49–53. doi:10.1126/science.1217330

Valeri, M., and Baggio, R. (2021). Social network analysis: organizational implications in tourism management. *Int. J. Organ. Analysis* 29 (2), 342–353. doi:10.1108/ijoa-12-2019-1971

Wang, Z., and Chen, C. (2017). Fuzzy comprehensive Bayesian network-based safety risk assessment for metro construction projects. *Tunn. Undergr. Space Technol.* 70, 330–342. doi:10.1016/j.tust.2017.09.012

Wirba, E., Tah, J., and Howes, R. (1996). *Risk interdependencies and natural language computations*. New York: Engineering, Construction and Architectural Management.

Wu, G., Peng, C., and Liao, T. W. (2018). Research on edges immunization strategy for complex network based on SIS-CA model. *Procedia Manuf.* 17, 1065–1072. doi:10.1016/j.promfg.2018.10.079

Xie, L., Han, T., and Skitmore, M. (2019). Governance of relationship risks in megaprojects: a social network analysis. *Adv. Civ. Eng.* 2019, 1–13. doi:10.1155/2019/1426139

Xu, J., Zhu, J., and Xie, J. (2023a). Research on risk evolution mechanism of urban river ecological governance project based on social network analysis. *Water* 15 (11), 2012. doi:10.3390/w15112012

Xu, J., Zhu, J., and Xie, J. (2023b). Study on the evolution of risk contagion in urban river ecological management projects based on SEIRS. *Water* 15 (14), 2622. doi:10.3390/w15142622

Yang, L., Lou, J., and Zhao, X. (2021). Risk response of complex projects: risk association network method. *J. Manag. Eng.* 37 (4), 05021004. doi:10.1061/(asce)me.1943-5479.0000916

Yu, G., Liu, D., Liao, X., Wang, T., Tian, Q., and Liao, Y. (2017). Quantitative research on regional ecological compensation from the perspective of carbon-neutral: the case of hunan province, China. *Sustainability* 9 (7), 1095. doi:10.3390/su9071095

Zhang, S., Sunindijo, R. Y., Loosemore, M., Wang, S., Gu, Y., and Li, H. (2021). Identifying critical factors influencing the safety of Chinese subway construction projects. *Eng. Constr. Archit. Manag.* 28 (7), 1863–1886. doi:10.1108/ecam-07-2020-0525

Zhao, X., and Huang, G. (2022). Urban watershed ecosystem health assessment and ecological management zoning based on landscape pattern and swmm simulation: a case study of yangmei river basin. *Environ. Impact Assess. Rev.* 95, 106794. doi:10.1016/j.eiar.2022.106794

Zhou, C., Ding, L., Skibniewski, M. J., Luo, H., and Zhang, H. (2018). Data based complex network modeling and analysis of shield tunneling performance in metro construction. *Adv. Eng. Inf.* 38, 168–186. doi:10.1016/j.aei.2018.06.011

Zhu, W., Shen, M., Dai, S., Liu, K., and Qi, Y. (2022). Channel evolution under the control of base-level cycle change and the influence on the sustainable development of the remaining oil—a case in jiang ling depression, jiang han basin, China. *Sustainability* 14 (19), 12518. doi:10.3390/su141912518

Frontiers in Earth Science

Investigates the processes operating within the major spheres of our planet

Advances our understanding across the earth sciences, providing a theoretical background for better use of our planet's resources and equipping us to face major environmental challenges.

Discover the latest Research Topics

See more →

Frontiers

Avenue du Tribunal-Fédéral 34
1005 Lausanne, Switzerland
frontiersin.org

Contact us

+41 (0)21 510 17 00
frontiersin.org/about/contact